Theory of eigenstate thermalization

Dissertation zur Erlangung des
naturwissenschaftlichen Doktorgrades
der Julius-Maximilians-Universität Würzburg

vorgelegt von

Tobias Thimo Helbig

aus Bad Urach

Würzburg 2023

Eingereicht am 05. Mai 2023
bei der Fakultät für Physik und Astronomie

1. Gutachter: Prof. Dr. Martin Greiter
2. Gutachterin: Prof. Dr. Johanna Erdmenger
3. Gutachter: Prof. Dr. Benoît Douçot
der Dissertation

Vorsitzender: Prof. Dr. Raimund Ströhmer

1. Prüfer: Prof. Dr. Martin Greiter
2. Prüferin: Prof. Dr. Johanna Erdmenger
3. Prüfer: Prof. Dr. Ralph Claessen
im Promotionskolloquium

Tag des Promotionskolloquiums: 18. Oktober 2023

Dedicated to Lina.

If you are out to describe the truth, leave elegance to the tailor.

Ludwig Boltzmann

Abstract

Next to the emergence of nearly isolated quantum systems such as ultracold atoms with unprecedented experimental tunability, the conceptualization of the eigenstate thermalization hypothesis (ETH) by Deutsch [1] and Srednicki [2] in the late 20th century has sparked exceptional interest in the mechanism of quantum thermalization. The ETH conjectures that the expectation value of a local observable within the quantum state of an isolated, interacting quantum system converges to the thermal equilibrium value at large times caused by a loss of phase coherence, referred to as dephasing. The thermal behavior within the quantum expectation value is traced back to the level of individual eigenstates, who locally act as a thermal bath to subsystems of the full quantum system and are hence locally indistinguishable to thermal states. The ETH has important implications for the understanding of the foundations of statistical mechanics, the quantum-to-classical transition, and the nature of quantum entanglement. Irrespective of its theoretical success, a rigorous proof has remained elusive so far.

An alternative approach to explain thermalization of quantum states is given by the concept of typicality. Typicality deals with typical states Ψ chosen from a subspace of Hilbert space with energy E and small fluctuations δ around it. It assumes that the possible microstates of this subspace of Hilbert space are uniformly distributed random vectors. This is inspired by the microcanonical ensemble in classical statistical mechanics, which assumes equal weights for all accessible microstates with energy E within an energy allowance δ. It follows from the ergodic hypothesis, which states that the time spent in each part of phase space is proportional to its volume leading to large time averages being equated to ensemble averages. In typicality, the Hilbert space of quantum mechanics is hence treated as an analogue of classical phase space where statistical and thermodynamic properties can be defined. Since typicality merely shifts assumptions of statistical mechanics to the quantum realm, it does not provide a complete understanding of the emergence of thermalization on a fundamental microscopic level.

To gain insights on quantum thermalization and derive it from a microscopic approach, we exclusively consider the fundamental laws of quantum mechanics. In the joint work with T. Hofmann, R. Thomale and M. Greiter [3], on which this thesis reports, we explore the ETH in generic local Hamiltonians in a two-dimensional spin-$1/2$ lattice with random nearest neighbor spin-spin interactions and random on-site magnetic fields. This isolated quantum system is divided into a small subsystem weakly coupled to the remaining part, which is assumed to be large and which we refer to as bath. Eigenstates of the full quantum system as well as the action of local operators on those can then be decomposed in terms of a product basis of eigenstates of the small subsystem and the bath. Central to our analysis is the fact that the coupling between the subsystem and the bath, represented in terms of the uncoupled product eigenbasis, is given by an energy dependent random band matrix, which is obtained from both analytical and numerical considerations.

Utilizing the methods of Dyson-Brownian random matrix theory for random band matrices, we analytically show that the overlaps of eigenstates of the full quantum system with the uncoupled product eigenbasis are described by Cauchy-Lorentz distributions close to their respective peaks. The result is supported by an extensive numerical study using exact diagonalization, where the numerical parameters for the overlap curve agree with the theoretical calculation. The information on the decomposition of the eigenstates of the full quantum system enables us to derive the reduced density matrix within the small subsystem given the pure density matrix of a single eigenstate. We show that in the large bath limit the reduced density matrix converges to a thermal density matrix with canonical Boltzmann probabilities determined by renormalized energies of the small subsystem which are shifted from their bare values due the influence of the coupling to the bath. The behavior of the reduced density matrix is confirmed through a finite size scaling analysis of the numerical data. Within our calculation, we make use of the pivotal result, that the density of states of a local random Hamiltonian is given by a Gaussian distribution under very general circumstances. As a consequence of our analysis, the quantum expectation value of any local observable in the subsystem agrees with its thermal expectation value, which proves the validity of the ETH in the equilibrium phase for the considered class of random local Hamiltonians and elevates it from hypothesis to theory.

Our analysis of quantum thermalization solely relies on the application of quantum mechanics to large systems, locality and the absence of integrability. With the self-averaging property of large random matrices, random matrix theory does not entail a statistical assumption, but is rather applied as a mathematical tool to extract information about the behavior of large quantum systems. The canonical distribution of statistical mechanics is derived without resorting to statistical assumptions such as the concepts of ergodicity or maximal entropy, nor assuming any characteristics of quantum states such as in typicality. In future research, with this microscopic approach it may become possible to exactly pinpoint the origin of failure of quantum thermalization, e.g. in systems that exhibit many body localization or many body quantum scars. The theory further enables the systematic investigation of equilibration, i.e. to study the time scales on which thermalization takes place.

Zusammenfassung

Neben der Entwicklung experimentell zugänglicher nahezu isolierter Quantensysteme wie ultrakalter Gase hat die Formulierung der "Eigenstate Thermalization Hypothesis" (ETH) durch Deutsch [1] und Srednicki [2] im späten 20. Jahrhundert ein gesteigertes Interesse am Mechanismus der Quantenthermalisierung geweckt. Die ETH postuliert, dass der Erwartungswert einer lokalen Observablen innerhalb des Quantenzustands eines isolierten, wechselwirkenden Quantensystems bei großen Zeiten zum thermischen Gleichgewichtswert konvergiert. Dies vollzieht sich durch den Verlust der Phasenkohärenz im Erwartungswert der lokalen Observable, was als "Dephasing" bekannt ist. Das thermische Verhalten innerhalb des Quantenerwartungswerts wird auf die Ebene einzelner Eigenzustände zurückgeführt, die lokal als thermisches Bad für Untersysteme des gesamten Quantensystems wirken und daher lokal nicht von thermischen Zuständen unterscheidbar sind. Die ETH hat wichtige Auswirkungen auf das Verständnis der Grundlagen der statistischen Mechanik, des Übergangs von der Quanten- zur klassischen Physik und der Natur der Quantenverschränkung. Ungeachtet ihres theoretischen Erfolges ist ein rigoroser Beweis der Hypothese bisher nicht erfolgt.

Ein alternativer Ansatz zur Erklärung der Thermalisierung von Quantenzuständen ist das Konzept der typicality. Typicality befasst sich mit typischen Zuständen Ψ, die aus einem Unterraum des Hilbertraums mit Energie E und kleinen Fluktuationen δ ausgewählt werden. Dabei wird angenommen, dass die möglichen Mikrozustände dieses Unterraums des Hilbertraums gleichmäßig verteilte Zufallsvektoren sind. Dies ist ein aus dem klassischen mikrokanonischen Ensemble übertragener Ansatz, der von einer Gleichgewichtung aller Mikrozustände mit der Energie E in einem Energiebereich δ ausgeht. Das geht auf die ergodische Hypothese zurück, die besagt, dass die verbrachte Zeit in jedem Teil des klassischen Phasenraums proportional zu dessen Volumen ist. Dies führt schlussendlich zu einer Gleichsetzung der Mittelwerte bei großen Zeiten mit Ensemblemittelwerten. Der Hilbertraum in der Quantenmechanik wird mit typicality daher als Analogon des klassischen Phasenraums behandelt, in dem statistische und thermodynamische Eigenschaften definiert werden können. Da typicality lediglich Annahmen der statistischen Mechanik auf den Quantenbereich überträgt, kann sie kein vollständiges mikroskopisches Bild der Entstehung von Thermalisierung liefern.

Um Erkenntnisse über die Quantenthermalisierung zu gewinnen und sie aus einem mikroskopischen Ansatz abzuleiten, stützen wir uns ausschließlich auf die grundlegenden Gesetze der Quantenmechanik. In der gemeinsamen Arbeit mit T. Hofmann, R. Thomale und M. Greiter [3], von der diese Arbeit berichtet, untersuchen wir die ETH in generischen lokalen Hamiltonians in einem zweidimensionalen Spin-$1/2$-Gitter mit zufälligen Spin-Spin-Wechselwirkungen zwischen nächsten Nachbarn und zufälligen lokalen Magnetfeldern. Dieses isolierte Quantensystem wird in ein kleines Untersystem aufgeteilt, das schwach an den verbleibenden Teil gekoppelt ist, der als groß angenommen und als Bad bezeichnet wird. Die Eigenzustände des gesamten Quantensystems sowie die Wirkung lokaler Operatoren auf diese können dann in Form einer Produktbasis von Eigenzuständen des kleinen Untersystems und des Bades zerlegt werden. Von zentraler Bedeutung für unsere Analyse ist die Tatsache, dass die Kopplung zwischen dem Untersystem und dem Bad, die in Form der ungekoppelten Produkteigenbasis dargestellt wird, durch eine energieabhängige Zufallsbandmatrix gegeben ist, welche sowohl aus analytischen als auch numerischen Überlegungen gewonnen wird.

Unter Verwendung der Methoden der mathematischen Theorie für zufällige Bandmatrizen finden wir analytisch heraus, dass der Überlapp von Quanteneigenzuständen mit der ungekoppelten Produkteigenbasis durch Cauchy-Lorentzverteilungen in den Badenergien in der Nähe ihrer jeweiligen Peaks beschrieben werden. Das Ergebnis wird durch eine umfangreiche numerische Studie mit exakter Diagonalisierung bestätigt, bei der die numerischen Parameter für die Überlapps mit der theoretischen Berechnung übereinstimmen. Die Information über die Form der Quanteneigenzustände ermöglicht es uns, die reduzierte Dichtematrix in dem kleinen Untersystem aus der reinen Dichtematrix eines einzelnen Eigenzustandes des isolierten Quantensystems abzuleiten. Wir zeigen, dass sie im Limes großer Bäder zu einer thermischen Dichtematrix mit kanonischen Boltzmann-Gewichten auf der Diagonalen konvergiert. Dies wird mithilfe einer numerischen Skalierungsanalyse für endliche Systeme bestätigt. In unseren Berechnungen verwenden wir das zentrale Ergebnis, dass die Zustandsdichte eines lokalen zufälligen Hamiltonians unter allgemeinen Bedingungen durch eine Gauß-Verteilung gegeben ist. Aus unserer Analyse folgt, dass der Quantenerwartungswert jeder lokalen Observablen in dem Untersystem mit ihrem thermischen Erwartungswert übereinstimmt, was die Gültigkeit der ETH in der Gleichgewichtsphase für die betrachtete Klasse von Hamiltonians beweist.

Unsere Analyse der Quantenthermalisierung beruht ausschließlich auf der Anwendung der Quantenmechanik auf große Systeme, der Lokalität und der fehlenden Integrabilität. Stützend auf der mathematischen Eigenschaft des “Self-averaging” von großen Zufallsmatrizen impliziert die Zufallsmatrixtheorie keine statistische Annahme, sondern wird vielmehr als mathematisches Instrument eingesetzt, um Informationen über das Verhalten großer Quantensysteme zu extrahieren. Die kanonische Verteilung der statistischen Mechanik wird abgeleitet, ohne auf die Konzepte der Ergodizität oder der maximalen Entropie zurückzugreifen und ohne irgendwelche Eigenschaften von Quantenzuständen anzunehmen wie es etwa bei typicality der Fall ist. Mit diesem mikroskopischen Ansatz könnte es zudem in zukünftiger Forschung möglich werden, den Ursprung des Nichterfüllens der Quantenthermalisierung, z.B. in Systemen mit Vielteilchenlokalisierung oder Quanten-Scar-Zuständen, exakt zu bestimmen. Die Theorie könnte außerdem eine systematische Untersuchung der Equilibrierung ermöglichen, d.h. die Bestimmung der Zeitskalen, auf denen Thermalisierung stattfindet.

Table of contents

Introduction

Thermal processes are ubiquitous in everyday life, from boiling water in the kettle, to heating or cooling our homes, to the internal combustion engine in our cars, to human metabolism, where food molecules are broken down to produce thermal energy. As an example consider the heating of a gas in a container. If the gas is initially at a lower temperature than its surroundings, heat will be transferred into the gas until an equilibrium state of uniform temperature is reached. From a microscopic perspective, the absorption of heat triggers a shift of the underlying velocity distribution of the gas particles, the Maxwell-Boltzmann distribution, to higher energies, which is associated with a temperature increase of the gas. A steady state is reached once the rate at which the gas absorbs energy from its surroundings balances out energy losses through thermal radiation or other processes. The processes to reach the thermal equilibrium are referred to as *thermalization*. In terms of measurable macroscopic physical quantities, they are quantitatively described by thermodynamics which is based on empirical observation. Later on, the thermodynamic laws have been conceptualized through *statistical mechanics* [4–7], a mathematical framework for predicting the macroscopic behavior of a system from the microscopic properties of its constituent particles. Statistical mechanics relates macroscopic observables such as temperature or pressure to microscopic parameters of the movement of individual particles characterized by probability distributions. Those statistical properties are derived from fundamental assumptions on the physical system, most notably *ergodicity*. The ergodic hypothesis [8, 9] states that for large times, every part of classical phase space of the physical system is visited uniformly, thereby relating the time average of a quantity to its ensemble average. It is equivalent to the *principle of maximal entropy* [10, 11], which presents an alternative assumption from which statistical mechanics can be deduced.

Ever since the enormous success of statistical mechanics in explaining the macroscopic behavior of physical systems, it has been an ongoing effort to relate it to the physical principles and equations that govern it on a microscopic level. In classical Newtonian mechanics, the equations of motions for individual particles are deterministic, which raises the question of how a probabilistic description can apply to the behavior of those particles. The answer is typically given in terms of lack of information. Nonlinearities in the dynamical equations for the individual particles leads to chaotic behavior, which becomes practically untraceable in large complex system causing the onset of thermalization. This relates to the ergodic hypothesis, since nonlinear dynamics at large times causes particle trajectories independent of their initial conditions with an ergodic covering of the constant energy manifold in phase space.

Soon after the quantum revolution in the beginning of the 20th century, first attempts have been made by E. Schrödinger [12, 13] as well as shortly after that in a seminal paper by J. von Neumann [14] and later by M. Berry [15, 16] at explaining the concept of thermalization on a quantum level. Isolated quantum systems are described by the Schrödinger equation, which presumes a linear and unitary time evolution of quantum states. Following from that, dynamical chaos is absent and it is not clear how statistical properties emerge from exact quantum states which would then lead to a description where a few thermodynamic variables such as energy, temperature or pressure suffice to capture the complexity of the dynamics in the quantum system. Particular interest in this regard was then invested in reconciling the seemingly random behavior of quantum systems with the deterministic and predictable dynamics of classical systems. Despite numerous attempts, a full microscopic understanding of thermalization has however remained elusive. In recent decades, the increased accessibility and tunability of experiments in nearly isolated quantum settings such as ultracold atom experiments [17–20] has sparked a renewed interest in this field. This renaissance was further inspired by a breakthrough that has put the understanding of thermalization from a microscopic perspective on a firmer footing. This breakthrough is conceptualized through the *eigenstate thermalization hypothesis (ETH)* as a powerful mathematical and predictive approach which was first put forward in seminal works by J. Deutsch [1] and M. Srednicki [2]. The ETH postulates that for sufficiently large and complex many-body quantum systems, the individual eigenstates behave thermally and exhibit the same statistical properties as those observed in thermal equilibrium. The investigation and explanation of the emergence of eigenstate thermalization is the main focus of the joint work with T. Hofmann, R. Thomale and M. Greiter [3], on which we report in this thesis. In [3] we establish the notion of quantum thermodynamics purely from the laws of quantum mechanics. The ETH has important implications for the understanding of the foundations of statistical mechanics, the quantum-to-classical transition, and the nature of quantum entanglement. Irrespective of its theoretical success, it is still a conjecture and a rigorous proof has remained elusive so far. Thorough and comprehensive reviews on the ETH are given in [21, 22].

In an effort to understand the ETH on a fundamental level, M. Rigol et al. [23] provided a theoretical study in which they show that the unitary time evolution in isolated quantum systems plays a merely auxiliary role in the relaxation to thermal equilibrium and that the knowledge of a single many-body eigenstate is sufficient to obtain thermal properties. Subsequent numerical studies [24–28] employing the method of *exact diagonalization (ED)* have observed the ETH in a variety of physical setups, including chaotic and integrable systems, quantum field theories and lattice systems [29–34], such as quantum spin chains [35–40] as well as for hard-core bosons [41, 42] and spinless fermions [29, 42, 43]. A review of numerical work performed in this context is given by [44] with concise methods for the investigation of quantum thermalization detailed in [45]. Next to providing a deeper understanding of thermalization on the quantum level, the ETH also predicts thermal transport coefficients [21, 46, 47], physical consequences for equilibration [48, 49] as well as fluctuations in the microscopic system relating to the fluctuation-dissipation theorem [50, 51]. It is worth considering complementary formulations [52, 53], where a distinction into a strong and a weak version of the ETH has been established. Deriving from the existence of quantum scars [54–56], in the weak ETH scenario, a fraction of eigenstates behave non-thermally, which was verified to hold even for integrable models. While this fraction of non-thermal states vanishes in the thermodynamic limit, the strong form of the ETH necessitates that non-thermal states completely disappear in the thermodynamic limit [57–59]. The notion of the weak ETH does not imply thermalization, as the initial conditions can have large support on non-thermal states, while in the case of the strong ETH thermalization always occurs.

The ETH is commonly studied through local reduced density matrices and the associated entanglement entropy in small subsystems of the isolated quantum system, which show thermal behavior at large system sizes. This approach is adopted in [3] where we find an analytic expression for the reduced density matrix in the thermodynamic limit. D. Page [60] conjectured an analytic expression for the average entanglement entropy of a subsystem, if the whole quantum system is in a random pure state, which became known as the Page curve. Later it was argued [61] that the entanglement entropy for those subsystems is equal to the thermodynamic entropy per degree of freedom in the smaller subsystem, which was verified in an ED study [62].

An alternative route to understanding quantum thermalization and in consequence statistical mechanics is *typicality*. The concept of typicality is closely related to the idea of randomness, where quantum eigenstates are expected to exhibit random-like behavior. It considers typical states, which are localized in energy with small fluctuations around the mean energy. Typicality in quantum mechanics, as well as in classical mechanics, involves a probability distribution on the possible microstates of the system. Under the hypothesis of equal weights for all those typical microstates in the corresponding subspace of Hilbert space, the canonical Boltzmann distribution was obtained [63]. Similar formulations of typicality regard Hilbert space in quantum mechanics as the analogue of phase space in classical mechanics, where entropy can be defined and thermal properties be derived [64]. A notion of canonical typicality was formulated in [65–68], where the authors argue that a single typical state suffices to produce a canonical distribution in a subsystem of the whole isolated quantum system [69], reconnecting typicality with the assumptions of the ETH. Typicality further addresses questions of *equilibration* [70], which concern the relaxation of an initial state to thermal equilibrium [71–73], that can for example be simulated by the time evolution after a quantum quench [57]. To relate typical quantum states to thermodynamic properties, the entanglement entropy of a subsystem is associated with a volume law, which converges to the thermodynamic entropy as the larger subsystem being traced out approaches unity [74]. Such a relation is denoted as strong typicality, whereas weak typicality allows for a definition of thermodynamic entropy using the diagonal entropy of the reduced density matrix when only a small part of the system is traced out [75]. Further evidence for this was found by considering the moments of the probability distribution that a subsystem has a specific entanglement entropy, where thermal entropy arises as the typical entanglement entropy of energy eigenstates [76]. In this context, later works by Goldstein et al. [77, 78] distinguish between a microscopic and macroscopic thermal equilibrium.

Since it deals with purely random states where all degrees of freedom (DOF) of the system are involved, the typicality argument has recently been demonstrated to be inapplicable to a set of local Hamiltonians and local observables [79]. In recent years, several counterexamples to the ETH have been identified, which challenge its validity in certain types of many-body systems. This has led to further criticism of the approach of typicality. Not all systems thermalize and since typicality is incapable of distinguishing between those types of systems and predicts that all such systems thermalize, it is not universally applicable. Furthermore, real experiments do not exhibit wave functions which are typical [22, 80]. In short, typicality cannot give a full microscopic picture on the emergence of thermalization, since it merely shifts assumptions of statistical mechanics to the quantum realm. In our work [3], we instead approach the problem from a different perspective and consider eigenstates of a random local isolated quantum system without making any assumptions on the shape of these quantum states.

One of the most prominent counterexamples to the ETH is the phenomenon of *many body localization (MBL)* [81–85]. MBL occurs in certain disordered systems in which quantum interference effects prevent the system from reaching thermal equilibrium. It is an extension of Anderson localization [86], which is a classical phenomenon where disorder prevents the propagation of waves. In a quantum many-body system, Anderson localization can lead to the formation of localized eigenstates in a particular region of Hilbert space [87], leading to a breakdown of thermalization. Numerically, it has been shown that MBL is present in one-dimensional lattice models such as interacting spinless fermions [88–90] or hard core bosons in a translation-invariant Hamiltonian [91]. Instead of a volume law entanglement in the thermalizing phase, the MBL phase is characterized by an area law entanglement entropy [90, 92, 93] and can display order protected by the localization [90, 92, 94]. A concise explanation for the breakdown of thermalization was given in [95], where the authors construct local conservation laws that characterize the MBL phase. The MBL phase may become relevant to the field of quantum information [96–98] as these systems locally remember the initial states in contrast to a thermalizing system, where the state of the system does not depend on the initial conditions. It can further „protect coherence of quantum states by suppressing relaxation between eigenstates with different local integrals of motion“ [95]. While the existence of MBL has been proven in one-dimensional spin chains [99], it seems unstable in higher dimensions [100, 101].

The ETH further breaks down in systems with *quantum many body scar states* [102–105]. Quantum scars first appeared as eigenstates of classically chaotic quantum systems with an increased probability density in the region of unstable classical periodic orbits [106–108]. Quantum many body scars are the many body analogue of quantum scars and are concentrated in certain parts of Hilbert space [55]. They have recently been experimentally observed in a kinetically constrained chain of 51 Rydberg atoms [54], subsequently theoretically identified and characterized [55] and systematically constructed [56]. The underlying mechanism responsible for the emergence of quantum many body scars is not yet understood. However, it has been shown [109], that quantum many-body scars are accompanied by a breaking of ergodicity and a subsequent strong breakdown of thermalization caused by continuous entanglement and disentanglement of the particles in the Rydberg chain [54]. Wether thermalization occurs in those systems hence crucially depends on its initial conditions, i.e. the overlap with scar states. Quantum many body scars have further been associated with a subthermal entanglement entropy [105], a suppression of quantum chaos caused by quantum scarring [110] as well as signs of integrability [111].

Other examples where the ETH has been shown to fail are systems with an extensive number of local conserved quantities, e.g. in a non-integrable model of hard core bosons [112]. If a system is exactly solvable through a complete set of integrals of motions, it is called integrable [45, 113]. The ETH has been shown to break down when approaching an integrable point [29, 41, 43, 114], while some states of prethermalization have been observed in integrable systems [114, 115]. Further research has been invested in the generalization of the Gibbs ensemble for integrable lattice systems with a full set of conserved quantities [116, 117].

The primary experimental platform to investigate ETH and MBL are *ultracold atoms*. In this setting, atoms are held at temperatures close to absolute zero where quantum effects are dominant [17–20]. Temperatures on the order of $10\,\mu\mathrm{K}$ are achieved by laser cooling and the combination of magnetic and optical trapping [118, 119]. The unprecedented tunability of this quantum setup allows for the realization of analogues of solid state systems of interest or the implementation of theoretical models such as the Bose-Hubbard model [119, 120]. As an example, the degree of experimental control has been demonstrated through the measurement of the interaction strength between a single fermion with a small bosonic field of an optical lattice [121, 122]. In this experimental testbed, relaxation processes towards a thermal equilibrium phase [123] can be traced in time resolved analyses [124–126]. It is further possible to investigate prethermalization properties [127] as well as thermalization with particle losses [128]. A prime focus of ultracold atom experiments has been concentrated on non-thermal behavior [129] as well as the demonstration of the MBL phase [130]. Recently, measurement protocols for the entanglement spectrum of cold atoms have been developed and illustrated on the Bose-Hubbard model [131–133].

Other notable experiments with nearly isolated systems include nuclear spins in diamonds [134] or in fermionic alkaline-earth atoms, where the entanglement spectrum of density operators has been measured through Ramsey spectroscopy [135]. Thermalization processes could further be investigated in heavy-ion collisions at ultrarelativistic energies [136] and in correlated electron materials probed through ultrafast spectroscopy [137, 138].

It is speculated that the underlying reason for the validity of the ETH is caused by an intimate connection of interacting systems to random matrix theory [139]. This hypothesis can be investigated in *Floquet systems* [139–141], which are time-periodic quantum systems, where the time dependence occurs due to an external driving. If we consider large system with a periodic driving, we can distinguish two distinct scenarios. First, if the driving period is much greater than the relaxation time, the driving protocol is not important. Violations of this statement apply for small system sizes [142]. If on the other hand the driving period is much smaller than the relaxation time, the Floquet formalism is needed to describe the time evolution after many periods [143]. As expected from a physical perspective, when in the thermal phase, the periodic driving heats a system up to infinite temperature [144]. Floquet systems further enable the study of relaxation towards an equilibrium state in systems that are initially driven out of equilibrium [145].

The theory of thermalization will be published in a joint work [3] with T. Hofmann, R. Thomale and M. Greiter. In our work [3], we investigate thermalization from a microscopic perspective in a non-integrable quantum system that is modeled through a random local Hamiltonian. We derive the canonical distribution [3] and hence statistical mechanics without resorting to the concepts of ergodicity or maximal entropy, nor assuming any characteristics of quantum states such as in typicality. Our analysis of quantum thermalization solely relies on the application of quantum mechanics to large systems, locality and the absence of integrability. This elevates the ETH from hypothesis to theory.

Beyond insights into the thermalization properties of quantum many body systems, the ETH can be applied to a plethora of open questions in physics. One such example are black holes, which are described by thermal states. The ETH and in general thermalization in the quantum regime can spark new insights into those objects, as recently demonstrated [146] when using the ETH to study the 'ER=EPR' conjecture of Maldacena and Susskind [147]. In this context, the ETH has been applied to investigate chaotic behavior of thermal states [148]. It has further been proposed that the ETH is a quantum version of the classical no-hair theorem [149] in the sense that the gravitational metric is given by an operator which obeys the ETH. Further discussions surround the entanglement entropy in black holes. In quantum field theory (QFT), it has been shown that the entanglement entropy of the free Klein Gordon field obeys an area law [150, 151], which has intriguing connections to the Bekenstein-Hawking entropy of black holes [152, 153], where an area law has been motivated from the second law of thermodynamics.

Methodological overview

To obtain universal properties of thermalization in quantum many body systems, we work with random Hamiltonians without integrability or symmetries. This way, we are able to use the results of random matrix theory (RMT) in order to analytically trace the universal behavior of the quantum many body system independent of its specific details. RMT deals with the statistical properties of matrices with random entries. General introductions to the topic are given in [154–156]. In a physical context, RMT was first introduced by E. Wigner to model the energy spacings in heavy atom nuclei [157, 158]. He conjectured that the level spacings resemble the statistics found in Gaussian random matrix ensembles, which was later experimentally verified [159]. This became known as Wigner's semicircle law which is named after the semicircle distribution of the density of states (DOS) in those systems. A recent review of the Wigner problem is found in [160].

In the prevailing approach of applying RMT to the thermalization of eigenstates, interactions are modeled through Gaussian orthogonal ensemble (GOE) or Gaussian unitary ensemble (GUE) matrices, sometimes also referred to as Wigner matrices. Those Gaussian ensembles contain real symmetric (GOE) or complex hermitian (GUE) matrices, where all entries above the main diagonal are independent random variables distributed according to a Gaussian distribution with mean zero and identical variance. In such matrices, all types of couplings exist, making them fully random matrices with non-local interactions. In our approach, we instead restrict ourselves to local Hamiltonians, which only contain local random interactions of arbitrary type. In a local basis, this leads to sparse Hamiltonians where the Wigner ensemble is not applicable anymore. Instead, numerical studies hint to an energy dependent structure of offdiagonal matrix elements of local operators [161] which form a band matrix structure in the energy basis. Furthermore, correlations between matrix elements depend on the energy window under consideration [162].

Using the methods of RMT, random system have been studied to determine the onset of chaotic behavior, e.g. for the Laplace operator on a domain [163]. Further studies have focused on a quantum analogue of ergodicity defined as an equidistribution of eigenvectors [164, 165], which was analyzed in fully random systems following the Wigner ensemble. Building on this result, the ETH has been rigorously proven for the case of generalized Wigner matrices [166, 167]. Going from thermalization towards localization, a delocalized non-ergodic regime as been identified as an intermediate phase between the fully delocalized ergodic and the MBL phase [168, 169].

In order to determine the microscopic properties of the quantum system, we study the eigenvector dynamics [170–175] resulting from a perturbation added to the Hamiltonian. The mathematical theory is based on *Brownian motion* [176, 177] which can be employed when assuming that the matrix elements in the pertubation are Gaussian distributed. By using the infinite divisibility of a Gaussian, one can derive an evolution equation for the eigenvalues of the initial matrix under the influence of the perturbation. This is captured in the theory of *Dyson-Brownian motion (DBM)* [178]. With the DBM applied to the resolvent, one can further derive *stochastic differential equations (SDEs)*, which determine the evolution of the eigenstates of the matrix. Having found the overlap of perturbed with unperturbed eigenstates, one can infer the structure of eigenstates and their properties. The theory on obtaining the eigenvector overlap was mathematically analyzed in [179], where R. Allez and J.-P. Bouchaud find a Lorentzian distribution for the eigenvector overlap from a perturbation by a Gaussian ensemble matrix. This theory was expanded to perturbations with random band matrices [165, 180, 181], where G. Casati and V. Girko [182] as well as D. Shlyakhtenko [183] determined a self consistency equation for the resolvent of the perturbed matrix. The equation of Casati and Girko enables us to study the overlap of eigenvectors in local Hamiltonians, which we extract from the resolvent analysis. From there we can further determine the behavior of a small subsystem locally coupled to the rest of the quantum system which dictates the properties of the quantum expectation value of local operators in that subsystem and in a single eigenstate.

A crucial ingredient to our approach is locality, which is violated in most RMT studies in the context of ETH, since they rely on the Wigner ensemble. While numerical studies of the ETH based on local RMT [184] have been invested, we approach the problem from an analytical angle based on results of RMT for random band matrices, where analytical results are probed and supported through numerical simulations. J. Cotler et al. [185] identified that the energy spectrum alone, which is the only basis invariant quantity of the Hamiltonian, almost always uniquely encodes the local degrees of freedom in the form of a local tensor factorization of Hilbert space. The result is connected to the DOS of local random Hamiltonians, which follows a Gaussian distribution instead of a semicircle law for the Wigner ensemble. M. Hartmann et al. [186, 187] have rigorously proven this statement using a variation of the central limit theorem when the full system is split into arrays of interacting quantum systems. We found an alternative proof that relies on the moments of the Hamiltonian to show that the DOS converges to the Gaussian distribution in the thermodynamic limit [188], which is detailed in the Ph.D. thesis of T. Hofmann [189].

All of the analytical calculations in this thesis are supplemented by numerical results. We numerically implement a finite size Hamiltonian of a two-dimensional spin-$\frac{1}{2}$ lattice containing up to 18 lattice sites. The spectrum and the corresponding eigenstates of the Hamiltonian are found by ED methods. For small system sizes up to 14 sites, we use the *algorithm of multiple relatively robust representations (MRRR)* [190] within the LAPACK package [191] to compute the spectrum as a whole. For large system sizes this becomes unfeasible as the Hilbert space dimension increases exponentially with the number of lattice sites. For large system sizes up to 18 sites, we use the *FEAST algorithm* [192, 193] to compute the spectrum and eigenstates in certain energy intervals under consideration. Since we are interested in energy states in the bulk of the spectrum for the ETH, iterative solvers such as Arnoldi, Lanczos or Davidson-Jacobi are not applicable, which is why we work with the FEAST algorithm. It maps the eigenvalue problem to a complex contour integral of the Green's function and is able to determine the eigensystem in any subspace without knowledge of the remainder of the spectrum.

Outline

This thesis is structured as follows.

In *chapter 1*, we introduce basic concepts of RMT, which are employed in the following chapters to calculate analytical results of the quantum system. We start by defining random variables, associated matrix ensembles and Brownian motion and continue by deriving the evolution of eigenvalues of a deterministic matrix under the addition of a GUE perturbation. Based on that, we obtain an SDE for the resolvent, which contains information on the overlap of unperturbed and perturbed eigenstates. The solution to the SDE is determined as the equation of Allez and Bouchaud. We conclude this chapter on the mathematical foundations with the equation of Casati and Girko, which provides a self consistency equation for the resolvent given a random band matrix perturbation. From this analysis, we extract the overlap of unperturbed and perturbed eigenstates.

In *chapter 2*, we expand on the structure of the quantum setup, which is chosen to be a two-dimensional spin-$\frac{1}{2}$ lattice under open boundary conditions (OBC) with a local Hamiltonian containing random nearest neighbor spin-spin interactions and random on-site magnetic fields on each site. For the quantum system, we distinguish between two different cases. First, the *single peak model* describes the behavior of the eigenstates when a local random perturbation is added to the Hamiltonian. Second, the *multi peak model* separates the quantum system into a small subsystem $\mathcal{S}$ and a bath $\mathcal{B}$, which are coupled by a small perturbation. The two scenarios are analyzed separately in the following chapters. We then briefly motivate the Gaussian shape of the DOS for the local Hamiltonian through numerical results and a heuristic sketch of the analytical proof in [188].

In *chapter 3*, the structure of the perturbation matrix, which connects the small subsystem and the bath is analyzed in terms of the unperturbed energy basis of the unconnected subsystems $\mathcal{S}$ and $\mathcal{B}$. Since the perturbation consists of merely local interactions along the boundary of the two subsystems, it forms a random band matrix in the unperturbed energy eigenbasis, where an analytic expression for the element dependent variance in the matrix is obtained using RMT and compared to numerical results. The energy dependent variance converges to a Gaussian distribution in the thermodynamic limit.

In *chapter 4*, we utilize the shape of the energy dependent variance of the perturbation matrix from chapter 3 to insert it into the equation by Casati and Girko from chapter 2. From the resulting recursive equation for the resolvent, we extract an approximate analytical expression for the overlap of eigenstates of the full system in terms of the unperturbed eigenstates. It turns out, that those are given by appropriately normalized Lorentzian curves, which have an additional energy cutoff reminiscent of the variance structure of the perturbation matrix in the energy representation. The parameters of the overlap curve as found from the analytical calculation are compared to an extensive numerical study through ED to achieve mutual consistency. We further estimate the influence of finite size effects intrinsic to the numerical computations.

In *chapter 5*, we use the results of chapter 4 to compute the entries of the reduced density matrix in the small subsystem $\mathcal{S}$ in terms of its eigenbasis. We find that the offdiagonal entries exponentially decrease with the number of lattice sites in the bath while the diagonal entries resemble a Boltzmann distribution in the thermodynamic limit with renormalized energies in $\mathcal{S}$. Those results agree with a numerical investigation where we additionally analyze the statistical distribution of the reduced density matrix with a finite size scaling. This is related to the ETH, where we establish a concise proof of the ETH in the equilibrium phase for the class of Hamiltonians introduced in chapter 2. The thesis is concluded by an analysis of a scattering of the Lorentzian overlap curves mediated by a time dependent perturbation which acts only in $\mathcal{S}$. We find that the scattering is sensitive to the renormalized energies in $\mathcal{S}$, which is supported by numerical data and propose that the predictions resulting from our theoretical analysis of thermalization could be probed in an experimental setting such as ultracold atoms.

The results presented in this thesis will be published in joint publications [3, 188] with T. Hofmann, R. Thomale and M. Greiter and are complemented by the thesis of T. Hofmann [189].

I

Random Matrix Theory and setup

In this part, we first introduce the basic concepts of *random matrix theory (RMT)*, which are needed for the analytic investigation of random Hamiltonians and their eigenvalues as well as eigenstates. We then further characterize the quantum system and its Hamiltonian, which we investigate in the this work.

Stochastic calculus

1.1 Definitions and identities

We begin by introducing the basic concepts necessary for the analysis of RMT inspired by [154–156]. First, we define random variables, probability densities as well as the Stieltjes transform and the resolvent. Second, we state common probability distributions used in the context of this work as well as the Gaussian matrix ensembles commonly employed in RMT. Third, we derive the Dirac identity and the associated Kramers-Kronig relation which is needed in the analysis of random matrices.

1.1.1 Random variables

Definitions. We define the *probability space* $(\Omega, \mathcal{F}, P)$ as consisting of three elements. Ω is the sample space, which is a set of possible outcomes. The event space $\mathcal{F}$ is a set of events, where an event is defined as a set of outcomes in Ω. Lastly, we need a probability function P, which assigns a probability $p \in [0, 1]$ to each element in $\mathcal{F}$.

In the following, we restrict ourselves to continuous random variables, where the sample space is the real axis, $\Omega = \mathbb{R}$ and P is a continuous function. Given a continuous random variable X, one can define its *probability density function (PDF)* $\rho(x)$. Then, the integral

$$\int_a^b \rho(x)\,\mathrm{d}x \tag{1.1}$$

provides the probability, that X takes a value in the interval $[a, b]$. The PDF must be normalized to one, such that

$$\int_\Omega \rho(x)\,\mathrm{d}x = 1, \tag{1.2}$$

where the integral is taken over the real axis. The PDF $\rho(x)$ can be visualized as the normalized histogram profile of the outcomes of a sufficiently large number of samples of the random variable X.

The *moments* of X are defined as

$$m_n = \langle X^n \rangle = \mathbb{E}\left[X^n\right] = \int \rho(x) x^n\,\mathrm{d}x, \tag{1.3}$$

where the average or expectation value of X is $\mu \equiv \langle X \rangle$. The *central moments* are given by

$$\langle (X - \mu)^n \rangle = \int \rho(x)(x - \mu)^n\,\mathrm{d}x, \tag{1.4}$$

around the *mean* μ. The *variance* is the second central moment, $Var(X) = \left\langle X^2 \right\rangle - (\langle X \rangle)^2$ and measures the width of the PDF. An alternative specification of the probability distribution to the PDF is given by the moment generating function of X,

$$M_X(t) = \mathbb{E}\left[e^{tX}\right]. \tag{1.5}$$

It generates the moments of the probability distribution by

$$m_n = \langle X^n \rangle = \left. \frac{\mathrm{d}^n M_X(t)}{\mathrm{d}\, t^n} \right|_{t=0}. \tag{1.6}$$

Using $M_X(t)$, one can define the cumulant-generating function $K_X(t)$, which is the logarithm of the moment generating function, $K_X(t) = \ln \mathbb{E}\left[e^{tX}\right]$. Analogous to the moments, the *cumulants* can be obtained by derivatives of $K(t)$,

$$c_n = \left. \frac{\mathrm{d}^n K_X(t)}{\mathrm{d}\, t^n} \right|_{t=0}. \tag{1.7}$$

The c_n are polynomial functions in the moments involving all moments m_p with $p \leq n$. The first cumulant is the mean value of the distribution, $c_1 = \mu$ and the second cumulant is its variance, $c_2 = Var(X)$. Building on that, we can define the *characteristic function* $\varphi_X(t)$, which is the Fourier transform of the PDF,

$$\varphi_X(t) = \mathbb{E}\left[e^{itX}\right] = \int_{-\infty}^{\infty} e^{itx} \rho(x)\, \mathrm{d}x. \tag{1.8}$$

It relates to the moment generating function as $\mathcal{M}_X(t) = \varphi_X(-it)$.

If we are dealing with two random variables X_1 and X_2, we can define the *joint probability density function (jPDF)* $\rho(x_1, x_2)$, such that the integral

$$\int_a^b \mathrm{d}x_1 \int_c^d \mathrm{d}x_2\, \rho(x_1, x_2) \tag{1.9}$$

yields the probability, that X_1 lies in the interval $[a, b]$ and X_2 in $[c, d]$. The jPDF factorizes if and only if the random variables are independent,

$$\rho(x_1, x_2) = \rho(x_1)\, \rho(x_2). \tag{1.10}$$

If additionally both variables X_1 and X_2 follow the same distribution, $\rho(x_1) = \rho(x_2)$, they are called *independent identically distributed (IID)*. These definitions can be generalized to an arbitrary number N of random variables having the jPDF $\rho(x_1, \ldots, x_N)$. If we make a change of basis to a different set of random variables $y_1, \ldots, y_N$, the jPDFs are related by the Jacobian determinant of the transformation,

$$\rho(x_1, \ldots, x_N)\, \mathrm{d}x_1 \ldots \mathrm{d}x_N = \rho(x_1(\mathbf{y}), \ldots, x_N(\mathbf{y}))\, |J(\mathbf{x} \to \mathbf{y})|\, \mathrm{d}y_1 \ldots \mathrm{d}y_N, \tag{1.11}$$

where $\rho(x_1(\mathbf{y}), \dots, x_N(\mathbf{y})) = \rho(y_1, \dots, y_N)$ and $J(\mathbf{x} \to \mathbf{y})$ is the Jacobian determinant of the transformation from $\mathbf{x}$ to $\mathbf{y}$ with

$$J(\mathbf{x} \to \mathbf{y}) = \det\left(\left\{\frac{\partial x_i}{\partial y_j}\right\}_{ij}\right) \tag{1.12}$$

Sum of random variables. Consider the sum $X = X_1 + X_2$ of two random variables X_1 and X_2, which are independent and distributed according to $\rho_1(x_1)$ and $\rho_2(x_2)$. To find the probability of X being equal to x within a range dx, we have to sum all combinations with the constraint $x_1 + x_2 = x$ and weight them with their respective probabilities. With X_1 and X_2 independent, the jPDF is given by the product $\rho_1(x_1)\rho_2(x - x_1)$, where we chose $X_1 = x_1$ and $X_2 = x - x_1$, such that their sum is equal to x. From there we obtain the PDF $\rho^{(2)}(x)$ of X,

$$\rho^{(2)}(x) = \int \mathrm{d}x' \rho_1(x')\rho_2(x - x'), \tag{1.13}$$

which is the *convolution* of ρ_1 and ρ_2, denoted as $\rho^{(2)} = \rho_1 \star \rho_2$. The characteristic functions are then simply multiplicative, $\varphi^{(2)}(k) = \varphi_1(k)\varphi_2(k)$ and their logarithms with $H(k) \equiv \ln(\varphi(k))$ are additive. A general, important property of cumulants follows, which is, that the cumulants of independent distributions add up. The mean and variance of independent random variables are additive, which is stating, that the mean (variance) of their sum is equal to the sum of their means (variances).

The procedure can be generalized to N independent random variables $X_1, \dots, X_N$ with their sum $X = X_1 + X_2 + \dots + X_N$. Each X_i is distributed according to $\rho_i(x_i)$. The sum X is then distributed according to the PDF [155]

$$\rho^{(N)}(x) = \int \prod_{i=1}^{N} \mathrm{d}x_i \rho_1(x_1) \dots \rho_N(x_N)\, \delta(x - \sum_{i=1}^{N} x_i) \tag{1.14}$$

with $\delta(x)$ being the Dirac-Delta distribution.

Resolvent and Stieltjes transform. The resolvent of an $(N \times N)$-dimensional Hermitian matrix A is defined as [155, 156]

$$R(z) = \frac{1}{z\mathbb{1} - A} = (z\mathbb{1} - A)^{-1}, \tag{1.15}$$

where z is a complex variable with nonzero imaginary part and $\mathbb{1}$ denotes the N-dimensional unit matrix. The real axis is excluded from the definition of z, since the real eigenvalues of the Hermitian matrix A produce poles along the real axis. From there, the Stieltjes transform is given by the trace of the resolvent

$$G_N(z) = \frac{1}{N}\mathrm{Tr}(R(z)) = \frac{1}{N}\sum_{k=1}^{N}\frac{1}{z - \lambda_k}, \tag{1.16}$$

where $\{\lambda_k, k = 1, \dots, N\}$ denotes the set of real eigenvalues of A. It is well defined for any $z \neq \lambda_k, k = 1, \dots, N$. The subscript N illustrates that G_N is the finite-N Stieltjes transform.

We define the *sample eigenvalue density* or *finite-size density of states* as

$$\rho_N(\lambda) = \frac{1}{N}\sum_{k=1}^{N}\delta(\lambda - \lambda_k). \tag{1.17}$$

In general, we intend to deal with random matrix ensembles as defined in Sec. 1.1.3, from which A is one random instance. The *eigenvalue density* or *normalized density of states (nDOS)* $\rho(\lambda)$ of the matrix ensemble is given by the expectation value of $\rho_N(\lambda)$. In the limit $N \to \infty$, matrices from the matrix ensemble obey a self-averaging property, which states, that

$$\rho(\lambda) = \lim_{N\to\infty}\left[\frac{1}{N}\sum_{k=1}^{N}\delta(\lambda - \lambda_l)\right] = \mathbb{E}\left[\frac{1}{N}\sum_{k=1}^{N}\delta(\lambda - \lambda_l)\right]. \tag{1.18}$$

The Stieltjes transform in terms of the complex z can be written in integral form

$$G_N(z) = \int_{-\infty}^{\infty}\frac{\rho_N(\lambda)}{z - \lambda}\,\mathrm{d}\lambda, \tag{1.19}$$

which is connected to the Hilbert transform of the density of states, as detailed in section 1.1.5.

If A is chosen from a random matrix ensemble, we can generalize the notion of expectation value and moments. The analogous definition of an expectation value for matrix variables is the normalized trace operator $\tau(.)$, defined as

$$\tau(A) := \frac{1}{N}\mathbb{E}\left[\mathrm{Tr}(A)\right]. \tag{1.20}$$

The prefactor $\frac{1}{N}$ is there to normalize the operator such that it remains finite in the limit $N \to \infty$. The k-th moment of the matrix ensemble is then simply given by $m_k \equiv \tau(A^k)$, which is equivalent to the k-th moment of the eigenvalue density $\rho(\lambda)$,

$$m_k^A = \frac{1}{N}\mathbb{E}\left[\mathrm{Tr}\left(A^k\right)\right] = \frac{1}{N}\mathbb{E}\left[\sum_{i=1}^{N}\lambda_i^k\right] = \int_{-\infty}^{\infty}\lambda^k\,\mathbb{E}\left[\frac{1}{N}\sum_{i=1}^{N}\delta(\lambda - \lambda_i)\right]\mathrm{d}\lambda = \int_{-\infty}^{\infty}\lambda^k\rho(\lambda)\,\mathrm{d}\lambda \tag{1.21}$$

The aforementioned *self-averaging property* can be expressed as the normalized trace of a function of the matrix A converging to its expectation value in the limit of large matrix dimensions,

$$\lim_{N\to\infty}\frac{1}{N}\mathrm{Tr}(f(A)) = \tau(f(A)), \tag{1.22}$$

where $f(.)$ denotes a smooth function. It states, that many scalar quantities, such as $\tau(A^k), k \in \mathbb{N}$ do not fluctuate much from sample to sample for large N and these fluctuations further vanish in the limit of $N \to \infty$. In mathematics, this property is also called *concentration of measure*. In the limit $N \to \infty$, the Stieltjes transform converges to the deterministic value $\mathcal{G}(z) = \lim_{N\to\infty} G_N(z) = \mathbb{E}\left[G_N(z)\right]$, which is well defined at large z. Its asymptotic expansion in the neighborhood of infinity is given by

$$\mathcal{G}(z) = \sum_{k=0}^{\infty}\frac{1}{z^{k+1}}\tau(A^k) = \sum_{k=0}^{\infty}\frac{m_k^A}{z^{k+1}}, \tag{1.23}$$

which is the Laurent series of $\mathcal{G}(z)$ for $|z| \to \infty$. As clear from Eq. (1.23), it serves as the moment generating function of A, which is in accordance with the definition in (1.5) by using $t = \frac{1}{z}$ [156]. The component-wise matrix expectation value of the resolvent is denoted by $\mathcal{R}(z) := \mathbb{E}\left[R(z)\right] \in \mathbb{C}^{N\times N}$ and $z \in \mathbb{C}$. If the diagonal elements of the resolvent only depend on the involved energy eigenvales, they also fulfill the property of self-averaging, since it can be expressed as the trace of a function of the resolvent. As shown in later chapters, this is the case when considering a setup perturbed by a random band matrix with the resolvent being represented in terms of the unperturbed eigenbasis.

1.1.2 Common distributions

Gaussian distribution. The Gaussian or normal distribution $\mathcal{N}(\mu, \sigma^2)$ is a continuous probability distribution of a real variable, which arises in various applications in statistics. The form of its PDF is given by

$$\rho(x) = \frac{1}{\sqrt{2\pi\sigma^2}} \exp\left\{-\frac{(x-\mu)^2}{2\sigma^2}\right\}, \tag{1.24}$$

where σ (σ^2) denotes its standard deviation (variance) and μ the mean or expectation value. As a notation, we write $X \sim \mathcal{N}(\mu, \sigma^2)$, if X is a random variable, which follows the normal distribution with mean μ and variance σ^2. The PDF is symmetric around $x = \mu$ and its central moments are given by

$$\mathbb{E}\left[(X-\mu)^p\right] = \begin{cases} 0 & \text{if } p \text{ is odd,} \\ \sigma^p (p-1)!! & \text{if } p \text{ is even.} \end{cases} \tag{1.25}$$

The moment generating function is equal to

$$M(t) = \mathbb{E}[e^{tX}] = \exp\left\{\mu t + \frac{1}{2}\sigma^2 t^2\right\} \tag{1.26}$$

and the cumulant generating function is

$$g(t) = \ln(M(t)) = \mu t + \frac{1}{2}\sigma^2 t^2. \tag{1.27}$$

Consequently, the only nonzero cumulants of the normal distribution are the first and the second one, whereas all higher ones are zero. The normal distribution is the only distribution with such a property. A characteristic parameter of a stochastic distribution is the *full width at half maximum (FWHM)*, which is the width of the curve measured as the distance between two points at half of the maximum amplitude. For the Gaussian, it is given by $2\sqrt{2\ln(2)}\,\sigma^2$.

Furthermore, the sum $X = X_1 + X_2$ of two normal distributed variables $X_1 \sim \mathcal{N}(\mu_2, \sigma_2^2)$, $X_2 \sim \mathcal{N}(\mu_2, \sigma_2^2)$ also follows a normal distribution. The reason is, that the convolution of two Gaussians is again a Gaussian. The rule of sums of random variables in (1.13) yields $X \sim \mathcal{N}(\mu_1 + \mu_2, \sigma_1^2 + \sigma_2^2)$, where the expectation values and the variances add up for X. This makes the Gaussian distribution infinitely divisible, as a Gaussian variable can be divided into arbitrarily many parts, whose sum follows the desired Gaussian distribution.

In the zero-variance limit $\sigma \to 0$, the probability density $f(x)$ tends to zero everywhere except at $x = \mu$, while it remains normalized to one. Therefore, it reaches the Dirac-Delta distribution, translated by μ in the weak limit,

$$\lim_{\sigma\to 0} \frac{1}{\sqrt{2\pi\sigma^2}} \exp\left\{-\frac{(x-\mu)^2}{2\sigma^2}\right\} = \delta(x-\mu). \tag{1.28}$$

An important application of the normal distribution is the central limit theorem.

Multivariate Gaussian distribution. We can extend the one-dimensional Gaussian to the dimension $d \in \mathbb{N}$. For that, we define the vector $\mathbf{X} = (X_1, \dots, X_d)^\top$, which is called *d-dimensional Gaussian*, if $X_1, \dots, X_d \sim \mathcal{N}(0, \sigma^2)$ are Gaussian distributed random variables and if they are all independent. From the independence of the random variables, we know, that the joint density of the d-dimensional Gaussian vector $\mathbf{X}$ is multiplicative and therefore given by

$$\rho_{X_1,\dots,X_n}(x_1, \dots, x_d) = \frac{1}{(\sqrt{2\pi})^d \sigma^d} \exp\left\{-\frac{1}{2\sigma^2}(x_1^2 + \dots + x_d^2)\right\} = \frac{1}{(\sqrt{2\pi\sigma^2})^d} \exp\left\{-\frac{1}{2\sigma^2}\mathbf{x}^\top \mathbf{x}\right\}, \tag{1.29}$$

where $\mathbf{x}^\top \mathbf{x}$ is the norm or length of $\mathbf{x}$ through the scalar product with itself. This is a quantity, which stays invariant under rotations by an orthogonal matrix A,

$$\mathbf{x}' = A\mathbf{x} \quad \to \quad (\mathbf{x}')^\top \mathbf{x}' = \mathbf{x}^\top A^\top A\, \mathbf{x} = \mathbf{x}^\top \mathbf{x} \tag{1.30}$$

and therefore $\rho_{A\mathbf{X}}(\mathbf{x}) = \rho_{\mathbf{X}}(\mathbf{x})$.

Cauchy distribution. The *Cauchy distribution* has the PDF

$$\rho(x; x_0, \gamma) = \frac{\gamma}{\pi} \frac{1}{(x - x_0)^2 + \gamma^2}, \tag{1.31}$$

where $x \in \mathbb{R}$. The function $\rho(x; x_0, \gamma)$ is also called *Lorentzian*. In (1.31), x_0 is a location parameter, which specifies the position of the peak of the distribution, which is centered symmetrically around the point $x = x_0$. γ marks a scale parameter or the width of the distribution. The FWHM is given by 2γ. It is convenient to parametrize the PDF in terms of a complex parameter $\psi \in \mathbb{C}$ with $\psi = x_0 + i\gamma$, such that

$$\rho(x; \psi) = \frac{1}{\pi} \Im\mathrm{m} \left(\frac{1}{x - \psi}\right). \tag{1.32}$$

The mean and the variance of the Cauchy distribution are undefined, as the distribution does not have well-defined or finite momenta m_n for $n \geq 1$. Consequently, there exists no moment generating function. The Lorentzian is normalized such that the integral over $\rho(x; x_0, \gamma)$ gives one, but the first moment

$$\mathbb{E}[x] = \int_{-\infty}^{\infty} x \rho(x)\, \mathrm{d}x \tag{1.33}$$

is undefined since the integral is not defined. This transfers to higher odd-power moments, who are undefined as well. The integral for the even-power moments is defined, but diverges, as illustrated on the example of the second moment,

$$\mathbb{E}\left[x^2\right] \propto \int_{-\infty}^{\infty} \frac{x^2}{1 + x^2}\, \mathrm{d}x = \int_{-\infty}^{\infty} \left(1 - \frac{1}{1 + x^2}\right) \mathrm{d}x = \int_{-\infty}^{\infty} \mathrm{d}x - \pi = \infty, \tag{1.34}$$

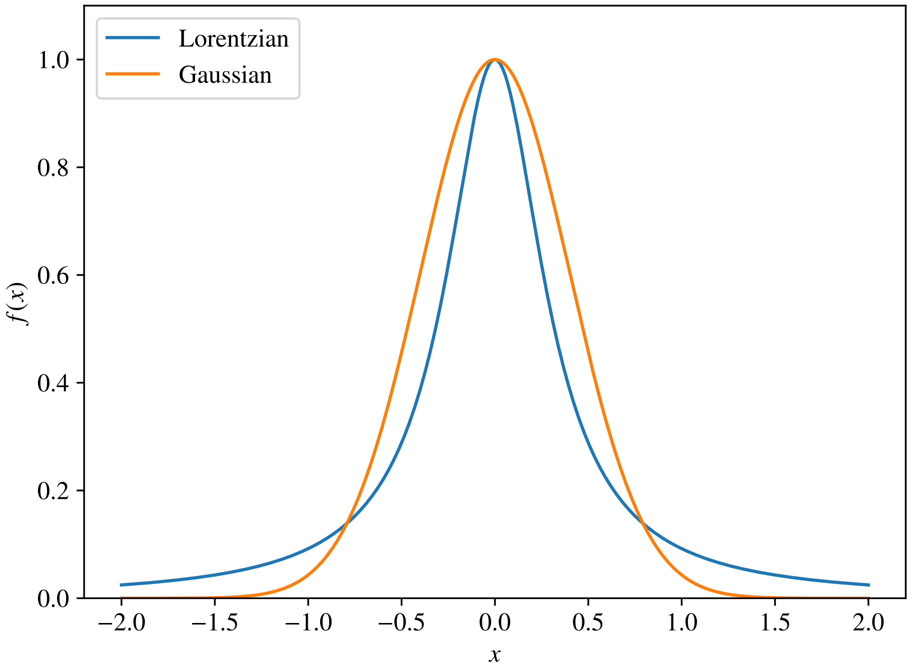

Figure 1.1: Comparison of a Gaussian to a Lorentzian distribution. Both functions are centered around zero, $\mu = x_0 = 0$. Their widths are adjusted, such that the height of the peak at the center is equal to one. For the Gaussian, this translates to $\sigma = \frac{1}{\sqrt{2\pi}}$ and for the Lorentzian $\gamma = \frac{1}{\pi}$.

which is an infinite integral of a constant equal to one. Therefore, all even-power moments diverge. Since the variance involves the mean value, it does not exist either, as none of the central moments do.

In Fig. 1.1, we compare the Gaussian PDF to the Lorentzian. Both distributions are centered around zero and we choose their width such that the maximum of the peak has a height of one. In comparison to the Gaussian, the Lorentzian falls off more quickly close to the peak location x_0, but its tail is longer ranged, such that at large x, the Gaussian goes to zero much faster and is much smaller with an exponentially decreasing tail as opposed to the algebraically decreasing tail of the Lorentzian. The Lorentzian marks a sequence, which converges to the Dirac-Delta distribution $\delta(x)$ for zero width in the weak limit via

$$\lim_{\gamma\to 0} \rho(x; 0, \gamma) = \lim_{\gamma\to 0} \frac{1}{\pi} \frac{\gamma}{x^2 + \gamma^2} = \delta(x). \tag{1.35}$$

1.1.3 Matrix ensembles

Wigner Matrix. In general, a random matrix is a matrix-valued random variable, which means that some or all elements of the matrix are random variables. A *Wigner matrix* is a random Hermitian matrix, such that all entries above the main diagonal are independent random variables with mean zero and the same variance. We can further constrain the Wigner matrix, e.g. demand the entries to be IID. If the entries are all distributed by a Gaussian distribution, we speak of a Gaussian ensemble.

Gaussian ensembles. A *Gaussian ensemble* is a Wigner matrix ensemble. where all elements follow a Gaussian distribution with mean zero. It is characterized by the Dyson index β, which counts the number of real elements per matrix entry. We thus distinguish the *Gaussian orthogonal ensemble (GOE)* with $\beta = 1$, which considers $(N \times N)$ real symmetric matrices, that are invariant under orthogonal transformations and describe time reversal symmetric (TRS) systems. $\beta = 2$ denotes the *Gaussian unitary ensemble (GUE)* with $(N \times N)$ Hermitian complex matrices, that are invariant under unitary transformations and describe systems, which break time-reversal symmetry. Lastly, the *Gaussian symplectic ensemble (GSE)* has $\beta = 4$ and consists of $(N \times N)$ Hermitian quaternionic matrices, which are invariant under symplectic transformations. Their elements are quaternions and the matrices describe time-reversal symmetric systems, which break rotational invariance.

As the mean of all elements of a matrix X drawn from a Gaussian ensemble is zero, $\langle X \rangle = 0$, the first moment of X vanishes as well, $m_1 = N^{-1}\,\mathbb{E}\left[\operatorname{Tr}(X)\right] = 0$. The two-point correlation is given by

$$\mathbb{E}\left[X_{ij}X^{*}_{mn}\right] = \mathbb{E}\left[X_{ij}X_{nm}\right] = \frac{1}{N}\,\delta_{im}\delta_{jn} + \frac{2-\beta}{N\beta}\delta_{in}\delta_{jm}. \tag{1.36}$$

The density up to a constant normalization factor is given by

$$P(\{X_{ij}\}) \propto e^{-\frac{\beta N}{4}\operatorname{Tr}\left(H^2\right)}, \tag{1.37}$$

which we shall show in the following by explicit construction of GOE and GUE matrices. The jPDF in terms of the eigenvalues of the Gaussian ensemble is given by [194]

$$\rho(\{\lambda_i\}) = \frac{1}{Z_{\beta,N}} \prod_{k=1}^{N} e^{-\frac{\beta}{4}\lambda_k^2} \prod_{i<j} \left|\lambda_i - \lambda_j\right|^{\beta}. \tag{1.38}$$

The eigenvalues $\lambda_i, i = 1, \ldots, N$ repel each other as there is a zero probability for coinciding eigenvalues $\lambda_i = \lambda_j$ at the roots of $\rho(\{\lambda_i\})$.

In the following, we discuss one way of constructing a GOE matrix. Take a non-symmetric random square matrix H of size N with real entries, that are IID and drawn from a Gaussian $\mathcal{N}(0, \frac{\sigma^2}{2N})$. The GOE matrix is then obtained by

$$X = H + H^{\top}, \tag{1.39}$$

which makes X a real, symmetric matrix. The variance of its offdiagonal elements is given by $\sigma_{\mathrm{od}}^2 = \frac{\sigma^2}{N}$, because they are constructed through the sum of two independent Gaussian variables (c.f. Sec. 1.1.2) with variance $\frac{\sigma^2}{2N}$. The variance on the diagonal is $\sigma_{\mathrm{d}}^2 = \frac{2\sigma^2}{N}$, as it is determined by the sum of twice the identical Gaussian variable. The jPDF of the GOE in terms of its matrix elements is therefore

$$P(\{X_{ij}\}) \propto \exp\left\{-\sum_{i=1}^{N}\frac{X_{ii}^2}{2\sigma_{\mathrm{d}}^2} - \sum_{\substack{i,j\\(i<j)}}\frac{X_{ij}^2}{2\sigma_{\mathrm{od}}^2}\right\} = \exp\left\{-\frac{N}{4\sigma^2}\operatorname{Tr}\left(X^2\right)\right\}, \tag{1.40}$$

where we inserted the values for σ_{d}^2 and σ_{od}^2 and extended the second sum over all matrix elements. In a change of variables via an orthogonal transformation O, $\tilde{X} = OXO^{\top}$, the measure in the jPDF stays invariant, $\operatorname{Tr}\left(\tilde{X}^2\right) = \operatorname{Tr}\left(X^2\right)$ and the absolute value of the Jacobian of the transformation is equal to one. Recalling Eq. (1.11) with the transformation property of a jPDF, we find that it stays invariant. Under a rotation of the basis, we therefore find, that $\tilde{X}$ is as probable as X and write

$$X \overset{\text{in law}}{=} OXO^{\top}. \tag{1.41}$$

We apply a similar procedure to construct a GUE matrix. Take a complex square matrix H of size N with both real and imaginary part in all matrix elements being IID and drawn from $\mathcal{N}(0, \frac{\sigma^2}{4N})$. Then, the GUE matrix is given by

$$X = H + H^{\dagger}, \tag{1.42}$$

where the diagonal entry obtains the variance $\sigma^2_{\mathrm{d}} = \frac{\sigma^2}{N}$ with the same argument as for the GOE. The variances of the real part $\sigma^2_{\mathrm{od,Re}} = \frac{\sigma^2}{2N}$ and of the imaginary part $\sigma^2_{\mathrm{od,Im}} = \frac{\sigma^2}{2N}$ of the offdiagonal elements are equal and individually obtained through the sum of two independent random variables. Then, the total offdiagonal variance of the absolute value is given by $\sigma^2_{\mathrm{od}} = \sigma^2_{\mathrm{od,Re}} + \sigma^2_{\mathrm{od,Im}} = \frac{\sigma^2}{N} = \sigma^2_{\mathrm{d}}$. The jPDF of one offdiagonal element is then

$$P(X_{ij}) \propto \exp\left\{-\frac{\mathfrak{Re}\,(X_{ij})^2}{2\sigma^2_{\mathrm{od,Re}}} - \frac{\mathfrak{Im}\,(X_{ij})^2}{2\sigma^2_{\mathrm{od,Im}}}\right\} = \exp\left\{-\frac{\left|X_{ij}\right|^2}{\sigma^2_{\mathrm{od}}}\right\}. \tag{1.43}$$

From this, we obtain the jPDF of the full matrix X to

$$P(\{X_{ij}\}) \propto \exp\left\{-\sum_{i=1}^{N}\frac{|X_{ii}|^2}{2\sigma^2_{\mathrm{d}}} - \sum_{\substack{i,j\\(i<j)}}\frac{\left|X_{ij}\right|^2}{\sigma^2_{\mathrm{od}}}\right\} = \exp\left\{-\frac{N}{2\sigma^2}\operatorname{Tr}\left(X^2\right)\right\}, \tag{1.44}$$

where we used, that $\operatorname{Tr}\left(X^2\right) = \sum_{i,j} X_{ij}X_{ji} = \sum_{i,j}\left|X_{ij}\right|^2$, i.e. the sum over the squared absolute values of all matrix elements. Then, the GUE matrix is invariant under unitary transformations and we have, analogously to the GOE case,

$$\tilde{X} = UXU^{\dagger} \overset{\text{in law}}{=} X \tag{1.45}$$

with U being a unitary matrix.

Finally, we compute the second moment of the Gaussian ensemble matrices X, which is equal to their variance, since their mean is zero. For the GOE, we have

$$\tau(X^2) = \frac{1}{N}\mathbb{E}\left[\operatorname{Tr}\left(X^2\right)\right] = \frac{1}{N}\left(\sum_{i}\mathbb{E}\left[X_{ii}^2\right] + \sum_{i\neq j}\mathbb{E}\left[X_{ij}^2\right]\right) = \frac{1}{N}\left(N\frac{2\sigma^2}{N} + N(N-1)\frac{\sigma^2}{N}\right) = \sigma^2 + \frac{\sigma^2}{N}, \tag{1.46}$$

which reaches σ^2 in the limit $N \to \infty$. For the GUE case,

$$\tau(X^2) = \frac{1}{N}\mathbb{E}\left[\operatorname{Tr}\left(X^2\right)\right] = \frac{1}{N}\sum_{i,j}\mathbb{E}\left[\left|X_{ij}\right|^2\right] = \sigma^2, \tag{1.47}$$

which is exactly equal to σ^2 for any N.

1.1.4 Dirac identity

The *Dirac identity*, in mathematics also known under the name of *Sokhostki-Plemelj theorem* [195, 196], states that

$$\lim_{\eta\to 0^+} \frac{1}{x \pm i\eta} = \mathcal{P}\left(\frac{1}{x}\right) \mp i\pi\,\delta(x) \tag{1.48}$$

with $\mathcal{P}(.)$ being the principle value. The identity is strictly speaking only valid in an integral sense and in the integral form written as

$$\lim_{\eta\to 0^+} \int_{-\infty}^{+\infty} \frac{\phi(x)}{x - x_0 \pm i\eta}\,\mathrm{d}x = ⨍_{-\infty}^{+\infty} \frac{\phi(x)}{x - x_0}\,\mathrm{d}x \mp i\pi\,\phi(x_0), \tag{1.49}$$

where $⨍$ denotes the Cauchy principal value integral. $\phi(x)$ is an arbitrary test function, which is assumed to be differentiable at $x = x_0$ and to fall off more quickly than $\frac{1}{x}$ for $x \to \pm\infty$. We proof the identity (1.48) by separating it into real and imaginary part,

$$\lim_{\eta\to 0^+} \int_{-\infty}^{\infty} \frac{\phi(x)}{x \pm i\eta}\,\mathrm{d}x = \lim_{\eta\to 0^+} \int_{-\infty}^{\infty} \frac{x}{x^2 + \eta^2}\,\phi(x)\,\mathrm{d}x \mp i\pi \lim_{\eta\to 0^+} \int_{-\infty}^{\infty} \frac{1}{\pi}\frac{\eta}{x^2 + \eta^2}\,\phi(x)\,\mathrm{d}x. \tag{1.50}$$

The imaginary part of $(x \pm i\eta)^{-1}$ is equal to $\pi\,\delta(x)$ in the limit of $\eta \to 0$, according to Eq. (1.35). To show the equivalence of the real part, we first note, that

$$\begin{aligned}
\lim_{\eta\to 0^+} \int_{-\infty}^{\infty} \frac{x}{x^2 + \eta^2}\,\phi(x)\,\mathrm{d}x &\overset{\text{P.I.}}{=} \left[\phi(x) \lim_{\eta\to 0^+} \frac{1}{2}\ln\left(\left|x^2 + \eta^2\right|\right)\right]_{-\infty}^{\infty} - \lim_{\eta\to 0^+} \int_{-\infty}^{\infty} \phi'(x)\frac{1}{2}\ln\left(\left|x^2 + \eta^2\right|\right)\mathrm{d}x \\
&= -\int_{-\infty}^{\infty} \phi'(x)\ln(|x|)\,\mathrm{d}x
\end{aligned} \tag{1.51}$$

by partial integration (P.I.). The boundary term vanishes as $\phi(x)\ln(|x|) \to 0$ in the limits $x \to \pm\infty$, as $\phi(x)$ goes to zero faster than $\frac{1}{x}$ and $\ln(x)$ diverges more slowly than any polynomial. What remains to show is, that the right hand side of this equation is equal to the principal value integral,

$$\begin{aligned}
⨍_{-\infty}^{+\infty} \frac{\phi(x)}{x}\,\mathrm{d}x &= \lim_{\eta\to 0^+} \left(\int_{-\infty}^{-\eta} + \int_{\eta}^{\infty}\right) \frac{\phi(x)}{x}\,\mathrm{d}x \\
&\overset{\text{P.I.}}{=} \lim_{\eta\to 0^+} \left[\phi(x)\ln(|x|)\Big|_{-\infty}^{-\eta} + \phi(x)\ln(|x|)\Big|_{\eta}^{\infty} - \left(\int_{-\infty}^{-\eta} + \int_{\eta}^{\infty}\right)\phi'(x)\ln(|x|)\right] \\
&= -\int_{-\infty}^{\infty} \phi'(x)\ln(|x|)\,\mathrm{d}x,
\end{aligned} \tag{1.52}$$

as $\ln(|x|)$ is integrable at $x = 0$. For that, we have used, that $\phi(x)$ is differentiable at $x = 0$ with $|[\phi(\eta) - \phi(-\eta)] \cdot \ln(|\eta|)| \leq \left|C \cdot \eta + O(\eta^2)\right| \cdot |\ln\eta| \to 0$ and $C \to \phi'(0)$ for small enough η. This completes the proof. The Dirac identity can be used to derive the Kramers-Kronig relations.

1.1.5 Kramers-Kronig relation

The *Kramers-Kronig relation* [197, 198] is a mathematical connection between the real and imaginary part of a complex function, which is analytic in the upper half of the complex plane. In physics, they are often used to analyze response functions. Consider a complex test function $\phi(z)$ of the complex variable z, which is assumed to be analytic in the upper half plane. This requirement is equivalent to the postulation of causality in physics. We further demand,

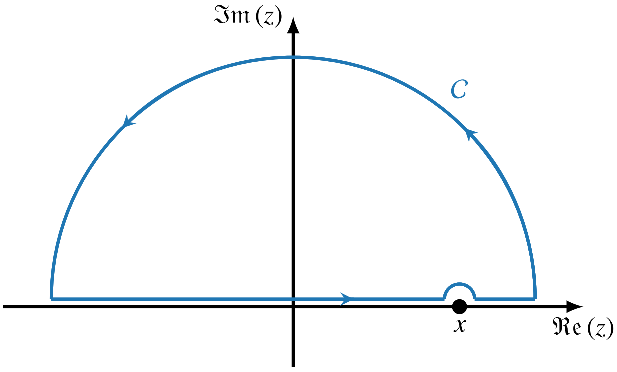

Figure 1.2: Illustration of the contour used to prove the Kramers-Kronig relation. The variable x is on the real axis.

that $\phi(z)$ vanishes faster than $\frac{1}{|z|}$ as $|z| \to \infty$. We derive the Kramers-Kronig relation by considering the contour integral

$$\oint_C \frac{\phi(z)}{z-x}\,\mathrm{d}z = 0, \tag{1.53}$$

where the contour C is a closed loop in the upper half plane as illustrated in Fig. 1.2 and $x \in \mathbb{R}$. The integral vanishes according to the residue theorem, as it does not enclose any singularities. We decompose C to a contour at $|z| \to \infty$, which vanishes due to the requirements on $\phi(z)$ and to a line integral along the real axis, which is shifted by a small regularization parameter η into the upper half plane, such as to avoid the singularity at x,

$$\oint_C \frac{\phi(z)}{z-x}\,\mathrm{d}z = \lim_{\eta\to 0^+}\int_{-\infty}^{-\infty} \frac{\phi(y)}{y+i\eta-x}\,\mathrm{d}y = ⨍ \frac{\phi(y)}{y-x}\,\mathrm{d}y - i\pi\,\phi(x) \tag{1.54}$$

with $y \in \mathbb{R}$. To find this result, we employed the Dirac identity in (1.48). Solving this for $\phi(x)$ gives

$$\phi(x) = \frac{1}{i\pi} ⨍ \frac{\phi(y)}{y-x}\,\mathrm{d}y. \tag{1.55}$$

The Kramers-Kronig relations are then obtained by splitting up the equation into its real and imaginary parts with $\phi(x) = \phi'(x) + i\phi''(x)$ and $\phi'(x), \phi''(x) \in \mathbb{R}$,

$$\phi'(x) = \frac{1}{\pi} ⨍ \frac{\phi''(y)}{y-x}\,\mathrm{d}y = -\mathcal{H}[\phi''](x) \tag{1.56a}$$

$$\phi''(x) = -\frac{1}{\pi} ⨍ \frac{\phi'(y)}{y-x}\,\mathrm{d}y = +\mathcal{H}[\phi'](x). \tag{1.56b}$$

This shows, that the real and imaginary part of the function $\phi(x)$ are not independent, but one part can be reconstructed given the other. In fact, they are connected by the *Hilbert transform* $\mathcal{H}[\phi](x)$, which is defined as [199]

$$\mathcal{H}[\phi](x) = \frac{1}{\pi} ⨍ \frac{\phi(y)}{x-y}\,\mathrm{d}y, \tag{1.57}$$

which is the convolution of the $\phi(x)$ with the function $h(x) \equiv \mathcal{P}\left(\frac{1}{\pi x}\right)$, $\mathcal{H}[\phi] = h \star \phi$. Furthermore, $\mathcal{H}$ is an anti-involution, meaning that the negative of the original function is recovered when it is applied twice,

$$\mathcal{H}\left[\mathcal{H}[\phi]\right](x) = -\phi(x). \tag{1.58}$$

From there, it follows, that $\mathcal{H}^{-1} = -\mathcal{H}$.

Analogous relations between the real and imaginary part of the complex function hold, if it is analytic in the lower half of the complex plane. In this case, the right hand side of the formulas in (1.56a,b) get an additional minus sign. We can apply this to the Stieltjes transform $G_N = G_N' + iG_N''$ written in the integral form in Eq. (1.18), as we approach the real axis from below, $z \to \lambda - i0^+$,

$$\begin{aligned} G_N(\lambda - i0^+) &= ⨍ \frac{\rho(\lambda')}{\lambda - \lambda'}\, \mathrm{d}\lambda + i\pi\rho(\lambda) \\ &= \pi\mathcal{H}[\rho](\lambda) + i\pi\rho(\lambda). \end{aligned} \tag{1.59}$$

The imaginary part of the Stieltjes is π times the eigenvalue density $\rho(\lambda)$, whereas the real part is π times the Hilbert transform of $\rho(\lambda)$, which is consistent with Eq. (1.56a) adjusted to the analyticity in the lower half of the complex plane, $\phi'(x) = \mathcal{H}[\phi''](x)$.

1.2 Dyson-Brownian motion

This section deals with the evolution of eigenvalues of a deterministic matrix given a GUE matrix perturbation. Building on the infinite divisibility property of the Gaussian distribution, a Brownian motion process [200] is employed and together with the works by Itô, who defined calculus tools for Brownian motion stochastic prcoesses [201, 202], Dyson-Brownian motion (DBM) is derived. It determines the evolution of an eigenvalue under the given perturbation.

1.2.1 Brownian motion

Given the probability space $(\Omega, \mathcal{F}, P)$, a *Brownian motion* [155, 156, 177] or *Wiener process* is a stochastic process $B = \{B(t) : t \geq 0\}$, which fulfills the following properties. It is zero for $t = 0$, $B(0) = 0$. $B(t)$ has independent increments, which means that under splitting t in n time steps $t_k = \frac{kt}{n}, k = 1, \ldots, n$, the random variables $B(t_1), B(t_2) - B(t_1), \ldots, B(t_n) - B(t_{n-1})$ are independent. Future increments $B(t+h) - B(t)$, $h \geq 0$ are independent of the past values $B(s)$ for $s \leq t$. Further, $B(t)$ has normal increments with mean zero and variance h,

$$B(t+h) - B(t) \sim \mathcal{N}(0, h) \tag{1.60}$$

for $t \geq 0, h \geq 0$. Lastly, $B(t)$ has continuous sample paths, which means that $\forall \omega \in \Omega$, the function $t \mapsto B(t;\omega)$ is continuous in t.

To make this explicit, we define the Brownian motion X_t as a Gaussian random variable of mean $\mu\, t$ and variance $\sigma^2\, t$. Utilizing the infinite divisibility of a Gaussian, we divide the Brownian motion into n discrete steps [155],

$$X_{t_k} = \sum_{l=0}^{k-1} \mu\, \delta t + \sum_{l=0}^{k-1} \sigma\, \delta B_l, \tag{1.61}$$

where $\delta B_l \sim \mathcal{N}(0, \delta t)$ for each l and $t_k = \frac{kt}{n}, 0 \leq k \leq n$ is the k-th step with the uniform step width $\delta t = \frac{t}{n}$. The first term in (1.61) adds up to the mean value

$$\mathbb{E}\left[X_{t_k}\right] = \mu\, k\, \delta t = \mu\, \frac{kt}{n}, \tag{1.62}$$

whereas the second term produces the total variance

$$Var(X_{t_k}) = \mathbb{E}\left[(X_{t_k} - \mathbb{E}\left[X_{t_k}\right])^2\right] = \sigma^2\, \mathbb{E}\left[\left(\sum_{l=0}^{k-1} \delta B_l\right)^2\right] = \sigma^2\, \frac{kt}{n}, \tag{1.63}$$

where we have used $\mathbb{E}\left[\delta B_l^2\right] = \delta t$. We then reach the value at t after n steps, $X_{t_n} = X_t$.

By taking the limit $n \to \infty$, we end up with a continuous time process from X_{t_k} with the limits $\delta t \to \mathrm{d}t$ and $\delta B_k \to \mathrm{d}B$ and an infinitesimal time step

$$\mathrm{d}X_t = \mu\, \mathrm{d}t + \sigma\, \mathrm{d}B_t \tag{1.64}$$

and $X_0 = 0$. Here, $\mathrm{d}B_t$ are independent, infinitesimal Gaussian variables with mean $\mathbb{E}\left[\mathrm{d}B\right] = 0$ and variance $\mathbb{E}\left[\mathrm{d}B^2\right] = \mathrm{d}t$, where $\mathrm{d}t$ is an infinitesimal quantity for the increment of time t. While the values of the process at different times X_t and $X_{t'}$ are not independent, their increments $X_t - X_{t'}$ are, if $t' < t$. Note, that we have employed Itô's prescription, where X_{t_k} is built from past increments δB_l for $l < k$, but independent of the step δB_k. In the continuous process, X_t is independent of the equal-time $\mathrm{d}B_t$, which necessitates a correction to the standard chain rule for differentiation, which is called Itô's term and described in Itô's Lemma.

1.2.2 Itô's Lemma

Consider now arbitrary functions $F(X_t)$ of the Brownian motion, X_t, which are at least twice differentiable. As $\mathrm{d}B^2$ is of the order $\mathcal{O}(\mathrm{d}t)$, we need to take care in building the derivative. In short, to compute the total differential $\mathrm{d}F$, it is not sufficient to consider the derivative by X_t, $\mathrm{d}F \neq \frac{\partial F}{\partial X_t}\,\mathrm{d}X_t$.

We first resort to the discretized version of the Brownian motion, where we Taylor-expand the function F,

$$F(X_{t+\delta t}) = F(X_t) + F'(X_t)\,\delta X + \frac{1}{2}F''(X_t)\,(\delta X)^2 + o(\delta t) \tag{1.65}$$

with the discretized version of the Brownian motion step $\delta X = \mu\delta t + \sigma\delta B_t$. Some parts in the quadratic term $(\delta X)^2$ are of the same order as the linear term with δB^2 being of the order $\mathcal{O}(\mathrm{d}t)$. We intend to keep all terms up to the order of δt, which yields for the quadratic term

$$(\delta X)^2 = \mu^2\,(\delta t)^2 + \sigma^2\,\delta t + \sigma^2\,\left[(\delta B)^2 - \delta t\right] + 2\mu\,\sigma\,\delta t\,\delta B = \sigma^2\,\delta t + o(\delta t). \tag{1.66}$$

We neglect the first term as it is of order $(\delta t)^2$ and keep the second term with order δt. The main statement of Itô's Lemma is to neglect the third term $\sigma^2\left[(\delta B)^2 - \delta t\right]$ as well, since it has mean zero and a standard deviation of $\sqrt{2}\,\sigma^2\delta t$ originating from the variance $2\,\sigma^4(\delta t)^2$ of the addition of the variables $(\delta B)^2$ and δt. The last term is of higher order than δt, since δB goes as $\sqrt{\delta t}$. In the continuum limit, we then obtain with Itô's lemma [203]

$$\mathrm{d}F_t = \mathrm{d}F(X_t) = \frac{\partial F}{\partial X_t}\,\mathrm{d}X_t + \frac{\sigma^2}{2}\frac{\partial^2 F}{\partial X_t^2}\,\mathrm{d}t. \tag{1.67}$$

The last term is called Itô's term [203], as this corrective term for the stochastic calculus appears additionally to standard differential calculus.

We can extend this analysis to functions of several stochastic variables. Consider a collection of N independent stochastic variables $\{X_{i,t}\}$ written as a vector $\mathbf{X}_t$. The differential of those functions $F(\mathbf{X}_t, t)$ can then be expressed as

$$\mathrm{d}F(\mathbf{X}_t, t) = \sum_{i=0}^{N}\frac{\partial F}{\partial X_i}\,\mathrm{d}X_{i,t} + \left[\frac{\partial F}{\partial t} + \sum_{i,j=1}^{N}\frac{c_{ij}(\mathbf{X}_t, t)}{2}\,\frac{\partial^2 F}{\partial X_i\,\partial X_j}\right]\mathrm{d}t, \tag{1.68}$$

where we used, that $\mathrm{d}X_{i,t} = \mu_i(\mathbf{X}_t, t)\,\mathrm{d}t + \mathrm{d}B_{i,t}$ with infinitesimal Brownian motion steps $\mathrm{d}B_{i,t}$. The mean and the variance may explicitly depend on $\mathbf{X}_t$ and t. The individual Brownian motions $X_{i,t}$ do not need to be independent, which is accounted for in Eq. (1.68) by the covariance matrix $c_{ij}(\mathbf{X}_t, t)$, which is defined through

$$\mathbb{E}\left[\mathrm{d}B_{i,t}\,\mathrm{d}B_{j,t}\right] := c_{i,j}(\mathbf{X}_t, t)\,\mathrm{d}t \tag{1.69}$$

with its diagonals containing the variances σ_i^2. The explicit time dependence of F is incorporated in Eq. (1.68) by the term $\frac{\partial F}{\partial t}$. The formula simplifies, if all Brownian motions are independent, which leads to a diagonal covariance matrix $c_{i,j} = \sigma_i^2\,\delta_{i,j}$.

1.2.3 Perturbation theory

In a recap of perturbation theory, we define $H = H_0 + \varepsilon H_1$ with H_0 and H_1 as $(N \times N)$ Hermitian matrices and ε being a small parameter. The unperturbed eigensystem of H_0 is given by $H_0\,\mathbf{v}_{i,0} = \lambda_{i,0}\,\mathbf{v}_{i,0}$ with $i = 1, \ldots, N$. Upon the addition of the perturbation εH_1, the perturbed eigenvectors of the full Hamiltonian H are defined by

$$H\,\mathbf{v}_i = \lambda_i\,\mathbf{v}_i. \tag{1.70}$$

We can expand those and their corresponding eigenvalues with a series expansion in ε,

$$\lambda_i = \lambda_{i,0} + \sum_{k=1}^{\infty} \varepsilon^k\,\lambda_{i,k}, \tag{1.71a}$$

$$\mathbf{v}_i = \mathbf{v}_{i,0} + \sum_{k=1}^{\infty} \varepsilon^k\,\mathbf{v}_{i,k} \tag{1.71b}$$

for $i = 1, \ldots, N$ with the additional constraint, that both the unperturbed and the perturbed eigenvectors are normalized to one, $|\mathbf{v}_i| = \left|\mathbf{v}_{i,0}\right| = 1\ \forall\, i$. Up to linear order in ε, $\mathbf{v}_i = \mathbf{v}_{i,0} + \varepsilon\,\mathbf{v}_{i,1}$, this results in the condition

$$1 \overset{!}{=} |\mathbf{v}_i|^2 = \left|\mathbf{v}_{i,0} + \varepsilon\,\mathbf{v}_{i,1}\right|^2 = \left|\mathbf{v}_{i,0}\right|^2 + 2\varepsilon\,\mathbf{v}_{i,0}^{\dagger}\mathbf{v}_{i,1} \quad \Leftrightarrow \quad \mathbf{v}_{i,0}^{\dagger}\mathbf{v}_{i,1} = 0, \tag{1.72}$$

that the first order correction $\mathbf{v}_{i,1}$ is orthogonal to the unperturbed eigenstate $\mathbf{v}_{i,0}$. Upon assuming a non-degenerate eigenspectrum, we can plug the expansion of (1.71a-b) in the defining equation for the eigensystem (1.70) and obtain

$$(H_0 + \varepsilon H_1)\,(\mathbf{v}_{i,0} + \varepsilon\,\mathbf{v}_{i,1} + \varepsilon^2\,\mathbf{v}_{i,2} + \ldots) = (\lambda_{i,0} + \varepsilon\,\lambda_{i,1} + \varepsilon^2\,\lambda_{i,2} + \ldots)\,(\mathbf{v}_{i,0} + \varepsilon\,\mathbf{v}_{i,1} + \varepsilon^2\,\mathbf{v}_{i,2} + \ldots). \tag{1.73}$$

Collecting the first order terms in ε, we obtain

$$\begin{aligned} H_1\mathbf{v}_{i,0} + H_0\mathbf{v}_{i,1} &= \lambda_{i,1}\,\mathbf{v}_{i,0} + \lambda_{i,0}\,\mathbf{v}_{i,1} \\ \Leftrightarrow\ \mathbf{v}_{j,0}^{\dagger}\,H_1\,\mathbf{v}_{i,0} + \lambda_{j,0}\mathbf{v}_{j,0}^{\dagger}\mathbf{v}_{i,1} &= \lambda_{i,1}\,\delta_{ij} + \lambda_{i,0}\mathbf{v}_{j,0}^{\dagger}\mathbf{v}_{i,1}, \end{aligned} \tag{1.74}$$

which leads to the first order corrections

$$i = j \ \rightarrow \quad \lambda_{i,1} = \mathbf{v}_{i,0}^{\dagger}\,H_1\,\mathbf{v}_{i,0} = (H_1)_{ii} \tag{1.75a}$$

$$i \neq j \ \rightarrow \quad \mathbf{v}_{i,1} = \sum_{j\ (j\neq i)} \frac{(H_1)_{ji}}{\lambda_{i,0} - \lambda_{j,0}}\,\mathbf{v}_{j,0} \tag{1.75b}$$

with the matrix elements of the perturbation Hamiltonian in the unperturbed basis defined as $(H_1)_{ij} := \mathbf{v}_{i,0}^{\dagger}\,H_1\,\mathbf{v}_{j,0}$. In second order of ε, we have

$$H_1\mathbf{v}_{i,1} + H_0\mathbf{v}_{i,2} = \lambda_{i,2}\,\mathbf{v}_{i,0} + \lambda_{i,1}\,\mathbf{v}_{i,1} + \lambda_{i,0}\,\mathbf{v}_{i,2}, \tag{1.76}$$

resulting in the second order correction of the eigenvalues

$$\lambda_{i,2} = \sum_{j\ (j\neq i)} \frac{\left|(H_1)_{ij}\right|^2}{\lambda_{i,0} - \lambda_{j,0}}. \tag{1.77}$$

Upon further sorting of (1.73) in terms of orders of ε, one can find all the higher order corrections.

1.2.4 Evolution of eigenvalues

The evolution of the eigenvalues of a matrix to which a Wigner ensemble is added is described by the *DBM* [178]. We define the Hermitian $(N \times N)$ matrix

$$M = A + X_t, \tag{1.78}$$

where A is the initial matrix. In the following, as we are interested in Hermitian matrices, we choose X_t to be a GUE matrix with the initial condition $X_0 = 0$ and a variance growing linearly with time. In an infinitesimal time step, the elements of the GUE X_t are given by

$$\mathrm{d}X_{kk} = \sqrt{\frac{1}{N}}\,\mathrm{d}B_{kk} \tag{1.79a}$$

$$\mathrm{d}X_{kl} = \sqrt{\frac{1}{2N}}\left(\mathrm{d}B'_{kl} + i\,\mathrm{d}B''_{kl}\right) \tag{1.79b}$$

for $k < l$. The remaining offdiagonal entries are obtained by the hermiticity condition, $\mathrm{d}X_{lk} = \mathrm{d}X^*_{kl}$. All of $\mathrm{d}B_{kk}$, $\mathrm{d}B'_{kl}$ and $\mathrm{d}B''_{kl}$ denote independent Brownian increments drawn from $\mathcal{N}(0, \mathrm{d}t)$ with variance $\mathrm{d}t$ and are hence IID. The elements of $\mathrm{d}X$ therefore have mean zero and a variance of $\sigma^2_{kk} = \mathbb{E}\left[|\mathrm{d}X_{kk}|^2\right] = \mathbb{E}\left[(\mathrm{d}X_{kk})^2\right] = \frac{1}{N}\,\mathrm{d}t$ on the diagonal as well as $\sigma^2_{kl} = \mathbb{E}\left[|\mathrm{d}X_{kl}|^2\right] = \frac{1}{N}\,\mathrm{d}t$ on the offdiagonal, while $\mathbb{E}\left[(\mathrm{d}X_{kl})^2\right] = 0$. As the GUE is rotationally invariant (c.f. Sec. 1.1.3), we choose to work in the diagonal basis of A, whose eigenvalues are given by $a_i, i = 1, \ldots, N$. The eigenvalues of the full matrix M are functions of the entries of the matrix X_t, $\lambda_i = \lambda_i(\{X_{kk}\}, \{X_{kl}\})$. We now apply Itô's Lemma from Eq. (1.68). Since the Brownian motions are all independent, the covariance matrix as defined in Eq. (1.69) can be determined by the two-point correlation

$$\mathbb{E}\left[\mathrm{d}X_{ij}\,\mathrm{d}X_{kl}\right] = \mathbb{E}\left[|\mathrm{d}X_{kl}|^2\right]\delta_{il}\delta_{jk} = \frac{\mathrm{d}t}{N}\,\delta_{il}\delta_{jk}, \tag{1.80}$$

as $\mathbb{E}\left[|\mathrm{d}X_{kl}|^2\right] = \sigma^2_{kl} = \frac{\mathrm{d}t}{N}$ for both $k = l$ and $k \neq l$. If we insert this into (1.68), we obtain

$$\mathrm{d}\lambda_i = \sqrt{\frac{1}{N}}\sum_k \frac{\partial\lambda_i}{\partial X_{kk}}\mathrm{d}B_{kk} + \sqrt{\frac{1}{2N}}\sum_{l>k}\frac{\partial\lambda_i}{\partial X_{kl}}\left(\mathrm{d}B'_{kl} + i\,\mathrm{d}B''_{kl}\right) + \frac{1}{2N}\left[\sum_k \frac{\partial^2\lambda_i}{\partial X^2_{kk}} + \sum_{l>k}\frac{\partial^2\lambda_i}{\partial X_{kl}\,\partial X_{lk}}\right]\mathrm{d}t, \tag{1.81}$$

where we have inserted the definition in (1.79a) and the covariance matrix from (1.80). The sums for the offdiagonal entries are restricted to $l > k$, because only those Brownian motions are independent with the ones for $k > l$ deriving from them.

To find all the derivatives of λ_i by elements of the perturbation matrix X_t appearing in (1.81), we employ perturbation theory, where we take A as the unperturbed matrix and X_t as its small perturbation. From the first and second order correction in (1.75a) and (1.77), we obtain

$$\lambda_i = a_i + X_{ii} + \sum_{j\ (j\neq i)}\frac{\left|X_{ij}\right|^2}{\lambda_i - \lambda_j} = a_i + X_{ii} + \sum_{j\ (j\neq i)}\frac{X_{ij}X_{ji}}{\lambda_i - \lambda_j}, \tag{1.82}$$

where we substituted $a_i \to \lambda_i$, as we are ultimately interested in an infinitesimal timestep dt with the Brownian increments $\mathrm{d}X_{kk}$ and $\mathrm{d}X_{kl}$ in (1.81). We then compute all the derivatives to

$$\frac{\partial \lambda_i}{\partial X_{kk}} = \delta_{ki}, \qquad \frac{\partial^2 \lambda_i}{\partial X_{kk}^2} = 0,$$
$$\frac{\partial \lambda_i}{\partial X_{kl}} = 0, \qquad \frac{\partial^2 \lambda_i}{\partial X_{kl}\,\partial X_{lk}} = \frac{2\delta_{ik}}{\lambda_k - \lambda_l} + \frac{2\delta_{il}}{\lambda_l - \lambda_k}.$$

These derivatives must be regarded in the context of a Taylor expansion of λ_i in terms of the matrix elements X_{ij}, where X_{ij} is set to zero in the derivatives. In the last derivative, there are two terms, the first for $i = k$ and $j = l$ and the second for $i = l$ and $j = k$. Inserting these results into the expression for $\mathrm{d}\lambda_i$ in Eq. (1.81) obtained from Itô's Lemma yields the final result [178]

$$\begin{aligned} \mathrm{d}\lambda_i &= \sqrt{\frac{1}{N}} \sum_k \mathrm{d}B_{kk}\,\delta_{ki} + \frac{1}{2N}\left[\sum_{k>l}\left(\frac{2\delta_{ik}}{\lambda_k - \lambda_l} + \frac{2\delta_{il}}{\lambda_l - \lambda_k}\right)\right]\mathrm{d}t \\ &= \left(\sqrt{\frac{1}{N}}\right)\mathrm{d}B_{ii} + \left(\frac{1}{N}\sum_{j\,(j\neq i)} \frac{1}{\lambda_i - \lambda_j}\right)\mathrm{d}t \end{aligned} \tag{1.83}$$

for a GUE perturbation of an initial matrix A. The stochastic evolution of the eigenvalues λ_i again assumes the form of a Brownian motion $\sigma \mathrm{d}B_{ii} + \mu \mathrm{d}t$ itself (c.f. (1.64)), with the first bracket in (1.83) as the root of the variance $\sigma^2 = \frac{1}{N}$ and the second bracket being the mean value. In summary, the DBM is a tool to find the evolution of eigenvalues and turns out to be a Brownian motion process itself, describing how much of a Wigner matrix is progressively added to the initial matrix A. Note, that the evolution of the eigenvalues $\lambda_i, i = 1, \ldots, N$ are independent of each other, as $\mathrm{d}\lambda_i$ in (1.83) only depends on $\mathrm{d}B_{ii}$ and $\mathrm{d}t$ and not on $\mathrm{d}B_{ij}$ or $\mathrm{d}\lambda_j$.

1.3 Burgers' equation

Given the eigenvalue evolution under the DBM, we derive a stochastic differential equation (SDE) for the Stieltjes transform of the time-evolved matrix under a GUE perturbation, which turns out to be the Burgers' equation, originally introduced in the context of fluid dynamics [204, 205]. With the Burgers' equation it is possible to determine the eigenvalue density of a Gaussian ensemble given by the semicircle law. Similarly, an SDE for the resolvent is derived, which contains information on the evolution of eigenvectors. Solutions to both SDEs for the Stieltjes and the resolvent are found by utilizing the method of characteristics.

1.3.1 Derivation of a stochastic differential equation for the Stieltjes transform

We now consider a matrix $M = A + X_t$, which undergoes a DBM with a GUE matrix X_t of variance t. It has eigenvalues $\lambda_i, i = 1, \dots, N$. In Sec. 1.1.1, we defined the Stieltjes transform of M as

$$G_N(z, \{\lambda_i\}) = \frac{1}{N} \sum_{i=1}^{N} \frac{1}{z - \lambda_i}, \tag{1.84}$$

where z is a constant complex parameter and the eigenvalues λ_i stochastically evolve as a Brownian motion according to Eq. (1.83) for $\mathrm{d}\lambda_i$. The application of Itô's Lemma in (1.68) to the Stieltjes G_N yields

$$\mathrm{d}G_N(z, \{\lambda_i\}) = \sum_{i=1}^{N} \frac{\partial G_N}{\partial \lambda_i} \mathrm{d}\lambda_i + \sum_{i,j=1}^{N} \frac{c_{ij}}{2} \frac{\partial^2 G_N}{\partial \lambda_i \partial \lambda_j} \mathrm{d}t. \tag{1.85}$$

We evaluate the derivatives of the Stieltjes to

$$\begin{aligned} \frac{\partial G_N}{\partial \lambda_i} &= \frac{1}{N} \frac{1}{(z - \lambda_i)^2}, \\ \frac{\partial^2 G_N}{\partial \lambda_i \partial \lambda_j} &= \frac{2}{N} \frac{1}{(z - \lambda_i)^3} \delta_{ij}. \end{aligned}$$

According to (1.83), the eigenvalues λ_i and their evolution are independent, which results in a diagonal covariance matrix $c_{ij} = \frac{1}{N} \delta_{ij}$. Inserting the derivatives and the equation for $\mathrm{d}\lambda_i$, we obtain

$$\mathrm{d}G_N = \sqrt{\frac{1}{N^3}} \sum_i \frac{\mathrm{d}B_{ii}}{(z - \lambda_i)^2} + \frac{1}{N^2} \sum_{\substack{i,j \\ (i \neq j)}} \frac{1}{\lambda_i - \lambda_j} \frac{1}{(z - \lambda_i)^2} \mathrm{d}t + \frac{1}{N^2} \sum_i \frac{1}{(z - \lambda_i)^3} \mathrm{d}t. \tag{1.86}$$

We further massage the second term

$$\begin{aligned} \frac{1}{N^2} \sum_{\substack{i,j \\ (i \neq j)}} \frac{1}{\lambda_i - \lambda_j} \frac{1}{(z - \lambda_i)^2} &= \frac{1}{2N^2} \sum_{\substack{i,j \\ (i \neq j)}} \left[\frac{1}{(z - \lambda_i)^2 (\lambda_i - \lambda_j)} + \frac{1}{(z - \lambda_j)^2 (\lambda_j - \lambda_i)} \right] \\ &= \frac{1}{2N^2} \sum_{\substack{i,j \\ (i \neq j)}} \frac{(z - \lambda_i) + (z - \lambda_j)}{(z - \lambda_i)^2 (z - \lambda_j)^2} = \frac{1}{N^2} \sum_{\substack{i,j \\ (i \neq j)}} \frac{1}{(z - \lambda_i)(z - \lambda_j)^2} \\ &= \left(\frac{1}{N} \sum_i \frac{1}{z - \lambda_i} \right) \left(\frac{1}{N} \sum_j \frac{1}{(z - \lambda_j)^2} \right) - \frac{1}{N^2} \sum_i \frac{1}{(z - \lambda_i)^3} \end{aligned}$$

$$= G_N \left(-\frac{\partial G_N}{\partial z} \right) - \frac{1}{N^2} \sum_i \frac{1}{(z-\lambda_i)^3}. \tag{1.87}$$

The third term in (1.86) is canceled out and we are left with

$$\mathrm{d}G_N = \sqrt{\frac{1}{N^3}} \sum_i \frac{\mathrm{d}B_{ii}}{(z-\lambda_i)^2} - G_N \frac{\partial G_N}{\partial z} \mathrm{d}t. \tag{1.88}$$

We now take the expectation value of the whole expression, as we are not interested in explicit random instances, but their expected behavior,

$$\mathbb{E}\left[\mathrm{d}G_N(z)\right] = -\mathbb{E}\left[G_N \frac{\partial G_N}{\partial z} \right] \mathrm{d}t, \tag{1.89}$$

where we used that the Brownian motions used to construct the elements of the perturbation matrix X_t are centered around zero, $\mathbb{E}\left[\mathrm{d}B_{ii}\right] = 0$. If we had used a GOE instead of a GUE for X_t, we would have ended up with an additional term [156],

$$\mathbb{E}\left[\mathrm{d}G_N(z)\right] = -\mathbb{E}\left[G_N \frac{\partial G_N}{\partial z} \right] \mathrm{d}t + \frac{1}{2N} \mathbb{E}\left[\frac{\partial^2 G_N}{\partial z^2} \right] \mathrm{d}t. \tag{1.90}$$

Here the additional viscosity term regularizes the equation for finite N. Note, that both (1.89) for the GUE and (1.90) are exact for any N. In the limit $N \to \infty$, we have $G_N(z) \to G(z)$ and use the self-averaging property of the Stieltjes transform, $\mathcal{G}(z) = \mathbb{E}\left[G(z)\right] = G(z)$ to determine the *SDE* [206]

$$\begin{aligned} \frac{\partial \mathcal{G}(z,t)}{\partial t} &= -\mathcal{G}(z,t) \frac{\partial \mathcal{G}(z,t)}{\partial z} \\ \text{with} \quad \mathcal{G}(z,0) = \mathcal{G}_0(z) &= \frac{1}{N} \sum_i (z-a_i)^{-1} \text{ at } t = 0 \end{aligned} \tag{1.91}$$

where the initial condition is evaluated from $X_t = 0$. This *partial differential equation (PDE)* holds for both a GUE and a GOE perturbation matrix X_t and is known as the inviscid Burgers' equation, as there is no viscosity term present.

1.3.2 Derivation of a stochastic differential equation for the resolvent

While the Stieltjes transform $G(z)$ contains the information about the eigenvalue density $\rho(\lambda)$ of the matrix M, the matrix-valued resolvent $R(z)$ also carries information about the eigenvectors of M. The Stieltjes is equal to the trace of the resolvent, $G(z) = \mathrm{Tr}(R(z))$. Analogously to Sec. 1.3.1, where we derived an SDE for the $G(z)$, we now apply Itô's calculus to obtain a stochastic differential equation for the resolvent. As in Sec. 1.3.1, we take $M = A + X_t$, where M is Hermitian and X_t is again a GUE with variance t. Together with the information, that $R(z)$ depends on all elements of the matrix M, $R_{ij}(\{M_{kl}\})$, we deduce the form of Itô's Lemma

$$\mathrm{d}R_{ij}(z) = \sum_{k,l=1}^{N} \frac{\partial R_{ij}}{\partial M_{kl}} \mathrm{d}X_{kl} + \sum_{k,l,m,n=1}^{N} \frac{c_{kl;mn}}{2} \frac{\partial^2 R_{ij}}{\partial M_{kl} \partial M_{mn}} \mathrm{d}t, \tag{1.92}$$

where $\mathrm{d}M_{kl} = \mathrm{d}X_{kl}$. We obtain the shape of the covariance matrix $c_{kl;mn}$ by the two point correlation

$$\mathbb{E}\left[\mathrm{d}X_{kl}\mathrm{d}X_{mn}\right] = \mathbb{E}\left[|\mathrm{d}X_{kl}|^2\right] \delta_{kn}\delta_{lm} = \frac{\mathrm{d}t}{N}\delta_{kn}\delta_{lm}. \tag{1.93}$$

As a next step, we evaluate the necessary derivatives through the identity

$$[R\,(z\mathbb{1}-M)]_{in}=\sum_m R_{im}\,(z\,\delta_{mn}-M_{mn})=\delta_{in}, \tag{1.94}$$

where we used, that $R(z)=(z\mathbb{1}-M)^{-1}$. If we take the derivative of this identity with respect to M_{kl}, we get

$$\sum_m \frac{\partial R_{im}}{\partial M_{kl}}(z\,\delta_{mn}-M_{mn})-\sum_m R_{im}\frac{\partial M_{mn}}{\partial M_{kl}}=0 \tag{1.95}$$

with $\frac{\partial M_{mn}}{\partial M_{kl}}=\delta_{mk}\delta_{nl}$. Multiplication by R_{nj} and summing over n yields

$$\frac{\partial R_{ij}}{\partial M_{kl}}=\sum_{m,n} R_{im}R_{nj}\,\delta_{mk}\delta_{nl}=R_{ik}R_{lj}. \tag{1.96}$$

The second derivative is straightforwardly obtained to

$$\frac{\partial R_{ij}}{\partial M_{kl}\partial M_{mn}}=\frac{\partial}{\partial M_{mn}}\left(R_{ik}R_{lj}\right)=R_{im}R_{nk}R_{lj}+R_{ik}R_{lm}R_{nj}. \tag{1.97}$$

In total, after insertion of all terms, Eq. (1.92) amounts to

$$\begin{aligned}
\mathrm{d}R_{ij}(z) &= \sum_{k,l} R_{ik}R_{lj}\mathrm{d}X_{kl}+\sum_{k,l,m,n}\frac{\mathrm{d}t}{2N}\,\delta_{kn}\delta_{lm}\left(R_{im}R_{nk}R_{lj}+R_{ik}R_{lm}R_{nj}\right)\\
&= \sum_{k,l} R_{ik}R_{lj}\mathrm{d}X_{kl}+\sum_{k,l}\frac{\mathrm{d}t}{2N}\left(R_{il}R_{kk}R_{lj}+R_{ik}R_{ll}R_{kj}\right)\\
&= \sum_{k,l} R_{ik}R_{lj}\mathrm{d}X_{kl}+\frac{1}{N}\,\mathrm{Tr}(R)\left[R^2\right]_{ij}\,\mathrm{d}t.
\end{aligned} \tag{1.98}$$

After taking the expectation value with $\mathbb{E}\,[\mathrm{d}X_{kl}]=0$, we end up with the SDE [156]

$$\frac{\partial\mathcal{R}(z,t)}{\partial t}=\mathcal{G}(z,t)\,\mathcal{R}^2(z,t). \tag{1.99}$$

The identification $\mathcal{R}^2(z,t)=-\partial_z\mathcal{R}(z,t)$ leads to the final result

$$\frac{\partial\mathcal{R}(z,t)}{\partial t}=-\mathcal{G}(z,t)\frac{\partial\mathcal{R}(z,t)}{\partial z} \tag{1.100}$$

with the initial conditions $\mathcal{R}(z,0)=\mathcal{R}_0(z)=(z\mathbb{1}-A)^{-1}$. Upon taking the trace of(1.100), we consistently end up with the Burgers' equation (1.91) for the Stieltjes transform $\mathcal{G}(z)$.

1.3.3 Solutions for the stochastic differential equations

Lastly, we solve the SDEs for the Stieltjes transform in (1.91) and for the resolvent in (1.100). The Burgers' equation (1.91) is a conservation equation and mathematically characterized as a first order quasilinear hyperbolic equation. We use the *methods of characteristics* [207] to solve it. This way, the PDE is transformed into an *ordinary differential equation (ODE)* along an appropriate curve, along which $\mathcal{G}$ is constant. The goal of this ansatz is to find those curves, which are called characteristic curves. The ODE, to which we intend to transform the differential equation must be of the general shape

$$\frac{\mathrm{d}}{\mathrm{d}s}\mathcal{G}(z(s),t(s)) = F(G,z(s),t(s)), \tag{1.101}$$

where F can be any function of its three variables and s is a new parameter, which characterizes the characteristic curve $(z(s),t(s))$. We apply the chain rule to find

$$\frac{\mathrm{d}}{\mathrm{d}s}\mathcal{G}(z(s),t(s)) = \frac{\partial\mathcal{G}}{\partial z}\underbrace{\frac{\mathrm{d}z}{\mathrm{d}s}}_{\overset{!}{=}\mathcal{G}} + \frac{\partial\mathcal{G}}{\partial t}\underbrace{\frac{\mathrm{d}t}{\mathrm{d}s}}_{\overset{!}{=}1} \overset{!}{=} 0, \tag{1.102}$$

where the total derivative is compared to the Burgers' equation in (1.91). The right hand side is zero in order to match it with the Burgers' equation in (1.91). Since it only contains partial derivatives of $\mathcal{G}(z,t)$ and no additional functions of $\mathcal{G}(z,t)$, the function $F(G,z(s),t(s))$ on the right-hand side of (1.101) must be zero. If these equations can be fulfilled, the ansatz leads to a solution along the characteristic line, where $\partial_s\mathcal{G} = 0$ and the solution is constant. The newly obtained ODEs for $\mathcal{G}$, z and t with their solutions read

$$\frac{\mathrm{d}z}{\mathrm{d}s} = \mathcal{G}, \quad z(0) = \xi \quad \to z(s) = \mathcal{G}\cdot s + \xi, \tag{1.103a}$$

$$\frac{\mathrm{d}t}{\mathrm{d}s} = 1, \quad t(0) = 0 \quad \to t(s) = s, \tag{1.103b}$$

$$\frac{\mathrm{d}\mathcal{G}}{\mathrm{d}s} = 0. \tag{1.103c}$$

We introduced ξ as a temporary variable for the initial condition of z. Since these equations are decoupled, the solutions can be readily obtained. As mentioned before, the third ODE guarantees, that $\mathcal{G}$ is constant along the characteristic

$$\mathcal{G}(z(s),t(s)) = \mathcal{G}(z(0),t(0)) = \mathcal{G}(\xi,0) = \mathcal{G}_0(\xi). \tag{1.104}$$

After insertion of $\xi = z - \mathcal{G}s = z - \mathcal{G}t$, we obtain the solution

$$\mathcal{G}(z,t) = \mathcal{G}(\xi,0) = \mathcal{G}(z-\mathcal{G}t,0) = \mathcal{G}_0(z-\mathcal{G}t), \tag{1.105}$$

which is an implicit algebraic equation for $\mathcal{G}(z,t)$ once the initial function $\mathcal{G}_0(z)$ is known.

A similar construction for the solution of the resolvent reads

$$\mathcal{R}(z,t) = \mathcal{R}_0(z - \mathcal{G}(z,t)t). \tag{1.106}$$

We show this by direct insertion into Eq. (1.100),

$$\begin{aligned}\Big(\mathcal{G}(z,t)\,\partial_z + \partial_t\Big)\mathcal{R}(z,t) &= \mathcal{G}\,\frac{\partial\mathcal{R}_0(z-\mathcal{G}t)}{\partial z} + \frac{\partial\mathcal{R}_0(z-\mathcal{G}t)}{\partial t}\\ &= \left(\mathcal{G} - \mathcal{G}\frac{\partial\mathcal{G}}{\partial z}t - \frac{\partial\mathcal{G}}{\partial t}t - \mathcal{G}\right)\mathcal{R}_0'(z-\mathcal{G}t)\end{aligned}$$

$$= -\mathcal{R}_0'(z - \mathcal{G}t)\, t\, \underbrace{\left[\frac{\partial \mathcal{G}}{\partial t} + \mathcal{G}\frac{\partial \mathcal{G}}{\partial z}\right]}_{=0,\ \text{Burgers' equation}} = 0,$$

which proves, that (1.106) is a solution. With these solutions, we can, under certain conditions, compute the eigenvalue density of M and the shape of its eigenvectors.

1.4 Eigenvector overlap

In the last section of chapter 1 we connect the resolvent to the eigenvectors of the underlying matrix composed of the initial matrix and the random perturbation matrix. Here, the diagonal elements of the resolvent are proportional to the squared absolute value of the overlap of perturbed and unperturbed eigenvectors with the proportionality constant given by the density of states (DOS) of the perturbed matrix multiplied by π. The equation of Allez and Bouchaud [179] determines the diagonal elements of the resolvent given a GOE or GUE perturbation. This is extended by the equation of Casati and Girko [182], which generalizes the perturbation matrix to the case of a random banded matrix. Both equations allow to extract the eigenvector overlap in their respective scenario.

1.4.1 Eigenvector percolation

We first show how the solution for the resolvent in (1.106) can be used to obtain information about the eigenvectors of a Hermitian matrix $M = A + X_t$, where A can be any Hermitian matrix with the eigenbasis $A\,|\phi_j\rangle = a_j\,|\phi_j\rangle$ and the eigenvalue density $\rho_0(a) = \frac{1}{N}\mathbb{E}\left[\sum_j \delta(a - a_j)\right]$. The full eigenbasis to M is given by $M\,|\psi_j\rangle = \lambda_j\,|\psi_j\rangle$ and the normalized eigenvalue density by $\rho_t(\lambda)$. The resolvent can be represented in terms of the outer products of its eigenvectors,

$$R(z) = \frac{1}{z\,\mathbb{1} - M} = \sum_k \frac{1}{z - \lambda_l}\,|\psi_l\rangle\,\langle\psi_l|\,. \tag{1.107}$$

In the following, we will represent the matrix elements of the resolvent in terms of the unperturbed basis of eigenvectors of A,

$$R_{ij}(z) \equiv \langle\phi_i|R(z)|\phi_j\rangle = \sum_l \frac{1}{z - \lambda_l}\,\langle\phi_i|\psi_l\rangle\,\langle\psi_l|\phi_j\rangle \tag{1.108}$$

with the diagonal entries equating to

$$R_{ii}(z) = \sum_l \frac{|\,\langle\phi_i|\psi_l\rangle|^2}{z - \lambda_l}. \tag{1.109}$$

We define the overlap as

$$\chi_{il} \equiv |\,\langle\phi_i|\psi_l\rangle|^2 \tag{1.110}$$

and its expectation value as

$$\mathcal{X}_{il} \equiv \mathbb{E}\left[\chi_{il}\right] = \mathbb{E}\left[|\,\langle\phi_i|\psi_l\rangle|^2\right]. \tag{1.111}$$

If we apply the Dirac identity (1.48) with $z \to \lambda - i0^+$ to the diagonals of the resolvent in Eq. (1.109) approaching the real axis from below and take the imaginary part with $\frac{1}{\pi}\Im\mathrm{m}\,(..)$ on both sides of the equation, we obtain

$$\frac{1}{\pi}\Im\mathrm{m}\,\left(R_{ii}(\lambda - i0^+)\right) = \sum_l |\,\langle\phi_i|\psi_l\rangle|^2\,\delta(\lambda - \lambda_l). \tag{1.112}$$

To extract the overlap χ_{il} from that equation, we introduce the function

$$\Gamma_l \equiv \int_{-\infty}^{\frac{\lambda_l+\lambda_{l+1}}{2}} \mathrm{d}\lambda \sum_k |\langle\phi_i|\psi_k\rangle|^2\, \delta(\lambda-\lambda_k) = \sum_{k=1}^{l} |\langle\phi_i|\psi_k\rangle|^2, \tag{1.113}$$

which sums up all eigenvector overlaps up to the state l while assuming the eigenvalue ordering $\lambda_l < \lambda_{l+1}$. Then the specific eigenvector overlap for the state l can be obtained through a difference of Γ_l and Γ_{l-1} as

$$\begin{aligned} \mathcal{X}_{il} &= \mathbb{E}\left[|\langle\phi_i|\psi_l\rangle|^2\right] = \mathbb{E}\left[\Gamma_l - \Gamma_{l-1}\right] \\ &= \mathbb{E}\left[\int_{\frac{\lambda_l+\lambda_{l-1}}{2}}^{\frac{\lambda_{l+1}+\lambda_l}{2}} \mathrm{d}\lambda \sum_k |\langle\phi_i|\psi_k\rangle|^2\, \delta(\lambda-\lambda_k)\right]. \end{aligned} \tag{1.114}$$

We can now use (1.112) to insert the left hand side into (1.114) in the integral and obtain

$$\begin{aligned} \mathcal{X}_{il} &= \mathbb{E}\left[\int_{\frac{\lambda_l+\lambda_{l-1}}{2}}^{\frac{\lambda_{l+1}+\lambda_l}{2}} \mathrm{d}\lambda\, \frac{1}{\pi}\Im\mathrm{m}\,\left(R_{ii}(\lambda - i0^+)\right)\right] \\ &= \mathbb{E}\left[\int_{\frac{\lambda_l+\lambda_{l-1}}{2}}^{\frac{\lambda_{l+1}+\lambda_l}{2}} \mathrm{d}\lambda\right] \frac{1}{\pi}\Im\mathrm{m}\,\left(\mathcal{R}_{ii}(\lambda_l - i0^+)\right) \\ &= \mathbb{E}\left[\frac{\lambda_{l+1}-\lambda_{l-1}}{2}\right] \frac{1}{\pi}\Im\mathrm{m}\,\left(\mathcal{R}_{ii}(\lambda_l - i0^+)\right). \end{aligned} \tag{1.115}$$

In the second line, we used that the integral covers only the single eigenvalue λ_l and we can effectively pull the resolvent out of the integral, by assuming that $\mathcal{R}_{ii}(z) = \mathbb{E}\left[R_{ii}(z)\right]$ is constant in this small energy interval. The resolvent is then evaluated at the discrete eigenvalue point λ_l. The expectation value of the eigenvalue difference in (1.115) is equal to the average energy spacing at the level λ_l and therefore given by the inverse DOS with

$$\mathbb{E}\left[\frac{\lambda_{l+1}-\lambda_{l-1}}{2}\right] = \frac{1}{N\rho_t(\lambda_l)}. \tag{1.116}$$

We hence find the important relation that connects the eigenvector overlap of the full eigenstates of M with the unperturbed eigenstates of A to the resolvent with

$$\mathcal{X}_{il} = \mathbb{E}\left[\chi_{il}\right] = \mathbb{E}\left[|\langle\phi_i|\psi_l\rangle|^2\right] = \frac{1}{\pi N\rho_t(\lambda_l)}\Im\mathrm{m}\,\left(\mathcal{R}_{ii}(\lambda_l - i0^+)\right), \tag{1.117}$$

which is valid for any N. Since $\mathcal{R}_{ii}(\lambda_l - i0^+)$ can be written as a continuous function $\mathcal{R}(a,\lambda)$ that is evaluated at the points $a = a_i$ and $\lambda = \lambda_l$, we infer that we can take the continuum limit for the overlap as well,

$$\mathbb{E}\left[|\langle\phi_i|\psi_l\rangle|^2\right] = \mathcal{X}_{il} = \mathcal{X}(a_i, \lambda_l) \tag{1.118}$$

with the continuous function $\mathcal{X}(a,\lambda)$ evaluated at the points $a = a_i$ and $\lambda = \lambda_l$.

1.4.2 Equation by Allez and Bouchaud

In the following, we employ equation (1.117) to find an explicit formula for the overlap $|\langle\phi_i|\psi_l\rangle|^2$ as a function of the unperturbed eigenvalues a_i and the full eigenvalues λ_l. For this, we use a perturbation matrix X_t, which is a GUE with

$$X_{ii} = \frac{1}{\sqrt{N}}\, B_{ii}(t), \tag{1.119a}$$

$$X_{ij} = \frac{1}{\sqrt{2N}}\left(B'_{ij}(t) + iB''_{ij}(t)\right) \tag{1.119b}$$

and $B_{ii}(t)$, $B'_{ij}(t)$, $B''_{ij}(t)$ are Brownian motions with variance t, drawn from $\mathcal{N}(0,t)$. We therefore have $\mathbb{E}[|X_{ij}|^2] = \frac{t}{N}$ and $\tau(X^2) = t$. In Sec. 1.3.3, we analyzed this scenario with RMT and found the solution (1.106) to the SDE of the resolvent in Eq. (1.100) with the initial condition $R_0 = (z\,\mathbb{1} - A)^{-1}$. The solution reads [156]

$$\mathcal{R}(z) = \mathcal{R}_0(z - \mathcal{G}(z)t) = \frac{1}{(z - t\,\mathcal{G}(z))\,\mathbb{1} - A}. \tag{1.120}$$

In the eigenbasis of A, the diagonal of the resolvent at $z = \lambda_l - i0^+$ is given by

$$R_{ii}(\lambda_l - i0^+) = \frac{1}{\lambda_l - i0^+ - t\,\mathcal{G}(\lambda_l - i0^+) - a_i} = \frac{1}{\lambda_l - a_i - \pi t\,\mathcal{H}[\rho_t](\lambda_l) - i\,\pi t\,\rho_t(\lambda_l)}, \tag{1.121}$$

where we inserted the complex value of the Stieltjes transform upon applying the Dirac identity at $\lambda_l - i0^+$ formulated in Eq. (1.59). We then use (1.117) and obtain the final result [170, 179]

$$\mathcal{X}(a_i,\lambda_l) = \mathbb{E}\left[|\langle\phi_i|\psi_l\rangle|^2\right] = \frac{1}{\pi N\rho_t(\lambda_l)}\,\mathfrak{Im}\,(\mathcal{R}_{ii}(\lambda_l)) = \frac{t}{N}\,\frac{1}{\left(\lambda_l - a_i - \pi t\,\mathcal{H}[\rho_t](\lambda_l)\right)^2 + \left(\pi t\,\rho_t(\lambda_l)\right)^2}. \tag{1.122}$$

We call this the equation by Allez and Bouchaud [179], as they mathematically derived this result with the use of RMT. If the DOS of the full perturbed system is known, one can compute the shape of the overlap curve χ_{il}. This is a significant result, since we do not need to resort to the explicit eigenvector equation, but it suffices to know the eigenvalue distribution of the random matrix in question. The eigenvector overlap $\mathcal{X}_{il}$ in terms of the unperturbed basis a_i is given by a Lorentzian $f(a; a_0, \gamma)$ with the peak position at $a_0 = \lambda_l - \pi t\,\mathcal{H}[\rho_t](\lambda_l)$ and the width $\gamma = \pi t\,\rho_t(\lambda_l)$. The Lorentzian is normalized, such that a summation over either i or l of the overlap $\mathcal{X}_{il}$ will provide one, as required from completeness of the basis. Note, that we required the perturbation matrix X_t to be a GUE with identical variance $\frac{t}{N}$ for all elements throughout the matrix. In the following, we loosen this constraint and allow for an element-dependent variance.

1.4.3 Equation by Casati and Girko

In previous sections, we considered $M = A + X_t$ with A being an arbitrary $(N \times N)$ Hermitian matrix with eigenvalue density $\rho_0(a)$ and X_t being a GUE of variance t. In the following, we loosen the latter constraint and consider X_t to be a random band matrix [180, 181], where each matrix element X_{ij} carries a variance of $\frac{t}{N} \cdot \sigma_{ij}^2$. It is therefore defined through

$$X_{ii} = \frac{\sigma_{ii}}{\sqrt{N}}\, B_{ii}(t), \tag{1.123a}$$

$$X_{ij} = \frac{\sigma_{ij}}{\sqrt{2N}}\left(B'_{ij}(t) + i\,B''_{ij}(t)\right) \tag{1.123b}$$

for $i < j$, where $B_{ii}(t), B'_{ij}(t), B''_{ij}(t) \sim \mathcal{N}(0,t)$ are independent Brownian motions of variance t. As X_t is Hermitian, we have $X_{ji} = X^*_{ij}$. We require the variance model σ^2_{ij} to be normalized, such that the variance of X_t is equal to t, as it was for the GUE case. This is fulfilled if

$$\sum_{i=1}^{N} \sigma^2_{ij} \frac{t}{N} = t = \sum_{j=1}^{N} \sigma^2_{ij} \frac{t}{N}, \tag{1.124}$$

where the sum over the variance in any row or column of X_t is normalized to t analogous to the GUE perturbation. Although the SDE describing the evolution of eigenvectors and eigenvalues in such a system remains elusive, Casati and Girko [182] as well as Shlyakthenko [183] provide an equation to evaluate the eigenvector overlap. Instead of the Stieltjes transform, which is the trace of the resolvent, we now consider an average of the diagonal of the resolvent $\mathcal{R}(z)$ weighted by the variance model σ^2_{ij},

$$\tilde{\mathcal{G}}_i(z) \equiv \sum_{\substack{j=1\\(j\neq i)}}^{N} \sigma^2_{ij} \mathcal{R}_{jj}(z) \tag{1.125}$$

for each $i = 1, \ldots, N$. Eq. (1.125) does not contain the diagonal element σ^2_{ii} of the variance model. Note, that we work in the unperturbed eigenbasis of A, where the diagonal elements of the resolvent are $\mathcal{R}_{jj}(z)$. The weighted trace $\tilde{\mathcal{G}}_i(z) = \tilde{\mathcal{G}}'_i(z) + i\,\tilde{\mathcal{G}}''_i(z)$ replaces the Stieltjes transform in previous formulas with the analogue of (1.120) given by

$$\mathcal{R}_{ii}(z) = \frac{1}{z - a_i - t\,\tilde{\mathcal{G}}_i(z)}. \tag{1.126}$$

From there, the eigenvector overlap is obtained as

$$\mathcal{X}(a_i, \lambda_l) = \mathbb{E}\left[|\langle\phi_i|\psi_l\rangle|^2\right] = \frac{1}{\pi N \rho(\lambda_l)} \frac{t\,\tilde{\mathcal{G}}''_i(\lambda_l)}{\left(\lambda_l - a_i - t\,\tilde{\mathcal{G}}'_i(\lambda_l)\right)^2 + \left(t\,\tilde{\mathcal{G}}''_i(\lambda_l)\right)^2}, \tag{1.127}$$

where we used the connection of the overlap to the resolvent in Eq. (1.117) and the Dirac identity in (1.48). In the limit, where X_t is a GUE with $\sigma^2_{ij} = 1$, we recover the equation of Allez and Bouchaud in (1.122). The real and imaginary part of $\tilde{\mathcal{G}}$ are connected by the negative Kramers-Kronig relations from (1.56a,b) due to $z \to \lambda - i0^+$,

$$\tilde{\mathcal{G}}'_i(\lambda_l) = \frac{1}{\pi} ⨍ \frac{\tilde{\mathcal{G}}''_i(\lambda_l)}{\lambda - \lambda_l}\,\mathrm{d}\lambda = \mathcal{H}[\tilde{\mathcal{G}}''_i](\lambda_l). \tag{1.128}$$

The two complex valued equations connecting $\mathcal{R}_{ii}$ and $\tilde{\mathcal{G}}$ in (1.125) and (1.126) can be combined to a recursive equation for either $\tilde{\mathcal{G}}$ or $\mathcal{R}_{ii}$, which reads

$$\mathcal{R}_{ii}(z) = \frac{1}{z - a_i - t \sum\limits_{\substack{j\\(j\neq i)}} \sigma^2_{ij} \mathcal{R}_{jj}(z)}, \tag{1.129}$$

which is now a self-consistency equation, which couples all the diagonal elements of the resolvent $\mathcal{R}_{ii}(z)$. We refer to (1.129) as the equation by Casati and Girko [182], where it first appeared. After finding its solution, we can compute the eigenvector overlap by the connection to the imaginary part of the resolvent in (1.117). Eq. (1.129) is significantly more complicated than it was the case for the GUE perturbation X_t in (1.122). Depending on the shape of the variance model σ_{ij}^2, it might not be possible to find an exact solution analytically. Nevertheless, one can obtain a numerical solution iteratively, which is arbitrarily close to the exact solution, depending on the numerical precision and the number of iteration steps.

Setup and Hamiltonian

2.1 The quantum system and its Hamiltonian

In our work [3], on which we report in this thesis, we study the thermalization of eigenstates and the resulting eigenstate distribution in an equilibrium phase of a closed quantum system. The system shall be of generic nature, such that the results are applicable to a wide array of quantum setups and encapsulate their general and shared universal properties. For this purpose, we design the system, such that it is not integrable and does not contain any spatial or other symmetries, such as time reversal symmetry, which could potentially feature degeneracies in the energy spectrum. To analyze the properties of such a quantum system, we employ the technique of *exact diagonalization (ED)*, where we set up the Hamiltonian as a matrix with the dimensionality of the underlying Hilbert space and numerically diagonalize it with the FEAST eigensolver [192] in order to find its eigenstates and corresponding eigenvalues. In further postprocessing of the eigenstates, we compute overlaps of eigenstates as detailed in chapter 4 and the reduced density matrix of subsystems of the quantum system described in chapter 5.

2.1.1 General setup

To investigate the thermalization properties analytically, we employ the results of RMT and thereby determine analytical predictions and formulas for the behavior of the quantum system. Those are then checked and compared to the numerical analysis. This way, we achieve a mutual consistency of analytical and numerical results which enables us to investigate and interpret the physical properties following from the results. To investigate generic features of thermalization, the quantum system under consideration consists of random interactions between individual particles. For our purposes, we consider a two dimensional spin lattice of d lattice sites where we place a spin-$\frac{1}{2}$ particle on each site. The Hamiltonian shall consist of random many-body interaction terms between the spin-$\frac{1}{2}$ particles and of a random local magnetic field, which provides an on-site energy to each spin configuration. By choosing different prefactors for all possible spin-spin interaction terms, we further avoid to implement a global SU(2) symmetry, which would induce a spin multiplet structure leading to degeneracies in the energy spectrum. The $\mathbb{Z}_2$ spin flip symmetry and the time reversal symmetry are broken by the magnetic on-site terms. The local basis of the lattice contains two states, $|\uparrow\rangle = (1,0)^\top$ and $|\downarrow\rangle = (0,1)^\top$, which are labeled spin-up and spin-down respectively. Those are eigenstates of the spin-S^z operator, which is the third component of the spin vector operator

$$\mathbf{S} = \frac{1}{2}\boldsymbol{\sigma}, \tag{2.1}$$

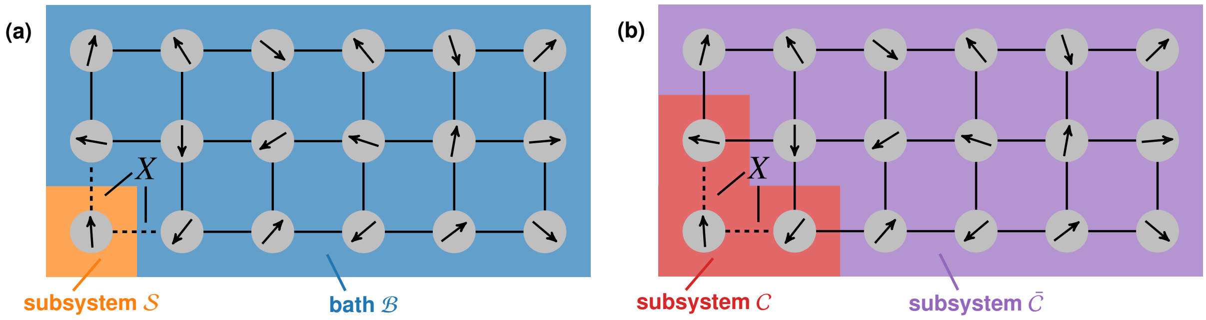

Figure 2.1: Two-dimensional spin lattice with a total of $d_{\mathcal{F}} = 18$ sites. We implement random nearest neighbor spin-spin interactions denoted by the solid lines connecting the spins on the lattice sites. On each site, there are additional random on-site magnetic fields indicated by the gray circles. **(a)** Subsystem $\mathcal{S}$ in orange is a single site on the corner of the lattice, while the remaining part of the spin lattice is called the bath $\mathcal{B}$ colored in blue. The perturbation X connects the subsystem $\mathcal{S}$ to the bath through weak interactions symbolized by dashed lines. The second moment of X is small compared to the second moment of $H^{\mathcal{S}}$ and $H^{\mathcal{B}}$. **(b)** Subsystem C is defined as the region of the spin lattice where X acts and marked in red, while the remaining subsystem $\bar{C}$ is colored in purple.

where $\hbar = 1$ and $\boldsymbol{\sigma}$ is the vector of Pauli matrices, $\boldsymbol{\sigma} = (\sigma^1, \sigma^2, \sigma^3)^\top$. Together with the (2×2) unit matrix σ^0, the Pauli matrices form a basis for (2×2) Hermitian matrices.

We demand that the Hamiltonian of the system is local. To fulfill this constraint, we restrict the interaction to involve only two spins at once and limit their real-space range to nearest neighbor terms only, the notion of which is stated more precisely in the next subsection. In order for the spin lattice to describe a generic quantum system, we establish a construction, where each interaction term between two spins consists of all possible combinations of σ^0 and the Pauli matrices on the respective sites. This way, it is possible to generate a random (4×4) interaction term exhausting all degrees of freedom (DOF) and allowing for scattering between all of the four states obtained for the two involved spins. The underlying spin structure therefore mainly serves as a way of constructing the random Hamiltonian and its eigenstates, whose properties are then decoupled from the spin nature of the quantum system.

2.1.2 The lattice structure and its subsystems

As detailed in the previous subsection, we create a random Hamiltonian on a two-dimensional spin lattice with a spin-$\frac{1}{2}$ particle on each lattice site. Due to the constraint of locality, we choose to limit the type of interaction terms to involve only two spins at once. The underlying lattice is a square lattice with local nearest neighbor connections, which couple the nearest spins in $\pm x-$ as well as $\pm y-$direction, as depicted in Fig. 2.1. A random number is attached to each of the individual two-body interaction terms. The local magnetic field, which is subject to each individual spin is randomized throughout the lattice with independent random numbers. As we investigate the properties of subsystems within the full quantum system, we choose the connections to be those of *open boundary conditions (OBC)*, where opposing boundaries of the lattice remain uncoupled to each other. With this choice, locality is preserved throughout the whole system and it is natural to separate out and define one part of the lattice as a distinct subsystem.

The full quantum system (label $\mathcal{F}$) as a whole is isolated and consequently does not allow for the exchange of information with the environment, e.g. in the form of matter or energy. We are interested in the reduced density matrix of a small subsystem (label $\mathcal{S}$) of it. Within this thesis, $\mathcal{S}$ typically consists a single spin and is then described by a Hilbert space of two states. The remaining part of the quantum system, which is not $\mathcal{S}$ is called the bath (label $\mathcal{B}$). $\mathcal{S}$ and $\mathcal{B}$ are mutually distinct and combine to the full system $\mathcal{F}$. Each subsystem is described by a Hamiltonian, which only acts within its denoted region and does not contain interaction terms between the two subsystems. In a preliminary analysis, we investigate the effects of a small local perturbation on the whole quantum system without separating out a small subset. In this scenario, we call the unperturbed setup the bath $\mathcal{B}$ and the perturbed one the full system $\mathcal{F}$. Such a configuration enables us to investigate the effects of a local perturbation on the large bath and how a local operator in general decomposes in terms of the energy basis. Depending on wether we separate out $\mathcal{S}$ or not, we consider two cases called *single peak model* and *multi peak model*, which are investigated individually.

In the single peak model, there is no subsystem $\mathcal{S}$ and the Hilbert space of $\mathcal{B}$ is identical to that of $\mathcal{F}$. Here, we model a setup, where the bath $\mathcal{B}$ is subjected to a small perturbation X and we evaluate the behavior of the perturbed eigenstates of the full system $\mathcal{F}$. The perturbation only acts on a partial region of the whole lattice, which is labeled by C. Similar to the Hamiltonian of $\mathcal{B}$, X contains interaction terms between nearest neighbors in the region C, which is typically two or three lattice sites. Accordingly, the full Hamiltonian is the sum of that of $\mathcal{B}$ and the perturbation X. In chapter 4, we analyze the overlaps between unperturbed eigenstates of $\mathcal{B}$ and $\mathcal{F}$, which give rise to a single peak.

In the multi peak model, we consider two distinct subsystems $\mathcal{S}$ and $\mathcal{B}$ of the total system $\mathcal{F}$, which are coupled by a small perturbation X. We investigate the decomposition of eigenstates of the full quantum system in terms of contributions for eigenstates of $\mathcal{S}$ and $\mathcal{B}$. In the following, we consider $\mathcal{S}$ to consist of a single lattice site in the multi peak model, which is located at the corner of the lattice, such that it carries the minimum amount of connections to other lattice sites. This is pictured in Fig. 2.1**a** with subsytem $\mathcal{S}$ in orange and the bath $\mathcal{B}$ in blue for a total lattice of $d_{\mathcal{F}} = 18$ sites. In the multi peak model, the full Hamiltonian can be split into three parts, one for each subsystem $\mathcal{S}$ and $\mathcal{B}$ and one for the interaction term X between them. The region of the lattice, where the small perturbation X acts is labeled by C. It contains only the lattice sites directly adjacent to the boundary between $\mathcal{S}$ and $\mathcal{B}$, which are those whose couplings are cut off with the separation into the two subsystems. This is depicted in Fig. 2.1**b** for the same configuration as in Fig. 2.1**a**. The three Hamiltonians $H^{\mathcal{S}}$, $H^{\mathcal{B}}$ and the perturbation X act on different, but not mutually distinct parts of the lattice. The overlaps between eigenstates of $\mathcal{F}$ and the unperturbed product eigenstates of $\mathcal{S}$ and $\mathcal{B}$ give rise to multiple peaks caused by the nontrivial internal eigenstate structure of $\mathcal{S}$.

In an analogous procedure, the full system can alternatively be split into different contributions, which are C, $\bar{C}$ and the interaction between the two. Here, $\bar{C}$ marks those lattice sites, which are not contained in C and the interaction between the two again acts on lattice sites directly adjacent to their boundary. While in the multi peak model with one lattice site in $\mathcal{S}$, the subsystem C involves the whole of $\mathcal{S}$ and a small part of $\mathcal{B}$, it is a subsystem of $\mathcal{B}$ itself in the single peak model. This distinction is helpful in the analysis of the variance model, which characterizes the perturbation X and its action on the whole unperturbed eigensystem as a consequence of its interaction terms in C.

2.1.3 The Hamiltonian

The Hilbert space of the full quantum system $\mathcal{H}^{\mathcal{F}}$ consists of a spin-$\frac{1}{2}$-degree of freedom on each of the d lattice sites, which individually produce a two-state Hilbert space $\mathcal{H}^{\frac{1}{2}}$ of spin-up and spin-down. Then

$$\mathcal{H}^{\mathcal{F}} = \underbrace{\mathcal{H}^{\frac{1}{2}} \otimes \mathcal{H}^{\frac{1}{2}} \otimes \cdots \otimes \mathcal{H}^{\frac{1}{2}}}_{\text{d times}} \tag{2.2}$$

with a dimensionality of $N = N_{\mathcal{F}} = 2^d$. In analogy, this holds for any subsystem of $\mathcal{F}$, where d must be replaced by the number of lattice sites in the corresponding subsystem given by $d_{\mathcal{S}}, d_{\mathcal{B}}, d_C$ and $d_{\bar{C}}$ for $\mathcal{S}$, $\mathcal{B}$, C and $\bar{C}$ respectively. Correspondingly, the number of states in the subsets are given by $N_{\mathcal{S}} = 2^{d_{\mathcal{S}}}, N_{\mathcal{B}} = 2^{d_{\mathcal{B}}}, N_C = 2^{d_C}$ and $N_{\bar{C}} = 2^{d_{\bar{C}}}$. Since the combinations of $\mathcal{S}$ and $\mathcal{B}$ or C and $\bar{C}$ constitute the whole system, it must hold that $d = d_{\mathcal{S}} + d_{\mathcal{B}} = d_C + d_{\bar{C}}$. The local real space basis of the Hilbert spaces is given by the product states of $|\uparrow\rangle$ or $|\downarrow\rangle$ on each lattice site in the system or subsystem.

The Hamiltonian of the quantum system is composed of random spin interactions. To generate a maximally random interaction between two spins, all possible terms are taken into account. For our spin-$\frac{1}{2}$ system, the interaction between the spins on sites i and j takes the form

$$H_{i,j} = \sum_{\alpha,\beta=1}^{3} J_{i,j}^{\alpha,\beta} S_i^\alpha \otimes S_j^\beta = \frac{1}{4} \sum_{\alpha,\beta=1}^{3} J_{i,j}^{\alpha,\beta} \sigma_i^\alpha \otimes \sigma_j^\beta \tag{2.3}$$

with the three Pauli matrices $\{\sigma_i^\alpha, \alpha = 1, 2, 3\}$ acting on site i. The symbol $\otimes$ denotes the tensor product between two operators. The on-site magnetic fields are defined as

$$H_i = \mathbf{h}_i \cdot \mathbf{S}_i = \frac{1}{2} \sum_{\alpha=1}^{3} h_i^\alpha \sigma_i^\alpha. \tag{2.4}$$

In this notation, we implicitly assume, that both the interaction term $\sigma_i^\alpha \otimes \sigma_j^\beta$ and the onsite term σ_i^α are enlarged to the full Hilbert space basis through the tensor product with identity matrices on each site not equal to i or j. Then H_i and $H_{i,j}$ are represented by matrices in terms of the *full local basis* of $\mathcal{H}^{\mathcal{F}}$. The real prefactors $J_{i,j}^{\alpha,\beta}$ of the spin-spin interactions in (2.3) are independent random coefficients drawn from a normal distribution with variance $(\sigma_{i,j}^{\alpha,\beta})^2$ and mean zero, $J_{i,j}^{\alpha,\beta} \sim \mathcal{N}(0, (\sigma_{i,j}^{\alpha,\beta})^2)$. Similarly, the on-site terms in (2.4) appear with variance $(\sigma_i^\alpha)^2, h_i^\alpha \sim \mathcal{N}(0, (\sigma_i^\alpha)^2)$.

We further define the *reduced basis* of any Hamiltonian H as the largest basis, in which H is not represented in a block diagonal form, i.e. where H is not further decomposable and all the identity terms on sites, where H does not act are removed. The reduced basis contains exactly all those spins, on which H acts and therefore has the smallest possible number of basis states to represent it. The identity term does not appear in either of the sums (2.3) and (2.4) such as to choose the full Hamiltonian to be traceless. Any additional unit matrix term merely adds a shift to the eigenvalues. The sum $H_{i,j} + H_i + H_j$, which contains all possible interaction and on-site terms for the sites i and j is represented by a traceless (4×4) random matrix in the reduced basis. While being Hermitian, it has complex entries and in total 15 real DOF, from which all matrix elements are determined. Within this construction, we can create a GUE by removing the prefactors of $\frac{1}{4}$ and $\frac{1}{2}$ in (2.3) and (2.4) and adding an identity term $g_0\mathbb{1}$ to account for the last DOF. On top of that, all variances must be chosen to be IID to obtain the GUE. Physically, the types of terms in (2.3) are spin-spin interactions, e.g. $\propto S^x \otimes S^y$ between the spin components on sites i and j, whereas the terms in (2.4) are on-site terms $\mathbf{h}_i \cdot \mathbf{S}$ mimicking a local on-site magnetic field of $\mathbf{h}_i = (h_i^1, h_i^2, h_i^3)^\top$ on lattice site i.

The Hamiltonian in subsystem $\mathcal{O}$ is given by the sum over all nearest-neighbor interactions of the type in (2.3) and over all on-site terms (2.4) of the lattice sites in $\mathcal{O}$ yielding

$$H^{\mathcal{O}} = \sum_{<i,j> \in \mathcal{O}} H_{i,j} + \sum_{i \in \mathcal{O}} H_i, \tag{2.5}$$

where $\mathcal{O} = \{\mathcal{S}, \mathcal{B}, \mathcal{C}, \bar{\mathcal{C}}\}$ can be any of the declared subsystems. $< \cdot, \cdot > \in \mathcal{O}$ denotes all nearest-neighbor type connections, that are contained in $\mathcal{O}$ to be summed over. If $d_{\mathcal{S}} = 1$ in the multi peak model, the subsystem Hamiltonian in $\mathcal{S}$ only contains a local magnetic field on the single site of subsystem $\mathcal{S}$ and no interaction terms.

In the multi peak model, we choose the interaction Hamiltonian between $\mathcal{S}$ and $\mathcal{B}$ as

$$X = \frac{1}{4} \sum_{<i,j>\in C} \left(\sum_{\alpha,\beta} J_{i,j}^{\alpha,\beta}\, \sigma_i^\alpha \otimes \sigma_j^\beta + \sum_{\alpha} \tilde{h}_i^\alpha\, \sigma_i^\alpha \otimes \mathbb{1}_j + \sum_{\beta} \tilde{h}_j^\beta\, \mathbb{1}_i \otimes \sigma_j^\beta + g_0\, \mathbb{1}_{4\times 4} \right), \tag{2.6}$$

where the set C contains lattice sites from both $\mathcal{S}$ and $\mathcal{B}$ along their boundary, which defines where X acts. It is indicated by the red region in Fig. 2.1**b**. $\mathbb{1}_i$ denotes a (2×2) unit matrix on site i. The couplings $H_{i,j}$ between $\mathcal{S}$ and $\mathcal{B}$ in X are not present in the unperturbed Hamiltonians $H^\mathcal{S}$ and $H^\mathcal{B}$ and are hence added as a perturbation trough X. The on-site terms in X are described by the terms $\tilde{H}_i$ for the corresponding lattice sites i, where similar on-site terms are already included in the unperturbed setup. We hence choose $\tilde{H}_i = \tilde{\mathbf{h}}_i \cdot \mathbf{S}_i$ to be form invariant to H_i, but with different random prefactors $\tilde{h}_i^\alpha \sim \mathcal{N}(0, (\tilde{\sigma}_i^\alpha)^2)$ independent of the random variables h_i^α contained in the unperturbed Hamiltonian. This way, $H^\mathcal{S}$, $H^\mathcal{B}$ and X are statistically independent. We further add a unit matrix term to X with a random prefactor $g_0 \sim \mathcal{N}(0, \sigma_0^2)$. It effects that for each link individually, X exhibits a total of 16 independent DOF, which exhausts the maximum DOF of this (4×4) Hermitian interaction matrix between the two sites. This way, we can explicitly tune the strength of all possible eigenstate scatterings in $\mathcal{S}$ under the action of X. Further owing to the construction of X in (2.6), by choosing all random prefactors $J_{i,j}^{\alpha\beta}$, $\tilde{h}_i^\alpha$, $\tilde{h}_j^\beta$, g_0 in X to be IID, we obtain a local (4×4) GUE perturbation on each individual link in X connecting $\mathcal{S}$ and $\mathcal{B}$. The full Hamiltonian is given by the sum of the subsystem Hamiltonians of $\mathcal{S}$ and $\mathcal{B}$ in (2.5) and the perturbation X in (2.6),

$$H^\mathcal{F} = H^\mathcal{S} + H^\mathcal{B} + X. \tag{2.7}$$

Recall, that we have enlarged the individual Hamiltonians to the local basis of the full quantum system, such that all terms have the same dimensionality and can be added up.

In the single peak model with $d_\mathcal{S} = 0$, i.e. where there is no subsystem $\mathcal{S}$, the set C on which X acts is defined as a small, connected local part of the bath $\mathcal{B}$. In the context of this work, we choose C to be either two or three sites. We choose

$$X = \sum_{<i,j>\in C} \tilde{H}_{i,j} = \frac{1}{4} \sum_{<i,j>\in C} \sum_{\alpha,\beta=1}^{3} \tilde{J}_{i,j}^{\alpha,\beta}\, \sigma_i^\alpha \otimes \sigma_j^\beta, \tag{2.8}$$

which involves only spin-spin interaction terms between the lattice sites in C. As those terms were already present in the unperturbed Hamiltonian $H^\mathcal{B}$, the prefactors of the terms in $\tilde{H}_{i,j}$ must be statistically independent of the prefactors of the terms present before the perturbation. This is ensured by drawing those from independent Gaussian distributions, $\tilde{J}_{i,j}^{\alpha,\beta} \sim \mathcal{N}(0, (\tilde{\sigma}_{i,j}^{\alpha,\beta})^2)$. As there is no $\mathcal{S}$, the subsystem Hamiltonian $H^\mathcal{S}$ is equal to the zero matrix. In contrast to the multi peak model, the single peak model merely features a Hamiltonian in the bath $\mathcal{B}$ and a perturbation matrix X added to that,

$$H^\mathcal{F} = H^\mathcal{B} + X. \tag{2.9}$$

Making use of the definitions of C and $\bar{C}$, we can split up the unperturbed Hamiltonian in a different manner with

$$H^{\mathcal{B}} + H^{\mathcal{S}} = H^{C} + H^{\bar{C}} + X^{C-\bar{C}} \tag{2.10}$$

for the multi peak model and

$$H^{\mathcal{B}} = H^{C} + H^{\bar{C}} + X^{C-\bar{C}} \tag{2.11}$$

for the single peak model. As H^{C} and $H^{\bar{C}}$ only contain interaction terms within their respective subsystems, the remaining terms make up their interaction $X^{C-\bar{C}}$. It consists of all and only those terms modulating an interaction between C and $\bar{C}$.

The eigensystems of the individual Hamiltonians are defined as follows,

$$H^{\mathcal{F}} \left|\psi_l^{\mathcal{F}}\right\rangle = \lambda_l \left|\psi_l^{\mathcal{F}}\right\rangle, l = 1, \ldots, N_{\mathcal{F}}, \tag{2.12a}$$

$$H^{\mathcal{S}} \left|\psi_\mu^{\mathcal{S}}\right\rangle = \epsilon_\mu \left|\psi_\mu^{\mathcal{S}}\right\rangle, \mu = 1, \ldots, N_{\mathcal{S}}, \tag{2.12b}$$

$$H^{O} \left|\psi_i^{O}\right\rangle = E_i^{O} \left|\psi_i^{O}\right\rangle, i = 1, \ldots, N_{O}, \tag{2.12c}$$

where O represents any of the subsystems $\mathcal{B}$, C, or $\bar{C}$. If it is clear from the context which state we are referring to, we omit the subsystem label.

The variance of an individual subsystem Hamiltonian can be readily computed to

$$\begin{aligned} Var(H^{O}) = m_2(H^{O}) = \tau\left((H^{O})^2\right) &= \frac{1}{16} \sum_{<i,j>\in D_O} \sum_{\alpha,\beta=1}^{3} \mathbb{E}\left[\left(J_{i,j}^{\alpha,\beta}\right)^2\right] + \frac{1}{4} \sum_{i\in D_O} \sum_{\alpha=1}^{3} \mathbb{E}\left[\left(h_i^{\alpha}\right)^2\right] \\ &= \frac{1}{16} \sum_{<i,j>\in D_O} \sum_{\alpha,\beta=1}^{3} \left(\sigma_{i,j}^{\alpha,\beta}\right)^2 + \frac{1}{4} \sum_{i\in D_O} \sum_{\alpha=1}^{3} \left(\sigma_i^{\alpha}\right)^2 \end{aligned} \tag{2.13}$$

as all mixed terms average to zero with the mean of all individual terms and of the total Hamiltonian being zero, $\tau(H^{O}) = 0$. The results states, that the total variance of H^{O} is simply given by the sum of variances of the individual terms in the Hamiltonian. In the following, we choose all variances within a single subsystem O to be equal, $\sigma_{i,j}^{\alpha,\beta} = \sigma_i^{\alpha} = s_O$, which means that the prefactors of all terms in the subsystem Hamiltonian are IID. Accordingly, the result can be simplified to

$$m_2(H^{O}) = \left(\frac{9n_O}{16} + \frac{3d_O}{4}\right) s_O^2 \equiv w_O\, s_O^2, \tag{2.14}$$

where n_O denotes the number of nearest-neighbor connections between the d_O lattice sites in O. In (2.14), the last equality defines w_O as the scaling factor between the local variance of any individual term in the Hamiltonian H^{O} and its total variance. We further define

$$\sigma_O^2 \equiv m_2\left(H^{O}\right), \tag{2.15a}$$

$$t \equiv m_2\left(X\right), \tag{2.15b}$$

$$t_C \equiv m_2\left(X^{C-\bar{C}}\right), \tag{2.15c}$$

where $O = \{\mathcal{S}, \mathcal{B}, \mathcal{F}, C, \bar{C}\}$. Due to the independence of the constituents of H^O, the variance of the full Hamiltonian is given by the sum of variances of its sub-Hamiltonians, $\sigma_{\mathcal{F}}^2 = \sigma_{\mathcal{S}}^2 + \sigma_{\mathcal{B}}^2 + t$. An equivalent relation holds for the bath $\mathcal{B}$ itself, $\sigma_{\mathcal{B}}^2 = \sigma_C^2 + \sigma_{\bar{C}}^2 + t_C$. As stated above, we choose X to be a small perturbation, which connects the two subsystems $\mathcal{S}$ and $\mathcal{B}$ in the multi peak model or merely perturbs the bath in the single peak model. In mathematical terms, the variance of X must be much smaller than that of the bath Hamiltonian $H^{\mathcal{B}}, t \ll \sigma_{\mathcal{B}}^2$, such that it can be viewed as a perturbation to the system. Moreover, t must also be small enough as to not completely mix the eigenstates of $\mathcal{S}$, which is fulfilled, if t is smaller than the average energy spacing in $\mathcal{S}, t \lessapprox \sigma_{\mathcal{S}}^2$. On the other hand, t must be chosen large enough such that X mixes the states of $\mathcal{B}$, which implies, that $\sqrt{t}$ must be larger than the average energy spacing of $\mathcal{B}$. The latter statement is captured by the inequality $\sqrt{t} \gg \frac{\sigma_{\mathcal{B}}}{N_{\mathcal{B}}}$, where $\sigma_{\mathcal{B}}$ is proportional to the expected energy spectral width of $\mathcal{B}$ and divided by the number of states $N_{\mathcal{B}}$ to obtain an estimate of the average energy spacing. We notice, that according to (2.14), while the spectral width $\sigma_{\mathcal{B}}$ scales at most quadratically with the number of lattice sites $d_{\mathcal{B}}$, the number of states scales exponentially, $N_{\mathcal{B}} = 2^{d_{\mathcal{B}}}$. This implies, that the average energy spacing decreases exponentially with the number of lattice sites. With t held constant, larger lattices and especially the thermodynamic limit with $d_{\mathcal{B}} \to \infty$ provide a better agreement of both inequalities involving the bath $\mathcal{B}$.

2.1.4 Schmidt decomposition and reduced density matrix

Singular value decomposition. The *Schmidt decomposition* [208–210] describes a certain way of expressing a state in a Hilbert space with the property that it factorizes in terms of a tensor product of two Hilbert subspaces. Assume, that the Hilbert space of total dimension $N = N_1 \cdot N_2$ is separable into $\mathcal{H} = \mathcal{H}_1 \otimes \mathcal{H}_2$, where N_1 and N_2 are the dimensions of $\mathcal{H}_1$ and $\mathcal{H}_2$, respectively and $N_1 \leq N_2$ w.l.o.g.. By construction, for the full Hilbert space of the spin lattice quantum system in (2.2), such a partition is always possible when choosing the subsystems to be mutually exclusive sets of lattice sites.

The Schmidt decomposition is a restatement of the singular value decomposition (SVD) and both terms are used synonymously in the following. It states, that any state $|\psi\rangle$ of the full Hilbert space $\mathcal{H}$ can be represented as a superposition of N_1 product states of $\mathcal{H}_1$ with $\mathcal{H}_2$,

$$|\psi\rangle = \sum_{\alpha=1}^{N_1} \kappa_\alpha \, |\phi_\alpha^1\rangle \otimes |\phi_\alpha^2\rangle \,. \tag{2.16}$$

Here $\{|\phi_\alpha^1\rangle\}$ and $\{|\phi_\alpha^2\rangle\}$ are orthonormal sets of states in $\mathcal{H}_1$ and $\mathcal{H}_2$ respectively and called singular vectors of the state $|\psi\rangle$. Further, $\kappa_\alpha \in \mathbb{R}_0^+$ are the singular values, chosen real and non-negative by employing the phase gauge DOF of the singular vectors. Note, that in (2.16), the sum runs over N_1 terms only, which is equal to the dimension of the smaller Hilbert space $\mathcal{H}_1$.

To show this, consider complete orthonormal bases in the two partitions with $\{|\psi_i^1\rangle, i = 1, \ldots, N_1\}$ in $\mathcal{H}_1$ and $\{|\psi_j^2\rangle, j = 1, \ldots, N_2\}$ in $\mathcal{H}_2$. Any state in $\mathcal{H}$ can then be represented in terms of product basis states with coefficients $D_{ij} \in \mathbb{C}$,

$$|\psi\rangle = \sum_{i,j} D_{ij} \, |\psi_i^1\rangle \otimes |\psi_j^2\rangle = \sum_i \sqrt{\sum_j \left|D_{ij}\right|^2} \, |\psi_i^1\rangle \otimes \left(\frac{\sum_j D_{ij} \, |\psi_j^2\rangle}{\sqrt{\sum_j \left|D_{ij}\right|^2}} \right) \equiv \sum_{i=1}^{N_1} \tilde{\kappa}_i \, |\psi_i^1\rangle \otimes |\tilde{\psi}_i^2\rangle \,, \tag{2.17}$$

where $\tilde{\kappa}_i \equiv \sqrt{\sum_j \left|D_{ij}\right|^2}$. Note, that this representation of the state $|\psi\rangle$ is very similar to the SVD in (2.16), but the states $\{|\tilde{\psi}_i^2\rangle\}$ although normalized w.r.t the basis in $\mathcal{H}_2$ are not orthogonal to each other, which is the crucial point of the Schmidt decomposition. We can consider the $(N_1 \times N_2)$ coefficient matrix D with matrix elements D_{ij} as a representation of $|\psi\rangle$ in the orthonormal bases of $\mathcal{H}_1$ and $\mathcal{H}_2$. The SVD expresses, that there exists a $(N_1 \times N_1)$ unitary matrix U, a $(N_2 \times N_2)$ unitary matrix V and a positive semidefinite $(N_1 \times N_1)$ diagonal matrix K, such that

$$D = U \begin{pmatrix} K & 0 \end{pmatrix} V^\dagger \tag{2.18}$$

Here, $(K \quad 0)$ is a $(N_1 \times N_2)$ dimensional matrix with K being extended by zeros. If we split the rows of $V^\dagger$ into $V_1^\dagger$ and $V_2^\dagger$, where $V_1^\dagger$ contains the first N_1 rows, we obtain

$$D = U \begin{pmatrix} K & 0 \end{pmatrix} V^\dagger = U \begin{pmatrix} K & 0 \end{pmatrix} \begin{pmatrix} V_1^\dagger \\ V_2^\dagger \end{pmatrix} = U K V_1^\dagger = \sum_{\alpha=1}^{N_1} \kappa_\alpha \, \mathbf{u}_\alpha \mathbf{v}_\alpha^\dagger. \tag{2.19}$$

The vectors $\mathbf{u}_\alpha$ and $\mathbf{v}_\alpha$ are the first N_1 column vectors of the matrices U and V respectively. Those are the singular vectors and κ_α the singular values of the SVD. If we return to a basis independent representation of (2.19), we end up with the final result of the SVD in Eq. (2.16). Assuming the state $|\psi\rangle$ is normalized, the singular values κ_α^2 fulfill the sum rule

$$\sum_\alpha \kappa_\alpha^2 = 1. \tag{2.20}$$

Reduced density matrix. We can represent the expectation value of an operator O in the state $|\psi\rangle$ in terms of its density matrix

$$\langle\psi|O|\psi\rangle = \mathrm{Tr}\left(O \rho_\psi\right), \tag{2.21}$$

where ρ_ψ is the outer product of $|\psi\rangle$ with itself, $\rho_\psi := |\psi\rangle\langle\psi|$. Any density matrix ρ is normalized such that $\mathrm{Tr}(\rho) = 1$. It is called pure, if $\rho^2 = \rho$ and otherwise called mixed. Only a pure density matrix, which can be viewed as a projection onto a quantum state has purity one, $\mathrm{Tr}\left(\rho^2\right) = 1$. This is the case for the density matrix ρ_ψ.

If we are interested in local measurements on entangled states, we can reduce ρ to its essential information in the local subset. This means considering operators, which just act on a subset of the full Hilbert space $\mathcal{H} = \mathcal{H}_1 \otimes \mathcal{H}_2$, say $\mathcal{H}_1$. We define the reduced density matrix in $\mathcal{H}_1$ as

$$\rho_1 = \mathrm{Tr}_2\left(\rho_\psi\right). \tag{2.22}$$

$\mathrm{Tr}_1(..)$ and $\mathrm{Tr}_2(..)$ are the partial traces in $\mathcal{H}_1$ and $\mathcal{H}_2$, respectively. If O just acts in $\mathcal{H}_1$ nontrivially with $O = O_1 \otimes \mathbb{1}_2$, the expectation value can be simplified with the use of the reduced density matrix,

$$\langle\psi|O|\psi\rangle = \mathrm{Tr}\left(O \rho_\psi\right) = \mathrm{Tr}_1\left(\mathrm{Tr}_2\left(O_1 \otimes \mathbb{1}_2 \rho_\psi\right)\right) = \mathrm{Tr}_1\left(O_1 \rho_1\right), \tag{2.23}$$

where O_1 only acts in $\mathcal{H}_1$. The reduced density matrix carries information about the state $|\psi\rangle$ in the subsystem 1, but the full information of ρ is lost. In general, ρ_1 is not a pure density matrix anymore. After taking the trace over ρ_ψ in subsystem 2, its reduced form is only pure if $|\psi\rangle$ can be written as a tensor product of states in $\mathcal{H}_1$ and $\mathcal{H}_2$. Otherwise, it is a mixed density matrix. In the SVD basis of $|\psi\rangle$ in (2.16), the reduced density matrix ρ_ψ of the quantum state $|\psi\rangle$ is diagonal,

$$\rho_1 = \sum_\alpha (\kappa_\alpha)^2 \, |\phi^1_\alpha\rangle \, \langle\phi^1_\alpha| \,, \tag{2.24}$$

where κ_α are the singular values of $|\psi\rangle$. ρ_1 is a superposition of all the pure density matrices constructed from the singular states in $\mathcal{H}_1$, $\{\,|\phi^1_\alpha\rangle\}$, with singular values κ_α as coefficients.

2.2 Density of states

We analytically and numerically study the DOS for different matrix ensembles. As detailed in the following, the DOS of a Hamiltonian with local interactions significantly differs from that of a GUE matrix ensemble. While a Gaussian ensemble in the form of a GOE or GUE matrix features a semicircle law, the DOS of a locally interacting Hamiltonian follows the normal distribution in the infinite size limit.

2.2.1 Gaussian Unitary Ensemble

To derive the DOS of a GUE, we use Burger's equation in (1.91) with the solution obtained in Eq. (1.105) for the Stieltjes transform. For that, we assumed a perturbed matrix $M = A + X_t$ with a perturbation X_t of variance t. In this case, the initial condition of the Stieltjes transform is given by

$$\mathcal{G}(z,0) = \mathcal{G}_0(z) = \frac{1}{N}\sum_i \frac{1}{z - a_i}, \tag{2.25}$$

where $a_i \in \mathbb{R}, i = 1,\dots,N$ are the eigenvalues of the Hermitian $(N \times N)$ matrix A. We now consider the case $A = 0$, which means that M is equal to a GUE. The initial condition for the Stieltjes reduces to $\mathcal{G}_0(z) = \frac{1}{z}$ and its solution following the Burger's equation is given by

$$\mathcal{G}(z,t) = \frac{1}{z - t\,\mathcal{G}(z,t)}, \tag{2.26}$$

which can be rearranged as a quadratic equation for $\mathcal{G}$ reading

$$t\,\mathcal{G}(z,t)^2 - z\,\mathcal{G}(z,t) + 1 = 0. \tag{2.27}$$

The solution to this self-consistency equation for $\mathcal{G}$ is given by

$$\mathcal{G}(z,t) = \frac{z \pm \sqrt{z^2 - 4t}}{2t}, \tag{2.28}$$

where the ± corresponds to the two different branches of the square root, separated by a branch cut in the complex plane. To choose the correct sign of the root, we look at the behavior of the Stieltjes at $|z| \to \infty$. For the + sign, we have $\mathcal{G} \sim \frac{z}{t}$, whereas the − sign gives rise to the correct behavior of $\mathcal{G} \sim \frac{1}{z}$ for $|z| \to \infty$. We therefore consider the branch with the − sign. In Eq. (1.59) we found, under application of Dirac's identity in (1.48), that the imaginary part of the Stieltjes is connected to the eigenvalue density of the corresponding matrix. With this, we find the DOS of the GUE as

$$N\rho(\lambda) = \frac{N}{\pi}\Im\mathrm{m}\left(\mathcal{G}(\lambda - i0^+, t)\right) = \frac{N}{\pi}\Im\mathrm{m}\left(\frac{(\lambda - i0^+) - \sqrt{(\lambda - i0^+)^2 - 4t}}{2t}\right). \tag{2.29}$$

The imaginary part of the expression is only nonzero, if $|\lambda| \leq 2\sqrt{t}$, in which case we find

$$N\rho(\lambda) = \begin{cases} \frac{2N}{\pi R}\sqrt{1 - \left(\frac{\lambda}{R}\right)^2} & \text{for } |\lambda| \leq R, \\ 0 & \text{else,} \end{cases} \tag{2.30}$$

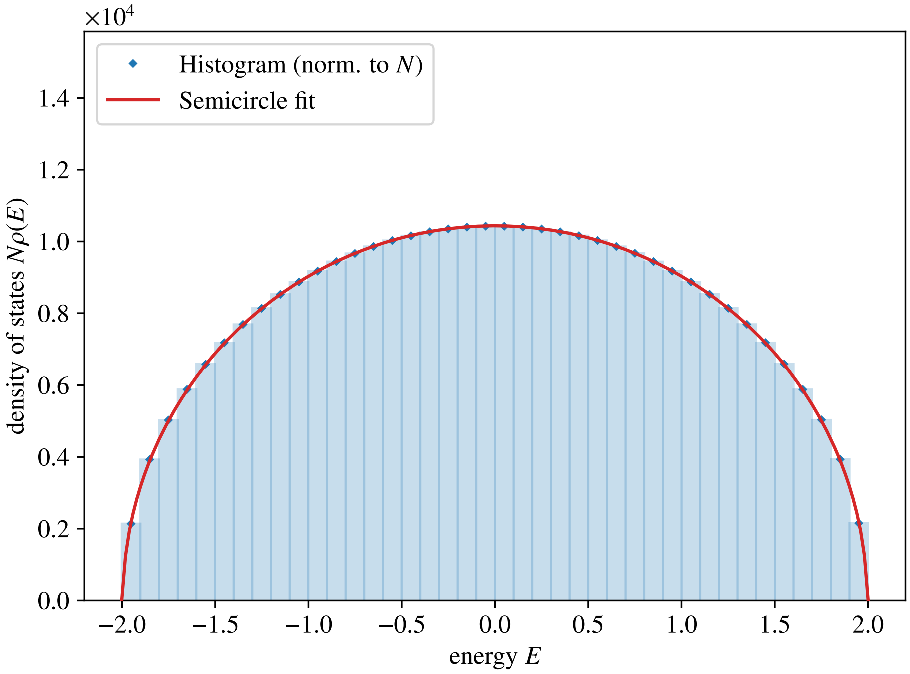

Figure 2.2: Averaged numerical DOS of 100 samples of a GUE with matrix dimension $N = 32768$ shown as blue points. We use the Freedman-Diaconis rule to select the number of bins in the histogram to $N_{\text{bins}} = 40$. A fit of a semicircle according to Eq. (2.30) through the data points is depicted as a red line and returns the radius $R = 1.998\,35(12)$, the area $\frac{A}{N} = 0.999\,49(11)$ and the center point $E_0 = 0.000\,02(11)$. The fit agrees with the numerical data.

for the GUE, where $R = 2\sqrt{t}$. This eigenvalue density is given by a semicircle [156], which is also known under the name of *Wigner's semicircle law* [157]. Wigner was the first to introduce RMT in a physical context [211, 212] to model the energy spacings in heavy atom nuclei [157, 158]. He conjectured that the level spacings resemble the statistics found in Gaussian random matrix ensembles, which was then experimentally verified [159]. The result can also be derived by considering the moments of the GUE matrix, which are given by

$$m_p^X = \tau\left(X_t^p\right) = \begin{cases} C_k\, t^k & \text{for } p = 2k \text{ (even)}, \\ 0 & \text{for } p = 2k+1 \text{ (odd)}. \end{cases} \tag{2.31}$$

C_k are called *Catalan numbers* and represent the number of noncrossing partitions of the set $\{1, \dots, k\}$ or equivalently the number of noncrossing pair partitions of the set $\{1, \dots, 2k\}$. From this it follows, that the Stieltjes transform can be written as

$$\mathcal{G}(z) = \sum_{k=0}^{\infty} \frac{C_k}{z^{2k+1}} t^{2k} \tag{2.32}$$

upon insertion of the moments into Eq. (1.23). $\mathcal{G}(z)$ returns the moment generating function of the eigenvalue density $\rho(\lambda)$ in (2.30). This approach leads to the same self-consistency equation as declared in Eq. (2.27). An alternative possibility to obtain (2.27) is the cavity method. There, we intend to find a relation between the Stieltjes transform of a GUE matrix of sizes N and $(N-1)$. We then use, that in the large N limit, both converge to the same limiting Stieltjes transform, which leads to the same self-consistency equation as in (2.27). In Fig. 2.2, we plot the DOS of a GUE of size $N = 2^{15} = 32768$ averaged over 100 samples obtained from a histogram of the eigenvalue data. A semicircle fit in red agrees with the numerical data. From the fit, we find, that the area $A \approx N$, as expected from the DOS, which is normalized to N.

2.2.2 Local Hamiltonian

Non-interacting system. Consider a local Hamiltonian of the construction in Sec. 2.1.3 containing only random on-site magnetic fields of the form in Eq. (2.4). The full Hamiltonian reads

$$H_{\text{non-int}} = \sum_{i=1}^{d} H_i, \tag{2.33}$$

where d is the number of sites in the spin lattice. This Hamiltonian is block diagonal and can be diagonalized by diagonalizing the (2×2) matrices on each lattice site, since the terms H_i act on different parts of the Hilbert space. Since all random prefactors of the on-site magnetic fields are independent, each eigenvalue λ of $H_{\text{non-int}}$ is given by a sum of eigenvalues λ_i of the on-site term H_i on each site,

$$\lambda = \sum_{i=1}^{d} \lambda_i. \tag{2.34}$$

Each λ_i can take two possible configurations $\pm|\lambda_i|$, which is symmetric around zero because we excluded the unit matrix term in H_i. It gives rise to a total of $N = 2^d$ possible eigenvalues λ, which is consistent with the size of $H_{\text{non-int}}$. The random prefactors of each Pauli matrix σ_i^α on site i in (2.4) are given by h_i^α and are drawn from normal distributions, $h_i \sim \mathcal{N}(0, (\sigma_i^\alpha)^2)$. Depending on the choice of the variances $(\sigma_i^\alpha)^2$, the eigenvalue λ_i of the random Hamiltonian on site i follows a probability distribution computed from the corresponding eigenvalue

$$\lambda_i = \pm\sqrt{\left(h_i^1\right)^2 + \left(h_i^2\right)^2 + \left(h_i^3\right)^2}. \tag{2.35}$$

Accordingly, $\{\lambda_1, \ldots, \lambda_i, \ldots\}$ is a sequence of independent random variables, each with mean zero, $\mu_i = 0$, and variance $\sigma_i^2 = \sum_\alpha (\sigma_i^\alpha)^2$. The total variance of the N-dimensional Hamiltonian of d sites is then given by $\sigma_d^2 = \sum_{i=1}^d \sigma_i^2$. Since the h_i^α are Gaussian distributed, the *Lindeberg condition* [213]

$$\lim_{d\to\infty} \frac{1}{\sigma_d^2} \sum_{i=1}^{d} \mathbb{E}\left[(\lambda_i)^2 1_{\{|\lambda_i| > \epsilon\sigma_d\}}\right] = 0 \tag{2.36}$$

for all $\epsilon > 0$ is satisfied. $1_{\{x\}}$ is the indicator function, which returns one, if the condition x is true and zero otherwise. The Lindeberg condition makes a statement on the tails of the individual distributions of the terms λ_i in the sum (2.34). Since the individual distributions are square integrable, by Lebesgue's dominated convergence theorem, expression (2.36) is fulfilled. Graphically, it means that the larger the system size d becomes, less of the real axis with $|\lambda_i| > \epsilon\sigma_d$ is integrated over and subsequently a smaller and smaller part of the tail is regarded. Since the tail of the distribution for λ_i falls off exponentially, the contribution of the tail for $|\lambda_i| > \epsilon\sigma_d$ goes to zero in the limit $d \to \infty$.

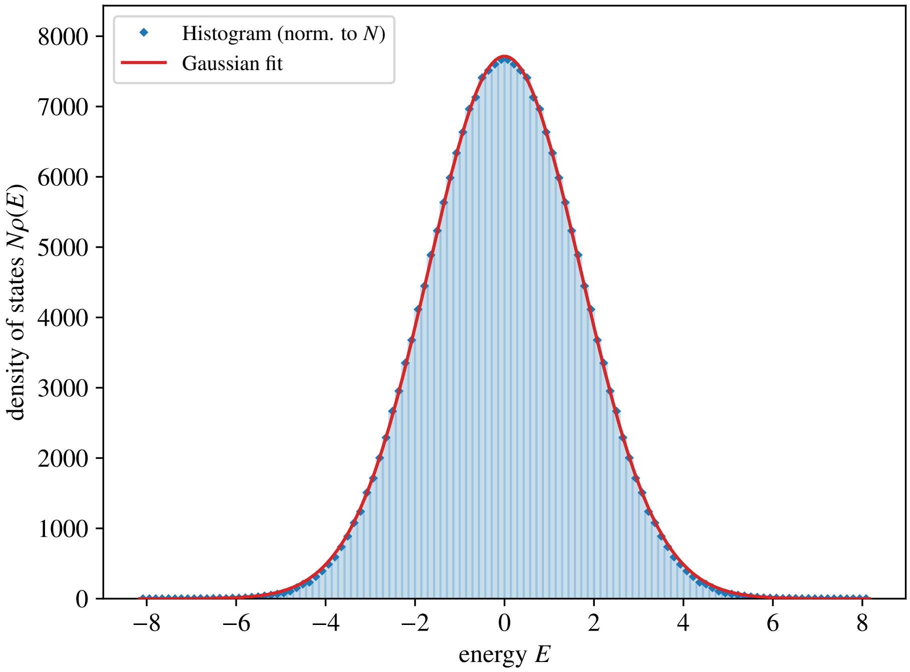

Figure 2.3: Numerical DOS of a spin-$\frac{1}{2}$ lattice of $d = 15$ sites with random local on-site magnetic fields on each site, but without interactions between the spins, according to the Hamiltonian in Eq. (2.33). The DOS is averaged over 100 samples and shown as blue dots. We use the Freedman-Diaconis rule to select the number of bins in the histogram to $N_{\text{bins}} = 98$. A fit of a Gaussian depicted in red returns the standard deviation $\sigma = 1.7009(20)$, the area $\frac{A}{N} = 1.0039(10)$ and the mean $E_0 = 0.0000(16)$. The Gaussian fit captures the shape of the DOS, with minor deviations at the boundary of the spectrum.

Additionally, the *Feller condition*

$$\lim_{d\to\infty} \max_{1\le i\le d} \left(\frac{\sigma_i^2}{\sigma_d^2} \right) = 0, \tag{2.37}$$

ensures, that the variance of any individual term in the sum for λ is asymptotically negligible. The Feller condition elevates the Lindeberg condition from a sufficient to a necessary condition for the central limit theorem to hold. The central limit theorem for the sequence $\{\lambda_1, \dots, \lambda_i, \dots\}$ then states, that the limiting form of the distribution for a properly normalized λ is the normal distribution,

$$\lim_{d\to\infty} \frac{1}{\sigma_d} \sum_{i=1}^{d} \lambda_i = \mathcal{N}(0, 1). \tag{2.38}$$

In Fig. 2.3, we show the DOS of a random Hamiltonian with local on-site magnetic fields on each site of a $d = 15$ spin lattice according to Eq. (2.33), where we choose all terms in $H_{\text{non-int}}$ to be IID with a variance of $s^2_{\text{non-int}} = \frac{1}{4}$. A Gaussian fit in red agrees with the numerical eigenvalue data obtained from 100 samples of the Hamiltonian $H_{\text{non-int}}$. We can insert $s_{\text{non-int}}$ into the equation of the second moment of the Hamiltonian in (2.14) and obtain $\sigma_{\text{non-int}} = 1.68$ for the square root of the second moment. The standard deviation obtained from the fit in Fig. 2.3 with $\sigma = 1.7009(20)$ is very close to that, where small corrections apply with the fit showing small deviations to the data towards the boundary of the spectrum due to the finite size of the lattice.

Interacting system: Moments and result. In a locally interacting spin system according to the construction in Sec. 2.1.3, the Hamiltonian consists of both local random on-site magnetic fields discussed in the previous subsection for the non-interacting Hamiltonian and additional random nearest neighbor spin-spin couplings through $H_{i,j}$ as introduced in Eq. (2.3). Despite the addition of spin-spin interactions, the DOS still remains Gaussian distributed, since all terms in the Hamiltonian are local. This was mathematically proven using a method that involves a variation of the central limit theorem [186, 187, 214]. We formulated an alternative proof [188], which relies on the moments of the Hamiltonian and is physically more intuitive. The central idea of this proof without claiming completeness is sketched in the following, while the detailed proof in full mathematical rigor can be read upon in [188]. In the following chapters, we then presume the Gaussian DOS.

The full interacting Hamiltonian under consideration is a combination of the two possible terms,

$$H_{\text{int}} = \sum_{<i,j>} J_{i,j}^{\alpha,\beta}\, \sigma_i^{\alpha} \otimes \sigma_j^{\beta} + \sum_i h_i^{\alpha}\, \sigma_i^{\alpha}, \tag{2.39}$$

where $< \cdot, \cdot >$ denotes nearest neighbor interactions between the sites $i, j = 1, \ldots, d$ in the spin lattice of d sites. Note, that in contrast to the previous definitions of the on-site magnetic fields in (2.4) and the interactions terms in (2.3), we omit all prefactors in front of the random variables in the following without loss of generality. Since all terms in the Hamiltonian have statistically independent prefactors, which are drawn from Gaussians with mean zero, the second moment of the Hamiltonian is computed to

$$\sigma_{\mathcal{B}}^2 = \tau\left(H_{\text{int}}^2\right) = \sum_{<i,j>} \sum_{\alpha,\beta=1}^{3} (\sigma_{i,j}^{\alpha,\beta})^2 + \sum_{i=1}^{d} \sum_{\alpha=1}^{3} (\sigma_i^{\alpha})^2. \tag{2.40}$$

which is equal to the matrix variance $\sigma_{\mathcal{B}}^2$, since the first moment of the Hamiltonian is zero. The total variance of H_{int} according to (2.40) is given by the sum of variances of all individual terms. If all variances of the individual terms are chosen to be equal and represented by σ_0^2, the variance simplifies to

$$\sigma_{\text{int}}^2 = L\sigma_0^2, \tag{2.41}$$

where L denotes the number of random terms in the Hamiltonian. Due to locality, L scales polynomially in the number of lattice sites d, while the Hilbert space dimension scales exponentially with d. Since the terms in (2.39) do not all mutually commute with each other, the commutators have to be taken into account in the computation of the exact expression for higher moments of H_{int}. We are however interested only in the leading order of L of the moments in order to find the behavior of the DOS in the large system size limit. To highest order of L, the $2p$-th moment is given by

$$m_{2p}(L) = \tau\left((H_{\text{int}})^{2p}\right) = \frac{(2p)^2}{2^p p!}(L\sigma_0^2)^p + O(L^{p-1}). \tag{2.42}$$

This highest order term given in (2.42) is equally obtained by setting all commutators, which appear in the computation, to zero. Since all spin-spin couplings and on-site magnetic fields act locally in the spin lattice, the only way a commutator can be nonzero is, if the terms in question involve the same sites in the lattice. As a consequence, the number of nonzero commutators is of lower order of L and do not appear in the highest order contribution in (2.42). In the limit of large lattices with $d \to \infty$, the leading order in L is the dominant contribution to the moments, while all other terms are negligible in comparison. If we normalize the second moment of the Hamiltonian to one with

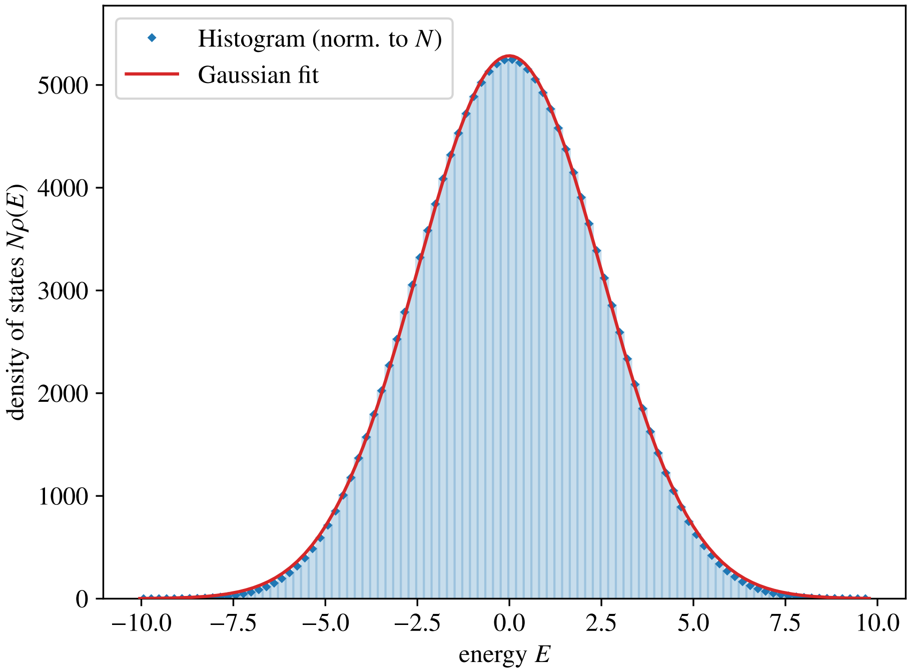

Figure 2.4: Numerical DOS of a two-dimensional spin-$\frac{1}{2}$ lattice of $d = 15$ sites with random local on-site magnetic fields on each site and random nearest neighbor spin-spin interactions, according to the Hamiltonian in Eq. (2.39). The DOS is averaged over 100 samples and shown as blue dots. We use the Freedman-Diaconis rule to select the number of bins in the histogram to $N_{\text{bins}} = 95$. A fit of a Gaussian depicted in red returns the standard deviation $\sigma = 2.4893(38)$, the area $\frac{A}{N} = 1.0063(13)$ and the mean $E_0 = -0.0016(38)$. The Gaussian fit captures the shape of the DOS, with minor deviations at the boundary of the spectrum.

$\tilde{H}_{\text{int}} = \sqrt{\frac{1}{L\sigma_0^2}} H_{\text{int}}$, we obtain the moments

$$\tilde{m}_{2p}(L) = \tau\left((\tilde{H}_{\text{int}})^{2p}\right) = \frac{(2p)!}{2^p p!} + O\left(\frac{1}{L}\right) \tag{2.43}$$

and in the limit $d \to \infty$ implying $L \to \infty$, only the highest order remains with

$$\lim_{d\to\infty} \tilde{m}_{2p}(L) = \frac{(2p)!}{2^p p!} = (2p-1)!!. \tag{2.44}$$

These moments are identical to the moments of the normal distribution with mean zero and variance one. Since they satisfy *Carleman's condition* [215]

$$\sum_{p=1}^{\infty} \tilde{m}_{2p}^{-\frac{1}{2p}} = +\infty, \tag{2.45}$$

the moment problem for $(\tilde{m}_{2p})$ is determinate and there exists only one measure with the moments $\tilde{m}_{2p}(L)$ and no other measure with the same moments. We define the sequence of random variables $\{\lambda_d\}_{d=1}^{\infty}$, where λ_d is an expected eigenvalue drawn from the matrix H_{int} for d sites. Each random variable λ_d is associated to a characteristic function $\varphi_d(t) = \mathbb{E}\left[e^{it\lambda_d}\right]$, which is defined through the moments of H_{int}. According to *Lévy's continuity theorem*, if the sequence of characteristic functions $\varphi_d(t) = \mathbb{E}\left[e^{it\lambda_d}\right]$ converges to the characteristic function $\varphi(t)$ for $d \to \infty$, the λ_d

converge in distribution to the random variable λ. The PDF of λ can be computed from the characteristic function $\varphi(t)$. This means, that the eigenvalue density of the matrix $\tilde{H}_{\text{int}}$ converges to the Gaussian distribution with variance one and mean zero. Consequently, the DOS of H_{int} is given by the number of states $N = 2^d$ multiplied by a normalized Gaussian with variance $\sigma^2_{\mathcal{B}}$. This mathematical proof outlined above is done in [188]. In the following chapters, we use that the considered class of Hamiltonians has a Gaussian DOS in the limit $d \to \infty$ with only small deviations in the finite size case. In Fig. 2.4, we show the DOS of the Hamiltonian in (2.5) obtained numerically from a spin lattice with $d = 15$ sites and 100 samples of H_{int}. All variances of the random prefactors in H_{int} are chosen to be equal to s^2_{int}. A Gaussian fit in red agrees with the numerical data. According to Eq. (2.14), the second moment of H_{int} can be computed by counting the number of spin-spin interaction terms n_{int} and the number of lattice sites d. By choosing $s_{\text{int}} = \frac{1}{2}$ in (2.14) and in the present case of a two-dimensional spin lattice with OBC, we find $n_{\text{int}} = 22$ and consequently $\sigma_{\text{int}} = 2.43$. This is very close to the numerical value $\sigma = 2.4893(38)$ obtained from the Gaussian fit in Fig. 2.4. The small deviation of 2.2% is due to the fact, that the numerical histogram data shows minor deviations to the Gaussian fit at the boundary of the spectrum for the finite sized lattice. From the calculation, we know, that the distribution converges to the normal distribution for $d \to \infty$, but finite size effects apply for finite d, which originate in the commutator contributions to the moments.

II

Eigenstate Thermalization

In this part, we investigate the eigenstate distribution of a small subset of a quantum system in an exact eigenstate. To this end, we characterize the interaction matrix that couples a small subsystem to a large bath by representing the coupling in the uncoupled eigenbasis. This way, it is possible to employ the methods of random matrix theory (RMT) to determine the overlap of eigenstates of the full quantum system with the product states of the uncoupled setup. Based on the structure and shape of the overlap functions, we compute the reduced density matrix and the distribution in the small subsystem. We conclude by taking the thermodynamic limit and exploring the implications of our results, where we find, that a single exact quantum state suffices to define a temperature and derive a thermal distribution in the small subsystem without resorting to the concepts of ergodicity or maximal entropy.

Structure of the perturbation matrix

3.1 General matrix structure

The general setup as described in 2.1.1 features a local Hamiltonian of a two-dimensional spin-$\frac{1}{2}$ lattice, which is perturbed by an operator X constructed from local, random interactions on a small, connected part of the lattice. We investigate the eigenstate distribution in a small subsystem of the spin lattice. For this, our intermediate objective is to compute and analyze the overlap between perturbed and unperturbed eigenvectors in this system. This is achieved by employing the methods of RMT, in particular the equation by Casati and Girko in (1.129). As detailed in Sec. 1.4.3, it deals with a general Hermitian matrix A, which is perturbed by a random band matrix with element-dependent variance σ_{ij}^2 at the matrix entry X_{ij}. As it turns out, the matrix X in the representation of the unperturbed eigenbasis is indeed a random band matrix and complies with the required prerequisites for the application of the equation by Casati and Girko. Its structure shall be investigated in the following, such as to determine the generic shape of its variance model σ_{ij}^2. It is then used as an input for the RMT calculation of the overlap function between perturbed and unperturbed eigenstates.

In our numerical analysis, we compute the matrix variance in boxes of uniform size and then average the results over random samples of X and $H^{\mathcal{B}}$. The numerical results are compared to analytical calculations with RMT. In the following, we start by investigating the structure of X in the single peak model and then generalize those results to the multi peak model in Sec. 3.2.3.

3.1.1 Definition and properties of the variance

We first define general properties of the perturbation matrix X and its associated element-wise variance σ_{ij}^2. Those become important in the analytical description and characterization of the shape of the variance model σ_{ij}^2.

We chose all prefactors of the Pauli matrices in the bath Hamiltonian $H^{\mathcal{B}}$ defined in Eq. (2.5) to be independent identically distributed (IID) and drawn from a Gaussian distribution $\mathcal{N}(0, s_{\mathcal{B}}^2)$. In the following, we first restrict ourselves to the analysis of the perturbation matrix X in the single peak model, while the results are extended to the multi peak model in Sec. 3.2.3. In the single peak model, the Hilbert space of $\mathcal{F}$ matches that of $\mathcal{B}$ with a total number of states $N_{\mathcal{F}} = N_{\mathcal{B}}$. If not stated otherwise, the perturbation X as defined in Eq. (2.8) acts on three sites on the boundary of the two dimensional spin lattice in Fig. 2.1 with $d_C = 3$ and has a variance of t. When represented in the local spin basis, we label it by X, while $\tilde{X}$ shall refer to the representation in the unperturbed eigenbasis of $\mathcal{B}$, $H^{\mathcal{B}} |\psi_i^{\mathcal{B}}\rangle = E_i^{\mathcal{B}} |\psi_i^{\mathcal{B}}\rangle$ with matrix entries

$$\tilde{X}_{ij} \equiv \langle\psi_i^{\mathcal{B}}|X|\psi_j^{\mathcal{B}}\rangle \,. \tag{3.1}$$

We can switch between the two representations by a transformation through the unitary matrix U,

$$\tilde{X} = U^{\dagger} X U, \tag{3.2}$$

where U is constructed out of the eigenbasis of $\mathcal{B}$ represented in terms of the local basis. It modulates a change of basis from local to eigenbasis with its matrix elements defined as $U_{ij} \equiv \langle \phi_i^{\mathcal{B}} | \psi_j^{\mathcal{B}} \rangle, (i, j = 1, \ldots, N)$, where $|\phi_i^{\mathcal{B}}\rangle$ denotes the local spin basis of product states of $|\uparrow\rangle$ and $|\downarrow\rangle$ on each of the d lattice sites. $X_{ij} \equiv \langle \phi_i^{\mathcal{B}} | X | \phi_j^{\mathcal{B}} \rangle$ are the matrix elements of X in the local basis.

While the total variance t of X stays invariant under unitary transformations as in (3.2), the element-wise variance might be subject to change in this ensemble. By way of construction of X with products of two Pauli matrices detailed in Sec 2.1.3, every random term appears in each row and column of the local basis representation of X exactly once. As a result, the number of nonzero elements as well as their value is identical in each row or column of the matrix. Each row or column of X must therefore contribute with the same factor of $\frac{t}{N}$ to the total variance of t, which is mathematically equivalent to the formulation

$$\mathbb{E}\left[\sum_i |X_{ij}|^2\right] = \mathbb{E}\left[\sum_j |X_{ij}|^2\right] = t. \tag{3.3}$$

As expected, the second moment of X returns t through a sum over both row and column variances,

$$\tau(X^2) = \frac{1}{N} \sum_{i,j} \mathbb{E}\left[|X_{ij}|^2\right] = \frac{1}{N} \sum_j t = t. \tag{3.4}$$

As compared to a Gaussian unitary ensemble (GUE), where each matrix entry has the same variance of $\frac{t}{N}$, the variance depends on the element in question for the block diagonal X in the local basis. This is also the case for $\tilde{X}$ in the unperturbed eigenbasis. Nevertheless, a weaker condition of a constant total row or column variance of $\frac{t}{N}$ independent of row i or column j is fulfilled for both a GUE and the local matrix X. In the local reduced basis of C, defined as only those spins on which X acts, it is very close to a GUE and would even be equivalent to it if X was chosen as in Eq. (2.6) in the multi peak model for $d_C = 2$. This way, the construction of X exhausts all 16 degrees of freedom (DOF) of the (4×4) Hermitian matrix X. The larger the subsystem C is, the more relevant the locality of its Hamiltonian becomes and the resemblance to a GUE is less pronounced, while importantly, Eq. (3.3) remains valid.

We define the element-wise variance model σ_{ij}^2 of $\tilde{X}$ in the eigenbasis of $\mathcal{B}$ as

$$\mathbb{E}\left[|\tilde{X}_{ij}|^2\right] =: t\,\sigma_{ij}^2 \quad \rightarrow \quad \sigma_{ij}^2 = \mathbb{E}\left[\frac{1}{t}\left|\langle \psi_i^{\mathcal{B}} | X | \psi_j^{\mathcal{B}} \rangle\right|^2\right] = \mathbb{E}\left[\frac{1}{t}|\tilde{X}_{ij}|^2\right] \tag{3.5}$$

In contrast to the sparse nature of X in the local basis, it acts on every eigenstate of $\mathcal{B}$ in some way, which renders $\tilde{X}$ in this basis a dense matrix. The variance model is subject to the constraint

$$\sum_i \sigma_{ij}^2 = \sum_j \sigma_{ij}^2 = 1, \tag{3.6}$$

which means, that the property of X having a constant row or column variance in (3.3) is valid in any basis representation. To derive this, we first compute the expectation value of the matrix elements in $\tilde{X}$ as

$$\left|\tilde{X}_{ij}\right|^2 = \tilde{X}_{ij}\tilde{X}_{ij}^* = \sum_{k,l,m,n} U_{ki}^* U_{mi} X_{kl} X_{mn}^* U_{lj} U_{nj}^* \tag{3.7}$$

and in the expectation value

$$\mathbb{E}\left[\left|\tilde{X}_{ij}\right|^2\right] = \sum_{k,l,m,n} U_{ki}^* U_{mi} U_{lj} U_{nj}^* \, \mathbb{E}\left[X_{kl} X_{mn}^*\right]. \tag{3.8}$$

A summation over the rows i returns

$$\begin{aligned}\sum_i \mathbb{E}\left[\left|\tilde{X}_{ij}\right|^2\right] &= \sum_{k,l,m,n}\left(\sum_i U_{ki}^* U_{mi}\right) U_{lj} U_{nj}^* \, \mathbb{E}\left[X_{kl} X_{mn}^*\right] = \sum_{k,l,m,n} \delta_{mk} U_{lj} U_{nj}^* \, \mathbb{E}\left[X_{kl} X_{mn}^*\right] \\ &= \sum_{k,l,n} U_{lj} U_{nj}^* \underbrace{\mathbb{E}\left[X_{kl} X_{kn}^*\right]}_{=\delta_{ln}\mathbb{E}\left[|X_{kn}|^2\right]} = \sum_l U_{lj} U_{lj}^* \underbrace{\sum_k \mathbb{E}\left[|X_{kl}|^2\right]}_{=t \text{ acc. to (3.3)}} = t \sum_l U_{lj} U_{lj}^* = t,\end{aligned} \tag{3.9}$$

which is equivalent to the demanded property of σ_{ij}^2 in (3.6) though division by t. In the calculation, we have used $\mathbb{E}\left[X_{kl} X_{kn}^*\right] = \delta_{ln}\mathbb{E}\left[|X_{kn}|^2\right]$, since according to the local construction in (2.8) each random term in X appears in each row or column only once. We have shown, that in any basis, the contribution of each row or column in X to the total variance t is $\frac{t}{N}$. The normalization criterion in (3.6) of the random band matrix with variances σ_{ij}^2 is a necessary criterion for the applicability of the equation by Casati and Girko. In chapter 4, we employ this equation to determine the overlap of eigenstates once the shape of the variance model of the band matrix $\tilde{X}$ is known.

A second required criterion for the validity of the equation by Casati and Girko is the statistical independence of all matrix entries of the perturbation X. If we choose X to be a GUE in the full basis, this requirement is fulfilled, as evident from the two-point correlation of the GUE in (1.93),

$$\mathbb{E}\left[X_{kl} X_{k'l'}^*\right] = \frac{t}{N}\delta_{kk'}\delta_{ll'}, \tag{3.10}$$

which holds in any basis. However, it is not true for the perturbation matrix X in the local basis as constructed through local Pauli matrix terms in (2.8) and (2.6) for the single and multi peak model, respectively. Since every random term appears exactly once in each row and each column of X, there are at most $\frac{N}{2}$ nonzero correlations for each individual offdiagonal element and N correlations for each element on the diagonal. The number of possible offdiagonal correlations is reduced by a factor of $\frac{1}{2}$, since the correlation is only nonzero, if the matrix entries in the two-point correlation combine to the squared absolute value $|X_{kl}|^2$ with nonzero variance. The expectation value of any squared complex valued entry instead vanishes with $\mathbb{E}\left[X_{kl}^2\right] = 0$. The actual number of correlations to any given matrix element of X while greater than one is up to a factor of four smaller because the individual scattering terms in X can combine to orthogonal random variables in linear superpositions. Since we include spin-spin interactions involving up to two spins with effective (4 × 4) matrices in the reduced basis, it maximally reduces the number of correlations by a factor of four. For example, this was exploited in the construction of X for the multi peak model in (2.6), where the reduced matrix for each link between two sites resembles a GUE with 16 DOF. The correlations of

X in the full local basis are however

$$\mathbb{E}\left[X_{kl}X^*_{k'l'}\right] = s^2_{kl}\left(\delta_{kk'}\delta_{ll'} + \delta_{k+r_1,k'}\delta_{l+c_1,l'} + \delta_{k+r_2,k'}\delta_{l+c_2,l'} + \ldots\right), \tag{3.11}$$

where $r_1, r_2, \ldots$ denote the row shift from k and $c_1, c_2, \ldots$ the column shift from l to find the same value in the matrix element again. s^2_{kl} is the variance of the matrix element X_{kl} in the local basis, which can be zero for some entries and nonzero for others as well as differ in value. Further correlations are of the same structure and indicated by the dots. In the unperturbed eigenbasis, the two-point correlation of the matrix elements of $\tilde{X}$ reads

$$\begin{aligned}\mathbb{E}\left[\tilde{X}_{ij}\tilde{X}^*_{i'j'}\right] &= \sum_{k,l} s^2_{kl}\, U^*_{ki}U_{lj}U_{ki'}U^*_{lj'} + \sum_{k,l} s^2_{kl}\, U^*_{ki}U_{lj}U_{k+r_1,i'}U^*_{l+c_1,j'} + \ldots \\ &= \underbrace{\sum_{k,l} s^2_{kl}\left(U^*_{ki}U_{ki'}\right)\left(U_{lj}U^*_{lj'}\right)}_{\textcircled{1}} + \underbrace{\sum_{k,l} s^2_{kl}\left(U^*_{ki}U_{k+r_1,i'}\right)\left(U_{lj}U^*_{l+c_1,j'}\right)}_{\textcircled{2}} + \ldots,\end{aligned} \tag{3.12}$$

where U is the unitary matrix, that transforms X from the local to the unperturbed eigenbasis of $\mathcal{B}$. The contribution of the individual terms can be evaluated by inserting the state representation of $U_{ij} = \langle\phi^{\mathcal{B}}_i|\psi^{\mathcal{B}}_j\rangle$, where we drop the superscript $\mathcal{B}$ for the following calculation. For the first term it results in

$$\textcircled{1} = \sum_l \left(\langle\psi_{j'}|\phi_l\rangle\, \langle\phi_l|\psi_j\rangle \sum_k \left(s^2_{kl}\, \langle\psi_i|\phi_k\rangle\, \langle\phi_k|\psi_{i'}\rangle \right)\right) \longrightarrow \left(\sum_{k,l} s^2_{kl}\, |\langle\psi_i|\phi_k\rangle|^2 \left|\langle\psi_j|\phi_l\rangle\right|^2\right)\delta_{ii'}\,\delta_{jj'} \quad \text{for } N \to \infty.$$

If the variance s^2_{kl} was constant throughout the matrix X as in a GUE, the proportionality to $\delta_{ii'}\,\delta_{jj'}$ would be obvious, since we could use the completeness of the local basis, $\sum_k |\phi_k\rangle\,\langle\phi_k| = \mathbb{1}$. In the present case with a local X, this is not possible due to the variance structure s^2_{kl}. Nevertheless, we assume, that all eigenstates $|\psi_i\rangle$ of $\mathcal{B}$ have uncorrelated random phases in each entry, which are drawn from a uniform distribution. The sum in ① therefore behaves as a random walk in two dimensions. In the limit $N \to \infty$, all terms are averaged out through their random complex phases, except for the contribution of the squared absolute values for $i = i'$ and $j = j'$ where the complex phases cancel out. We apply the same logic to the second term, which gives

$$\textcircled{2} = \sum_l \left(\langle\psi_{j'}|\phi_{l+c_1}\rangle\, \langle\phi_l|\psi_j\rangle \sum_k \left(s^2_{kl}\, \langle\psi_i|\phi_k\rangle\, \langle\phi_{k+r_1}|\psi_{i'}\rangle \right)\right) \longrightarrow 0 \quad \text{for } N \to \infty.$$

Due to the shifts r_1 and c_1 of the local states, the phases of the scalar products in the sums over k and l never cancel out and all terms are averaged out to zero in the 2D random walk. Any other term in the correlation $\mathbb{E}\left[\tilde{X}_{ij}\tilde{X}^*_{i'j'}\right]$ is of the same form as ② and for $N \to \infty$ averages to zero as well. Putting everything together in the limit of large system size, we obtain

$$\mathbb{E}\left[\tilde{X}_{ij}\tilde{X}^*_{i'j'}\right] \longrightarrow \left(\sum_{k,l} s^2_{kl}\, |\langle\psi_i|\phi_k\rangle|^2 \left|\langle\psi_j|\phi_l\rangle\right|^2\right)\delta_{ii'}\,\delta_{jj'} = t\,\sigma^2_{ij}\,\delta_{ii'}\,\delta_{jj'} \quad \text{for } N \to \infty, \tag{3.13}$$

where we inserted the definition of the variance model $\sigma^2_{ij} = \mathbb{E}\left[\frac{1}{t}\left|\langle\psi^{\mathcal{B}}_i|X|\psi^{\mathcal{B}}_j\rangle\right|^2\right]$. This result is remarkable and important, as it shows that the perturbation matrix $\tilde{X}$ in the unperturbed eigenbasis can be treated as a GUE with additional element-wise variance structure, where all random entries in the matrix are independent random variables with an additional constraint of hermiticity $X^\dagger = X$. The same result is obtained by taking an average over the

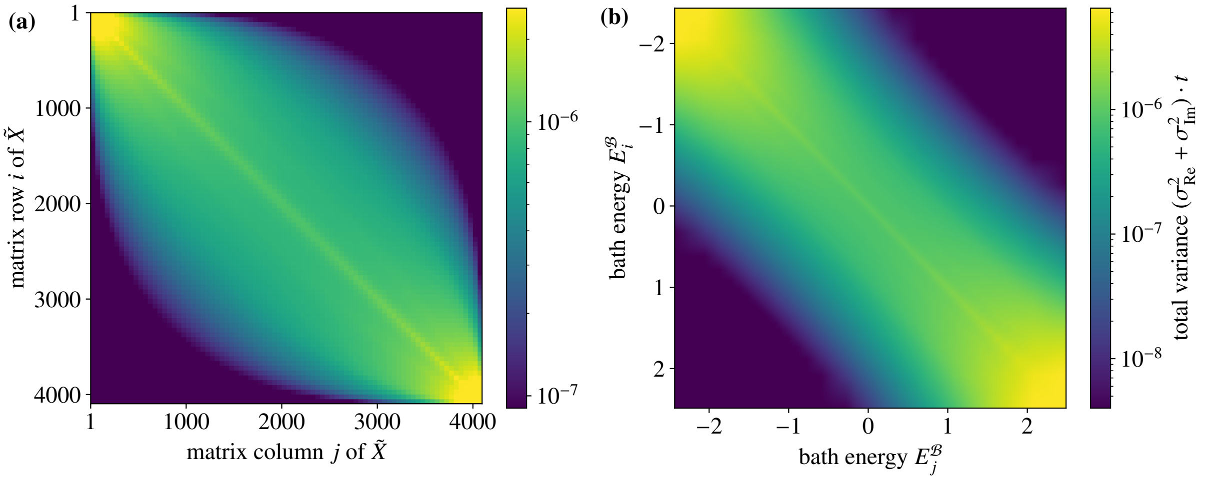

Figure 3.1: Matrix plot of the variance of the absolute value of the offdiagonal elements in the matrix $\tilde{X}$ with $t = 2.435(31) \times 10^{-3}$ computed in terms of boxes of size 25×25 in a single peak setup with $d_{\mathcal{B}} = 12$ sites and $d_{\mathcal{S}} = 0$. The variance is averaged over 100 random samples of X and 50 samples of $H^{\mathcal{B}}$ and represented on a logarithmic scale. **(a)** Representation in terms of the matrix indices, where we use nearest shading, in which the color in quadrilaterals spanned by the data points is chosen from the value of the closest data point. **(b)** Representation in terms of the bath energy corresponding to the matrix indices. We use Gouraud shading, where the color is linearly interpolated in quadrilaterals spanned by the data points.

unperturbed bath $\mathcal{B}$, which is a restatement of the property of self-averaging. This result shows, that the equation by Casati and Girko in (1.129) is applicable.

3.1.2 Influence of the density of states

We first investigate the general structure of the perturbation matrix $\tilde{X}$ in the eigenbasis of $\mathcal{B}$ by both analytical considerations and numerical simulations. As detailed in Sec. 2.1, the perturbation matrix to the bath acts only on the subsystem C. It can change the spin configurations by flipping spins in this subsystem. Equivalently, if we decompose the local basis states in terms of product states in C and $\bar{C}$, X can scatter between different states in C, while the states in $\bar{C}$ are not affected by X. Given that C is a small and connected region of $\mathcal{B}$, we want to address the question of what the contribution of an initial state $|\psi_j^{\mathcal{B}}\rangle$ under a scattering of X to a specific final state $|\psi_i^{\mathcal{B}}\rangle$ is. This scattering is inherently accompanied by an energy change of $\delta E = E_i^{\mathcal{B}} - E_j^{\mathcal{B}}$, where $E_j^{\mathcal{B}}$ and $E_i^{\mathcal{B}}$ are the eigenenergies corresponding to the initial and final state respectively. From a physical point of view, we expect, that the scattering amplitude from the ground state to the highest energy state of $\mathcal{B}$ is very small, as X only acts in a small part of $\mathcal{B}$. Naturally, there exists an intrinsic energy scale Δ associated with the scattering of eigenstates of $\mathcal{B}$. It depends on the properties of the bath Hamiltonian $H^{\mathcal{B}}$ and its eigenstates and eigenvalues, where Δ is set by how much the energy of the state $|\psi_j^{\mathcal{B}}\rangle$ can maximally change upon altering its spin configurations in a small subregion of $\mathcal{B}$. Note that this statement does not specify the variance distribution itself, but only its width while its shape depends on the specifics of the system. Moreover, Δ is independent of the variance t associated with X, as t merely sets the overall scale of the amplitudes of the scattering throughout the whole matrix. This is why we divide by t in the definition of the variance model σ_{ij}^2 in (3.5).

To get a general idea of the matrix structure, we plot the variances throughout the matrix $\tilde{X}_{ij}$ in a heatmap in Fig. 3.1 for $d = 12$ lattice sites. For the plot, we split the matrix in boxes of size (25×25) and determine the sample variance of the elements in each box. Each box value is then averaged over 100 random samples of X and 50 of $H^{\mathcal{B}}$. First note, that the variance of the absolute value of $\tilde{X}_{ij}$ is given by the sum of the variances of its real and imaginary part,

$$\sigma_{ij}^2 = \frac{1}{t}\mathbb{E}\left[\left|\tilde{X}_{ij}\right|^2\right] = \frac{1}{t}\left(\mathbb{E}\left[\Re\mathfrak{e}\,(\tilde{X}_{ij})^2\right] + \mathbb{E}\left[\Im\mathfrak{m}\,(\tilde{X}_{ij})^2\right]\right) =: \sigma_{ij,\mathrm{Re}}^2 + \sigma_{ij,\mathrm{Im}}^2. \tag{3.14}$$

In Fig. 3.1**a**, the variance of the matrix elements is plotted with respect to the row i and column j. We observe a *belly shaped distribution*, where the scattering width in terms of the matrix indices increases towards the middle of the matrix and becomes smaller towards the corners. In an additional numerical study, we cut out the boxes and construct a lower-dimensional effective matrix from those. When diagonalizing this effective matrix, we obtain widths for the Lorentzian peaks, which are close to those obtained from the full matrix. It shows, that the shape of the Lorentzians and their width is primarily determined by the matrix elements in the vicinity of $\tilde{X}$. We further notice, that a smaller scattering width is paralleled by a larger average variance. While probing along the diagonal direction of the matrix, this means, that the average variance decreases towards the middle of the matrix and diverges at the corners. This is an artifact of the normalization property of σ_{ij}^2 and the Gaussian density of states (DOS)

$$N_{\mathcal{B}}\rho_{\mathcal{B}}(E) = \frac{N_{\mathcal{B}}}{\sqrt{2\pi\sigma_{\mathcal{B}}^2}}\exp\left(-\frac{E^2}{2\sigma_{\mathcal{B}}^2}\right) \tag{3.15}$$

of the bath (c.f. Sec. 2.2) with width $\sigma_{\mathcal{B}}$, centered around $E_0 = 0$.

In Fig. 3.1**b**, we account for the DOS of $\mathcal{B}$ in the scaling of the axes by plotting the box variances with respect to the averaged bath energy of the corresponding rows and columns. We notice, that the belly shaped distribution of Fig. 3.1**a** disappears and the band property of the random band matrix is visible. Since the variance data itself remains unchanged, the increase of the variance towards the boundary of the spectrum is still present in accordance with the observation in Fig. 3.1**a**. Since there are straight lines of approximately constant variance with constant distance to $E^{\mathcal{B}} = 0$ in the plot, it can be estimated, that the scattering width Δ remains constant throughout the matrix. Further evidence for that is the clearly discernible energy cutoff at which the matrix elements become very small. The structure in Fig. 3.1**b** implies, that apart from an overall scaling along the diagonal direction of the matrix, the variance model predominantly depends on the energy difference $\delta E = E_i^{\mathcal{B}} - E_j^{\mathcal{B}}$. In total, the variance structure in $\tilde{X}$ can be modeled to be a product of two functions, u and v. The first function $u(E_i^{\mathcal{B}} - E_j^{\mathcal{B}})$ depends only on the energy difference and encodes the scattering behavior due to the action of X in the eigenbasis of $\mathcal{B}$. It formulates the structure of the matrix along its *anti-diagonal*, which is defined as a straight line starting at the lower left and ending at the upper right corner of the matrix or any lines parallel to that in Fig. 3.1**b**. The second function $v(E_i^{\mathcal{B}} + E_j^{\mathcal{B}})$ determines the scaling factor along the diagonal direction from the upper left to the lower right of the matrix and any lines parallel to that. Fig. 3.1**b** suggests that such a separation is in accordance with the variance structure. In the following, we examine the validity of that approach and detail the shape of both functions u and v.

To model the variance increase in $\tilde{X}$ towards the boundary of the spectrum, we assume that the part of the variance model, which depends on the energy difference δE is constant in the scattering range given by Δ. This is reflected in choosing the function $u(E_i^{\mathcal{B}} - E_j^{\mathcal{B}})$ to be a rectangular function with width Δ and height chosen accordingly to fulfill the normalization condition of the variance model. Though this assumption is unphysical and does not reflect the structure of the matrix, it can be employed to deduct the scaling factor along the diagonal of the matrix. Hence, only the remaining part of the matrix structure remains for analysis, namely the increase of variance towards the edge of the energy spectrum. We then write

$$\sigma_{ij}^2 = \begin{cases} \frac{1}{N_\Delta(E_i^{\mathcal{B}},E_j^{\mathcal{B}})} & \text{for } \;|E_i^{\mathcal{B}} - E_j^{\mathcal{B}}| \le \frac{\Delta}{2}, \\ 0 & \text{else.} \end{cases} \tag{3.16}$$

This model enables us to separately investigate the contribution of the DOS to the variance model reflected in the function $v(E_i^{\mathcal{B}} + E_j^{\mathcal{B}})$ and then add an energy-dependent structure through the function $u(E_i^{\mathcal{B}} - E_j^{\mathcal{B}})$ to it resulting from the scattering of X in C. With (3.16), each initial state $|\psi_j^{\mathcal{B}}\rangle$ can scatter to states $|\psi_i^{\mathcal{B}}\rangle$ when the final energy resides within the range $E_i^{\mathcal{B}} \in [E_j^{\mathcal{B}} - \frac{\Delta}{2}, E_j^{\mathcal{B}} + \frac{\Delta}{2}]$, which itself depends on the initial energy $E_j^{\mathcal{B}}$. In order to properly normalize the *rectangular model* in (3.16) according to the normalization condition (3.6) of $\sum_i \sigma_{ij}^2 = 1$, $N_\Delta(E_i^{\mathcal{B}}, E_j^{\mathcal{B}})$ must equal the number of available states to scatter into within the energy range $\delta E \in [-\frac{\Delta}{2}, +\frac{\Delta}{2}]$. To count the number of states with an energy $E < E'$ below the cutoff E', we compute

$$N_{<E'} = \sum_{i\,(E_i^{\mathcal{B}}<E')} = \int_{-\infty}^{E'} N_{\mathcal{B}}\rho_{\mathcal{B}}(E)\,\mathrm{d}E = \frac{N_{\mathcal{B}}}{2}\,\mathrm{erf}\left(\frac{E}{\sqrt{2}\sigma_{\mathcal{B}}}\right)\Bigg|_{-\infty}^{E'} = \frac{N_{\mathcal{B}}}{2}\left(\mathrm{erf}\left(\frac{E'}{\sqrt{2}\sigma_{\mathcal{B}}}\right) + 1\right), \tag{3.17}$$

where $\mathrm{erf}(x)$ is the error function with $\lim_{x\to-\infty}\mathrm{erf}(x) = -1$. In the following, we assume the scattering width to be very small, $\Delta \ll \sigma_{\mathcal{B}}$. We then compute the number of states in one column j of the matrix corresponding to the energy $E_j^{\mathcal{B}}$. This is done by summing over all rows i in column j while assuming that $E_i^{\mathcal{B}} - E_j^{\mathcal{B}}$ is approximately constant in the energy interval $[-\Delta, +\Delta]$ for small Δ. As a consequence of integrating out $E_i^{\mathcal{B}}$, the result will only depend on $E_j^{\mathcal{B}}$. We symmetrize it in the indices i and j such that it holds in approximation for each row and column individually. N_Δ is given by

$$N_\Delta = \int_{E_j^{\mathcal{B}}-\frac{\Delta}{2}}^{E_j^{\mathcal{B}}+\frac{\Delta}{2}} N_{\mathcal{B}}\rho_{\mathcal{B}}(E^{\mathcal{B}})\,\mathrm{d}E = \frac{N_{\mathcal{B}}}{2}\left(\mathrm{erf}\left(\frac{E_j^{\mathcal{B}} + \frac{\Delta}{2}}{\sqrt{2}\sigma_{\mathcal{B}}}\right) - \mathrm{erf}\left(\frac{E_j^{\mathcal{B}} - \frac{\Delta}{2}}{\sqrt{2}\sigma_{\mathcal{B}}}\right)\right). \tag{3.18}$$

In the limit $\Delta \to 0$, it resembles the first derivative of the error function

$$N_\Delta = \frac{N_{\mathcal{B}}\Delta}{2}\frac{\mathrm{d}}{\mathrm{d}x}\,\mathrm{erf}\left(\frac{x}{\sqrt{2}\sigma_{\mathcal{B}}}\right)\Bigg|_{x=E_j^{\mathcal{B}}} + \mathcal{O}(\Delta^3) = \Delta\left(\frac{N_{\mathcal{B}}}{\sqrt{2\pi\sigma_{\mathcal{B}}^2}}\exp\left\{-\frac{(E_j^{\mathcal{B}})^2}{2\sigma_{\mathcal{B}}^2}\right\}\right) + \mathcal{O}(\Delta^3) = \Delta\left(N_{\mathcal{B}}\rho_{\mathcal{B}}(E_j^{\mathcal{B}})\right) + \mathcal{O}(\Delta^3), \tag{3.19}$$

which gives back the density of states of $\mathcal{B}$ multiplied by the scattering width Δ. The result makes sense, as $\rho_{\mathcal{B}}(E)$ is the eigenvalue density of $H^{\mathcal{B}}$ with the property, that $\rho_{\mathcal{B}}(E)\,\mathrm{d}E$ returns the probability of finding an eigenvalue in the infinitesimal interval $[E, E + \mathrm{d}E]$. The next order correction to N_Δ is of third order in Δ, since all even orders of Δ cancel out in (3.18) due to the symmetry $N_{-\Delta} = -N_\Delta$. Since we have only considered the normalization in column j, we need to symmetrize the result between row i and column j to achieve approximate normalization for both. As a means of symmetrization we use the arithmetic mean of the bath energies $E_i^{\mathcal{B}}$ and $E_j^{\mathcal{B}}$ to insert into the DOS, which yields

$$\frac{1}{N_\Delta(E_i^{\mathcal{B}}, E_j^{\mathcal{B}})} = \frac{1}{N_{\mathcal{B}}\Delta}\,\frac{1}{\rho_{\mathcal{B}}\left(\frac{E_i^{\mathcal{B}}+E_j^{\mathcal{B}}}{2}\right)} \tag{3.20}$$

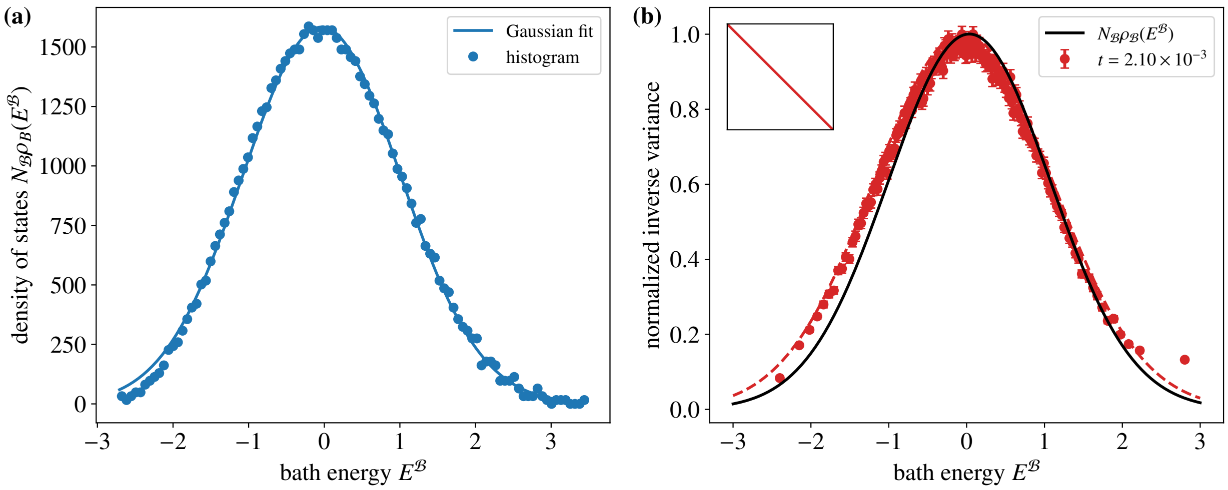

Figure 3.2: **(a)** Numerical DOS of the bath $\mathcal{B}$, complemented by a Gaussian fit as a blue line with best fit standard deviation $\sigma_{\mathcal{B}} = 1.0439(47)$. **(b)** Inverse element-wise variance of $\tilde{X}$ in the single peak model of $d_{\mathcal{B}} = 12$ and $d_{\mathcal{S}} = 0$ sites with $t = 2.10 \times 10^{-3}$ along the diagonal of the matrix, indicated by the inset. We consider only the offdiagonal elements, obtain the variance in terms of boxes of size (25×25) and average it over 100 samples of X. The data is normalized, such that the maximum is equal to one. A Gaussian fit to the data shown as a dashed line returns the Gaussian standard deviation of $\sigma_{\text{dia}} = 1.149(20)$. For comparison, the Gaussian fit of the DOS, normalized such that the peak height is one, is shown in black.

inside the energy range $|E_i^{\mathcal{B}} - E_j^{\mathcal{B}}| \leq \frac{\Delta}{2}$. This result is an approximation to the normalization for all rows and columns, since the expansion of N_Δ is up to second order in Δ and the DOS is not a pure exponential in terms of the energy.

To summarize, when accounting for the row and column normalization of σ_{ij}^2, we find that the variance in X increases towards the corners of the matrix at larger $|E|$ as depicted in Fig. 3.1. The reason is that at larger $|E|$, the average energy spacing ϵ increases in an inverse proportionality to the DOS $(N\rho_{\mathcal{B}}(E))$. Combined with a constant scattering width Δ throughout the matrix as evident in Fig. 3.1**b**, the number of available scattering states in Δ is given by $\frac{\Delta}{\epsilon}$, which causes both the specified variance increase as well as the belly shaped distribution of the index plot in Fig. 3.1**a**. This general logic carries over to a non-constant variance profile in terms of $E_i^{\mathcal{B}} - E_j^{\mathcal{B}}$, which is analyzed in the following section.

3.1.3 Structure and properties of the offdiagonal variance distribution

In Sec. 3.1.2, we analyzed the overall matrix structure and the influence of the DOS of the bath on the variance profile. As a next step, we investigate the offdiagonal variance structure of the matrix with respect to the difference of final and initial energy $E_i^{\mathcal{B}} - E_j^{\mathcal{B}}$ under the scattering by X. The variance model $\sigma_{ij}^2 = \sigma^2(E_i^{\mathcal{B}}, E_j^{\mathcal{B}})$ can be rewritten in terms of the energy sum and difference,

$$\left.\begin{aligned} E_+ &= \frac{E_i^{\mathcal{B}}+E_j^{\mathcal{B}}}{2} \\ E_- &= \frac{E_i^{\mathcal{B}}-E_j^{\mathcal{B}}}{2} \end{aligned}\right\} \rightarrow \sigma^2(E_i^{\mathcal{B}}, E_j^{\mathcal{B}}) = \sigma^2\left(E_+ + E_-, E_+ - E_-\right) \equiv \tilde{\sigma}^2(E_+, E_-) \tag{3.21}$$

The behavior of $\tilde{\sigma}^2$ at constant E_- is an inverse proportionality to the DOS in terms of E_+, as illustrated in Sec. 3.1.2. This is supported by numerical analysis in Fig. 3.2 and 3.3. There, to probe the variance model along the direction E_+,

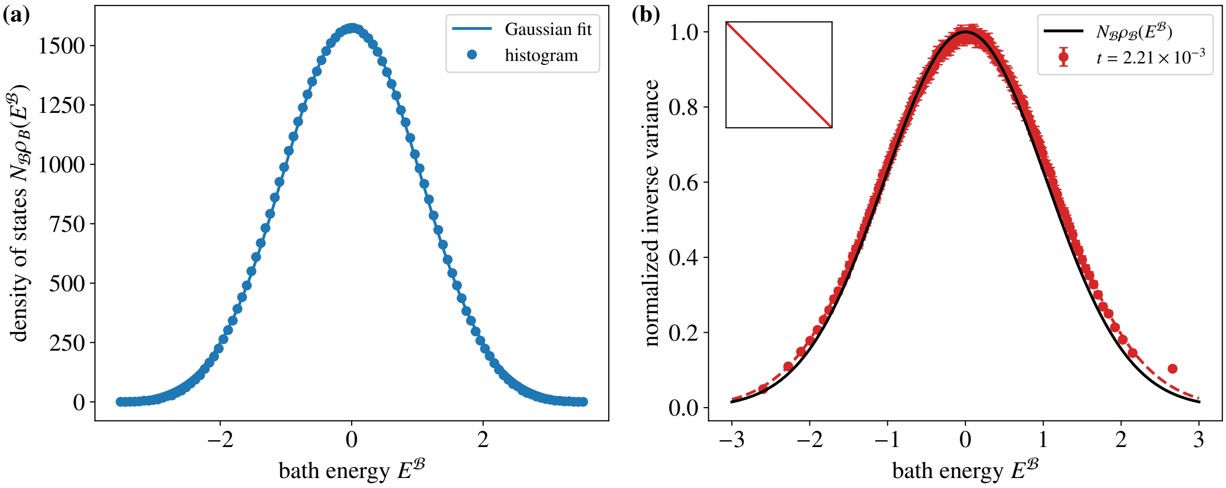

Figure 3.3: **(a)** Numerical DOS of the bath $\mathcal{B}$, which is averaged over 50 samples of $H^\mathcal{B}$ and complemented by a Gaussian fit as a blue line with best fit standard deviation $\sigma_\mathcal{B} = 1.0378(25)$. **(b)** Inverse element-wise variance of $\tilde{X}$ in the single peak model of $d_\mathcal{B} = 12$ and $d_\mathcal{S} = 0$ sites with $t = 2.208(26) \times 10^{-3}$ along the diagonal of the matrix, indicated by the inset. We consider only the offdiagonal elements, obtain the variance in terms of boxes of size (25×25) and average it over 100 samples of X. Compared to Fig. 3.2**b**, we additionally average over 50 samples of $H^\mathcal{B}$. The data is normalized, such that the maximum is equal to one. A Gaussian fit to the data shown as a dashed line returns a standard deviation of $\sigma_\text{dia} = 1.110(19)$. For comparison, the Gaussian fit of the DOS, normalized such that the peak height is one, is shown in black.

we use boxes of dimension (25×25) and compute the sample variance along the diagonal of the matrix, where $E_- \approx 0$. In this analysis, the diagonal matrix elements are taken out and analyzed separately in Sec. 3.1.4. With an average over 100 random samples of X, we obtain the result for the offdiagonal variance in Fig. 3.2, where we plot the DOS of $\mathcal{B}$ in 3.2**a** to compare it to the inverse variance σ_{ij}^{-1} in 3.2**b** without averaging over the bath Hamiltonian. A Gaussian fit of the histogram of the bath energies in Fig. 3.2**a** is shown in Fig. 3.2**b** and agrees well with the general shape of the inverse variance data, although the width σ_{ij}^{-1} is slightly larger than expected from the DOS. After an additional averaging over 50 random samples of $H^\mathcal{B}$ in Fig. 3.3, the shape of the eigenvalue distribution of $\mathcal{B}$ is entirely captured by the Gaussian fit in Fig. 3.3**a**. Moreover, the Gaussian fit agrees with the normalized inverse variance data along the diagonal in Fig. 3.3**b**. This confirms the inverse proportionality of σ_{ij}^2 to the DOS along the diagonal direction of the matrix, which was derived through the rectangular model in Sec. 3.1.2 using Eq. (3.20).

To investigate the dependence of the variance model on E_-, we analyze different sections of the matrix. In Fig. 3.4, we plot the variance along several lines of the matrix normalized such that the maximum value along each line is equal to one. Analogous to previous analysis of the matrix, the variance was found by considering the offdiagonal matrix elements in quadratic boxes of size (25×25) along the investigated lines, with an additional average over 100 samples of X. The lines are chosen parallel to the anti-diagonal. Along these straight lines, the variable E_+ is approximately constant. This is exactly fulfilled for the anti-diagonal line itself, as $E_+ = 0$ there due to the reflection symmetry of the DOS $\rho_\mathcal{B}(E)$ with $E \to -E$. Owing to the influence of the DOS in the index plot of the matrix in Fig. 3.1**a**, leading to the belly shaped distribution as pointed out in Sec. 3.1.2, the other lines fulfill this criterion only in approximation. In fact, lines for constant E_+ need to be curved when plotted with respect to the matrix indices, as well as lines for constant E_-.

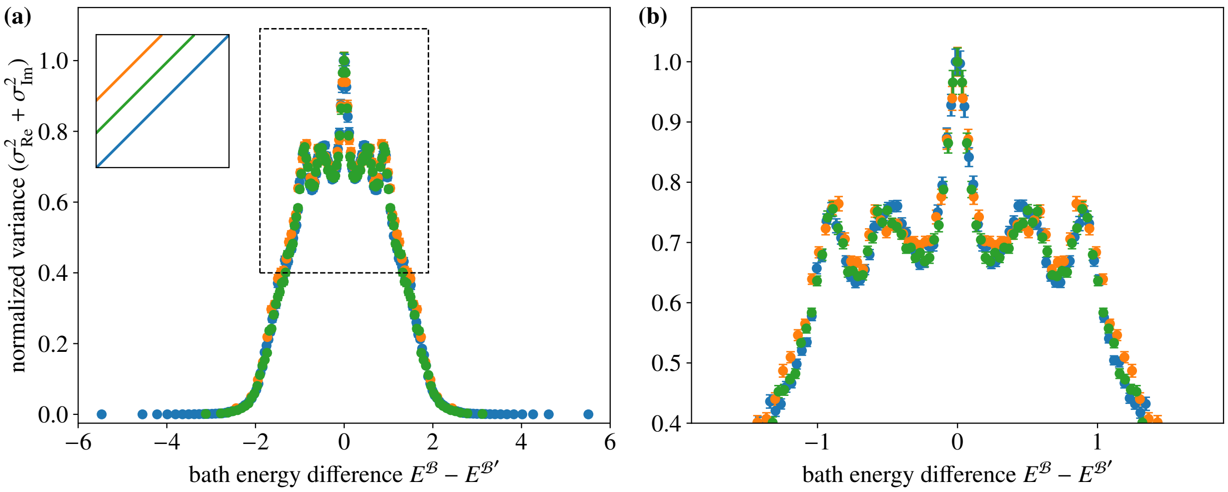

Figure 3.4: Element wise variance of $\tilde{X}$ in the single peak model of $d_{\mathcal{B}} = 12$ and $d_{\mathcal{S}} = 0$ sites with $t = 2.10 \times 10^{-3}$ along three lines in the matrix, indicated in the inset. Only the variance of the offdiagonal elements is considered, which is obtained in terms of boxes of size (25×25), averaged over 100 samples of X and normalized, such that their peak heights are one. **(a)** Plot of the full data. **(b)** Cutout of the variance data around zero, indicated by the dashed rectangular box in **(a)**.

Nevertheless, Fig. 3.4 shows a nearly perfect agreement of all the investigated lines. We identify several peaks of the variance at different positions of the difference between column and row energies. This peak structure originates from the eigenvector properties of $\mathcal{B}$, since it remains even after the specific properties of X are averaged out. Not only is the scattering width Δ constant throughout the matrix, as deduced from the matrix plot in Fig. 3.1, but the whole variance structure with all its peaks is identical. This is a significant result, which points to a more general intrinsic structure of the eigenvectors of $\mathcal{B}$. Up to an overall scaling factor, a scattering modulated by X between two eigenstates is a function only of their corresponding energy difference and does not explicitly depend on their eigenvalues individually. This behavior is further investigated in Sec. 3.2, where we explicitly calculate the element-wise variance using the methods of RMT. As it turns out, the action of X on an eigenstate of $\mathcal{B}$ can be viewed as a scattering between different singular vectors in the region C, where X acts. Since X acts on the whole of C, it scatters between all singular vectors and this scattering averages out with the average over X. As a result, we are left with all of the possible overlaps of singular vectors in the region $\bar{C}$. Since the shape of those singular vectors is very similar across the spectrum of $\mathcal{B}$ except for overall normalization factors, the variance σ^2_{ij} along the plotted lines merely depends on the energy difference of the energetic position of the center of those singular vectors. This positional difference then translates to a difference in bath energies.

The several peaks of the variance model in Fig. 3.4 are a residual artifact of the eigenvalue density of C and of the general shape of the singular vectors in $\bar{C}$ and are therefore subject to the specific choice of the bath Hamiltonian $H^{\mathcal{B}}$. We hence obtain a *quasi translational invariance* of the variance model $\sigma^2(E^{\mathcal{B}}_i, E^{\mathcal{B}}_j)$ in the matrix $\tilde{X}$, which is translational invariant up to a scaling factor. The scaling factor is symmetric in $E^{\mathcal{B}}_i$ and $E^{\mathcal{B}}_j$. When an additional averaging over 50 samples of $\mathcal{B}$ is taken, all peaks in Fig. 3.4 except for the one at $E = 0$ are averaged out, since their position depends on the specific details of $H^{\mathcal{B}}$. We end up with a monotonic function in the positive or negative energy range, which is symmetric around $E_- = 0$ as depicted in Fig. 3.5. Here, the one remaining peak, which is not averaged out is located at $E = 0$, since its position is the same throughout all random samples of $H^{\mathcal{B}}$. This peak at

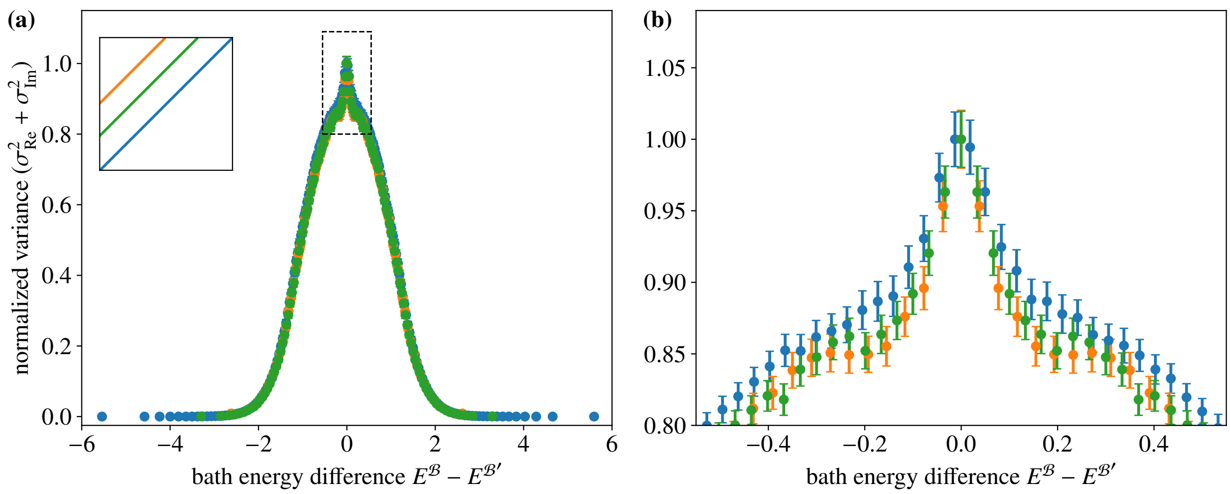

Figure 3.5: Element wise variance of $\tilde{X}$ in the single peak model of $d_{\mathcal{B}} = 12$ and $d_{\mathcal{S}} = 0$ sites with $t = 2.208(26)\times10^{-3}$ along three lines in the matrix, indicated in the inset. Only the variance of the offdiagonal elements is considered, which is obtained in terms of boxes of size (25×25), averaged over 100 samples of X and 50 samples of $H^{\mathcal{B}}$ and normalized, such that their peak heights are one. **(a)** Plot of the full data. **(b)** Cutout of the variance data around zero, indicated by the dashed rectangular box in **(a)**.

zero is a finite size effect and vanishes in the limit $N_{\mathcal{B}} \to \infty$, as detailed in Sec. 3.2. The remaining part of the variance model resembles the shape of a Gaussian. In chapter 4, when computing the overlaps of perturbed and unperturbed eigenstates of the full quantum system, we model the variance distribution explicitly and determine its parameters with a fit in order to compare the analytic calculation to the numerical results. As expected from previous results, the variances at different lines of the matrix in Fig. 3.5 still agree with each other within their expected error, after the average over $\mathcal{B}$ is carried out. These results numerically show that the variance model can be split into the two independent contributions $u(E_-)$ and $v(E_+)$.

3.1.4 Diagonal of the matrix

The elements at the exact diagonal of $\tilde{X}$ are omitted in the analysis of the offdiagonal part of the variance model σ^2_{ij} in Sec. 3.1.3 and are therefore analyzed separately in the following. With the diagonal elements of $\tilde{X}$ being defined as $\tilde{X}_{ii} = \langle\psi_i^{\mathcal{B}}|X|\psi_i^{\mathcal{B}}\rangle$, they are equal to the first order energy correction in perturbation theory as declared in (1.75a) with X acting as the perturbation to the bath Hamiltonian $H^{\mathcal{B}}$. In Fig. 3.6, we plot the diagonal elements $\tilde{X}_{ii}$ of several random samples of the matrix X, which are averaged in intervals of uniform size of 82 elements each with $\tilde{X}_{ii}$ being the expectation value of X in the state $|\psi_i^{\mathcal{B}}\rangle$, we observe a correlation between the value of $\tilde{X}_{ii}$ and the corresponding eigenvalue $E_i^{\mathcal{B}}$. This correlation is randomized through the randomness of X and $H^{\mathcal{B}}$. Generally, we notice, that $|\tilde{X}_{ii}|$ is larger at larger energy magnitudes $|E_i^{\mathcal{B}}|$. It originates in the fact, that the energy pertaining to each eigenstate is on average uniformly distributed throughout the whole bath $\mathcal{B}$ and through X we probe the amount of energy in region C. Put differently, since all interaction terms between the spins in the lattice of the bath $\mathcal{B}$ are IID, each coupling between two sites on average contributes the same amount of energy to the total energy of the state. As the same couplings, which appear in the perturbation X are already present in the Hamiltonian $H^{\mathcal{B}}$, the first order perturbation probes the available energy in the part of the system, where X acts, which is defined as subsystem C. Then the expectation value

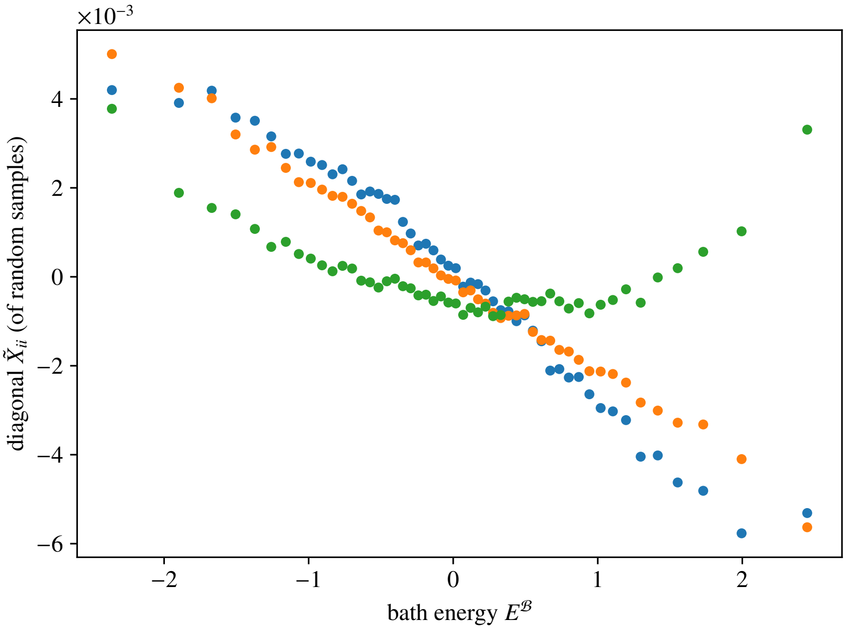

Figure 3.6: Diagonal elements of three random samples of the perturbation matrix $\tilde{X}$ in the single peak model of $d_{\mathcal{B}} = 12$ and $d_{\mathcal{S}} = 0$ sites with $t = 2.10 \times 10^{-3}$, averaged in intervals of 82 elements corresponding to a total of 50 bins.

$\tilde{X}_{ii}$ is a linear function of the total energy $E_i^{\mathcal{B}}$ with real prefactors, expressed as

$$\frac{1}{\sqrt{t}} \tilde{X}_{ii} \sim c_1 + c_2 \frac{E_i^{\mathcal{B}}}{\sigma_{\mathcal{B}}} + O(E_i^{\mathcal{B}2}), \tag{3.22}$$

where c_1 and c_2 are random variables following a normal distribution with mean zero and yet undetermined variance, $c_1 \sim \mathcal{N}(0, \sigma_1^2)$ and $c_2 \sim \mathcal{N}(0, \sigma_2^2)$. The standard deviation $\sigma_{\mathcal{B}}$ of the DOS of the bath sets the energy scale for $E_i^{\mathcal{B}}$ in (3.22).

In the expectation value, we find that the diagonal elements vanish, $\mathbb{E}\left[\tilde{X}_{ii}\right] = 0 \, \forall i = 1, \ldots, N$, as do all matrix element of X or $\tilde{X}$, since the prefactors of the interaction terms are drawn from a Gaussian with mean zero. However, the variance of those elements is nonzero. From Eq. (3.22), we obtain in second order of the bath energy $E_i^{\mathcal{B}}$,

$$\begin{aligned} \sigma_{ii}^2 = \mathbb{E}\left[\frac{\tilde{X}_{ii}^2}{t}\right] &= \mathbb{E}\left[\left(c_1 + c_2 \frac{E_i^{\mathcal{B}}}{\sigma_{\mathcal{B}}}\right)^2\right] + O\left((E_i^{\mathcal{B}})^4\right) \\ &= \mathbb{E}\left[c_1^2 + 2 c_1 c_2 \frac{E_i^{\mathcal{B}}}{\sigma_{\mathcal{B}}} + c_2^2 \left(\frac{E_i^{\mathcal{B}}}{\sigma_{\mathcal{B}}}\right)^2\right] + O\left((E_i^{\mathcal{B}})^4\right) \\ &\approx \sigma_1^2 + \sigma_2^2 \left(\frac{E_i^{\mathcal{B}}}{\sigma_{\mathcal{B}}}\right)^2 \end{aligned} \tag{3.23}$$

with $\sigma_1^2 = \mathbb{E}\left[c_1^2\right]$ and $\sigma_2^2 = \mathbb{E}\left[c_2^2\right]$, as the mixed terms vanish due to their zero mean. This shows that the diagonal variance of $\tilde{X}$ is a quadratic function in energy.

To analytically determine the variances σ_1^2 and σ_2^2, we consider the average amount of energy that each term in the bath Hamiltonian $H^{\mathcal{B}}$ contributes to the total energy $E_i^{\mathcal{B}}$. For this, we rewrite the Hamiltonian $H^{\mathcal{B}}$ defined in Eq. (2.5) as a sum of terms H_l with variance one and prefactors J_l drawn from $\mathcal{N}(0, \sigma_l^2)$, which are adjusted to fit the definition of the prefactors in the local Pauli matrix construction. This gives

$$H^{\mathcal{B}} = \sum_{l=1}^{L} J_l\, H_l, \tag{3.24}$$

where L denotes the total number of independent terms in $H^{\mathcal{B}}$. The variances of all terms follow the sum rule $\sum_l \sigma_l^2 = \sigma_{\mathcal{B}}^2$. A similar relation holds for the perturbation matrix X with prefactors x_l,

$$X = x_1 \mathbb{1} + \sum_{l=2}^{L_X} x_l\, H_l, \tag{3.25}$$

where $x_l \sim \mathcal{N}(0, t_l)$ for $l = 1, ..., L_X$ with a total of L_X terms in X. Here, the sum rule $\sum_l t_l = t$ holds with t_l denoting the variance of a single term in X. The perurbation contains the same terms H_l, which were already present in the unperturbed Hamiltonian. We can additionally introduce a unit matrix term. Such a term is present in the multi peak model with X in (2.6), but not for the single peak model. To be as general as possible, we include it in (3.25) with a prefactor x_1. We assume, that on average, the distribution of the bath energy $E_i^{\mathcal{B}}$ throughout the lattice matches the strength of the lattice couplings. It corresponds to a uniform energy distribution in the lattice, if all couplings are of equal strength. In general, each term in $H_{\mathcal{B}}$ contributes as

$$\mathbb{E}_{\mathcal{B}}\left[\langle\psi_i^{\mathcal{B}}|J_l\, H_l|\psi_i^{\mathcal{B}}\rangle\right] = \frac{\sigma_l^2}{\sigma_{\mathcal{B}}^2} E_i^{\mathcal{B}} \tag{3.26}$$

with the fraction $\frac{\sigma_l^2}{\sigma_{\mathcal{B}}^2}$ to the total energy $E_i^{\mathcal{B}}$. $\mathbb{E}_{\mathcal{B}}$ denotes the expectation value over $H^{\mathcal{B}}$. If all terms in $\mathcal{B}$ had the same variance, the energy in each term would be equal to $\frac{E_i^{\mathcal{B}}}{L}$, which corresponds to a uniform energy distribution over all terms. It is consistent with the total energy in $\mathcal{B}$ reading

$$\mathbb{E}\left[E_i^{\mathcal{B}}\right] = \mathbb{E}\left[\langle\psi_i^{\mathcal{B}}|H^{\mathcal{B}}|\psi_i^{\mathcal{B}}\rangle\right] = \sum_l \mathbb{E}\left[\langle\psi_i^{\mathcal{B}}|J_l\, H_l|\psi_i^{\mathcal{B}}\rangle\right] = \sum_l \frac{\sigma_l^2}{\sigma_{\mathcal{B}}^2} E_i^{\mathcal{B}} = E_i^{\mathcal{B}} \tag{3.27}$$

upon using the sum rule for the individual variances σ_l^2. From (3.26) we follow

$$\mathbb{E}_{\mathcal{B}}\left[\left(\langle\psi_i^{\mathcal{B}}|J_l\, H_l|\psi_i^{\mathcal{B}}\rangle\right)^2\right] = \frac{\sigma_l^4}{\sigma_{\mathcal{B}}^4}(E_i^{\mathcal{B}})^2. \tag{3.28}$$

This equation implies, that the variance of each term $\langle\psi_i^{\mathcal{B}}|J_l\, H_l|\psi_i^{\mathcal{B}}\rangle$ vanishes. We assume that all such terms are uncorrelated and therefore independent. Since $E_i^{\mathcal{B}}$ is an exact eigenenergy corresponding to the state $|\psi_i^{\mathcal{B}}\rangle$, its variance is zero, which implies, that all individual independent terms $\langle\psi_i^{\mathcal{B}}|J_l\, H_l|\psi_i^{\mathcal{B}}\rangle$ must have zero variance and (3.28) holds. Eq. (3.28) further suggests that

$$\mathbb{E}_{\mathcal{B}}\left[\left(\langle\psi_i^{\mathcal{B}}|H_l|\psi_i^{\mathcal{B}}\rangle\right)^2\right] = \frac{\sigma_l^2}{\sigma_{\mathcal{B}}^4}(E_i^{\mathcal{B}})^2, \tag{3.29}$$

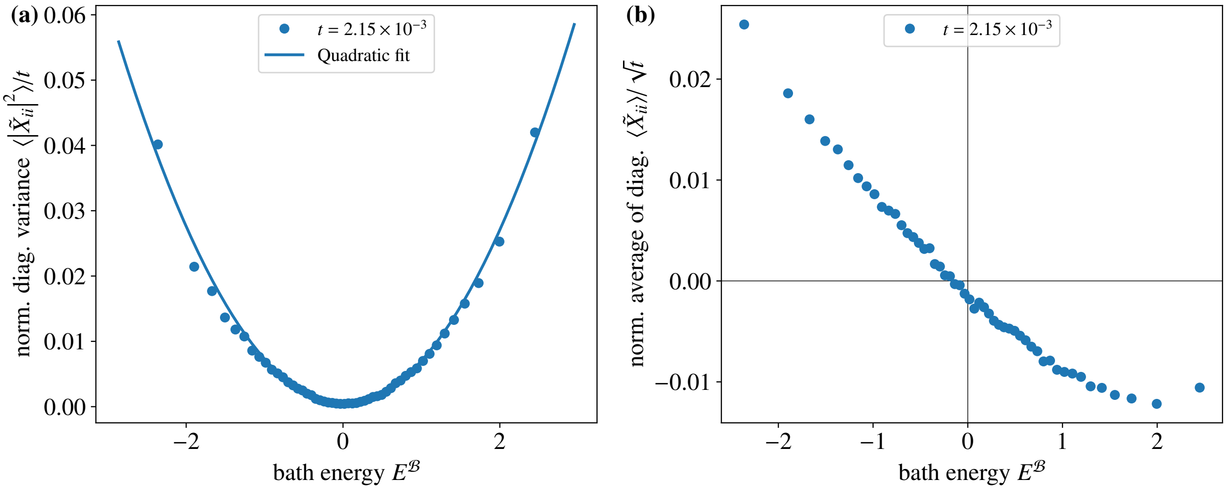

Figure 3.7: **(a)** Sample variance of the diagonal elements of $\tilde{X}$ for 100 samples of X. In each sample, the diagonal values $\tilde{X}_{ii}$ are averaged in intervals of 82 elements, then the sample variance of each interval with respect to X is computed and normalized by t. A quadratic fit $\sigma_1^2 + \left(\frac{\sigma_2}{\sigma_{\mathcal{B}}}\right)^2 \cdot \left(E_i^{\mathcal{B}} - E_0\right)^2$ gives the best fit parameters $\sigma_1^2 = 8.38(35) \times 10^{-4}$, $\sigma_2^2 = 5.79(12) \times 10^{-3}$ and $E_0 = -6.78(47) \times 10^{-3}$. **(b)** Diagonal elements of $\tilde{X}$ averaged over 100 samples of X and in intervals of 82 elements each. The result is normalized by $\sqrt{t}$.

which is mathematically reformulated as $\mathbb{E}_{\mathcal{B}}\left[\left(\langle\psi_i^{\mathcal{B}}|J_l H_l|\psi_i^{\mathcal{B}}\rangle\right)^2\right] = \mathbb{E}_{\mathcal{B}}\left[J_l^2\right]\mathbb{E}_{\mathcal{B}}\left[\left(\langle\psi_i^{\mathcal{B}}|H_l|\psi_i^{\mathcal{B}}\rangle\right)^2\right]$, where J_l is on average pulled out as an independent variable. As $\mathbb{E}_{\mathcal{B}}\left[J_l^2\right] = \sigma_l^2$, the effect of pulling out the contribution from J_l is equivalent to dividing the right hand side by σ_l^2. For this, we assume, that the only effect of J_l is that it sets the scale for the term H_l and how much it contributes to the energy, but has on average no other effect than that of a prefactor, which we treat separately here with the Hamiltonian structure contained in H_l. Eq. (3.29) is consistent with (3.28), which we followed from the energy distribution in terms of the Hamiltonian terms H_l in (3.26). Since X in (3.25) contains the same terms as the Hamiltonian H_l, the second moment of each individual term in X is given by

$$\mathbb{E}_{X,\mathcal{B}}\left[\left(\langle\psi_i^{\mathcal{B}}|x_l H_l|\psi_i^{\mathcal{B}}\rangle\right)^2\right] = \mathbb{E}_X\left[x_l^2\right]\mathbb{E}_{\mathcal{B}}\left[\left(\langle\psi_i^{\mathcal{B}}|H_l|\psi_i^{\mathcal{B}}\rangle\right)^2\right] = t_l\,\frac{\sigma_l^2}{\sigma_{\mathcal{B}}^4}(E_i^{\mathcal{B}})^2, \tag{3.30}$$

which is equal to its variance, since the mean of each prefactor in X is zero, $\mathbb{E}\left[x_l\right] = 0$. From this, we follow for the variance of the whole perturbation matrix $\tilde{X}$ on its diagonal

$$\mathbb{E}_{X,\mathcal{B}}\left[\left(\langle\psi_i^{\mathcal{B}}|X|\psi_i^{\mathcal{B}}\rangle\right)^2\right] = \mathbb{E}_X\left[x_1^2\right] + \sum_{l=2}^{L_X}\mathbb{E}_{X,\mathcal{B}}\left[\left(\langle\psi_i^{\mathcal{B}}|x_l H_l|\psi_i^{\mathcal{B}}\rangle\right)^2\right] = t_1 + \sum_{l=2}^{L_X}\frac{t_l\,\sigma_l^2}{\sigma_{\mathcal{B}}^2}\left(\frac{E_i^{\mathcal{B}}}{\sigma_{\mathcal{B}}}\right)^2. \tag{3.31}$$

In a system where all prefactors J_l in (3.24) are IID with $\sigma_{\mathcal{B}}^2 = L\sigma_l^2$ with a total of L terms in $H^{\mathcal{B}}$, we obtain the final result for the diagonal variance of $\tilde{X}$

$$\mathbb{E}_{\mathcal{B}}\left[\sigma_{ii}^2\right] = \mathbb{E}_{X,\mathcal{B}}\left[\frac{1}{t}\left(\langle\psi_i^{\mathcal{B}}|X|\psi_i^{\mathcal{B}}\rangle\right)^2\right] = \frac{1}{t}\left(t_1 + (t-t_1)\frac{1}{L}\left(\frac{E_i^{\mathcal{B}}}{\sigma_{\mathcal{B}}}\right)^2\right) = \sigma_1^2 + \sigma_2^2\left(\frac{E_i^{\mathcal{B}}}{\sigma_{\mathcal{B}}}\right)^2, \tag{3.32}$$

where we identify the variances $\sigma_1^2 = \frac{t_1}{t}$ and $\sigma_2^2 = \frac{t-t_1}{t}\frac{1}{L}$ in a comparison with the initial equation (3.23). In Eq. (3.32), we take the average over $\mathcal{B}$ as well, which is equivalent to taking the large system size limit with $N_{\mathcal{B}} \to \infty$ given the

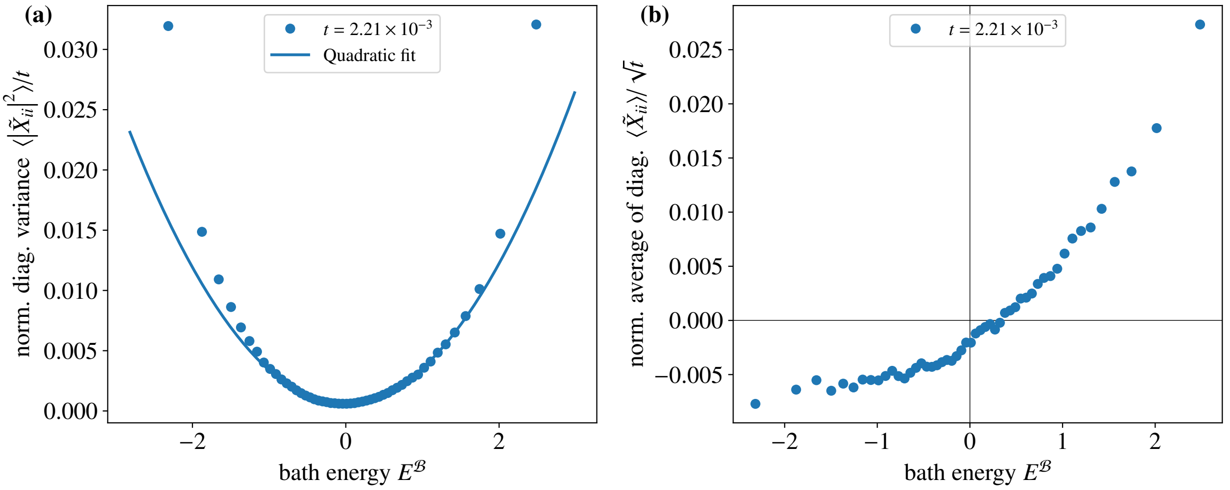

Figure 3.8: (**a**) Sample variance of the diagonal elements of $\tilde{X}$ for 100 samples of X. In contrast to Fig. 3.7 the depicted results are additionally averaged over 50 samples of $H^{\mathcal{B}}$. In each sample, the diagonal values $\tilde{X}_{ii}$ are averaged in intervals of 82 elements, then the sample variance of each interval with respect to X is computed and normalized by t. A quadratic fit $\sigma_1^2 + \left(\frac{\sigma_2}{\sigma_{\mathcal{B}}}\right)^2 \cdot \left(E_i^{\mathcal{B}} - E_0\right)^2$ gives the best fit parameters $\sigma_1^2 = 5.89(10) \times 10^{-4}$, $\sigma_2^2 = 3.047(33) \times 10^{-3}$ and $E_0 = -1.39(25) \times 10^{-2}$. (**b**) Diagonal elements of $\tilde{X}$ averaged over 100 samples of X, 50 samples of $H^{\mathcal{B}}$ and in intervals of 82 elements each. The result is normalized by $\sqrt{t}$.

self averaging property. σ_1^2 is equal to the fraction of t, which contributes with a unit matrix term in X and gives a constant term to the diagonal variance σ_{ii}^2. σ_2^2 is equal to the remaining fraction of t divided by the number of terms in the bath Hamiltonian $H^{\mathcal{B}}$, which is proportional to the number of lattice sites $L \propto d_{\mathcal{B}}$ for the Pauli matrix construction in (2.5). Its contribution is proportional to the square of the eigenenergy $E_i^{\mathcal{B}}$ in $\mathcal{B}$ itself and is therefore responsible for the locally varying trace contribution to the matrix X, which appears in a finite size average. Contrary to the offdiagonal variance, the diagonal variance does not scale inversely to the number of states $\frac{1}{N_{\mathcal{B}}}$, but remains constant when increasing the size of $\mathcal{B}$ while assuming the energy $E_i^{\mathcal{B}}$ to be extensive and to scale with the system size $d_{\mathcal{B}}$.

In Fig. 3.7, we plot the average mean and variance of the diagonal of $\tilde{X}$ for 100 samples of X, normalized by t. In accordance with the analytical results, the variance in Fig. 3.7**a** is quadratic in the bath energy $E_i^{\mathcal{B}}$ and the square of the mean value throughout the matrix in Fig. 3.7**b** is much smaller than the order of magnitude set by the variance values. It implies, that the sample averaging over X already significantly reduced the mean value, which is expected as the theoretical mean value is zero for all entries. Note, that in this case the box variance computed in intervals along the diagonal differs significantly from the sample variance over X. This derives from the correlation to $E_i^{\mathcal{B}}$, as elements in close proximity in the matrix are also close in value. Contrary to the offdiagonal entries, where the box variance gives an equivalent result, we have to be careful here to first average the diagonal elements in intervals and then compute the sample variance of the averaged values. Similar results are obtained when additionally averaging over 50 samples of $H^{\mathcal{B}}$, which are depicted in Fig. 3.8. A quadratic fit of the variance is shown both in Fig. 3.7**a** and Fig. 3.8**a**, which agrees well with the data at small energies. From the calculation in (3.32), we obtain the theoretical expectations of $\sigma_1^2 \approx 0$ and $\sigma_2^2 = 5.29 \times 10^{-3}$. It results from the perturbation matrix X defined in (2.8) for the single peak model, which has no unit matrix term and the number of terms in $H^{\mathcal{B}}$ with $L = 189$ for $d_{\mathcal{B}} = 12$ sites. Those values are of the same order as the fit results $\sigma_2^2 = 5.79(12) \times 10^{-3}$ in Fig. 3.7 and $\sigma_2^2 = 3.047(33) \times 10^{-3}$ in Fig. 3.8 and hence confirm the analytical result. From the fits, we additionally confirm, that $\sigma_1^2 \ll \sigma_2^2$. We assert the deviations to the finite sized averaging. At larger energies, the variance grows faster than quadratic and higher order terms play a role.

When added with the offdiagonals to give the total variance σ_{ij}^2, the diagonal variance contributes with a Kronecker-Delta, $(\sigma_1^2 + \sigma_2^2\,(E_i^{\mathcal{B}})^2)\,\delta_{ij}$. In the continuum limit, the volume ϵ of a unit cell of discretization has to be taken into account with $\delta_{ij} \to \epsilon\,\delta(E_i^{\mathcal{B}} - E_j^{\mathcal{B}})$, where $\delta(x)$ is the Dirac Delta function. In this case it is given by the average energy spacing at $E_i^{\mathcal{B}}$, which is the inverse DOS at that point and we obtain

$$\sigma_{ij}^2 \to \sigma^2(E_i^{\mathcal{B}}, E_j^{\mathcal{B}}) = \sigma_{\mathrm{od}}^2\left(E_i^{\mathcal{B}}, E_j^{\mathcal{B}}\right) + \sigma_{\mathrm{d}}^2\left(E_i^{\mathcal{B}}, E_j^{\mathcal{B}}\right) = \sigma_{\mathrm{od}}^2(E_i^{\mathcal{B}}, E_j^{\mathcal{B}}) + \left(\sigma_1^2 + \sigma_2^2 \cdot \left(\frac{E_i^{\mathcal{B}}}{\sigma_{\mathcal{B}}}\right)^2\right) \frac{\delta(E_i^{\mathcal{B}} - E_j^{\mathcal{B}})}{N_{\mathcal{B}}\rho_{\mathcal{B}}(E_i^{\mathcal{B}})}, \tag{3.33}$$

where $\sigma_{\mathrm{od}}^2(E_i^{\mathcal{B}}, E_j^{\mathcal{B}})$ is the contribution of the offdiagonal and $\sigma_{\mathrm{d}}^2(E_i^{\mathcal{B}}, E_j^{\mathcal{B}})$ of the diagonal elements to the variance model. A fundamental property of the diagonal variance σ_{ii}^2 is, that it does not scale with $N_{\mathcal{B}}$. In contrast to the offdiagonal variance, where each element decreases as $\frac{1}{N_{\mathcal{B}}}$, the diagonal variance does not scale with $N_{\mathcal{B}}$, but remains constant upon changing the size of the bath $\mathcal{B}$. This is reflected in Eq. (3.32), where we assume an extensive behavior of the energy $E^{\mathcal{B}}$ with the system size of $\mathcal{B}$, which exactly compensates the extensive behavior of $\sigma_{\mathcal{B}}$ and the inverse extensive property of the prefactor to the energy dependence σ_2^2. Consequently, the diagonal entries of $\tilde{X}$ contribute significantly to the total matrix and are much larger than any single offdiagonal entry. In a sum over one row or column, in contrast to any single offdiagonal element, they can not be neglected or disregarded as a null set for $N_{\mathcal{B}} \to \infty$.

3.2 The variance model

In the previous section we analyzed the diagonal of the perturbation matrix X represented in the unperturbed eigenbasis as $\tilde{X}$. To complete the analysis of $\tilde{X}$ we perform a random matrix calculation to find the variance model of its offdiagonal elements. This is then compared to numerical results. Lastly we describe how to extend the results obtained within the single peak model to the multi peak model.

3.2.1 Random matrix computation of the variance

Having treated the diagonal variance of the matrix elements of $\tilde{X}$ in Sec. 3.1.4 analytically, we employ RMT to also find an analytical expression for the variance of the offdiagonal elements. For that, we use the singular value decomposition (SVD) of the eigenstates in $\mathcal{B}$ defined in (2.16) for the partition into the subsystems C and $\bar{C}$,

$$|\psi_i^{\mathcal{B}}\rangle = \sum_{\alpha=1}^{N_C} \kappa_\alpha^{(i)} \; |\phi_\alpha^{C,i}\rangle \otimes |\phi_\alpha^{\bar{C},i}\rangle \tag{3.34}$$

with the singular values $\kappa_\alpha^{(i)} > 0$. With the SVD of the bath eigenstates, we find the relation

$$\langle\psi_i^{\mathcal{B}}|X|\psi_j^{\mathcal{B}}\rangle = \sum_{\alpha,\beta=1}^{N_C} \kappa_\alpha^{(i)}\kappa_\beta^{(j)} \; \langle\phi_\alpha^{C,i}|X|\phi_\beta^{C,j}\rangle \; \langle\phi_\alpha^{\bar{C},i}|\phi_\beta^{\bar{C},j}\rangle = \sum_{\alpha,\beta=1}^{N_C} \kappa_\alpha^{(i)}\kappa_\beta^{(j)} \; X_{\alpha,\beta}^{(i,j)} \; \langle\phi_\alpha^{\bar{C},i}|\phi_\beta^{\bar{C},j}\rangle \tag{3.35}$$

for the matrix elements, which utilizes the definition of X in the SVD basis of C. Taking the expectation value of the squared modulus yields the variance model σ_{ij}^2 as defined in Eq. (3.5) for the case $i \neq j$,

$$\begin{aligned}
\sigma_{ij}^2 = \frac{1}{t}\,\mathbb{E}\left[\left|\langle\psi_i^{\mathcal{B}}|X|\psi_j^{\mathcal{B}}\rangle\right|^2\right] &= \frac{1}{t}\sum_{\alpha,\beta,\alpha',\beta'} \kappa_\alpha^{(i)}\kappa_\beta^{(j)}\kappa_{\alpha'}^{(i)}\kappa_{\beta'}^{(j)} \; \langle\phi_\alpha^{\bar{C},i}|\phi_\beta^{\bar{C},j}\rangle \; \langle\phi_{\beta'}^{\bar{C},j}|\phi_{\alpha'}^{\bar{C},i}\rangle \; \underbrace{\mathbb{E}\left[X_{\alpha,\beta}^{(i,j)}\left(X_{\alpha',\beta'}^{(i,j)}\right)^*\right]}_{\approx\delta_{\alpha\alpha'}\,\delta_{\beta\beta'}\,\mathbb{E}\left[|X_{\alpha,\beta}^{(i,j)}|^2\right]} \\
&= \frac{1}{t}\sum_{\alpha,\beta}\left(\kappa_\alpha^{(i)}\right)^2\left(\kappa_\beta^{(j)}\right)^2\left|\langle\phi_\alpha^{\bar{C},i}|\phi_\beta^{\bar{C},j}\rangle\right|^2\mathbb{E}\left[|X_{\alpha,\beta}^{(i,j)}|^2\right] \\
&= \frac{1}{t}\sum_{\alpha,\beta}\left|\langle\tilde{\phi}_\alpha^{\bar{C},i}|\tilde{\phi}_\beta^{\bar{C},j}\rangle\right|^2 \; \underbrace{\mathbb{E}\left[|X_{\alpha,\beta}^{(i,j)}|^2\right]}_{\approx\frac{t}{N_C}} \\
&\approx \frac{1}{N_C}\sum_{\alpha,\beta}\left|\langle\tilde{\phi}_\alpha^{\bar{C},i}|\tilde{\phi}_\beta^{\bar{C},j}\rangle\right|^2 .
\end{aligned} \tag{3.36}$$

With the definition $|\tilde{\phi}_\alpha^{\bar{C},i}\rangle \equiv \kappa_\alpha^{(i)} \; |\phi_\alpha^{\bar{C},i}\rangle$, the singular values in the SVD are absorbed into the states $|\tilde{\phi}_\alpha^{\bar{C},i}\rangle$ in subsystem $\bar{C}$. The SVD basis $X^{(i,j)}$ with elements $X_{\alpha,\beta}^{(i,j)}$ is obtained through a transformation of X from the reduced basis of C. We assume, that for a small subsystem C, the matrix $X^{(i,j)}$ is approximately given by a GUE in the sense, that the variance of all elements is identical and given by $\frac{t}{N_C}$. This is fulfilled exactly only if we started with a GUE for X in the reduced basis of C. However, each scattering of the matrix $X_{\alpha,\beta}$ between different singular vectors in the small subsystem C can be approximated to be uniform with X being close to a dense matrix for small C. Since the bath Hamiltonian $H^{\mathcal{B}}$ consists of random interactions as well, which are statistically independent of the random interactions in X, the scattering in C is approximately uniform after taking an average over $\mathcal{B}$. When C is larger, the local structure of the interaction terms needs to be taken into account. In this case, we can use the diagonal two-point correlation in Eq. (3.13), which derives from random phases of the states in the rotated basis, in this case the SVD basis. This explains the identity in the first line of the calculation. The variances in the matrix $X^{(i,j)}$ are not constant anymore, but will in some way decline with the difference in scattering energy. It introduces a background decrease of the variance for larger energies additional to the structure inherent to the SVD scattering $\left|\langle\tilde{\phi}_\alpha^{\bar{C},i}|\tilde{\phi}_\beta^{\bar{C},j}\rangle\right|^2$. In the following, we neglect this background contribution as its width is much larger than what is expected from the SVD scattering in (3.36) with X having access to all spins in C. As the scattering of X in subsystem C is averaged out, the variance model in Eq. (3.36) depends only on the singular vectors in $\bar{C}$ and on their corresponding singular values. The spectral structure of the final result in (3.36) is dictated by all possible overlaps between the singular vectors of i and j in the region $\bar{C}$.

Alternatively, the offdiagonal variance can be represented by the use of reduced density matrices in $\bar{C}$,

$$\rho_{\bar{C}}^{(i)} = \mathrm{Tr}_C(\,|\psi_i^{\mathcal{B}}\rangle\,\langle\psi_i^{\mathcal{B}}|) = \sum_{\alpha=1}^{N_C}(\kappa_\alpha^{(i)})^2\,|\phi_\alpha^{\bar{C},i}\rangle\,\langle\phi_\alpha^{\bar{C},i}|\,. \tag{3.37}$$

Massaging Eq. (3.36) gives

$$\begin{aligned}
\sigma_{ij}^2 &= \frac{1}{N_C}\sum_{\alpha,\beta}\left(\kappa_\alpha^{(i)}\right)^2\left(\kappa_\beta^{(j)}\right)^2\,\langle\phi_\alpha^{\bar{C},i}|\phi_\beta^{\bar{C},j}\rangle\,\langle\phi_\beta^{\bar{C},j}|\phi_\alpha^{\bar{C},i}\rangle\\
&= \frac{1}{N_C}\sum_{\alpha}\left(\kappa_\alpha^{(i)}\right)^2\,\langle\phi_\alpha^{\bar{C},i}|\rho_{\bar{C}}^{(j)}|\phi_\alpha^{\bar{C},i}\rangle\\
&= \frac{1}{N_C}\sum_{\alpha,m,n}\left(\kappa_\alpha^{(i)}\right)^2\,\langle\phi_\alpha^{\bar{C},i}|\psi_m^{\bar{C}}\rangle\,\langle\psi_m^{\bar{C}}|\rho_{\bar{C}}^{(j)}|\psi_n^{\bar{C}}\rangle\,\langle\psi_n^{\bar{C}}|\phi_\alpha^{\bar{C},i}\rangle\\
&= \frac{1}{N_C}\sum_{m,n}\left[\rho_{\bar{C}}^{(i)}\right]_{nm}\left[\rho_{\bar{C}}^{(j)}\right]_{mn} = \frac{1}{N_C}\,\mathrm{Tr}_{\bar{C}}\left[\rho_{\bar{C}}^{(i)}\rho_{\bar{C}}^{(j)}\right],
\end{aligned} \tag{3.38}$$

where $\left[\rho_{\bar{C}}^{(i)}\right]_{nm} \equiv \langle\psi_n^{\bar{C}}|\rho_{\bar{C}}^{(i)}|\psi_m^{\bar{C}}\rangle$ is the matrix representation of the reduced density matrix $\rho_{\bar{C}}^{(i)}$ in terms of the eigenbasis of $H^{\bar{C}}$, which is $|\psi_n^{\bar{C}}\rangle\,, n = 1, \ldots, N_{\bar{C}}$. In Eq. (3.36), the variance is given by SVD vector overlaps. The overlap can be represented in terms of the eigenbasis of $H^{\bar{C}}$ as

$$\sigma_{ij}^2 = \frac{1}{N_C}\sum_{\alpha,\beta,m,n}\langle\tilde{\phi}_\alpha^{\bar{C},i}|\psi_m^{\bar{C}}\rangle\,\langle\psi_m^{\bar{C}}|\tilde{\phi}_\beta^{\bar{C},j}\rangle\,\langle\tilde{\phi}_\beta^{\bar{C},j}|\psi_n^{\bar{C}}\rangle\,\langle\psi_n^{\bar{C}}|\tilde{\phi}_\alpha^{\bar{C},i}\rangle\,. \tag{3.39}$$

We can split up the involved overlaps into an absolute value and a phase contribution,

$$\langle\psi_n^{\bar{C}}|\tilde{\phi}_\alpha^{\bar{C},i}\rangle \equiv \left|\langle\psi_n^{\bar{C}}|\tilde{\phi}_\alpha^{\bar{C},i}\rangle\right|\,e^{i\varphi_{n,\alpha}^{(i)}} \tag{3.40}$$

and insert it into the expression to obtain

$$\sigma_{ij}^2 = \frac{1}{N_C}\sum_{\alpha,\beta,m,n}\left|\langle\tilde{\phi}_\alpha^{\bar{C},i}|\psi_m^{\bar{C}}\rangle\right|\left|\langle\psi_m^{\bar{C}}|\tilde{\phi}_\beta^{\bar{C},j}\rangle\right|\left|\langle\tilde{\phi}_\beta^{\bar{C},j}|\psi_n^{\bar{C}}\rangle\right|\left|\langle\psi_n^{\bar{C}}|\tilde{\phi}_\alpha^{\bar{C},i}\rangle\right|\exp\left\{i\left(\varphi_{n,\alpha}^{(i)} - \varphi_{m,\alpha}^{(i)}\right) + i\left(\varphi_{m,\beta}^{(j)} - \varphi_{n,\beta}^{(j)}\right)\right\}. \tag{3.41}$$

The phases $\varphi_{n,\alpha}^{(i)}$ are random real numbers, which leads to the sums over m and n being averaged out to zero for $m \neq n$, where $N_{\bar{C}}$ random complex phases are added. Only in the case $m = n$, the phases cancel and the sum contributes with the modulus squared of the overlap terms,

$$\sigma_{ij}^2 = \frac{1}{N_C}\sum_{\alpha,\beta,n}\left|\langle\psi_n^{\bar{C}}|\tilde{\phi}_\alpha^{\bar{C},i}\rangle\right|^2\left|\langle\psi_n^{\bar{C}}|\tilde{\phi}_\beta^{\bar{C},j}\rangle\right|^2. \tag{3.42}$$

Those are the diagonal terms of the reduced density matrices $\rho^{(i)}_{\bar{C}}$ and $\rho^{(j)}_{\bar{C}}$ represented in the eigenbasis of $H^{\bar{C}}$, which are the only terms left from the matrix product in (3.38). We define the overlaps as

$$\tilde{\chi}^{(i)}_{\alpha,n} \equiv \left|\langle\psi^{\bar{C}}_n|\tilde{\phi}^{\bar{C},i}_\alpha\rangle\right|^2. \tag{3.43}$$

The states $|\tilde{\phi}^{\bar{C},i}_\alpha\rangle$ are chosen such that they are collectively normalized in a sum over α with $\sum_{\alpha,n}\tilde{\chi}^{(i)}_{\alpha,n} = 1$. In the continuum limit with $N \to \infty$ and $\tilde{\chi}^{(i)}_{\alpha,n} \to \tilde{\chi}(\epsilon_\alpha, E^{\bar{C}}_n, E^{\mathcal{B}}_i)$, the summation in (3.42) is replaced by an integral with the corresponding DOS

$$\sigma^2_{ij} \to \sigma^2_{\text{od}}\left(E^{\mathcal{B}}_i, E^{\mathcal{B}}_j\right) = \frac{1}{N_C}\int \mathrm{d}\epsilon\,(N_C\rho_C(\epsilon))\int \mathrm{d}\epsilon'\,(N_C\rho_C(\epsilon'))\int \mathrm{d}E^{\bar{C}}\,(N_{\bar{C}}\rho_{\bar{C}}(E^{\bar{C}}))\tilde{\chi}(\epsilon, E^{\bar{C}}, E^{\mathcal{B}}_i)\tilde{\chi}(\epsilon', E^{\bar{C}}, E^{\mathcal{B}}_j),$$

where σ^2_{od} represents the offdiagonal contribution to the variance model, considering the case $i \neq j$. There are two integrals over the energy in C corresponding to the sums over α and β and one integration over the energy in $\bar{C}$, which results from the sum over n. Consider a weak coupling limit, where the subsystems C and $\bar{C}$ are coupled by an interaction $X^{C-\bar{C}}$, which is very small compared to the whole bath, $\tau((X^{C-\bar{C}})^2) = t_C \ll \sigma^2_{\mathcal{B}}$. In the limit $t_C \to 0$, the overlap reduces to a Delta function

$$\tilde{\chi}(\epsilon, E^{\bar{C}}, E^{\mathcal{B}}_i) \;\to\; \frac{\delta(\epsilon - (E^{\mathcal{B}}_i - E^{\bar{C}}))}{N_{\mathcal{B}}\rho_{\mathcal{B}}(E^{\mathcal{B}}_i)} \tag{3.44}$$

since the eigenstates in $\mathcal{B}$ are product states of the eigenstates in C and in $\bar{C}$. The Delta function divided by the DOS is the continuum limit of the Kronecker-Delta, which matches the energies of the corresponding eigenstates. In this limit, we obtain

$$\sigma^2_{\text{od}}\left(E^{\mathcal{B}}_i, E^{\mathcal{B}}_j\right) = \frac{1}{N_{\mathcal{B}}}\,\frac{\int \mathrm{d}E^{\bar{C}}\,\rho_C(E^{\mathcal{B}}_i - E^{\bar{C}})\rho_C(E^{\mathcal{B}}_j - E^{\bar{C}})\rho_{\bar{C}}(E^{\bar{C}})}{\rho_{\mathcal{B}}(E^{\mathcal{B}}_i)\rho_{\mathcal{B}}(E^{\mathcal{B}}_j)} \tag{3.45}$$

as the final result. The formula is similar to a convolution, but involves three functions instead of two, where the DOS in $\bar{C}$ is integrated with twice the DOS in C, which are shifted by $E^{\mathcal{B}}_i$ and $E^{\mathcal{B}}_j$. We notice, that a single offdiagonal element scales with $\frac{1}{N_{\mathcal{B}}}$ as determined by the first factor. The second quotient in (3.45) contains the eigenvalue densities, which are normalized to one and provide the structure of the matrix in the energies $E^{\mathcal{B}}_i$ and $E^{\mathcal{B}}_j$. In the limit $N_{\mathcal{B}} \to \infty$, any individual offdiagonal element can be treated as a null set, since it gives a vanishing contribution to the total model. However, in a fixed energy interval, the sum of elements gives a finite nonzero contribution. As the system size increases, the matrix becomes more and more diagonal-heavy as the diagonal elements do not scale with $\frac{1}{N_{\mathcal{B}}}$, but only with $\frac{1}{N_C}$. Although the result (3.45) is only exact in the limit of small coupling t_C between C and $\bar{C}$, it still holds approximately, if t_C is much smaller than the variance $\sigma^2_{\mathcal{B}}$ in $\mathcal{B}$. In the case of nonzero t_C, the width of the overlaps $\tilde{\chi}^{(i)}_{\alpha,n}$ in (3.42) although nonzero remains small, since C is a small region of the whole bath $\mathcal{B}$, which ensures $t_C \ll \sigma^2_{\mathcal{B}}$. To match the case of nonzero t_C to the result (3.45), we further have to assume, that the variation of $\tilde{\chi}(\epsilon_\alpha, E^{\bar{C}}_n, E^{\mathcal{B}}_i)$ occurs on a much smaller energy scale than that of the DOS of C. This is the case if $t_C \ll \sigma^2_C$, such that the main contribution from the integrals over the energy in C comes from the peak positions of $\tilde{\chi}(\epsilon_\alpha, E^{\bar{C}}_n, E^{\mathcal{B}}_i)$. In this approximation, the width of the overlaps is neglected. In summary, formula (3.45) is valid in the limit $N_{\mathcal{B}} \to \infty$. As expected, the result is symmetric under the interchange of i and j. It also fulfills the normalization condition of the variance model,

$$\begin{aligned}\sum_j \sigma_{ij}^2 = \sum_i \sigma_{ij}^2 &= \int \mathrm{d}E^{\mathcal{B}} \left(N_{\mathcal{B}}\rho_{\mathcal{B}}(E^{\mathcal{B}})\right) \frac{1}{N_{\mathcal{B}}} \frac{\int \mathrm{d}E^{\bar{C}} \rho_C(E^{\mathcal{B}} - E^{\bar{C}})\rho_C(E_j^{\mathcal{B}} - E^{\bar{C}})\rho_{\bar{C}}(E^{\bar{C}})}{\rho_{\mathcal{B}}(E^{\mathcal{B}})\rho_{\mathcal{B}}(E_j^{\mathcal{B}})} \\ &= \frac{1}{\rho_{\mathcal{B}}(E_j^{\mathcal{B}})} \int \mathrm{d}E^{\bar{C}} \rho_C(E_j^{\mathcal{B}} - E^{\bar{C}})\rho_{\bar{C}}(E^{\bar{C}}) = 1,\end{aligned}$$

where the convolution of the eigenvalue densities in C and $\bar{C}$ returns the eigenvalue density $\rho_{\mathcal{B}}(E)$ in $\mathcal{B}$. Note, that the diagonal contribution of the matrix $\tilde{X}$ to the variance model σ_{ij}^2 is not included here. The full model is obtained by inserting the final result for σ_{od} from (3.45) into Eq. (3.33), which contains the result for the diagonal in the continuum

$$\sigma^2\left(E_i^{\mathcal{B}}, E_j^{\mathcal{B}}\right) = \frac{A}{N_{\mathcal{B}}} \frac{\int \mathrm{d}E^{\bar{C}} \rho_C(E_i^{\mathcal{B}} - E^{\bar{C}})\rho_C(E_j^{\mathcal{B}} - E^{\bar{C}})\rho_{\bar{C}}(E^{\bar{C}})}{\rho_{\mathcal{B}}(E_i^{\mathcal{B}})\rho_{\mathcal{B}}(E_j^{\mathcal{B}})} + \left(\sigma_1^2 + \sigma_2^2 \left(\frac{E_i^{\mathcal{B}}}{\sigma_{\mathcal{B}}}\right)^2\right) \frac{\delta(E_i^{\mathcal{B}} - E_j^{\mathcal{B}})}{N_{\mathcal{B}}\rho_{\mathcal{B}}(E_i^{\mathcal{B}})}. \tag{3.46}$$

We added a prefactor A to the offdiagonal part to account for the now unfulfilled normalization condition due to the contribution from the diagonal part. Crucially, the diagonal part cannot be approximated as a null set for large $N_{\mathcal{B}}$, as it does not scale with $\frac{1}{N_{\mathcal{B}}}$ in contrast to each individual offdiagonal element. If the spectral width in C is much smaller than the total spectral width in $\mathcal{B}$ with $\sigma_C \ll \sigma_{\mathcal{B}}$, the normalization prefactor can be approximated to

$$A = 1 - \sigma_1^2 - \sigma_2^2\, E_i^{\mathcal{B}} E_j^{\mathcal{B}} \tag{3.47}$$

after symmetrization in i and j to fulfill the sum rule for the variance normalization.

3.2.2 Comparison to numerical results

We compare the analytical results for the offdiagonal part of the variance of $\tilde{X}$ obtained in Sec. 3.2.1 through RMT to numerical simulations. We first investigate Eq. (3.36), which connects the variance σ_{ij}^2 to the overlaps between the SVD vectors from $|\psi_i^{\mathcal{B}}\rangle$ and $|\psi_j^{\mathcal{B}}\rangle$ in the subsystem $\bar{C}$. Fig. 3.9 shows the result for four values of t_C with the joined orange curve denoting the sum of SVD overlaps from the right-hand side of (3.36) while the blue points represent the actual variance $\sigma^2(E_i^{\mathcal{B}}, E_j^{\mathcal{B}})$ along the anti-diagonal in $\tilde{X}$. To analyze the dependence of E_- we choose the anti-diagonal, as along this line $E_i^{\mathcal{B}} \approx -E_j^{\mathcal{B}}$ and therefore $E_+ \approx 0$. In all figures throughout this section, the bath $\mathcal{B}$ contains $d_{\mathcal{B}} = 12$ lattice sites with the same coupling strengths in C and $\bar{C}$, which are IID. Hence, only the coupling between C and $\bar{C}$ is subject to change, which has a negligible effect on the total width $\sigma_{\mathcal{B}}^2$ of the Gaussian DOS $N_{\mathcal{B}}\rho_{\mathcal{B}}(E)$. It is therefore reasonable to compare the results for the absolute values of different t_C in the following. In Fig. 3.9, an average over X is taken, while $H^{\mathcal{B}}$ remains the same operator as it is represented by just one randomly drawn sample.

Since t_C is very small in Fig. 3.9**a**, the SVD overlaps are very narrow. This can be understood from the limit $t_C \to 0$, where the perturbed basis coincides with the product basis of C and $\bar{C}$ and the overlaps are delta peaks. The peaks are located at all possible differences of the eigenvalues of H^C, which are plotted as dashed lines for reference. X scatters between different states in C which requires the bath energy $E^{\mathcal{B}}$ to change according to those energy differences in C. Note, that the peaks stay at the same positions throughout the averaging over random samples of X, which confirms that they depend on features of the unperturbed system $\mathcal{B}$, while X just decides the separation of the lattice into the subsystems C and $\bar{C}$. The eigenvalue differences marked with dashed lines in Fig. 3.9**a** are matched by the peak positions of the variance σ_{ij}^2.

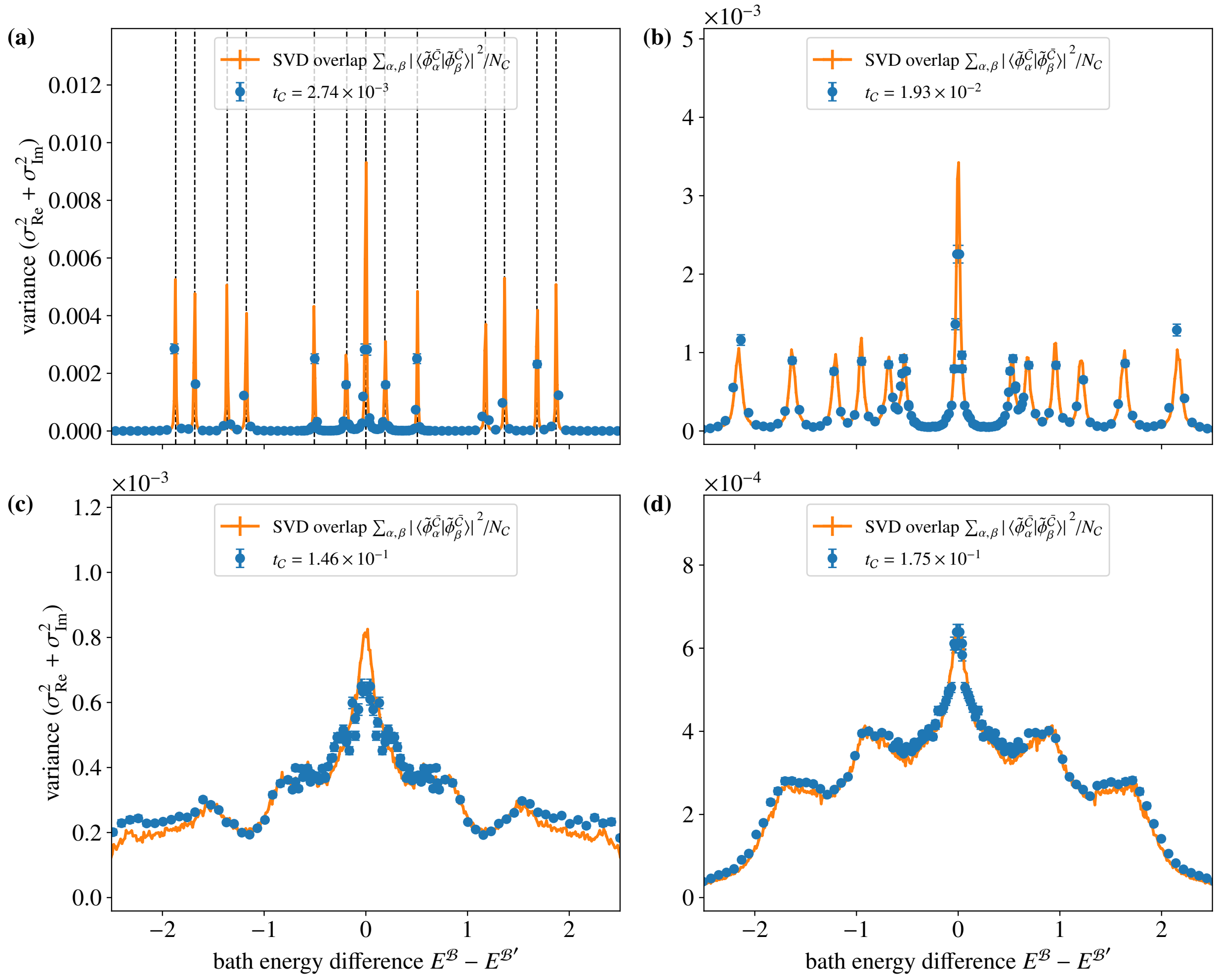

Figure 3.9: Element wise variance along the anti-diagonal line of the matrix $\tilde{X}$ in the single peak model of $d_{\mathcal{B}} = 12$ and $d_{\mathcal{S}} = 0$ sites with $t = 0.01$. We analyze different coupling strengths t_C between the subsystems C and $\bar{C}$ in the bath. The variance is depicted as blue points and compared to the SVD overlap formula in (3.36), plotted as a joined orange line. We average over 100 samples of X, while $H^{\mathcal{B}}$ stays constant. Relative to all other local terms in $H^{\mathcal{B}}$, we choose the width of the terms in $H^{C-\bar{C}}$ to be of strength **(a)** 10%, **(b)** 20%, **(c)** 50%, and **(d)** 100%. **(d)** corresponds to all terms being IID with $\tau\left((H^{\mathcal{B}})^2\right) = 4.64$. **(a)** additionally shows all possible differences of eigenvalues in the subsystem C, where X acts.

In Fig. 3.9**b** with slightly larger t_C, the peaks are no longer as sharply pronounced because the widths of the SVD overlaps have increased. This trend is reinforced in Fig. 3.9**c** and Fig. 3.9**d**, when there are no single peaks distinguishable anymore due to the large width of the SVD overlaps, which average to a curve with a broad discernible scattering width. In all of the plots in Fig. 3.9, the SVD prediction agrees with the shape of the actual variance data.

To probe the validity of the approximation of random phases, which was used to obtain Eq. (3.42) from (3.36), we compare the numerical results of the two equations in Fig. 3.10 for the same setup and the same values of t_C as in Fig. 3.9. When we assume, that the SVD vectors in $\bar{C}$ possess purely random phases in the eigenstate representation of $\bar{C}$, the only term, which remains from the SVD vector overlap in Eq. (3.36) is the diagonal term for $m = n$ in Eq. (3.42). Here, the joint orange line again corresponds to the full SVD overlap, while the blue points represent the diagonal term in the eigenstate representation. As evident from the agreement of the two expressions in Fig. 3.10**a**-

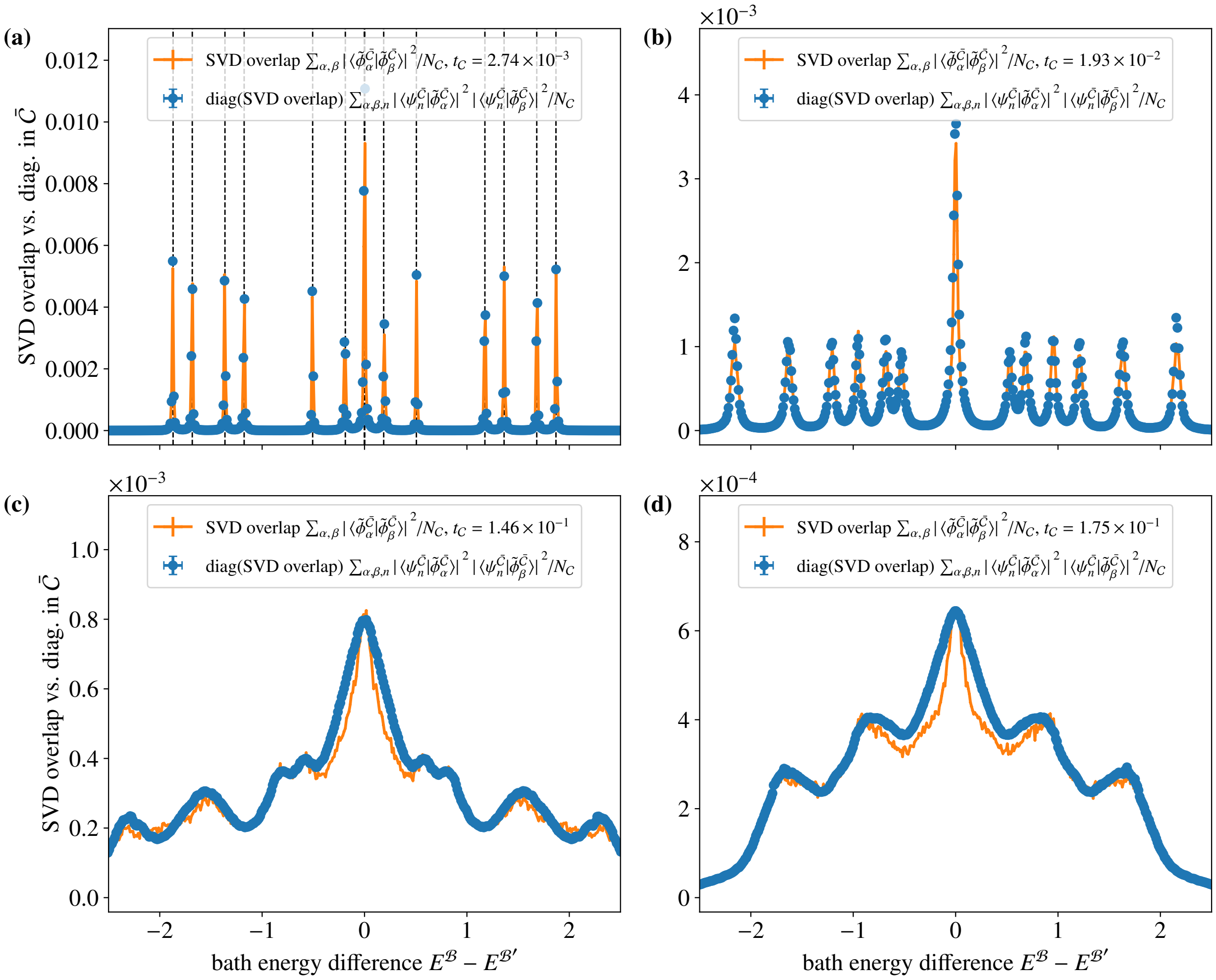

Figure 3.10: SVD overlap of the singular vectors in $\bar{C}$ in Eq. (3.36) in orange compared to the approximation of random phases represented in terms of the eigenbasis of $\bar{C}$ in Eq. (3.42) as blue points. An average is taken over 100 samples of X, whereas $H^{\mathcal{B}}$ stays constant. For this, we work with the single peak model with $d_{\mathcal{B}} = 12$ and $d_{\mathcal{S}} = 0$ sites. Relative to all other local terms in $H^{\mathcal{B}}$, we choose the width of the terms in $H^{C-\bar{C}}$ to be of strength **(a)** 10%, **(b)** 20%, **(c)** 50%, and **(d)** 100%. **(a)** additionally shows all possible differences of eigenvalues in the subsystem C, where X acts.

d, the approximation of random phases is also numerically justified and is henceforth applied in different contexts throughout this work. In Fig. 3.10**a-c**, there is a near perfect agreement of the two expressions, while in Fig. 3.10**d**, the only distinctive remaining peak at zero cannot be resolved with the diagonal of the SVD overlap, as there is an overshoot compared to the full overlap at energy differences close to zero. While the reason remains an open question for further investigation, we formulate the conjecture, that there exists a minor correlation in the phases of SVD states, which are computed from eigenstates $|\psi_i^{\mathcal{B}}\rangle$ and $|\psi_j^{\mathcal{B}}\rangle$ close to each other in energy. Due to this correlation, the actual peaked SVD overlap vanishes faster when we go away from the peak than what is estimated from its diagonal part in the eigenbasis representation. This leads to an overestimate of the blue points in Fig. 3.10 in comparison to the orange line. It does not matter far away from the peak positions of the SVD overlaps and is balanced out for energy differences far away from zero in Fig. 3.10**d**. But since the peak at zero is a superposition of a total of N_C peaks at

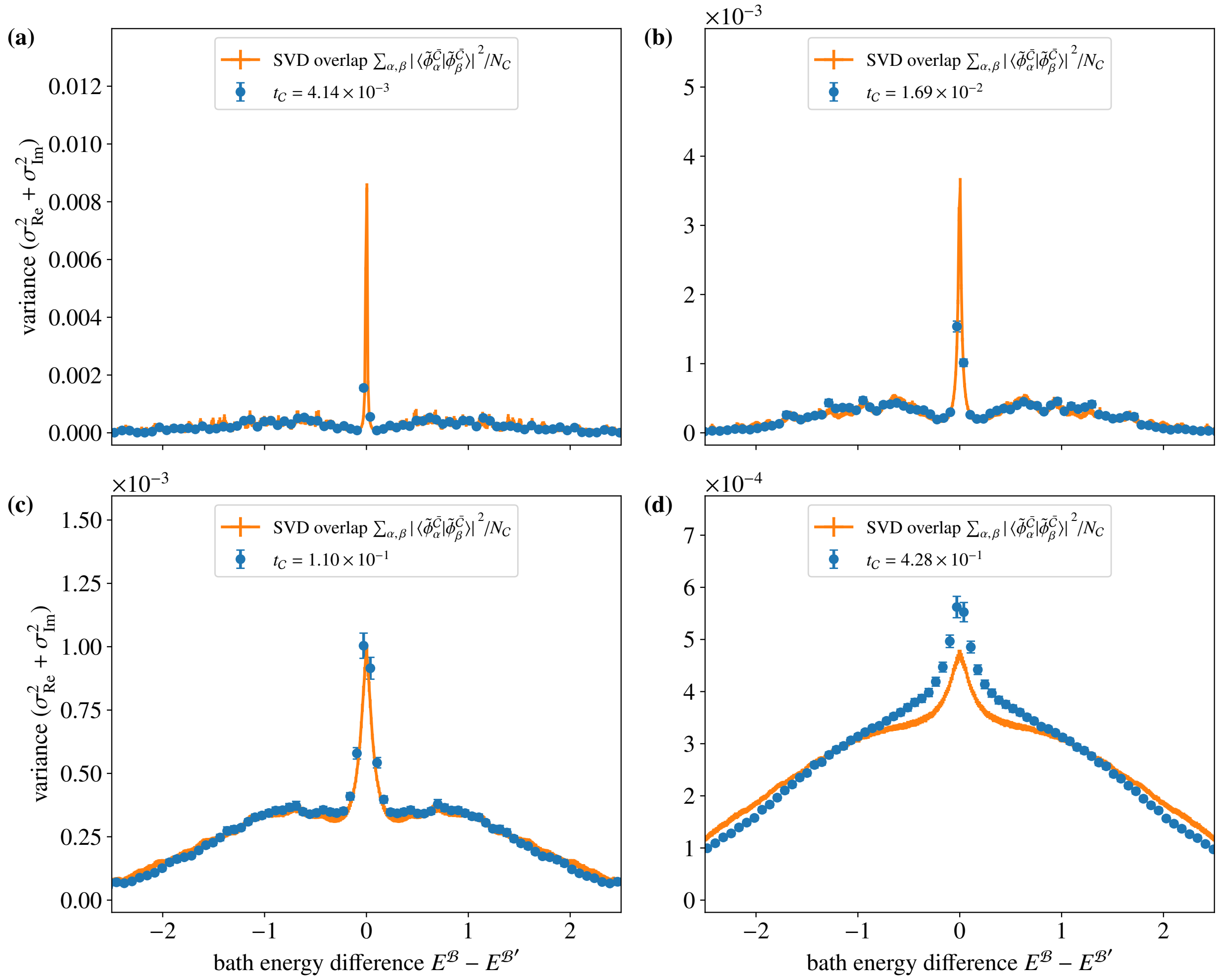

Figure 3.11: Element wise variance along the anti-diagonal line of the matrix $\tilde{X}$ in the single peak model of $d_{\mathcal{B}} = 12$ and $d_S = 0$ sites with $t = 0.01$ with $t = 0.01$ for different coupling strengths t_C between the subsystems C and $\bar{C}$ in the bath. The variance is depicted as blue points and compared to the SVD overlap formula in (3.36), plotted as a joined orange line. An average is taken over 100 samples of X and 50 samples of $H^{\mathcal{B}}$. Relative to all other local terms in $H^{\mathcal{B}}$, we choose the width of the terms in $H^{C-\bar{C}}$ to be of strength **(a)** 10%, **(b)** 20%, **(c)** 50%, and **(d)** 100%.

that position, this discrepancy becomes especially prominent. For now, we disregard this point as a minor correction to the description of the variance model.

In Fig. 3.11 and Fig. 3.12, we perform an additional average over 50 samples of $H^{\mathcal{B}}$. The comparison of the SVD vector overlap to the total variance along the anti-diagonal is shown in Fig. 3.11. For small t_C in Fig. 3.11**a**,**b**, there is a prominent peak at zero, while the remaining structure is averaged out. This roots in the averaging over $\mathcal{B}$, which causes the peaks to appear at different positions for each individual sample except for the peak at zero, which is present in every sample and hence remains. As we consider larger t_C in Fig. 3.11**c**,**d**, the SVD overlaps become broader and a variance structure remains after the averaging. The deviation of the two quantities close to zero in Fig. 3.11**d** remains after the average over $\mathcal{B}$, but the general shape of the variance model is captured well by the SVD result. We find similar results in Fig. 3.12, where we again compare formulas (3.42) and (3.45) in a numerical analysis with an additional average over $\mathcal{B}$. The data of both quantities agrees, once more confirming the approximation of random

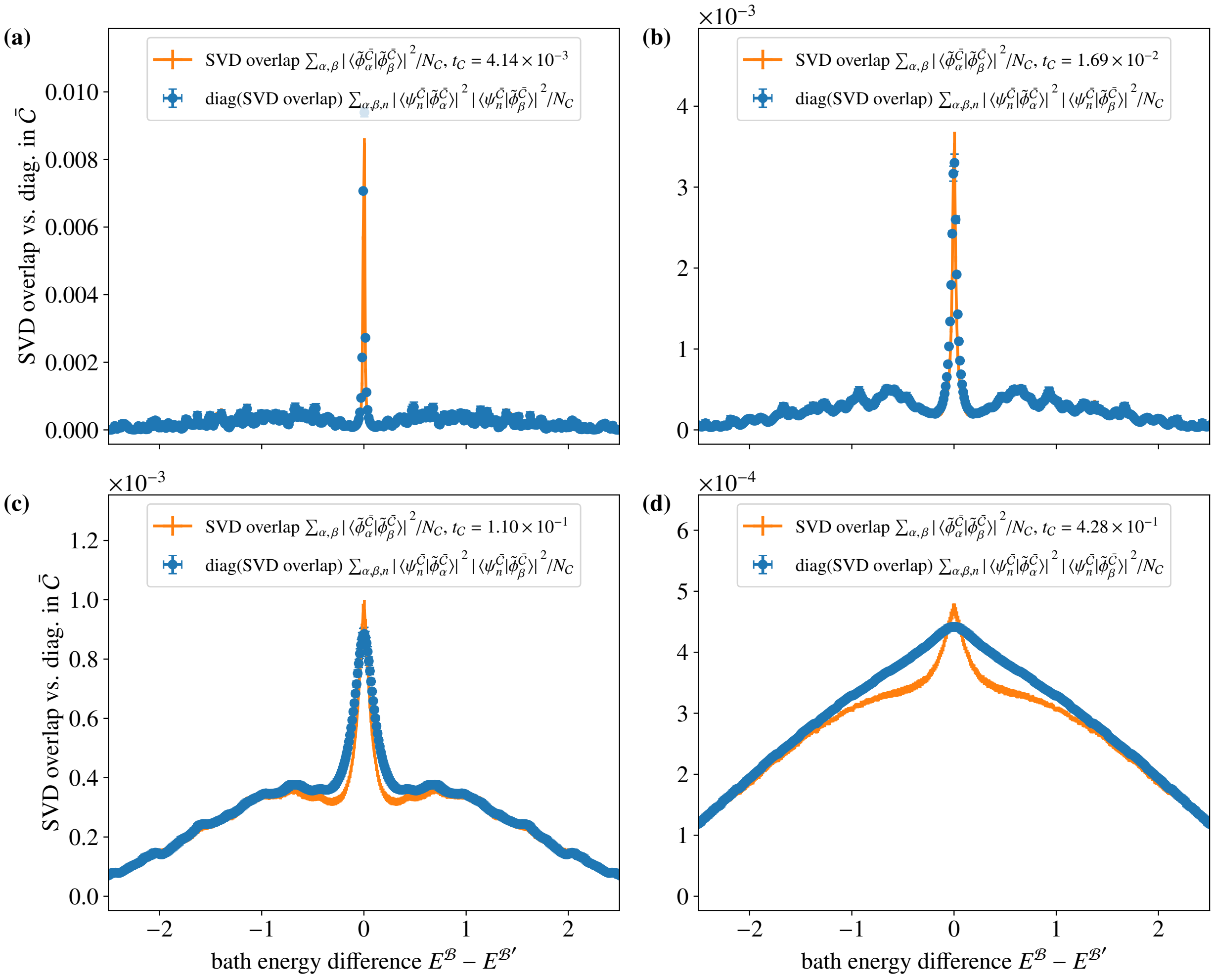

Figure 3.12: SVD overlap of the singular vectors in $\bar{C}$ in Eq. (3.36) in orange compared to the approximation of random phases of the SVD overlap represented in terms of the eigenbasis of $\bar{C}$ in Eq. (3.42) as blue points. For this, we work with the single peak model with $d_{\mathcal{B}} = 12$ and $d_{\mathcal{S}} = 0$ sites. An average is taken over 100 samples of X and 50 samples of $H^{\mathcal{B}}$. Relative to all other local terms in $H^{\mathcal{B}}$, we choose the width of the terms in $H^{C-\bar{C}}$ to be of strength **(a)** 10%, **(b)** 20%, **(c)** 50%, and **(d)** 100%.

phases. Similar to Fig. 3.10**d**, we find in Fig. 3.12**d**, that the peak at zero in the SVD overlap is not captured by the diagonal terms in the $\bar{C}$ eigenbasis.

Fig. 3.13 shows a comparison of the final result for the offdiagonal variance in Eq. (3.45) with numerical results at $t_C = 4.28 \times 10^{-3}$. The general structure of the variance is reproduced by the analytical formula. However, it also does not accurately represent the peak at zero, which is a consequence of the approximation of random phases, on which the analytic result builds. In the limit $N_{\mathcal{B}} \to \infty$, the peak at zero vanishes and the variance model has the shape of a Gaussian shown in orange in Fig. 3.13.

3.2.3 Extension to the multi peak model

Contrary to the previous analysis for the single peak model, the full quantum system in the multi peak model consists of a small subsystem $\mathcal{S}$ and a bath $\mathcal{B}$. The unperturbed basis is constructed out of the product states $|\psi_\mu^{\mathcal{S}}\rangle \otimes |\psi_i^{\mathcal{B}}\rangle$

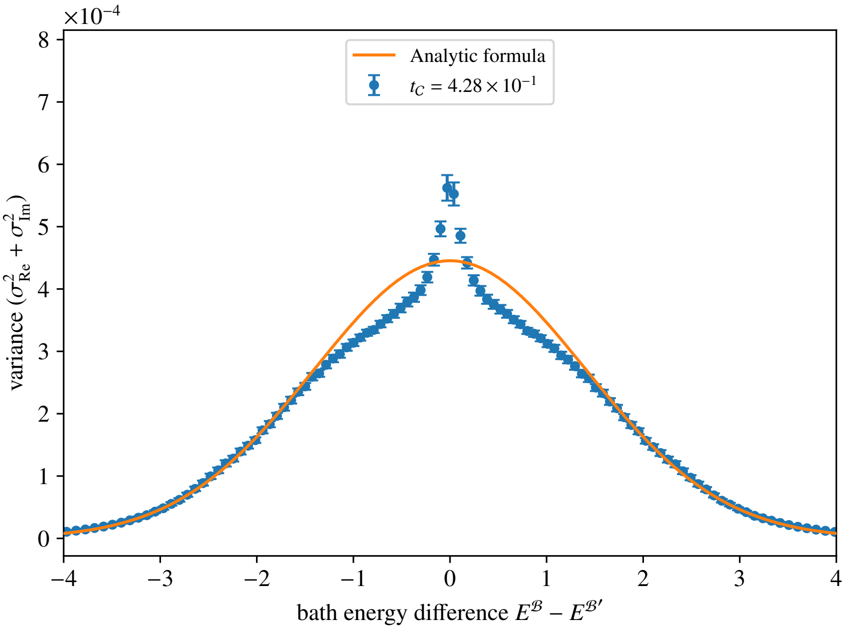

Figure 3.13: Comparison of the variance along the antidiagonal line in $\tilde{X}$ in the single peak model of $d_{\mathcal{B}} = 12$ and $d_{\mathcal{S}} = 0$ sites with $t = 0.01$ as blue points to the analytic formula in (3.45) in orange. All terms in $H^{\mathcal{B}}$ are chosen to be IID. An average is taken over 100 samples of X and 50 samples of $H^{\mathcal{B}}$. To compute the result in (3.45), we assume Gaussian DOS for C, $\bar{C}$, and $\mathcal{B}$, which are normalized to N_C, $N_{\bar{C}}$, and $N_{\mathcal{B}}$ respectively. The parameters of the Gaussians are obtained from fits to the numerical eigenvalue data. The best fit parameters are determined to $\sigma_{\mathcal{B}} = 2.2397(48)$, $\sigma_C = 0.911(85)$, $\sigma_{\bar{C}} = 2.0201(56)$ for the standard deviations and $E_0^{\mathcal{B}} = -0.36(48) \times 10^{-4}$, $E_0^{C} = -0.30(73) \times 10^{-3}$, $E_0^{\bar{C}} = -0.49(56) \times 10^{-4}$ for the mean values.

and the perturbation X couples the subsystems $\mathcal{S}$ and $\mathcal{B}$ with a variance of t. In the multi peak model, we define the element-wise variance with four indices as

$$\sigma^2_{\mu i;\nu j} \equiv \frac{1}{t} \mathbb{E}\left[\left| \langle \psi^{\mathcal{S}}_\mu | \, \langle \psi^{\mathcal{B}}_i | \, X \, | \psi^{\mathcal{S}}_\nu \rangle \, | \psi^{\mathcal{B}}_j \rangle \right|^2 \right], \tag{3.48}$$

where X contains the nearest neighbor spin-spin interaction terms along the boundary of $\mathcal{S}$ and $\mathcal{B}$, as well as local random magnetic fields for the spins and an additional unit matrix term,

$$X = \sum_{\substack{<k,l> \\ k \in \mathcal{S},\, l \in \mathcal{B}}} \sum_{\alpha,\beta=0}^{3} \tilde{r}^{\alpha,\beta}_{k,l} \, \sigma^\alpha_k \otimes \sigma^\beta_l \tag{3.49}$$

as defined in Eq. (2.6). Note, that in (3.49), the on-site magnetic fields and the unit matrix term are included through the σ^0 Pauli matrices with $\sigma^0_i = \mathbb{1}_{i;2\times 2}$ on site i. We further absorbed all analytic prefactors into the random variables $\tilde{r}^{\alpha,\beta}_{k,l} \sim \mathcal{N}(0, (\sigma^{\alpha,\beta}_{k,l})^2)$. The sum over k and l goes over the nearest neighbor lattice sites, on which X acts, where k must be in $\mathcal{S}$ and l in $\mathcal{B}$ since X acts along their boundary. For completeness, we included all combinations of two Pauli matrix terms in (3.49), which corresponds to a GUE for each link if all random variables $\tilde{r}^{\alpha,\beta}_{k,l}$ are IID. The sum rule in the multi peak model is then extended to

$$\sum_\mu \sum_i \sigma^2_{\mu i;\nu j} = \sum_\nu \sum_j \sigma^2_{\mu i;\nu j} = 1. \tag{3.50}$$

Inserting (3.49) into (3.48) yields

$$
\begin{aligned}
\sigma^2_{\mu i;\nu j} &= \frac{1}{t}\,\mathbb{E}\left[\left|\sum_{<k,l>}\sum_{\alpha,\beta=0}^{3} \tilde{r}^{\alpha,\beta}_{k,l}\ \langle\psi^{\mathcal{S}}_{\mu}|\sigma^{\alpha}_{k}|\psi^{\mathcal{S}}_{\nu}\rangle\ \langle\psi^{\mathcal{B}}_{i}|\sigma^{\beta}_{l}|\psi^{\mathcal{B}}_{j}\rangle\right|^2\right] \\
&= \frac{1}{t}\sum_{<k,l>}\sum_{<k',l'>}\sum_{\alpha,\alpha'\beta,\beta'} \mathbb{E}\left[\tilde{r}^{\alpha,\beta}_{k,l}\,\tilde{r}^{\alpha',\beta'}_{k',l'}\right] \langle\psi^{\mathcal{S}}_{\mu}|\sigma^{\alpha}_{k}|\psi^{\mathcal{S}}_{\nu}\rangle\ \langle\psi^{\mathcal{S}}_{\nu}|\sigma^{\alpha'}_{k'}|\psi^{\mathcal{S}}_{\mu}\rangle\ \langle\psi^{\mathcal{B}}_{i}|\sigma^{\beta}_{l}|\psi^{\mathcal{B}}_{j}\rangle\,\langle\psi^{\mathcal{B}}_{j}|\sigma^{\beta'}_{l'}|\psi^{\mathcal{B}}_{i}\rangle \\
&= \frac{1}{t}\sum_{\substack{<k,l>\\ k\in\mathcal{S},\, l\in\mathcal{B}}}\sum_{\alpha,\beta=0}^{3} \left(\sigma^{\alpha,\beta}_{k,l}\right)^2 \left|\langle\psi^{\mathcal{S}}_{\mu}|\sigma^{\alpha}_{k}|\psi^{\mathcal{S}}_{\nu}\rangle\right|^2 \left|\langle\psi^{\mathcal{B}}_{i}|\sigma^{\beta}_{l}|\psi^{\mathcal{B}}_{j}\rangle\right|^2,
\end{aligned}
\tag{3.51}
$$

where all mixed terms vanish, since the random prefactors are independent, normal distributed and have zero mean. The only remaining terms are those with variance $\mathbb{E}\left[(\tilde{r}^{\alpha,\beta}_{k,l})^2\right] = (\sigma^{\alpha,\beta}_{k,l})^2$. As before, we choose all prefactors of the individual terms in the Hamiltonian of a specific subsystem to be IID. In this case, all terms in X are defined to have the variance $(\sigma^{\alpha,\beta}_{k,l})^2 = t_0\ \forall\ k,l,\alpha,\beta$.

For the most part of this work, we choose subsystem $\mathcal{S}$ to be a single site with $k = 1$, as the total number of sites due to the numerical implementation is limited to 18 sites and we want $\mathcal{S}$ to be a small subset of the total quantum system. In the scenario $d_{\mathcal{S}} = 1$, the sum over k returns only one term and we can separate the result into a product of two terms,

$$
\sigma^2_{\mu i;\nu j} = \sigma^2_{\mu\nu}\cdot\sigma^2_{ij}
\tag{3.52}
$$

with

$$
\sigma^2_{\mu\nu} = \frac{1}{N^2_{\mathcal{S}}}\sum_{\alpha=0}^{3}\left|\langle\psi^{\mathcal{S}}_{\mu}|\sigma^{\alpha}_{k}|\psi^{\mathcal{S}}_{\nu}\rangle\right|^2 = \frac{1}{N_{\mathcal{S}}},
\tag{3.53a}
$$

$$
\sigma^2_{ij} = N^2_{\mathcal{S}}\,\frac{t_0}{t}\sum_{\substack{l\in\mathcal{B}\\ (<1,l>)}}\sum_{\beta=0}^{3}\left|\langle\psi^{\mathcal{B}}_{i}|\sigma^{\beta}_{l}|\psi^{\mathcal{B}}_{j}\rangle\right|^2,
\tag{3.53b}
$$

where the sum over l contains all neighbors to the site $k = 1$, which is subsystem $\mathcal{S}$. In this case of a two-state subsystem $\mathcal{S}$, $\sigma^2_{\mu\nu}$ contains four different scatterings with $\mu,\nu = 1,2$ between the eigenstates in $\mathcal{S}$. Displayed in Fig. 3.14 for 12 sites in $\mathcal{B}$ and a single site in $\mathcal{S}$, we can represent the scattering matrix in terms of $N^2_{\mathcal{S}}$ blocks with identical variance profiles σ^2_{ij} up to a scaling prefactor. Each block corresponds to one scattering of eigenstates in $\mathcal{S}$ and is correspondingly scaled by $\sigma^2_{\mu\nu}$. The evaluation of the variance σ^2_{ij} in $\mathcal{B}$ is identical to the single peak model. Since all possible scattering terms in $\mathcal{S}$ are included in (3.53a) and have the same prefactor of one, the scattering probability between all eigenstates in $\mathcal{S}$ is uniform. It implies that all $N^2_{\mathcal{S}}$ blocks are exactly identical with $\sigma^2_{\mu\nu} = \frac{1}{N_{\mathcal{S}}}$. Fig. 3.14 shows an example, where this is the case. For a direct comparison of the four blocks, we plot their variance along the anti-diagonal on top of each other in Fig. 3.15. We find that the variances in the four blocks agree and the variance model is independent of μ and ν. The sum rule for the uniform scattering in $\mathcal{S}$ reduces to the sum rule for σ^2_{ij} as known from the single peak model,

$$
\sum_{\mu=1}^{N_{\mathcal{S}}}\sum_{i=1}^{N_{\mathcal{B}}}\sigma^2_{\mu i;\nu j} = \sum_{\mu=1}^{N_{\mathcal{S}}}\sigma^2_{\mu\nu}\sum_{i=1}^{N_{\mathcal{B}}}\sigma^2_{ij} = \sum_{\mu=1}^{N_{\mathcal{S}}}\frac{1}{N_{\mathcal{S}}}\sum_{i=1}^{N_{\mathcal{B}}}\sigma^2_{ij} = \sum_{i=1}^{N_{\mathcal{B}}}\sigma^2_{ij} = 1.
\tag{3.54}
$$

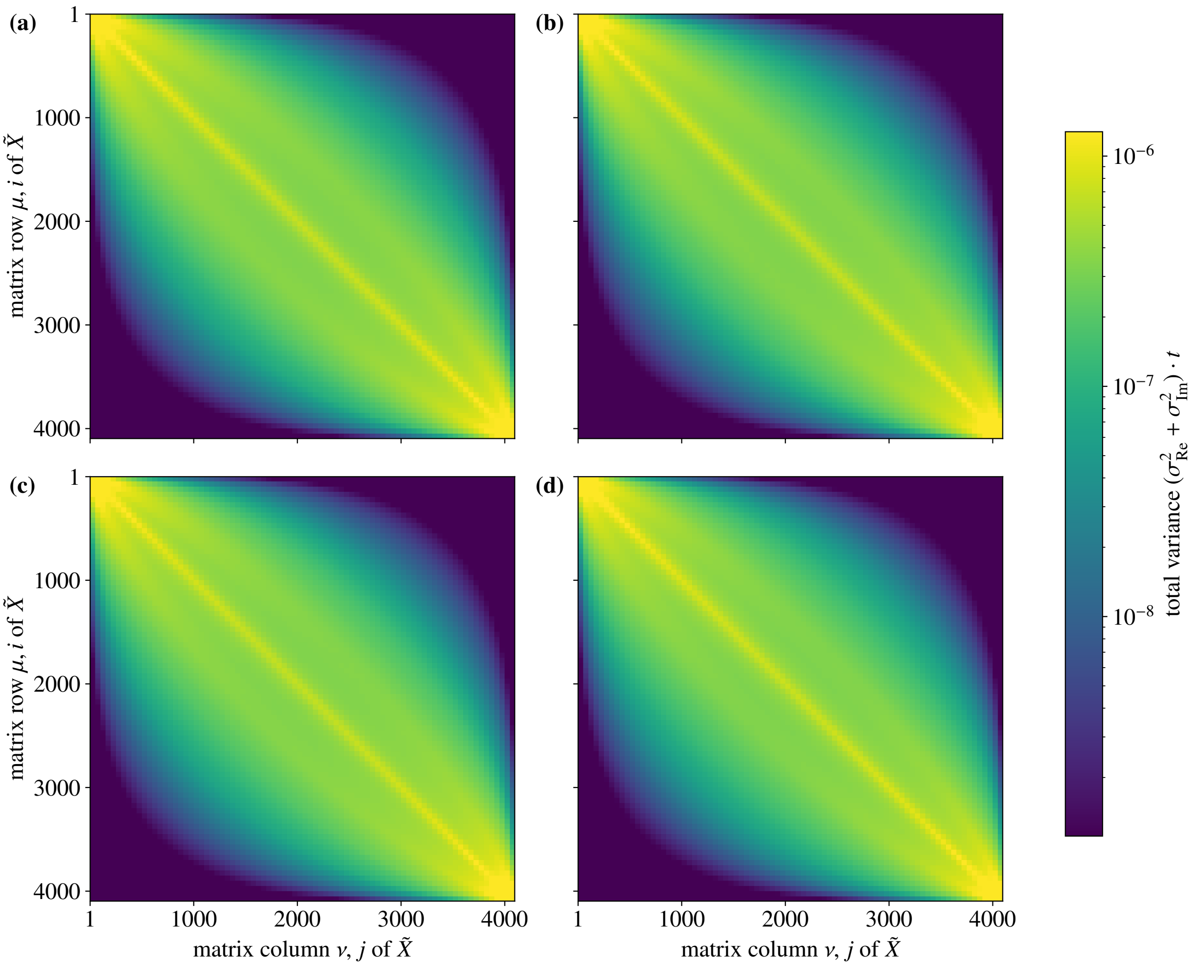

Figure 3.14: Matrix plot of the variance of the absolute value of the offdiagonal elements in the matrix $\tilde{X}$ with $t = 2.470(36) \times 10^{-3}$ computed in terms of boxes of size 25×25 in the multi peak setup with a bath of $d_{\mathcal{B}} = 12$ sites and a small subsystem $\mathcal{S}$ with $d_{\mathcal{S}} = 1$ site. The variance is averaged over 100 random samples of X and 50 samples of $H^{\mathcal{B}}$ and plotted on a logarithmic scale. The matrix is separated into four blocks, where the substructure describes the scattering of states (i, j) in $\mathcal{B}$. In each block, the variance is represented in terms of the matrix indices. We use nearest shading, in which the color in quadrilaterals spanned by the data points is chosen from the value of the closest data point. Each block corresponds to a scattering of eigenstates in $\mathcal{S}$ with **(a)** $(\mu, \nu) = (1, 1)$, **(b)** $(\mu, \nu) = (1, 2)$, **(c)** $(\mu, \nu) = (2, 1)$ and **(d)** $(\mu, \nu) = (2, 2)$.

This means, that all properties of the single peak variance model transfer to the multi peak model with one site in $\mathcal{S}$ and the full variance model $\sigma^2_{\mu i;\nu j}$ is a uniform extension of σ^2_{ij}.

In general, the variance in the multi peak model can be separated into a diagonal and an offdiagonal contribution,

$$\sigma^2_{\mu i;\nu j} \rightarrow \sigma^2_{\mu\nu}(E_i^{\mathcal{B}}, E_j^{\mathcal{B}}) = \sigma^2_{\mathrm{od},\mu\nu}(E_i^{\mathcal{B}}, E_j^{\mathcal{B}}) + \sigma^2_{\mathrm{d},\mu\nu}(E_i^{\mathcal{B}}, E_j^{\mathcal{B}}), \tag{3.55}$$

where we took the continuum limit such that the variance model in $\mathcal{B}$ depends on the eigenenergies between which X scatters, $E_i^{\mathcal{B}}$ and $E_j^{\mathcal{B}}$. For each block (μ, ν) corresponding to the scattering in $\mathcal{S}$, the shape of the variance model

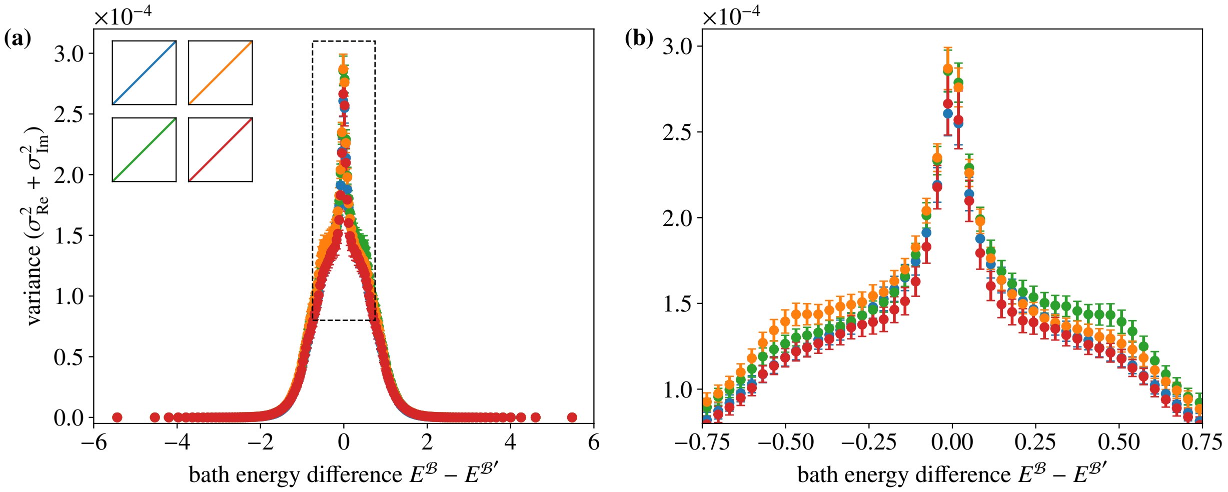

Figure 3.15: Element wise variance of $\tilde{X}$ with $t = 2.269(26) \times 10^{-3}$ along one line in each block of the full matrix, indicated by the inset. The results are obtained from a multi peak setup with $d_{\mathcal{B}} = 12$, $d_{\mathcal{S}} = 1$ and the blocks correspond to the scattering in $\mathcal{S}$. Only the variance of the offdiagonal elements is considered, which is obtained in terms of boxes of size (25×25), averaged over 100 samples of X and 50 samples of $H^{\mathcal{B}}$ and normalized by t. **(a)** Plot of the full data. **(b)** Cutout of the variance data around zero, indicated by the dashed rectangular box in **(a)**.

can be different. If a general relation for the variance model in $\mathcal{B}$ is found, e.g. a Gaussian in the limit of large $N_{\mathcal{B}}$ as in Eq. (3.45), the parameters in each block can be adjusted to depend on μ and ν such as to fit the variance model in the corresponding block. In the following, we argue that a similar separation as for $d_{\mathcal{S}} = 1$ is possible in the large system size limit. For this consider the general Eq. (3.51), where we use IID prefactors in front of all terms in X and $H^{\mathcal{B}}$ respectively. We then obtain

$$\begin{aligned}\sigma^2_{\mu i;\nu j} &= \frac{t_0}{t} \sum_{\substack{k \in \mathcal{S} \\ \text{w/}\, k \in \partial(\mathcal{S},\mathcal{B})}} \underbrace{\left(\sum_{\alpha=0}^{3} \left| \langle \psi^{\mathcal{S}}_{\mu} | \sigma^{\alpha}_{k} | \psi^{\mathcal{S}}_{\nu} \rangle \right|^2 \right)}_{=:\sigma^2_{k,\mu\nu}} \underbrace{\left(\sum_{\substack{l \\ (<k,l>)}} \sum_{\beta=0}^{3} \left| \langle \psi^{\mathcal{B}}_{i} | \sigma^{\beta}_{l} | \psi^{\mathcal{B}}_{j} \rangle \right|^2 \right)}_{=:\sigma^2_{k,\mathcal{B}}(E^{\mathcal{B}}_i, E^{\mathcal{B}}_j)} \\ &= \frac{t_0}{t} \sum_{\substack{k \in \mathcal{S} \\ \text{w/}\, k \in \partial(\mathcal{S},\mathcal{B})}} \sigma^2_{k,\mu\nu}\, \sigma^2_{k,\mathcal{B}}(E^{\mathcal{B}}_i, E^{\mathcal{B}}_j) \end{aligned} \tag{3.56}$$

with $k \in \partial(\mathcal{S}, \mathcal{B})$ indicating the sites k in subsystem $\mathcal{S}$, which lie at the boundary to the bath $\mathcal{B}$. Since the first term does not depend on l, we pulled the sum over l inside, which runs over all sites in $\mathcal{B}$ that are nearest neighbors to the site k in $\mathcal{S}$. Here, we defined $\sigma^2_{k,\mu\nu}$ as the variance originating from a scattering of states μ and ν in subsystem $\mathcal{S}$ mediated by all possible Pauli matrix terms on site k. Further, for $\sigma^2_{k,\mathcal{B}}(E^{\mathcal{B}}_i, E^{\mathcal{B}}_j)$ we take the continuum limit in $\mathcal{B}$ as the scattering of eigenstates from $E^{\mathcal{B}}_j$ to $E^{\mathcal{B}}_i$. It is defined as the variance from all Pauli matrix terms on those sites in $\mathcal{B}$ which are neighbors to site k in $\mathcal{S}$. For large system sizes of $\mathcal{S}$ and $\mathcal{B}$, we expect that the variance $\sigma^2_{k,\mathcal{B}}(E^{\mathcal{B}}_i, E^{\mathcal{B}}_j)$ in $\mathcal{B}$ does not depend on k, when all terms in $\mathcal{H}^{\mathcal{S}}$ and $\mathcal{H}^{\mathcal{B}}$ are IID. In this case there is a translational invariance on average in the bulk, since the coordination number is constant throughout the bulk of the lattice. This means, that the scattering $\sigma^2_{k,\mathcal{B}}(E^{\mathcal{B}}_i, E^{\mathcal{B}}_j) = \sigma^2_{\mathcal{B}}(E^{\mathcal{B}}_i, E^{\mathcal{B}}_j)$ is invariant upon translation of the site k when neglecting boundary effects, where the coordination number can differ. Defining the sum over the variances associated to the scattering on site k

in $\mathcal{S}$ in (3.56) as $\sigma^2_{\mu\nu} := \frac{t_0}{t} \sum_{\substack{k \in \mathcal{S} \\ \text{w}/\, k \in \partial(\mathcal{S},\mathcal{B})}} \sigma^2_{k,\mu\nu}$, we obtain the final result

$$\sigma^2_{\mu i;\nu j} = \sigma^2_{\mu\nu} \cdot \sigma^2_{\mathcal{B}}(E^{\mathcal{B}}_i, E^{\mathcal{B}}_j), \tag{3.57}$$

where the variances in $\mathcal{S}$ and $\mathcal{B}$ are on average decoupled and multiplied. For $d_{\mathcal{S}} = 1$, we assume a uniform scattering $\sigma^2_{\mu\nu}$ in $\mathcal{S}$, which also forms an energy dependent scattering structure similar to $\mathcal{B}$ as $\mathcal{S}$ becomes larger.

Eigenvector overlap

4.1 Shape of the overlap curve

We start the analysis of the overlap between perturbed and unperturbed states by delineating the principle shape of the overlap curve for the single and multi peak model. It relies on numerical results for a system with $d_{\mathcal{B}} = 17$ bath sites and zero or one site for the subsystem $\mathcal{S}$ in the single and multi peak model respectively. We find that the overlap curve close to its peak for small X is described by a Lorentzian curve where the real and imaginary part of each individual data point are distributed according to the normal distribution. We further confirm that the phases of the overlaps are fully random, i.e. follow a uniform distribution. Lastly, we numerically confirm, that the squared magnitude of the overlap decreases as $\frac{1}{N_{\mathcal{F}}}$ as demanded by the normalization condition of the full eigenstate.

4.1.1 Setup

Recap of the lattice structure. As illustrated in chapter 2, the underlying quantum system is a two-dimensional square lattice of d lattice sites, on which we model spin-$\frac{1}{2}$ particles with random nearest-neighbor spin-spin interactions and random on-site magnetic fields, such that the system as a whole preserves locality.

The total quantum system is divided into a small subsystem $\mathcal{S}$ and a bath $\mathcal{B}$, which together combine to the full system $\mathcal{F}$. For the eigenstate thermalization, we study the eigenstate distribution in $\mathcal{S}$ in an eigenstate of the full quantum system $\mathcal{F}$ by tracing out the bath. The interaction X between $\mathcal{S}$ and $\mathcal{B}$ is chosen to be local and small, such that it can be treated as a perturbation. Mathematically speaking, the second moment of X must be much smaller than the second moment of the full Hamiltonian $H^{\mathcal{F}}$, $\tau(X^2) \ll \tau((H^{\mathcal{F}})^2)$.

To find the occupation in $\mathcal{S}$, we analyze how a full eigenstate of $H^{\mathcal{F}}$ decomposes in terms of the unperturbed eigenbasis. We first employ the single peak model with no subsystem $\mathcal{S}$, where the unperturbed system consists only of the bath Hamiltonian $H^{\mathcal{B}}$. In this case, the local perturbation X acts on a small connected subset of $\mathcal{B}$ and we are interested in the overlap of eigenstates in $\mathcal{F}$ with those of the unperturbed bath. It produces just one overlap curve in terms of the bath eigenstates. In the multi peak model, the subsystem $\mathcal{S}$ contains at least one lattice site and a total number of states $N^{\mathcal{S}} \geq 2$. The overlap of a full eigenstate of $H^{\mathcal{F}}$ is then computed in terms of the product eigenbasis of $\mathcal{S}$ and $\mathcal{B}$, and we can separate out an individual overlap curve in $\mathcal{B}$ for each eigenstate in $\mathcal{S}$. The eigenstate occupation in $\mathcal{S}$ is then found by tracing out the associated overlap curves in $\mathcal{B}$.

Eigenstates and overlaps. The eigenstates of the full system $\mathcal{F}$, the subsystem $\mathcal{S}$ and the bath $\mathcal{B}$ are given by their respective stationary Schrödinger equations reading

$$H^{\mathcal{F}} |\psi_l^{\mathcal{F}}\rangle = \lambda_l |\psi_l^{\mathcal{F}}\rangle, \quad \text{with } l = 1, \dots, N_{\mathcal{F}}, \tag{4.1a}$$

$$H^{\mathcal{S}} |\psi_\mu^{\mathcal{S}}\rangle = \epsilon_\mu |\psi_\mu^{\mathcal{S}}\rangle, \quad \text{with } \mu = 1, \dots, N_{\mathcal{S}}, \tag{4.1b}$$

$$H^{\mathcal{B}} |\psi_i^{\mathcal{B}}\rangle = E_i |\psi_i^{\mathcal{B}}\rangle, \quad \text{with } i = 1, \dots, N_{\mathcal{B}}. \tag{4.1c}$$

For this section, we drop the subsytem labels in the eigenvalues, $\lambda_l = \lambda_l^{\mathcal{F}}$, $\epsilon_\mu = \epsilon_\mu^{\mathcal{S}}$ and $E_i = E_i^{\mathcal{B}}$. The sizes of the Hilbert spaces are given by $N_{\mathcal{F}} = 2^{d_{\mathcal{F}}}$, $N_{\mathcal{S}} = 2^{d_{\mathcal{S}}}$ and $N_{\mathcal{B}} = 2^{d_{\mathcal{B}}}$. A basis for the full Hilbert space $\mathcal{H}^{\mathcal{F}}$ is given by all eigenstates of $H^{\mathcal{F}}$, $|\psi_l^{\mathcal{F}}\rangle, l = 1, \dots N_{\mathcal{F}}$ or by the product eigenbasis of subsystems $\mathcal{S}$ and $\mathcal{B}$, $|\psi_\mu^{\mathcal{S}}\rangle \otimes |\psi_i^{\mathcal{B}}\rangle$ with all combinations of $\mu = 1, \dots, N_{\mathcal{S}}$ and $i = 1, \dots, N_{\mathcal{B}}$.

In the following, we are interested in the decomposition of a full eigenstate $|\psi_l^{\mathcal{F}}\rangle$ in terms of the unperturbed eigenbasis. For the single peak model, the relevant quantity is the overlap

$$\chi_{i,l} \equiv \left| \langle \psi_i^{\mathcal{B}} | \psi_l^{\mathcal{F}} \rangle \right|^2 \tag{4.2}$$

and its expectation value

$$X_{i,l} \equiv \mathbb{E}\left[\left| \langle \psi_i^{\mathcal{B}} | \psi_l^{\mathcal{F}} \rangle \right|^2 \right]. \tag{4.3}$$

$\chi_{i,l}$ can be plotted with respect to E_i, the eigenenergy in the bath $\mathcal{B}$, showing how a perturbed eigenstate is distributed in terms of the unperturbed eigenbasis. An analogous quantity for the multi peak model is given by

$$\chi_{\mu i,l} \equiv \left| \left(\langle \psi_\mu^{\mathcal{S}} | \otimes \langle \psi_i^{\mathcal{B}} | \right) |\psi_l^{\mathcal{F}}\rangle \right|^2 \tag{4.4}$$

and

$$X_{\mu i,l} \equiv \mathbb{E}\left[\left| \left(\langle \psi_\mu^{\mathcal{S}} | \otimes \langle \psi_i^{\mathcal{B}} | \right) |\psi_l^{\mathcal{F}}\rangle \right|^2 \right]. \tag{4.5}$$

Given a full eigenstate $|\psi_l^{\mathcal{F}}\rangle$, we obtain an individual overlap curve for each eigenstate μ in $\mathcal{S}$ in terms of the bath eigenstates, which can be resolved in terms of E_i. By the information gained from the overlap curves, one can investigate how the perturbation X and the bath $\mathcal{B}$ shapes the eigenstate distribution in subsystem $\mathcal{S}$ within one full eigenstate.

In the numerical analysis, we choose the prefactors of all terms in each subsystem Hamiltonian to be IID. Furthermore, the unperturbed Hamiltonian of the bath $H^{\mathcal{B}}$ is normalized such that its second moment is one, $\tau_2(H^{\mathcal{B}}) = 1$. The resulting Gaussian DOS in $\mathcal{B}$ then has a variance of $\sigma_{\mathcal{B}}^2 = 1$ independent of the system size d and the number of terms in the Hamiltonian. It allows for comparisons between different system sizes and guarantees reproducibility of the results. The perturbation X must be small, such that we demand $t \ll \sigma_{\mathcal{B}}^2 = 1$. In the multi peak model, where $\mathcal{S}$ is not zero, we normalize its Hamiltonian such that the spectral width is smaller than that of $H^{\mathcal{B}}$ with $\sigma_{\mathcal{S}}^2 \approx 0.01 < 1$. With this choice, the eigenvalues in $\mathcal{S}$ are on the order of 0.1.

In this section, we present the general shape of the overlap curves $X_{i,l}$ and $X_{\mu i,l}$ in the single and multi peak model respectively. For that, the size of the bath is $d_{\mathcal{B}} = 17$ lattice sites and $\mathcal{S}$ contains no site or one site in the single and multi peak model respectively. In further sections, we employ RMT to compute the overlap analytically and compare the results with an extensive numerical analysis.

4.1.2 Single peak model

The perturbation matrix. In the single peak model, we investigate the decomposition of a full eigenstate in terms of the unperturbed eigenbasis of $\mathcal{B}$. We demand the variance t of the perturbation matrix X to be small compared to the variance $\sigma^2_{\mathcal{B}}$ of $H^{\mathcal{B}}$. In the limit $t \to 0$, we expect the full eigenstate to be identical to one of the unperturbed eigenstates, which results in a Kronecker-Delta shaped overlap, $\chi_{i,l} = \delta_{il}$. In a setup with finite, but very small $t \ll \sigma^2$, we expect the eigenvectors close to $E_i \approx \lambda_l$ to provide the main contribution to the overlap, as it can not deviate substantially from a Dirac-Delta distribution. The energy expectation value of the full Hamiltonian $H^{\mathcal{F}} = H^{\mathcal{B}} + X$ in the state $|\psi_l^{\mathcal{F}}\rangle$ can be written as

$$\begin{aligned} \lambda_l = \langle\psi_l^{\mathcal{F}}|H^{\mathcal{F}}|\psi_l^{\mathcal{F}}\rangle &= \langle\psi_l^{\mathcal{F}}|H^{\mathcal{B}}|\psi_l^{\mathcal{F}}\rangle + \langle\psi_l^{\mathcal{F}}|X|\psi_l^{\mathcal{F}}\rangle \\ &= \sum_i \left|\langle\psi_i^{\mathcal{B}}|\psi_l^{\mathcal{F}}\rangle\right|^2 E_i + \langle\psi_l^{\mathcal{F}}|X|\psi_l^{\mathcal{F}}\rangle \\ \Rightarrow \mathbb{E}\left[\lambda_l\right] &= \sum_i \mathcal{X}_{i,l}\, E_i + \epsilon_X^{(l)}, \end{aligned} \tag{4.6}$$

where we took the statistical expectation value over X to obtain the last line and defined $\epsilon_X^{(l)} := \langle\psi_l^{\mathcal{F}}|X|\psi_l^{\mathcal{F}}\rangle$. The expected energy eigenvalue $\mathbb{E}\left[\lambda_l\right]$ is given by the energy expectation value of its corresponding state $|\psi_l^{\mathcal{F}}\rangle$ in the unperturbed Hamiltonian $H^{\mathcal{B}}$ and its expectation value in the perturbation, $\epsilon_X^{(l)}$, which scales with t. Since the perturbation X is small according to $t \ll \sigma^2_{\mathcal{B}}$, the main contribution on the right-hand side in (4.6) lies in an energy window close to $E_i \approx \lambda_l$, where $\mathcal{X}_{i,l}$ must be maximal and is much smaller for energies far away from the point $E_i \approx \lambda_l$,, where $\mathcal{X}_{i,l}$ must then have dropped off significantly.

As a first step, we examine the perturbation matrix X in terms of the unperturbed eigenbasis represented by $\tilde{X}$ and detailed in section 3 with matrix elements

$$\tilde{X}_{ij} := \langle\psi_i^{\mathcal{B}}|X|\psi_j^{\mathcal{B}}\rangle\,. \tag{4.7}$$

This is necessary to compare the structure of the full Hamiltonian $H^{\mathcal{F}} = H^{\mathcal{B}} + X$ in terms of the eigenbasis of $\mathcal{B}$ to the structure of the properties of the perturbation employed in the equations of Allez-Bouchaud in (1.122) and of Casati-Girko in (1.129). We numerically analyze the overlap curve $\chi_{i,l}$ at the full energy $\lambda_l \approx -1.45$. Since the dominant contribution in $\chi_{i,l}$ will be close to $E_i \approx -1.45$, we analyze the statistical properties of $\tilde{X}_{ij}$ in an energy window $\Delta E^{\mathcal{B}} = 0.1$ around $E_i = -1.45$. This selects the matrix elements of $\tilde{X}_{ij}$ inside a square-shaped box of base 0.1 in the row E_i and column E_j, which are then arranged in histograms to find their statistical distributions. The results are shown in Fig 4.1, where the real and imaginary part of the off-diagonal entries and the diagonal values are analyzed separately in **c**, **d**, and **b** respectively. All three follow a Gaussian distribution, which is fitted through the data as an orange curve. The Gaussian standard deviation is given by $\sigma_{\text{Re}} = 1.6426(11) \times 10^{-4}$, $\sigma_{\text{Im}} = 1.643\,62(82) \times 10^{-4}$ and $\sigma_{\text{dia}} = 2.325(54) \times 10^{-4}$ for the real and imaginary part of the off-diagonal entries and the diagonal values respectively. We notice, that the variance of the real and imaginary part of the Gaussian fits agree, $\sigma^2_{\text{Re}} = \sigma^2_{\text{Im}}$, while the diagonal variance is twice as large, $\sigma^2_{\text{dia}} = 2\,\sigma^2_{\text{Re}}$. This fulfills the requirements of a GUE and we can approximate the analyzed box in $\tilde{X}$ as an effective GUE close to the expected location of the overlap curve.

While the mean value of the real and imaginary part of $\tilde{X}_{ij}$ is zero for $i \neq j$, it is finite and equal to $\mu_{\text{dia}} = -1.8322(54) \times 10^{-3}$ for the diagonal $\tilde{X}_{ii}$ in the considered energy interval as shown in Fig. 4.1**b**. The nonzero center of the normal distribution for the diagonal entries $\tilde{X}_{ii}$ originates from a local trace contribution. This structure was analyzed in Sec. 3.1.4 and derives from the local construction of the Hamiltonian and the perturbation X. The

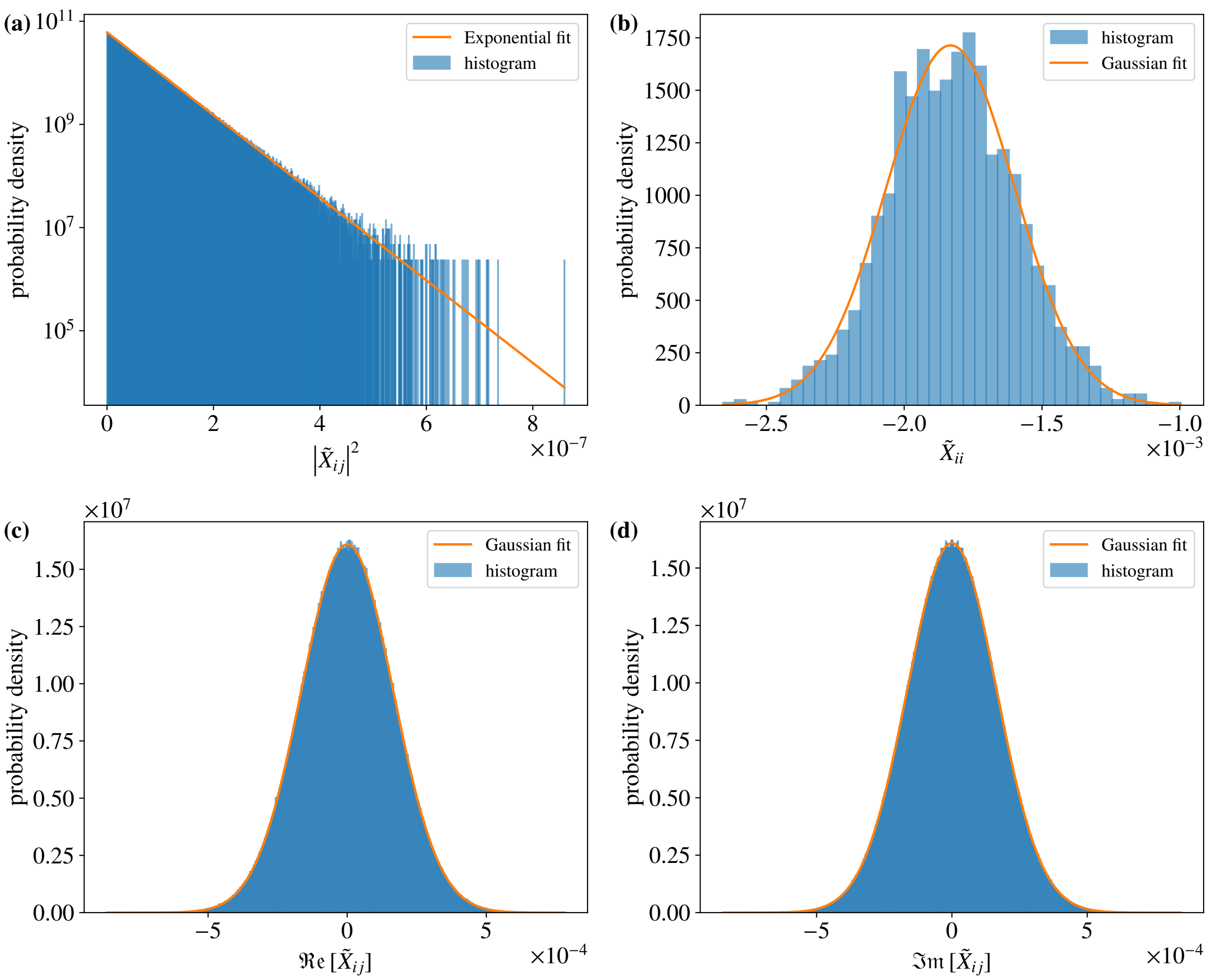

Figure 4.1: Analysis of the perturbation matrix $\tilde{X}$ with variance $t = 1.52 \times 10^{-3}$ in the single peak model with $d_{\mathcal{B}} = 17$ sites in an interval of width $\Delta E^{\mathcal{B}} = 0.1$ around the energy $E_i = -1.45$ at the expected location of the peak of the overlap $\mathcal{X}_{il}$ with $E_i \approx \lambda_l$. **(a)** shows the distribution of the squared magnitude in the considered box on a logarithmic scale with an exponential fit. The slope is given by $\alpha = 1.8343(34) \times 10^7$. In **(b)**, **(c)** and **(d)**, we plot the distribution of the diagonal values, and the real and the imaginary part of the offdiagonal values respectively with Gaussian fits. The best fit standard deviations are given by $\sigma_{\mathrm{Re}} = 1.6426(11) \times 10^{-4}$, $\sigma_{\mathrm{Im}} = 1.643\,62(82) \times 10^{-4}$ and $\sigma_{\mathrm{dia}} = 2.325(54) \times 10^{-4}$. While the Gaussians for the real and imaginary part are centered around zero, the mean of the diagonal values is given by $\mu_{\mathrm{dia}} = -1.8322(54) \times 10^{-3}$.

diagonal values $\tilde{X}_{ii}$ in each sample are on the order of E_i with additional random fluctuations about that value. Note, that σ^2_{dia} is the box variance, while the sample variance in terms of X is much larger, as detailed in Sec. 3.1.4. The local trace due to μ_{dia} can be regarded as a unit matrix term additional to the local GUE, which acts as a shift to the energy eigenvalues.

In Fig. 4.1**a**, we plot the distribution of the square modulus of the offdiagonal elements of $\tilde{X}$ in the considered box. As expected, we obtain an exponential distribution

$$p(|\tilde{X}_{ij}|^2) = \alpha\, e^{-\alpha|\tilde{X}_{ij}|^2} \tag{4.8}$$

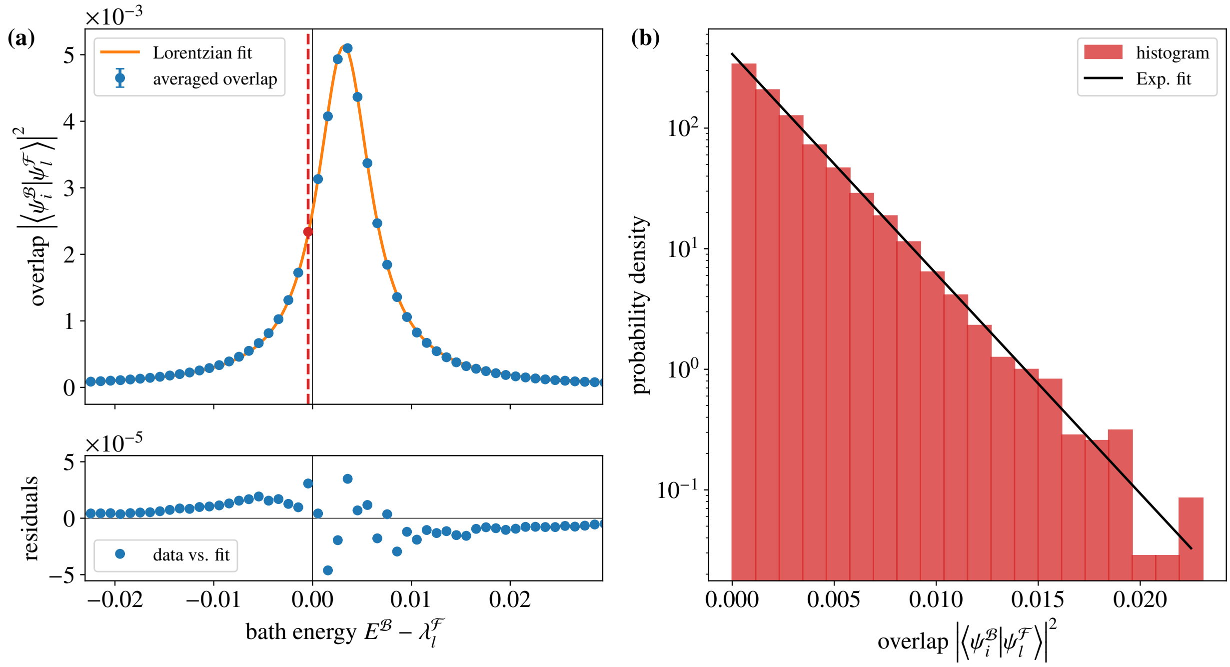

Figure 4.2: **(a)** Averaged overlap $\left|\langle\psi_i^{\mathcal{B}}|\psi_l^{\mathcal{F}}\rangle\right|^2$ using $N_{\text{av}} = 1600$ full states in an interval around the mean eigenvalue $\bar{\lambda}_l = -1.457\,29(60)$ in the single peak model. The bath $\mathcal{B}$ of $d_{\mathcal{B}} = 17$ sites is perturbed by a local interaction X with variance $t = 1.52 \times 10^{-3}$, whose element-wise variance close to the overlap peak is shown in Fig. 4.1. The overlap is represented as blue points in terms of the bath energy shifted by λ_l and averaged in intervals of width $w = 0.001$. A Lorentzian fit in orange returns the fit parameters for the shift $\eta = 3.1716(39) \times 10^{-3}$ and the width $\gamma = 3.2743(55) \times 10^{-3}$. Below, we show the residuals of the non-linear fit. **(b)** shows the distribution of overlap values for one data point marked in red in **(a)** close to the left-handed half width at half maximum (HWHM) at $x \approx -\gamma$. We plot the probability density on a logarithmic scale, on which the slope is given by $\alpha = 3.94(10) \times 10^2$.

with $\alpha = \frac{1}{2\sigma^2} = -1.8451(42) \times 10^7$ resulting from the combination of the Gaussian distribution for the real and imaginary part within the numerically verified assumption $\sigma^2 = \sigma^2_{\text{Re}} = \sigma^2_{\text{Im}}$.

The overlap curve and its statistics. The total number of states in the full quantum system with $d_{\mathcal{F}} = 17$ sites is equal to $N_{\mathcal{F}} = 2^{17} = 131072$. To find the overlap curve close to $\lambda_l \approx -1.45$, we take $N_{\text{av}} = 1600$ full states $|\psi_l^{\mathcal{F}}\rangle$ and average the squared absolute value of the overlap $\left|\langle\psi_i^{\mathcal{B}}|\psi_l^{\mathcal{F}}\rangle\right|^2$ of those states with the unperturbed eigenbasis of $\mathcal{B}$. The mean value of the full eigenvalue in this interval is given by $\bar{\lambda}_l = -1.457\,29(60)$. The average is performed by sorting the overlap values into boxes of uniform energy width $w = 0.001$ according to the bath energy shifted by their respective eigenvalue, $E_i^{\mathcal{B}} - \lambda_l^{\mathcal{F}}$. The bath energies are shifted by the investigated value of $\lambda^{\mathcal{F}}$, as we expect their peak close to the position $E_i^{\mathcal{B}} \approx \lambda_l^{\mathcal{F}}$. The overlap average is shown in Fig. 4.2**a** in a small energy window around $E_i^{\mathcal{B}} - \lambda_l^{\mathcal{F}} = 0$. We notice a pronounced peak, which falls off at larger energies. The overlap data points are fitted well by a Lorentzian curve, which is shown in orange in Fig. 4.2**a**. Below that, we plot the corresponding fit residuals, which are two orders of magnitude smaller than the actual data points, hereby confirming the validity of the Lorentzian fit. We notice, that the center position $\eta = 3.1716(39) \times 10^{-3}$ of the Lorentzian is slightly shifted from the position $\lambda_l = E_i$ towards larger bath eigenvalues $E^{\mathcal{B}}$. There are two contributions to this shift. First, as discussed above, the local trace of the perturbation matrix $\tilde{X}$ is nonzero, since its diagonal values $\tilde{X}_{ii}$ correlate with E_i, which leads to the mean of the Gaussian distribution in Fig. 4.1**b** to be $\mu_{\text{dia}} = -1.8322(54) \times 10^{-3}$. This accounts for about

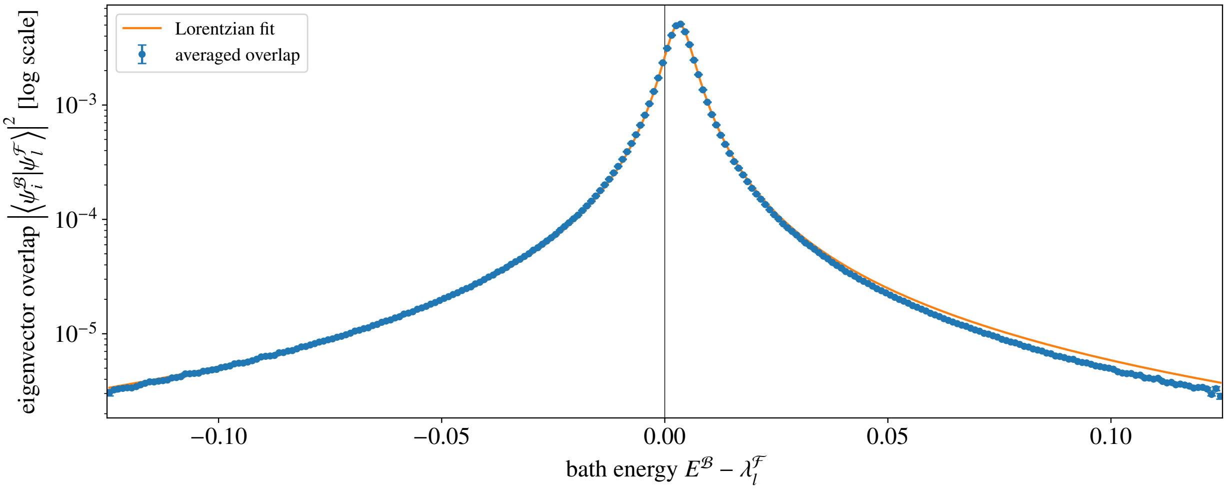

Figure 4.3: Logarithmic representation of the averaged overlap $\left|\langle\psi_i^{\mathcal{B}}|\psi_l^{\mathcal{F}}\rangle\right|^2$ from $N_{\text{av}} = 1600$ states around $\bar{\lambda}_l = -1.457\,29(60)$ in terms of the shifted bath energy $E_i^{\mathcal{B}} - \lambda_l^{\mathcal{F}}$. The data is the same as shown in Fig. 4.2(**a**) in a larger energy range and the matrix variance of X is $t = 1.52 \times 10^{-3}$. A Lorentzian fit is shown as an orange curve additional to the data points in blue.

half of the present shift of the Lorentzian in Fig.4.2**a**. The second contribution for the remaining part is caused by the shape of the variance model σ_{ij}^2, which needs to be taken into account in its entirety over the whole energy axis as demonstrated by the analytic calculation in Sec. 4.3.1. Fig. 4.3 shows the overlap data points together with the Lorentzian fit from Fig. 4.1**a** on a logarithmic scale. The fit matches well with the data points in the extended energy range in Fig. 4.3 although we notice a small asymmetry of the data with respect to its center position. This asymmetry appears when the Lorentzian has fallen off by about two orders of magnitude from its peak height and is therefore a minor effect, which we attribute to finite size effects.

The width of the Lorentzian fit in Fig. 4.2**a** is $\gamma = 3.2743(55) \times 10^{-3}$. Suppose that the box of $\tilde{X}$ around the Lorentzian as analyzed in Fig. 4.1 is a GUE with an additional constant energy shift resulting from the nonzero local trace and assume that the remaining part of the matrix $\tilde{X}$ plays a negligible role for the shape of the overlap curve. In this scenario we can apply the equation by Allez and Bouchaud in (1.122). It predicts the width $\gamma_0 = \pi\, t\, \rho_{\mathcal{F}}(\lambda_l) = \pi N_{\mathcal{B}}(\sigma_{\text{Re}}^2 + \sigma_{\text{Im}}^2)\rho_{\mathcal{F}}(\lambda_l) = 2.88 \times 10^{-3}$, where we made the identification, that the element-wise variance of the box GUE is given by $(\sigma_{\text{Re}}^2 + \sigma_{\text{Im}}^2) = \frac{t}{N_{\mathcal{B}}}$. This first rough estimate is of the same order as the numerical value γ with a relative deviation of about 14%. A refined calculation of the overlap curve paralleled by a systematic comparison to numerical data is found in Sec. 4.3.

In Fig. 4.2**b**, we plot the statistical distribution of a single overlap data point closest to the HWHM of the Lorentzian curve. The values for the overlap in this box interval are obtained from the 1600 full states, which we average over. The square modulus of the overlap is distributed according to an exponential, as fitted by a black line through the red histogram data points in Fig. 4.2**b**, shown on a logarithmic scale. It occurs as a consequence of Gaussian distributions in the real and imaginary part of the overlap with matching variance in the average over the 1600 full states. Although the individual Gaussians of the real and imaginary part have mean zero, the mean of the square modulus is nonzero. The characterizing parameter of the exponential distribution

$$p\left(r^2 = \left|\langle\psi_i^{\mathcal{B}}|\psi_l^{\mathcal{F}}\rangle\right|^2\right) = \alpha e^{-\alpha r^2} \tag{4.9}$$

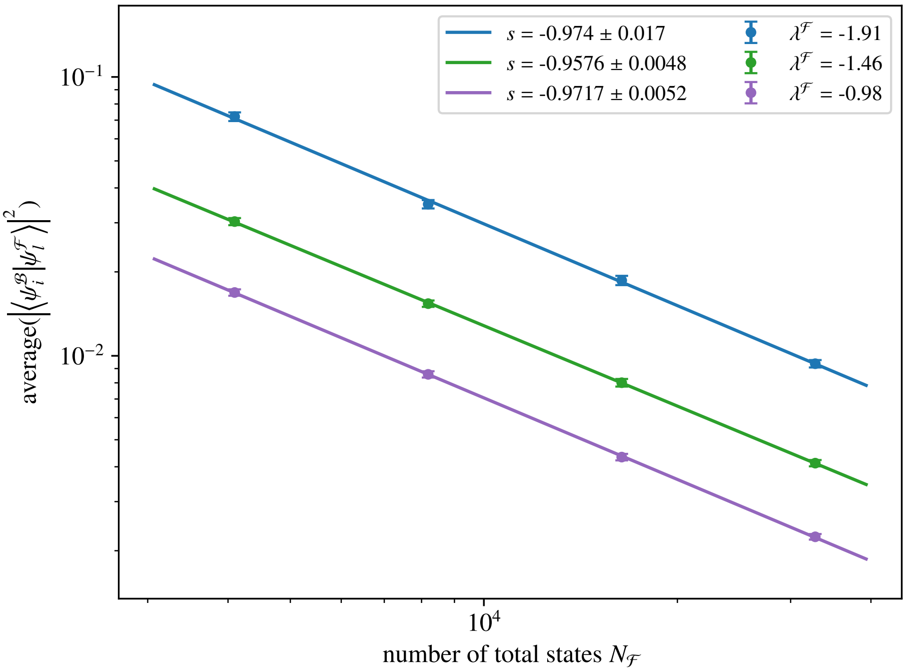

Figure 4.4: Average of the Lorentzian overlap points closest to the left-handed HWHM at $x \approx -\gamma$ with respect to the total number of states in the full quantum system with $d_{\mathcal{F}} = \{12, 13, 14, 15\}$ sites. The data is averaged over 100 samples of $H^{\mathcal{B}}$ and 200 samples of X for each data point and plotted on a double logarithmic scale. The colors indicate three different full energies λ_l. Linear fits are performed for each data set for λ_l individually, where the slope s is indicated in the legend.

is equal to $\alpha = 3.94(10) \times 10^2$. The mean value of this distribution in r^2 is given by its first moment $\langle\left|\langle\psi_i^{\mathcal{B}}|\psi_l^{\mathcal{F}}\rangle\right|^2\rangle = \langle r^2\rangle = \frac{1}{\alpha}$. The second moment is $\langle r^4\rangle = \frac{2}{\alpha^2}$, which yields a variance of

$$Var\left(\left|\langle\psi_i^{\mathcal{B}}|\psi_l^{\mathcal{F}}\rangle\right|^2\right) = \langle r^4\rangle - (\langle r^2\rangle)^2 = \frac{1}{\alpha^2} = \left(\langle\left|\langle\psi_i^{\mathcal{B}}|\psi_l^{\mathcal{F}}\rangle\right|^2\rangle\right)^2. \tag{4.10}$$

In the exponential distribution, the variance is equal to the square of the mean value, which implies that its standard deviation is equal to its mean value. In Fig. 4.4, we plot the sample mean at a fixed position of the overlap with respect to the total number of states $N_{\mathcal{F}}$. The position is selected to be the closest value to the HWHM, which is the point, where the overlap has dropped to half its maximum value. In the double logarithmic plot of Fig. 4.4, the data points follow a linear relation, which is shown by a corresponding linear fit. Since the slope of the linear fit is approximately $s = -1$ in Fig. 4.4, the mean value of the square modulus of the overlap is inversely proportional to the number of states,

$$\langle\left|\langle\psi_i^{\mathcal{B}}|\psi_l^{\mathcal{F}}\rangle\right|^2\rangle \propto \frac{1}{N_{\mathcal{F}}} \tag{4.11}$$

and hence $\alpha \propto N_{\mathcal{F}}$. The result makes sense, as the average energy spacing is also inversely proportional to $N_{\mathcal{F}}$. By adding one site to the lattice, there are twice as many states $N_{\mathcal{F}} \rightarrow 2N_{\mathcal{F}}$, leading to twice the number of overlap data points and a higher resolution of the overlap curve. The overlap is represented in the complete basis of the full Hilbert space in terms of the perturbed states $|\psi_l^{\mathcal{F}}\rangle$ or the unperturbed states $|\psi_i^{\mathcal{B}}\rangle$, which results in the sum

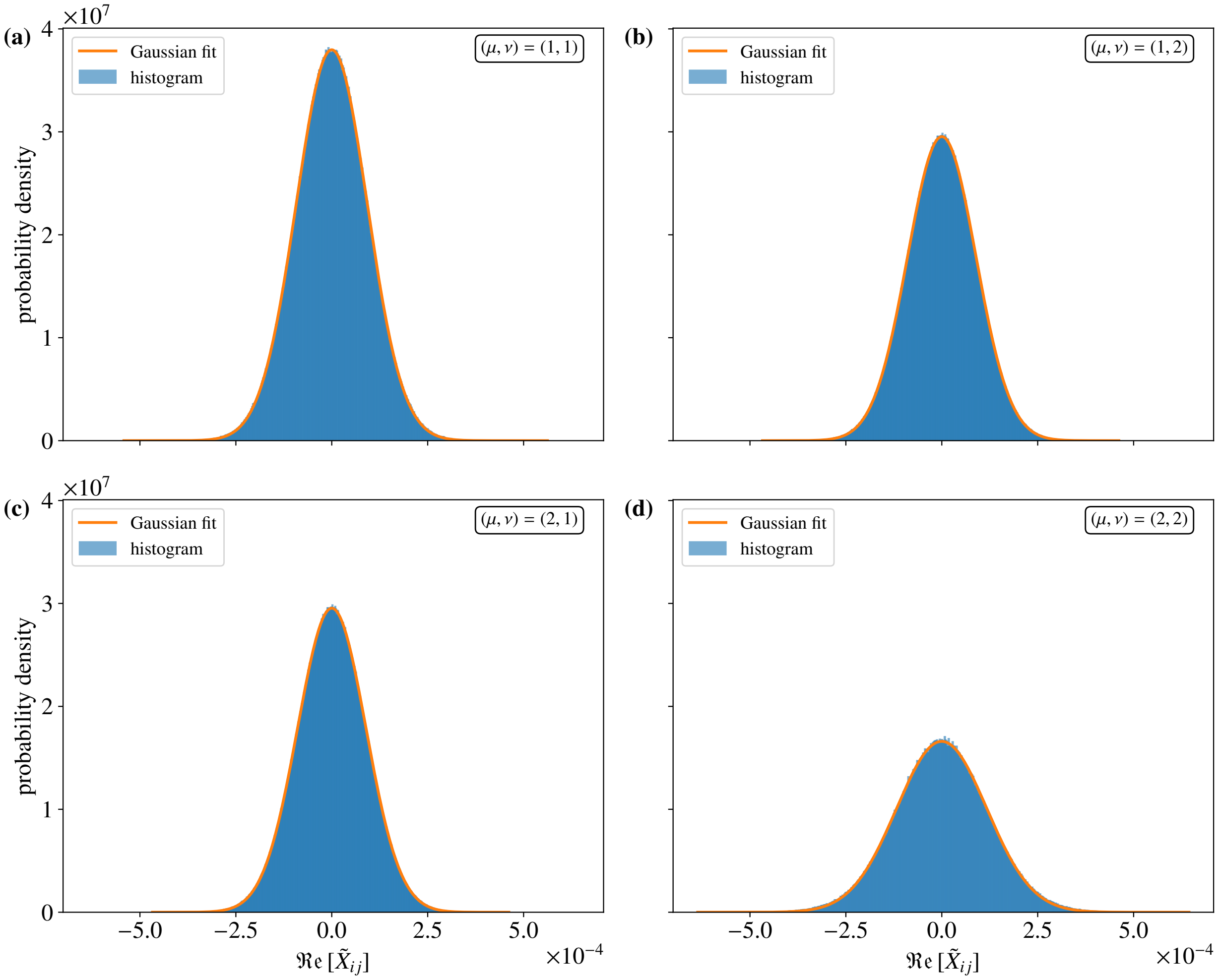

Figure 4.5: Analysis of the perturbation matrix $\tilde{X}$ with variance $t = 1.63 \times 10^{-3}$ in the multi peak model with $d_{\mathcal{B}} = 17$ and $d_{\mathcal{S}} = 1$ sites. With the eigenenergies $\epsilon_1 = -0.1$ and $\epsilon_2 = 0.1$, we extract boxes of width $\Delta E^{\mathcal{B}} = 0.1$ around the bath energies $(E_i, E_j) = (-1.45 - \epsilon_\mu, -1.45 - \epsilon_\nu)$ of the block (μ, ν) corresponding to the scattering in $\mathcal{S}$ in $\tilde{X}$, where E_i is the row and E_j the column energy. This coincides with the expected location of the overlap peak $\mathcal{X}_{\mu i,l}$ at $E_i \approx \lambda_l - \epsilon_\mu$ for $\mu = 1, 2$. For comparison of the four boxes, we only show the distribution of the real part of the offdiagonal elements in the blocks **(a)** $(1, 1)$, **(b)** $(1, 2)$, **(c)** $(2, 1)$ and **(d)** $(2, 2)$. From Gaussian fits in orange, we obtain the standard deviations **(a)** $\sigma_{1,1;\mathrm{Re}} = 9.2505(52) \times 10^{-5}$, **(b)** $\sigma_{1,2;\mathrm{Re}} = 8.9034(40) \times 10^{-5}$, **(c)** $\sigma_{2,1;\mathrm{Re}} = 8.9034(40) \times 10^{-5}$ and **(d)** $\sigma_{2,2;\mathrm{Re}} = 1.1779(13) \times 10^{-4}$.

rule $\sum_i \chi_{i,l} = \sum_l \chi_{i,l} = 1$ for the normalized state. While the shape of the overlap curve stays roughly the same, each overlap point must go to half of its value after the addition of the site in order to satisfy the sum rule for the normalization. Consequently, the variance of the overlap $\chi_{i,l}$ scales as $\frac{1}{N_{\mathcal{F}}^2}$, which decreases as the system grows in size.

4.1.3 Multi peak model

The perturbation matrix. Similar to the single peak model, we start by investigating the perturbation matrix $\tilde{X}$ in the representation of the unperturbed eigenbasis for the multi peak model. The subsystem $\mathcal{S}$ consists of a single lattice site resulting in $N_{\mathcal{S}} = 2$ states. As detailed in Sec. 3.2.3, the perturbation matrix can be arranged in four

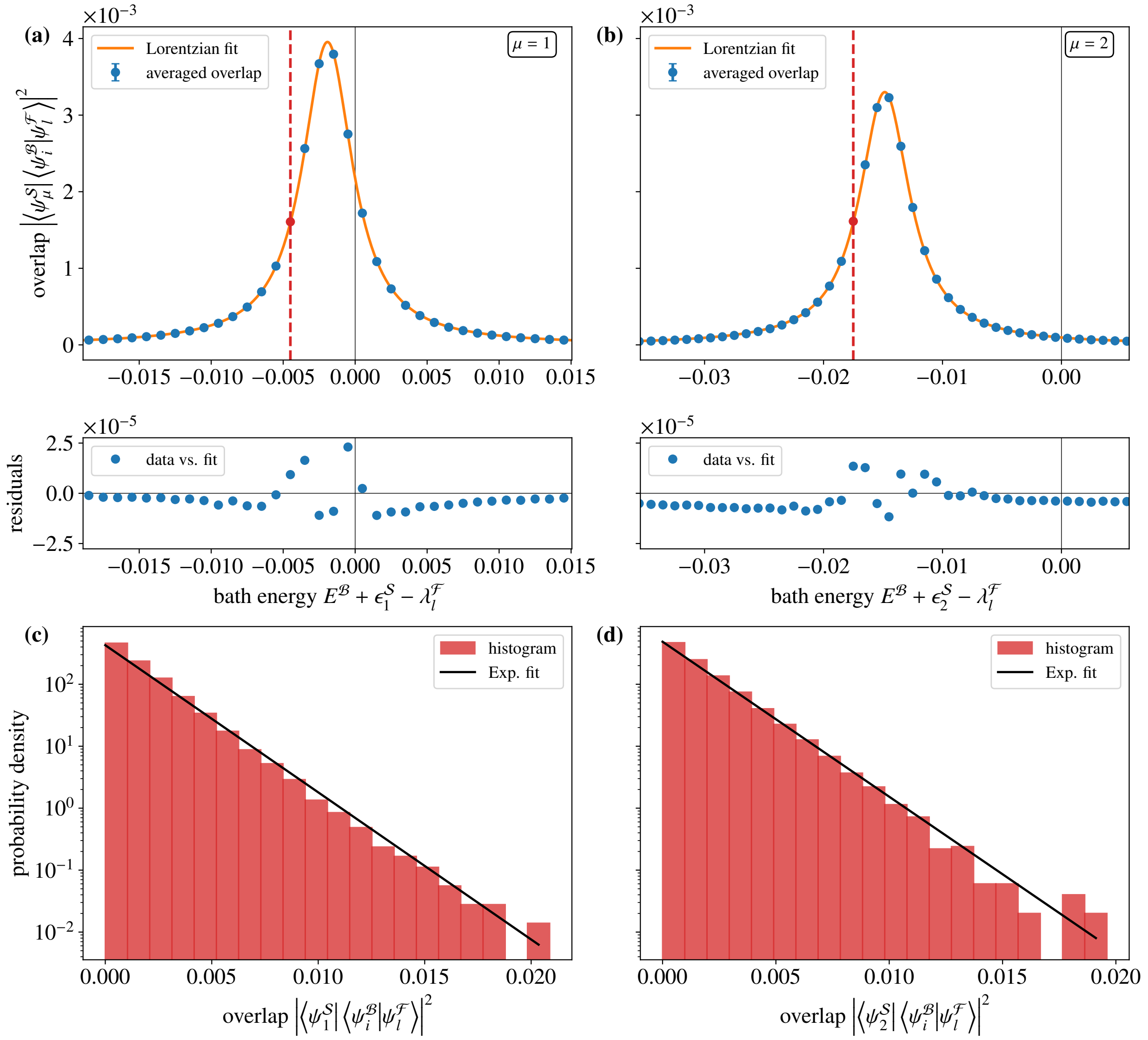

Figure 4.6: Averaged overlaps $\left|\langle\psi_\mu^{\mathcal{S}}|\,\langle\psi_i^{\mathcal{B}}|\psi_l^{\mathcal{F}}\rangle\right|^2$ in the multi peak model with $d_{\mathcal{B}} = 17$ and $d_{\mathcal{S}} = 1$ sites at $t = 1.63\times10^{-3}$. We employ $N_{\mathrm{av}} = 3200$ full states averaged in intervals of width $w = 0.001$ around the mean eigenvalue $\bar{\lambda}_l = -1.457\,29(60)$ and split up the overlap into contributions for $\mu = 1$ in **(a)** and $\mu = 2$ in **(b)**. A Lorentzian fit in orange returns the fit parameters shift η_μ and width γ_μ with **(a)** $\eta_1 = -1.9223(20)\times10^{-3}$, $\gamma_1 = 2.1224(29)\times10^{-3}$ and **(b)** $\eta_2 = -1.485\,30(24)$, $\gamma_2 = 2.5682(34)\times10^{-3}$. Below the overlap data, we show the residuals of the non-linear fit. **(c)** and **(d)** show the distribution of overlap values for one data point marked in red in **(a)** for $\mu = 1$ and **(b)** for $\mu = 2$ respectively close to the left-handed HWHM at $x \approx -\gamma$. A linear fit returns the slope **(c)** $\alpha_1 = -5.47(12)\times10^{2}$ and **(d)** $\alpha_2 = -5.76(20)\times10^{2}$.

blocks corresponding to the four possible scatterings between the states in subsystem $\mathcal{S}$. With the given choice of X, the four blocks are on average identical. Since the unperturbed eigenbasis is a product basis of $|\psi_\mu^{\mathcal{S}}\rangle \otimes |\psi_i^{\mathcal{B}}\rangle$, we are interested in $\chi_{\mu i,l}$, the square modulus of the overlap of the product states with the full eigenstates $|\psi_l^{\mathcal{F}}\rangle$, arising from the small perturbation X with variance $t \ll \sigma_{\mathcal{B}}^2$ for each μ individually. We expect those overlaps to be peaked close to $E_i \approx \lambda_l - \epsilon_\mu$, which refers to two different positions in the bath $\mathcal{B}$ for $\mu = 1, 2$. As determined for the single peak model, $\chi_{i,l}$ forms a localized peak in energy and we expect a similar structure for the multi peak model. We again

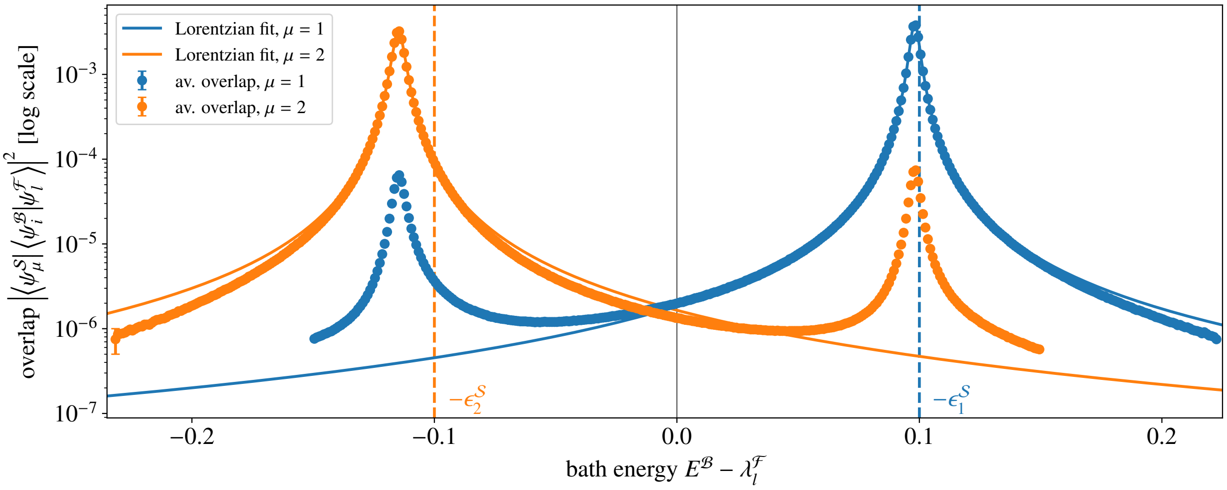

Figure 4.7: Logarithmic representation of the averaged overlaps $\left|\langle\psi_\mu^S|\langle\psi_i^{\mathcal{B}}|\psi_l^{\mathcal{F}}\rangle\right|^2$ from $N_{\text{av}} = 3200$ states around $\bar{\lambda}_l = -1.457\,29(60)$ in terms of the shifted bath energy $E_i^{\mathcal{B}} - \lambda_l^{\mathcal{F}}$, split up into the contributions for $\mu = 1$ in blue and $\mu = 2$ in orange. The data is the same as shown in Fig. 4.6**a,b** in a larger energy range and the matrix variance of X is $t = 1.63 \times 10^{-3}$. Lorentzian fits are added as blue and orange curves for $\mu = 1$ and $\mu = 2$ respectively. We further mark the expected position of the overlap peak without shifts $E_i^{\mathcal{B}} = \lambda_l^{\mathcal{F}} - \epsilon_\mu^S$ for $\mu = 1, 2$ as dashed lines.

choose $\lambda_l^{\mathcal{F}} \approx -1.45$ as our point of investigation to be able to qualitatively compare the results to the single peak model.

With H^S normalized, such that its variance is $\sigma_S^2 = 0.01$, we obtain the eigenvalues $\epsilon_1 = -0.1$ and $\epsilon_2 = +0.1$ in the subsystem $\mathcal{S}$. From the four blocks in the matrix $\tilde{X}$, we each select boxes of equal energy width $\Delta E_i = 0.1$ around the expected location of the overlap peaks. This corresponds to boxes centered around the (row, column) energies $(E_i^{(\mu)} \approx -1.45 - \epsilon_\mu, E_j^{(\nu)} \approx -1.45 - \epsilon_\nu)$ in the block (μ, ν). The four boxes are centered around different energies. The diagonal blocks have the same energy center for their respective row and column, while in the offdiagonal blocks this differs. The DOS is energy dependent which leads to different number of states in a fixed energy window $\Delta E_i = 0.1$ around different energy centers. It results in rectangular shapes of the boxes for the offdiagonal blocks and in square boxes for the diagonal blocks. The structure of the boxes is similar to the single peak model in Fig. 4.1 featuring an effective GUE in each box with a Gaussian distribution of real and imaginary part of equal variance and twice of that variance on the diagonal. Additionally, the trace of the diagonal in each box is nonzero leading to a nonzero mean of the Gaussian for the diagonal elements. In Fig. 4.5, we plot the distribution of the real part of the matrix elements in the boxes of each matrix block as a reference for comparison. Due to the fact, that the boxes are centered around different bath energies, the variances of their matrix elements do not agree. From the Gaussian fits in Fig. 4.5 we obtain the standard deviations $\sigma_{1,1;\text{Re}} = 9.2505(52) \times 10^{-5}$, $\sigma_{1,2;\text{Re}} = 8.9034(40) \times 10^{-5}$, $\sigma_{2,1;\text{Re}} = 8.9034(40) \times 10^{-5}$ and $\sigma_{2,2;\text{Re}} = 1.1779(13) \times 10^{-4}$ for the real part. Due to hermiticity, the variances for the offdiagonal parts are exactly equal, $\sigma_{1,2;\text{Re}}^2 = \sigma_{2,1;\text{Re}}^2$. They are smaller than $\sigma_{1,1;\text{Re}}^2$ and $\sigma_{2,2;\text{Re}}^2$ with $\sigma_{2,2;\text{Re}}^2$ being the largest. The relation $\sigma_{2,2;\text{Re}}^2 > \sigma_{1,1;\text{Re}}^2$ is a result of their center positions with $E_i^{(1)} \approx -1.45 + 0.1 = -1.35$ and $E_i^{(2)} \approx -1.45 - 0.1 = -1.55$, causing the box $(2, 2)$ to be further on the boundary of the spectrum than the box $(1, 1)$. In Sec. 3.1.4, we associated this positional relation with an increased variance due to the reduced DOS of $\mathcal{B}$ towards the boundary. The variance of the boxes in the offdiagonal blocks is the smallest because its elements are not distributed symmetrically around the diagonal of the matrix, but are shifted in energy by $|\epsilon_2 - \epsilon_1| = 0.2$ on average over the whole box.

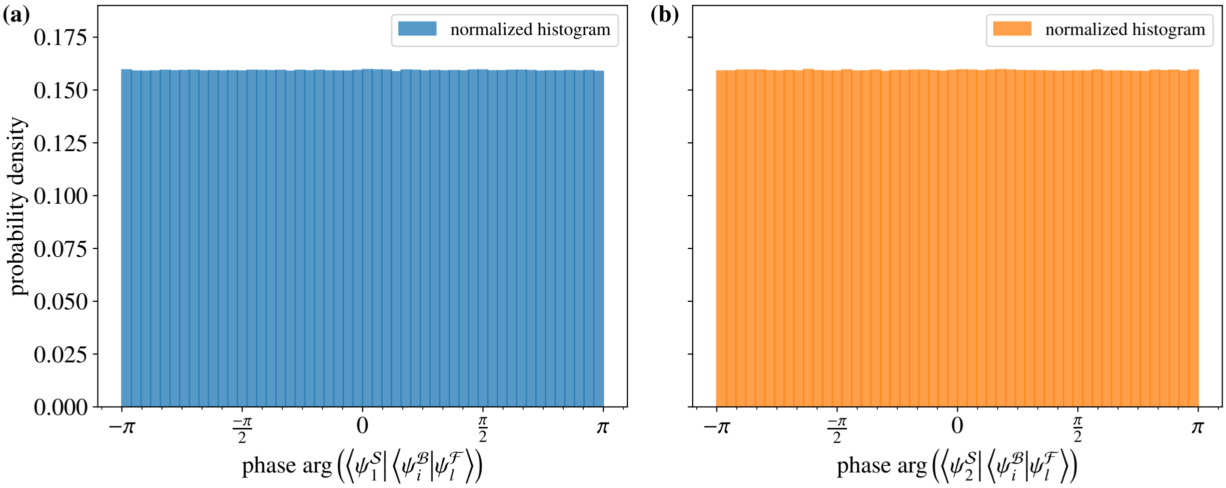

Figure 4.8: Normalized probability distributions of the phases of the complex valued overlaps, $\arg\left(\langle\psi_\mu^{\mathcal{S}}|\,\langle\psi_i^{\mathcal{B}}|\psi_l^{\mathcal{F}}\rangle\right)$, for $\mu = 1$ in **(a)** and $\mu = 2$ in **(b)**. To obtain the distributions of the phases, we take $N_{\mathrm{av}} = 3200$ full states around $\bar{\lambda}_l = -1.457\,29(60)$ and evaluate the overlaps in terms of the bath eigenstates in an energy range of $\Delta E^{\mathcal{B}} = 0.2$ around the peak of its squared magnitude. The results are compiled in normalized histograms of 50 bins. The phases correspond to the squared magnitude of the overlaps in Fig. 4.7 as well as Fig. 4.6**(a,b)**.

The overlap curve and its statistics. If the box variances $\sigma^2_{1,1;\mathrm{Re}}$, $\sigma^2_{1,2;\mathrm{Re}}$, $\sigma^2_{2,1;\mathrm{Re}}$ and $\sigma^2_{2,2;\mathrm{Re}}$ were all identical, we could describe the matrix $\tilde{X}$ around all of the overlap peaks by an effective GUE. This includes the combination of all boxes, not only each box individually. In such a case and when omitting the influence of the matrix elements outside of the boxes, the overlap $\chi_{\mu i,l}$ would give rise to a single peak for all μ as predicted by the equation of Allez and Bouchaud in (1.122). If we split it up into the contributions for $\mathcal{S}$, we would find identically shaped overlap curves for $\mu = 1, 2$ at different positions in terms of the bath energies E_i. However, according to the matrix structure of $\tilde{X}$ with the variance model $\sigma^2_{\mu\nu;ij}$ of the multi peak model described in Sec. 3.2.3 this is not the case, since the variance in the boxes depends on their position in the matrix. This behavior is confirmed again in Fig. 4.5. With different box variances, we expect differing overlap curves for $\mu = 1$ and $\mu = 2$.

Numerical results for $d_{\mathcal{F}} = 18$ lattice sites from which subsystem $\mathcal{S}$ occupies $d_{\mathcal{S}} = 1$ site are shown in Fig. 4.6. We consider $N_{\mathrm{av}} = 3200$ full eigenstates to obtain the mean overlap points averaged in intervals of width $\Delta E^{\mathcal{B}} = 0.001$. The overlap data is plotted with respect to the bath energies shifted by the expected approximate position of the peak, $E_i - (\lambda_l - \epsilon_\mu)$. Both the peak for $\mu = 1$ in Fig. 4.6**a** and for $\mu = 2$ in Fig. 4.6**b** have a Lorentzian shape in the vicinity of the peak position, as confirmed by the Lorentzian fits in the plot. Below these plots, the residuals are shown to be two orders of magnitude smaller than the actual data points, confirming the validity of the fit. The width of the two Lorentzians differs with $\gamma_1 = 2.1224(29) \times 10^{-3}$ and $\gamma_2 = 2.5682(34) \times 10^{-3}$. In first order, this derives from the different variances of the matrix $\tilde{X}$ around their peak positions, as described in Fig. 4.5. We further notice the different peak positions of $\chi_{1i,l}$ and $\chi_{2i,l}$ in terms of their respective shifted bath energy axes $E_i - (\lambda_l - \epsilon_\mu)$ with the fit results $\eta_1 = -1.9223(20) \times 10^{-3}$ and $\eta_2 = -1.485\,30(24) \times 10^{-3}$ for the shifts from zero. The shift partially derives from the nonzero local trace of $\tilde{X}$, which is different at different bath energies $E^{\mathcal{B}}$ of the matrix. On top of those influences, the offdiagonal blocks of the perturbation matrix $\tilde{X}$ introduce a coupling between the two Lorentzians, which can hence not be treated as being independent. The interaction between the overlaps triggers an effective repulsion between them, which shifts them away from each other. Similarly, the

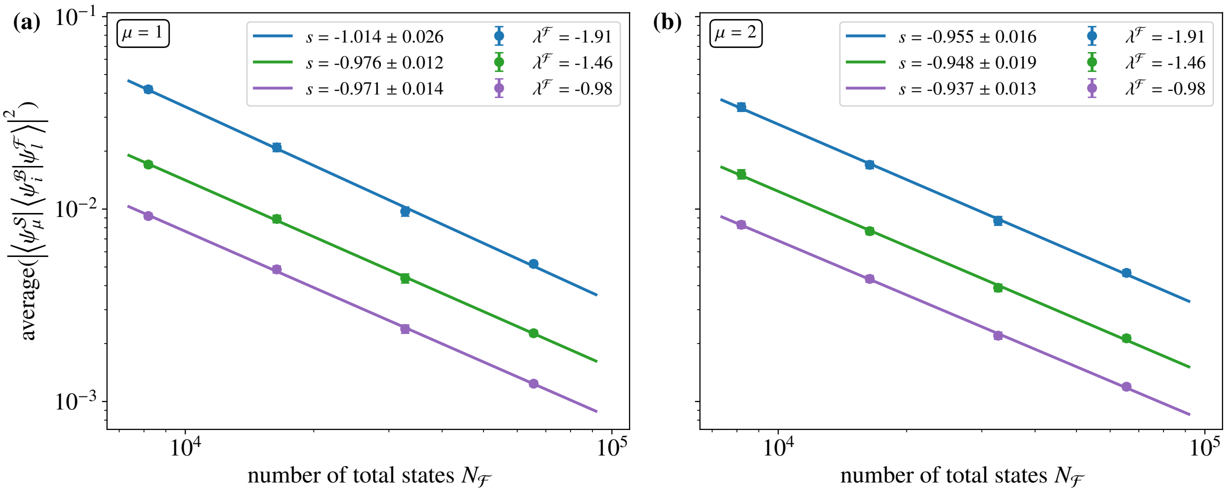

Figure 4.9: Average of the Lorentzian overlap points closest to the left-handed HWHM at $x \approx -\gamma_\mu$ with respect to the total number of states in the quantum system with $N_{\mathcal{F}} = \{2^{13}, 2^{14}, 2^{15}, 2^{16}\}$ for the overlap curve $\mu = 1$ in **(a)** and $\mu = 2$ in **(b)**. The data is averaged over 100 samples of $H^{\mathcal{B}}$ and 200 samples of X for each data point and plotted on a double logarithmic scale. The colors indicate three different full energies λ_l. Linear fits are performed for each data set for λ_l individually, where the slope s is indicated in the legend.

widths of the overlap curves are distorted due to the scattering between them. A detailed calculation for the multi peak model with a systematic comparison to numerical results is conducted in Sec 4.4. Fig. 4.7 shows the overlap curves from Fig. 4.6**a,b** for $\mu = 1$ in blue and $\mu = 2$ in orange on a broader energy range and on a logarithmic scale. The respective Lorentzian fits are shown as a blue and orange line. The fits match the overlap data well close to the expected peak positions at $E_i \approx \lambda_l - \epsilon_\mu$ indicated by dashed vertical lines. Each numerical overlap curve however has an additional secondary peak located at the position of the main peak of the respective other overlap curve. This structure arises due to the coupling of the Lorentzians through the offdiagonal blocks of the perturbation matrix $\tilde{X}$ with $\sigma^2_{1,2;i,j}$ and $\sigma^2_{2,1;i,j}$ and is primarily caused by the diagonal variance contribution in those blocks. The secondary peaks are two orders of magnitude smaller than the main peaks and therefore contribute of lower order.

In Fig. 4.8, we probe the phases of the overlap data, for which we plot the squared magnitude in Fig. 4.7. The phases of the full eigenstate $|\psi_l^{\mathcal{F}}\rangle$ in terms of the unperturbed product eigenbasis of $\mathcal{S}$ and $\mathcal{B}$, $|\psi_\mu^S\rangle \otimes |\psi_i^{\mathcal{B}}\rangle$, are shown for $\mu = 1$ in blue in Fig. 4.8**a** and for $\mu = 2$ in orange in Fig. 4.8**b**. We collect all phases of the $N_{\text{av}} = 3200$ full states in an energy range of $\Delta E^{\mathcal{B}} = 0.2$ around the overlap peak in the bath and determine the probability density by computing the normalized histogram. We find uniform probability densities and hereby confirm again, that the eigenstates originating from the random Hamiltonians have completely random phases, both in terms of their entries in the local basis and between each other.

In Fig. 4.6**c,d** we show the associated statistics of the data point at about the HWHM point of each Lorentzian curve. The statistics is shown for the interval of width 0.001, which was considered to compute the average of this overlap data point. For both data points, we find an exponential distribution of the squared modulus of the overlap values. In Fig. 4.9, we plot the average of this the overlap at the HWHM point in relation to the total number of states $N_{\mathcal{F}}$. We identify a power law dependence, which manifests itself as a linear relationship in the double logarithmic plot, supported by linear fits. The slope of the linear fits is close to -1 with a deviation of less than 8%. This shows, that in total the individual Lorentzian curve for each μ scale as $\frac{1}{N_{\mathcal{F}}}$. The deviation to the nominal value of -1 is caused by the discrete resolution of the overlap curve in terms of the bath eigenstates and their corresponding eigenvalues. Since the numerical results are obtained in a finite size lattice, the overlap curve is sampled through discrete points. With the same argument as in the single peak model, the energy resolution of the overlap curve increases with the lattice size and the investigated point at the HWHM of the peak is sampled more precisely at large $N_{\mathcal{F}}$. Since the full eigensystem forms a complete basis, the squared modulus overlaps $\chi_{\mu i,l}$ fulfill a sum rule over l for the normalization of the state $|\psi_\mu^S\rangle \otimes |\psi_i^{\mathcal{B}}\rangle$ which is involved in the overlap $\chi_{\mu i,l}$. This holds for each μ independently, as numerically confirmed in Fig. 4.9.

4.2 Resolvent iteration

We outline the analytical approach on how to theoretically calculate the overlap curve based on the equation by Casati and Girko. As described in chapter 1, the equation of Casati and Girko gives rise to a recursive equation for the resolvent. Our analytical approach relies on a single insertion of an initial Delta peak into the recursive equation. Since we showed in the previous section 4.1 that the overlap peak is a Lorentzian peak and can be viewed as a broadened Dirac-Delta distribution for small X, the single insertion suffices to approximately describe the shape of the overlap curve. This is confirmed by numerical results in the following sections.

4.2.1 Statement of the problem

As outlined in Sec. 2.1, the single peak model consists of a bath Hamiltonian $H^{\mathcal{B}}$ perturbed by small local interaction X, while the multi peak model is made up of two subsystems, a small subset $\mathcal{S}$ and a large bath $\mathcal{B}$, which are coupled by the perturbation X. In the following, we choose to operate in the basis of the unperturbed eigenstates for both models. The representation of X in the unperturbed eigenbasis is labeled by $\tilde{X}$.

In chapter 3, we analyzed the variance structure of the perturbation matrix $\tilde{X}$ and found that it is a random band matrix, where the elements are drawn from the normal distribution with an element dependent variance. We assume random complex phases of the unperturbed eigenstates, which means that the matrix entries in $\tilde{X}$ are uncorrelated as shown in Sec. 3.1.1. Consequently, all matrix elements $\tilde{X}_{ij}$ can be treated as independent random variables, which was shown to hold in the large system limit culminating with a diagonal two-point correlation in Eq. (3.13). For the single peak model we then use

$$\tilde{X}_{ii} = \sigma_{ii}\, B_{ii}(t), \tag{4.12a}$$

$$\tilde{X}_{ij} = \frac{\sigma_{ij}}{\sqrt{2}} \left(B'_{ij}(t) + i\, B''_{ij}(t) \right) \tag{4.12b}$$

for $i < j$, where $B_{ii}(t), B'_{ij}(t), B''_{ij}(t) \sim \mathcal{N}(0,t)$ are independent Brownian motions of variance t. The diagonal variance of the elements of $\tilde{X}$ is σ^2_{ii} and the offdiagonal variance for $i \neq j$ is σ^2_{ij}. In total, the variance of $\tilde{X}$ is equal to t. The equation of Casati and Girko (1.129) in Sec. 1.4.3 provides a self-consistency relation for the diagonal of the resolvent of $H^{\mathcal{F}}$. The resolvent is represented in the unperturbed eigenbasis of bath eigenstates with diagonal elements $\mathcal{R}_{ii} \equiv \langle \psi_i^{\mathcal{B}} | (z\mathbb{1} - H^{\mathcal{F}})^{-1} | \psi_i^{\mathcal{B}} \rangle$. With this definition, the application of (1.129) yields

$$\mathcal{R}_{ii}(z) = \frac{1}{z - E_i - t \sum\limits_{j\,(j\neq i)} \sigma^2_{ij}\, \mathcal{R}_{jj}(z)}, \tag{4.13}$$

where use the variable E_i for the bath energies to connect to the equation of Casati and Girko. When the solution to this equation for a particular shape of σ^2_{ij} is known, we can use the connection of the resolvent to the overlap determined in Eq. (1.117),

$$X_{il} = \mathbb{E}\left[\left| \langle \psi_i^{\mathcal{B}} | \psi_l^{\mathcal{F}} \rangle \right|^2 \right] = \frac{1}{\pi\, N_{\mathcal{F}} \rho_{\mathcal{F}}(\lambda_l)} \Im\mathrm{m}\, \left(\mathcal{R}_{ii}(\lambda_l - i0^+) \right), \tag{4.14}$$

to find the statistical expectation value of the overlap. Alternatively, the solution to Eq. (4.13) can be obtained iteratively. With this approach, we use an initial guess of the overlap to find the initial value of the resolvent with (4.14), which is then iterated recursively by application of (4.13) with repeated insertion of the resolvent. In the continuum representation with $E_i \to E, \mathcal{R}_{ii}(z) \to \mathcal{R}(E, z)$ and $\sum_j \to \int \mathrm{d}E\,(N_{\mathcal{B}}\rho_{\mathcal{B}}(E))$, the iteration formula of the resolvent reads

$$\mathcal{R}(E, z) = \frac{1}{z - E - t\int \mathrm{d}E'\ (N_{\mathcal{B}}\rho_{\mathcal{B}}(E'))\ \sigma^2_{\mathrm{od}}(E, E')\,\mathcal{R}(E', z)}, \tag{4.15}$$

where $\sigma^2_{\mathrm{od}}(E, E')$ is the variance model of the offdiagonal entries of $\tilde{X}$. The diagonal variance model does not appear in the equation, since the term $i = j$ is excluded in the sum in (4.13). Note, that similar to the Stieltjes, the resolvent obeys a Kramers-Kronig relation (1.56a) with $z \to \lambda - i0^+$,

$$\mathfrak{Re}\ (\mathcal{R}(E, \lambda)) = \fint \frac{\frac{1}{\pi}\mathfrak{Im}\ (\mathcal{R}(E, \xi))}{\lambda - \xi}\,\mathrm{d}\xi = \mathcal{H}[\mathfrak{Im}\,(\mathcal{R})](E, \lambda). \tag{4.16}$$

For the multi peak model, we can extend the analysis to include the subsystem $\mathcal{S}$ with $N_{\mathcal{S}}$ states. The perturbation matrix $\tilde{X}$ with statistically independent elements then takes the form

$$\tilde{X}_{\mu i;\mu i} = \sigma_{\mu i;\mu i}\,B_{ii}(t), \tag{4.17a}$$

$$\tilde{X}_{\mu i;\nu j} = \frac{\sigma_{\mu i;\nu j}}{\sqrt{2}}\left(B'_{\mu i;\nu j}(t) + i\,B''_{\mu i;\nu j}(t)\right) \tag{4.17b}$$

for $i < j$ with independent Brownian motions $B_{\mu i;\mu i}(t), B'_{\mu i;\nu j}(t), B''_{\mu i;\nu j}(t) \sim \mathcal{N}(0, t)$ of variance t. The indices μ and ν refer to the small subsystem $\mathcal{S}$, while i and j correspond to the scattering of X in $\mathcal{B}$. This way, the matrix is separated into the different scattering blocks in $\mathcal{S}$ for μ and ν, where in each block individually $\sigma^2_{\mu i;\nu i}$ represents the diagonal variance of $\tilde{X}$ and $\sigma^2_{\mu i;\nu j}$ with $i \neq j$ the offdiagonal variance. The unperturbed eigenbasis is given by the product basis of $\mathcal{S}$ and $\mathcal{B}$ and we separate the indices of the resolvent into those two contributions with the diagonal elements defined as $\mathcal{R}_{\mu i;\mu i} \equiv \langle\psi^{\mathcal{S}}_{\mu}|\,\langle\psi^{\mathcal{B}}_{i}|\,(z\mathbb{1} - H^{\mathcal{F}})^{-1}\,|\psi^{\mathcal{S}}_{\mu}\rangle\,|\psi^{\mathcal{B}}_{i}\rangle$. The self-consistency equation for the diagonal of the resolvent is then given by

$$\mathcal{R}_{\mu i;\mu i}(z) = \frac{1}{z - E_i - \epsilon_\mu - t \displaystyle\sum_{\substack{\nu, j\\(\nu, j)\neq(\mu, i)}} \sigma^2_{\mu i;\nu j}\,\mathcal{R}_{\nu j;\nu j}(z)} \tag{4.18}$$

and in the continuum version by

$$\begin{aligned}&\mathcal{R}_{\mu\mu}(E, z) \\ &= \frac{1}{z - E - \epsilon_\mu - t\displaystyle\sum_{\nu}\int \mathrm{d}E'\,N_{\mathcal{B}}\rho_{\mathcal{B}}(E')\,\sigma^2_{\mathrm{od},\mu\nu}(E, E')\,\mathcal{R}_{\nu\nu}(E', \lambda) - t\sum_{\substack{\nu\\(\nu\neq\mu)}}\int \mathrm{d}E'\,N_{\mathcal{B}}\rho_{\mathcal{B}}(E')\,\sigma^2_{\mathrm{d},\mu\nu}(E, E')\,\mathcal{R}_{\nu\nu}(E', \lambda)}\end{aligned} \tag{4.19}$$

with $\sigma^2_{\mathrm{od},\mu\nu}(E, E')$ and $\sigma^2_{\mathrm{d},\mu\nu}(E, E')$ denoting the offdiagonal and diagonal variance in the scattering block from the states ν to μ in $\mathcal{S}$ respectively. As in the single peak model, the exact diagonal of the variance model is taken out of the analysis as required by the Casati and Girko equation. in (1.129).

4.2.2 Calculation of the resolvent

To analytically approximate the shape of this curve, we employ the resolvent iteration formula (4.15) in the single peak and (4.19) in the multi peak model. From the numerical analysis in Sec. 4.1, we know that for small $\tilde{X}$ with $t \ll \sigma_{\mathcal{B}}^2 = 1$, the overlap curve is given by a shifted Lorentzian with small width $\gamma \approx t$. This leads to the choice of the initial value to be a Dirac-Delta distribution for the overlap, which reads

$$\mathcal{X}_{il} \to \mathcal{X}(E_i, \lambda_l) = \frac{1}{N_{\mathcal{F}} \rho_{\mathcal{F}}(\lambda_l)} \delta(E_i - \lambda_l - \eta^{(l)}) \tag{4.20}$$

for the single peak model with appropriate normalization. The Delta peaks are shifted from the expected location of $t = 0$ in order to determine the shift parameter η self-consistently. We terminate the resolvent iteration after one recursive loop, which amounts to a single insertion of the initial value since we are interested in the overlap curve for small t. This is justified by the preliminary numerical results in Sec. 4.1, from which we conclude, that the energy resolved overlap curve is a broadened Dirac-Delta distribution. Since we assume that the perturbation matrix X is small as it has a small variance compared to the spectral width of the unperturbed system, we expect the featured overlap peak to have a small width as well. The shape of this narrow peak can be approximated by the single recursive insertion into the equation by Casati and Girko (1.129) with further insertions providing merely minor adjustments and a parametric rescaling. This was confirmed in a numerical analysis where the solution of the equation by Casati and Girko was found through numerical iterations where a termination condition adjusted to the desired numerical precision was employed. We found that for small t the analytic calculation approximates the solution well. An analytic calculation beyond the single insertion is further not available due to the complexity of the result. With the initial overlap, we find the imaginary part of the initial value of the resolvent through application of Eq. (4.14) as

$$\Im\mathfrak{m}\,(\mathcal{R}_{ii}(\lambda_l)) = \pi\,\delta(E_i - \lambda_l - \eta^{(l)}). \tag{4.21}$$

With the Kramers-Kronig relation for the resolvent in (4.16), we find the complex valued resolvent as

$$\mathcal{R}(E_i, z) = \frac{1}{z - E_i + \eta^{(l)}} \tag{4.22a}$$

$$\to \mathcal{R}(E_i, \lambda_l - i0^+) = \mathcal{P}\left(\frac{1}{\lambda_l - E_i + \eta^{(l)}}\right) + i\pi\,\delta(\lambda_l - E_i + \eta^{(l)}) \tag{4.22b}$$

with $z \in \mathbb{C}$ and with applying the Dirac identity in Eq. (1.48). To apply the resolvent iteration formula, we calculate the weighted trace $\tilde{\mathcal{G}}(E, \lambda) = \tilde{\mathcal{G}}'(E, \lambda) + i\,\tilde{\mathcal{G}}''(E, \lambda)$ of the resolvent to

$$\tilde{\mathcal{G}}(E_i, z) = \int \mathrm{d}E'\ (N_{\mathcal{B}} \rho_{\mathcal{B}}(E'))\ \sigma_{\mathrm{od}}^2(E_i, E')\,\mathcal{R}(E', z) \tag{4.23a}$$

$$\Rightarrow \tilde{\mathcal{G}}(E_i, \lambda_l - i0^+) = ⨍ \mathrm{d}E'\ \frac{(N_{\mathcal{B}} \rho_{\mathcal{B}}(E'))\ \sigma_{\mathrm{od}}^2(E_i, E')}{\lambda_l - E' + \eta^{(l)}} + i\pi\, N_{\mathcal{B}} \rho_{\mathcal{B}}(\lambda_l + \eta^{(l)})\,\sigma_{\mathrm{od}}^2(E_i, \lambda_l + \eta^{(l)}), \tag{4.23b}$$

which can be split into the real and imaginary part

$$\tilde{\mathcal{G}}'(E_i, \lambda_l) = \pi N_{\mathcal{B}} \mathcal{H}\left[\rho_{\mathcal{B}}(E_j)\,\sigma_{\mathrm{od}}^2(E_i, E_j)\right](E_j \to \lambda_l + \eta^{(l)}), \tag{4.24a}$$

$$\tilde{\mathcal{G}}''(E_i, \lambda_l) = \pi\, N_{\mathcal{B}}\, \rho_{\mathcal{B}}(\lambda_l + \eta^{(l)})\,\sigma_{\mathrm{od}}^2(E_i, \lambda_l + \eta^{(l)}). \tag{4.24b}$$

The real part is given by the Hilbert transform of the imaginary part in terms of its second variable E_j, as found in (4.16). This solution can be inserted into the resolvent equation (4.13),

$$\mathcal{R}(E_i, z) = \frac{1}{z - E_i - t\tilde{\mathcal{G}}(E_i, z)} \tag{4.25}$$

to obtain the final result for the resolvent, from which the overlap can be extracted by means of Eq. (1.117).

The variance model in the multi peak model is given by $\sigma^2_{\mu i;\nu j}$, which is given Eq. (3.55) in the continuum limit reading

$$\sigma^2_{\mu i;\nu j} \to \sigma^2_{\mu\nu}(E_i^{\mathcal{B}}, E_j^{\mathcal{B}}) = \sigma^2_{\mathrm{od},\mu\nu}(E_i^{\mathcal{B}}, E_j^{\mathcal{B}}) + \sigma^2_{\mathrm{d},\mu\nu}(E_i^{\mathcal{B}}, E_j^{\mathcal{B}}). \tag{4.26}$$

Here, $\sigma^2_{\mathrm{od},\mu\nu}(E_i^{\mathcal{B}}, E_j^{\mathcal{B}})$ corresponds to the offdiagonal variance in the block (μ, ν) of the matrix $\tilde{X}$ while $\sigma^2_{\mathrm{d},\mu\nu}(E_i^{\mathcal{B}}, E_j^{\mathcal{B}})$ denotes the diagonal variance in the same block. The diagonal of the variance model, which is proportional to a Dirac-Delta distribution divided by the DOS in the continuum is further explicated as

$$\sigma_{\mathrm{d},\mu\nu}(E, E') = \frac{1}{N_{\mathcal{B}}\rho_{\mathcal{B}}(E)}\,\tilde{\sigma}^2_{\mathrm{d},\mu\nu}(E)\,\delta(E - E') \tag{4.27}$$

with the prefactor $\tilde{\sigma}^2_{\mathrm{d},\mu\nu}(E)$. This relation is derived and explained in Sec. 3.1.4. In the multi peak model, we choose the initial overlap curve as

$$X_{\mu i,l} \to X_\mu(E_i, \lambda_l) = \frac{1}{N_{\mathcal{F}}\rho_{\mathcal{F}}(\lambda_l)}\,\delta(E_i + \epsilon_\mu - \lambda_l - \eta_\mu^{(l)}), \tag{4.28}$$

which determines the complex valued diagonal of the resolvent to

$$\mathcal{R}_{\mu\mu}(E_i, z) = \frac{1}{z - E_i - \epsilon_\mu + \eta_\mu^{(l)}}. \tag{4.29}$$

The resolvent iteration in (4.19) yields

$$\begin{aligned}
\tilde{\mathcal{G}}_\mu(E_i, z) &= \sum_\nu \int \mathrm{d}E'\, N_{\mathcal{B}}\rho_{\mathcal{B}}(E')\,\sigma^2_{\mathrm{od},\mu\nu}(E, E')\,\mathcal{R}_{\nu\nu}(E', z) + \sum_{\substack{\nu \\ (\nu\neq\mu)}} \int \mathrm{d}E'\, N_{\mathcal{B}}\rho_{\mathcal{B}}(E')\,\sigma^2_{\mathrm{d},\mu\nu}(E, E')\,\mathcal{R}_{\nu\nu}(E', z) \\
\Rightarrow \tilde{\mathcal{G}}_\mu(E_i, \lambda_l - i0^+) &= \sum_\nu \fint \mathrm{d}E'\, \frac{N_{\mathcal{B}}\rho_{\mathcal{B}}(E')\,\sigma^2_{\mathrm{od},\mu\nu}(E_i, E')}{\lambda_l - E' - \epsilon_\nu + \eta_\nu^{(l)}} + \sum_{\substack{\nu \\ (\nu\neq\mu)}} \frac{\tilde{\sigma}^2_{\mathrm{d},\mu\nu}(E_i)}{\lambda_l - E_i - \epsilon_\nu + \eta_\nu^{(l)}} \\
&\quad + i\pi \left(\sum_\nu N_{\mathcal{B}}\rho_{\mathcal{B}}(\lambda_l - \epsilon_\nu + \eta_\nu^{(l)})\,\sigma^2_{\mathrm{od},\mu\nu}(E_i, \lambda_l - \epsilon_\nu + \eta_\nu^{(l)}) + \sum_{\substack{\nu \\ (\nu\neq\mu)}} \tilde{\sigma}^2_{\mathrm{d},\mu\nu}(E_i)\,\delta(E_i + \epsilon_\nu - \lambda_l - \eta_\nu^{(l)}) \right)
\end{aligned} \tag{4.30}$$

for the weighted trace of the resolvent, where the overlap curve for each μ is evaluated separately using the resolvent input. Due to the coupling of the overlaps with the offdiagonal blocks of the variance model, each iteration result involves a sum ν over all resolvents in $\mathcal{S}$, which contribute to $\tilde{\mathcal{G}}_\mu(E_i, z)$. The first line in (4.30) corresponds to the real part $\tilde{\mathcal{G}}'_\mu$, while the second line is its imaginary part $\tilde{\mathcal{G}}''_\mu$. It involves both the diagonal and offdiagonal part of the variance model. It can be inserted in

$$\mathcal{R}_{\mu\mu}(E_i, z) = \frac{1}{z - E_i - \epsilon_\mu - t\,\tilde{\mathcal{G}}_\mu(E_i, z)} \tag{4.31}$$

to obtain the final result of the resolvent, from which the overlap curve in terms of the bath energies $E_i = E_i$ can be extracted for each μ in $\mathcal{S}$ individually. To find the final result for the resolvent, we need to assume a specific shape of the DOS and the variance model $\sigma^2(E, E')$ in $\mathcal{B}$ and insert it into the formulas for $\tilde{\mathcal{G}}$. This is done in the following chapter.

4.3 Quantitative analysis of the single peak model

We quantitatively analyze the shape of the overlap curve in the single peak model, where a small local perturbation is added to the bath. To investigate it analytically, we employ the resolvent iteration from Sec. 4.2 based on the equation by Casati and Girko. We find that the overlap close to the peak is described by a Lorentzian curve. This is supported by a numerical analysis, where we compare the parameters of the Lorentzian with the analytical prediction. We conclude the analysis by a study of the finite size averaging as well as the influence of the finite size lattice.

4.3.1 Analytic calculation of the overlap curve

X-matrix: The physical model. From a physical standpoint, we want to take the thermodynamic limit where the number of states as well as the volume of the bath in the system goes to infinity, $N \to \infty$ and $V \to \infty$ such as to analyze the behavior of macroscopically large systems. In Sec. 2.2, we stated, that the DOS of the bath $\mathcal{B}$ is a Gaussian, $N_{\mathcal{B}}\rho_{\mathcal{B}}(E) = N_{\mathcal{B}}\sqrt{\frac{1}{2\pi\sigma^2}}\, e^{-\frac{1}{2\sigma^2}E^2}$. To find the behavior of the DOS close to the energy E, we look at the expansion $E + x$ in terms of x,

$$\frac{\rho_{\mathcal{B}}(E+x)}{\rho_{\mathcal{B}}(E)} = e^{\beta_E x - \frac{1}{2\sigma^2}x^2}, \tag{4.32}$$

which is exact for the Gaussian with $\beta_E = -\frac{1}{\sigma^2}E$ depending on the point of expansion E. In statistical mechanics, the entropy $S_{\mathcal{B}}$ of the bath is defined as the logarithm of the DOS, $S_{\mathcal{B}}(x) = k_{\mathrm{B}} \ln(\rho_{\mathcal{B}}(x))$. The inverse temperature β changes linearly with x,

$$\beta = \frac{1}{k_{\mathrm{B}}T} = \frac{1}{k_{\mathrm{B}}}\frac{\partial}{\partial x} S_{\mathcal{B}}(x) = \beta_E - \frac{x}{\sigma^2}, \tag{4.33}$$

where β_E is the inverse temperature at energy E for $x = 0$. Rewriting Eq. (4.32) in terms of the entropy, we find

$$\frac{\rho_{\mathcal{B}}(E+x)}{\rho_{\mathcal{B}}(E)} = e^{\frac{1}{k_{\mathrm{B}}}(S_{\mathcal{B}}(E+x) - S_{\mathcal{B}}(E))} \tag{4.34}$$

with

$$S_{\mathcal{B}}(E+x) - S_{\mathcal{B}}(E) = \underbrace{\left.\frac{\partial S_{\mathcal{B}}(E)}{\partial E}\right|_E}_{=\frac{1}{T}} \cdot x + \frac{1}{2}\left.\frac{\partial^2 S_{\mathcal{B}}(E)}{\partial^2 E}\right|_E \cdot x^2 + \dots \tag{4.35}$$

with a general expansion of the entropy $S_{\mathcal{B}}(E)$ around the energy E. The heat capacity defined as $c(T) \equiv \frac{\partial E}{\partial T}$ is then computed by

$$\frac{1}{c} = \frac{\partial T}{\partial E} = \frac{\partial}{\partial E}\left(\frac{\partial S_{\mathcal{B}}(E)}{\partial E}\right)^{-1} = -\left(\frac{\partial S_{\mathcal{B}}(E)}{\partial E}\right)^{-2}\frac{\partial^2 S_{\mathcal{B}}(E)}{\partial E^2} = -T^2\frac{\partial^2 S_{\mathcal{B}}(E)}{\partial E^2}. \tag{4.36}$$

Reconnecting this result to Eq. (4.32), we obtain the relation

$$\frac{1}{\sigma^2} = -\frac{1}{k_{\mathrm{B}}}\frac{\partial^2 S_{\mathcal{B}}(E)}{\partial E^2} = \frac{1}{k_{\mathrm{B}}T^2 c} = \beta^2\frac{k_{\mathrm{B}}}{c} \tag{4.37}$$

for the prefactor of the quadratic term of the DOS in the expansion around E. Since the inverse temperature β stays constant and the heat capacity c is proportional to the volume V in the thermodynamic limit, the factor $\frac{1}{\sigma^2}$ goes to zero with $\frac{1}{\sigma^2} \propto \frac{1}{c} \propto \frac{1}{V} \to 0$ as $V \to \infty$. As a result, the Gaussian DOS reduces to an exponential in the thermodynamic limit with $\rho_{\mathcal{B}}(E) \propto e^{\beta E}$, where β is constant.

The exponential approximation for the DOS is one approach on how the variance model can be evaluated. In chapter 3, we split up the quantum system in a part C on which X acts and the remaining part $\bar{C}$. Consistent with the approximation $\rho_{\mathcal{B}}(E) \propto e^{\beta E}$, we assume that the bath is so large, that the DOS in $\bar{C}$ is equal to the DOS in $\mathcal{B}$. Invoking the final formula for the offdiagonal variance model in (3.45), we can pull all factors out of the integral, which do not depend on the energy difference $E_- = \frac{E_i - E_j}{2}$, but only on their mean, $E_+ = \frac{E_i + E_j}{2}$. The result for σ^2_{od} up to a normalization factor is given by

$$\begin{aligned}
\sigma^2_{\mathrm{od}}\left(E_i, E_j\right) &= \frac{1}{N_{\mathcal{B}}} \frac{\int \mathrm{d}E\, \rho_C(E_i - E)\, \rho_C(E_j - E)\, \rho_{\bar{C}}(E)}{\rho_{\mathcal{B}}(E_i)\, \rho_{\mathcal{B}}(E_j)} \\
&\propto e^{-\beta(E_i + E_j)} \int \mathrm{d}E\, e^{\beta E} \rho_C(E_i - E)\, \rho_C(E_j - E) \\
&\propto e^{-\frac{\beta}{2}(E_i + E_j)} \underbrace{\int \mathrm{d}E\, e^{-\beta E} \rho_C(E + E_-)\, \rho_C(E - E_-)}_{=:u(E_-)} \\
&\propto \frac{1}{N_{\mathcal{B}} \rho_{\mathcal{B}}(E_+)}\, u(E_-),
\end{aligned} \tag{4.38}$$

where we substituted $E \to E_+ - E$ in the integral. As discussed and illustrated in chapter 3, the result for the variance model can be represented in terms of a product of a function $v(E_+) := (N_{\mathcal{B}} \rho_{\mathcal{B}}(E_+))^{-1}$, the inverse of the DOS, which depends only on the mean energy E_+ and another function $u(E_-)$ depending only on the energy difference E_-. This is consistent with the numerical data presented in Sec. 3.1.3. Since the interactions in the subsystem C where X acts, are local, ρ_C has the shape of a Gaussian. Therefore the function $u(E_-)$ must be proportional to a Gaussian as well,

$$u(E_-) \propto e^{-\frac{E_-^2}{\Delta_0^2}} = e^{-\frac{(E_i - E_j)^2}{4\Delta_0^2}}, \tag{4.39}$$

for which we use the scattering scale $\sqrt{2}\Delta_0$, which renders the full width at half maximum (FWHM) to be $4\sqrt{\ln(2)}\Delta_0$. In the definition of $u(E_-)$, we can view the exponential $e^{-\beta E}$ as a background function, while the integral varies on the scale of the DOS of C. This results in an effective convolution of ρ_C with itself. As ρ_C is a Gaussian, the resulting convolution returns a Gaussian as well with twice the variance σ_C^2. The variance of the scattering function $u(E_-)$ is therefore $2\Delta_0$ with $\Delta_0 = \sigma_C$. This makes sense, because the variance model originates from a scattering between all states in C whose width is accordingly given by $\sqrt{2}$ times the width in C. We compute the normalization factor $\mathcal{N}_0$ with the exponential DOS in the bath such that the sum of variances in each row or column is equal to one,

$$\begin{aligned}
1 = \sum_j \sigma_{ij}^2 &= \int \mathrm{d}E_j \left(N_{\mathcal{B}} \rho_{\mathcal{B}}(E_j)\right) \frac{\mathcal{N}_0}{N_{\mathcal{B}} \rho_{\mathcal{B}}\left(\frac{E_i + E_j}{2}\right)}\, e^{-\frac{(E_i - E_j)^2}{4\Delta_0^2}} \\
&= \mathcal{N}_0 \int \mathrm{d}E_j \exp\left\{\beta E_j - \beta \frac{E_i + E_j}{2} - \frac{(E_i - E_j)^2}{4\Delta_0^2}\right\} \\
&= \mathcal{N}_0 \int \mathrm{d}E_j \exp\left\{-\beta \frac{E_i - E_j}{2} - \frac{(E_i - E_j)^2}{4\Delta_0^2}\right\}
\end{aligned}$$

$$= \mathcal{N}_0\, 2\sqrt{\pi}\Delta_0\, e^{\frac{\beta^2\Delta_0^2}{4}} \tag{4.40}$$

and consequently

$$\sigma^2_{\mathrm{od}}(E_+, E_-) = \frac{1}{2\sqrt{\pi}\Delta_0}\,\frac{1}{N_{\mathcal{B}}\rho_{\mathcal{B}}(E_+)}\, e^{-b_0^2}\, e^{-\frac{E_-^2}{\Delta_0^2}}, \tag{4.41}$$

where we defined $b_0 := \frac{\beta\Delta_0}{2}$. This result was obtained under the assumption of constant β, which is fulfilled in the limit $\frac{1}{\sigma^2} \to 0$. Note, that the offdiagonal variance multiplied with the DOS can be written in the compact form

$$\begin{aligned} N_{\mathcal{B}}\rho_{\mathcal{B}}(E_i)\,\sigma^2_{\mathrm{od}}\left(E_i, E_j\right) &= \frac{1}{2\sqrt{\pi}\Delta_0}\,\frac{\rho_{\mathcal{B}}(E_i)}{\rho_{\mathcal{B}}\left(\frac{E_i+E_j}{2}\right)}\, e^{-\frac{(E_i-E_j)^2}{4\Delta_0^2}}\, e^{-\frac{\beta^2\Delta_0^2}{4}} \\ &= \frac{1}{2\sqrt{\pi}\Delta_0}\, e^{-\frac{1}{4\Delta_0^2}\left(E_i-E_j-\beta\Delta_0^2\right)^2} = \frac{1}{2\sqrt{\pi}\Delta_0}\, e^{-\left(\frac{E_-}{\Delta_0}-b_0\right)^2}, \end{aligned} \tag{4.42}$$

which is a function of E_- only. This means, that an integration over E_i gives a constant, in this case one. As we analyzed in Sec. 3.1.4, the diagonal contribution to the matrix is not a null set. It can be superimposed with the offdiagonal term, where the overall normalization is accounted for by a prefactor to $\sigma^2_{\mathrm{od}}(E_i, E_j)$.

In the case of a finite system size, the normalization factor of σ^2_{ij} depends on the energy itself through $\beta = -\frac{1}{\sigma^2}E$ and therefore can be computed to normalize either the rows or the columns of $\tilde{X}$ depending on wether we choose the inverse temperature to be $\beta = -\frac{1}{\sigma^2}E_i$ or $\beta = -\frac{1}{\sigma^2}E_j$. But the resolvent iteration in (4.13) involves only the sum over j of the variance model σ^2_{ij} paired with the diagonal of the resolvent $\mathcal{R}_{jj}$. Hence the i-th row of σ^2_{ij} can be normalized by approximating $\beta = -\frac{1}{\sigma^2}E_i$ to be constant in this row. This way, the sum over j is taken for a normalized row i, as $\mathcal{N}_0$ does not depend on j and the difference to an overall normalized variance model is neglected. Moreover, the DOS of the bath is a full Gaussian in the finite lattice. However, due to the small perturbation X with variance $t \ll 1$, the energetic width of the resolvent is very small and the expansion of $\rho_{\mathcal{B}}$ as an exponential around the center of the resolvent in the integral is justified.

X-matrix: The mathematical model. A different approach to find an analytical form of the variance model is to assume a Gaussian DOS for each of the subsystems and then use Eq. (3.45) to calculate the result. The result must be an exponential function with up to quadratic order in the energy E_i and E_j in the exponent. Since the variance is symmetric in the exchange of indices i and j, $\sigma^2_{ij} = \sigma^2_{ji}$, the only terms which can appear in the exponent are $E_i + E_j = 2E_+$, $E_i^2 + E_j^2 = E_+^2 + E_-^2$, $E_i \cdot E_j = E_+^2 - E_-^2$ and $(E_i - E_j)^2 = 4E_-^2$. As a consequence, the variance model σ^2_{od} constructed from Gaussian DOS in all subsystems can always be written as a product of two functions, $v(E_+)$ and $u(E_-)$, which depend only on E_+ and E_- respectively. This split into $v(E_+)$ and $u(E_-)$ was seen to be consistent with the numerical results of $\tilde{X}$ in Sec. 3.1.3. Since in the exponent the highest order of the energy is the second order, each of these functions must be a Gaussian as well. To connect to the physical model of $\tilde{X}$, we choose $u(E_-)$ to have the same form and adjust the width of the Gaussian in $v(E_+)$ such that whole variance model is normalized to one. In total, we obtain

$$\sigma^2_{\mathrm{od}}(E_i, E_j) = \frac{\sqrt{2\pi}\sigma_{\mathcal{B}}}{\sqrt{4\pi c^2}}\, \frac{\exp\left\{-\frac{1}{\Delta_0^2}\left(\frac{E_i-E_j}{2}\right)^2\right\}}{N_{\mathcal{B}}\exp\left\{-\frac{1}{1+r_0}\frac{1}{2\sigma_{\mathcal{B}}^2}\left(\frac{E_i+E_j}{2}\right)^2\right\}}, \tag{4.43}$$

for the offdiagonal variance model, where $r_0 = \frac{\Delta_0^2}{2\sigma_{\mathscr{B}}^2}$ is a small parameter and

$$c = \sigma_{\mathscr{B}} \frac{\sqrt{2r_0(r_0+1)}}{2r_0+1} = \frac{(\Delta_0')^2}{\overline{\Delta}_0} \tag{4.44}$$

when defining

$$\frac{1}{{\Delta_0'}^2} := \frac{1}{\Delta_0^2} + \frac{1}{\sigma_{\mathscr{B}}^2}, \tag{4.45a}$$

$$\frac{1}{\overline{\Delta}_0^2} := \frac{1}{\Delta_0^2} + \frac{1}{2\sigma_{\mathscr{B}}^2}. \tag{4.45b}$$

In (4.43), the denominator is very close to being the DOS of the bath evaluated at E_+, $N_{\mathscr{B}}\rho_{\mathscr{B}}(E_+)$, however with a slightly larger variance of $(r_0+1)\sigma_{\mathscr{B}}^2 = (\sigma_{\mathscr{B}}^2 + \frac{\Delta_0^2}{2}) > \sigma_{\mathscr{B}}^2$ due to $\Delta_0 > 0$ to fulfill the normalization condition with a Gaussian DOS. In the thermodynamic limit with $N \to \infty$, we have $r_0 \to 0$ and the denominator is equal to $N_{\mathscr{B}}\rho_{\mathscr{B}}(E_+)$, which is consistent with the physical model and with the numerical observations in Sec. 3.1.2. The numerator of σ_{od}^2 in (4.43) is equivalent to the physical model and describes the scattering in the subsystem C. The variance of the Gaussian scattering term is then $2\Delta_0^2$ and twice as large as the variance of the Gaussian DOS in C with $\Delta_0 \approx \sigma_C$. Multiplied with the DOS in the bath, we obtain

$$\begin{aligned} N_{\mathscr{B}}\rho_{\mathscr{B}}(E_j)\,\sigma_{\mathrm{od}}^2\left(E_i, E_j\right) &= \frac{1}{\sqrt{4\pi c^2}} \exp\left\{-\frac{1}{4c^2}\left(E_i - E_j + x_0\right)^2\right\} \\ &= \frac{1}{\sqrt{4\pi}} \frac{\overline{\Delta}_0}{{\Delta_0'}^2} \exp\left\{-\left(\frac{\overline{\Delta}_0}{{\Delta_0'}^2} E_- + \overline{b}_0\right)^2\right\} \end{aligned} \tag{4.46}$$

with

$$x_0 := -\frac{2r_0}{2r_0+1} E_i = -\frac{(\Delta_0')^2}{\sigma_{\mathscr{B}}^2} E_i, \tag{4.47a}$$

$$\overline{b}_0 := \frac{x_0}{2c} = -\frac{\overline{\Delta}_0 E_i}{2\sigma_{\mathscr{B}}^2} \tag{4.47b}$$

In an integration over E_j, which only appears through E_-, the term in (4.46) returns one as expected from the normalization. In the definitions of Δ_0' and $\overline{\Delta}_0$, we can see, that there are corrections to the scattering width Δ_0 with $\Delta_0' < \overline{\Delta}_0 < \Delta_0$ due to the finite width of the DOS of the bath $\sigma_{\mathscr{B}}$.

In the thermodynamic limit we have $r_0 \to 0$, which leads to $\overline{\Delta}_0 \to \Delta_0$ and $\Delta_0' \to \Delta_0$, as well as $\overline{b}_0 \to b_0$. In this limit, the result of the physical model in (4.42) and the mathematical model in (4.46) coincide as demanded from their construction. In a finite system, the mathematical model gives more precise results even though the parameter $r_0 \ll 1$, because C is only a small part of $\mathscr{B}$ already in the finite system with a much smaller variance $\sigma_C^2 \ll \sigma_{\mathscr{B}}^2$ accordingly.

X-matrix: The numerical model. To check the validity of the analytic calculation, we compare it to numerical results of a spin lattice with $d_{\mathscr{B}} = 15$ sites in the bath. The Hamiltonian is chosen according to the introduction in Sec. 2.1.3. We again normalize $H^{\mathscr{B}}$ such that its second moment is $\tau((H^{\mathscr{B}})^2) = 1$. In Fig. 4.10, we show the DOS of the bath with a Gaussian fit, whose best fit standard deviation is extracted to $\sigma_{\mathscr{B}} = 1.0296(19)$. Note, that there is a small 3% deviation to the second moment of $H^{\mathscr{B}}$, which is caused by finite size effects, as the Gaussian in Fig. 4.10 fits the

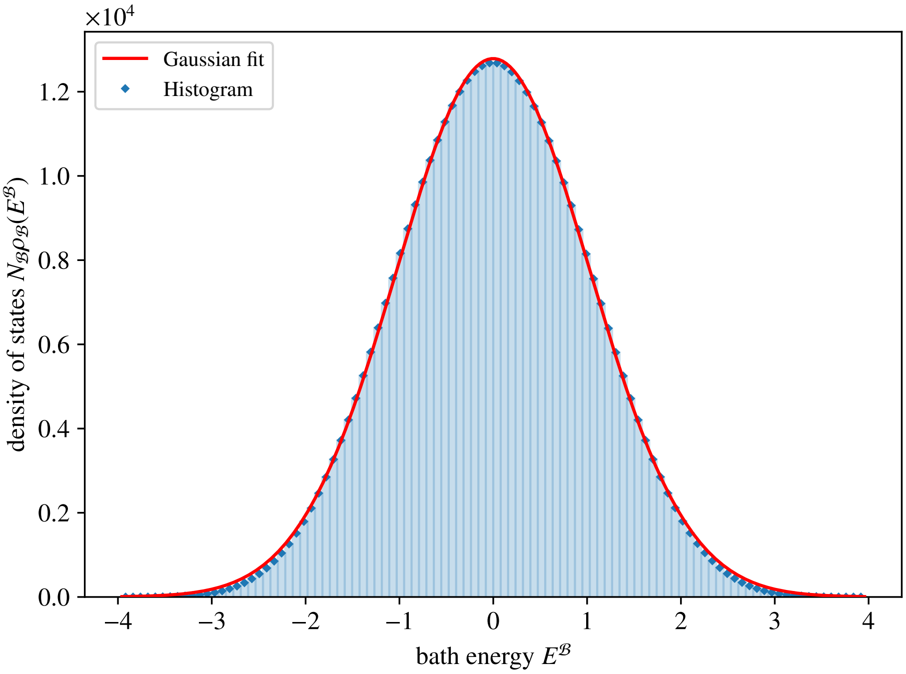

Figure 4.10: Density of states of the bath $\mathcal{B}$ with $d_{\mathcal{B}} = 15$ sites, in an average over 100 samples of $H^{\mathcal{B}}$. A Gaussian fit returns the standard deviation $\sigma_{\mathcal{B}} = 1.0299(19)$.

numerically obtained eigenvalue distribution very well, but not exactly with deviations towards the boundary of the spectrum. The Gaussian is the limit distribution for $N_{\mathcal{B}} \to \infty$, where finite size corrections apply for $N_{\mathcal{B}}$ finite. In the following, all numerical data is obtained after averaging over 200 samples of the perturbation X and 100 samples of the bath Hamiltonian $H^{\mathcal{B}}$. We average over the bath Hamiltonian as well to compensate for finite size effects and a reduced self-averaging property, which would become exact at $N_{\mathcal{B}} \to \infty$ in the thermodynamic limit. To compare the results at different interaction strengths, three different values of t are investigated. The variance data of the matrix $\tilde{X}$ is obtained as the sample variance from square boxes each containing 100×100 matrix elements.

We individually analyze the contributions $v(E_+)$ and $u(E_-)$ to the offdiagonal part of the variance model and conclude on their shape in comparison to what we assumed analytically. A separate analysis of the diagonal elements of $\tilde{X}$ follows. In Fig. 4.11, we plot the anti-diagonal of the variance model along the line $E_i \approx -E_j$, along which $E_+ \approx 0$ to investigate the function $u(E_-)$. The data is normalized by t and we observe only minor deviations between the data points for the three different values of t. As already observed in Sec. 3.1.3, the variance in Fig. 4.11 follows a Gaussian distribution with an additional peak at zero. To model this structure, we fit a sum of two Gaussians of different widths to the data and normalize each Gaussian term in the same way as in Eq. (4.43) for the mathematical model. This gives the numerical model for the offdiagonal variance

$$\sigma^2_{\text{od;num}}(E_i, E_j) = \frac{A_0\,\sqrt{2\pi}\,\sigma_{\mathcal{B}}}{\sqrt{4\pi}\,(1+\vartheta)} \left(\frac{\overline{\Delta}_1}{{\Delta'_1}^2} \frac{\exp\left\{-\frac{1}{\Delta_1^2}\left(\frac{E_i-E_j}{2}\right)^2\right\}}{N_{\mathcal{B}} \exp\left\{-\frac{1}{1+r_1}\frac{1}{2\sigma_{\mathcal{B}}^2}\left(\frac{E_i+E_j}{2}\right)^2\right\}} + \vartheta\, \frac{\overline{\Delta}_2}{{\Delta'_2}^2} \frac{\exp\left\{-\frac{1}{\Delta_2^2}\left(\frac{E_i-E_j}{2}\right)^2\right\}}{N_{\mathcal{B}} \exp\left\{-\frac{1}{1+r_2}\frac{1}{2\sigma_{\mathcal{B}}^2}\left(\frac{E_i+E_j}{2}\right)^2\right\}} \right) \tag{4.48}$$

with $r_1 := \frac{\Delta_1^2}{2\sigma_{\mathcal{B}}^2}$, $r_2 := \frac{\Delta_2^2}{2\sigma_{\mathcal{B}}^2}$ as well as Δ'_1, $\overline{\Delta}_1$ and Δ'_2, $\overline{\Delta}_2$ analogously defined to Eq. (4.45a,b) with Δ_0 substituted by Δ_1 and Δ_2. In Fig. 4.11, we fit the function $\sigma^2_{\text{od;num}}(\frac{x}{2}, -\frac{x}{2})$ to the data points with $x = E_i - E_j = 2E_-$, as the variance is

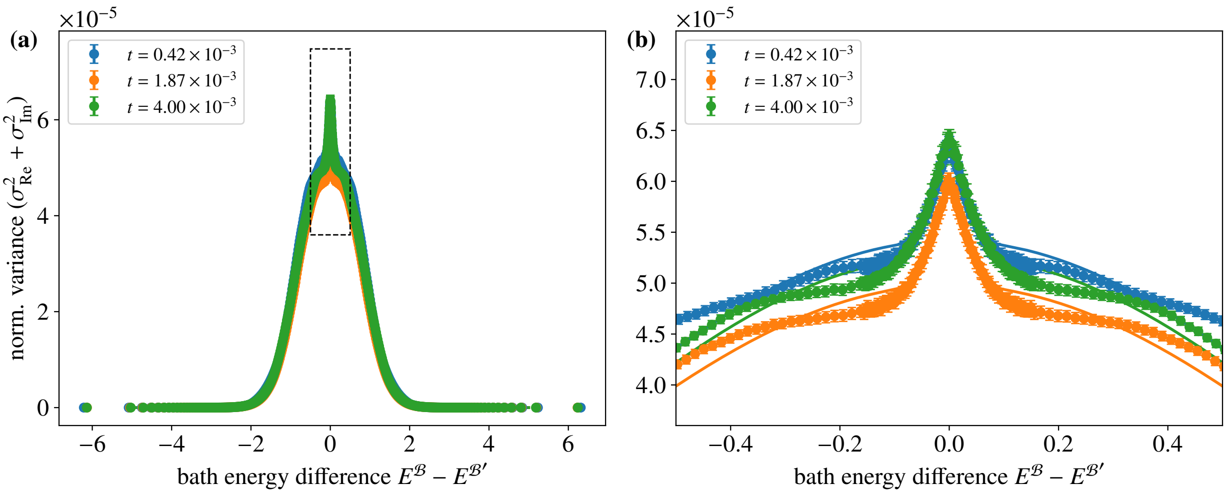

Figure 4.11: Element wise variance of the offdiagonal elements along the anti-diagonal line in the matrix $\tilde{X}$ from the lower left to the upper right, normalized by t and shown for three different values of t. We use $d_{\mathcal{B}} = 15$ and $d_{\mathcal{S}} = 0$ in the single peak model. The data points are computed in terms of boxes of size (100×100) and for a higher resolution around zero with size (20×20). An average is taken over 100 samples of $H^{\mathcal{B}}$ and 200 samples of X. **(a)** shows the variance as a whole along the analyzed line, while **(b)** shows a segment of that indicated by the dashed rectangle in **(a)**. We fit a sum of two Gaussians according to Eq. (4.48) to the data with the best fit parameters being collected in Tab. 4.1.

plotted with respect to the bath energy difference x. The parameter Δ_1 represents the width of the broad underlying Gaussian, while Δ_2 models the much smaller width of the peak at zero on top of the broad Gaussian. Both best fit values from Fig. 4.11 are compiled in Tab. 4.1. The parameter ϑ determines the relative weight of the two Gaussians and the prefactor A_0 accounts for an overall scaling factor of the variance model. With $A_0 = 1$, the sum over each row i or column j in $\sigma^2_{\text{od;num}}(E_i, E_j)$ is normalized to one. We add $A_0 < 1$ as an additional fit parameter to account for the contribution of the diagonal variance of the element $\tilde{X}_{ii}$ to the normalization of the full model. Adapting the result in Eq. (4.46) for the mathematical model, the product of the Gaussian DOS in $\mathcal{B}$ with the numerical offdiagonal model is determined to

$$N_{\mathcal{B}}\rho_{\mathcal{B}}(E_j)\,\sigma^2_{\text{od;num}}\left(E_i, E_j\right) = \frac{A_0}{\sqrt{4\pi}(1+\vartheta)}\left[\frac{\overline{\Delta}_1}{\Delta_1'^2}\exp\left\{-\left(\frac{\overline{\Delta}_1}{\Delta_1'^2}E_- + \overline{b}_1\right)^2\right\} + \vartheta\,\frac{\overline{\Delta}_2}{\Delta_2'^2}\exp\left\{-\left(\frac{\overline{\Delta}_2}{\Delta_2'^2}E_- + \overline{b}_2\right)^2\right\}\right] \tag{4.49}$$

with $\overline{b}_1 := \frac{\beta\overline{\Delta}_1}{2}$ and $\overline{b}_2 := \frac{\beta\overline{\Delta}_2}{2}, \beta = \beta(E_i) = -\frac{E_i}{\sigma^2_{\mathcal{B}}}$.

In Fig. 4.12, we plot the numerically obtained inverse variance along the diagonal of the matrix $\tilde{X}$, where the exact diagonal elements are taken out of the analysis to identify the shape of the offdiagonal variance contribution. This diagonal line is chosen along $E_i \approx E_j$, which means $E_- = 0$ and the function $v(E_+)$ can be investigated. Combined with the above analysis of $u(E_-)$ and the diagonal elements below, the full model is obtained. We identify a Gaussian shape of the data points in Fig. 4.12 for all three values of t, which is supported by the Gaussian fits shown as dashed lines with best fit variance σ_{dia}. For reference, the DOS of the bath is added to the plot. We notice two things in the plot. First, the overall scale of the inverse variance is larger than that of the DOS $N_{\mathcal{B}}\rho_{\mathcal{B}}(E)$ due to the normalization prefactor of the offdiagonal variance model appearing in (4.43) for the mathematical model and in (4.48) for the numerical model. Second, from Tab. 4.1, we conclude that the width σ_{dia} of the inverse variance along the diagonal is

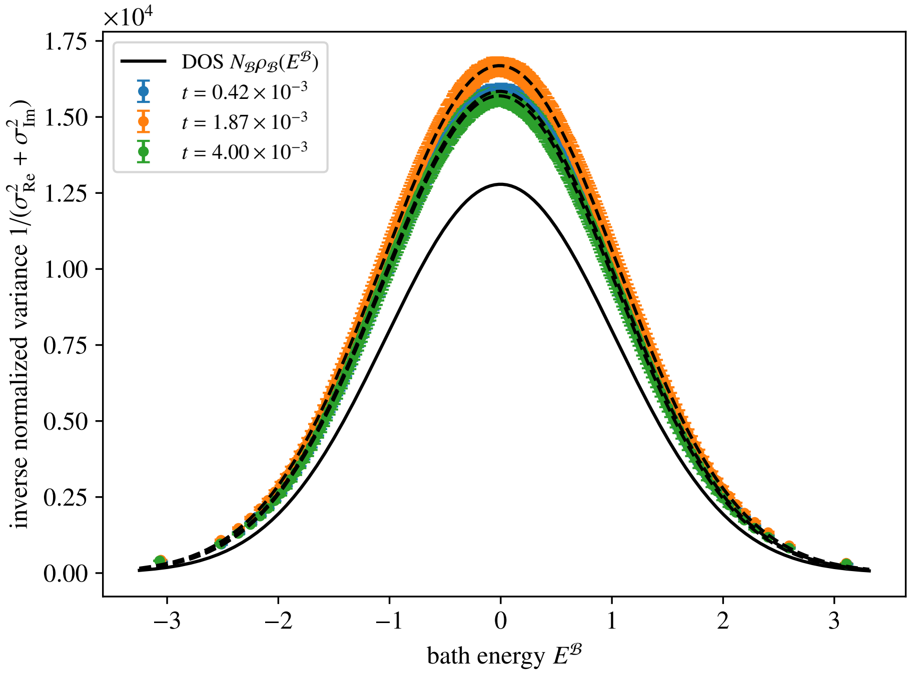

Figure 4.12: Inverse element-wise variance for three values of t on a line along the diagonal of $\tilde{X}$ which considers only the offdiagonal elements with $d_{\mathcal{B}} = 15$ and $d_{\mathcal{S}} = 0$. The data points are computed in terms of boxes of size (100×100) and in an average over 100 samples of $H^{\mathcal{B}}$ and 200 samples of X. For comparison, we plot the fit of the Gaussian DOS $N_{\mathcal{B}}\rho_{\mathcal{B}}(E)$ as a black joined line. Gaussians fits to the data for each value of t are shown as black dashed lines where the fit parameter of the Gaussian variance σ^2_{dia} is noted in Tab. 4.1.

larger than the width $\sigma_{\mathcal{B}} = 1.0296(19)$ of the DOS in $\mathcal{B}$. This is reflected in the fact, that for $\Delta_0 > 0$, the denominator in (4.43) describing the function $v(E_+)$ as well as in each term in (4.48) is a broadened Gaussian of the DOS $\rho_{\mathcal{B}}(E)$ to obtain an exact normalization. The expected broadened width $\sqrt{1 + r_1}\,\sigma_{\mathcal{B}}$ is calculated from the fitted width Δ_1 of the underlying Gaussian of $v(E_-)$ and shown in Tab. 4.1. The fit values for σ_{dia} from Fig. 4.12 lie between $\sigma_{\mathcal{B}}$ and $\sqrt{1 + r_1}\,\sigma_{\mathcal{B}}$.

To complete the analysis of the matrix $\tilde{X}$, we plot the variance σ^2_{ii} for the exact diagonal elements of the matrix $\tilde{X}_{ii}$ in Fig. 4.13**a**. The data points are obtained with the method prescribed in Sec. 3.1.4, where it is important, that the variance is obtained with respect to the random samples of X and not in terms of intervals or boxes, as it was done for the offdiagonal variances. It is relevant for the diagonal, as there is a correlation between the diagonal element and the bath energy in each sample, which is visible in Fig. 4.13**b**, where the sample average of the diagonal values is shown and also discussed in detail in Sec. 3.1.4. This local trace leads to a quadratic dependence of σ^2_{ii} in lowest order of energy. We adopt the notation of Sec. 3.1.4 with

$$\sigma^2_{ii} = \sigma^2_1 + \sigma^2_2 \frac{(E_i - E_0)^2}{\sigma^2_{\mathcal{B}}}, \tag{4.50}$$

where we added the center point E_0 to the quadratic function. E_0 can be nonzero in a finite size average,is zero in although its theoretical statistical expectation value is zero. The parameters are obtained from fits in Fig. 4.13**a** and noted in Tab. 4.2. From the analytical calculation of the diagonal variance culminating in Eq. (3.32), we know that σ^2_1

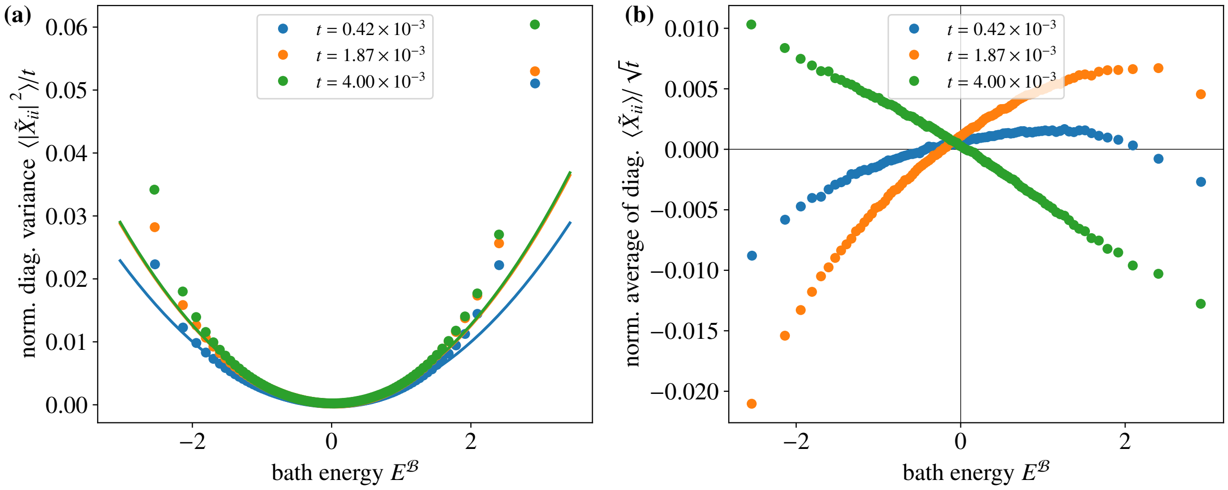

Figure 4.13: (**a**) Sample variance of the diagonal elements of $\tilde{X}$ in the single peak model with $d_{\mathcal{B}} = 15$ and $d_{\mathcal{S}} = 0$ for 200 samples of X and 100 samples of $H^{\mathcal{B}}$ for three values of t. For each sample, the diagonal values $\tilde{X}_{ii}$ are averaged in intervals of 328 elements, then the sample variance of each interval with respect to X is computed and normalized by t. The best fit parameters of a quadratic fit according to Eq. (4.50) to the data for each t are found in Tab. 4.2. **b** Diagonal elements of $\tilde{X}$ averaged over 200 samples of X, 100 samples of $H^{\mathcal{B}}$ and in intervals of 328 elements each. The result is normalized by $\sqrt{t}$. This leads to a total of 100 intervals along the energy axis.

is given by the fraction to which the unit matrix terms contribute to t. Since there are no such terms in the definition of X for the single peak model in (2.8), we have $\sigma_1^2 \approx 0$, which is reflected in the fit results in Tab. 4.2 with $\sigma_1^2 \ll \sigma_2^2$. We further found, that $\sigma_2^2 = \frac{1}{L}$ with L being the number of terms in $H^{\mathcal{B}}$. For $d_{\mathcal{B}} = 15$ sites, there are $L = 243$ terms, which yields a theoretical result of $\sigma_2^2 = 4.12 \times 10^{-3}$. The average of the fit parameters σ_2^2 for all values of t in Tab. 4.2 is $\langle\sigma_2^2\rangle = 3.39(48) \times 10^{-3}$, which is of the same order and close to the analytical expectation. In Fig. 4.13**b**, the sample average of the diagonal elements $\langle\tilde{X}_{ii}\rangle$ is plotted. From this plot, we conclude that with the given number of samples, the average of the diagonal is much smaller than their standard deviation, $\langle\tilde{X}_{ii}\rangle \ll \sqrt{t}\,\sigma_{ii}$. It is consistent with the statistical expectation value, which is zero, $\mathbb{E}\left[\tilde{X}_{ii}\right] = 0$.

Result for the overlap curve. After characterizing the perturbation matrix $\tilde{X}$ in the representation of the unperturbed eigenbasis, we can employ it to calculate the resolvent and from there the overlap $\mathcal{X}_{il}$. In Sec. 4.2.2, we found the real and imaginary part of the weighted trace of the resolvent $\tilde{\mathcal{G}}$ in the single peak model in Eq. (4.24a,b) after one iteration of an initial Delta peak of the overlap. Both in the physical model with (4.42) and in the mathematical model with (4.46), we found that the product of the Gaussian DOS in $\mathcal{B}$ and the offdiagonal variance model σ^2_{od} is again represented by a Gaussian. For the numerical model of the $\tilde{X}$-matrix, the product in (4.49) can be written as a sum of two Gaussians, since we started with a sum of two Gaussians for the offdiagonal matrix. Consider a general Gaussian form for the product

$$N_{\mathcal{B}}\rho_{\mathcal{B}}(E_j)\,\sigma^2_{\text{od}}(E_i, E_j) = \frac{1}{\sqrt{4\pi\Delta^2}}\, e^{-\left(\frac{E_i-E_j}{2\Delta}+b\right)^2}, \tag{4.51}$$

where Δ and b are parameters, which can be adjusted to match the variance model. Δ is a constant, while we allow for a dependence of b on the bath energy E_i with $b = c \cdot E_i$, while b is independent of the bath energy E_j for the following

Fit parameters of the offdiagonal variance						
$t\,[10^{-3}]$	Δ_1	Δ_2	A_0	ϑ	$\sqrt{1+r_1}\,\sigma_{\mathcal{B}}$	σ_{dia}
0.42	0.5371(21)	0.017 99(98)	1.1021(30)	0.006 53(39)	1.0974(12)	1.042 75(51)
1.87	0.5363(22)	0.020 09(88)	1.0084(24)	0.008 62(39)	1.0972(12)	1.078 72(43)
4.00	0.5432(23)	0.0218(11)	1.0683(23)	0.010 15(38)	1.0989(13)	1.039 70(41)

Table 4.1: Fit parameters of the offdiagonal variance in the single peak model with $d_{\mathcal{B}} = 15$ employing the numerical variance model in (4.48). The data together with the resulting fit are depicted in Fig. 4.11. The Gaussian fit standard deviation of the DOS is given by $\sigma_{\mathcal{B}} = 1.0299(19)$. The parameter σ_{dia} is obtained as the Gaussian standard deviation from a fit to the inverse offdiagonal variance data along the diagonal direction of $\tilde{X}$ shown in Fig.4.12.

calculation to be valid. This ansatz inserted into Eq. (4.24b) determines the imaginary part of $\tilde{\mathcal{G}}$ to be

$$\tilde{\mathcal{G}}''(E_i, \lambda_l) = \frac{\sqrt{\pi}}{2\Delta}\, e^{-\left(\frac{E_i-\lambda_l-\eta^{(l)}}{2\Delta}+b\right)^2} = \frac{\sqrt{\pi}}{2\Delta}\, e^{-(x+b)^2} =: \tilde{\mathcal{G}}''(x), \tag{4.52}$$

where we defined $x = x(E_i) := \frac{E_i-\lambda_l-\eta^{(l)}}{2\Delta}$. The Hilbert transform of the imaginary part returns the real part of $\tilde{\mathcal{G}}$ as given in Eq. (4.24a),

$$\tilde{\mathcal{G}}'(E_i, \lambda_l) = \mathcal{H}\left[N_{\mathcal{B}}\rho_{\mathcal{B}}(E_j)\,\sigma_{\text{od}}^2(E_i, E_j)\right](E_i, E_j \to \lambda_l - \eta^{(l)}) = -\frac{\sqrt{\pi}}{2\Delta}\, e^{-(x+b)^2}\, \operatorname{erfi}(x+b)\,, \tag{4.53}$$

where $\operatorname{erfi}(x)$ denotes the *imaginary error function* $\operatorname{erfi}(x) = -i\,\operatorname{erf}(ix)$. The Hilbert transform of the Gaussian is also known under the name of *Dawson function*. The negative sign in the result of the Hilbert transform comes from the fact that it is computed with respect to the second variable in $\tilde{\mathcal{G}}''$, which is E_j. The result can be inserted into the formula for the resolvent in (4.25), from which the overlap follows as

$$\begin{aligned} \mathcal{X}(E_i, \lambda_l) = \mathbb{E}\left[\left|\langle\psi_i^{\mathcal{B}}|\psi_l^{\mathcal{F}}\rangle\right|^2\right] &= \frac{1}{\pi N_{\mathcal{F}}\rho_{\mathcal{F}}(\lambda_l)}\, \Im\mathrm{m}\,(\mathcal{R}(E_i, \lambda_l - i0^+)) \\ &= \frac{1}{\pi N_{\mathcal{F}}\rho_{\mathcal{F}}(\lambda_l)}\, \frac{t\tilde{\mathcal{G}}''(E_i, \lambda_l)}{\left(\lambda_l - E_i - t\tilde{\mathcal{G}}'(E_i, \lambda_l)\right)^2 + \left(t\tilde{\mathcal{G}}''(E_i, \lambda_l)\right)^2}, \end{aligned} \tag{4.54}$$

which in terms of $x = \frac{E_i-\lambda_l-\eta^{(l)}}{2\Delta}$ is given by

$$\mathbb{E}\left[\left|\langle\psi_i^{\mathcal{B}}|\psi_l^{\mathcal{F}}\rangle\right|^2\right] = \frac{1}{\pi N_{\mathcal{F}}\rho_{\mathcal{F}}(\lambda_l)}\, \frac{t\tilde{\mathcal{G}}''(x)}{\left(2\Delta\, x + \eta^{(l)} + t\tilde{\mathcal{G}}'(x)\right)^2 + \left(t\tilde{\mathcal{G}}''(x)\right)^2}. \tag{4.55}$$

Note that the function $\tilde{\mathcal{G}}$ depends only on the energy difference x. The shift $\eta^{(l)}$ of the overlap peak from the position $E_i = \lambda_l$ can be determined self-consistently using Eq. (4.55) by demanding that the peak of the curve be at the position $x = 0$. In Sec. 4.1, we numerically identified the shape of the overlap curve close to its peak position to be a Lorentzian. In the theoretical calculation, we want to recast the overlap close to the center position $x = 0$ in terms of a Lorentzian shape. For this purpose, we expand the denominator

$$\mathcal{D} \equiv \left(2\Delta\, x + \eta^{(l)} + t\tilde{\mathcal{G}}'(x)\right)^2 + \left(t\tilde{\mathcal{G}}''(x)\right)^2 \tag{4.56}$$

Fit parameters of the diagonal variance			
$t\,[10^{-3}]$	$\sigma_1^2\,[10^{-3}]$	$\sigma_2^2\,[10^{-3}]$	E_0
0.42	0.188(16)	2.565(24)	−0.009 53(32)
1.87	0.171(14)	4.222(22)	−0.009 71(29)
4.00	0.1687(58)	3.3869(92)	−0.014 93(33)

Table 4.2: Fit parameters of the diagonal sample variance in the single peak model with $d_{\mathcal{B}} = 15$ according to Eq. (4.50) with the data being plotted in Fig. 4.13.

in Eq. (4.55) around the position $x = 0$ in second order of x, which means $E_i - \lambda_l - \eta^{(l)} \ll \Delta$. The self-consistency equation for $\eta^{(l)}$ can then be extracted by demanding, that the linear order of x in $\mathcal{D}$ vanishes. We further use, that the matrix X is a small perturbation to the bath and further expand the denominator in first order of the interaction strength $t \ll \sigma_{\mathcal{B}}^2$. The denominator $\mathcal{D}$ can be recast in the form

$$\mathcal{D} = (2\Delta x)^2 + (\gamma^{(l)})^2 + O(x^3, t^2) = (E_i - \lambda_l - \eta^{(l)})^2 + (\gamma^{(l)})^2 + O(x^3, t^2) \tag{4.57}$$

with the shift $\eta^{(l)}$ and the width $\gamma^{(l)}$ of a Lorentzian written in terms of the energy difference $E_i - \lambda_l$.

The parameters $\eta^{(l)}$ and $\gamma^{(l)}$ can be obtained by the following logic using an expansion around $x = 0$ of $\mathcal{D}$ in (4.56). By choosing $\eta^{(l)} = -t\tilde{\mathcal{G}}'(0)$, the first bracket corresponding to the real part $\lambda_l - E_i - t\tilde{\mathcal{G}}'(E_i, \lambda_l)$ is proportional to $x + O(x^2)$ and its square is proportional to $x^2 + O(x^3)$. The imaginary part of the function $\tilde{\mathcal{G}}$ with $t\tilde{\mathcal{G}}''(E_i, \lambda_l)$ contributes in second order of t to the denominator $\mathcal{D}$ and therefore plays no role in determining the shift $\eta^{(l)}$ in first order of t. Consequently the constant term of $t\tilde{\mathcal{G}}''(E_i, \lambda_l)$ is identified as the width $\gamma^{(l)}$, which enters as a square in $\mathcal{D}$ and is independent of x. This way, $\mathcal{D}$ has a constant term and a quadratic term $\propto x^2$ and we obtain the final result

$$\gamma^{(l)} = t\tilde{\mathcal{G}}''(0) = \frac{\sqrt{\pi}t}{2\Delta}\, e^{-b^2} + O(t^2), \tag{4.58a}$$

$$\eta^{(l)} = -t\tilde{\mathcal{G}}'(0) = \frac{\sqrt{\pi}t}{2\Delta}\, e^{-b^2}\, \mathrm{erfi}\,(b) + O(t^2) \tag{4.58b}$$

with $b := -\frac{\Delta\lambda_l}{2\sigma_{\mathcal{B}}^2}$. Note that the result in (4.58a,b) for the parameters of the Lorentzian in linear order of t is remarkably simple as they are given by the evaluation of the real and imaginary part of $\tilde{\mathcal{G}}(x)$ at $x = 0$. Different to b_0, b_1 and b_2, we used λ_l instead E_i in the definition of b, since we want to analyze the overlap in terms of the bath energy E_i with $\eta^{(l)}$ and $\gamma^{(l)}$ being parameters that depend on the energy λ_l of the considered eigenstate of the full quantum system. This is possible, as those parameters depending on λ_l are then constants in terms of E_i, having been evaluated at $x = 0$ in Eq. (4.58a,b). At $x = 0$ the relation $E_i = \lambda_l + \eta^{(l)}$ holds, which inserted into (4.58a,b) yields $b = -\frac{\Delta\lambda_l}{2\sigma_{\mathcal{B}}^2}$ for the first order expansion of the parameters in t. This is the general result of the first resolvent iteration for the overlap curve when using (4.51) for the offdiagonal variance model.

In total, the result for the overlap close to the peak position $E_i = \lambda_l + \eta^{(l)}$ is given by

$$\mathbb{E}\left[\left|\langle\psi_i^{\mathcal{B}}|\psi_l^{\mathcal{F}}\rangle\right|^2\right] = \mathcal{X}(E_i, \lambda_l) \approx \frac{1}{N_{\mathcal{F}}\rho_{\mathcal{F}}(\lambda_l)}\left(\frac{1}{\pi}\frac{\gamma^{(l)}}{(E_i - \lambda_l - \eta^{(l)})^2 + (\gamma^{(l)})^2}\right)\exp\left\{-\left(\frac{E_i - \lambda_l - \eta^{(l)}}{2\Delta} + b\right)^2 + b^2\right\}, \tag{4.59}$$

where the denominator is expanded in second order of x and the parameters are determined in first order of t. In total, there are three contributions to the overlap. The first term is the normalization of the overlap, which originates from the prefactor of the connection of the resolvent to the overlap in Eq. (4.14). This term causes the $\frac{1}{N}$ proportionality of

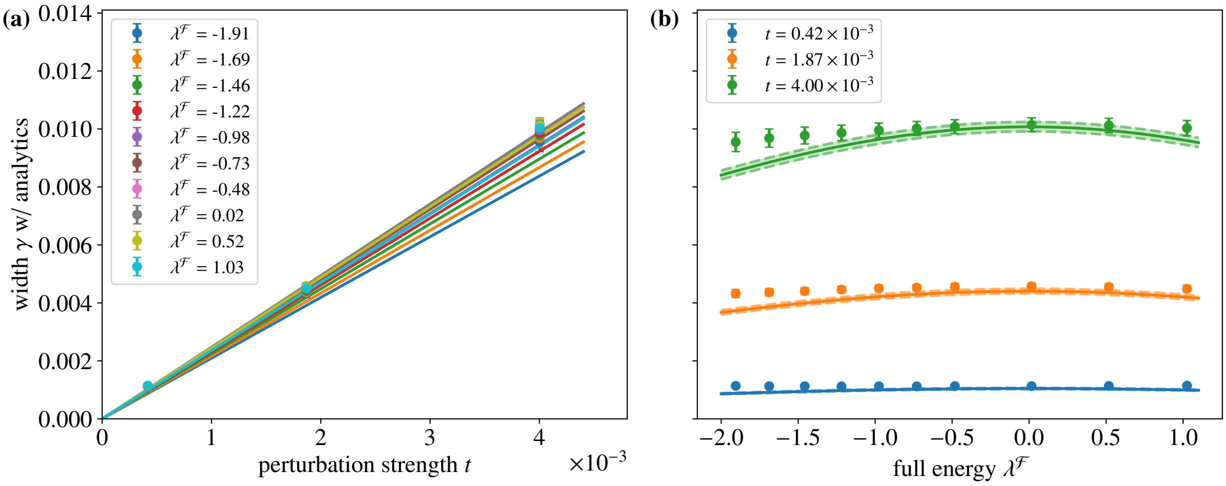

Figure 4.14: Lorentzian width γ in the single peak model with $d_{\mathcal{B}} = 15$ and $d_{\mathcal{S}} = 0$ obtained from fits to the overlaps $\left|\langle\psi_i^{\mathcal{B}}|\psi_l^{\mathcal{F}}\rangle\right|^2$ close to the peak for three different values of t. An analysis of the corresponding perturbation matrix $\tilde{X}$ is shown in Fig. 4.11, 4.12 and 4.13. The numerical overlap data is obtained from averaging over $N_{\text{av}} = 400$ eigenstates of $H^{\mathcal{F}}$ in intervals around the desired full energies λ_l. The Lorentzian fit parameter γ is then averaged over 200 samples of X and 100 samples of $H^{\mathcal{B}}$. In **(a)**, we plot γ with respect to the perturbation strength t of X and in **(b)** to the eigenenergy λ_l of the full quantum state. In both **(a)** and **(b)**, we plot the analytical results of Eq. (4.62a), while in **(b)** analytical margins of error are added, which are computed from the errors of the numerical fit parameters inserted into (4.62b).

the overlap, which is required due to the sum rule for the normalization of the quantum state. This proportionality is explored in detail in Sec. 4.1.2 and illustrated in Fig. 4.4. The second term enclosed in brackets is a Lorentzian. Close to the peak of the overlap on the order of $O(\gamma^{(l)})$, the overlap has the shape of a Lorentzian, which is supported by fits to the numerical data in Fig. 4.2 when analyzing the general shape of the overlap curve for the single peak model in Sec. 4.1.2. The third term in (4.59) is a Gaussian originating from the variance model and inheriting the intrinsic scattering width Δ as an energy scale with a Gaussian variance of $2\Delta^2$. It regularizes the whole overlap, such that all its moments exist, which is not the case for a pure Lorentzian as the result of a GUE perturbation matrix. This term can be viewed as an envelope function multiplied with the Lorentzian, which derives from the decreased scattering amplitude in the perturbation matrix $\tilde{X}$ for larger energy differences. It is fundamentally caused by the locality of the quantum system in the way it is constructed, as argued in Sec. 3.1.3. The constraint of locality produces a local perturbation or scattering matrix, which induces an emergent energy scale in the scattering of unperturbed states due to its limited access to the system. This energy scale in $\tilde{X}$ must carry over to the overlap between perturbed and unperturbed states, since the shape of the overlap is ultimately mediated by $\tilde{X}$ and therefore reflects the shape of the scattering amplitude in the variance model. The term is important, as it provides locality in the energy by cutting off the non-local algebraic tail of the Lorentzian.

To obtain the results of the Lorentzian parameters η and γ for the three variance models of the $\tilde{X}$-matrix discussed above, we simply need to substitute the parameters b and Δ as introduced in Eq. (4.51) to match the desired model. For the mathematical model, we obtain the result

$$\gamma^{(l)} = \frac{\sqrt{\pi}t}{2}\,\frac{\overline{\Delta}_0}{{\Delta_0'}^2}\,e^{-\overline{b}_0^{-2}} = \frac{\sqrt{\pi}t}{2}\,\frac{\overline{\Delta}_0}{{\Delta_0'}^2}\left(1-\overline{b}_0^{-2}\right)+O\left(\overline{b}_0^{-3}\right), \tag{4.60a}$$

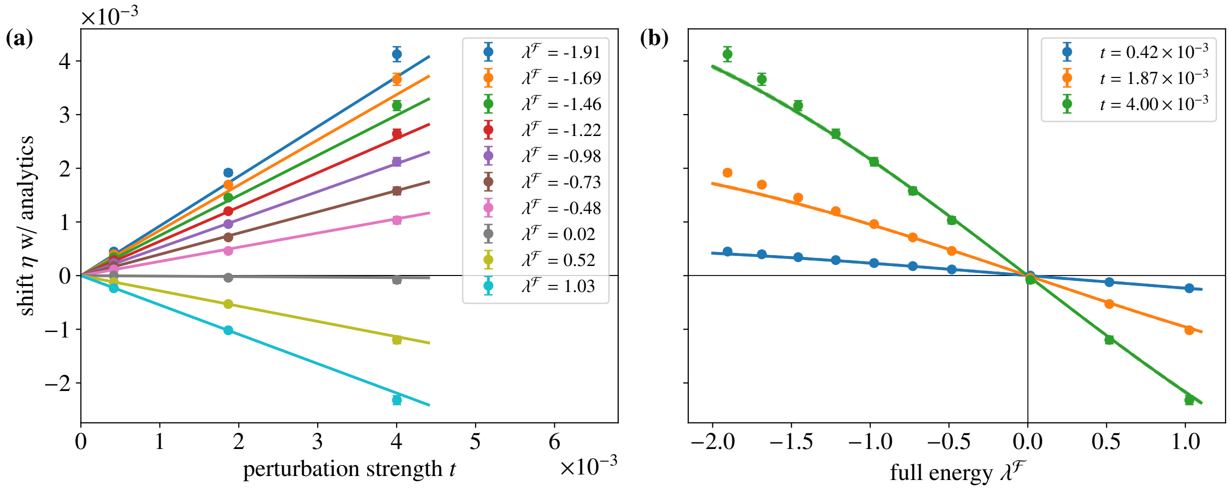

Figure 4.15: Lorentzian shift η in the single peak model with $d_{\mathcal{B}} = 15$ and $d_{\mathcal{S}} = 0$ obtained from fits to the overlaps $\left|\langle\psi_i^{\mathcal{B}}|\psi_l^{\mathcal{F}}\rangle\right|^2$ close to the peak for three different values of t. An analysis of the corresponding perturbation matrix $\tilde{X}$ is shown in Fig. 4.11, 4.12 and 4.13. The numerical overlap data is obtained from averaging over $N_{\text{av}} = 400$ eigenstates of $H^{\mathcal{F}}$ in intervals around the desired full energies λ_l. From the raw data of the shifts, we subtract the contribution from the nonzero local trace of $\tilde{X}$. The resulting Lorentzian fit parameter η is then averaged over 200 samples of X and 100 samples of $H^{\mathcal{B}}$. In **(a)**, we plot η with respect to the perturbation strength t of X and in **(b)** to the eigenenergy λ_l of the full quantum state. In both **(a)** and **(b)**, we plot the analytical results of Eq. (4.62b), while in **(b)** analytical margins of error are added, which are computed from the errors of the numerical fit parameters inserted into (4.62b).

$$\eta^{(l)} = \frac{\sqrt{\pi}t}{2}\frac{\bar{\Delta}_0}{\Delta_0'^2}\, e^{-\bar{b}_0^2}\operatorname{erfi}\left(\bar{b}_0\right) = t\,\frac{\bar{\Delta}_0}{\Delta_0'^2}\,\bar{b}_0 + O\left(\bar{b}_0^3\right) = \left(\frac{\bar{\Delta}_0}{\Delta_0'}\right)^2\frac{\beta t}{2} + O\left(\bar{b}_0^3\right) \tag{4.60b}$$

in linear order of t after comparison with Eq. (4.46). The parameters are given by $(\Delta_0')^{-2} = (\Delta_0^{-2} + \sigma_{\mathcal{B}}^{-2})$, $(\bar{\Delta}_0)^{-2} = (\Delta_0^{-2} + (2\sigma_{\mathcal{B}})^{-2})$ and

$$\bar{b}_0 = -\frac{\bar{\Delta}_0\,\lambda_l}{2\sigma_{\mathcal{B}}^2} = \frac{\beta\bar{\Delta}_0}{2}, \tag{4.61}$$

where the inverse temperature is obtained as $\beta = \frac{\partial S_{\mathcal{B}}(E)}{\partial E}\Big|_{E=\lambda_l} = -\frac{\lambda_l}{\sigma_{\mathcal{B}}^2}$ with the bath entropy $S_{\mathcal{B}}(E)$. We expand the result (4.60a,b) in terms of small $\bar{b}_0$, which is only fulfilled for energies λ_l close to zero. Since the shift $\eta^{(l)}$ is proportional to β and it arises due to the non-constant DOS, which can be expanded as an exponential $\propto e^{\beta(E_i)x}$ close to E_i, we call this term the *thermal shift*. The full overlap curve is given by the insertion of the Lorentzian width and shift in (4.60a,b) as well as $b \to \bar{b}_0$ into the general equation (4.59). The result for the physical model is obtained from (4.60a,b) in the limit $\Delta_0' \to \Delta_0$ and $\bar{\Delta}_0 \to \Delta_0$, which includes $\bar{b}_0 \to b_0$. For the numerical model of the offdiagonal variance defined in (4.48), we obtain the Lorentzian parameters

$$\gamma_{\text{num}}^{(l)} = \frac{A_0\sqrt{\pi}t}{2(1+\vartheta)}\left(\frac{\bar{\Delta}_1}{\Delta_1'^2}\, e^{-\bar{b}_1^2} + \vartheta\,\frac{\bar{\Delta}_2}{\Delta_2'^2}\, e^{-\bar{b}_2^2}\right), \tag{4.62a}$$

$$\eta_{\text{num}}^{(l)} = \frac{A_0\sqrt{\pi}t}{2(1+\vartheta)}\left(\frac{\bar{\Delta}_1}{\Delta_1'^2}\, e^{-\bar{b}_1^2}\operatorname{erfi}\left(\bar{b}_1\right) + \vartheta\,\frac{\bar{\Delta}_2}{\Delta_2'^2}\, e^{-\bar{b}_2^2}\operatorname{erfi}\left(\bar{b}_2\right)\right), \tag{4.62b}$$

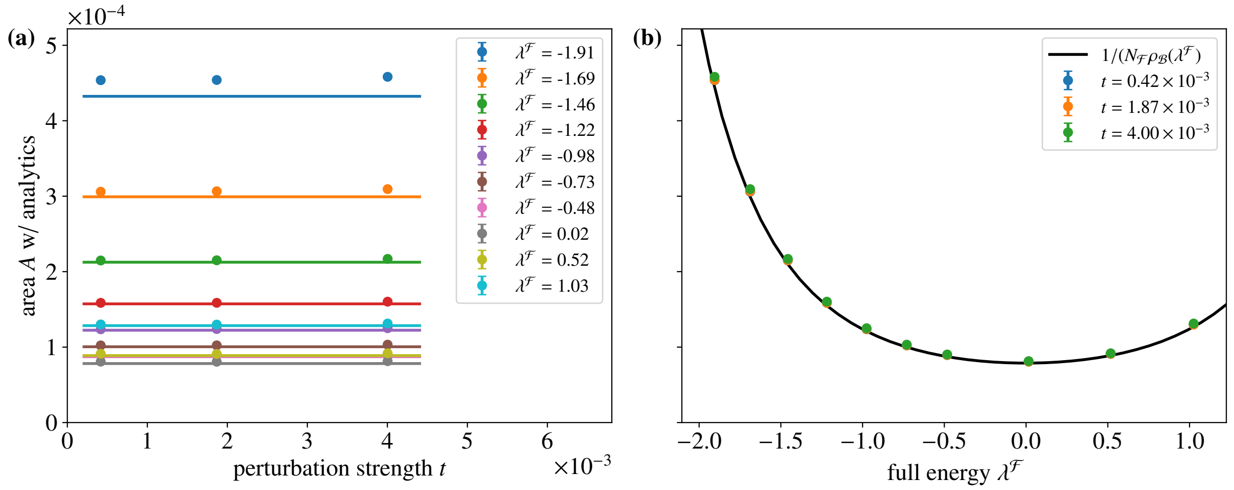

Figure 4.16: Lorentzian area A in the single peak model with $d_{\mathcal{B}} = 15$ and $d_{\mathcal{S}} = 0$ obtained from fits to the overlaps $\left|\langle\psi_i^{\mathcal{B}}|\psi_l^{\mathcal{F}}\rangle\right|^2$ close to the peak for three different values of t. An analysis of the corresponding perturbation matrix $\tilde{X}$ is shown in Fig. 4.11, 4.12 and 4.13. The numerical overlap data is obtained from averaging over $N_{\text{av}} = 400$ eigenstates of $H^{\mathcal{F}}$ in intervals around the desired full energies λ_l. The Lorentzian fit parameter A is then averaged over 200 samples of X and 100 samples of $H^{\mathcal{B}}$. In **(a)**, we plot A with respect to the perturbation strength t of X and in **(b)** to the eigenenergy λ_l of the full quantum state. In **(a)**, we additionally show the inverse value of the Gaussian fit of the DOS of $\mathcal{B}$ evaluated at the full energy λ_l and in **(b)**, we plot the inverse of the numerical DOS of the bath $\mathcal{B}$ at λ_l.

where Δ_1', $\overline{\Delta}_1$ and $\overline{b}_1$ as well as Δ_2', $\overline{\Delta}_2$ and $\overline{b}_2$ are defined analogously to Δ_0', $\overline{\Delta}_0$ and $\overline{b}_0$. A_0 and ϑ are parameters from the numerical model $\sigma^2_{\text{od;num}}$, that correspond to a scaling factor and to the relative weight of the two Gaussians in the model. With the result for the overlap, we now compare the analytical results for the Lorentzian parameters to the numerical fit parameters in the following section.

4.3.2 Comparison to numerical results

In Sec. 4.1.2, numerical data showed that the overlap around its peak position can be modeled by a Lorentzian curve, which was supported by a fit to the data points for an example overlap in Fig. 4.2. Given our numerical approach with exact diagonalization (ED), we are working with finite size systems where self-averaging is not fully present. To simulate the behavior of an infinite system, we not only average over random samples of the perturbation X, as demanded for the stochastic analysis of the overlap, but also over the unperturbed bath Hamiltonian $H^{\mathcal{B}}$. This is possible, because all Hamiltonians in the quantum system are random due to the prefactors of the interaction terms being drawn from a normal distribution. With the average over X and over the bath $\mathcal{B}$, we gather information on the behavior of a generic local quantum system without symmetries or integrability, that is subject to a local perturbation. The final results depend only on general parameters, such as the perturbation strength t, the expected DOS of $\mathcal{B}$ and the scattering width Δ of the perturbation matrix $\tilde{X}$ in the unperturbed eigenbasis. In Sec. 4.3.1 we obtained analytical expressions for the Lorentzian parameters, which we now compare to the numerically obtained fit parameters. In the numerical analysis, we adhere to the same procedure as applied and described in Sec. 4.1.2, adjusted to a bath size of $d_{\mathcal{B}} = 15$ sites. To find the overlap data points, we collect $N_{\text{av}} = 400$ full states $|\psi_l^{\mathcal{F}}\rangle$ in an interval around the desired energy λ_l and collect the squared magnitude of their overlap with the bath states $|\psi_i^{\mathcal{B}}\rangle$ in terms of the energy difference $E_i - \lambda_l$. The average overlap data points are then found by dividing the energy axis in intervals of uniform

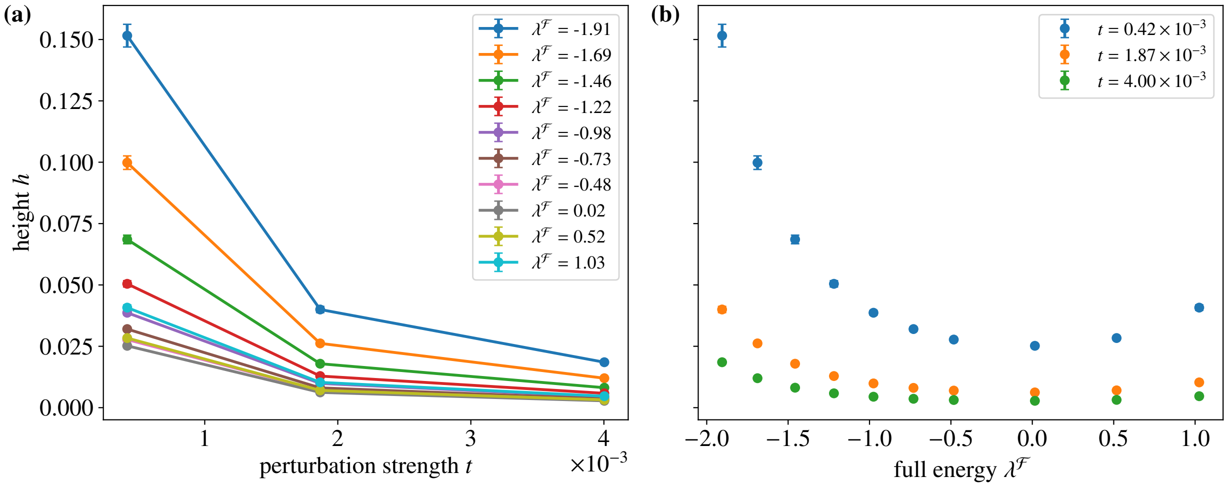

Figure 4.17: Lorentzian height h in the single peak model with $d_{\mathcal{B}} = 15$ and $d_{\mathcal{S}} = 0$ obtained from the fit parameters of the overlaps $\left|\langle\psi_i^{\mathcal{B}}|\psi_l^{\mathcal{F}}\rangle\right|^2$ close to the peak for three different values of t. We compute h from the width γ and the area A as $h = \frac{A}{\pi\gamma}$. An analysis of the corresponding perturbation matrix $\tilde{X}$ is shown in Fig. 4.11, 4.12 and 4.13. The numerical overlap data is obtained from averaging over $N_{\mathrm{av}} = 400$ eigenstates of $H^{\mathcal{F}}$ in intervals around the desired full energies λ_l. The height h is averaged over 200 samples of X and 100 samples of $H^{\mathcal{B}}$. In **(a)**, we plot h with respect to the perturbation strength t of X with lines connecting the data points as a guide to the eye and in **(b)** to the eigenenergy λ_l of the full quantum state.

width $w = 1 \times 10^{-3}$ and averaging over the values in each interval. Once the overlap data points are determined, we fit a Lorentzian with an additional scaling prefactor A to them and read out the best fit parameters for the width γ, the center position η and the area A. Those fit parameters are then averaged over 200 samples of X and 100 samples of $H^{\mathcal{B}}$ to find their sample expectation value. The standard error is calculated using the sample standard deviation to estimate the precision of the data points. For comparison to the analytical results, we use the final results obtained from the numerically adjusted model of the $\tilde{X}$-matrix in (4.62a,b). The necessary parameters of the numerical model are obtained from fits of $\sigma^2_{\mathrm{od;num}}$ to the numerical data as shown in Fig. 4.11 and with the best fit parameters compiled in Tab. 4.1. The Lorentzian fit parameters shown below correspond to the variance data shown in Fig. 4.11-4.13 in the way that the data result from a collective analysis of the Hamiltonians and their eigenstates in the quantum system.

In Fig. 4.14, we show the results for the fit parameter γ, in **a** plotted versus the variance t of the perurbation matrix X and in **b** with respect to the perturbed energy λ_l of the full quantum state. The solid lines in the plot denote the analytical results as found in Eq. (4.62a). To get a general idea of the dependencies of γ on t and λ_l, we use Eq. (4.60a), which is obtained from the mathematical model of the variance. In Fig. 4.14**a**, we observe, that the linear dependence of γ on t is accurate in the analyzed range for small $t \ll \sigma^2_{\mathcal{B}}$. The data points in Fig. 4.14**b** are of the same magnitude and very close in value to the analytical prediction, although we notice small finite size effects, which increase towards the boundary of the spectrum. Eq. 4.14**a** predicts a quadratic drop $\propto (1 - \overline{b}_0^2)$ of the Lorentzian width towards larger energy magnitudes from the maximum at $\lambda = 0$. This drop is less pronounced in the numerical data than in the analytical predicition. We attribute this difference to finite-size effects originating towards the eigenstate density decreases towards the boundary of the spectrum. In section 4.3.4 we quantify this in a system size-resolved analysis, where we notice a general trend of the discrepancy between analytical and numerical data decreasing for

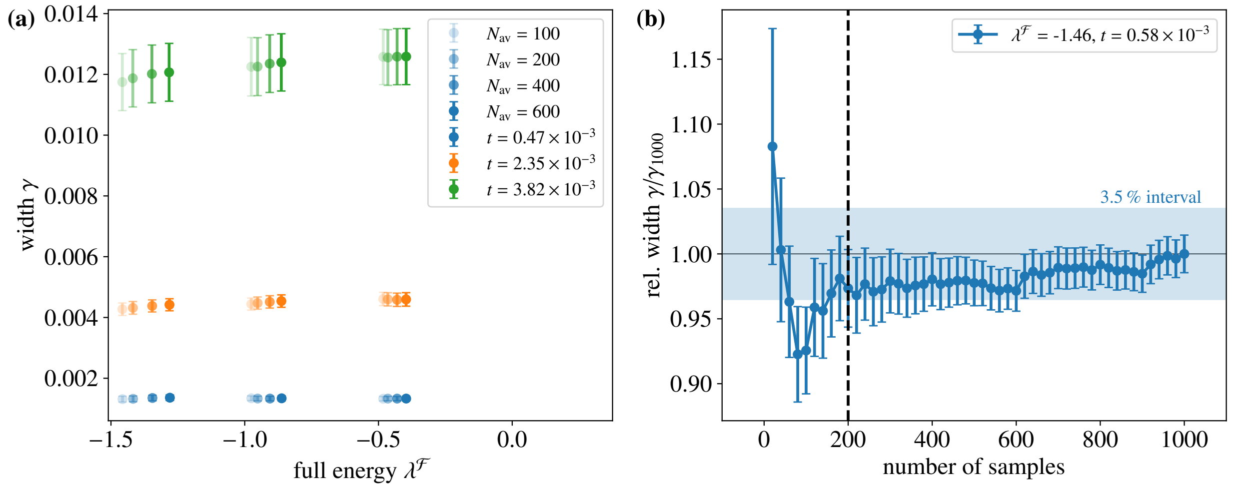

Figure 4.18: Consistency review of the width γ in the single peak model with $d_{\mathcal{B}} = 13$ and $d_{\mathcal{S}} = 0$ sites. In (**a**), we plot γ with respect to the full energy λ_l for three values of t while varying the number of full states N_{av}, which are taken into account for the average of the overlap data. We choose $N_{\text{av}} = \{100, 200, 400, 600\}$ and average each data point over 20 samples of X and 10 samples of $H^{\mathcal{B}}$. (**b**) shows the width γ in the same setup as in (**a**) at the point $\lambda_l = 1.46$ and $t = 0.58 \times 10^{-3}$ relative to the value γ_{1000} obtained from 1000 samples of X. The plot shows γ/γ_{1000} relative to the number of samples employed in the average. The number of samples of $H^{\mathcal{B}}$ is half of that of X. The point at a sample size of 200 is marked as a black dashed line and a deviation interval of 3.5% is shown as a blue band.

larger systems.

Fig. 4.15 shows the center position η of the Lorentzian fit obtained from the fit of the overlap data with respect to the energy axis $E_i - \lambda_l$. Before the average is taken, the value for η in each sample is corrected by the local trace of the perturbation matrix $\tilde{X}$ read off from the averaged diagonal of the matrix in a small interval $[-\gamma^{(l)}, \gamma^{(l)}]$ around the position of the overlap peak at the bath energy $E_i = \lambda_l - \eta^{(l)}$. The final values for η plotted in Fig. 4.15 are therefore corrected by the trace shift, which is subtracted out. This is possible because the local trace acts as a unit matrix term close to the peak position and merely causes a shift of the eigenvalues. This way, we are able to compare the numerical values to the analytical results in Eq. (4.60b) or (4.62b), which do not incorporate the contribution from the local trace. After taking out this additional randomness, we notice that the standard error computed from the sample standard deviation significantly decreases. This makes sense, as the spread of the data around the mean value reduces. This fact supports the approach of taking out the trace as an additive factor to the shift. Similar to the width γ, we confirm the linear dependence of the shift η for small $t \ll \sigma^2_{\mathcal{B}}$ as depicted in Fig. 4.15**a**, although there is a small deviation to the slope predicted from the analytical values. In Fig. 4.15**b**, we plot η with respect to the eigenvalue of the perturbed quantum state. We observe the approximately linear dependence of η on $\overline{b}_0$ and therefore on λ_l for small energy magnitudes λ_l predicted by Eq. (4.60b). At larger $|\lambda_l|$, the nonlinear character of $\overline{b}_0$ in the analytical result for η manifests itself, while the data show a slight discrepancy with a linear trend. Nevertheless, the general behavior of the shift is accurately predicted by Eq. (4.62b).

Since we fitted a Lorentzian shape with an additional prefactor A through the data points, we also plot this parameter, which describes the area of the Lorentzian in Fig. 4.16 with respect to t and to λ_l. The analytical result is taken from Eq. (4.59) as the prefactor to the Lorentzian, which returns the inverse DOS of the full quantum system $(N_{\mathcal{F}}\rho_{\mathcal{F}}(\lambda_l))^{-1}$.

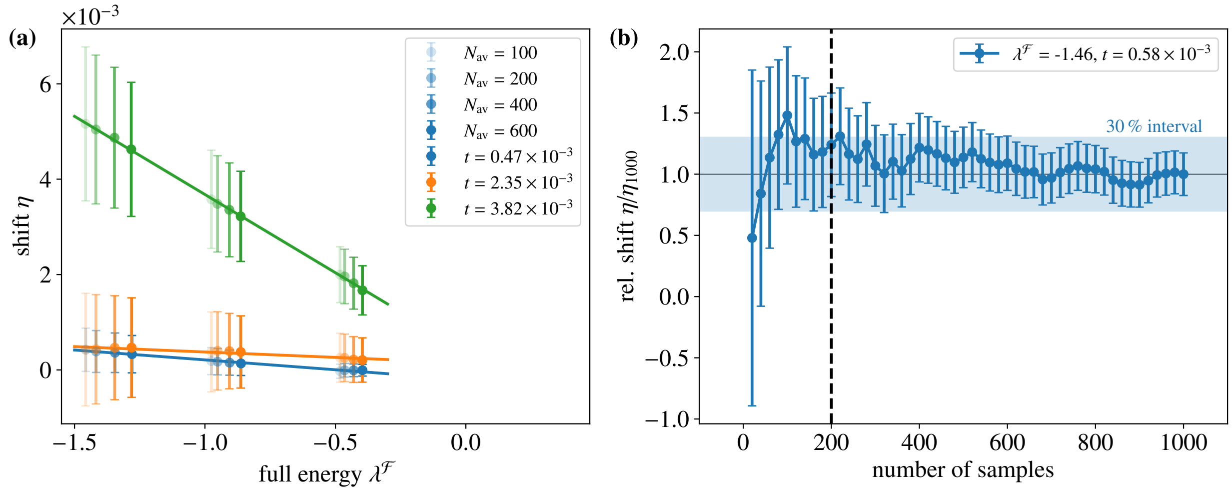

Figure 4.19: Consistency review of the shift η in the single peak model with $d_{\mathcal{B}} = 13$ and $d_{\mathcal{S}} = 0$ sites. In **(a)**, we plot η with respect to the full energy λ_l for three values of t while varying the number of full states N_{av}, which are taken into account for the average of the overlap data. We choose $N_{\mathrm{av}} = \{100, 200, 400, 600\}$ and average each data point over 20 samples of X and 10 samples of $H^{\mathcal{B}}$. Linear fits to each data set for t are added. **(b)** shows the shift η in the same setup as in **(a)** at the point $\lambda_l = 1.46$ and $t = 0.58 \times 10^{-3}$ relative to the value η_{1000} obtained from 1000 samples of X. The plot shows η/η_{1000} relative to the number of samples employed in the average. The number of samples of $H^{\mathcal{B}}$ is half of that of X. The point at a sample size of 200 is marked as a black dashed line and a deviation interval of 30% is shown as a blue band.

It equals the value of the overlap curve in Eq. (4.59) evaluated at $x = 0 \rightarrow E_i - \lambda_l - \eta^{(l)} = 0$ and multiplied with the Lorentzian height at $x = 0$. Since we only diagonalized the full Hamiltonian $H^{\mathcal{F}}$ along specific energy intervals to obtain the states $|\psi_l^{\mathcal{F}}\rangle$ in order to compute the overlap, the full eigenvalue density $\rho_{\mathcal{F}}(\lambda_l)$ is not available. We hence compare the numerical values to the unperturbed DOS of the bath $N_{\mathcal{B}}\rho_{\mathcal{B}}(E)$, whose variance differs by t to the variance of the full DOS with the difference equal to the small amount of $\frac{t}{\sigma_{\mathcal{B}}^2} \sim 10^{-3}$. The area A stays constant with t, as apparent in Fig. 4.16**a**. In Fig. 4.16**a**, the analytical predictions are obtained from the Gaussian fit to the DOS of $\mathcal{B}$ as shown in Fig. 4.10. The standard error of the data points is very small, suggesting precise knowledge of the numerical value for A. There is a deviation of up to 5% of numerical versus analytical values with the Gaussian fit overestimating the numerical values of the DOS at large $|E|$. The deviation is significantly reduced in Fig. 4.16**b**, where instead of the Gaussian fit, we use the exact data points of the numerical DOS in $\mathcal{B}$ from Fig. 4.10 to plot as a joined black line. This indicates, that due to finite size effects, the Gaussian fit differs from the numerical DOS data at large energies $|E|$, while the inverse proportionality of the area A to the DOS is accurate throughout the whole spectrum. The inverse proportionality of the Lorentzian area to the number of states, $\frac{1}{N_{\mathcal{F}}}$, causes the whole overlap to be proportional to $\frac{1}{N_{\mathcal{F}}}$, which is a necessary condition for the normalization of the state $|\psi_l^{\mathcal{F}}\rangle$ and explained in detail in Sec. 4.1.2 and shown in Fig. 4.4.

For completeness, we plot the height h of the Lorentzian in Fig. 4.17. It is evaluated at the position $x = 0 \rightarrow E_i - \lambda_l - \eta^{(l)} = 0$ of the Lorentzian, which gives $h = \frac{A}{\pi\gamma}$ in terms of the area A and the width γ. h is the maximum value of the overlap curve. In Fig. 4.17**a**, we note, that it is inversely proportional to t due to the inverse dependence of h on γ. The pattern of the data points with respect to the full energy λ_l is mainly caused by the inverse proportionality of A to the DOS in Fig. 4.17**b**, whereas the relation variation of γ with respect to λ_l is much smaller than that of A. However, the data splits up for the three different values of t due to the strong dependence of γ on t. Since h is not an

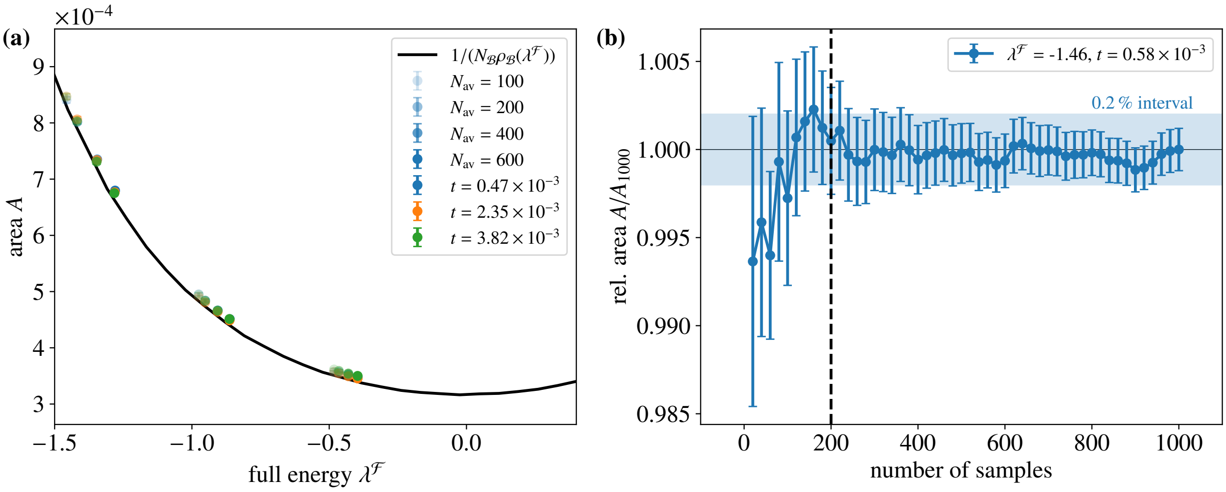

Figure 4.20: Consistency review of the area A in the single peak model with $d_{\mathcal{B}} = 13$ and $d_{\mathcal{S}} = 0$ sites. In (**a**), we plot A with respect to the full energy λ_l for three values of t while varying the number of full states N_{av}, which are taken into account for the average of the overlap data. We choose $N_{\text{av}} = \{100, 200, 400, 600\}$ and average each data point over 20 samples of X and 10 samples of $H^{\mathcal{B}}$. Additionally, we show the inverse DOS of the bath $\mathcal{B}$ evaluated at the full energy λ_l. **(b)** shows the area A in the same setup as in **(a)** at the point $\lambda_l = 1.46$ and $t = 0.58 \times 10^{-3}$ relative to the value A_{1000} obtained from 1000 samples of X. The plot shows A/A_{1000} relative to the number of samples employed in the average. The number of samples of $H^{\mathcal{B}}$ is half of that of X. The point at a sample size of 200 is marked as a black dashed line and a deviation interval of 0.2% is shown as a blue band.

independent fit parameter, but directly follows from two other Lorentzian parameters, we refrain from showing it for the multi peak model.

4.3.3 Influence of finite size averaging

In Sec. 4.3.2, we explained that the displayed numerical data for the $d_{\mathcal{B}} = 15$ site lattice for the overlap curve are obtained by considering $N_{\text{av}} = 400$ full states in an interval around the desired energy λ_l and averaging over the squared magnitude of the overlap data to find the final curve. This averaging is necessary, as the random fluctations of a single state $|\psi_l^{\mathcal{F}}\rangle$ are too large and the number of overlap data points around the peak position too small to draw conclusions about its shape and fit a nonlinear curve, such as a Lorentzian. After their extraction from the fit, we further average the Lorentzian parameters over 200 random samples of X to find the expected value, which can be compared to the analytical findings of the overlap, where the expectation value is always taken in the calculation. Another averaging over 100 samples of the unperturbed Hamiltonian $H^{\mathcal{B}}$ is done to compensate for the finite size and the weak indication of self averaging.

In this section, we review the influence of both types of averaging on the Lorentzian parameters in order to evaluate the consistency of the numerical results. The analysis is done in a $d_{\mathcal{B}} = 13$ site lattice. In Fig. 4.18, the consistency checks for the Lorentzian width γ are shown. From Fig. 4.18**a** we conclude that changing N_{av} has only a small effect. We show the numerically obtained width γ of the Lorentzian for each of three values of t and λ_l as well as choose $N_{\text{a}} = \{100, 200, 400, 600\}$. For each data point of γ at (t, λ_l), all values obtained with different N_{av} agree with each other within the scope of their error. Because we choose the starting value of the analyzed interval the same and independent of N_{av}, the average for λ_l is smaller when we include fewer states in it. As a conseqence, we notice a

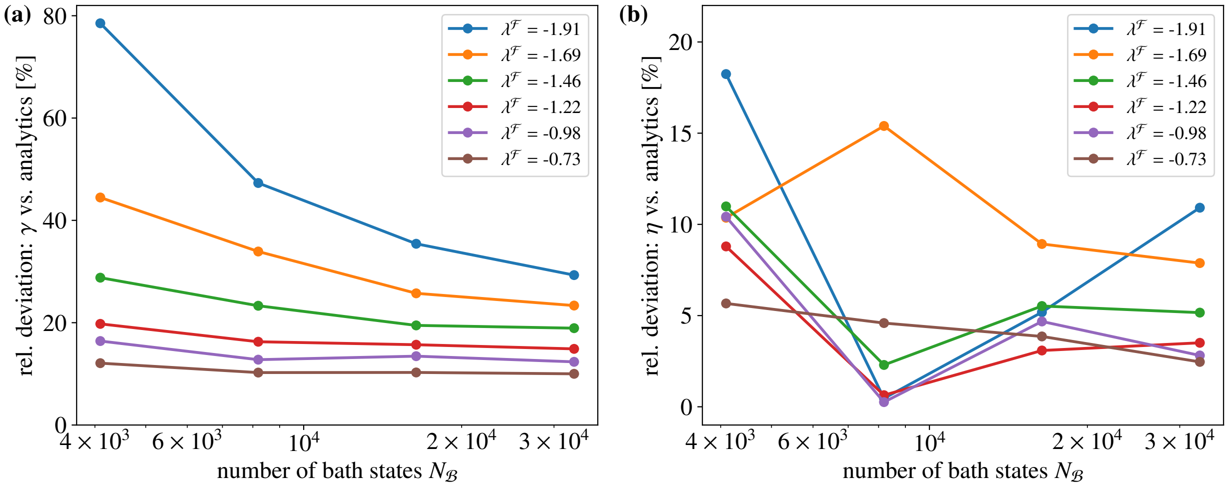

Figure 4.21: Finite size analysis of the width γ in **(a)** and the shift η in **(b)** in the single peak model plotted with respect to the number of bath states $N_{\mathcal{B}}$ on a logarithmic scale. We choose $d_{\mathcal{B}} = \{12, 13, 14, 15\}$ for the analysis, which corresponds to $t = \{4.4, 4.9, 5.5, 4.2\} \times 10^{-4}$ and $N_{\text{av}} = \{50, 100, 200, 400\}$ full states averaged over for the final overlap curve. The values of t differ for different number of sites in $\mathcal{B}$, because X is normalized by the square root of the second moment of $H^{\mathcal{B}}$. This is done in accordance to the normalization of $H^{\mathcal{B}}$ to have a variance of one, which causes the local couplings in $H^{\mathcal{B}}$ to decrease with increasing system size. We show the relative deviation in percent of the numerical values of γ to the analytical calculation in Eq. (4.62a) in **(a)** and the relative deviation in percent of η to the analytics in Eq. (4.62b) in **(b)**.

small decrease in γ for smaller mean values of λ_l, which is consistent with the analytical dependence of γ on λ_l. In Fig. 4.18**b**, we show the sample average of one example data point of γ with its standard error with respect to the number of samples of X and relative to γ_{1000}, the value of γ at 1000 samples. The number of samples in the bath Hamiltonian for each data point is half the sample size of X. For the analysis, we choose a data point at $\lambda_l = 1.46$, $t = 0.58 \times 10^{-3}$ and $N_{\text{av}} = 100$. Naturally, by increasing the sample size, the standard error decreases. All mean values of γ in a sample size of 200 or more samples lie inside a confidence interval of 3.5%. Convergence to the value γ_{1000} is achieved gradually and with increasing precision, indicating a purely random underlying process, where both accuracy and precision increase with larger sample size.

A similar behavior is observed for the shift η in Fig. 4.19, where an identical analysis as for γ is performed. The Lorentzian fit parameters are obtained from the same underlying overlap data. For this analysis, we do not collect the data of the perturbation matrix $\tilde{X}$ in the unperturbed eigenbasis. With this data unavailable, the average is taken over the raw shift values obtained from the fit without correcting for the local trace of $\tilde{X}$ by subtraction of the trace shift, as we did for the data in Fig. 4.19. The averaged full energy λ_l is again smaller at smaller sample sizes N_{av}. While the values for η with different N_{av} in Fig. 4.19**a** agree with each other for each parameter pair (t, λ_l), we identify a linear dependence of η on λ_l as indicated by linear fits. This is consistent with analytical expectations, where η is proportional to $-\lambda_l$ in first order. The values for the shift η should therefore not be compared with each other, but with the best fit line, which shows excellent agreement, with the deviations from the linear fit being much smaller than the error bars of the individual values. In Fig. 4.19**b** we see that the mean value of η for a sample size of X of 200 samples or more deviates at most with 30% relative to the value obtained from an average of 1000 samples. This deviation interval for $\frac{\eta}{\eta_{1000}}$ is one order of magnitude greater than that for $\frac{\gamma}{\gamma_{1000}}$, which is caused by the additional randomness of the local trace of $\tilde{X}$ that is still included in the data when taking the average.

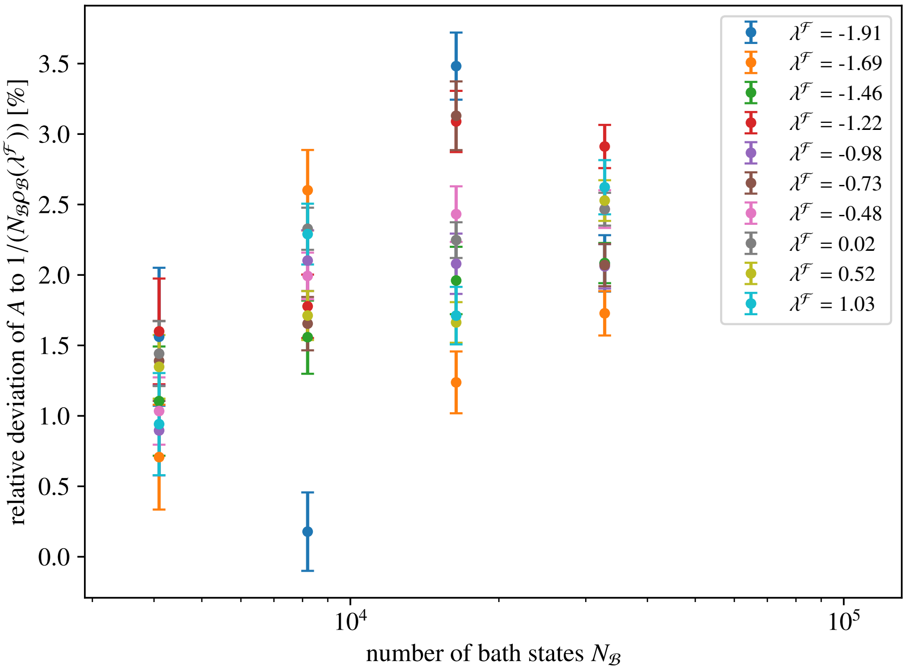

Figure 4.22: Finite size analysis of the Lorentzian area A in the single peak model plotted with respect to the number of bath states $N_{\mathcal{B}}$ on a logarithmic scale. The plot depicts the relative deviation of A to the inverse numerically obtained DOS of $\mathcal{B}$ evaluated at the full energy λ_l. We choose $d_{\mathcal{B}} = \{12, 13, 14, 15\}$ for the analysis, which corresponds to $t = \{4.4, 4.9, 5.5, 4.2\} \times 10^{-4}$ and $N_{\text{av}} = \{50, 100, 200, 400\}$ full states averaged over for the final overlap curve.

Lastly, we do the same consistency analysis for the area A from the Lorentzian fit. In Fig. 4.20**a**, we compare the area obtained for different values of N_{av} to the numerical DOS, where we use the DOS of the unperturbed bath evaluated at the perturbed energies of the full system, since we do not have $\rho_{\mathcal{F}}(E)$ available. With the average full energy λ_l being smaller for smaller N_{av}, the values follow the numerical DOS, which is expected analytically and confirms that the only influence of N_{av} in this analysis is to shift the mean value λ_l, which can be compensated by shifting the boundaries of the analyzed interval accordingly. In Fig. 4.20**b**, the influence of the sample size on A in the averaging over X and $H^{\mathcal{B}}$ is shown, where the number of samples of $H^{\mathcal{B}}$ is half of that of X. We notice that all mean values of A for 200 or more samples deviate by less than 2% to the value of A at 1000 samples. This supports the observation in Fig. 4.16, where we conclude that with the error bars of A being much smaller than those of γ and η, the numerical value of A is known more precisely.

We conclude that the effect that different choices of N_{av} have on the resulting overlap data is consistent with the analytical results and that the numerical results of the Lorentz parameters show no inconsistencies in the finite sample size averaging.

4.3.4 Finite size effects

The effects that are present in the finite size numerical analysis lead to deviations of the Lorentzian parameters compared to a hypothetical analysis in the thermodynamic limit. To estimate the finite size effect, we analyze the overlap curve for different sizes of the bath with the number of lattice sites $d_{\mathcal{B}} = \{12, 13, 14, 15\}$ and plot the relative deviation of the Lorentzian parameters to the analytical results, which are obtained in the limit $N_{\mathcal{F}} \to \infty$. For this comparison, we choose $t = \{4.4, 4.9, 5.5, 4.2\} \times 10^{-4}$, $N_{\text{av}} = \{50, 100, 200, 400\}$ and 200 samples for X and 100 for $H^{\mathcal{B}}$ for the averaging. The investigated points of energy λ_l coincide with that of the numerical results presented in Sec. 4.3.2, but for the sake of clarity of the plot, we show only the values for $\lambda_l < -0.5$. In Fig.4.21**a**, the results for γ are depicted. We observe a trend of decreasing relative deviation of numerical to analytical results for larger systems, which we attribute to an enhanced self-averaging. We further notice that the finite size effects are stronger towards the boundary of the spectrum, where the relative deviation to the analytical values is much larger for smaller system sizes, whereas this trend is not as pronounced for the analysis with λ_l closer to zero. This is in accordance with Fig. 4.14, where we attribute the larger deviations of the numerical data to the analytical calculation at larger λ_l to stronger finite size effects, since the average energy spacing increases resulting in a smaller eigenvalue density and an effectively smaller sized system close to those points. In Fig. 4.21**b**, the same analysis is performed for the shift η. We draw the same conclusion as for γ, that the general trend with some outliers points towards a smaller relative deviation of numerical and analytical results at larger system sizes. It supports the assumption, that the presence of self-averaging increases for larger systems. Fig. 4.22 depicts the relative deviation of the Lorentzian area A to the inverse DOS. For the comparison we use again the eigenvalue density $\rho_{\mathcal{B}}(E)$ instead of the analytical prediction $\rho_{\mathcal{F}}(E)$, since $\rho_{\mathcal{B}}(E) \approx \rho_{\mathcal{F}}(E)$. The relative deviation for the area in Fig. 4.22 with $< 4\%$ is much smaller than that of γ and η in Fig.4.21. Of all the three Lorentzian fit parameters, we conclude that the area A is the closest to the analytical predictions, whilst also being the one with the highest numerical precision due to the smallest standard deviation for the same sample set of random Hamiltonians and perturbations.

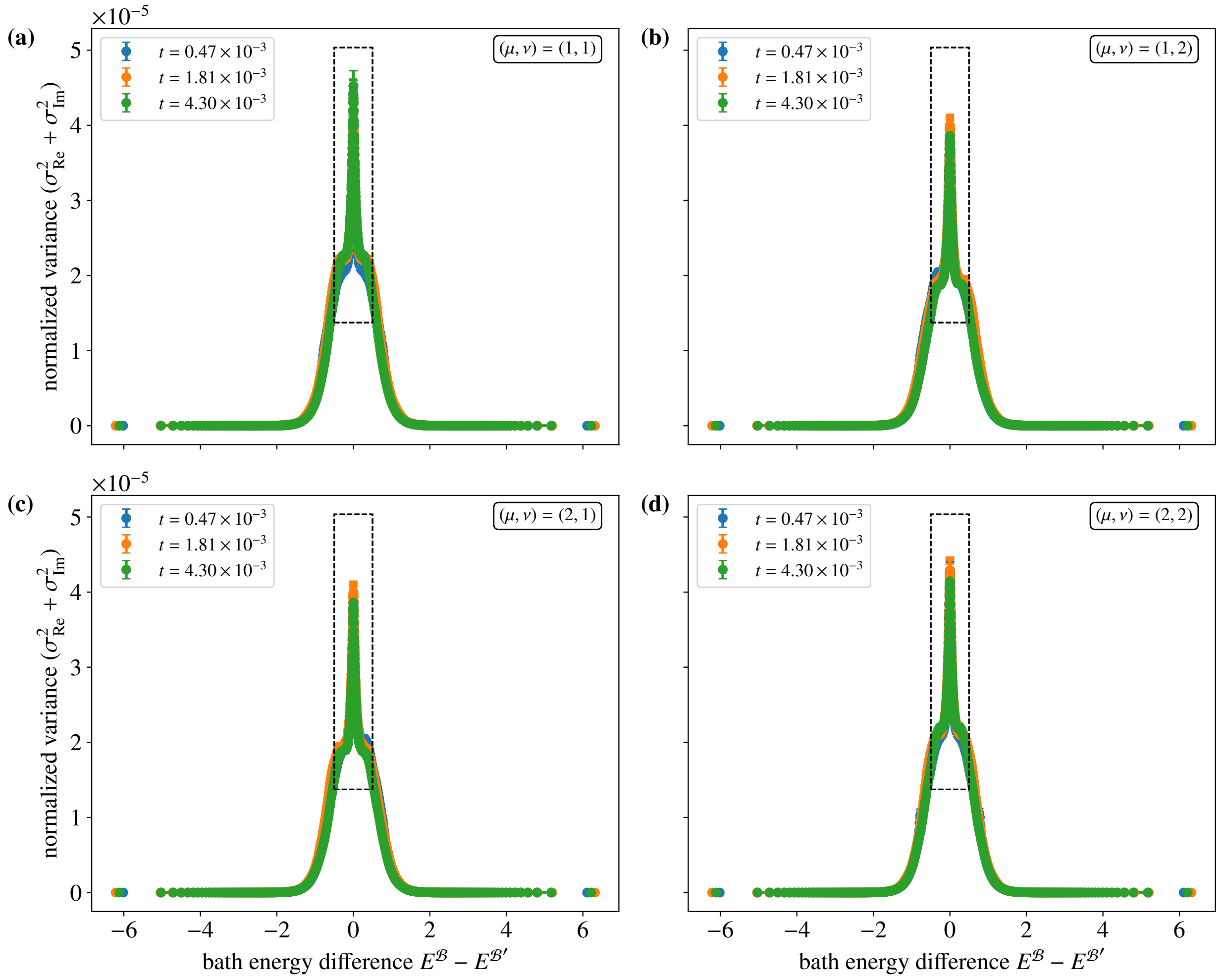

Figure 4.23: Element wise variance of the offdiagonal elements along the anti-diagonal line in the four blocks of the matrix $\tilde{X}$ in the multi peak model with $d_{\mathcal{B}} = 15$ and $d_{\mathcal{S}} = 1$, normalized by t and shown for three different values of t. Each block corresponds to a scattering in $\mathcal{S}$ under X with (μ, ν) being **(a)** $(1, 1)$, **(b)** $(1, 2)$, **(c)** $(2, 1)$ and **(d)** $(2, 2)$. The data points are computed in terms of boxes of size (100×100) and for a higher resolution close to zero with size (20×20). An average is taken over 100 samples of $H^{\mathcal{B}}$ and 200 samples of X. We show the variance as a whole along the analyzed line and fit a sum of two Gaussians according to Eq. (4.65) to the data, with the best fit parameters being compiled in Tab. 4.3.

4.4 Quantitative analysis of the multi peak model

Analogous to the single peak model, we quantitatively analyze the properties of the overlap curves in the multi peak model. Here, we investigate the overlaps between the eigenstates of the full quantum system and the unperturbed eigenstates of the small subsystem $\mathcal{S}$ and the bath $\mathcal{B}$, which are separated into different overlap curves for each eigenstate in $\mathcal{S}$. Analytically we again refer to the resolvent iteration in Sec. 4.2 and obtain Lorentzian curves close to the peak of each individual overlap curve. The numerical fit parameters of the Lorentzian are compared to the analytical calculation for a system with $d_{\mathcal{S}} = 1$ site in $\mathcal{S}$ and $d_{\mathcal{B}} = 15$ sites in the bath. We further study the influence of the energy spacing of the two states in $\mathcal{S}$ on the parameters of the overlap curve. The section is concluded by a description of the finite size effects occurring in the numerical study.

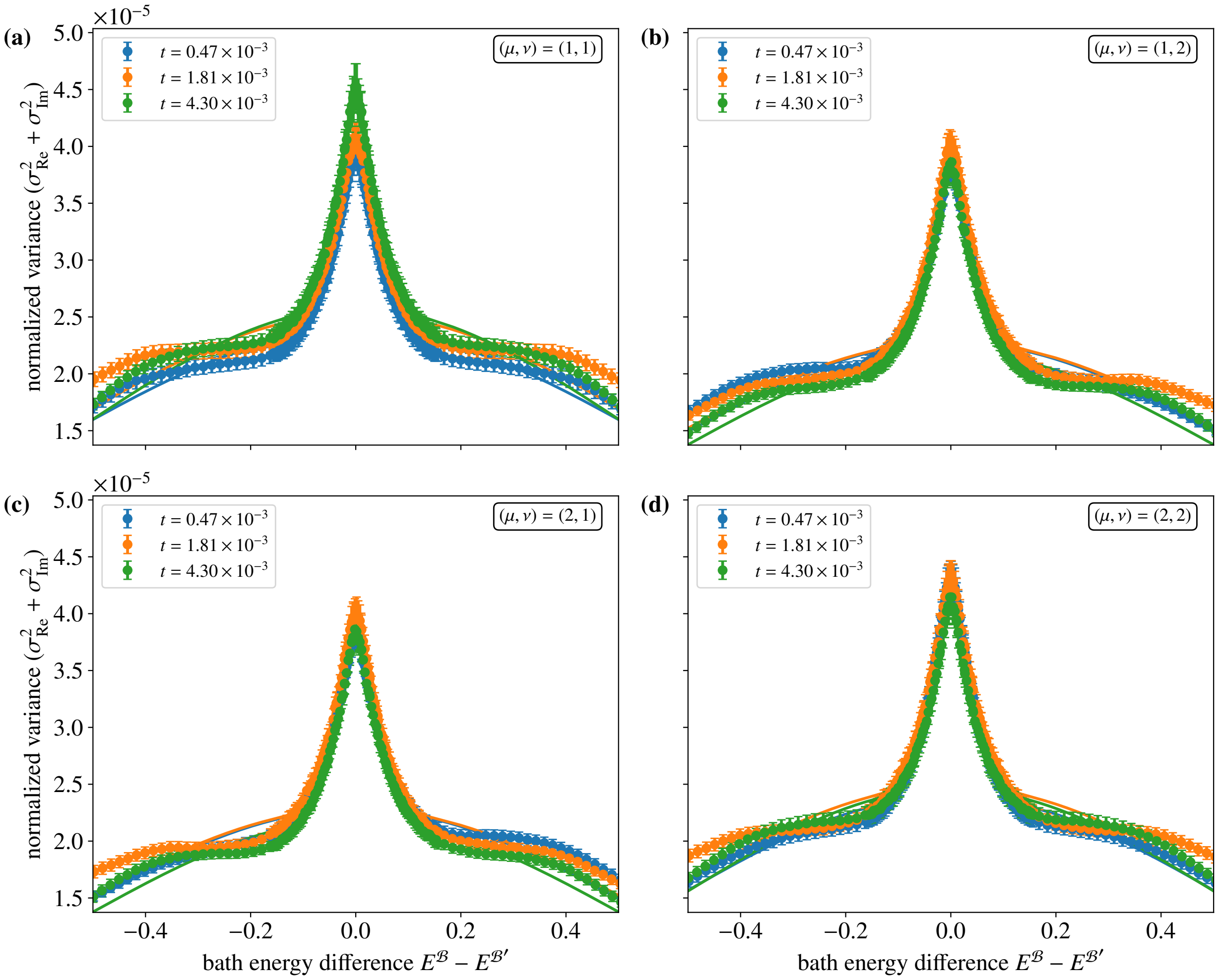

Figure 4.24: Extracts of the variance along the anti-diagonal indicated by the dashed rectangle in Fig. 4.23 for three different values of t. The system details are described in the caption of Fig. 4.23. A sum of two Gaussians according to the numerical variance model in Eq. (4.65) is fitted to the data, with the best fit parameters being compiled in Tab. 4.3.

4.4.1 Analytic calculation of the overlap curves

Model for the X-matrix in the multi peak model. In the following analysis of the multi peak model, the unperturbed system consists of a small subsystem $\mathcal{S}$ with $d_{\mathcal{S}} = 1$ and a bath $\mathcal{B}$ with $d_{\mathcal{B}} = 15$ sites. To calculate the analytical expressions of the Lorentzian parameters for the multi peak model, we return to the analysis of the perturbation matrix $\tilde{X}$, where the unperturbed eigenbasis now consists of a product basis of eigenstates of $\mathcal{S}$ and $\mathcal{B}$. The perturbation X in terms of the local basis consists of all interaction and on-site terms between the single site in $\mathcal{S}$ and its nearest neighbors of the lattice, which are in $\mathcal{B}$. In Sec. 3.2.3, we conclude, that in this configuration with $N_{\mathcal{S}} = 2$, the variance model can be split up as a product $\sigma^2_{\mu i;\nu j} = \sigma^2_{\mu\nu}\sigma^2_{ij}$, giving rise to four blocks of the matrix, where each block (μ, ν) corresponds to the specific scattering from $|\psi^{\mathcal{S}}_{\mu}\rangle$ to $|\psi^{\mathcal{S}}_{\nu}\rangle$ in subsystem $\mathcal{S}$. The numerical setup is chosen with the second moment of the bath Hamiltonian to be normalized to one, $\tau((H^{\mathcal{B}})^2) = 1$. For the Gaussian fit of the numerical DOS in $\mathcal{B}$, we obtain the standard deviation $\sigma_{\mathcal{B}} = 1.0298(19)$, which has a small deviation to $\tau((H^{\mathcal{B}})^2)$

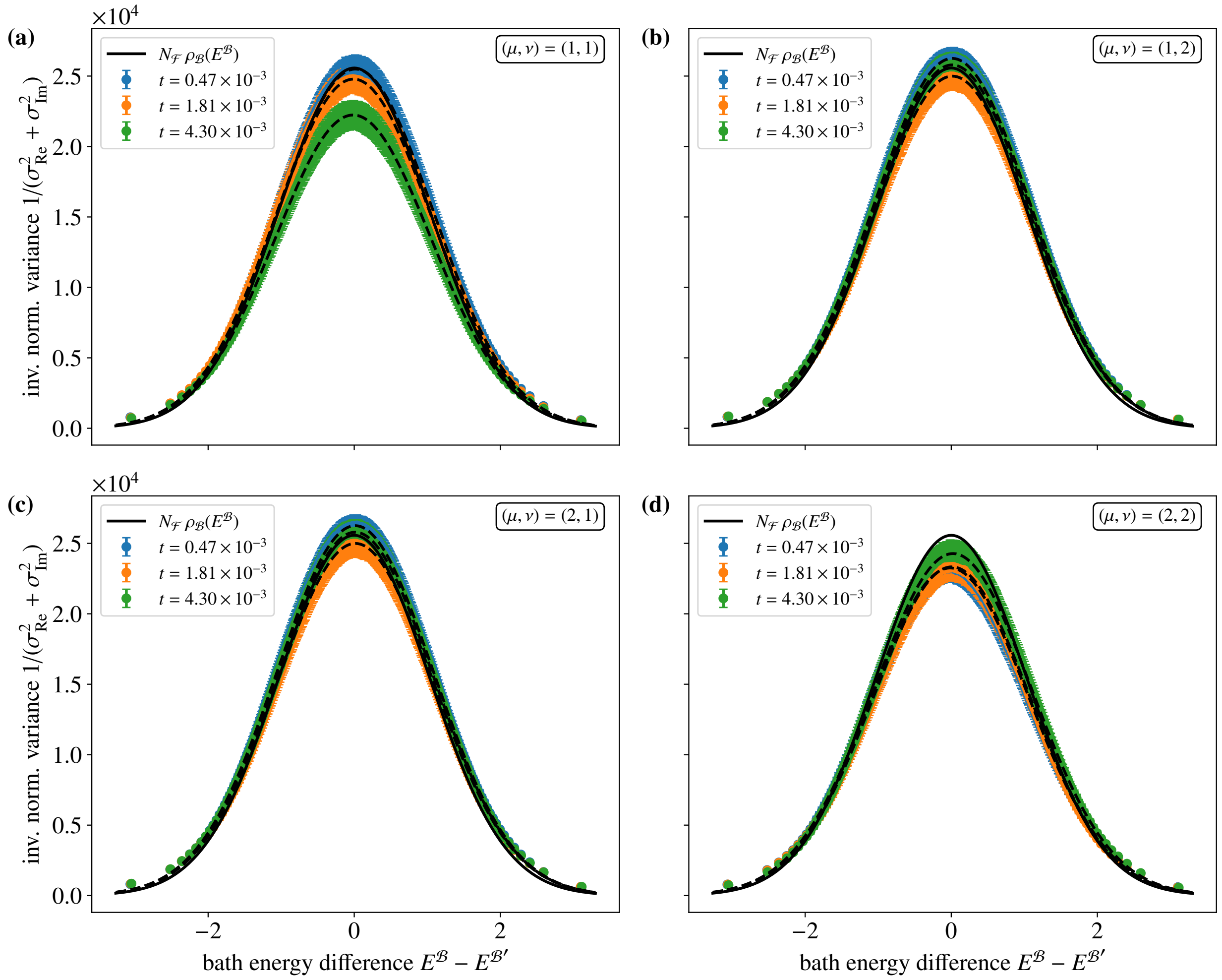

Figure 4.25: Inverse element-wise variance for three values of t on a line along the diagonal of $\tilde{X}$ which considers only the offdiagonal elements. Each block of $\tilde{X}$ represents a specific scattering in $\mathcal{S}$ and analyzed separately with (μ, ν) being **(a)** $(1,1)$, **(b)** $(1,2)$, **(c)** $(2,1)$ **(d)** $(2,2)$. The data points are computed in terms of boxes of size (100×100) and in an average over 100 samples of $H^{\mathcal{B}}$ and 200 samples of X. For reference, we plot the fit of the Gaussian DOS multiplied by $N_{\mathcal{S}}$, $N_{\mathcal{F}}\rho_{\mathcal{B}}(E)$ as a black joined line. Gaussians fits to the data are shown as black dashed lines with the fit parameter of the variance σ^2_{dia} added to Tab. 4.3.

originating in the finite size of the system. The second moment of $H^{\mathcal{S}}$ is chosen to $\tau((H^{\mathcal{S}})^2) = 0.01$, which results in the two eigenvalues in $\mathcal{S}$ to be $\epsilon_1 = -0.1$ and $\epsilon_2 = 0.1$.

In Fig. 4.23, we plot the element-wise variance of the perturbation matrix $\tilde{X}$ divided by the matrix variance t, which is defined as the variance model $\sigma^2_{\mu i;\nu j}$. In this analysis, only the offdiagonal elements of $\tilde{X}$ are taken into account, while the diagonal elements are evaluated separately. The result is depicted in terms of the four blocks of the matrix $\tilde{X}$ corresponding to the scattering of the states μ to ν in $\mathcal{S}$. An enlarged cutout of the offdiagonal variance model around zero highlighted in Fig. 4.23 is depicted in Fig. 4.24. Combining the two figures, we conclude that the four blocks of the variance model are very similar to each other, but not exactly the same due to the limited sample rate used for the averaging. This statement is supported by the fact that the variances in each block for different choices of t also slightly differ. In each matrix block individually, the general shape of the variance model is the same as in the single peak model, where $N_{\mathcal{S}} = 1$. It consists of a Gaussian model with an additional peak at zero. As explained

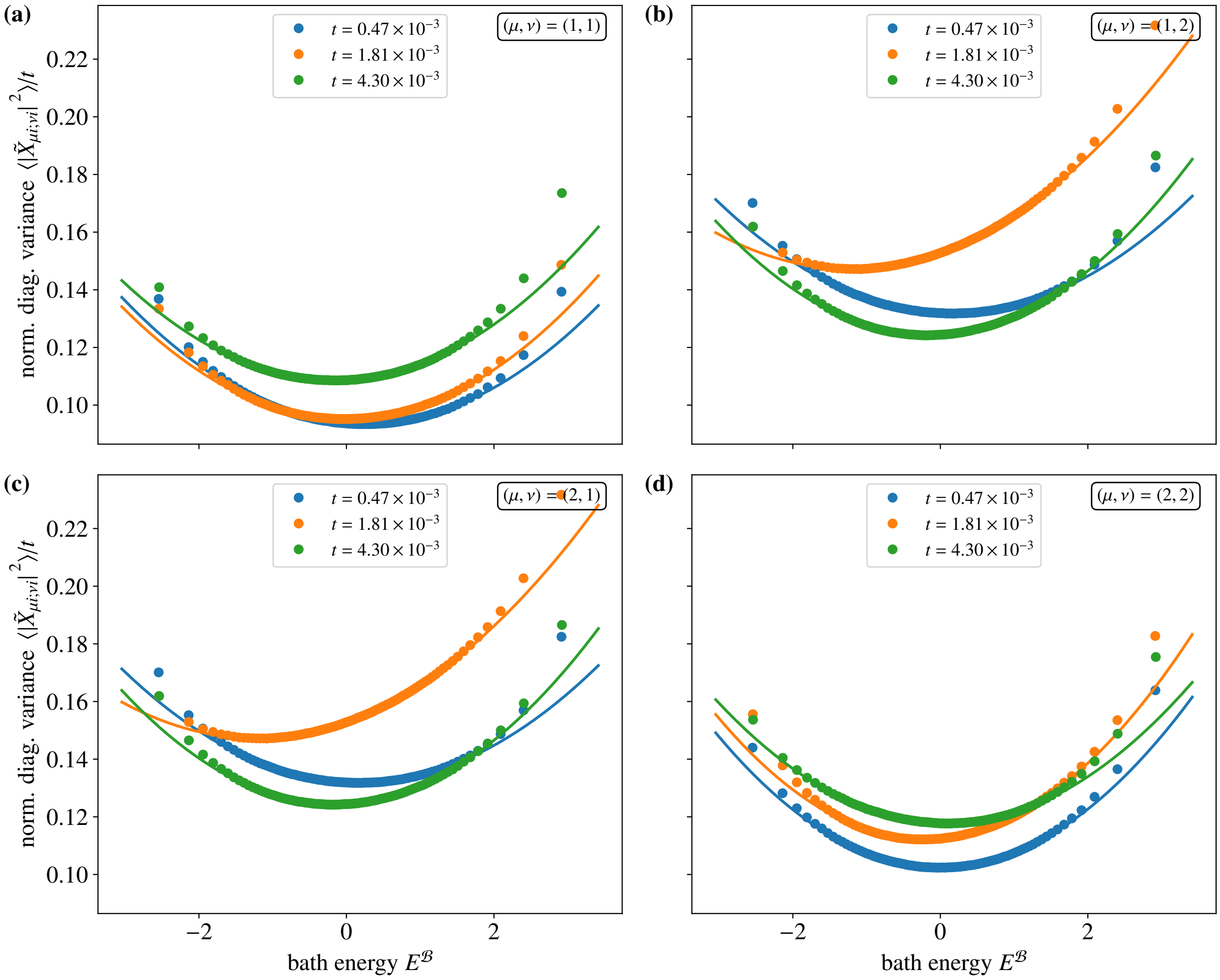

Figure 4.26: Sample variance of the diagonal elements in each block of $\tilde{X}$ for 200 samples of X and 100 samples of $H^{\mathcal{B}}$ for three values of t in the multi peak model with $d_{\mathcal{B}} = 15$ and $d_{\mathcal{S}} = 1$. For each sample, the diagonal values $\tilde{X}_{ii}$ are averaged in intervals of 328 elements, then the sample variance of each interval with respect to X is computed and normalized by t. The blocks of $\tilde{X}$ represent the eigenvector scattering in $\mathcal{S}$ and are analyzed separately with (μ, ν) being **(a)** $(1, 1)$, **(b)** $(1, 2)$, **(c)** $(2, 1)$ **(d)** $(2, 2)$. We fit quadratic functions according to Eq. (4.66) to the data for each t with the best fit parameters arranged in Tab. 4.4.

in Sec. 3.2 with the final result for the variance model in (3.45), this peak is a finite size effect and vanishes in the thermodynamic limit resulting in a pure Gaussian model for $N_{\mathcal{B}} \to \infty$. For this reason, we employ two different models for the perturbation matrix $\tilde{X}$ to calculate the analytical overlap curve for $X_{\mu i,l} = \mathbb{E}\left[\langle \psi^{\mathcal{S}}_{\mu} | \langle \psi^{\mathcal{B}}_{i} | \psi^{\mathcal{F}}_{l} \rangle \right]$. In the mathematical model, which we introduced in Sec. 4.3.1 for the single peak model, we assume a Gaussian shape of the scattering term $u(E_-)$ as well as for the DOS in $\mathcal{B}$. In the block (μ, ν), the offdiagonal variance model is described by $\sigma^2_{\mathrm{od},\mu\nu} = u(E_-) \cdot v(E_+)$. The function $v(E_+)$ is then chosen such that the combination of variance blocks is normalized to fulfill the sum rule $\sum_{\nu,j} \sigma^2_{\mu i;\nu j} = 1$. The mathematical model for the offdiagonal variances in $\tilde{X}$ in the multi peak

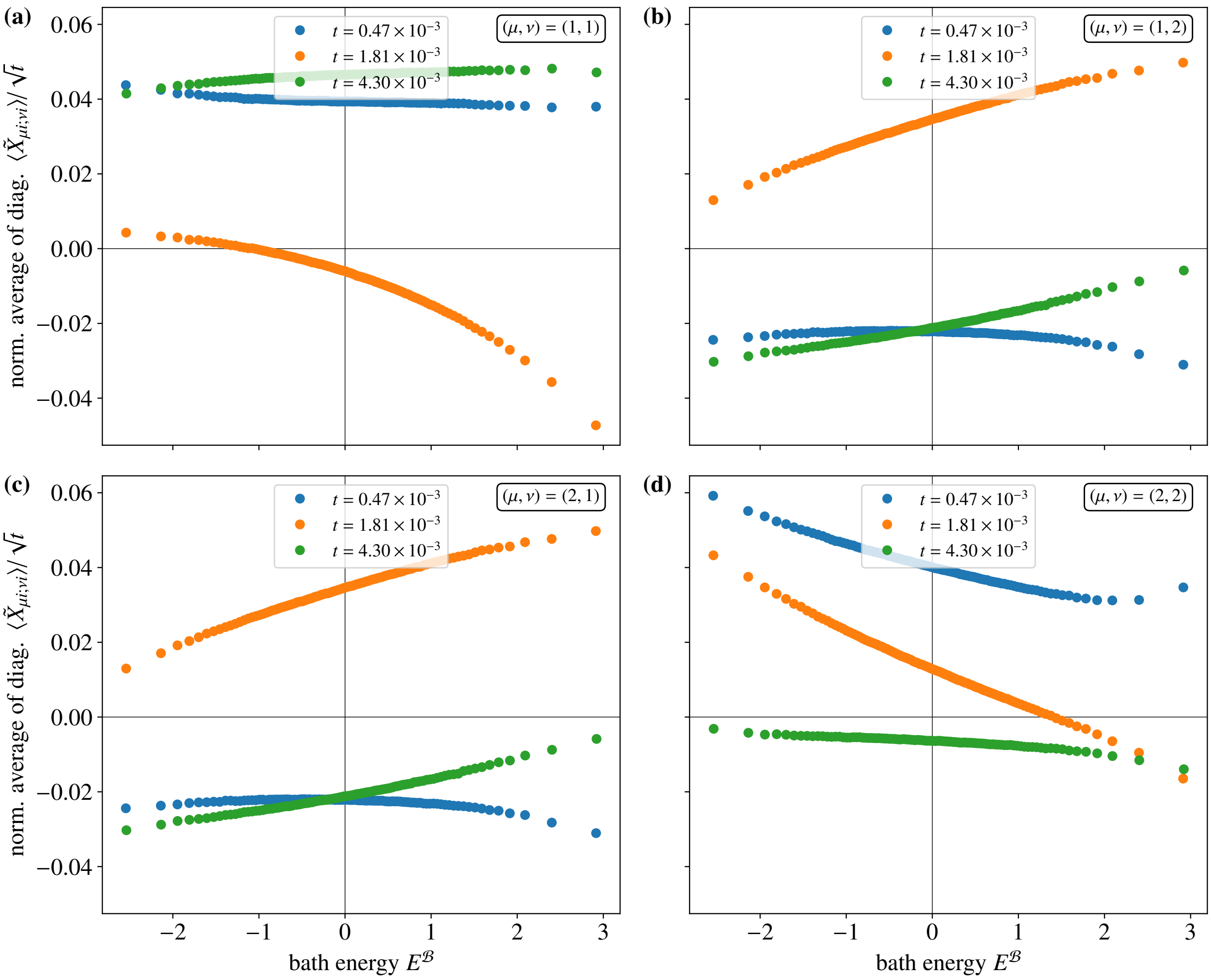

Figure 4.27: Real part of the diagonal elements of $\tilde{X}$ averaged separately in each block over 200 samples of X, 100 samples of $H^\mathcal{B}$ and in intervals of 328 elements each in the multi peak model with $d_\mathcal{B} = 15$ and $d_\mathcal{S} = 1$. The blocks of $\tilde{X}$ represent the eigenvector scattering in $\mathcal{S}$ and are analyzed separately with (μ,ν) being **(a)** $(1,1)$, **(b)** $(1,2)$, **(c)** $(2,1)$ **(d)** $(2,2)$. The result is normalized by $\sqrt{t}$. The average leads to a total of 100 intervals along the energy axis.

model is then equal to

$$\sigma^2_{\mu i;\nu j} \to \sigma^2_{\mathrm{od},\mu\nu}(E_i,E_j) = \frac{1}{N_\mathcal{S}}\sigma^2_{\mathrm{od}}(E_i,E_j) = \frac{1}{N_\mathcal{F}}\frac{\sigma_\mathcal{B}\,\bar{\Delta}_0}{\sqrt{2}{\Delta'_0}^2}\,\frac{\exp\left\{-\frac{1}{\Delta_0^2}\left(\frac{E_i-E_j}{2}\right)^2\right\}}{\exp\left\{-\frac{1}{2\sigma_\mathcal{B}^2+\Delta_0^2}\left(\frac{E_i+E_j}{2}\right)^2\right\}}, \tag{4.63}$$

where $\sigma^2_{\mathrm{od}}(E_i,E_j)$ corresponds to the offdiagonal variance of the single peak model, in this case chosen to be the mathematical model defined in Eq. (4.43) in Sec. 4.3.1. We further use $N_\mathcal{S} \cdot N_\mathcal{B} = N_\mathcal{F}$, while $(\bar{\Delta}_0)^{-2} = (\Delta_0^{-2} + (2\sigma_\mathcal{B})^{-2})$ and $(\Delta'_0)^{-2} = (\Delta_0^{-2} + \sigma_\mathcal{B}^{-2})$ as previously defined. Multiplied with the DOS in the bath, we obtain

$$N_\mathcal{B}\,\rho_\mathcal{B}(E_j)\,\sigma^2_{\mathrm{od},\mu\nu}(E_i,E_j) = \frac{1}{\sqrt{4\pi}N_\mathcal{S}}\,\frac{\bar{\Delta}_0}{{\Delta'_0}^2}\exp\left\{-\left(\frac{\bar{\Delta}_0}{{\Delta'_0}^2}\,E_- + \bar{b}_0\right)^2\right\} \tag{4.64}$$

Fit parameters of the offdiagonal variance							
$t\,[10^{-3}]$	μ	ν	Δ_1	Δ_2	A	ϑ	σ_{dia}
0.47	1	1	0.3963(22)	0.026 36(45)	0.7993(30)	0.044 15(89)	1.062 53(39)
		2	0.3847(22)	0.026 93(45)	0.7497(29)	0.047 87(96)	1.068 45(37)
	2	1	0.3847(22)	0.026 93(45)	0.7497(29)	0.047 86(96)	1.068 45(37)
		2	0.3842(20)	0.026 68(34)	0.7497(29)	0.055 88(86)	1.074 98(49)
1.81	1	1	0.3971(26)	0.026 20(50)	0.8463(38)	0.0413(10)	1.065 49(38)
		2	0.3931(23)	0.027 47(42)	0.7689(30)	0.0534(10)	1.068 75(48)
	2	1	0.3931(23)	0.027 47(42)	0.7689(30)	0.0535(10)	1.068 75(48)
		2	0.3921(25)	0.027 26(48)	0.7688(30)	0.0516(11)	1.067 70(51)
4.30	1	1	0.3628(18)	0.026 42(35)	0.8110(28)	0.052 78(85)	1.065 70(41)
		2	0.3676(19)	0.026 72(36)	0.6976(24)	0.054 03(87)	1.067 01(38)
	2	1	0.3676(19)	0.026 72(36)	0.6976(24)	0.054 04(87)	1.067 01(38)
		2	0.3707(17)	0.025 13(35)	0.6976(24)	0.045 17(73)	1.072 78(38)

Table 4.3: Fit parameters of the offdiagonal and variance in the multi peak model with $d_{\mathcal{B}} = 15$ and $d_{\mathcal{S}} = 1$ employing the numerical variance model in (4.65). The data along the anti-diagonal together with the resulting fits for all four blocks are depicted in Fig. 4.23 and Fig. 4.24. The Gaussian fit standard deviation of the DOS of the bath $\mathcal{B}$ is given by $\sigma_{\mathcal{B}} = 1.0300(19)$. The parameter σ_{dia} is obtained as the Gaussian standard deviation from a fit to the inverse offdiagonal variance data along the diagonal direction of $\tilde{X}$ in each block shown in Fig.4.25.

with $E_- = \frac{E_i - E_j}{2}$ and $\bar{b}_0 = -\frac{\bar{\Delta}_0 E_i}{2\sigma_{\mathcal{B}}^2}$ as before. A second approach to model the variance is to adjust it to fit the numerically obtained shape displayed in Fig. 4.23 and Fig. 4.24. With this approach, we compare the numerical results for the Lorentzian parameters with the analytical results obtained from the calculation. For this purpose, we use a sum of two Gaussians for each block individually to incorporate the shape of the peak at zero in the numerical variance model. In each block (μ, ν), the model is given by

$$\sigma^2_{\mathrm{od;num},\,\mu\nu}(E_i, E_j) = \frac{\sigma_{\mathcal{B}}}{\sqrt{2}N_{\mathcal{F}}}\,\frac{A_{\mu\nu}}{(1+\vartheta_{\mu\nu})}\left(\frac{\bar{\Delta}_{1,\mu\nu}}{{\Delta'}_{1,\mu\nu}^{2}}\,\frac{\exp\left\{-\frac{1}{\Delta_{1,\mu\nu}^2}\left(\frac{E_i-E_j}{2}\right)^2\right\}}{\exp\left\{-\frac{1}{2\sigma_{\mathcal{B}}^2+\Delta_{1,\mu\nu}^2}\left(\frac{E_i+E_j}{2}\right)^2\right\}} + \vartheta_{\mu\nu}\frac{\bar{\Delta}_{2,\mu\nu}}{{\Delta'}_{2,\mu\nu}^{2}}\,\frac{\exp\left\{-\frac{1}{\Delta_{2,\mu\nu}^2}\left(\frac{E_i-E_j}{2}\right)^2\right\}}{\exp\left\{-\frac{1}{2\sigma_{\mathcal{B}}^2+\Delta_{2,\mu\nu}^2}\left(\frac{E_i+E_j}{2}\right)^2\right\}}\right). \tag{4.65}$$

The overall prefactor $A_{\mu\nu}$ is added to account for different weight of the blocks while $\vartheta_{\mu\nu}$ determines the weight of the two Gaussians within each block. Since the variance in the four blocks show small deviations, a fit according to Eq. (4.65) is performed for each block separately. The best fit parameters are compiled in Tab. 4.3. Analogous to the mathematical model, we define $N_{\mathcal{S}} \cdot N_{\mathcal{B}} = N_{\mathcal{F}}$, while $(\bar{\Delta}_{i,\mu\nu})^{-2} = (\Delta_{i,\mu\nu}^{-2} + (2\sigma_{\mathcal{B}})^{-2})$ and $(\Delta'_{i,\mu\nu})^{-2} = (\Delta_{i,\mu\nu}^{-2} + \sigma_{\mathcal{B}}^{-2})$ for $i = 1, 2$. Multiplied with the Gaussian DOS in $\mathcal{B}$, we obtain

$$\begin{aligned} &N_{\mathcal{B}}\,\rho_{\mathcal{B}}(E_j)\,\sigma^2_{\mathrm{od;num},\,\mu\nu}(E_i, E_j) \\ &\quad= \frac{1}{\sqrt{4\pi}N_{\mathcal{S}}}\,\frac{A_{\mu\nu}}{(1+\epsilon_{\mu\nu})}\left[\frac{\bar{\Delta}_{1,\mu\nu}}{{\Delta'}_{1,\mu\nu}^{2}}\exp\left\{-\left(\frac{\bar{\Delta}_{1,\mu\nu}}{{\Delta'}_{1,\mu\nu}^{2}}E_- + \bar{b}_{1,\mu\nu}\right)^2\right\} + \vartheta_{\mu\nu}\frac{\bar{\Delta}_{2,\mu\nu}}{{\Delta'}_{2,\mu\nu}^{2}}\exp\left\{-\left(\frac{\bar{\Delta}_{2,\mu\nu}}{{\Delta'}_{2,\mu\nu}^{2}}E_- + \bar{b}_{2,\mu\nu}\right)^2\right\}\right], \end{aligned}$$

Fit parameters of the diagonal variance					
$t\,[10^{-3}]$	μ	ν	$\sigma_1^2\,[10^{-3}]$	$\sigma_2^2\,[10^{-3}]$	E_0
0.47	1	1	186.759(14)	8.759(21)	0.014 98(32)
		2	263.524(14)	8.156(21)	0.013 26(30)
	2	1	263.524(14)	8.156(21)	0.013 26(29)
		2	204.687(13)	10.732(21)	−0.014 92(39)
1.81	1	1	190.296(20)	8.9860(302)	−0.009 71(30)
		2	294.356(44)	7.999(28)	0.015 39(39)
	2	1	294.356(44)	7.999(28)	0.015 39(39)
		2	224.322(26)	11.457(40)	0.007 13(41)
4.30	1	1	217.060(19)	8.839(30)	−0.014 74(32)
		2	248.480(18)	10.110(28)	0.012 07(30)
	2	1	248.480(18)	10.110(28)	0.012 07(30)
		2	235.432(26)	9.325(40)	0.023 71(31)

Table 4.4: Fit parameters of the diagonal sample variance in the multi peak model with $d_{\mathcal{B}} = 15$ and $d_{\mathcal{S}} = 1$ according to Eq. (4.66) with the data being plotted in Fig. 4.26. Note, that the factors σ_1^2 and σ_2^2 are twice as large as expected from a direct comparison with Fig. 4.13, since the diagonal variance in Eq. (4.50) is normalized by $N_{\mathcal{S}} = 2$ to account for the number of blocks in $\tilde{X}$ in each row or column.

where $E_- = \frac{E_i - E_j}{2}$ and $\overline{b}_i = -\frac{\overline{\Delta}_{i,\mu\nu} E_i}{2\sigma_{\mathcal{B}}^2}$ for $i = 1, 2$. The fits in Fig. 4.23 and Fig. 4.24 match the general shape of the data well. There are small deviations as compared to the data points, which are not of greater importance, since primarily the width of the two Gaussians enters the description of the overlap curve as calculated below.

Analogously, the inverse by t normalized variance along the diagonal direction of the perturbation matrix $\tilde{X}$ is shown in Fig. 4.25 for each block of the matrix individually. As expected from the analysis in Sec. 3.1.4, the variance along this direction is given by the inverse Gaussian DOS. This is confirmed by Gaussian fits on the data sets for each value of t individually. The best fit parameter for the Gaussian variance σ_{dia}^2 is added to Tab. 4.3. Additionally, the DOS of the bath is plotted in each frame of Fig. 4.25 as a black solid line and compares well with the general shape of the data. As elaborated in Sec. 4.3.1 for the single peak model, σ_{dia} is slightly larger than the standard deviation of the DOS with $\sigma_{\mathcal{B}} = 1.0300(19)$. This is caused by the normalization condition of the variance model with the slightly increased variance $\sigma_{\mathcal{B}}^2 + \Delta_0^2$ of the Gaussian in the denominator of the offdiagonal variance model (4.63) and similarly with $\sigma_{\mathcal{B}}^2 + \Delta_{1,\mu\nu}^2$ and $\sigma_{\mathcal{B}}^2 + \Delta_{2,\mu\nu}^2$ in the denominators in (4.65).

In Fig. 4.26, we plot the variance of the diagonal elements of $\tilde{X}$ normalized by t. In Sec. 3.1.4, we argue, that the diagonal variance is a sum of two terms, one being constant in energy, while the second is proportional to the square of the bath energy E_i. It derives from the relation, that the diagonal element $\tilde{X}_{ii}$ can have a constant term and one proportional to E_i. The diagonal element is relevant, since in contrast to any other element in the matrix, it does not scale with $\frac{1}{N_{\mathcal{B}}}$, but merely decreases as the inverse of a polynomial in $d_{\mathcal{B}}$. In accordance with Eq. (3.33), the variance of the diagonal elements of $\tilde{X}$ in each block assume the form

$$\sigma^2_{\text{d;num},\mu\nu}(E_i, E_j) = \frac{1}{N_{\mathcal{S}}} \left(\sigma^2_{1,\mu\nu} + \sigma^2_{2,\mu\nu} \cdot \frac{\left(E_i - E_{0,\mu\nu}\right)^2}{\sigma^2_{\mathcal{B}}} \right) \frac{\delta(E_i - E_j)}{N_{\mathcal{B}} \rho_{\mathcal{B}}(E_i)} \tag{4.66}$$

for the continuum case. The parameters $E_{0,\mu\nu}$, $\sigma^2_{1,\mu\nu}$ and $\sigma^2_{2,\mu\nu}$ are obtained from quadratic fits to the variance $\sigma^2_{\mu i,\nu i}$ in each block (μ,ν) depicted in Fig. 4.26. Their best fit parameters are collected in Tab. 4.4. From the analytic analysis of the diagonal elements in Sec. 3.1.4, we extract the analytically expected values for $\frac{\sigma^2_{1,\mu\nu}}{N_S} = \frac{t_1}{t}$ and $\frac{\sigma^2_{2,\mu\nu}}{N_S} = \frac{1}{N_S}(1-\sigma^2_{1,\mu\nu})\frac{1}{L}$. t_1 denotes the fraction of t, which contributes as a unit matrix term in the bath $\mathcal{B}$ in each block (μ,ν), while the remaining part $(1-\sigma^2_{1,\mu\nu})$ contributes to the variance of the E_i^2 term. L stands for the total number of terms in $\mathcal{B}$. With the construction of X in (2.6) for the multi peak model, we read off, that $t_1 = \frac{t}{8}$, since two out of the 16 terms in X contribute as unit matrix terms in subsystem $\mathcal{B}$ in each block. The number of terms in $\mathcal{B}$ is given by $L = 243$. These definitions imply the theoretically expected values $\sigma^2_{1,\mu\nu} = \frac{N_S\,t}{8}0.25$ and $\sigma^2_{2,\mu\nu} = \frac{3}{4}\frac{1}{L} = 3.09\times 10^{-3}$. We compare those to the mean values over all t, μ and ν in Tab. 4.4, which are $\bar{\sigma}^2_{1,\mu\nu} = 0.239(10)$ and $\bar{\sigma}^2_{2,\mu\nu} = 9.22(33)\times 10^{-3}$, which are on the same order of magnitude as the theoretical results. For comparison, we plot the sample average $\langle \mathfrak{Re}\,(\tilde{X}_{ii})\rangle$ of the real part of the diagonal elements in Fig. 4.27 normalized by $\sqrt{t}$, which show an approximate linear behavior, from which their quadratic variance in E_i derives. Since the perturbation matrix is Hermitian, the diagonal entries on the diagonal blocks are real valued, while those on the offdiagonal blocks are complex. The imaginary part on the offdiagonal blocks is of the same order as the real part. We notice, that the square of the average in Fig. 4.27 is much smaller than its variance in Fig. 4.26, $\langle \tilde{X}_{ii}\rangle \ll t\,\sigma^2_{ii}$. This is consistent with the analytical expectation, that $\mathbb{E}\left[\tilde{X}_{ii}\right] = 0$, which derives from the fact, that all random values in $\tilde{X}$ are drawn from Gaussians with mean zero.

For the mathematical model, we choose the parameters of the diagonal variance as they are expected from analytical considerations. We choose the perturbation matrix X such that the variance can be separated into a product, $\sigma^2_{\mu i,\nu j} = \sigma^2_{\mu\nu}\cdot\sigma^2_{ij}$ as shown in Sec. 3.2.3. With the choice of X for the multi peak model in (2.6), all parameters in the four blocks are equal and further $E_{0,\mu\nu} = 0$ as discussed in Sec. 3.1.4. This results in

$$\sigma^2_{\mathrm{d},\mu\nu}(E_i,E_j) = \frac{1}{N_S}\left(\sigma_1^2 + \sigma_2^2\cdot\left(\frac{E_i}{\sigma_{\mathcal{B}}}\right)^2\right)\frac{\delta(E_i-E_j)}{N_{\mathcal{B}}\rho_{\mathcal{B}}(E_i)} \tag{4.67}$$

for the mathematical model.

Results for the parameters of the overlap curves. With the concrete form of the diagonal and offdiagonal variance in the perturbation matrix $\tilde{X}$, we can now compute the overlap function in the multi peak model. The calculation is based on Sec. 4.2, where we discussed the application of the equation by Casati and Girko. For that, we split up the resolvent into blocks corresponding to the contributions in $\mathcal{S}$ with diagonal elements $\mathcal{R}_{\mu i,\nu i}(z) \to \mathcal{R}_{\mu\mu}(E_i,z)$ for $\mu = 1,\ldots,N_{\mathcal{S}}$. We found the result for the trace of $\mathcal{R}$ weighted by the variance model $\sigma_{\mu i,\nu j}$, which we defined as $\tilde{\mathcal{G}}_{\mu,i}(z) = \sum_{\nu,j}\mathcal{R}_{\mu j,\nu j}(z)$. With an initial Delta peak for the overlap, the first resolvent iteration is given by Eq. (4.30). Similar to the single peak model, we assume the general form

$$N_{\mathcal{B}}\rho_{\mathcal{B}}(E_i)\,\sigma^2_{\mathrm{od},\mu\nu}(E_i,E_j) = \frac{1}{N_S}\frac{1}{\sqrt{4\pi\Delta^2}}e^{-\left(\frac{E_i-E_j}{2\Delta}+c\cdot E_i\right)^2} \tag{4.68}$$

for the product of the Gaussian DOS and the offdiagonal variance model. According to Eq. (4.30), the imaginary part of the function $\tilde{\mathcal{G}}_{\mu,i}(\lambda_l)$ is given by

$$\tilde{\mathcal{G}}''_{\mu}(E_i,\lambda_l - i0^+) = \pi\left(\sum_{\nu} N_{\mathcal{B}}\rho_{\mathcal{B}}(\lambda_l-\epsilon_\nu+\eta^{(l)}_\nu)\,\sigma^2_{\mathrm{od},\mu\nu}(E_i,\lambda_l-\epsilon_\nu+\eta^{(l)}_\nu) + \sum_{\substack{\nu\\(\nu\neq\mu)}}\tilde{\sigma}^2_{\mathrm{d},\mu\nu}(E_i)\,\delta(E_i+\epsilon_\nu-\lambda_l-\eta^{(l)}_\nu)\right)$$

$$
\begin{aligned}
&= \frac{\sqrt{\pi}}{2\Delta N_{\mathcal{S}}} \sum_{\nu} \exp\left\{ -\left[\frac{x_\mu - (\epsilon_{\mu\nu} - \eta_{\mu\nu})}{2\Delta} + c\left(x_\mu + \lambda_l - \epsilon_\mu + \eta_\mu^{(l)}\right) \right]^2 \right\} \\
&\quad + \frac{\pi}{N_{\mathcal{S}}} \sum_{\substack{\nu \\ (\nu \neq \mu)}} \left(\sigma_1^2 + \frac{\sigma_2^2}{\sigma_{\mathcal{B}}^2} \cdot \left(x_\mu + \lambda_l - \epsilon_\mu + \eta_\mu^{(l)}\right)^2 \right) \delta\left(x_\mu - (\epsilon_{\mu\nu} - \eta_{\mu\nu})\right),
\end{aligned}
$$

where we define $x_\mu = x_\mu(E_i) := E_i - \lambda_l + \epsilon_\mu - \eta_\mu^{(l)}$, $\epsilon_{\mu\nu} = \epsilon_\mu - \epsilon_\nu$ and $\eta_{\mu\nu} = \eta_\mu - \eta_\nu$. The part originating from the offdiagonal variance is obtained by setting $E_j \to \lambda_l - \epsilon_\mu + \eta_\mu$ in Eq. (4.68) and summing over all ν. The corresponding real part is obtained by the Hilbert transform in the second variable,

$$
\begin{aligned}
&\tilde{\mathcal{G}}'_\mu(E_i, \lambda_l - i0^+) = \mathcal{H}\left[G''_\mu(E_i, E_j)\right](E_j \to \lambda_l - \epsilon_\mu + \eta_\mu^{(l)}) \\
&= -\frac{\sqrt{\pi}}{2\Delta N_{\mathcal{S}}} \sum_{\nu} \exp\left\{ -\left[\frac{x_\mu - (\epsilon_{\mu\nu} - \eta_{\mu\nu})}{2\Delta} + c\left(x_\mu + \lambda_l - \epsilon_\mu + \eta_\mu^{(l)}\right) \right]^2 \right\} \operatorname{erfi}\left(\frac{x_\mu - (\epsilon_{\mu\nu} - \eta_{\mu\nu})}{2\Delta} + c\left(x_\mu + \lambda_l - \epsilon_\mu + \eta_\mu^{(l)}\right) \right) \\
&\quad - \frac{1}{N_{\mathcal{S}}} \sum_{\substack{\nu \\ (\nu \neq \mu)}} \frac{\sigma_1^2 + \frac{\sigma_2^2}{\sigma_{\mathcal{B}}^2} \cdot \left(x_\mu + \lambda_l - \epsilon_\mu + \eta_\mu^{(l)}\right)^2}{x_\mu - (\epsilon_{\mu\nu} - \eta_{\mu\nu})}.
\end{aligned}
$$

With the resolvent in Eq. (4.31), we can compute the overlap curve for the state $|\psi_\mu^{\mathcal{S}}\rangle$ in terms of the bath energy E_i,

$$
X_\mu(E_i, \lambda_l) = \mathbb{E}\left[\left| \left(\langle \psi_\mu^{\mathcal{S}} | \otimes \langle \psi_i^{\mathcal{B}} | \right) | \psi_l^{\mathcal{F}} \rangle \right|^2 \right] = \frac{1}{\pi N_{\mathcal{F}} \rho_{\mathcal{F}}(\lambda_l)} \frac{t \tilde{\mathcal{G}}''_\mu(E_i, \lambda_l)}{\left(x_\mu + \eta_\mu^{(l)} + t\tilde{\mathcal{G}}'_\mu(E_i, \lambda_l)\right)^2 + \left(t\tilde{\mathcal{G}}''_\mu(E_i, \lambda_l)\right)^2}. \tag{4.69}
$$

Analogous to the single peak model, we expand the denominator in second order of x_μ to find the shape of the overlap close to its peak. We then read off the shift parameter in first order of t, which is equal to the real part of $\tilde{\mathcal{G}}_\mu(E_i, \lambda_l)$ evaluated at the peak position,

$$
\begin{aligned}
\eta_\mu^{(l)} &= -t\,\tilde{\mathcal{G}}'_\mu(E_i, \lambda_l)\Big|_{E_i = \lambda_l - \epsilon_\mu + \eta_\mu^{(l)}} \\
&= \frac{t}{N_{\mathcal{S}}} \left(\frac{\sqrt{\pi}}{2\Delta} \sum_{\nu} \exp\left\{ -\left[c\left(\lambda_l - \epsilon_\mu\right) - \frac{\epsilon_\mu - \epsilon_\nu}{2\Delta} \right]^2 \right\} \operatorname{erfi}\left(c\left(\lambda_l - \epsilon_\mu\right) - \frac{\epsilon_\mu - \epsilon_\nu}{2\Delta} \right) - \sum_{\substack{\nu \\ (\nu \neq \mu)}} \frac{\sigma_1^2 + \sigma_2^2 \frac{(\lambda_l - \epsilon_\mu)^2}{\sigma_{\mathcal{B}}^2}}{\epsilon_\mu - \epsilon_\nu} \right),
\end{aligned} \tag{4.70}
$$

which is equivalent to setting $x_\mu = 0$. Since $\eta_\mu^{(l)}$ is itself at least first order in t, it was set to zero to obtain Eq. (4.70), since we are only interested in the first order of t. The result for the first order of t of the shift $\eta_\mu^{(l)}$ in (4.70) is exact in terms of the eigenvalues ϵ_μ in $\mathcal{S}$ as well as the full eigenvalue λ_l. It is obtained by assuming a Lorentzian shape of the overlap curve close to its maximum, which is why we designate $\eta_\mu^{(l)}$ and $\gamma_\mu^{(l)}$ as the analytical Lorentzian parameters. Similarly, the Lorentzian width $\gamma_\mu^{(l)}$ is obtained by evaluating the imaginary part of $\tilde{\mathcal{G}}_\mu(E_i, \lambda_l)$ at the position $x_\mu = 0$,

$$
\begin{aligned}
\gamma_\mu^{(l)} &= t\,\tilde{\mathcal{G}}''_\mu(E_i, \lambda_l)\Big|_{E_i = \lambda_l - \epsilon_\mu + \eta_\mu^{(l)}} \\
&= \frac{t}{N_{\mathcal{S}}} \frac{\sqrt{\pi}}{2\Delta} \sum_{\nu} \exp\left\{ -\left[c\left(\lambda_l - \epsilon_\mu\right) - \frac{\epsilon_\mu - \epsilon_\nu}{2\Delta} \right]^2 \right\},
\end{aligned} \tag{4.71}
$$

where we again set $\eta_\mu^{(l)} = 0$ in $\tilde{\mathcal{G}}''$ to find the first order in t. The second contribution from $\tilde{\mathcal{G}}''$ is proportional to $\delta(\epsilon_\mu - \epsilon_\nu)$, which vanishes since $\mu \neq \nu$ in the corresponding sum.

We can match the definitions with the mathematical variance model, which are declared in Eq. (4.63) for the offdiagonal part and in Eq. (4.67) for the diagonal part. From that, we obtain the Lorentzian parameters

$$\gamma_\mu^{(l)} = \frac{\sqrt{\pi}t}{2N_\mathcal{S}} \frac{\overline{\Delta}_0}{{\Delta_0'}^2} \sum_\nu \exp\left\{-\left(\overline{b}_\mu - \frac{\overline{\Delta}_0}{2{\Delta_0'}^2}(\epsilon_\mu - \epsilon_\nu)\right)^2\right\}, \tag{4.72a}$$

$$\eta_\mu^{(l)} = \frac{t}{N_\mathcal{S}} \left(\frac{\sqrt{\pi}}{2} \frac{\overline{\Delta}_0}{{\Delta_0'}^2} \sum_\nu \exp\left\{-\left(\overline{b}_\mu - \frac{\overline{\Delta}_0}{2{\Delta_0'}^2}(\epsilon_\mu - \epsilon_\nu)\right)^2\right\} \operatorname{erfi}\left(\overline{b}_\mu - \frac{\overline{\Delta}_0}{2{\Delta_0'}^2}(\epsilon_\mu - \epsilon_\nu)\right) - \sum_{\substack{\nu \\ (\nu\neq\mu)}} \frac{\sigma_1^2 + \sigma_2^2 \frac{(\lambda_l - \epsilon_\mu)^2}{\sigma_\mathcal{B}^2}}{\epsilon_\mu - \epsilon_\nu} \right), \tag{4.72b}$$

where we substitute $\Delta \to \frac{{\Delta_0'}^2}{\overline{\Delta}_0}$, $c \to -\frac{\overline{\Delta}_0}{2\sigma_\mathcal{B}^2}$ and define $\overline{b}_\mu = -\frac{\overline{\Delta}_0(\lambda_l - \epsilon_\mu)}{2\sigma_\mathcal{B}^2}$ in the mathematical multi peak model. To get a general idea of the dependence of the Lorentzian parameters on the eigenenergies in $\mathcal{S}$ and in $\mathcal{F}$, we expand Eq. (4.72a,b) in first order order of $\epsilon_{\mu\nu}$ and in second order of $\overline{b}_\mu$, which gives

$$\gamma_\mu^{(l)} = \frac{\sqrt{\pi}t}{2} \frac{\overline{\Delta}_0}{{\Delta_0'}^2} \left(1 - \overline{b}_\mu^2 + \frac{\overline{\Delta}_0}{{\Delta_0'}^2} \frac{\overline{b}_\mu}{N_\mathcal{S}} \sum_\nu \epsilon_{\mu\nu}\right) + O(\overline{b}_\mu^3, \{\epsilon_\mu^2\}), \tag{4.73a}$$

$$\eta_\mu^{(l)} = \frac{\sqrt{\pi}t}{2} \frac{\overline{\Delta}_0}{{\Delta_0'}^2} \left(2\overline{b}_\mu - \frac{\overline{\Delta}_0}{{\Delta_0'}^2} \frac{1 - 2\overline{b}_\mu^2}{N_\mathcal{S}} \sum_\nu \epsilon_{\mu\nu}\right) - \frac{t}{N_\mathcal{S}} \left(\sigma_1^2 + \sigma_2^2 \frac{\lambda_l(\lambda_l - 2\epsilon_\mu)}{\sigma_\mathcal{B}^2}\right) \sum_{\substack{\nu \\ (\nu\neq\mu)}} \frac{1}{\epsilon_{\mu\nu}} + O(\overline{b}_\mu^3, \{\epsilon_\mu^2\}), \tag{4.73b}$$

where $\{\epsilon_\mu^2\}$ represents the squared eigenvalue for all $\mu = 1, \ldots, N_\mathcal{S}$. We use Eq. (4.73a,b) to be able to estimate the approximate structure of the Lorentzian parameters in a comparison with the numerical results. Similarly, the result can be adjusted to fit the numerical multi peak model for the offdiagonal and diagonal variance in (4.65) and (4.66) respectively, which gives

$$\gamma_{\text{num},\mu}^{(l)} = \frac{\sqrt{\pi}t}{2N_\mathcal{S}} \sum_\nu \frac{A_{\mu\nu}}{1 + \vartheta_{\mu\nu}} \left(\frac{\overline{\Delta}_{1,\mu\nu}}{{\Delta'_{1,\mu\nu}}^2} e^{-\left(\overline{b}_{1,\mu\nu} - \frac{\overline{\Delta}_{1,\mu\nu}}{2{\Delta'_{1,\mu\nu}}^2}(\epsilon_\mu - \epsilon_\nu)\right)^2} + \vartheta_{\mu\nu} \frac{\overline{\Delta}_{2,\mu\nu}}{{\Delta'_{2,\mu\nu}}^2} e^{-\left(\overline{b}_{2,\mu\nu} - \frac{\overline{\Delta}_{2,\mu\nu}}{2{\Delta'_{2,\mu\nu}}^2}(\epsilon_\mu - \epsilon_\nu)\right)^2} \right), \tag{4.74a}$$

$$\begin{aligned} \eta_{\text{num},\mu}^{(l)} = \frac{\sqrt{\pi}t}{2N_\mathcal{S}} \sum_\nu \frac{A_{\mu\nu}}{1 + \vartheta_{\mu\nu}} \Bigg\{ & \frac{\overline{\Delta}_{1,\mu\nu}}{{\Delta'_{1,\mu\nu}}^2} e^{-\left(\overline{b}_{1,\mu\nu} - \frac{\overline{\Delta}_{1,\mu\nu}}{2{\Delta'_{1,\mu\nu}}^2}(\epsilon_\mu - \epsilon_\nu)\right)^2} \operatorname{erfi}\left(\overline{b}_{1,\mu\nu} - \frac{\overline{\Delta}_{1,\mu\nu}}{2{\Delta'_{1,\mu\nu}}^2}(\epsilon_\mu - \epsilon_\nu)\right) \\ & + \vartheta_{\mu\nu} \frac{\overline{\Delta}_{2,\mu\nu}}{{\Delta'_{2,\mu\nu}}^2} e^{-\left(\overline{b}_{2,\mu\nu} - \frac{\overline{\Delta}_{2,\mu\nu}}{2{\Delta'_{2,\mu\nu}}^2}(\epsilon_\mu - \epsilon_\nu)\right)^2} \operatorname{erfi}\left(\overline{b}_{2,\mu\nu} - \frac{\overline{\Delta}_{2,\mu\nu}}{2{\Delta'_{2,\mu\nu}}^2}(\epsilon_\mu - \epsilon_\nu)\right) \Bigg\} \\ - \frac{t}{N_\mathcal{S}} \sum_{\substack{\nu \\ (\nu\neq\mu)}} \frac{\sigma_{1,\mu\nu}^2 + \sigma_{2,\mu\nu}^2 \cdot \frac{(\lambda_l - \epsilon_\mu - E_{0,\mu\nu})^2}{\sigma_\mathcal{B}^2}}{\epsilon_\mu - \epsilon_\nu}, \end{aligned} \tag{4.74b}$$

where we defined $\overline{b}_{i,\mu,\nu} = -\frac{\overline{\Delta}_{i,\mu\nu}(\lambda_l - \epsilon_\mu)}{2\sigma_\mathcal{B}^2}$ for $i = 1, 2$ additional to the definitions in $\sigma_{\text{od;num},\mu\nu}^2$ and $\sigma_{\text{d;num},\mu\nu}^2$. The fit parameters from the variance model, which are inserted into Eq. (4.74a,b) to find the numerically adjusted results are posted in Tab. 4.3. The result from Eq. (4.74a,b) is then used as a comparison of the analytical calculation to the numerical values of the Lorentzian parameters obtained from Lorentzian fits to the data.

4.4.2 Comparison to numerical results

In Sec. 4.1.3, we saw, that the overlap curves $|\langle\psi_\mu^{\mathcal{S}}|\,\langle\psi_i^{\mathcal{B}}|\psi_\mu^{\mathcal{F}}\rangle|^2$, depicted individually for each μ with respect to the bath energy E_i, have the shape of a Lorentzian close to the peak of the overlap curve. The total system size is $d_{\mathcal{F}} = 16$, which splits up into a bath of $d_{\mathcal{B}} = 15$ sites and a small subsystem $\mathcal{S}$ with one site. The bath Hamiltonian $H^{\mathcal{B}}$ and the perturbation X, which adds an interaction between the subsystems $\mathcal{S}$ and $\mathcal{B}$ are random matrices according to Sec. 2.1.3, while $H^{\mathcal{S}}$ has fixed eigenvalues of $\epsilon_1 = -0.1$ and $\epsilon_2 = +0.1$ due to the normalization of the second moment of the Hamiltonian to $\tau\left((H^{\mathcal{S}})^2\right) = 0.01$. For each random sample of X and $H^{\mathcal{B}}$, we use $N_{\mathrm{av}} = 400$ full states $|\psi_l^{\mathcal{F}}\rangle$ in an interval around the desired full energy λ_l to compute the averaged overlap curve for λ_l. From a Lorentzian fit with an additional prefactor A to the average overlap curve, we obtain the Lorentzian best fit parameters for the width γ, the shift η and the area A. Those fit parameters are averaged over 200 samples of X and 100 samples of $H^{\mathcal{B}}$, while $H^{\mathcal{S}}$ is constant throughout the analysis. Those Lorentzian parameters are compared with the analytical result in (4.74a,b), which is adjusted to the numerical shape of the variance model in the perturbation matrix $\tilde{X}$, that is the representation of X in terms of the unperturbed eigenbasis. Note, that the depicted variance model in Fig. 4.23-4.27 is obtained from the same data set as the Lorentzian fit parameters presented in the following. Since the small subsystem $\mathcal{S}$ consists of only two states, $N_{\mathcal{S}} = 2$, there are two individual overlap curves for $\mu = 1$ and $\mu = 2$ in terms of the bath energies E_i. In Sec. 4.1.3, we discussed that if the perturbation matrix $\tilde{X}$ was a GUE, we would obtain two identical overlap curves for $\mu = 1$ and $\mu = 2$ with them being extracted from a single overlap curve in the unperturbed product eigenbasis. Due to the energy dependent variance structure in the matrix $\tilde{X}$, this is not the case and the variance at the Lorentzian peak for $\mu = 1$ differs from the variance around the peak for $\mu = 2$. We hence expect the two overlap curves to differ slightly with small differences in width and shift for small ϵ_{12}.

In Fig. 4.28, we plot the widths γ with respect to the perturbation strength t and the averaged eigenvalue λ_l of the full quantum system in the considered interval. It is convenient to recast the Lorentzian parameters in terms of their sum and differences, $\gamma_1 + \gamma_2$ and $\gamma_1 - \gamma_2$, which are plotted in Fig. 4.28**a,c** and Fig. 4.28**b,d** respectively. To compare the numerical results to the analytical calculation, we use Eq. (4.74a), where the parameters of the variance model are obtained from fits to the numerical data in $\tilde{X}$. Together with their maximum error estimate computed from the error of the best fit parameters, the analytical values are plotted as a joint line with the corresponding margin of error in Fig. 4.28**b,d**. To obtain an estimate of the analytical expressions, we use Eq. (4.73a) and keep all terms of second order in the full energy λ_l and first order in the subsystem energy ϵ_μ,

$$\gamma_1^{(l)} + \gamma_2^{(l)} \approx \sqrt{\pi} t \, \frac{\overline{\Delta}_0}{\Delta_0'^{\,2}} \, (1 - \overline{b}_0^{\,2}) = 2\,\gamma^{(l)}, \tag{4.75a}$$

$$\gamma_1^{(l)} - \gamma_2^{(l)} \approx \frac{\sqrt{\pi} t}{2\Delta_0} \left(\frac{\overline{\Delta}_0}{\Delta_0'}\right)^2 \frac{\epsilon_{12}}{\Delta_0} \, \overline{b}_0 = \frac{\sqrt{\pi}}{4} \, \frac{\overline{\Delta}_0^{\,3}}{\Delta_0 \Delta_0'^{\,2}} \, \frac{\epsilon_{12}}{\Delta_0} \, (\beta t), \tag{4.75b}$$

where we used the single peak definition of $\overline{b}_0 = -\frac{\overline{\Delta}_0 \lambda_l}{2\sigma_{\mathcal{B}}^2} = \frac{\beta \overline{\Delta}_0}{2}$. We find, that the mean of the two widths $\gamma_1^{(l)}$ and $\gamma_2^{(l)}$ in this expansion is equal to the Lorentzian width of the single peak model $\gamma^{(l)}$, which can be viewed as the base contribution to the width in the multi peak model. In Fig. 4.28**a**, we confirm the linear dependence of $\gamma_1^{(l)} + \gamma_2^{(l)}$ on t, while Fig. 4.28**b** shows, that the numerical data agrees with the analytical calculation. On top of that, there is a broadening or narrowing of the Lorentzians in the multi peak model, which is reflected in the nonzero difference of their widths. There are two contributions to this. First, the Lorentzian width decreases with a factor of $e^{-\overline{b}_0^2}$ towards the edge of the spectrum, as we saw in the single peak model. In the first resolvent iteration, this originates in the

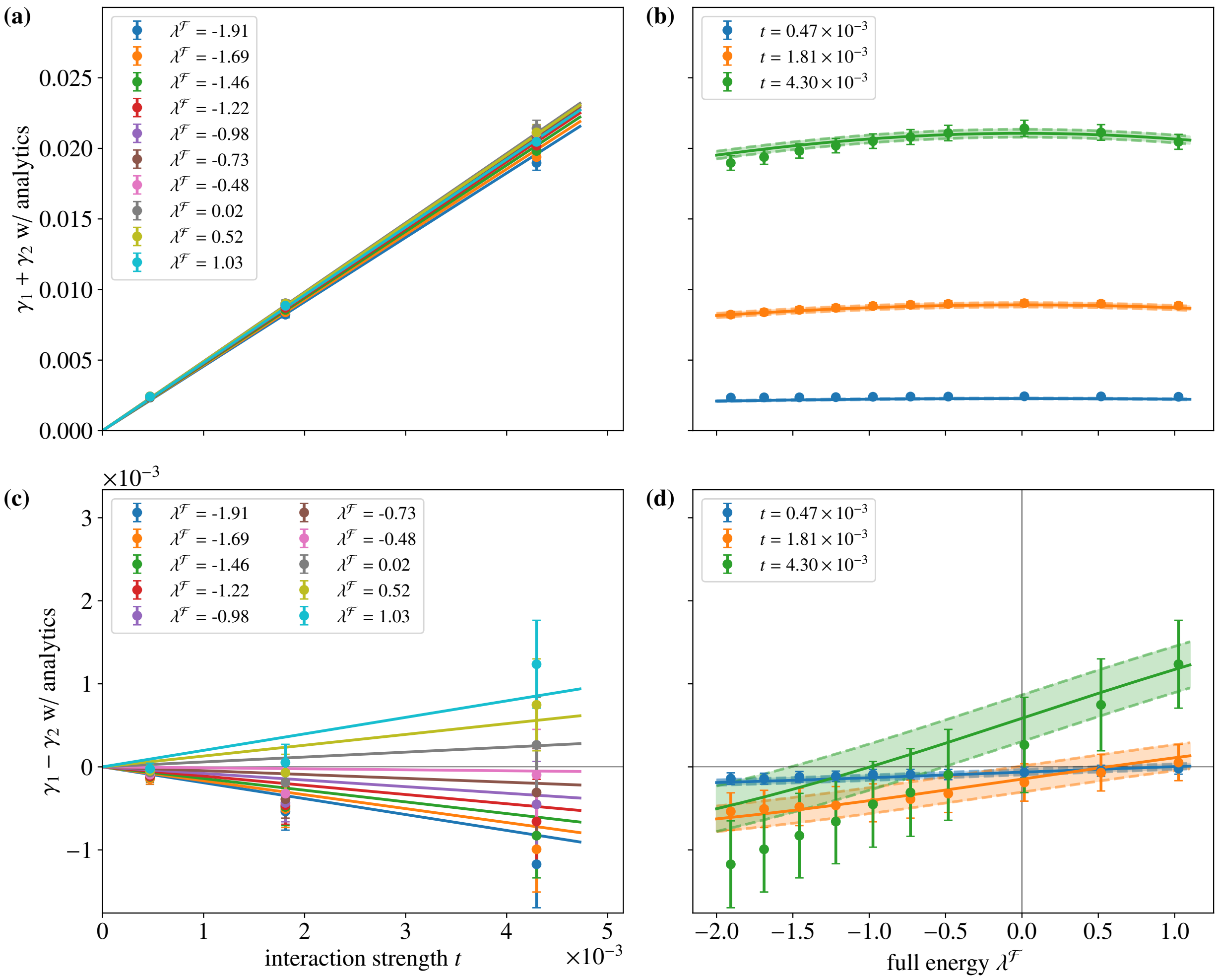

Figure 4.28: Lorentzian widths γ_μ in the multi peak model with $d_{\mathcal{B}} = 15$ and $d_{\mathcal{S}} = 1$ obtained from fits to the overlaps $\left|\langle\psi_\mu^{\mathcal{S}}|\,\langle\psi_i^{\mathcal{B}}|\psi_l^{\mathcal{F}}\rangle\right|^2$ close to their respective peaks for $\mu = 1, 2$ and three different values of t. An analysis of the corresponding perturbation matrix $\tilde{X}$ is shown in Fig. 4.23-4.27. The numerical overlap data is obtained from averaging over $N_{\mathrm{av}} = 400$ eigenstates of $H^{\mathcal{F}}$ in intervals around the desired full energies λ_l. The Lorentzian fit parameters γ_μ for $\mu = (1, 2)$ are averaged over 200 samples of X and 100 samples of $H^{\mathcal{B}}$. **(a)** and **(c)** show $\gamma_1 + \gamma_2$ and $\gamma_1 - \gamma_2$ depending on the perturbation strength t of X, while **(b)** and **(d)** show them with respect to the eigenenergy λ_l of the full quantum state. In all plots, we show the analytical results of Eq. (4.74a) as a joint line, while in **(b)** and **(d)**, margins of error of the analytical calculation are added, which are computed from the errors of the numerical fit parameters inserted into (4.74a).

width being proportional to the product of the DOS of $\mathcal{B}$ and the variance model, $N_{\mathcal{B}}\rho_{\mathcal{B}}(E_j)\sigma^2_{\mathrm{od}}(E_i, E_j)$ evaluated at the Lorentzian peak position. This product decreases with the exponential $e^{-\bar{b}_0^2}$, which comes from the normalization condition of the variance model in each row. Since the Lorentzian peak positions for each μ are located close to $E_i \approx \lambda_l - \epsilon_\mu$, their order in terms of the bath energy E_i is reversed as compared to the eigenenergy order of ϵ_μ in $\mathcal{S}$. In the present case with $N_{\mathcal{S}} = 2$, this means that for $\lambda_l < 0$, the overlap peak for $\mu = 1$ is closer to zero energy in $\mathcal{B}$ than the peak for $\mu = 2$, while for $\lambda_l > 0$ it is reversed. As a consequence, this effect causes $\gamma_1^{(l)}$ to be larger than $\gamma_2^{(l)}$ for $\lambda_l < 0$ and smaller for $\lambda_l > 0$. Second, there is an interaction between the Lorentzians due to the offdiagonal blocks in $\tilde{X}$, which mediate a scattering between different states in $\mathcal{S}$. Since the DOS of the bath is different at the two Lorentzian positions, the scattering between them has an unequal effect on their widths. The Lorentzian with the smaller associated DOS in $\mathcal{B}$ is broadened, while the other is narrowed. Opposed to the first effect, this causes $\gamma_2^{(l)}$ to be larger than $\gamma_1^{(l)}$ for $\lambda_l < 0$ and vice versa for $\lambda_l > 0$, since the Lorentzian located closer to zero in terms of E_i corresponds to a larger DOS in $\mathcal{B}$. While the second effect is larger than the first overall leading to $\gamma_1^{(l)} - \gamma_2^{(l)} < 0$ for $\lambda_l < 0$ and $\gamma_1^{(l)} - \gamma_2^{(l)} > 0$ for $\lambda_l > 0$, both terms are proportional to $\epsilon_1 - \epsilon_2$ and therefore much smaller than the sum of the widths $\gamma_1^{(l)} + \gamma_2^{(l)}$. Being proportional to (βt), the difference of the Lorentzian widths has a similar dependence as the single peak shift $\eta^{(l)}$ with an additional scaling by ϵ_{12}. From the plots in Fig. 4.28**c,d**, we find, that the analytical results for $\gamma_1^{(l)} - \gamma_2^{(l)}$ agree with the numerics. We additionally note that $\gamma_1^{(l)} - \gamma_2^{(l)}$ is one order of magnitude smaller than $\gamma_1^{(l)} + \gamma_2^{(l)}$ demonstrating that the scattering between the Lorentzians is only a small effect due to ϵ_{12} being small.

In Fig. 4.29, we plot the sum and difference of the shifts $\eta_1^{(l)}$ and $\eta_2^{(l)}$ of the Lorentzian fits for the overlap curve of $\mu = 1$ and $\mu = 2$ in the multi peak model. Analogous to the procedure in the single peak model described in Sec. 4.3.2, the bare values of the shifts are corrected by the value of the trace of $\tilde{X}$ close to the respective Lorentzian peak position in $\mathcal{B}$. As discussed in Sec. 3.1.4, the nonlocal trace in $\tilde{X}$ originates from a correlation of its diagonal elements to the eigenvalue E_i of $H^{\mathcal{B}}$. The trace shift occurring due to the trace being nonzero locally is therefore not contained in the final numerical results. In Fig. 4.29**a,c** they are shown with respect to the variance t of the perturbation matrix X, while in Fig. 4.29**b,d** their dependence on the eigenenergy λ_l of the full quantum state is shown. We additionally plot the analytical results from Eq. (4.74b) in Fig. 4.29**b,d**, which are obtained from the numerical model of the offdiagonal variance. The parameters of this model are taken from best fit values to the numerical variance data of $\tilde{X}$, whose errors produce a corresponding margin of error of the analytical values. As with the widths, we estimate the analytical dependencies of the shifts by employing the result of the mathematical model in Eq. (4.72b), which is expanded in first order of ϵ_μ and second order of λ_l,

$$\eta_1^{(l)} + \eta_2^{(l)} \approx t\,\frac{\overline{\Delta}_0}{{\Delta_0'}^2}\,(2\bar{b}_0) + t\,\frac{\sigma_2^2}{\sigma_{\mathcal{B}}^2}\lambda_l = 2\,\eta^{(l)} + t\,\frac{\sigma_2^2}{\sigma_{\mathcal{B}}^2}\lambda_l, \tag{4.76a}$$

$$\eta_1^{(l)} - \eta_2^{(l)} \approx -\frac{t}{2\Delta_0}\left(\frac{\overline{\Delta}_0}{\Delta_0'}\right)^2\left(1 - 2\bar{b}_0^2\left(\frac{\Delta_0}{\Delta_0'}\right)^2\right)\frac{\epsilon_{12}}{\Delta_0} - \frac{(\sigma_1^2 + \sigma_2^2\,\frac{\lambda_l^2}{\sigma_{\mathcal{B}}^2})\,t}{\epsilon_{12}}. \tag{4.76b}$$

In contrast to the widths, the result for the shifts contains a contribution from the diagonal term of the offdiagonal block of the variance model, which mediates an additional interaction between the Lorentzians and was computed in Sec. 4.4.1. The mean of the shifts $\eta_1^{(l)}$ and $\eta_2^{(l)}$ in this expansion is given by the the single peak shift $\eta^{(l)}$ and a much smaller term added to it, which results from the diagonal of the offdiagonal variance block. In Fig. 4.29**a**, we confirm that the sum of the Lorentzian shifts for the considered values of t is approximately proportional to t, while we show in Fig. 4.29**b**, that the numerical and analytical results agree. Both plots are very similar to the plots of $\eta^{(l)}$ in the single peak model, which illustrates that $\eta_1^{(l)} + \eta_2^{(l)} \approx 2\,\eta^{(l)}$. The base contribution to each shift $\eta_\mu^{(l)}$ is hence mainly given by the thermal shift known from the single peak model. The first term in (4.76b) in the difference $\eta_{\mu\nu}^{(l)} = \eta_1^{(l)} - \eta_2^{(l)}$ has a similar shape as the single peak result of the width $\gamma^{(l)}$ with an additional proportionality to ϵ_{12}, while the second term is inversely proportional to ϵ_{12}. While $\eta_{\mu\nu}^{(l)} > 0$ corresponds to an increased distance between the Lorentzians and therefore a repulsion, $\eta_{\mu\nu}^{(l)} < 0$ is associated with an attraction of the Lorentzians. Overall, the Lorentzians repulse each other as visible in Fig. 4.29**c,d** compared to their expected positions from the single peak model. There are in total three contributions to $\eta_{\mu\nu}^{(l)}$. First, with $\epsilon_{12} \neq 0$, the Lorentzian for $\mu = 1$ is located at larger bath energies $E_i \approx \lambda_l - \epsilon_1$ than that for $\mu = 2$ with $E_i \approx \lambda_l - \epsilon_2$. This effectively reduces η_1 and increases η_2 as read off from the single peak result of $\eta^{(l)}$ leading to a small attraction of the peaks. Second, the offdiagonal variance on the

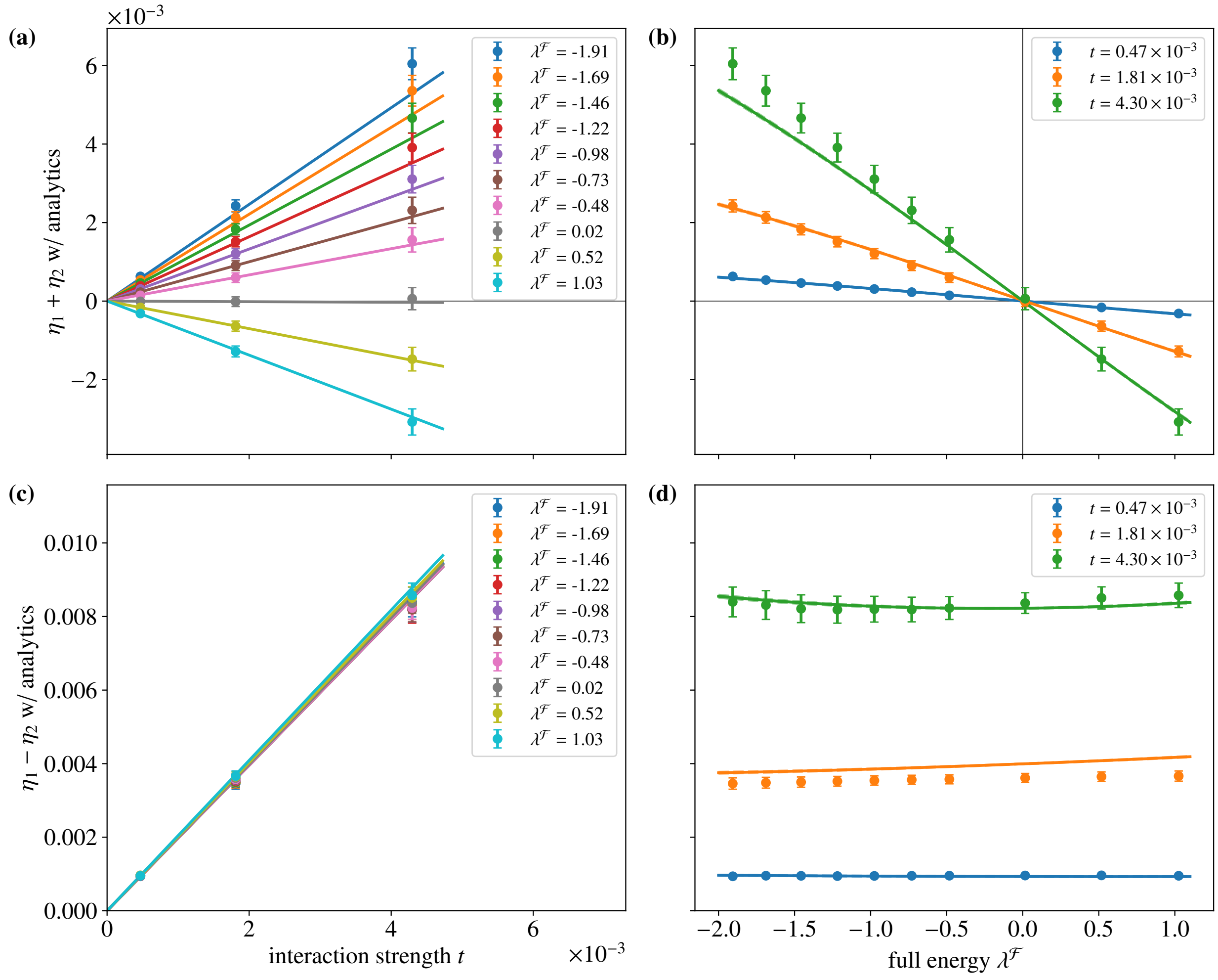

Figure 4.29: Lorentzian shifts η_μ in the multi peak model with $d_{\mathcal{B}} = 15$ and $d_{\mathcal{S}} = 1$ obtained from fits to the overlaps $\left|\langle\psi^{\mathcal{S}}_\mu|\,\langle\psi^{\mathcal{B}}_i|\psi^{\mathcal{F}}_l\rangle\right|^2$ close to their respective peaks for $\mu = 1, 2$ and three different values of t. An analysis of the corresponding perturbation matrix $\tilde{X}$ is shown in Fig. 4.23-4.27. The numerical overlap data is obtained from averaging over $N_{\text{av}} = 400$ eigenstates of $H^{\mathcal{F}}$ in intervals around the desired full energies λ_l. From the raw data of the shifts, we subtract the contribution from the nonzero local trace of $\tilde{X}$. The resulting Lorentzian fit parameters η_μ for $\mu = (1, 2)$ are averaged over 200 samples of X and 100 samples of $H^{\mathcal{B}}$. **(a)** and **(c)** show $\eta_1 + \eta_2$ and $\eta_1 - \eta_2$ depending on the perturbation strength t of X, while **(b)** and **(d)** show them with respect to the eigenenergy λ_l of the full quantum state. In all plots, we show the analytical results of Eq. (4.74b) as a joint line, while in **(b)** and **(d)**, additional margins of error of the analytical calculation are added, which are computed from the errors of the numerical fit parameters inserted into (4.74b).

offdiagonal blocks of the variance model of $\tilde{X}$ introduces an interaction between the two Lorentzians. This scattering leads to a repulsive effect between the Lorentzians labeled as *interaction shift*, which is conceptually similar to the level repulsion in RMT. The third contribution is called *overlap shift* and results from the finite diagonal variance $\sigma_{\text{d},\mu\nu}$ for $\mu \neq \nu$ in the offdiagonal blocks of $\tilde{X}$. The finite extent of the real part of the resolvents results in a repulsion, which is proportional to the value of the resolvent at the position of the other Lorentzian peak. Since the peak distance is given by ϵ_{12} and the resolvent in appropriately chosen variables is proportional to $\frac{1}{z}$, the overall repulsion is proportional to $\frac{1}{\epsilon_{12}}$. This is the strongest effect of the three, since ϵ_{12} is small. It is evident in Fig. 4.29**c,d**, where

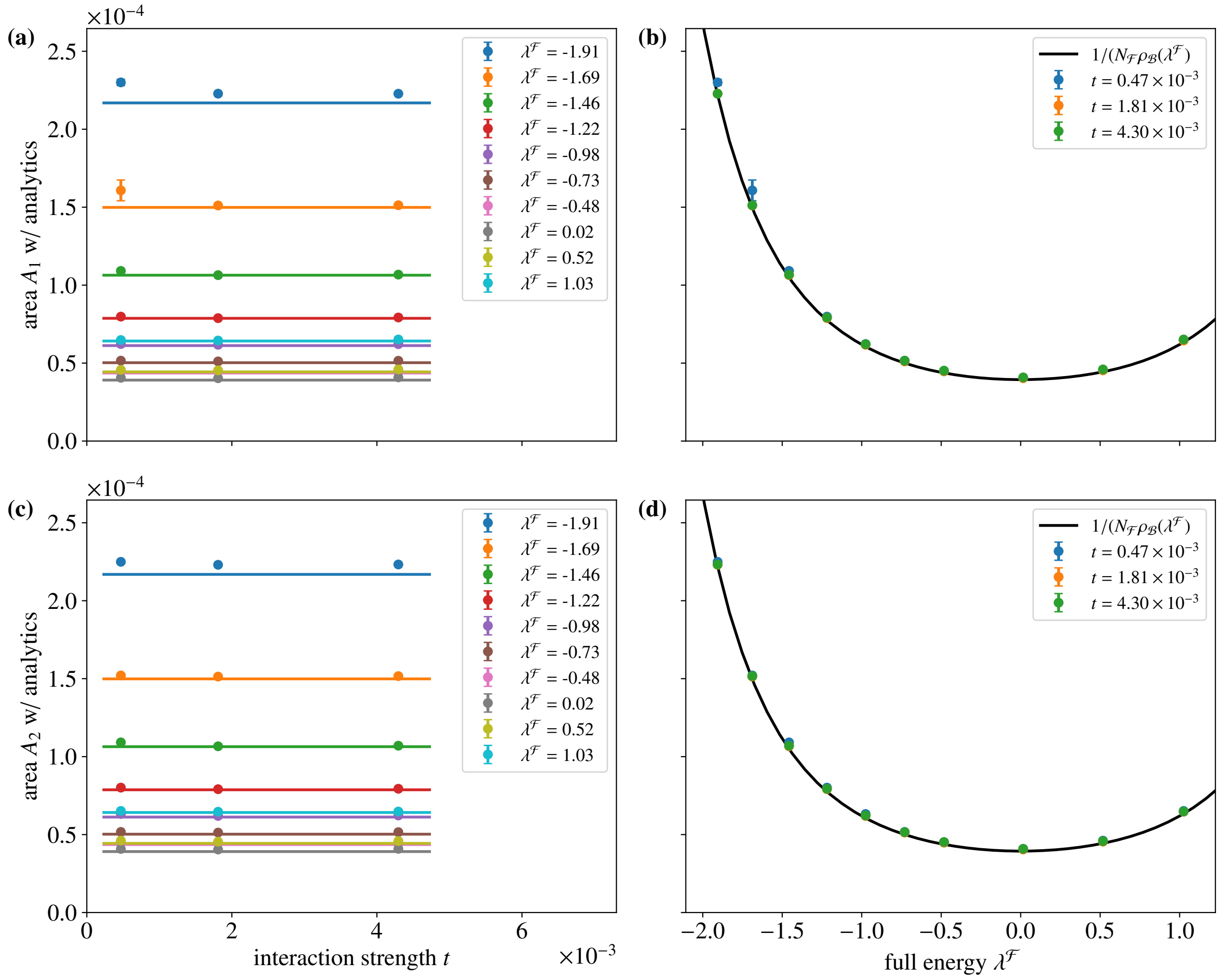

Figure 4.30: Lorentzian area A_μ in the multi peak model with $d_{\mathcal{B}} = 15$ and $d_{\mathcal{S}} = 1$ obtained from fits to the overlaps $\left|\langle\psi_\mu^{\mathcal{S}}|\,\langle\psi_i^{\mathcal{B}}|\psi_l^{\mathcal{F}}\rangle\right|^2$ close to their respective peaks for $\mu = 1, 2$ and three different values of t. An analysis of the corresponding perturbation matrix $\tilde{X}$ is shown in Fig. 4.23-4.27. The numerical overlap data is obtained from averaging over $N_{\mathrm{av}} = 400$ eigenstates of $H^{\mathcal{F}}$ in intervals around the desired full energies λ_l. The Lorentzian fit parameter A is then averaged over 200 samples of X and 100 samples of $H^{\mathcal{B}}$. In **(a)** and **(c)**, we plot A_1 and A_2 with respect to the perturbation strength t of X and in **(b)** and **(d)** the same values with respect to the eigenenergy λ_l of the full quantum state. In **(a)** and **(c)**, we additionally show the inverse value of the Gaussian fit of the DOS of $\mathcal{B}$ multiplied by $N_{\mathcal{S}}$ evaluated at the full energy λ_l. In **(b)** and **(d)**, we plot the inverse of the numerical DOS of the bath $\mathcal{B}$ at λ_l multiplied by $N_{\mathcal{S}}$.

we notice that $\eta_1^{(l)} - \eta_2^{(l)}$ is positive and overall larger than $\eta_1^{(l)} + \eta_2^{(l)}$, which highlights the strong repulsion between the Lorentzians resulting from the offdiagonal blocks in $\tilde{X}$. This result is in stark contrast to the widths in the multi peak model, where opposing narrowing and broadening effects balance each other out for small ϵ_{12} leading to a difference in widths $\gamma_1^{(l)} - \gamma_2^{(l)}$, which is much smaller than the base contribution of their sum $\gamma_1^{(l)} + \gamma_2^{(l)}$.

In Fig. 4.30, we show the areas A_1 and A_2 of the two Lorentzians being resolved with respect to t in Fig. 4.30**a,c** and with respect to λ_l in Fig. 4.30**b,d**. In the latter plots, the data points for the area are compared to the inverse numerically obtained DOS of $\mathcal{B}$ multiplied with $N_{\mathcal{S}}$ to obtain an estimate of the full perturbed DOS $N_{\mathcal{F}}\rho_{\mathcal{F}}(\lambda)$, which

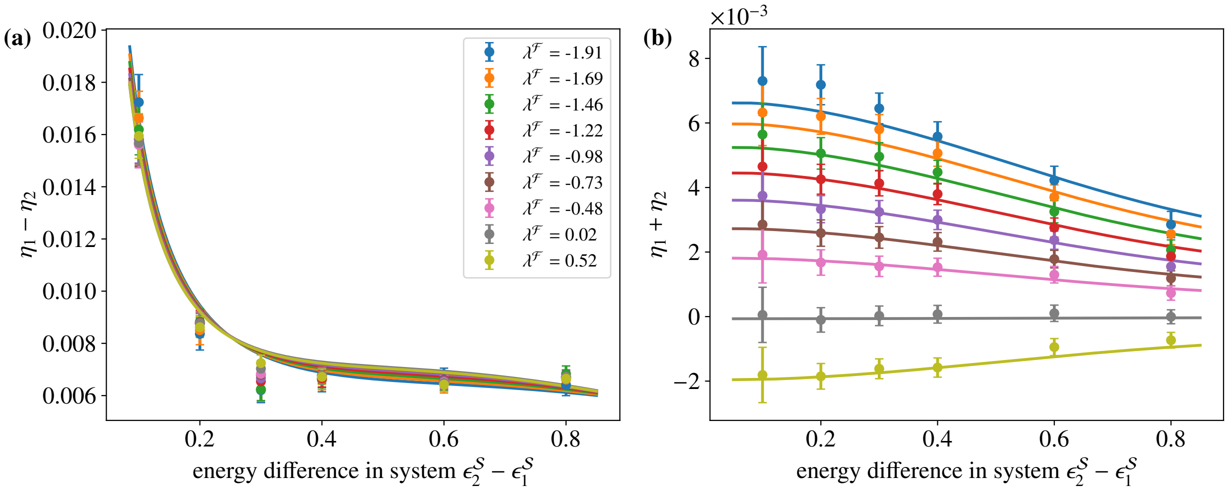

Figure 4.31: Analysis of the behavior of the shifts η_μ in the multi peak model for $d_{\mathcal{B}} = 12$ and $d_{\mathcal{S}} = 1$ sites with respect to the energy spacing $|\epsilon_{12}| = \epsilon_2 - \epsilon_1$ in the small subsystem $\mathcal{S}$. The variance of the interaction matrix X between $\mathcal{S}$ and $\mathcal{B}$ is $t = 4.79 \times 10^{-3}$. The numerical overlap data is obtained from averaging over $N_{\text{av}} = 100$ eigenstates of $H^{\mathcal{F}}$ in intervals around the desired full energies λ_l. The Lorentzian fit parameters for η are averaged over 100 samples of X and 50 samples of $H^{\mathcal{B}}$. In (**a**), we plot the difference $\eta_1 - \eta_2$, while (**b**) shows the sum $\eta_1 + \eta_2$. In both plots, the analytical formula in Eq. (4.74b) is shown as a joined line for comparison. We consider the same values for the full energy λ_l as in Sec. 4.4.2.

holds approximately with $\sigma_{\mathcal{F}}^2 = \sigma_{\mathcal{B}}^2 + \sigma_{\mathcal{S}}^2 + t$ and $\sigma_{\mathcal{S}}^2 = 10^{-2} \ll \sigma_{\mathcal{B}}^2$ as well as $t \sim 10^{-3} \ll \sigma_{\mathcal{B}}^2$. We add the expected area of the Gaussian fit of the DOS of $\mathcal{B}$ as horizontal lines in Fig. 4.30**a,c**. We notice, that both plots for A_1 and for A_2 are very similar to the area plot in the single peak model. The standard error of the data is much smaller than that of the widths and shifts, signifying higher numerical precision of the area parameter. Moreover, both areas A_1 and A_2 agree with the inverse numerical DOS, which implies that the Lorentzian area is accurately described by the inverse DOS of the full quantum system. As A is a prefactor to the Lorentzian, this dependence causes each point in the overlap curves to scale with $\frac{1}{N_{\mathcal{F}}}$ as mathematically expected and shown in Fig. 4.9 in Sec. 4.1. This means, that the areas A_1 and A_2 also agree with each other.

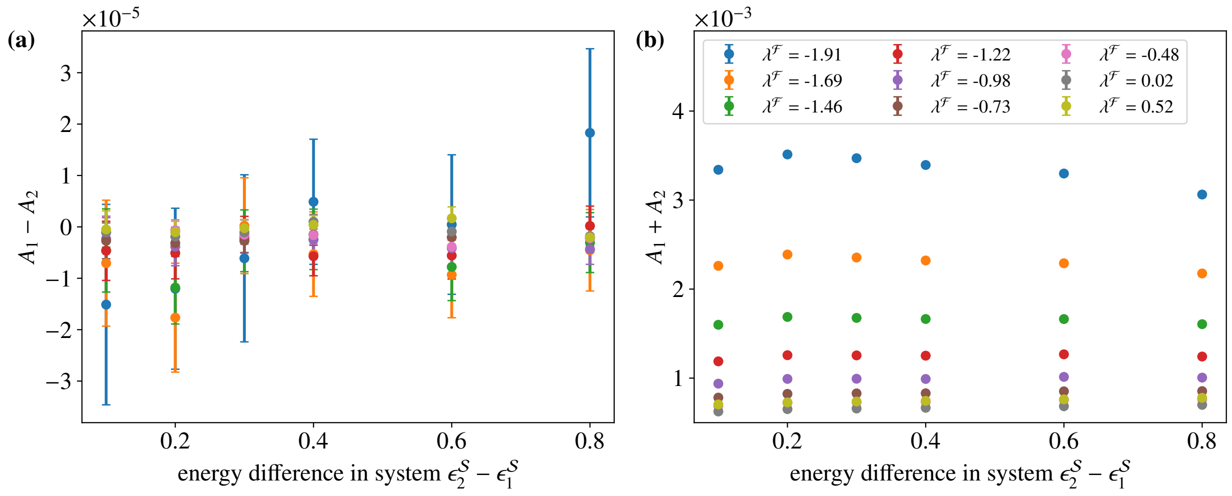

Figure 4.32: Plot of the difference and sum of areas A_μ in the multi peak model for $d_\mathcal{B} = 12$ and $d_\mathcal{S} = 1$ sites with $t = 4.79 \times 10^{-3}$, resolved with respect to the energy spacing $|\epsilon_{12}| = \epsilon_2 - \epsilon_1$ in the small subsystem $\mathcal{S}$. The numerical overlap data is obtained from averaging over $N_\mathrm{av} = 100$ eigenstates of $H^\mathcal{F}$ in intervals around the desired full energies λ_l. The fit parameters A_μ are averaged over 100 samples of X and 50 samples of $H^\mathcal{B}$. **(a)** shows the difference $A_1 - A_2$ and **(b)** the sum $A_1 + A_2$ for the same values of λ_l as in Sec. 4.4.2.

4.4.3 Influence of overlap distance

As we saw in Sec. 4.4.2, the Lorentzian widths and the shifts depend on the distance of the overlap peaks, which is approximately given by $|\epsilon_{12}| = |\epsilon_1 - \epsilon_2|$ for the considered system with $N_\mathcal{S} = 2$. Most prominently, this is expressed in the difference of the shifts $\eta_1^{(l)} - \eta_2^{(l)}$ in the expansion in Eq. (4.76b), which contains one term directly proportional to ϵ_{12} and one inversely proportional to ϵ_{12}. The latter originates from the variance of the diagonal entries on the offdiagonal blocks of $\tilde{X}$. For this point, it is crucial that the diagonal variance in each block of $\tilde{X}$ does not scale with $\frac{1}{N_\mathcal{B}}$ as the variance of each offdiagonal element does. This means that for large $N_\mathcal{B}$, the variance on the diagonal is much larger than each individual offdiagonal variance, while the latter give a significant contribution in a sum over one row. In such a system, the individual diagonal variances in all blocks of $\tilde{X}$ are the only ones that cannot be treated as a null set for $N_\mathcal{B} \to \infty$.

In Fig. 4.31, we resolve the sum and difference of the shifts $\eta_1^{(l)}$ and $\eta_2^{(l)}$ with respect to the energy difference $|\epsilon_{12}| = -\epsilon_{12} = \epsilon_2 - \epsilon_1$ with ϵ_1 being the lower state energy. The numerical values are compared to the analytical results in (4.74b) obtained from the variance model adjusted to its numerical shape with the additional peak at zero discussed in Sec. 4.4.1. The final data for the shifts is obtained for a system with a total of $d_\mathcal{F} = 13$ sites, of which one site on the corner of the lattice is subsystem $\mathcal{S}$. The perturbation strength is $t = 4.79 \times 10^{-3}$. To obtain the Lorentzian parameters from the fits, we average $N_\mathrm{av} = 100$ states in an interval around the full energy λ_l, while the parameters are additionally averaged over 100 samples of X and 50 samples of $H^\mathcal{B}$. For each investigated value of ϵ_{12}, the subsystem Hamiltonian H^S is constant, as we only average over the randomness in X and $H^\mathcal{B}$. In Fig. 4.31**a**, we observe the strong dependence of $\eta_1^{(l)} - \eta_2^{(l)}$ on $\frac{1}{|\epsilon_{12}|}$ towards zero $|\epsilon_{12}|$, which translates to a stronger repulsion of the Lorentzians originating from their interaction mediated by the offdiagonal variance blocks. The analytical calculation correctly predicts the general dependence on $|\epsilon_{12}|$, while the numerical data suggests a slightly stronger divergence for $|\epsilon_{12}| \to 0$, which is not captured in the first resolvent iteration. In Fig. 4.31**a**, we show the numerical values for $\eta_1^{(l)} - \eta_2^{(l)}$ which, within their error, agree to the analytical results. There is a small dependence on $|\epsilon_{12}|$, which is of higher order than one, since it does not appear in the expansion in (4.76b).

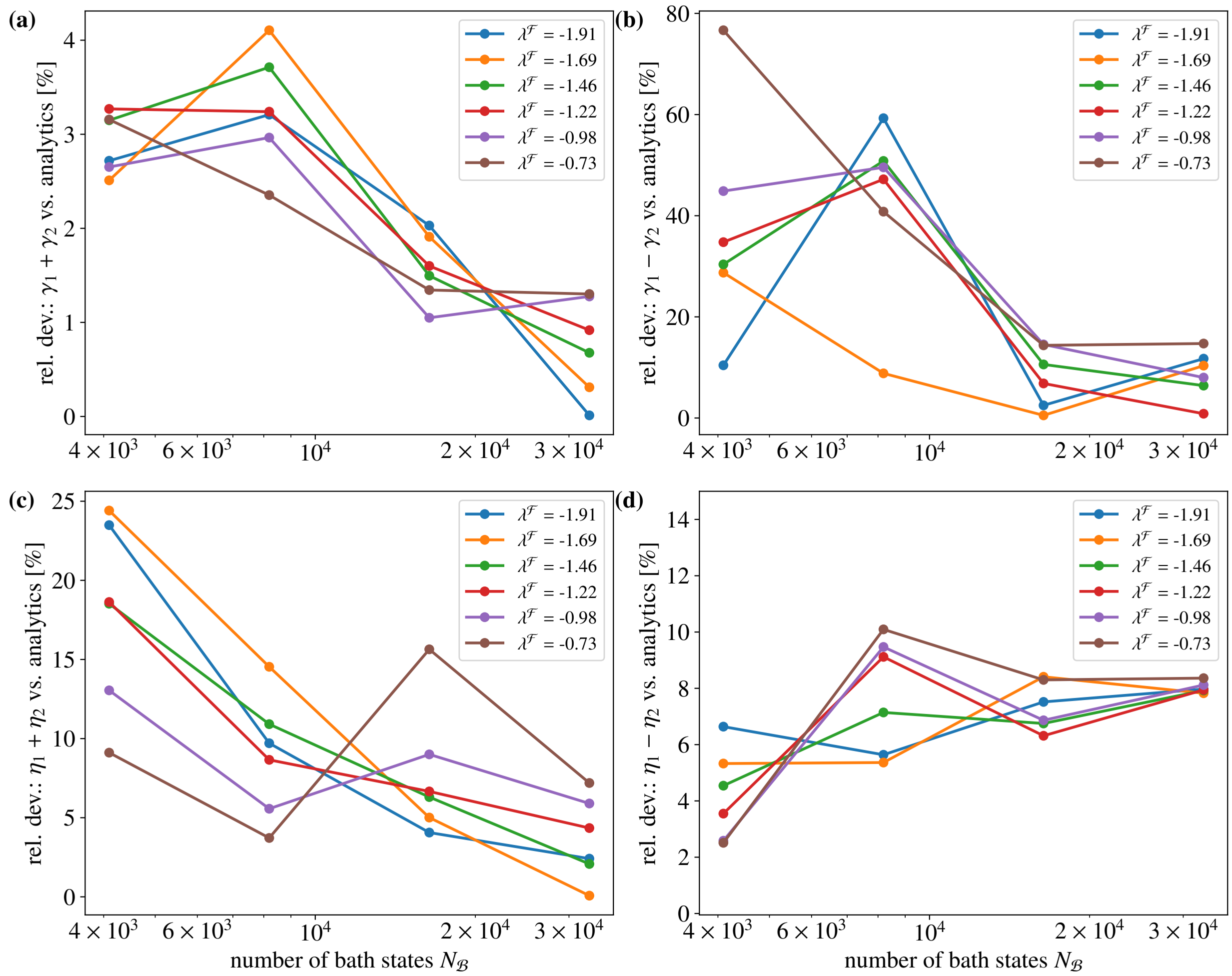

Figure 4.33: Finite size study of the width γ_μ and shift η_μ in the multi peak model plotted with respect to the number of bath states $N_{\mathcal{B}}$ on a logarithmic scale. We choose $d_{\mathcal{B}} = \{12, 13, 14, 15\}$ for the analysis, which corresponds to $t = \{5.7, 5.8, 4.3, 4.7\} \times 10^{-4}$ and $N_{\text{av}} = \{50, 100, 200, 400\}$ full states, which are taken into account for the average of the final overlap curve. We show the relative deviation in percent of the numerical values to the analytical calculation of **(a)** $\gamma_1 + \gamma_2$ to Eq. (4.74a), **(b)** $\gamma_1 - \gamma_2$ to Eq. (4.74a), **(c)** $\eta_1 + \eta_2$ to Eq. (4.74b) and **(d)** $\eta_1 - \eta_2$ to Eq. (4.74b). As a guide to the eye, the individual data points are connected by straight lines.

Fig. 4.32 shows the sum and difference of the Lorentzian areas A_1 and A_2 on $|\epsilon_{12}|$. We observe, that the difference $A_1 - A_2$ in Fig. 4.32**a** is much smaller than the sum $A_1 + A_2$ in Fig. 4.32**b** and within their errors, it holds that $A_1 - A_2 = 0$. This numerical data supports the previous statement, that the areas of the two Lorentzians are equal. It is an important piece of the derivation of the thermal distribution in subsystem $\mathcal{S}$, which is considered in Sec. 5.2.2.

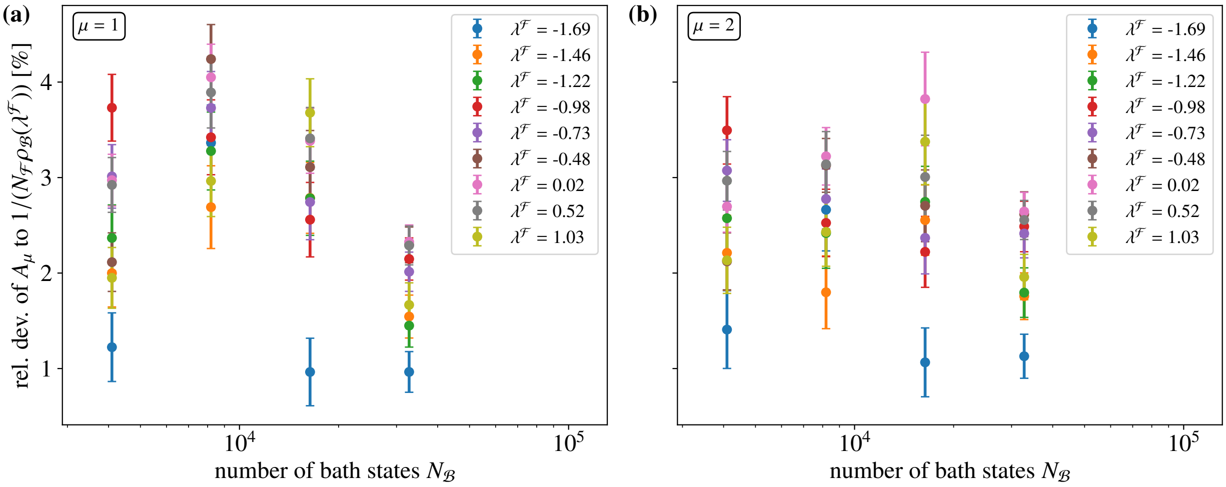

Figure 4.34: Finite size analysis of the Lorentzian areas $A_\mu, \mu = 1, 2$ in the multi peak model plotted with respect to the number of bath states $N_\mathcal{B}$ on a logarithmic scale. The plot depicts the relative deviation of A_μ to the inverse numerically obtained DOS of $\mathcal{B}$, multiplied with $N_\mathcal{S}$ to get an estimate of the full DOS and evaluated at the full energy λ_l. We choose $d_\mathcal{B} = \{12, 13, 14, 15\}$ for the analysis, which corresponds to $t = \{5.7, 5.8, 4.3, 4.7\} \times 10^{-4}$ and $N_\text{av} = \{50, 100, 200, 400\}$ full states averaged over for the final overlap curve. **(a)** shows the analysis of the area A_1 and **(b)** that of A_2.

4.4.4 Finite size effects

Similar to the single peak model, we look at finite size effects, that are introduced due to the finite sized lattice of the bath. We analyze the overlap curves for $\mu = 1$ and $\mu = 2$ in subsystem $\mathcal{S}$ coupled to a bath of $d_\mathcal{B} = \{12, 13, 14, 15\}$ sites. We use $t = \{5.7, 5.8, 4.3, 4.7\} \times 10^{-4}$, $N_\text{av} = \{50, 100, 200, 400\}$ respectively and average over 200 samples of X and 100 samples of $H^\mathcal{B}$. We investigate the difference and sum of the widths $\gamma_1^{(l)}$ and $\gamma_2^{(l)}$ as well as the shifts $\eta_1^{(l)}$ and $\eta_2^{(l)}$ in the multi peak model. In Fig. 4.33, we show the relative deviation of those values compared to the analytical results in Eq. (4.74a,b), which are obtained in the limit $N_\mathcal{B} \to \infty$. We plot the same points in the energy λ_l of the full quantum system as in the detailed analysis of $d_\mathcal{B} = 15$ sites, but restricted to $\lambda_l < -0.5$.

For the sum and difference of γ in Fig. 4.33**a,b**, we notice a clear trend towards stronger agreement of numerical and analytical results with increasing bath size $d_\mathcal{B}$, which is even more pronounced for larger $|\lambda_l|$. The relative deviation of the difference in Fig. 4.33**b** is overall much larger than that of the sum in Fig. 4.33**a**, which is explained by the fact, that the absolute values of the difference are more than one order of magnitude smaller than those of the sum. The numerical precision therefore leads to a much larger relative error of both the numerical and analytical values for $\gamma_1^{(l)} - \gamma_2^{(l)}$, the latter being calculated upon insertion of the numerical best fit parameters of the variance model. The relative deviation of the sum and difference of η in Fig. 4.33**c,d** also becomes smaller for larger baths, while the trend towards smaller deviation is not as pronounced with it being already less than 20% for 12 sites in $\mathcal{B}$.

In Fig. 4.34, we plot the deviation of the area of the overlap A_1 and A_2 relative to the DOS of $\mathcal{B}$ multiplied by the Hilbert space dimension of $\mathcal{S}$ giving $N_\mathcal{F}\rho_\mathcal{B}(E)$. It is chosen as an approximation to the full DOS, which is not available numerically. We notice, that the relative deviation of the area to the analytically predicted value is much smaller than that of the width or the shift. This indicates, that the area of each individual overlap curve in both the single and multi peak model is accurately captured by the inverse DOS of the perturbed full quantum system. In Sec. 4.4.3, we further noted, that the areas A_1 and A_2 agree with each other within the scope of their errors, which is the one the most precise and important statements of the numerical analysis of the overlap curves.

Theory of eigenstate thermalization

5.1 Reduced density matrix

The final goal of the analysis of thermalization concerns the reduced density matrix in a small subsystem of the isolated quantum system. The eigenstate thermalization hypothesis (ETH) involves the expectation value of local operators A in a quantum state which converge to their thermal expectation value at large times described by a canonical ensemble. For this, the ETH conjectures that each single eigenstate behaves thermally. Since we deal with local operators A, our approach directly investigates the reduced density matrix in the subsystem where A acts, which is obtained from a single eigenstate of the quantum system. Utilizing the results of the overlap curves from chapter 4, we derive that the reduced density matrix converges to a thermal density matrix for the single quantum eigenstate in the thermodynamic limit, which proves the ETH. The result is compared to numerical studies, which confirm that the offdiagonal entries of the reduced density matrix exponentially decrease with the number of lattice sites in the system.

5.1.1 Analytic evaluation

In the following, we consider the properties of a small subsystem of a single eigenstate of the full quantum system $\mathcal{F}$. The expectation value of any observable A in the quantum state $|\psi_l^{\mathcal{F}}\rangle$ can be computed in terms of the pure density matrix

$$\rho^l = |\psi_l^{\mathcal{F}}\rangle \langle\psi_l^{\mathcal{F}}| \tag{5.1}$$

by taking the trace, $\langle\psi_l^{\mathcal{F}}|A|\psi_l^{\mathcal{F}}\rangle = \mathrm{Tr}\left(A\rho^l\right)$. If $A = A_{\mathcal{S}} \otimes \mathbb{1}_{\mathcal{B}}$ is a local operator, which acts non-trivially only on the small subsystem $\mathcal{S}$ with $A_{\mathcal{S}}$, we can reduce the expectation value to a trace over $\mathcal{S}$ with

$$\langle\psi_l^{\mathcal{F}}|A_{\mathcal{S}} \otimes \mathbb{1}_{\mathcal{B}}|\psi_l^{\mathcal{F}}\rangle = \mathrm{Tr}_{\mathcal{S}}\left(A_{\mathcal{S}}\rho^{l,\mathcal{S}}\right), \tag{5.2}$$

where $\rho^{l,\mathcal{S}}$ denotes the reduced density matrix in terms of the subsystem $\mathcal{S}$ by taking the trace over the bath $\mathcal{B}$,

$$\rho^{l,\mathcal{S}} = \mathrm{Tr}_{\mathcal{B}}\left(\rho^l\right). \tag{5.3}$$

The reduced density matrix therefore describes the properties of the full eigenstate $|\psi_l^{\mathcal{F}}\rangle$ within subsystem $\mathcal{S}$. We denote the unperturbed product basis of $\mathcal{S}$ and $\mathcal{B}$ by $|\psi_{\mu i}\rangle \equiv |\psi_\mu^{\mathcal{S}}\rangle \otimes |\psi_i^{\mathcal{B}}\rangle$ and compute the reduced density matrix in

$\mathcal{S}$ as

$$\begin{aligned}\rho^{l,\mathcal{S}} &= \sum_{\mu,\nu}\sum_{i,j}\mathrm{Tr}_{\mathcal{B}}\left(|\psi_{\mu i}\rangle\langle\psi_{\mu i}|\psi_l^{\mathcal{F}}\rangle\langle\psi_l^{\mathcal{F}}|\psi_{\nu j}\rangle\langle\psi_{\nu j}|\right)\\ &= \sum_{\mu,\nu}|\psi_\mu^{\mathcal{S}}\rangle\langle\psi_\nu^{\mathcal{S}}|\sum_i\left(\langle\psi_{\mu i}|\psi_l^{\mathcal{F}}\rangle\langle\psi_l^{\mathcal{F}}|\psi_{\nu i}\rangle\right)\\ &= \sum_{\mu,\nu}\rho_{\mu\nu}^{l,\mathcal{S}}|\psi_\mu^{\mathcal{S}}\rangle\langle\psi_\nu^{\mathcal{S}}|,\end{aligned} \tag{5.4}$$

where $\rho_{\mu\nu}^{l,\mathcal{S}}$ are the matrix elements of $\rho^{l,\mathcal{S}}$ in terms of the eigenbasis of $\mathcal{S}$. If we represent the full eigenstate in terms of the complete unperturbed basis of $\mathcal{S}$ and $\mathcal{B}$ as $|\psi_l^{\mathcal{F}}\rangle = \sum_{\mu i} c_{\mu i}^{(l)}|\psi_{\mu i}\rangle$ with coefficients $c_{\mu i}^{(l)}$, the elements of the reduced density matrix are given by

$$\rho_{\mu\nu}^{l,\mathcal{S}} = \sum_i c_{\mu i}^{(l)} c_{\nu i}^{(l)*}. \tag{5.5}$$

The coefficients connect to the overlaps in the multi peak model in chapter 4 through $\chi_{\mu i,l} = |c_{\mu i}^{(l)}|^2 = |\langle\psi_{\mu i}|\psi_l^{\mathcal{F}}\rangle|^2$. We analyze the diagonal and offdiagonal elements of $\rho^{l,\mathcal{S}}$ separately in the following.

The offdiagonal entries are given in (5.5) for $\mu \neq \nu$ and their expectation value vanishes, $\mathbb{E}\left[\rho_{\mu\nu}^{l,\mathcal{S}}\right] = 0$, since the coefficients $c_{\mu i}^{(l)}$ have random phases as confirmed multiple times in chapters 3 and 4, e.g. in Fig. 4.8. The random phases average the result to zero. With random complex phases attached to the coefficients $c_{\mu i}^{(l)}$, the evaluation of an element $\rho_{\mu\nu}^{l,\mathcal{S}}$ for $\mu \neq \nu$ in (5.5) is mathematically equivalent to a random walk in two dimensions, since $c_{\mu i}^{(l)} \in \mathbb{C}$. Its expectation value is zero, but we can find the expected translation distance in the random walk. The coefficients are subject to the sum rule

$$\sum_{\mu,i}\left|c_{\mu i}^{(l)}\right|^2 = 1 = \sum_l\left|c_{\mu i}^{(l)}\right|^2 \tag{5.6}$$

derived from the normalization of the eigenstates $|\psi_l^{\mathcal{F}}\rangle$ and $|\psi_{\mu i}\rangle$. This property is regarded in Sec. 4.1.3, i.e. Fig. 4.8, where we show that the squared magnitude of the overlap scales inversely with the number of states, $\chi_{\mu i,l} \propto \frac{1}{N_{\mathcal{F}}}$. The coefficients therefore decrease with the square root of $N_{\mathcal{F}}$, $c_{\mu i}(l) \propto \frac{1}{\sqrt{N_{\mathcal{F}}}}$. We hence define the size invariant coefficients $\tilde{c}_{\mu i}^{(l)}$ through

$$c_{\mu i}^{(l)} = \frac{1}{\sqrt{N_{\mathcal{F}}}}\tilde{c}_{\mu i}^{(l)}, \tag{5.7}$$

which capture the overlap function and do not decrease with $N_{\mathcal{F}}$. Inserting this into (5.5) gives

$$\rho_{\mu\nu}^{l,\mathcal{S}} = \frac{1}{N_{\mathcal{F}}}\sum_{i=1}^{N_{\mathcal{B}}}\tilde{c}_{\mu i}^{(l)}\tilde{c}_{\nu i}^{(l)*}, \tag{5.8}$$

where the sum goes over all states i in the bath $\mathcal{B}$. To find the scaling of the absolute value $\left|\rho_{\mu\nu}^{l,\mathcal{S}}\right|$, we look at its expectation value

$$\mathbb{E}\left[\left|\rho_{\mu\nu}^{l,\mathcal{S}}\right|\right] = \frac{1}{N_{\mathcal{F}}}\mathbb{E}\left[\left|\sum_{i=1}^{N_{\mathcal{B}}} \tilde{c}_{\mu i}^{(l)}\, \tilde{c}_{\nu i}^{(l)*}\right|\right] \propto \frac{1}{\sqrt{N_{\mathcal{F}}}} \quad \text{for } \mu \neq \nu. \tag{5.9}$$

We assume, that the coefficients $\tilde{c}_{\mu i}^{(l)}$ and $\tilde{c}_{\nu i}^{(l)*}$ are uncorrelated for $\mu \neq \nu$. Then the problem is equivalent to finding the expected translation distance in a random two-dimensional walk with $N_{\mathcal{B}}$ steps due to the sum of $N_{\mathcal{B}}$ terms. This is of the order of square root of number of terms $\sqrt{N_{\mathcal{B}}}$, from which we obtain (5.9) for the scaling in terms of $N_{\mathcal{F}}$. The result can also be motivated by the second moment of $\left|\rho_{\mu\nu}^{l,\mathcal{S}}\right|$, which reads

$$\begin{aligned}
\mathbb{E}\left[\left|\rho_{\mu\nu}^{l,\mathcal{S}}\right|^2\right] &= \mathbb{E}\left[\sum_{i,j=1}^{N_{\mathcal{B}}} c_{\mu i}^{(l)}\, c_{\nu i}^{(l)*} c_{\mu j}^{(l)*}\, c_{\nu j}^{(l)}\right] \\
&= \sum_{i=1}^{N_{\mathcal{B}}} \mathbb{E}\left[\left|c_{\mu i}^{(l)}\right|^2 \left|c_{\nu i}^{(l)}\right|^2\right] = \sum_{i=1}^{N_{\mathcal{B}}} \underbrace{\mathbb{E}\left[\left|c_{\mu i}^{(l)}\right|^2\right]}_{=\mathcal{X}_{\mu i,l}} \underbrace{\mathbb{E}\left[\left|c_{\nu i}^{(l)}\right|^2\right]}_{=\mathcal{X}_{\nu i,l}} \\
&= \int_{-\infty}^{\infty} \mathrm{d}E\, \left(N_{\mathcal{B}}\rho_{\mathcal{B}}(E)\right) \mathcal{X}_{\mu}(E,\lambda_l)\, \mathcal{X}_{\nu}(E,\lambda_l).
\end{aligned} \tag{5.10}$$

In the first line, the only term which remains after taking the expectation value is the one where the complex phases cancel out and the coefficient combine to the absolute value, which is the case for $i = j$. For the other terms, the uniformly distributed random complex phases of the coefficients average the result to zero. In the second line, we assumed, that the coefficients for different μ, ν are uncorrelated by separating the expectation value into two terms. Those two terms are equal to the overlap curves $\mathcal{X}_{\mu i,l}$, which we convert to the continuum by substituting the sum over i with the integral over the energy in $\mathcal{B}$ with the corresponding DOS. To determine the scaling of the expression with system size, we approximate the overlap curves as

$$\mathcal{X}_{\mu}(E,\lambda_l) \approx \frac{1}{N_{\mathcal{F}}\rho_{\mathcal{F}}(\lambda_l)}\, f_{\mu}(E,\lambda_l) \tag{5.11}$$

with the normalization factor $\frac{1}{N_{\mathcal{F}}\rho_{\mathcal{F}}(\lambda_l)}$ and a normalized Lorentzian curve $f_{\mu}(E,\lambda_l)$. The normalization factor is present due to the sum rule of the coefficients in (5.7) and confirmed in an analysis in Sec. 4.4. As compared to the actual overlap, e.g. in (4.59) for the single peak model, we dropped the energy cutoff introduced by the locality of the perturbation matrix X. The additional factor due to the energy distribution of X in terms of the unperturbed eigenbasis would give a Gaussian, which further decreases the overlap between Lorentzians, but does not influence the scaling with $N_{\mathcal{F}}$. With this, we obtain

$$\mathbb{E}\left[\left|\rho_{\mu\nu}^{l,\mathcal{S}}\right|^2\right] = \frac{1}{N_{\mathcal{F}}}\underbrace{\frac{1}{N_{\mathcal{S}}}\int_{-\infty}^{\infty} \mathrm{d}E\, \rho_{\mathcal{B}}(E) f_{\mu}(E,\lambda_l)\, f_{\nu}(E,\lambda_l)}_{\substack{\text{depends on overlap of Lorentzians and on DOS,}\\ \text{but does not scale with } N_{\mathcal{F}}}} \propto \frac{1}{N_{\mathcal{F}}} \quad \text{for } \mu \neq \nu. \tag{5.12}$$

The second moment of an offdiagonal element of the absolute value of the reduced density matrix scales as $\frac{1}{N_{\mathcal{F}}}$, which implies the scaling of the root mean square and the expectation value

$$\sqrt{\mathbb{E}\left[\left|\rho_{\mu\nu}^{l,\mathcal{S}}\right|^2\right]} \propto \frac{1}{\sqrt{N_{\mathcal{F}}}} \quad \longrightarrow \quad \mathbb{E}\left[\left|\rho_{\mu\nu}^{l,\mathcal{S}}\right|\right] \propto \frac{1}{\sqrt{N_{\mathcal{F}}}} \quad \text{for } \mu \neq \nu, \tag{5.13}$$

as also argued above in Eq. (5.9).

The diagonal elements of the reduced density matrix $\mu = \nu$ are given by

$$\mathbb{E}\left[\rho^{l,\mathcal{S}}_{\mu\mu}\right] = \sum_{i=1}^{N_\mathcal{B}} \mathbb{E}\left[\left|c^{(l)}_{\mu i}\right|^2\right] = \sum_{i=1}^{N_\mathcal{B}} \mathcal{X}_{\mu i,l} = \frac{1}{N_\mathcal{F}\rho_\mathcal{F}(\lambda_l)} \int_{-\infty}^{\infty} \mathrm{d}E\,(N_\mathcal{B}\rho_\mathcal{B}(E))\, f_\mu(E,\lambda_l), \tag{5.14}$$

where we insert the form of the overlap from (5.11). For this, we assume, that the areas A_μ of all Lorentzian are identical and given by $A_\mu = \frac{1}{N_\mathcal{F}\rho_\mathcal{F}(\lambda_l)}$. This assumption is numerically verified in Sec. 4.4 and agrees very well with the numerical data. The function $f_\mu(E,\lambda_l)$ is a normalized Lorentzian centered around the energy $E = \lambda_l - \epsilon^\mathcal{S}_\mu + \eta^{(l)}_\mu$ with the shift $\eta^{(l)}_\mu$. The width of the Lorentzian is much smaller than that of the Gaussian DOS of the bath, $\gamma^{(l)}_\mu \ll \sigma_\mathcal{B}$. Even more, $\gamma^{(l)}_\mu$ is approximately proportional to the perturbation strength, which is the variance t of the matrix X and stays constant with system size, while the spectral variance in $\mathcal{B}$ scales with the number of sites in the bath, $\sigma^2_\mathcal{B} \propto d_\mathcal{B}$. The integral in (5.14) is a convolution between a Lorentzian and a Gaussian, which is called *Voigt profile* [216, 217]. The Voigt profile reproduces a Gaussian in the limit $\frac{\gamma^{(l)}_\mu}{\sigma_\mathcal{B}} \to 0$. At large system sizes, we therefore obtain

$$\mathbb{E}\left[\rho^{l,\mathcal{S}}_{\mu\mu}\right] \approx \frac{\rho_\mathcal{B}(\lambda_l - \epsilon^\mathcal{S}_\mu + \eta^{(l)}_\mu)}{N_\mathcal{S}\,\rho_\mathcal{F}(\lambda_l)} \tag{5.15}$$

with $N_\mathcal{F} = N_\mathcal{B}N_\mathcal{S}$. The normalization of any density matrix such that its trace equals unity implies the sum rule

$$\sum_\mu \frac{\rho_\mathcal{B}(\lambda_l - \epsilon^\mathcal{S}_\mu + \eta^{(l)}_\mu)}{N_\mathcal{S}\rho_\mathcal{F}(\lambda_l)} = 1, \tag{5.16}$$

which is equal to

$$N_\mathcal{F}\rho_\mathcal{F}(\lambda_l) = \int_{-\infty}^{\infty} \mathrm{d}\epsilon\,(N_\mathcal{S}\rho_\mathcal{S}(\epsilon))\,(N_\mathcal{B}\rho_\mathcal{B}(\lambda_l - \epsilon)) \tag{5.17}$$

by converting the sum over μ to the integral in the continuum description and neglecting the small contribution of the shift $\eta^{(l)}_\mu$ for the integral. The full DOS is given by the convolution of the DOS in $\mathcal{S}$ and $\mathcal{B}$ for large systems with a negligible contribution from the perturbation matrix X, since X only acts on a very small part of the system. The partition function $Z_\mathcal{S}(\lambda_l) = N_\mathcal{S}\rho_\mathcal{F}(\lambda_l)$ is therefore the sum of the raw probabilities $\rho^{l,\mathcal{S}}_{\mu\mu} \propto \rho_\mathcal{B}(\lambda_l - \epsilon^\mathcal{S}_\mu + \eta^{(l)}_\mu)$ to find the subsystem $\mathcal{S}$ in the eigenstate $|\psi^\mathcal{S}_\mu\rangle$ within an exact eigenstate $|\psi^\mathcal{F}_l\rangle$ of the full quantum system. Note, that the result for the reduced density matrix with the diagonals in (5.15) and the offdiagonals in (5.9) is qualitatively the same as when employing a GUE on the full basis as a perturbation matrix X. As compared to the general overlap form in (4.59), the GUE perturbation has no natural energy cutoff which would be implied by a local X, since it is a GUE in any basis. According to Eq. (1.122) by Allez and Bouchaud, the Lorentzian form (5.11) then becomes exact for the GUE perturbation and the other results follow. However, a GUE violates the locality condition of the system, as it contains all possible spin interaction terms with IID prefactors independent of the distance. Furthermore, the GUE acts within the whole quantum system $\mathcal{F}$, which means that its variance t scales with $d_\mathcal{F}$ in the same way as $\sigma^2_\mathcal{F}$ does and is therefore not negligible in the large system size limit. Returning to the reduced density matrix, we can expand the diagonal entries by expanding the DOS of the bath and the full system. This is possible, as we assumed $\sigma^2_\mathcal{S} \ll \sigma^2_\mathcal{B}$ in the construction of the Hamiltonian. We expand the DOS of $\mathcal{B}$ in the exponent in first order of $\epsilon_\mu^\mathcal{S} - \eta_\mu^{(l)}$, which yields

$$\begin{aligned}\rho_\mathcal{B}(\lambda_l - \epsilon_\mu^\mathcal{S} + \eta_\mu^{(l)}) &= \frac{1}{\sqrt{2\pi}\sigma_\mathcal{B}} \exp\left\{-\frac{1}{2\sigma_\mathcal{B}^2}\left(\lambda_l^2 - 2\lambda_l\,(\epsilon_\mu^\mathcal{S} - \eta_\mu^{(l)}) + (\epsilon_\mu^\mathcal{S} - \eta_\mu^{(l)})^2\right)\right\} \\ &\approx \frac{1}{\sqrt{2\pi}\sigma_\mathcal{B}}\,\mathrm{e}^{-\frac{\lambda_l^2}{2\sigma_\mathcal{B}^2}}\,\mathrm{e}^{\frac{\lambda_l\,(\epsilon_\mu^\mathcal{S}-\eta_\mu^{(l)})}{\sigma_\mathcal{B}^2}} = \frac{1}{\sqrt{2\pi}\sigma_\mathcal{B}}\mathrm{e}^{-\frac{\beta^2\sigma_\mathcal{B}^2}{2}}\,\mathrm{e}^{-\beta(\epsilon_\mu^\mathcal{S}-\eta_\mu^{(l)})}\end{aligned} \tag{5.18}$$

with $\beta \equiv -\frac{\lambda_l}{\sigma_\mathcal{B}^2}$ as defined in Sec. 4.4.2. The inverse temperature is set by the bath $\mathcal{B}$, which is in equilibrium with the small subsystem $\mathcal{S}$. It can be computed by considering the entropy of the bath,

$$S_\mathcal{B}(E) \equiv \log\left(N_\mathcal{B}\,\rho_\mathcal{B}\right) = -\frac{E^2}{2\sigma_\mathcal{B}^2} + \log\frac{N_\mathcal{B}}{\sqrt{2\pi}\sigma_\mathcal{B}}. \tag{5.19}$$

The inverse temperature associated to an eigenstate of the full system is given by the derivative of the entropy $S_\mathcal{B}(E)$ evaluated at the full energy λ_l,

$$\beta = \left.\frac{\partial S_\mathcal{B}(E)}{\partial E}\right|_{E=\lambda_l} = -\frac{\lambda_l}{\sigma_\mathcal{B}^2}. \tag{5.20}$$

Similarly, the DOS of the full quantum system is expanded in first order of $\frac{\sigma_\mathcal{S}^2}{\sigma_\mathcal{B}^2}$ in the exponent as

$$\begin{aligned}\rho_\mathcal{F}(\lambda_l) &= \frac{1}{\sqrt{2\pi}\sigma_\mathcal{F}}\,\mathrm{e}^{-\frac{\lambda_l^2}{2\sigma_\mathcal{F}^2}} = \frac{1}{\sqrt{2\pi}\sigma_\mathcal{F}}\,\mathrm{e}^{-\frac{\beta^2\sigma_\mathcal{B}^4}{2\sigma_\mathcal{F}^2}} = \frac{1}{\sqrt{2\pi}\sigma_\mathcal{F}}\exp\left\{-\frac{\beta^2\sigma_\mathcal{B}^2}{2}\left(\frac{\sigma_\mathcal{B}^2}{\sigma_\mathcal{B}^2+\sigma_\mathcal{S}^2}\right)\right\} \\ &\approx \frac{1}{\sqrt{2\pi}\sigma_\mathcal{F}}\exp\left\{-\frac{\beta^2\sigma_\mathcal{B}^2}{2}\left(1-\frac{\sigma_\mathcal{S}^2}{\sigma_\mathcal{B}^2}\right)\right\},\end{aligned} \tag{5.21}$$

where we inserted $\sigma_\mathcal{F}^2 = \sigma_\mathcal{S}^2 + \sigma_\mathcal{B}^2$. This is a direct consequence of Eq. (5.17), where we assumed that the convolution of the DOS in $\mathcal{S}$ and $\mathcal{B}$ returns the full DOS and the contribution from their coupling X is negligible in the large system limit. After insertion of (5.18) and (5.21) for the diagonal entries in (5.15) we obtain

$$\mathbb{E}\left[\rho_{\mu\mu}^{l,\mathcal{S}}\right] \approx \frac{\rho_\mathcal{B}(\lambda_l - \epsilon_\mu^\mathcal{S} + \eta_\mu^{(l)})}{N_\mathcal{S}\rho_\mathcal{F}(\lambda_l)} \approx \frac{\mathrm{e}^{-\beta(\epsilon_\mu^\mathcal{S}-\eta_\mu^{(l)})}}{N_\mathcal{S}\,\mathrm{e}^{\frac{\beta^2\sigma_\mathcal{S}^2}{2}}} = \frac{\mathrm{e}^{-\beta(\epsilon_\mu^\mathcal{S}-\eta_\mu^{(l)})}}{Z_\mathcal{S}(\beta)}, \tag{5.22}$$

where we set the prefactor $\frac{\sigma_\mathcal{F}}{\sigma_\mathcal{B}} \to 1$ to conform with the normalization conditions. We further define the partition function

$$Z_\mathcal{S}(\beta) \equiv \sum_{\mu=1}^{N_\mathcal{S}} \mathrm{e}^{-\beta(\epsilon_\mu^\mathcal{S}-\eta_\mu^{(l)})} \approx \int_{-\infty}^{\infty} \mathrm{d}\epsilon\,(N_\mathcal{S}\rho_\mathcal{S}(\epsilon))\,\mathrm{e}^{-\beta\epsilon} = \frac{N_\mathcal{S}}{\sqrt{2\pi}\sigma_\mathcal{S}}\int_{-\infty}^{\infty}\mathrm{d}\epsilon\,\mathrm{e}^{-\frac{\epsilon^2}{2\sigma_\mathcal{S}^2}}\,\mathrm{e}^{-\beta\epsilon} = N_\mathcal{S}\,\mathrm{e}^{\frac{\beta^2\sigma_\mathcal{S}^2}{2}}, \tag{5.23}$$

as obtained from the expansion of $\rho_{\mu\mu}^{l,\mathcal{S}}$. Eq. (5.22) contains the correct normalization for the reduced density matrix, $\mathrm{Tr}_\mathcal{S}(\rho_{\mu\mu}^{l,\mathcal{S}}) = 1$. The diagonal elements can be interpreted as the normalized probabilities to find the system in the eigenstate $|\psi_\mu^\mathcal{S}\rangle$ of the small subsystem $\mathcal{S}$ given an exact eigenstate of the full quantum system. Those probabilities are exponentials and form equivalent to the *Boltzmann factors* from statistical mechanics with a redefinition of the energy levels to the shifted levels $\epsilon_\mu^\mathcal{S} \to \epsilon_\mu^\mathcal{S} - \eta_\mu^{(l)}$ due to the influence of the perturbation matrix X with variance t.

Slope s in Fig. 5.5**a**,**b**		
λ_l	s of var$(\rho^{\mathcal{S}}_{0,0})$	s of var$(\lvert\rho^{\mathcal{S}}_{0,1}\rvert)$
−1.72	−0.821(45)	−0.910(59)
−0.91	−0.864(34)	−1.065(25)
−0.43	−0.857(32)	−0.910(56)
0.06	−0.866(29)	−0.876(63)
0.57	−0.855(30)	−0.997(47)
1.10	−0.853(29)	−1.108(32)

Table 5.1: Exponent s of the power function of the variance of the entries of the reduced density matrix $\rho^{\mathcal{S}}$ with respect to the number of states, $\rho^{\mathcal{S}} \propto (N_{\mathcal{F}})^s$. s is obtained as the slope from a linear fit to the double logarithmic plot of the variance in Fig. 5.5 for each investigated value of the full energy λ_l individually. We consider the variance of the first diagonal element var$(\rho^{\mathcal{S}}_{0,0})$ in Fig. 5.5**a** as well as the variance of the absolute value of the upper right offdiagonal entry var$(\lvert\rho^{\mathcal{S}}_{0,1}\rvert)$ in Fig. 5.5**b**.

In summary, in the large system size limit, the reduced density matrix of a small subsystem $\mathcal{S}$ in the eigenstate $\lvert\psi^{\mathcal{F}}_l\rangle$ of the full quantum system with eigenvalue λ_l converges to the diagonal form

$$\rho^{l,\mathcal{S}} \to \frac{1}{Z_{\mathcal{S}}(\beta)} \sum_{\mu} \mathrm{e}^{-\beta(\epsilon^{\mathcal{S}}_{\mu}-\eta^{(l)}_{\mu})} \lvert\psi^{\mathcal{S}}_{\mu}\rangle \langle\psi^{\mathcal{S}}_{\mu}\rvert \quad \text{for } N_{\mathcal{B}} \to \infty, \tag{5.24}$$

where the self averaging assumes the role of an expectation value. The offdiagonal entries of $\rho^{l,\mathcal{S}}$ go to zero with $\frac{1}{\sqrt{N_{\mathcal{B}}}}$ for increasing bath $\mathcal{B}$ and subsystem $\mathcal{S}$ of constant size. The reduced density matrix in (5.24) is a mixed density matrix, which resembles a thermal density matrix with renormalized energy levels in $\mathcal{S}$ according to the shift $\eta^{(l)}_{\mu}$, which depend on the variance t of the interaction matrix X. The subsystem $\mathcal{S}$ is in thermal contact with the bath, which determines the temperature as $\beta = -\frac{\lambda_l}{\sigma^2_{\mathcal{B}}}$ in this thermal equilibrium state. We have shown, that to obtain the result in (5.24), a single eigenstate of the full quantum system suffices, which means that a single quantum eigenstate already incorporates statistical mechanics and a well-defined temperature can be associated to it. For that, we merely applied the principles and equations of quantum mechanics without resorting to the principles of maximal entropy or ergodicity, which are employed in textbook derivations of statistical mechanics. The shifts $\eta^{(l)}_{\mu}$ can be measured as spectral lines through the scattering between eigenstates of different energy of the full quantum system, e.g. by an external light pulse. We detail this in Sec. 5.3.

5.1.2 Numerical results

In the following section, we investigate the analytical results for the reduced density matrix $\rho^{l,\mathcal{F}}$ in Sec. 5.1.1 in a numerical study. For that, we use a subsystem $\mathcal{S}$ consisting of a single site, $d_{\mathcal{S}} = 1$, and investigate the behavior of one diagonal and one offdiagonal entry in the (2×2) reduced density matrix with increasing system size $d_{\mathcal{F}}$. We choose $d_{\mathcal{F}} = \{10, 11, 12, 13, 14, 15\}$ and similar to chapter 4 average the reduced density matrix in intervals of $N_{\text{av}} = \{50, 100, 200, 400, 800, 1600\}$ full states around the investigated full energy λ_l of $H^{\mathcal{F}}$. On top of that, we average over 100 samples of $H^{\mathcal{F}}$. The results are shown in Fig. 5.1 for different investigated points of λ_l. Since $\rho^{l,\mathcal{F}}_{22} = 1 - \rho^{l,\mathcal{F}}_{11}$ due to the normalization of the density matrix, we show only the entry $\rho^{l,\mathcal{F}}_{11}$ in Fig. 5.1**a**. The eigenvalues of $\mathcal{S}$ are plotted in Fig. 5.1**a**, which are normalized to $\epsilon_{\mu} = \pm 0.15$ at all system sizes. Throughout the whole numerical analysis, we normalize $\tau\left((H^{\mathcal{B}})^2\right) = 1$. As expected from the analytical results, the diagonal entry stays approximately

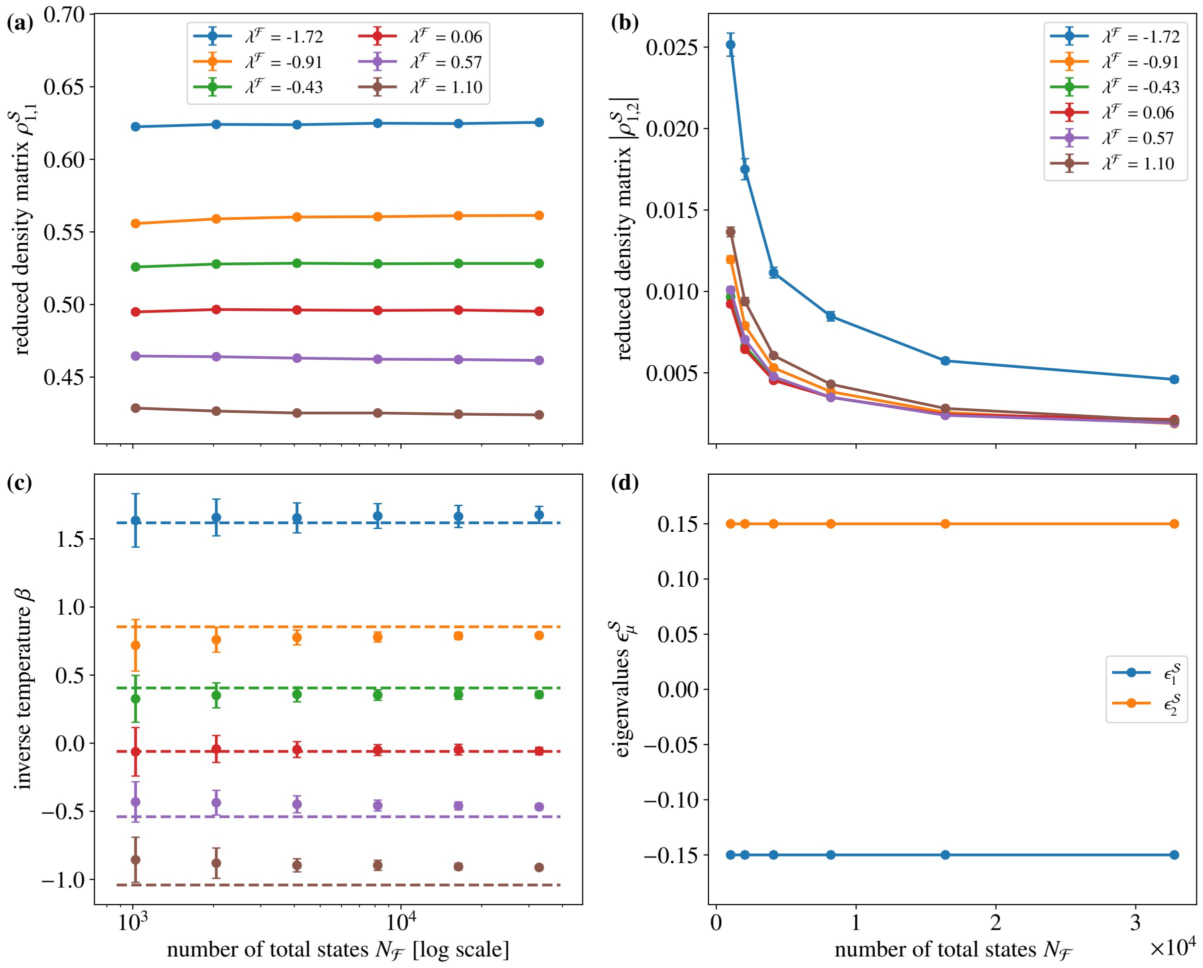

Figure 5.1: Analysis of the reduced density matrix $\rho^{\mathcal{S}}$ in a small subsystem $\mathcal{S}$ with $d_{\mathcal{S}} = 1$ site obtained from an exact quantum eigenstate of a spin lattice with $d_{\mathcal{F}}$ total sites. $\rho^{\mathcal{S}}$ is represented in terms of the eigenbasis of $\mathcal{S}$. The corresponding matrix variance of the perturbation X is given by $t = \{3.33, 2.98, 2.66, 2.44, 2.23, 2.03\} \times 10^{-3}$, while the second moment of the bath Hamiltonian is normalized to $\tau(H^{\mathcal{B}^2}) = 1$. All plots are resolved with respect to the number of total states $N_{\mathcal{F}}$ in the quantum system, shown on a logarithmic scale. We choose $d_{\mathcal{F}} = \{10, 11, 12, 13, 14, 15\}$ and average the reduced density matrix in intervals of $N_{\text{av}} = \{50, 100, 200, 400, 800, 1600\}$ full states around the investigated full energy λ_l of $H^{\mathcal{F}}$. At each system size, the results are obtained by additionally averaging over 100 random samples of $H^{\mathcal{F}}$. **(a)** shows the first diagonal entry and **(b)** the absolute value of the upper right offdiagonal entry of $\rho^{\mathcal{S}}$ for different full energies λ_l, with the data points connected by straight lines. **(c)** depicts the inverse temperature β computed from the diagonal entries of $\rho^{\mathcal{S}}$ in **(a)**. In **(d)**, the eigenvalues in subsystem $\mathcal{S}$ are plotted, which are normalized to be ±0.15 at all system sizes.

constant with increasing Hilbert space dimension $N_{\mathcal{F}}$. We read off the inverse temperature β from $\rho^{l,\mathcal{F}}_{11}$ by assuming an exponential distribution as derived in (5.22). The results for the corresponding β are shown in Fig. 5.1**c**. Additional dashed lines indicate the theoretically expected value of $\beta = -\frac{\lambda_l}{\sigma^2_{\mathcal{B}}}$ using $\sigma^2_{\mathcal{B}} = 1.03$ taken from the Gaussian fit in Fig. 4.10. The results agree with the theoretical expectation for each interval around λ_l individually. We attribute the deviations to the computation of the numerical values of β, which we obtained by using the bare energy levels $\epsilon^{\mathcal{S}}_{\mu}$ in $\mathcal{S}$. Comparing that to (5.22), it is actually the renormalized energy levels $\epsilon^{\mathcal{S}}_{\mu} - \eta^{(l)}_{\mu}$, which follow the exponential

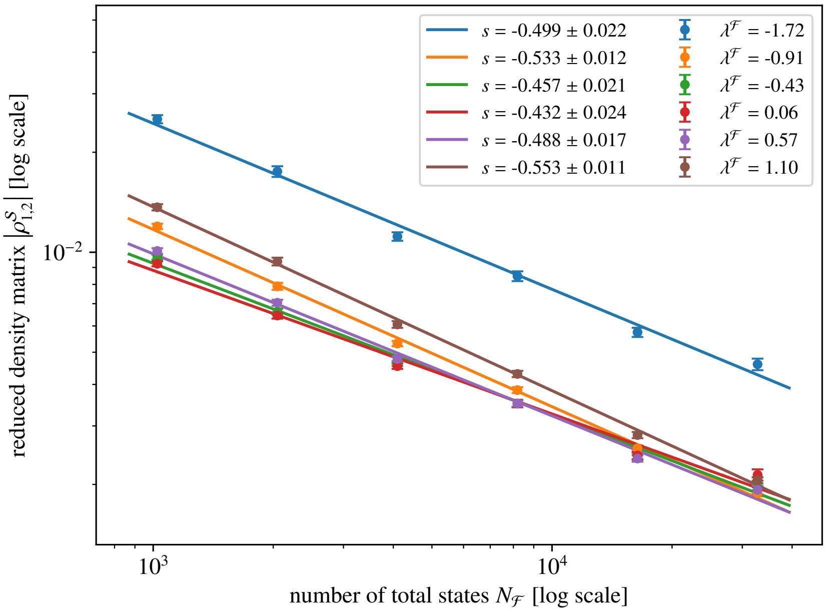

Figure 5.2: Logarithmic plot of the absolute value of the upper right offdiagonal entry of the reduced density matrix $\rho^{\mathcal{S}}$ in a small subsystem $\mathcal{S}$ with $d_{\mathcal{S}} = 1$ site, resolved with respect to the number of total states $N_{\mathcal{F}} = 2^{d_{\mathcal{F}}}$. $\rho^{\mathcal{S}}$ is represented in terms of the eigenbasis of $\mathcal{S}$. We choose $d_{\mathcal{F}} = \{10, 11, 12, 13, 14, 15\}$ and average the reduced density matrix in intervals of $N_{\text{av}} = \{50, 100, 200, 400, 800, 1600\}$ full states around the investigated full energy λ_l of $H^{\mathcal{F}}$. At each system size, the results are obtained by additionally averaging over 100 random samples of $H^{\mathcal{F}}$. It is the same data as shown in Fig. 5.1(**b**). We perform linear fits to find the scaling behavior of the offdiagonal of $\rho^{\mathcal{S}}$ with respect to $N_{\mathcal{F}}$ through the slope s of the linear fit.

Boltzmann distribution. The shifts may increase or decrease the effective energy distance in subsystem $\mathcal{S}$ as compared to the bare levels and are not taken into account, since they are not available in this numerical analysis. This causes a small inaccuracy in the numerically extracted value for β as compared to the actual numerical value of β. An in-depth analysis of the inverse temperature β obtained at different sizes of subsystem $\mathcal{S}$ is done in Sec. 5.2.2. We further notice that the standard error of the data points in Fig. 5.1**c** decreases with increasing system size $N_{\mathcal{F}}$, which is a direct consequence of a decreasing variance in the sample distribution of the data points, from which the average is taken. The statistics of the data points are analyzed in Sec. 5.1.3. In Fig. 5.1**b**, we plot the absolute value of the offdiagonal entry $\left|\rho^{l,\mathcal{S}}_{12}\right|$ on the upper right of the reduced density matrix. The average taken for this is identical to the diagonal averaging, except for the fact that we take the absolute value since the average would yield zero otherwise, as discussed in Sec. 5.1.1. We observe, that for all investigated points λ_l, the absolute offdiagonal entry decreases with the total number of states $N_{\mathcal{F}}$. To find the scaling with respect to $N_{\mathcal{F}}$, we plot the results on a double logarithmic scale in Fig. 5.2. In this plot, the data for each individual λ_l follows a linear relation, which is shown by linear fits. The resulting slopes of the linear fits are close to the value $s = 0.5$ and combine to an average value of $s = 0.494(19)$, which agrees with the analytically obtained scaling of $\left|\rho^{l,\mathcal{F}}_{12}\right| \propto \frac{1}{\sqrt{N_{\mathcal{F}}}}$ in Eq. (5.9). This finite size scaling analysis shows that the offdiagonal matrix elements in the reduced density matrix decrease with the size of the bath. The numerical analysis hence confirms the diagonal form of the reduced density matrix with exponential Boltzmann factors obtained in the large system size limit in Eq. (5.24).

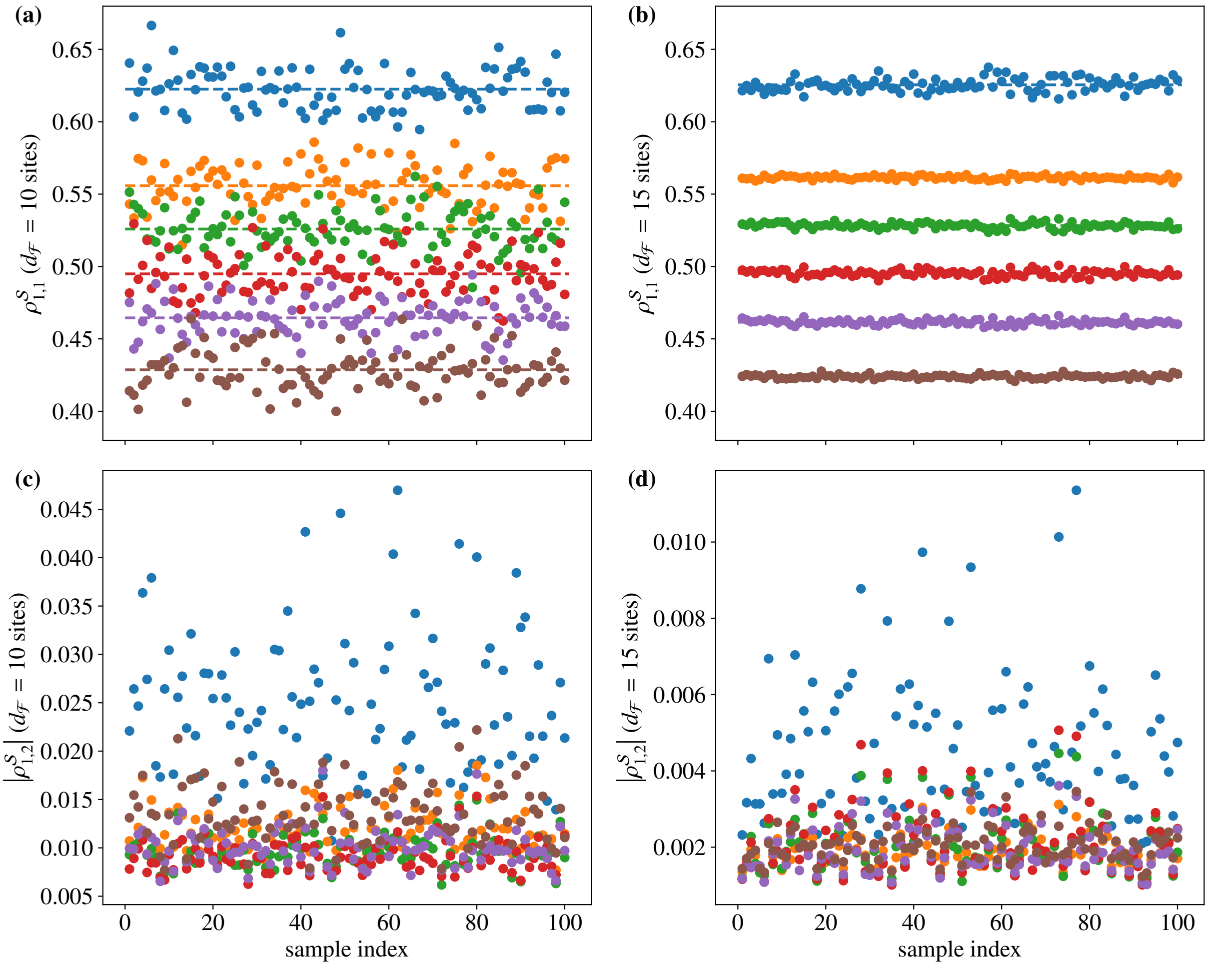

Figure 5.3: Values of the reduced density matrix $\rho^{\mathcal{S}}$ in a small subsystem $\mathcal{S}$ with $d_{\mathcal{S}} = 1$ site for each individual sample run of $H^{\mathcal{F}}$ used to obtain the average values in Fig. 5.1. $\rho^{\mathcal{S}}$ is represented in terms of the eigenbasis of $\mathcal{S}$. The investigated points of the full energy $\lambda_{\mathcal{F}}$ are the same as in Fig. 5.1 with $\lambda_l = \{-1.72, -0.91, -0.43, 0.06, 0.57, 1.10\}$ for the blue, orange, green, red, purple and brown data points respectively. In each sample of $H^{\mathcal{F}}$, we average the reduced density matrix in intervals of $N_{\text{av}} = 50$ full states for $d_{\mathcal{F}} = 10$ sites and $N_{\text{av}} = 1600$ full states for $d_{\mathcal{F}} = 15$ around the investigated full energy λ_l. In all plots, we normalize $\tau(H^{\mathcal{B}^2}) = 1$. We compare the results for $d_{\mathcal{F}} = 10$ sites at $t = 3.33 \times 10^{-3}$ in **(a)**, **(c)** to $d_{\mathcal{F}} = 15$ sites at $t = 2.03 \times 10^{-3}$ in **(b)**, **(d)**. We plot the average of the first diagonal value of $\rho^{\mathcal{S}}$ for each sample in **(a)** for $d_{\mathcal{F}} = 10$ sites and in **(b)** for $d_{\mathcal{F}} = 15$ sites. The average values for each λ_l are shown as dotted lines. **(c)** and **(d)** show the average of the absolute value of the upper right offdiagonal entry of $\rho^{\mathcal{S}}$ for each sample and for $d_{\mathcal{F}} = 10$ and $d_{\mathcal{F}} = 15$ sites respectively.

5.1.3 Statistics of the reduced density matrix

We conclude the numerical analysis of the reduced density matrix by an investigation of the statistical distribution of the individual data points plotted in Fig. 5.1 and Fig. 5.2. The numerical data in Sec. 5.1.2 resolved with respect to the total Hilbert space dimension $N_{\mathcal{F}}$ was obtained through averaging the entries of the reduced density matrix in a small energy window containing $N_{\text{av}} = \{50, 100, 200, 400, 800, 1600\}$ full states around the individually investigated points of total energy λ_l. The width w of the investigated energy window depends on λ_l and ranges from $w \approx 0.15$ for $\lambda_l = 0.06$ to $w \approx 0.50$ for $\lambda_l = -1.72$. Additional to that, we averaged over 100 samples of $H^{\mathcal{F}}$ to obtain the final

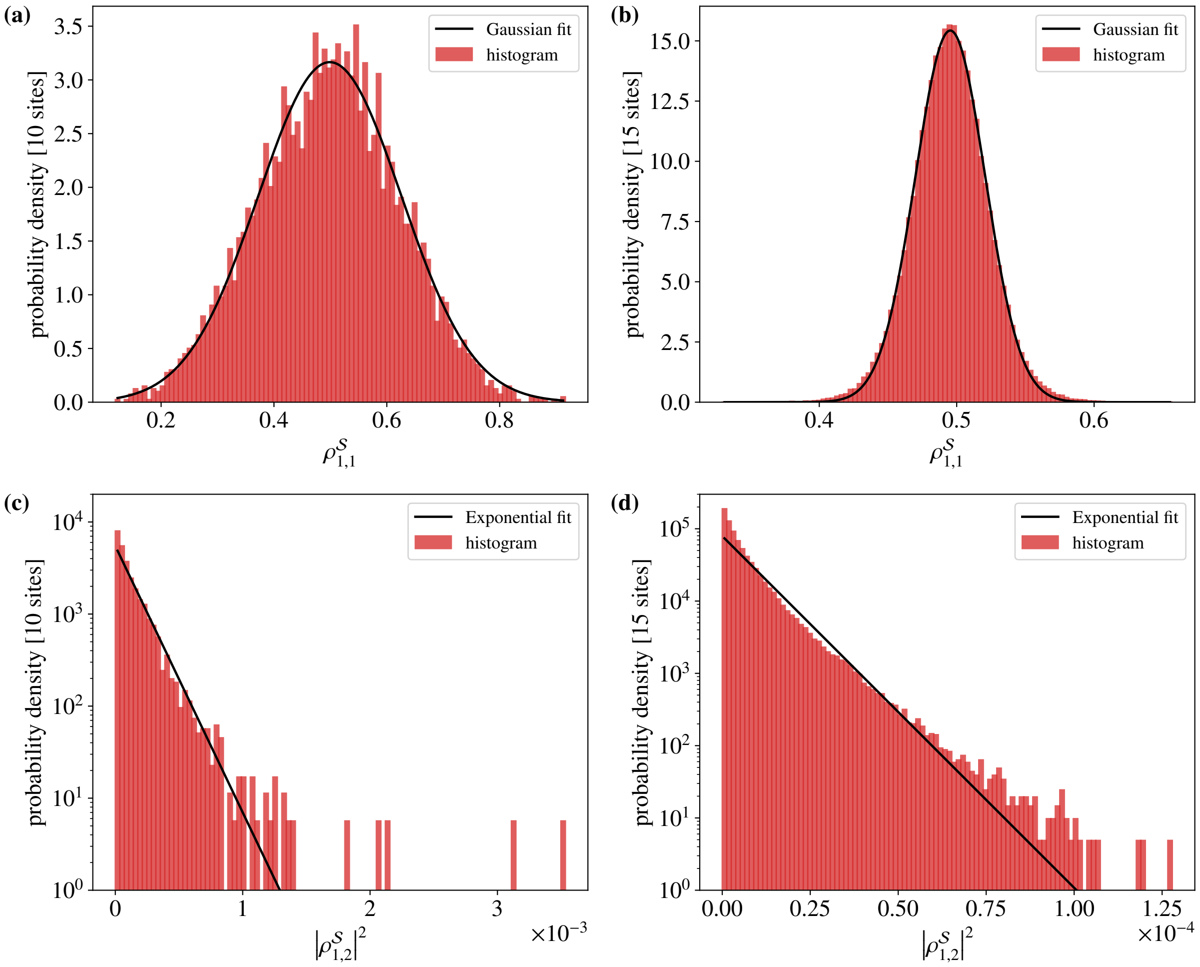

Figure 5.4: Probability distribution of the entries of ρ^{S} in an exact eigenstate of $H^{\mathcal{F}}$ at the investigated full energy $\lambda_{\mathcal{F}} = 0.06$ with an average of N_{av} full states around $\lambda_{\mathcal{F}}$ and of 100 samples of $H^{\mathcal{F}}$. The distribution corresponds to the data points shown in Fig. 5.3 and is used to obtain the average values in Fig. 5.1. We compare the results for $d_{\mathcal{F}} = 10$ sites at $t = 3.33 \times 10^{-3}$ in **(a)**, **(c)** to $d_{\mathcal{F}} = 15$ sites at $t = 2.03 \times 10^{-3}$ in **(b)**, **(d)**, while we normalize $\tau(H^{\mathcal{B}^2}) = 1$. The probability distribution of the first diagonal value of ρ^{S} is shown in **(a)** for $d_{\mathcal{F}} = 10$ sites and $N_{\text{av}} = 50$ and in **(b)** for $d_{\mathcal{F}} = 15$ sites and $N_{\text{av}} = 1600$. We fit Gaussians through both numerically obtained distributions, which return mean values of $\mu_{10} = 0.5011(18)$ and $\mu_{15} = 0.504\,660(90)$ as well as standard deviations of $\sigma_{10} = 12.68(18) \times 10^{-2}$ and $\sigma_{15} = 2.5435(90) \times 10^{-2}$ for **(a)** and **(b)** respectively. **(c)** and **(d)** depict the probability distribution of the squared absolute value of the upper right offdiagonal value of ρ^{S} on a logarithmic scale for $d_{\mathcal{F}} = 10$, $N_{\text{av}} = 50$ and $d_{\mathcal{F}} = 15$, $N_{\text{av}} = 1600$ respectively. Exponential distributions are fitted as straight lines through the logarithmically plotted data points returning the slope parameters $\alpha = -6.66(31) \times 10^{3}$ and $\alpha = -1.120(24) \times 10^{5}$ for **(c)** and **(d)** respectively.

result of the reduced density matrix. In Fig. 5.3, we show the results corresponding to individual samples of $H^{\mathcal{F}}$ for $d_{\mathcal{F}} = 10$ sites and $d_{\mathcal{F}} = 15$ sites. Fig. 5.3**a,b** show the diagonal $\rho^{l,\mathcal{F}}_{11}$ of the reduced density matrix in subsystem $\mathcal{S}$. We observe, that the results for $d_{\mathcal{F}} = 15$ sites in Fig. 5.3**b** have a much smaller variance than those for $d_{\mathcal{F}} = 10$ sites in Fig. 5.3**a** and hence have a higher precision due to the smaller spread of the data. We attribute this effect to increased self averaging due to the larger sized bath. This supports the statement, that the diagonal values of the reduced density matrix converge to well defined values in the large system size limit $N_{\mathcal{B}} \to \infty$. In Sec. 5.1.1, we

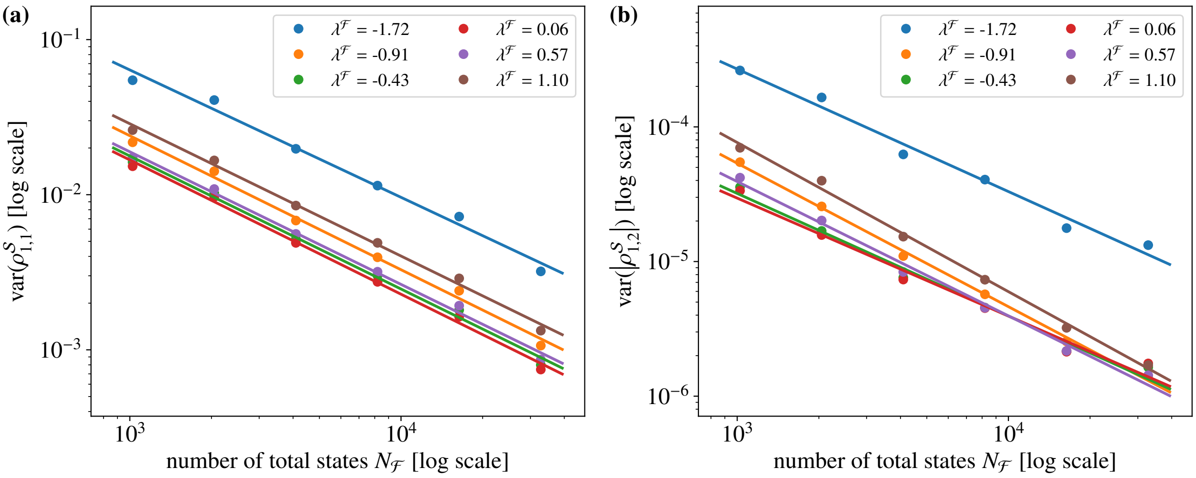

Figure 5.5: Variances of the entries of $\rho^{\mathcal{S}}$ with $d_{\mathcal{S}} = 1$ in an exact eigenstate of $H^{\mathcal{F}}$ at the eigenenergy $\lambda^{\mathcal{F}}$ by considering N_{av} full states around $\lambda_{\mathcal{F}}$ and 100 samples of $H^{\mathcal{F}}$. $\rho^{\mathcal{S}}$ is represented in terms of the eigenbasis of $\mathcal{S}$. The results are plotted on a double logarithmic scale and resolved with respect to the Hilbert space dimension $N_{\mathcal{F}}$ of the full quantum system. We choose $d_{\mathcal{F}} = \{10, 11, 12, 13, 14, 15\}$ and consider intervals of $N_{\mathrm{av}} = \{50, 100, 200, 400, 800, 1600\}$ full states at $t = \{3.33, 2.98, 2.66, 2.44, 2.23, 2.03\} \times 10^{-3}$ to compute the variance of the entries of the reduced density matrix at different λ_l. The variance is obtained from the same numerical data as the average values in Fig. 5.1. **(a)** shows the variance of the first diagonal entry of $\rho^{\mathcal{S}}$, while **(b)** shows the variance of the absolute value of the upper right offdiagonal entry of $\rho^{\mathcal{S}}$. We fit linear functions through the data points with the resulting slopes collected in Tab. 5.1.

found that those limiting values are given by the exponential Boltzmann distribution. Moreover, here we see that the fluctuations around those limiting values approach zero in the same limit $N_{\mathcal{B}} \to \infty$, thus increasing the precision of these values. Fig. 5.3**c,d** shows the absolute value of the upper right offdiagonal entry of the (2×2) reduced density matrix resolved for all samples of $H^{\mathcal{F}}$ individually. The relative spread of the data points is much larger than that of the diagonal values in Fig. 5.3**a,b**. The absolute value of the data in Fig. 5.3**d** for $d_{\mathcal{F}} = 15$ sites is much smaller than that in Fig. 5.3**c** for $d_{\mathcal{F}} = 10$ sites. This is consistent with the analytical result, that the offdiagonal of the reduced density matrix scales with $\frac{1}{\sqrt{N_{\mathcal{B}}}}$, which was explored in Sec. 5.1.1 and numerically confirmed with Fig. 5.2.

To obtain the statistical distribution of the individual entries of the reduced density matrix, we plot the numerically obtained probability density from the normalized histogram of all data points contributing to that element in Fig. 5.4. Note, that in this plot, all N_{av} values for each of the 100 samples of $H^{\mathcal{F}}$ are taken into account for the creation of the histogram. The statistical distribution is evaluated exemplary for the mean value of $\lambda_l = 0.06$, whose mean values for each sample of $H^{\mathcal{F}}$ is shown in red in Fig. 5.3. We obtain probability distributions with Gaussian shape for the first diagonal value $\rho^{l,\mathcal{F}}_{11}$ of the reduced density matrix in Fig. 5.4**a** for $d_{\mathcal{F}} = 10$ and in Fig. 5.4**b** for $d_{\mathcal{F}} = 15$ sites. This is confirmed by Gaussian fits, from which we obtain numerical best fit parameters for the mean value and the standard deviation. While the mean values are almost identical with $\mu_{10} = 0.5011(18)$ and $\mu_{15} = 0.504\,660(90)$, the standard deviation for $d_{\mathcal{F}} = 15$ sites is much smaller than that for $d_{\mathcal{F}} = 10$ sites, $\sigma_{10} \gg \sigma_{15}$ with $\sigma_{10} = 12.68(18) \times 10^{-2}$ and $\sigma_{15} = 2.5435(90) \times 10^{-2}$. This confirms the above reasoning that the fluctuations of the diagonal entries of the reduced density matrix decrease for larger bath sizes. An analogous relation holds for the offdiagonal entries of the reduced density matrix. As depicted on a logarithmic scale in Fig. 5.4**c,d**, the squared absolute value of the upper right offdiagonal element of the reduced density matrix follows an exponential probability distribution. A linear fit on the logarithmic axis returns the slope $\alpha_{10} = -6.66(31) \times 10^3$ for $d_{\mathcal{F}} = 10$ sites in Fig. 5.4**c** and $\alpha_{15} = -1.120(24) \times 10^5$ for $d_{\mathcal{F}} = 15$ sites in Fig. 5.4**d**. Since the distribution is obtained for the squared absolute value $\left|\rho_{12}^{l,\mathcal{F}}\right|^2$, we conclude, that the spread of the data points also decreases with system size for the offdiagonal element in the reduced density matrix. Not only does the absolute value $\left|\rho_{12}^{l,\mathcal{F}}\right|$ go to zero with $\frac{1}{\sqrt{N_{\mathcal{F}}}}$, but also its variance decreases with $N_{\mathcal{F}}$.

A full analysis of the variance of the entries of the reduced density matrix is shown in Fig. 5.5. Here, we use the full data set for each system size $d_{\mathcal{F}}$ to compute the variance of the data for each investigated point of full energy λ_l individually. The variance is plotted on a double logarithmic scale with respect to the total number of states $N_{\mathcal{F}}$ for the first diagonal element in Fig. 5.5**a** and the absolute value of the offdiagonal element in Fig. 5.5**b**. Linear fits indicate the approximate linear relationship in the double logarithmic plot, which translates to a power law behavior $\mathrm{var}(\rho_{11}^{l,\mathcal{F}}) \propto N_{\mathcal{F}}^s$ and $\mathrm{var}(\left|\rho_{12}^{l,\mathcal{F}}\right|) \propto N_{\mathcal{F}}^s$, where the power law exponent s equals the slope of the linear fit. In Tab. 5.1, we enter the best fit parameters for the slope s for all investigated full energies in Fig. 5.5 individually. In an average over all slopes, we obtain $\bar{s}_{\mathrm{dia}} = -0.8527(67)$ for the diagonal variance $\mathrm{var}(\rho_{11}^{l,\mathcal{F}})$ and $\bar{s}_{\mathrm{offdia}} = -0.978(39)$ for the offdiagonal variance $\mathrm{var}(\left|\rho_{12}^{l,\mathcal{F}}\right|)$ in the reduced density matrix. As expected and analytically derived in Sec. 5.1.1, the variance of the offdiagonal elements in the reduced density matrix scales with $\frac{1}{N_{\mathcal{F}}}$ consistent with the scaling $\frac{1}{\sqrt{N_{\mathcal{F}}}}$ of the element itself. The variance of the diagonal element is not quite $\frac{1}{N_{\mathcal{F}}}$, but with a slightly reduced exponent in the denominator, which we attribute to insufficient self averaging due to the finite system size. The results quantitatively confirm, that the variance of the entries in the reduced density matrix decrease with system size. This supports the analytical calculation where the reduced density matrix is represented by a diagonal matrix of Boltzmann factors in the large system size limit $N_{\mathcal{B}} \to \infty$ according to Eq. (5.24). Not only do the matrix entries converge to the analytical results, but also their fluctuations vanish in the large system size limit.

5.2 Thermalization

To compare our findings with the ETH, we first outline the principle idea of the ETH and its main explanation up to now, which is typicality. We explicitly delineate the approximations which go into the ETH and the assumptions made for typicality, which are an extension of classical statistical mechanics to the quantum realm. We then summarize our derivation of statistical mechanics, which relies solely on the principles of quantum mechanics, as well as locality and non-integrability. Our approach is compared to typicality and reconnected to the ETH, which is elevated from hypothesis to theory.

5.2.1 Eigenstate Thermalization Hypothesis

The ETH is a conjecture about the thermalization of eigenstates. To formulate it, we look at a quantum state of the full system $\mathcal{F}$

$$|\psi\rangle = \sum_l c_l \, |\psi_l^{\mathcal{F}}\rangle \tag{5.25}$$

with the mean energy

$$\bar{E} \equiv \langle\psi|H^{\mathcal{F}}|\psi\rangle = \sum_l |c_l|^2 \lambda_l \tag{5.26}$$

and variance

$$(\delta E)^2 = \langle\psi|(H^{\mathcal{F}} - \bar{E})^2|\psi\rangle = \sum_l |c_l|^2 (\lambda_l - \bar{E})^2 \ll \bar{E}^2 \tag{5.27}$$

determining the fluctuations around the mean value. The mean energy $\bar{E}$ is assumed to lie in the bulk of the energy spectrum of the quantum system. For thermal properties to arise, we require that the energy difference $\bar{E} - E_0$ with respect to the ground state energy E_0 scales extensively with the number of DOF in the system. It is possible that the ground state and the states close to it have intricate correlations that prevent thermalization. In the ETH, the energy fluctuations are assumed to be much smaller than the mean value in the state $|\psi\rangle$. Since the state follows the Schrödinger equation

$$i\partial_t \, |\psi(t)\rangle = H^{\mathcal{F}} \, |\psi(t)\rangle \tag{5.28}$$

with $\hbar$ set to unity, its time evolution is given by

$$|\psi(t)\rangle = \sum_l c_l \, \mathrm{e}^{-i\lambda_l t} \, |\psi_l^{\mathcal{F}}\rangle \tag{5.29}$$

with the initial condition $|\psi(0)\rangle = |\psi\rangle$. The ETH considers local operators A, which only act in a subsystem of the quantum system, in this case chosen as subsystem $\mathcal{S}$ with $A = A_{\mathcal{S}} \otimes \mathbb{1}_{\mathcal{B}}$ and $\mathbb{1}_{\mathcal{B}}$ being an identity in the bath. The quantum expectation value in the state $|\psi(t)\rangle$ at time t is given by

$$\langle A\rangle_\psi (t) = \langle\psi(t)|A|\psi(t)\rangle = \sum_{l,l'} c_{l'}^* c_l \mathrm{e}^{-i(\lambda_l - \lambda_{l'})t} \underbrace{\langle\psi_{l'}^{\mathcal{F}}|A|\psi_l^{\mathcal{F}}\rangle}_{=:A_{l'l}} \xrightarrow{t\to\infty} \sum_l |c_l|^2 A_{ll}. \tag{5.30}$$

Due to loss of the phase coherence between different eigenstates of $H^{\mathcal{F}}$, the offdiagonal elements of A are averaged out and only the diagonal ones remain. In a thermal system, the ETH assumes that each single eigenstate $|\psi_l^{\mathcal{F}}\rangle$ of the full Hamiltonian is a thermal state. From this assumption, it follows that in the energy range given by δE, where the main contribution of the coefficients c_l originates from, the diagonal values of A are equal to the thermal expectation value

$$A_{ll} = \langle\psi_l^{\mathcal{F}}|A|\psi_l^{\mathcal{F}}\rangle \approx \langle A\rangle_\beta = \mathrm{Tr}\left(A\,\rho_\beta\right). \tag{5.31}$$

Here, ρ_β is the thermal density matrix for the quantum system with

$$\rho_\beta = \frac{1}{Z}\mathrm{e}^{-\beta H^{\mathcal{F}}}, \tag{5.32}$$

where Z is the partition function. The inverse temperature β is fixed by equating the energy $\bar{E}$ in the state ψ with the thermal energy,

$$\bar{E} \overset{!}{=} \mathrm{Tr}\left(H^{\mathcal{F}}\rho_\beta\right), \tag{5.33}$$

where it is assumed that the inverse temperature β is constant within the energy range δE. Since each eigenstate is assumed to behave thermally, the quantum expectation value of A in the state $|\psi\rangle$ in Eq. (5.30) is given by the thermal expectation value

$$\langle\psi(t)|A|\psi(t)\rangle \overset{t\to\infty}{\longrightarrow} \sum_l |c_l|^2 A_{ll} \approx \langle A\rangle_\beta\,, \tag{5.34}$$

where we used the normalization of the state $|\psi\rangle$ with $\sum_l |c_l|^2 = 1$. The quantum expectation value at large times t when an equilibrium state is reached is thus equal to the thermal expectation value with inverse temperature β. For this result to be physically meaningful, the fluctuations around the thermal equilibrium value need to be small as well. The fluctuations of $\langle A\rangle_\psi$ in the state $|\psi\rangle$ to the thermal value are given by

$$\left(\langle A\rangle_\psi(t) - \langle A\rangle_\beta\right)^2 \overset{t\to\infty}{\longrightarrow} \sum_{\substack{k,l\\(k\neq l)}} |c_k|^2\,|A_{kl}|\,|c_l|^2. \tag{5.35}$$

From the time evolution of the quantum expectation value $\langle A\rangle_\psi(t)$ in the state $|\psi(t)\rangle$, we can define a thermal equilibrium at time t through

$$\left|\langle A\rangle_\psi(t) - \langle A\rangle_\beta\right| < \epsilon, \tag{5.36a}$$

$$|A_{kl}| < \epsilon \text{ for } k \neq l, \tag{5.36b}$$

where $\epsilon > 0$ is a small parameter. With (5.36a,b), the ETH hence boils down to two main assumptions. The first equation concerns the diagonal values A_{ll} and ensures that the deviation to the thermal expectation value is small, while the second states that the offdiagonal values $A_{ll'}$ are small. Eq. (5.36b) makes sure, that the fluctations of $\langle A\rangle_\psi(t)$ around the thermal value $\langle A\rangle_\beta$ at large times are small with $\left(\langle A\rangle_\psi - \langle A\rangle_\beta\right)^2 < \epsilon^2$ according to Eq. (5.35). This means that independent of the initial value of $\langle A\rangle_\psi$, the expectation value relaxes to its equilibrium value [47].

The ETH formulates a mathematical statement about when exact quantum states that are represented by a pure density matrix can show thermal behavior. It has been numerically verified to hold in a plethora of systems such as quantum lattices [29–34]. An alternative prevailing approach to explain the occurrence of thermalization in quantum systems is typicality. We sketch the main idea of this approach in the following, which is taken from Ref. [65]. Similar to classical statistical mechanics, typicality involves a probability distribution on the possible microstates of the system. In classical mechanics, a microcanonical ensemble is defined to be isolated from the environment and to sit at energy E with nonzero energy allowance δ. The possible microstates therefore lie in the energy window $[E, E+\delta]$. Following from the ergodic hypothesis we assign equal weights to all possible microstates, which corrresponds to a uniform probability distribution in the considered energy shell. When considering typicality in quantum systems, the possible microstates are taken to be normalized wave functions Ψ with energies in the range $[E, E+\delta]$, i.e. states in a subspace of the Hilbert space labeled as $\mathcal{H}_{[E,E+\delta]}$. The probability distribution for the states in $\mathcal{H}_{[E,E+\delta]}$ is proposed to be uniform. We randomly choose one state $|\Psi\rangle$ in this subspace and expand it in terms of the energy eigenstates $|E_i\rangle$ of the Hamiltonian of the quantum system,

$$|\Psi\rangle = \sum_i c_i \, |E_i\rangle \, . \tag{5.37}$$

Here, c_i are coefficients restricted to energy eigenvalues within the interval $[E, E+\delta]$. Since the ETH deals with local observables A acting only within the subsystem $\mathcal{S}$, we split up the quantum system into the small subsystem $\mathcal{S}$ and a large bath $\mathcal{B}$. The random state $|\Psi\rangle$ can be viewed as arising from a Gaussian random vector $\Phi \in \mathcal{H}_{[E,E+\delta]}$, which is additionally being normalized through $|\Psi\rangle = |\Phi\rangle \, / \, \langle\Phi|\Phi\rangle$. The Gaussian random vector has mean zero and its two-point correlation is given by the identity on $\mathcal{H}_{[E,E+\delta]}$. It therefore has the same properties as an eigenvector of a GUE and is fully random with no correlations between eigenvectors to different eigenvalues. Its expansion in terms of the energy eigenbasis $|\psi_\mu^{\mathcal{S}}\rangle$ in $\mathcal{S}$ and $|\psi_i^{\mathcal{B}}\rangle$ in $\mathcal{B}$ is given by

$$|\Phi\rangle = \sum_{\mu,i} c_{\mu i} \, |\psi_\mu^{\mathcal{S}}\rangle \, |\psi_i^{\mathcal{B}}\rangle = \sum_{\mu} |\psi_\mu^{\mathcal{S}}\rangle \, |\Phi_\mu\rangle \, , \tag{5.38}$$

where the real and imaginary part of $c_{\mu i}$ are real Gaussian random variables with mean zero and variance $\frac{1}{2}$ for all μ, i which fulfill the energy constraint $\epsilon_\mu^{\mathcal{S}} + E_i^{\mathcal{B}} \in [E, E+\delta]$. After the last equal sign in (5.38), we have defined the bath states

$$|\Phi_i\rangle \equiv \sum_{i \in I_\mu} c_{\mu i} \, |\psi_i^{\mathcal{B}}\rangle \, , \tag{5.39}$$

which have nonzero coefficients for the bath states i only in the intervals I_μ defined as $E_i^{\mathcal{B}} \in [E - \epsilon_\mu^{\mathcal{S}}, E - \epsilon_\mu^{\mathcal{S}} + \delta]$ such that the total energy lies in $[E, E+\delta]$. Hence the interval I_μ depends on the state μ in $\mathcal{S}$ through its energy $\epsilon_\mu^{\mathcal{S}}$. The reduced density matrix in the subsystem $\mathcal{S}$ is obtained from the pure density matrix corresponding to the state $|\Psi\rangle$ by taking the trace over the bath

$$\rho_\Psi^{\mathcal{S}} = \frac{1}{\langle\Phi|\Phi\rangle} \mathrm{Tr}_{\mathcal{B}} \left(|\Phi\rangle \, \langle\Phi| \right) = \frac{1}{\langle\Phi|\Phi\rangle} \sum_{\mu,\nu} \langle\Phi_\mu|\Phi_\nu\rangle \, |\psi_\mu^{\mathcal{S}}\rangle \, \langle\psi_\nu^{\mathcal{S}}| \, . \tag{5.40}$$

A crucial step in the analysis is the evaluation of the overlap of the bath states $\langle\Phi_\mu|\Phi_\nu\rangle$. If the energy spacings in $\mathcal{S}$ are greater than δ, the intervals I_μ and I_ν are disjoint and $\langle\Phi_\mu|\Phi_\nu\rangle \propto \delta_{\mu\nu}$. Goldstein et al. in [65] argue that if even the intervals I_μ and I_ν have significant overlap, the states $|\Phi_\mu\rangle$ and $|\Phi_\nu\rangle$ are still approximately orthogonal since they are uniformly distributed random vectors in a high-dimensional space. This originates from the expectation value of the overlap of two random vectors drawn from a uniform distribution in an N-dimensional space, which is $\frac{1}{N}$. This means that

$$\langle \Phi_\mu | \Phi_\nu \rangle = \delta_{\mu\nu} \, \langle \Phi_\mu | \Phi_\mu \rangle = \delta_{\mu\nu} \cdot \sum_{i \in I_\mu} \left| c_{\mu i} \right|^2 \approx \delta_{\mu\nu} \cdot \dim\left(\mathcal{H}^{\mathcal{B}}_\mu \right). \tag{5.41}$$

The subspace $\mathcal{H}^{\mathcal{B}}_\mu$ of the Hilbert space of the bath corresponds to the bath eigenstates in the interval I_μ,

$$\mathcal{H}^{\mathcal{B}}_\mu = \mathcal{H}^{\mathcal{B}}_{[E-\epsilon^{\mathcal{S}}_\mu, E-\epsilon^{\mathcal{S}}_\mu+\delta]}. \tag{5.42}$$

Inserting Eq. (5.41) into (5.40), we obtain for the reduced density matrix in $\mathcal{S}$ of the pure state $|\psi\rangle$ the result

$$\rho^{\mathcal{S}}_\Psi \approx \frac{1}{\dim\left(\mathcal{H}_{[E,E+\delta]}\right)} \sum_\mu \dim\left(\mathcal{H}^{\mathcal{B}}_\mu \right) |\psi^{\mathcal{S}}_\mu\rangle \langle \psi^{\mathcal{S}}_\mu| , \tag{5.43}$$

where the prefactor $\dim\left(\mathcal{H}_{[E,E+\delta]}\right)$ denotes the number of states of the full quantum in the interval $[E, E+\delta]$, from which $|\Psi\rangle$ is picked. It accounts for the overall normalization of the uniform probability distribution of the states in $[E, E+\delta]$. Eq. (5.43) is the final result and one can recover the canonical distribution with the inverse temperature as $\beta = \frac{\partial S(E)}{\partial E}$ when defining the entropy of the bath as $S(E) \approx \log\left(\dim\left(\mathcal{H}^{\mathcal{B}}_{[E,E+\delta]}\right)\right)$ in [65]. With the saddle point expansion around the energy $\epsilon^{\mathcal{S}}_\mu$ in the small subsystem

$$\dim\left(\mathcal{H}^{\mathcal{B}}_\mu \right) \approx \mathrm{e}^{S(E-\epsilon^{\mathcal{S}}_\mu)} \approx \mathrm{e}^{S(E)-\beta\epsilon^{\mathcal{S}}_\mu} \propto \mathrm{e}^{-\beta\epsilon^{\mathcal{S}}_\mu} \tag{5.44}$$

and under appropriate normalization, Eq. (5.43) becomes

$$\rho^{\mathcal{S}}_\Psi \approx \frac{1}{Z_{\mathcal{S}}} \sum_\mu \mathrm{e}^{-\beta\epsilon^{\mathcal{S}}_\mu} |\psi^{\mathcal{S}}_\mu\rangle \langle \psi^{\mathcal{S}}_\mu| = \rho^{\mathcal{S}}_{\mathrm{can}}, \tag{5.45}$$

where $Z_{\mathcal{S}}$ is the partition function. This is equal to the thermal density matrix $\rho^{\mathcal{S}}_{\mathrm{can}}$ in a canonical ensemble, where $\mathcal{S}$ is coupled to a heat bath. The derivation of the canonical ensemble and its probability distribution in typicality necessitates the definition of an energy allowance δ reminiscent of the derivation of the canonical ensemble in classical statistical mechanics. It further requires a uniform probability distribution on all possible microstates in the interval $[E, E+\delta]$, where δ denotes a sharp cutoff and all other states outside of that interval are not considered. This is also similar to classical mechanics, where the possible microstates are characterized by an energy shell in phase space and the uniform probability results from the ergodic hypothesis. In typicality it is assumed that all quantum states in $[E, E+\delta]$ are Gaussian random vectors, which corresponds to a Hamiltonian that contains all possible random interaction terms including non-local ones, i.e. in a GUE or Gaussian orthogonal ensemble (GOE). In contrast, with our approach we directly consider the exact eigenstates of a non-integrable quantum system with a random local Hamiltonian. Instead, in our approach to quantum thermalization, we merely apply the principles of quantum mechanics and obtain the thermal density matrix of a canonical ensemble in a small subset of the local non-integrable quantum system [3] in Eq. (5.24) from a single eigenstate in Sec. 5.1.1 without requiring further assumptions. A summary of our theory is sketched in the following section and the inverse temperature β is obtained from a numerical analysis.

5.2.2 Thermal distribution in a quantum subsystem

To derive the ETH for the considered Hamiltonians consider a single eigenstate $|\psi_l^{\mathcal{F}}\rangle$ with eigenenergy λ_l of the full quantum system, which is described by a local random Hamiltonian $H^{\mathcal{F}}$. The isolated quantum system is hence in a state described by the pure density matrix $\rho^l = |\psi_l^{\mathcal{F}}\rangle\langle\psi_l^{\mathcal{F}}|$ defined in (5.1). In Fig. 5.6 we visually illustrate how the canonical distribution emerges in the two-level subsystem $\mathcal{S}$ of the quantum system from ρ^l by taking the trace over the remaining part, which is the bath $\mathcal{B}$. In chapter 4, we used the methods of RMT to obtain the overlap $\mathcal{X}_{\mu i,l}$ of the eigenstate $|\psi_l^{\mathcal{F}}\rangle$ with the unperturbed eigenbasis of $\mathcal{S}$ and $\mathcal{B}$, $|\psi_\mu^{\mathcal{S}}\rangle\,|\psi_i^{\mathcal{B}}\rangle$. In Fig. 5.6, the overlap curve is plotted with respect to the bath energy $E_i^{\mathcal{B}}$ and is close to its peak position approximated by a Lorentzian distribution with an additional area prefactor A. In Sec. 5.1.1, we showed that the offdiagonal entries in the reduced density matrix $\rho^{l,\mathcal{S}} = \mathrm{Tr}_{\mathcal{B}}\left(\rho^l\right)$ for subsystem $\mathcal{S}$ go to zero with $\frac{1}{\sqrt{N_{\mathcal{F}}}}$. As discussed in Eq. (5.14), the μ-th diagonal entry of the reduced density matrix can be computed by

$$\mathbb{E}\left[\rho_{\mu\mu}^{l,\mathcal{S}}\right] = \sum_{i=1}^{N_{\mathcal{B}}} \mathcal{X}_{\mu i,l} = \int_{-\infty}^{\infty} \mathrm{d}E\, N_{\mathcal{B}}\,\rho_{\mathcal{B}}(E)\,\mathcal{X}_\mu(E,\lambda_l), \tag{5.46}$$

where $\mathcal{X}_\mu(E_i^{\mathcal{B}},\lambda_l)$ is the continuum version of the overlap $\mathcal{X}_{\mu i,l}$. Eq. (5.46) holds in general for any overlap function $\mathcal{X}_\mu(E_i^{\mathcal{B}},\lambda_l)$. We now split up the overlap function into a normalized part and a normalization factor

$$\mathcal{X}_\mu(E_i^{\mathcal{B}},\lambda_l) = A_\mu\, f_\mu(E_i^{\mathcal{B}},\lambda_l), \tag{5.47}$$

where the function f_μ is normalized to one in an integral over the full energy λ_l for all μ with

$$\int \mathrm{d}\lambda\, f_\mu(E_i^{\mathcal{B}},\lambda) = 1. \tag{5.48}$$

The prefactor A_μ is labeled as the area of the overlap curve in chapter 4. It makes sure that the overlap is normalized according to the completeness of the full Hilbert space. This results in the relation

$$1 \overset{!}{=} \sum_{l=1}^{N_{\mathcal{F}}} \mathbb{E}\left[\left|c_{\mu i}^{(l)}\right|^2\right] = \sum_{l=1} N_{\mathcal{F}}\mathcal{X}_{\mu i,l} = \int_{-\infty}^{\infty} \mathrm{d}\lambda\, N_{\mathcal{F}}\,\rho_{\mathcal{F}}(\lambda)\,\mathcal{X}_\mu(E_i^{\mathcal{B}},\lambda) = \int_{-\infty}^{\infty} \mathrm{d}\lambda\, \underbrace{N_{\mathcal{F}}\,\rho_{\mathcal{F}}(\lambda)\,A_\mu}_{\overset{!}{=}1}\, f_\mu(E_i,\lambda), \tag{5.49}$$

where $c_{\mu i}^{(l)}$ are the coefficients of the expansion of the eigenstate $|\psi_l^{\mathcal{F}}\rangle$ in terms of the unperturbed eigenbasis as defined in Sec. 5.1.1, from which the sum rule in (5.49) originates. In (5.49) to fulfill the sum rule, the normalization factor for the overlap $\mathcal{X}_{\mu i,l}$ from (5.47) is determined to

$$A_\mu = \frac{1}{N_{\mathcal{F}}\,\rho_{\mathcal{F}}(\lambda_l)} \tag{5.50}$$

since the overlap curve $\mathcal{X}_\mu(E_i^{\mathcal{B}},\lambda)$ is evaluated at the position $\lambda = \lambda_l$. Note that the area A_μ does not depend on the considered overlap curve for the state μ in $\mathcal{S}$. This is confirmed by the analytical and numerical analysis in Sec. 4.4. For the numerical analysis, A_μ was determined from a Lorentzian fit with A_μ as an additional area prefactor. In Fig. 4.30 we found from a numerical analysis with $d_{\mathcal{S}} = 1$ and $d_{\mathcal{B}} = 1$ that both areas A_1 and A_2 of the two overlap curves agree with the inverse of the numerical DOS $N_{\mathcal{F}}\rho_{\mathcal{B}}(\lambda^{\mathcal{F}})$ supporting the result in (5.50). The areas are compared to $\rho_{\mathcal{B}}$ instead of $\rho_{\mathcal{F}}$, since the latter was not computed in the numerical analysis due to computation power limitations. In Fig. 4.32 we further numerically analyzed the difference of the two areas, $A_1 - A_2$ with respect to the energy

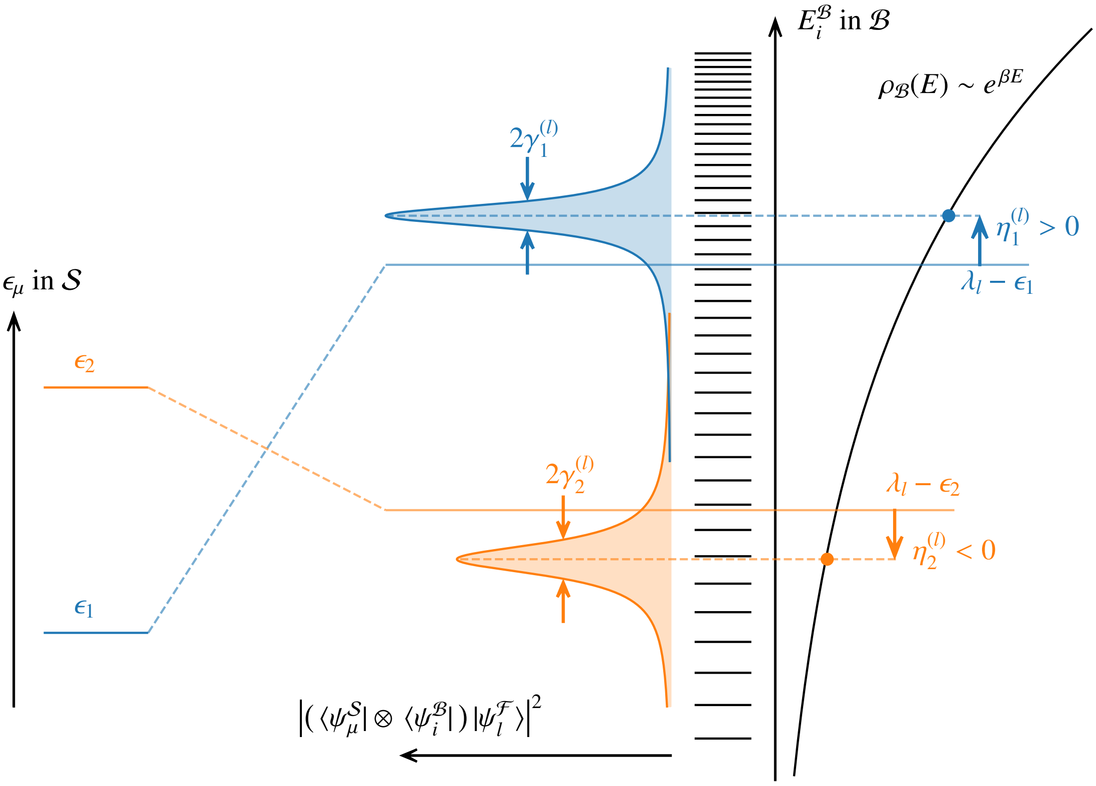

Figure 5.6: Illustration of a thermal distribution in a small subsystem $\mathcal{S}$ in an exact eigenstate $|\psi_l^{\mathcal{F}}\rangle$ of an isolated quantum system. The subsystem $\mathcal{S}$ is coupled weakly to the bath $\mathcal{B}$ and gives rise to Loretzian overlap curves $|\left(\langle\psi_\mu^{\mathcal{S}}|\otimes\langle\psi_i^{\mathcal{B}}|\right)|\psi_l^{\mathcal{F}}\rangle|^2$ in terms of the bath energies $E_i^{\mathcal{B}}$ centered at the position $E_i^{\mathcal{B}} = \lambda_l - \epsilon_\mu + \eta_\mu^{(l)}$, with a respective shift of $\eta_\mu^{(l)}$. Their width $\gamma_\mu^{(l)}$ is much smaller than the width of the DOS of $\mathcal{B}$. Given the Gaussian DOS in the bath, which can locally be expanded in terms of an exponential function, we obtain an exponential eigenstate occupation in the subsystem $\mathcal{S}$, which determines the diagonal of the reduced density matrix in the subsystem $\mathcal{S}$.

difference $\epsilon_2 - \epsilon_1$ in subsystem $\mathcal{S}$ and found that the data agrees with zero within the error margin. This is a strong confirmation, that the area A_μ of the overlap curves is independent of the considered state $|\psi_\mu^{\mathcal{S}}\rangle$, which is important in the derivation of the canonical distribution in the following. The result (5.50) with (5.47) can be inserted into (5.46) to find the diagonal entry of the reduced density matrix

$$\mathbb{E}\left[\rho_{\mu\mu}^{l,\mathcal{S}}\right] = \frac{\int_{-\infty}^{\infty} \mathrm{d}E\, N_{\mathcal{B}}\, \rho_{\mathcal{B}}(E)\, f_\mu(E, \lambda_l)}{N_{\mathcal{F}}\, \rho_{\mathcal{F}}(\lambda_l)}. \tag{5.51}$$

Since the result is obtained from (5.46), it holds in general for any overlap curve. In the thermodynamic limit, it converges to the canonical distribution, as shown in the following. For the thermodynamic limit, we increase the size of the bath $\mathcal{B}$ with $d_{\mathcal{B}}$ lattice sites, while the size of subsystem $\mathcal{S}$ stays constant. Since the interaction matrix between $\mathcal{S}$ and the bath does not change because it only acts at the boundary between $\mathcal{S}$ and $\mathcal{B}$, the overlap function $\mathcal{X}_\mu(E, \lambda)$ is approximately unchanged with the increase of $\mathcal{B}$. As explained in chapter 2, the DOS of the bath in the limit $d_{\mathcal{B}} \to \infty$

is given by a Gaussian distribution. Its variance scales as $\sigma^2_{\mathcal{B}} \propto d_{\mathcal{B}}$. At large $\mathcal{B}$, the width of the DOS $N_{\mathcal{B}}\,\rho_{\mathcal{B}}(E)$ is hence much larger than the width of the peak of the overlap curve $f_\mu(E,\lambda_l)$ and we have

$$\mathbb{E}\left[\rho^{l,\mathcal{S}}_{\mu\mu}\right] \to \frac{N_{\mathcal{B}}\,\rho_{\mathcal{B}}\left(\lambda_l - (\epsilon_\mu - \eta^{(l)}_\mu)\right)}{N_{\mathcal{F}}\,\rho_{\mathcal{F}}(\lambda_l)} \underbrace{\int \mathrm{d}E\, f_\mu(E,\lambda_l)}_{\circledast} \quad \text{for } N_{\mathcal{B}} \to \infty. \tag{5.52}$$

The integral $\circledast$ is equal to one if the normalized part of the overlap function depends only on the energy difference between the full energy and the bath energy $f_\mu(E^{\mathcal{B}}_i, \lambda_l) = f_\mu(E^{\mathcal{B}}_i - \lambda_l)$. This is the case for the Lorentzian function obtained for the overlap close to its maximum peak as described by analytical and numerical investigation in chapter 4. It was also used for the derivation of the reduced density matrix in Sec. 5.1.1 with Eq. (5.11) resulting in the canonical thermal density matrix for $\mathcal{S}$. The reason is that in this case the integral $\circledast$ is equal to the normalization integral over λ in (5.48), which is one by definition. It means that the overlap function is also normalized with respect to an integral over the bath energy $E^{\mathcal{B}}$. Since the normalization A_μ in (5.50) does not depend on $E^{\mathcal{B}}_i$, it corresponds to the area of the overlap curve $\mathcal{X}_\mu(E^{\mathcal{B}}_i, \lambda_l)$ in terms of the bath energy with

$$\int \mathrm{d}E\, \mathcal{X}_\mu(E,\lambda_l) = A_\mu \int \mathrm{d}E\, f_\mu(E,\lambda_l) = A_\mu. \tag{5.53}$$

In the thermodynamic limit the reduced density matrix in $\mathcal{S}$ takes the form

$$\mathbb{E}\left[\rho^{l,\mathcal{S}}\right] = \frac{1}{N_{\mathcal{F}}\,\rho_{\mathcal{F}}(\lambda_l)} \sum_\mu N_{\mathcal{B}}\,\rho_{\mathcal{B}}\left(\lambda_l - (\epsilon_\mu - \eta^{(l)}_\mu)\right) |\psi^{\mathcal{S}}_\mu\rangle\,\langle\psi^{\mathcal{S}}_\mu| \tag{5.54}$$

as emergent from a single eigenstate of the full quantum system. Crucial for this result is the fact that the areas A_μ of the overlap curves are identical for all μ, which was confirmed multiple times in the analytical and numerical analysis in Sec. 4.4. Only in this case is the diagonal entry of the reduced density matrix $\mathbb{E}\left[\rho^{l,\mathcal{S}}_{\mu\mu}\right] \propto N_{\mathcal{B}}\,\rho_{\mathcal{B}}\left(\lambda_l - (\epsilon_\mu - \eta^{(l)}_\mu)\right)$ which results from (5.52) and the area A_μ is a global prefactor. Except for the shifts $\eta^{(l)}_\mu$, the result (5.54) is analogous to the result from typicality in (5.43), but in contrast to typicality which makes a lot of assumption, e.g. on the probability distribution for the possible microstates, it was derived purely from the microscopic equations, i.e. from the laws of quantum mechanics. It can hence give a microscopic approach based on the actual eigenstates in the local quantum system to thermalization and provides a systematic study of the ETH.

Since the DOS of the bath $N_{\mathcal{B}}\rho_{\mathcal{B}}(E)$ is a Gaussian and its width is much larger than the spectral width of the small subsystem $\mathcal{S}$ with $\sigma_{\mathcal{S}} \ll \sigma_{\mathcal{B}}$, we can expand it in an exponential with constant inverse temperature $\beta = \frac{\partial S_{\mathcal{B}}(E)}{\partial E}$ and $S_{\mathcal{B}}(E) = \log(N_{\mathcal{B}}\,\rho_{\mathcal{B}})$ to obtain

$$N_{\mathcal{B}}\,\rho_{\mathcal{B}}\left(\lambda_l - (\epsilon_\mu - \eta^{(l)}_\mu)\right) \propto N_{\mathcal{B}}\,\mathrm{e}^{-\beta(\epsilon_\mu - \eta^{(l)}_\mu)} \tag{5.55}$$

This can be inserted into the reduced density matrix in (5.54) to obtain the canonical distribution in terms of the energy levels $\epsilon_\mu - \eta^{(l)}_\mu$, which are renormalized through the shifts $\eta^{(l)}_\mu$ that occur due the influence of the perturbation matrix X. The derivation is sketched in Fig. 5.6. To each of the two levels in $\mathcal{S}$, there is a corresponding overlap curve in terms of the bath eigenstates and energies $E^{\mathcal{B}}_i$, colored in blue and orange for the levels $\mu = 1$ and $\mu = 2$ respectively. The overlap peaks are centered around the positions $\lambda_l - (\epsilon_\mu - \eta^{(l)}_\mu)$, which is shifted by $\eta^{(l)}_\mu$ about the difference of the full energy λ_l and the corresponding energy in $\mathcal{S}$ indicated by the dashed versus the solid line in

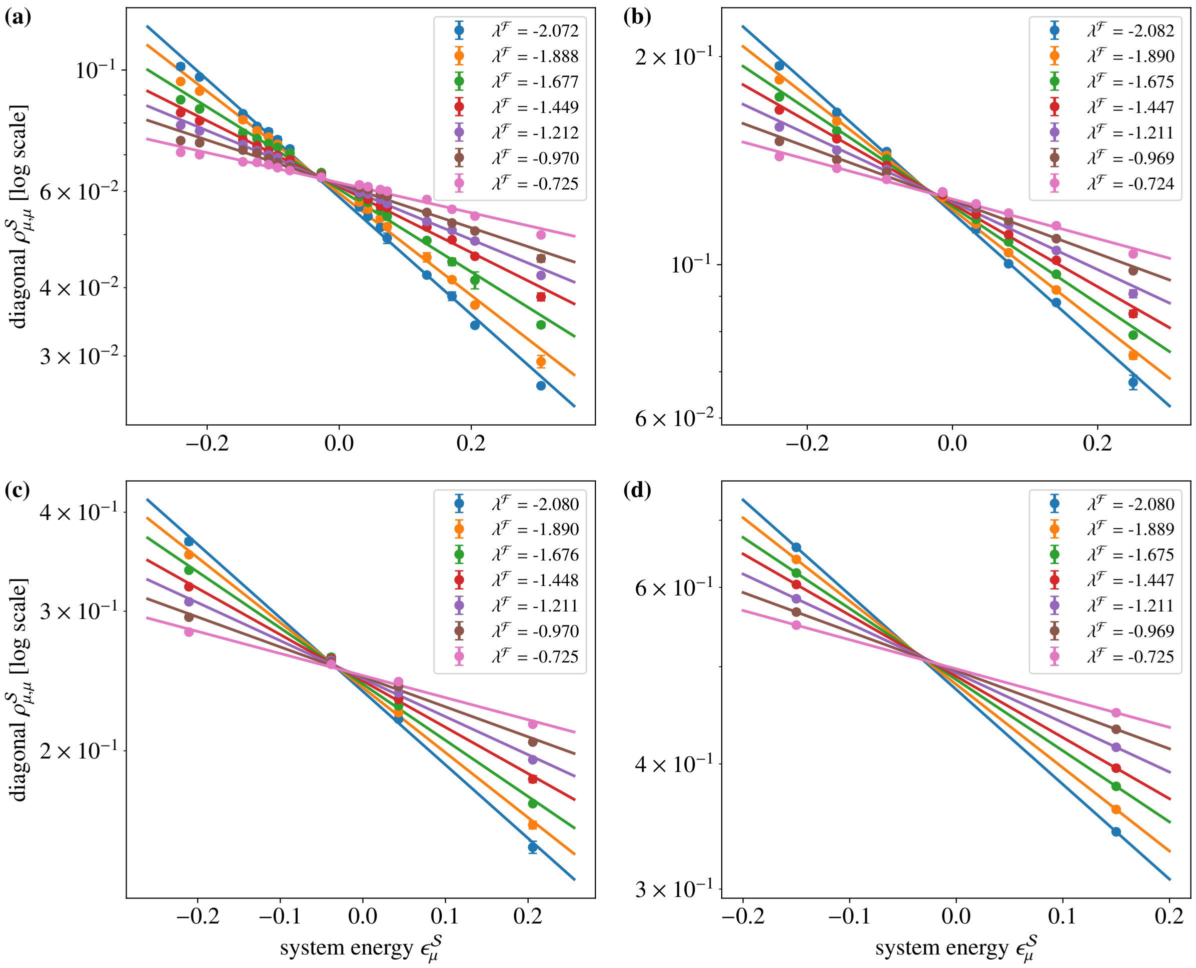

Figure 5.7: Diagonal entries of a reduced density matrix $\rho^{\mathcal{S}}$ in a small subsystem $\mathcal{S}$ obtained from an exact eigenstate of $H^{\mathcal{F}}$ at the eigenenergy $\lambda^{\mathcal{F}}$. $\rho^{\mathcal{S}}$ is represented in terms of the eigenbasis of $\mathcal{S}$ and its diagonal elements are plotted on a logarithmic scale with respect to the eigenenergy $\epsilon^{\mathcal{S}}_{\mu}$ in $\mathcal{S}$. We consider $N_{\text{av}} = 1000$ full states around different values of $\lambda_{\mathcal{F}}$ and average the result over 40 samples of $H^{\mathcal{F}}$. The variance of the perturbation matrix is given by t. The full quantum systems contains $d_{\mathcal{F}} = 16$ sites, of which subsystem $\mathcal{S}$ occupies **(a)** $d_{\mathcal{S}} = 4$ at $t = 2.22 \times 10^{-3}$, **(b)** $d_{\mathcal{S}} = 3$ at $t = 1.93 \times 10^{-3}$, **(c)** $d_{\mathcal{S}} = 2$ at $t = 2.12 \times 10^{-3}$ and **(d)** $d_{\mathcal{S}} = 1$ at $t = 2.03 \times 10^{-3}$ sites. We perform linear fits in each plot for all investigated values of λ_l individually to read off the inverse temperature β of the assumed exponential distribution as the slope of the linear fit. The result is plotted in Fig. 5.8.

Fig. 5.6. The Gaussian DOS expanded into an exponential curve is indicated on the right side of the figure and is evaluated at the peak position of the respective overlap curves to give the diagonal entries of the reduced density matrix in $\mathcal{S}$ given by Eq. (5.24) or (5.54) with (5.55).

In a numerical analysis of the quantum lattice with $d_{\mathcal{F}} = 16$ sites we compare the entries of the reduced density matrix with the analytical results for different sizes of the subsystem $\mathcal{S}$. In Fig. 5.7, the diagonal $\rho^{l,\mathcal{S}}_{\mu\mu}$ is plotted on a logarithmic scale for $d_{\mathcal{S}} = 4$ in **(a)**, $d_{\mathcal{S}} = 3$ in **(b)**, $d_{\mathcal{S}} = 2$ in **(c)** and $d_{\mathcal{S}} = 1$ in **(d)**. We consider different values of the full energy λ_l, around which we take $N_{\text{av}} = 1000$ full states to average the entries of the reduced density matrix. Those are then averaged over 40 samples of the Hamiltonian $H^{\mathcal{F}}$, where the subsystem Hamiltonian $H^{\mathcal{S}}$ in $\mathcal{S}$ is kept constant and normalized to $\tau\left((H^{\mathcal{S}})^2\right) = 0.0225$ such as to have identical energy levels to compare to in all runs. The diagonal values $\rho^{l,\mathcal{S}}_{\mu\mu}$ approximately follow an exponential distribution as indicated by the linear fits on the logarithmic scale. This confirms the analytical result in Eq. (5.24) and (5.54) with (5.55) that the reduced density matrix in the subsystem $\mathcal{S}$ follows an exponential distribution. Although the numerical results were obtained in a finite size system at $d_{\mathcal{F}} = 16$ sites, the diagonals of the reduced matrix already show thermal behavior. They assume the form

$$\rho^{l,\mathcal{S}}_{\mu\mu} \approx \frac{1}{Z_{\mathcal{S}}(\beta)} \mathrm{e}^{-\beta(\epsilon_\mu - \eta^{(l)}_\mu)} \tag{5.56}$$

where $Z_{\mathcal{S}} = (\beta) = \sum_\mu \mathrm{e}^{-\beta(\epsilon_\mu - \eta^{(l)}_\mu)}$ is the partition function. Since the shifts $\eta^{(l)}_\mu$ are not available in the present numerical analysis and since they are much smaller than the energies in $\mathcal{S}$, they are omitted in the further analysis of the inverse temperature β obtained from the numerical data. β is obtained as the negative slope of the linear fits with respect to the energy in $\mathcal{S}$ on the logarithmic scale in Fig. 5.7 reading

$$\ln\left(\rho_{\mu\mu}\right) = -\ln(Z_{\mathcal{S}}(\beta)) - \beta\epsilon_\mu. \tag{5.57}$$

In every panel of Fig. 5.7, we observe a crossing point of the linear functions, which from the scale of Fig. 5.7 seems to be at the same point for all β, but actually differs slightly for all combinations of curve crossings. It is also not at the point $\epsilon_\mu = 0$ since there we have $\rho^{l,\mathcal{S}}_{\mu\mu} = (Z_{\mathcal{S}}(\beta))^{-1}$ which depends on β. We expand $Z_{\mathcal{S}}(\beta)$ in second order of $\beta\epsilon_\mu$ with

$$\ln(Z_{\mathcal{S}}(\beta)) \approx \ln\left(N_{\mathcal{S}} + \frac{1}{2}\beta^2 \sum_\mu \epsilon_\mu^2\right) \approx \ln(N_{\mathcal{S}}) + \frac{1}{2}\beta^2 \underbrace{\frac{1}{N_{\mathcal{S}}}\sum_\mu \epsilon^2_\mu}_{=\sigma^2_{\mathcal{S}}} \tag{5.58}$$

where we have used the fact that the trace of the Hamiltonian in subsystem $\mathcal{S}$ is zero, $\sum_\mu \epsilon_\mu = 0$ such that the first order of $\beta\epsilon_\mu$ vanishes in (5.58). We further identified the second moment of $H^{\mathcal{S}}$ being the variance $\sigma^2_{\mathcal{S}}$ of the DOS in (5.58). In terms of this expansion we have

$$Z_{\mathcal{S}}(\beta) \approx N_{\mathcal{S}}\, \mathrm{e}^{\frac{1}{2}\beta^2\sigma^2_{\mathcal{S}}} \tag{5.59}$$

which agrees with the result obtained in Eq. (5.23). If we want to compute the crossing point of two different linear fits with slopes $-\beta_1$ and $-\beta_2$, we have to solve the equation

$$\begin{aligned} -\ln(Z_{\mathcal{S}}(\beta_1)) - \beta_1 x_0 &\overset{!}{=} -\ln(Z_{\mathcal{S}}(\beta_2)) - \beta_2 x_0 \\ \rightarrow x_0 &= -\frac{1}{\beta_2 - \beta_1}\left(\ln(Z_{\mathcal{S}}(\beta_2)) - \ln(Z_{\mathcal{S}}(\beta_2))\right) \\ &= -\frac{1}{\beta_2 - \beta_1}\frac{\sigma^2_{\mathcal{S}}}{2}(\beta_2^2 - \beta_1^2) \\ &= -\frac{1}{2}\sigma^2_{\mathcal{S}}(\beta_1 + \beta_2) \end{aligned} \tag{5.60}$$

where x_0 marks the crossing point of the two lines. It is not at zero but slightly shifted to negative values due to the effect of $\ln(Z_{\mathcal{S}}(\beta))$ which is the y-intersect of the linear fit equation in (5.57). This behavior is consistently observed in Fig. 5.7, where the crossing region in each panel is located at negative energies of small magnitude. Since $\sigma_{\mathcal{S}} = 0.15$ uniformly for all investigated sizes of subsystem $\mathcal{S}$, the crossing points are located approximately in same region of

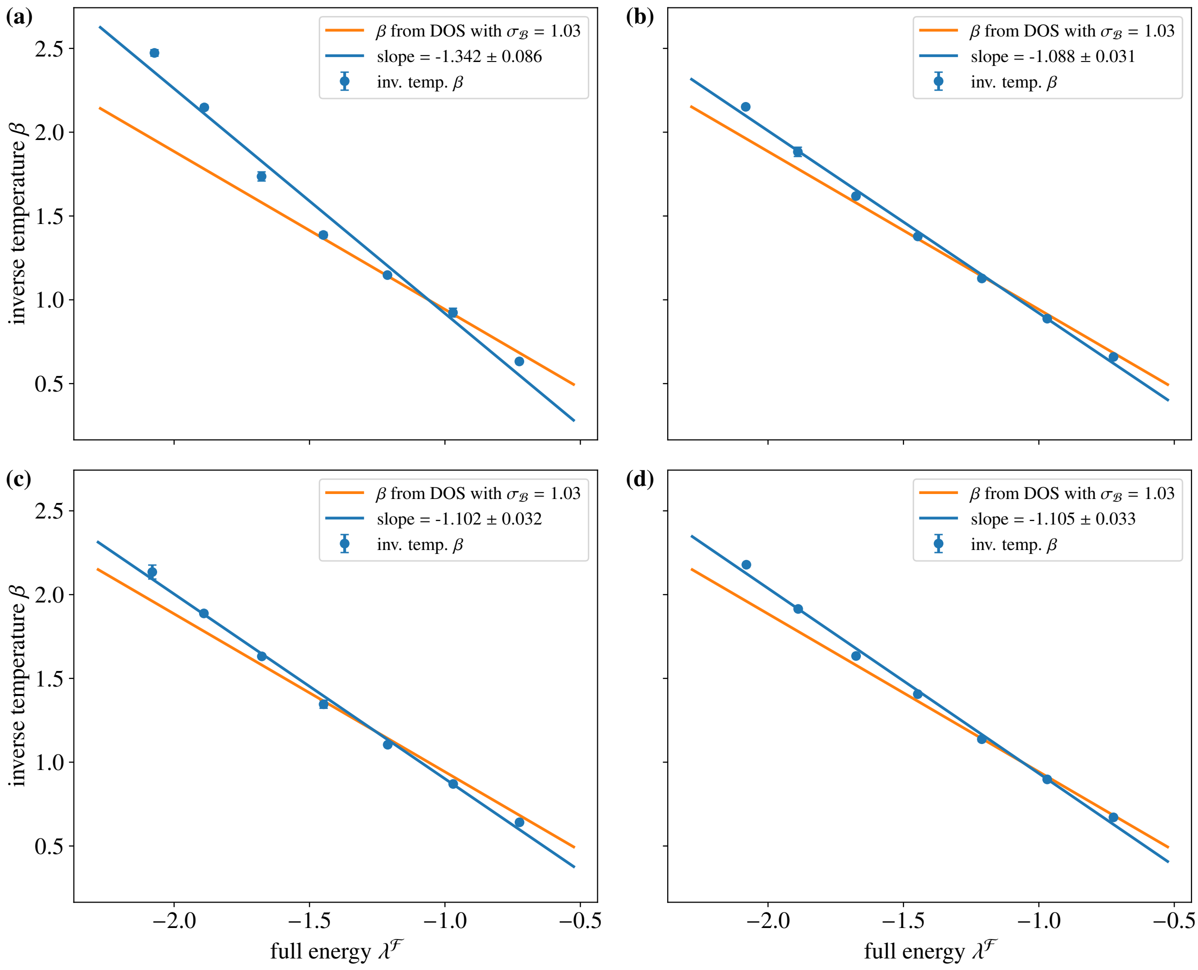

Figure 5.8: Result for the inverse temperature β obtained from linear fits to the logarithmic plot of the diagonal entries of the reduced density matrix $\rho^{\mathcal{S}}$ in Fig. 5.7 as blue data points. In accordance with Fig. 5.7, the full quantum systems contains $d_{\mathcal{F}} = 16$ sites, of which subsystem $\mathcal{S}$ occupies **(a)** $d_{\mathcal{S}} = 4$, **(b)** $d_{\mathcal{S}} = 3$, **(c)** $d_{\mathcal{S}} = 2$ and **(d)** $d_{\mathcal{S}} = 1$ sites. β is plotted with respect to the full energy λ_l of the full quantum system. In each plot, we perform a linear fit in blue to find the relation between the inverse temperature β and the full energy λ_l. An additional straight line in orange shows the analytical expectation of β in terms of the energy λ_l from the Gaussian DOS of the bath $\mathcal{B}$ with variance $\sigma_{\mathcal{B}}^2$.

$\epsilon_\mu^{\mathcal{S}}$ within all panels in Fig. 5.7. The diagonal value of the reduced density matrix at the crossing is given by

$$\rho_{\mu\mu} = \frac{1}{Z_{\mathcal{S}}(\beta_1)} \mathrm{e}^{-\beta_1 x_0} = \frac{1}{N_{\mathcal{S}}} \mathrm{e}^{\frac{1}{2}\beta_1\beta_2\sigma_{\mathcal{S}}^2} \tag{5.61}$$

and

$$\ln\left(\rho_{\mu\mu}\right) = -\ln(N_{\mathcal{S}}) + \frac{1}{2}\beta_1\beta_2\,\sigma_{\mathcal{S}}^2 \tag{5.62}$$

in terms of the given expansion. With $\sigma_{\mathcal{S}}^2 \ll \sigma_{\mathcal{B}}^2$, the diagonal values of the reduced density matrix at the crossing points of the linear fits are slightly larger than $\frac{1}{N_{\mathcal{S}}}$ which is supported by the observation in Fig. 5.7. The inverse temperature β obtained from the best fit parameters from Fig. 5.7 for the slopes are plotted with respect to the investigated points of the full energy λ_l for each panel individually in Fig. 5.8. Equivalent to Fig. 5.7 we have $d_{\mathcal{S}} = 4$ in **(a)**, $d_{\mathcal{S}} = 3$ in **(b)**, $d_{\mathcal{S}} = 2$ in **(c)** and $d_{\mathcal{S}} = 1$ in **(d)** in Fig. 5.8. In Sec. 5.1.1 the inverse temperature was obtained as

$$\beta = \frac{\partial S_{\mathcal{B}}(E)}{\partial E}\bigg|_{E=\lambda_l} = -\frac{\lambda_l}{\sigma_{\mathcal{B}}^2} \tag{5.63}$$

in Eq. (5.20). As a reference, we plot this relation as orange colored straight lines in each panel of Fig. 5.8, where we use $\sigma_{\mathcal{B}} = 1.03$ which was obtained from the numerical fit in chapter 4 in Fig. 4.10. Linear fits to the data points in blue in Fig. 5.8 confirm the linear relation between β and the full energy λ_l in (5.63). In Fig. 5.8**a**, the data shows a slight curvature which we attribute to finite size effects as the subsystem $\mathcal{S}$ with $d_{\mathcal{S}} = 4$ denotes a quarter of the whole quantum system of $d_{\mathcal{F}} = 16$ sites. In this case the bath only contains $d_{\mathcal{B}} = 12$ sites and its DOS is not large enough to obtain reliable results with a main assumption $\sigma_{\mathcal{B}}^2 \gg \sigma_{\mathcal{S}}^2$ being violated. This panel also contains the largest deviation of the slopes between the linear fit of the numerical data and the theoretically expected slope $-\frac{1}{\sigma_{\mathcal{B}}^2}$. From the slope of the linear fits in the remaining panels Fig. 5.8**b-c** we can compute the expected standard deviation of the DOS of the bath $\mathcal{B}$ for the reduced density matrix data, which is given by $\sigma_{\mathcal{B}}^{(\text{num},\beta)} = 0.9542(39)$. It is slightly smaller than the actual value of $\sigma_{\mathcal{B}} = 1.03$, which is attributed to two effects. First, the finite width of the Gaussian obtained from the numerical data does not represent the thermodynamic limit and introduces finite size effects. Here, the curvature of the Gaussian DOS plays a role for the data since the exponential expansion of the DOS in the investigated energy interval only becomes exact in the limit $d_{\mathcal{B}} \to \infty$. Second, the inverse temperature β was obtained from the pure energy levels ϵ_μ instead of the shifted levels $(\epsilon_\mu - \eta_\mu^{(l)})$ which actually occur in the thermal density matrix of the eigenstate $|\psi_l^{\mathcal{F}}\rangle$ in Sec. 5.1.1, since the shifts $\eta_\mu^{(l)}$ are not available in this numerical study.

The reduced density matrix in subsystem $\mathcal{S}$ can alternatively be represented in terms of the SVD states, c.f. Sec. 2.1.4, which is stated as

$$|\psi_l^{\mathcal{F}}\rangle = \sum_\mu \kappa_\mu^{(l)} |\phi_\mu^{l,\mathcal{S}}\rangle \otimes |\phi_\mu^{l,\mathcal{B}}\rangle, \tag{5.64}$$

where $|\phi_\mu^{l,\mathcal{S}}\rangle$ and $|\phi_\mu^{l,\mathcal{B}}\rangle$ are the singular vectors in $\mathcal{S}$ and $\mathcal{B}$ respectively. The singular values are chosen real and larger than zero, $\kappa_\mu^{(l)} > 0$. The pure density matrix of the single eigenstate $|\psi_l^{\mathcal{F}}\rangle$ of $H^{\mathcal{F}}$ is then given by

$$\rho^l = |\psi_l^{\mathcal{F}}\rangle\langle\psi_l^{\mathcal{F}}| = \sum_{\mu,\mu'=1}^{N_{\mathcal{S}}} \kappa_\mu^{(l)}\kappa_{\mu'}^{(l')} |\phi_\mu^{l,\mathcal{S}}\rangle\langle\phi_{\mu'}^{l,\mathcal{S}}| \otimes |\phi_\mu^{l,\mathcal{B}}\rangle\langle\phi_{\mu'}^{l,\mathcal{B}}| . \tag{5.65}$$

Taking the trace over the bath $\mathcal{B}$ results in the reduced density matrix of subsystem $\mathcal{S}$,

$$\rho^{l,\mathcal{S}} = \mathrm{Tr}\left(|\psi_l^{\mathcal{F}}\rangle\langle\psi_l^{\mathcal{F}}|\right) = \sum_{\mu=1}^{N_{\mathcal{S}}} \left(\kappa_\mu^{(l)}\right)^2 |\phi_\mu^{l,\mathcal{S}}\rangle\langle\phi_\mu^{l,\mathcal{S}}| , \tag{5.66}$$

which is diagonal in the SVD basis. If the two subsystems $\mathcal{S}$ and $\mathcal{B}$ of the quantum lattice are weakly coupled through the perturbation X, the singular vectors in $\mathcal{S}$ are approximately equivalent to the eigenstates in $\mathcal{S}$ with $|\phi_\mu^{l,\mathcal{S}}\rangle \approx |\psi_\mu^{\mathcal{S}}\rangle$ since the states in $\mathcal{S}$ are not being mixed. This assumption is numerically confirmed for the choices of X and t that were analyzed in chapter 4. Additionally, in Sec. 5.1.1 we show that the reduced density matrix in $\mathcal{S}$ obtained from a single eigenstate of the full quantum system becomes diagonal in the thermodynamic limit with $N_{\mathcal{F}} \to \infty$ thereby

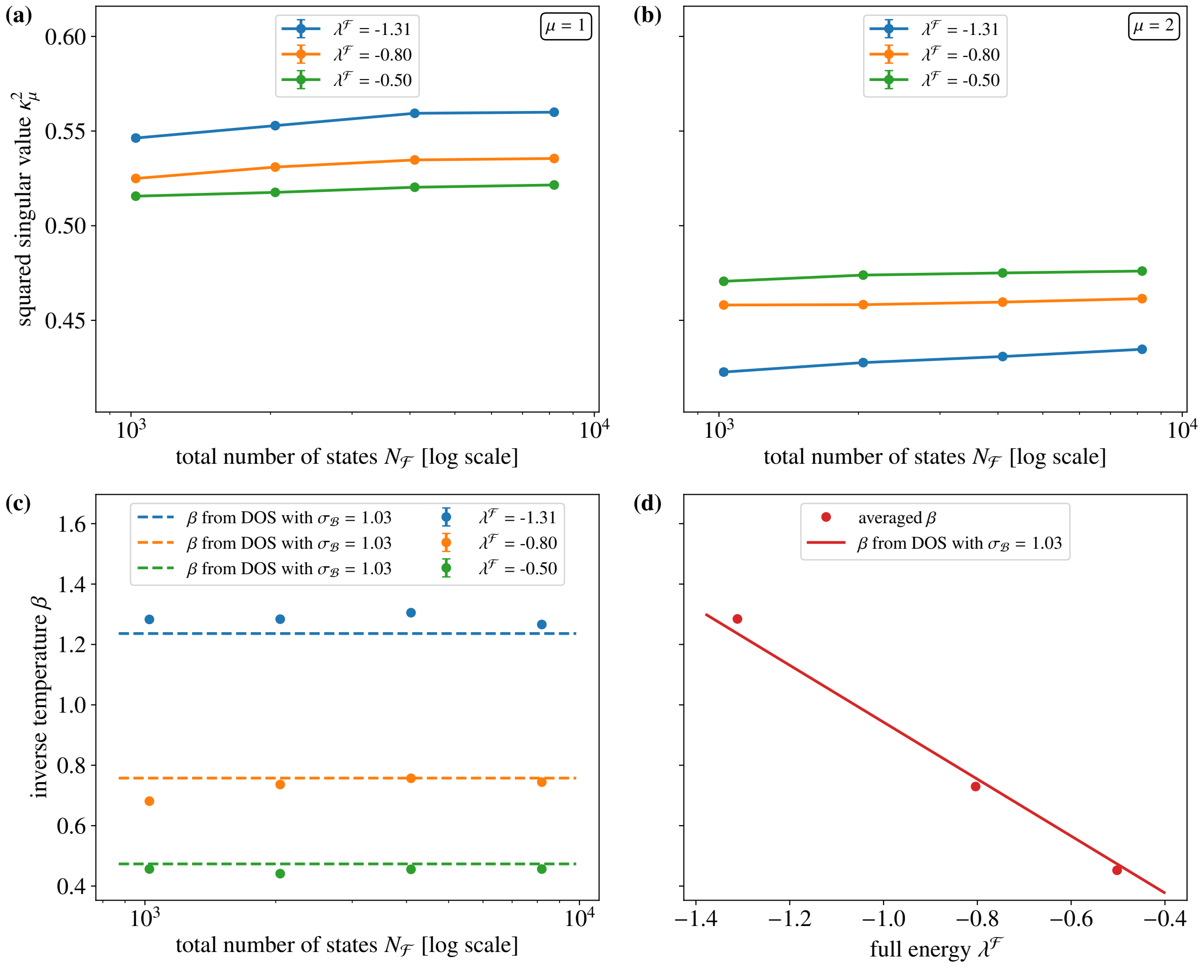

Figure 5.9: Analysis of the thermal properties of the reduced density matrix $\rho^{\mathcal{S}}$ represented in terms of the SVD in the subsystem $\mathcal{S}$ with $d_{\mathcal{S}} = 1$ site obtained from an eigenstate of a quantum system with a total size of $d_{\mathcal{F}} = \{10, 11, 12, 13\}$ sites. The variance of X is given by $t = \{7.66, 6.66, 5.98, 5.53\} \times 10^{-3}$ accordingly. The result is averaged over 100 samples of $H^{\mathcal{B}}$ and 200 samples of X. **(a)** and **(b)** show the squared singular values κ_μ^2 at different eigenvalues λ_l for $\mu = 1$ and $\mu = 2$ respectively with respect to the number of total states $N_{\mathcal{F}}$ on a logarithmic scale. **(c)** depicts the inverse temperature β for each system size $N_{\mathcal{F}}$ and full energy λ_l with respect to a logarithmic scale of $N_{\mathcal{F}}$. The data is computed from the squared singular values κ_μ^2 in **(a)** and **(b)**. Dashed lines show the analytically expected value of β from the Gaussian DOS of the bath $\mathcal{B}$ with variance $\sigma_{\mathcal{B}}^2$. **(d)** depicts the inverse temperature β averaged over all system sizes $d_{\mathcal{F}}$ in **(c)** with respect to the full energy λ_l. A straight line shows the expected relation between β and λ_l from the Gaussian DOS of $\mathcal{B}$.

showing that the singular vectors are effectively equivalent to the eigenvectors in $\mathcal{S}$. In this case, the singular vectors in the bath scaled with their corresponding singular value $\kappa_\mu^{(l)} |\phi_\mu^{l,\mathcal{B}}\rangle$ are equivalent to the decomposition of the full states in the unperturbed basis with coefficients $c_{\mu i}^{(l)}$ defined in Sec. 5.1.1 and we have

$$\kappa_\mu^{(l)} |\phi_\mu^{l,\mathcal{B}}\rangle \approx \sum_i c_{\mu i}^{(l)} |\psi_i^{\mathcal{B}}\rangle \,. \tag{5.67}$$

The overlaps of the full eigenstates in terms of the unperturbed eigenbasis in chapter 4 are then given by $X_{\mu i,l} \approx \left(\kappa_\mu^{(l)}\right)^2 \left|\langle\phi_\mu^{l,\mathcal{B}}|\psi_i^{\mathcal{B}}\rangle\right|^2$. In the thermodynamic limit, we can reconnect the result in (5.66) to the thermal density matrix (5.24) obtained in Sec. 5.1.1. The diagonal values in the reduced density matrix of the SVD representation in (5.66) are then equal to the Boltzmann factors

$$\left(\kappa_\mu^{(l)}\right)^2 \approx \frac{1}{Z_{\mathcal{S}}}\,\mathrm{e}^{-\beta(\epsilon_\mu-\eta_\mu^{(l)})}. \tag{5.68}$$

This result is obtained from a comparison to Eq. (5.24) as the shifts $\eta_\mu^{(l)}$ which were found from the overlap analysis are not accessible to the SVD approach. For this reason, it cannot provide a complete microscopic picture, and we have used the overlap analysis in the previous part of this work. A numerical analysis of the reduced density matrix in subsystem $\mathcal{S}$ containing a single site in terms of the SVD representation is shown in Fig. 5.9. We plot the squared singular values $\left(\kappa_\mu^{(l)}\right)^2$ for three different investigated points of full energy λ_l with respect to a logarithmic representation of the total number of states $N_{\mathcal{F}}$ in Fig. 5.9**a,b**. In total, we investigate the total system sizes of $d_{\mathcal{F}} = \{10, 11, 12, 13\}$ sites. In Fig. 5.9**c** we plot the computed values of the inverse temperature β from a linear fit to the singular values $\left(\kappa_\mu^{(l)}\right)^2$ represented on a logarithmic scale. Underlying to that is Eq. (5.68), where the shifts $\eta_\mu^{(l)}$ are omitted since they are not available from the SVD approach. The theoretical values of β obtained from (5.63) for the investigated values of λ_l are plotted as dashed lines in Fig. 5.9**c**. The theoretical and numerical values are close to each other and their deviation is smaller for larger $N_{\mathcal{F}}$. In Fig. 5.9**d** we show the mean values of β averaged from the results in Fig. 5.9**c** plotted with respect to the investigated full energy λ_l. A straight line shows the theoretical relation between β and λ_l given by $-\frac{1}{\sigma_{\mathcal{B}}^2}$. It fits well to the numerical results and confirms (5.68) for the investigated systems with small coupling X between $\mathcal{S}$ and $\mathcal{B}$. This alternative approach to the description of thermal states is inferior to the one in Sec. 5.1.1 since it does not take the full microscopic details of the system into account, which is traced through the overlaps of the perturbed and unperturbed states under the addition of the coupling X. This is why we choose to primarily investigate the latter approach in this work.

The results presented in this section and in Sec. 5.1.1 explain and derive the thermal behavior of a single eigenstate in a small subsystem of a local, isolated, non-integrable quantum system from a microscopic perspective. As a basis of our calculations we only use the theory of quantum mechanics and make no assumptions on the shape of the eigenstates. The theory can be connected to the description of the ETH which was detailed in Sec. 5.2.1. For this purpose, we use a local operator $A = A_{\mathcal{S}} \otimes \mathbb{1}_{\mathcal{B}}$ which acts non-trivially only in subsystem $\mathcal{S}$. Then our analysis shows that the expectation value of A in a single eigenstate $|\psi_l^{\mathcal{F}}\rangle$ behaves thermally,

$$A_{ll} = \langle\psi_l^{\mathcal{F}}|A|\psi_l^{\mathcal{F}}\rangle \longrightarrow \frac{1}{Z_{\mathcal{S}}}\,\mathrm{Tr}_{\mathcal{S}}\left(\mathrm{e}^{-\beta\tilde{H}^{\mathcal{S}}} A_{\mathcal{S}}\right) \equiv \langle A_{\mathcal{S}}\rangle_{\beta,\mathcal{S}} \tag{5.69}$$

in the thermodynamic limit with $N_{\mathcal{B}} \to \infty$. The subscript $\beta, \mathcal{S}$ refers to the canonical thermal expectation value in subsystem $\mathcal{S}$ and not in the whole quantum system. Equation (5.69) holds, since we have shown that the reduced density matrix $\rho^{l,\mathcal{S}}$ of the single full eigenstates $|\psi_l^{\mathcal{F}}\rangle$ converges to its thermal density matrix with energy levels $\epsilon_\mu - \eta_\mu^{(l)}$ renormalized by the interaction X as determined in Eq. (5.24). For that we define the effective Hamiltonian $\tilde{H}^{\mathcal{S}}$ in the subsystem $\mathcal{S}$ that enters the thermal density matrix as

$$\tilde{H}^{\mathcal{S}} \equiv \sum_{\mu=1}^{N_{\mathcal{S}}} \left(\epsilon_\mu - \eta_\mu^{(l)}\right) |\psi_\mu^{\mathcal{S}}\rangle\,\langle\psi_\mu^{\mathcal{S}}| \tag{5.70}$$

with the shifted energies. Both β and $\eta_\mu^{(l)}$ depend on the full eigenvector $|\psi_l^{\mathcal{F}}\rangle$ in question and its associated eigenvalue λ_l. The ETH in Sec. 5.2.1 is formulated in terms of states $|\psi\rangle$ in (5.25) whose fluctuations in energy are much smaller than their mean energy, $(\delta\lambda)^2 \ll \bar{\lambda}$. Mathematically, this equates to an approximation of constant β in the energy window $\delta\lambda$, which means that also $\eta_\mu^{(l)}$ is constant within this small window. Since with (5.69) we have proven that each single state behaves thermally, the ETH follows by using Eq. (5.30)

$$\langle A\rangle_\psi (t) = \langle\psi(t)|A|\psi(t)\rangle \overset{t\to\infty}{\longrightarrow} \sum_l |c_l|^2 A_{ll} \overset{N_{\mathcal{B}}\to\infty}{\longrightarrow} \langle A_{\mathcal{S}}\rangle_{\beta,\mathcal{S}} \tag{5.71}$$

under the application of (5.69) for every single eigenstate l. here, c_l are the expansion coefficients of $|\psi\rangle$ in terms of the full eigenstates. Note that our theory makes a statement about the equilibrium phase and not about the equilibration to the equilibrium which can be investigated in future research.

Further note that the ETH is slightly more general as it identifies the pure density matrix of a single eigenstate $|\psi_l^{\mathcal{F}}\rangle$ with its thermal density matrix for the whole system

$$A_{ll} = \mathrm{Tr}\left(A\rho^l\right) \approx \langle A\rangle_\beta = \mathrm{Tr}\left(A\,\rho_\beta\right) = \frac{1}{Z}\,\mathrm{Tr}\left(A\,\mathrm{e}^{-\beta H^{\mathcal{F}}}\right). \tag{5.72}$$

which only holds in the expectation value of the local operator A, as initially described in Eq. (5.31). Since $A = A_{\mathcal{S}} \otimes \mathbb{1}_{\mathcal{B}}$ is a local operator, it results in

$$\langle A\rangle_\beta = \frac{1}{Z_{\mathcal{S}}}\,\mathrm{Tr}_{\mathcal{S}}\left[A_{\mathcal{S}}\left(\frac{1}{Z_{\mathcal{B}}}\,\mathrm{Tr}_{\mathcal{B}}\left(\mathrm{e}^{-\beta(H^{\mathcal{B}}+H^{\mathcal{S}}+X)}\right)\right)\right] \tag{5.73}$$

with $Z = Z_{\mathcal{S}}\cdot Z_{\mathcal{B}}$. Using the notion of the *approximate ETH* [62], we obtain for the thermal density matrix of the whole quantum system traced over $\mathcal{B}$

$$\frac{1}{Z_{\mathcal{B}}}\,\mathrm{Tr}_{\mathcal{B}}\left(\mathrm{e}^{-\beta(H^{\mathcal{B}}+H^{\mathcal{S}}+X)}\right) \approx \mathrm{e}^{-\beta H^{\mathcal{S}}}, \tag{5.74}$$

where X is assumed much smaller than $H^{\mathcal{B}}$ while $H^{\mathcal{S}}$ can be pulled out of the trace since it does not act in the bath. In this approximation, the influence of X in the trace over $\mathcal{B}$ is neglected and the thermal density matrix of $\mathcal{S}$ with the bare Hamiltonian $H^{\mathcal{S}}$ emerges. It therefore equates the thermal expectation value $\langle A\rangle_\beta$ in the whole quantum system with the thermal expectation value of $A_{\mathcal{S}}$ in subsystem $\mathcal{S}$. From our analysis, we find that the influence of X can effectively be captured through a shift of the energy levels in $\mathcal{S}$ by taking the thermal density matrix with the renormalized Hamiltonian $\tilde{H}^{\mathcal{S}}$ as in (5.69). It results in the identification

$$\langle A\rangle_\beta = \langle A_{\mathcal{S}}\rangle_{\beta,\mathcal{S}} \tag{5.75}$$

confirming the general version of the ETH. From the point of view of statistical mechanics, this makes sense, since a subsystem of a thermal system must also behave thermally at the same temperature, since the remaining part of the system can be assigned to the bath. In our analysis we require that the coupling X between $\mathcal{S}$ and $\mathcal{B}$ is much smaller than the spectral width in $\mathcal{S}$ and $\mathcal{B}$ itself, $t \ll \sigma_{\mathcal{S}}^2 \ll \sigma_{\mathcal{B}}^2$. This situation can always be achieved with a very large bath by increasing the size of $\mathcal{S}$. Since X scales with the boundary between $\mathcal{S}$ and $\mathcal{B}$, it is inherently much smaller than $H^{\mathcal{S}}$ and $H^{\mathcal{B}}$. Our analysis further uses the averaging over X and the self-averaging of $H^{\mathcal{B}}$. If we had a specifically tuned situation, e.g. $\mathcal{S}$ is locally coupled to a region of $\mathcal{B}$ with a strong local magnetic field, the analysis would break down. However by the scheme of increasing the defined size of $\mathcal{S}$ taken from a very large bath, we can always achieve the prescribed situation $t \ll \sigma_{\mathcal{S}}^2 \ll \sigma_{\mathcal{B}}^2$ where self-averaging is applicable and we obtain a generic coupling between $\mathcal{S}$ and $\mathcal{B}$ which leads to the thermal density matrix in $\mathcal{S}$ as in (5.24) and consequently proves the ETH.

Lastly, we remark that the ETH was already visible from the matrix elements of the perturbation matrix X in the unperturbed basis in chapter 3. We found that the diagonal elements $\tilde{X}_{ii}$ are correlated with the energy $E_i^{\mathcal{B}}$ in a quadratic energy dependence of their variance. This behavior originates from the uniform energy distribution of the thermal states throughout the spin lattice and can be obtained, alternative to the derivation in 3.1.4, when assuming that the states are thermal. We further found that the diagonal variance of $\tilde{X}$ do not scale with the system size of the bath $\mathcal{B}$, while the offdiagonal variance of $\tilde{X}$ scales with $\frac{1}{N_{\mathcal{B}}}$ and is therefore much smaller than the diagonal one, the difference being amplified as $N_{\mathcal{B}}$ increases. Those properties are the same and only ones demanded in (5.36a,b) for the ETH to hold within the original formulation by Deutsch and Srednicki.

5.3 Scattering of Lorentzians

To conclude the analysis, we propose an experiment where the small subsystem $\mathcal{S}$ is excited by an external source, e.g. a light pulse. In this experiment, we are interested in the transition probability from an initial to a final state of the full quantum system $\mathcal{F}$ depending on the input energy of the light. We treat the incoming light as a time dependent perturbation on the whole quantum system, which acts only within subsystem $\mathcal{S}$. Since the scattering only acts in $\mathcal{S}$, its transition probability is determined by the scattering of the corresponding states in the bath $\mathcal{B}$, which occur in the decomposition of a full eigenstate in terms of the unperturbed setup. The overlap of eigenstates of the full quantum system with the unperturbed eigenbasis form shifted Lorentzian peaks and we expect that the transition probability due to the external perturbation is sensitive to the shifts of the Lorentzians. In such a setting, the renormalized energy levels according to the coupling of $\mathcal{S}$ to the bath which enter the Boltzmann factors in the reduced density matrix of subsystem $\mathcal{S}$ in (5.24) are accessible. We first review Fermi's golden rule through time-dependent perturbation theory and then analytically investigate the scattering amplitude to compare it to a numerical analysis.

5.3.1 Fermi's golden rule

Fermi's golden rule [218, 219] determines the transition rate from an initial eigenstate to a group of final eigenstates of the full quantum system in a continuum. For that, we add a time dependent perturbation to the Hamiltonian, which is assumed to be weak. To analytically trace the eigenstate transition, we employ time dependent perturbation theory in first order. The unperturbed full quantum system is described by the *Schrödinger equation (SEQ)*

$$i\partial_t \left|\psi_0(t)\right\rangle = H^{\mathcal{F}} \left|\psi_0(t)\right\rangle \tag{5.76}$$

with $\hbar = 1$, where $\left|\psi_0(t)\right\rangle$ is the initial state of the quantum system at times $t < 0$. At $t = 0$ we then switch on a perturbation $V(t)$, which is added to the Hamiltonian. The perturbed state $\left|\psi(t)\right\rangle$ is then described by the SEQ

$$i\partial_t \left|\psi(t)\right\rangle = \left(H^{\mathcal{F}} + V(t)\right) \left|\psi(t)\right\rangle \tag{5.77}$$

which follows the boundary condition $\left|\psi(t)\right\rangle = \left|\psi_0(t)\right\rangle$ for times $t \leq 0$. In the *Dirac* or *interaction picture*, the time evolved state due to the unperturbed Hamiltonian is given by

$$\left|\psi(t)\right\rangle_{\mathrm{I}} = \mathrm{e}^{iH^{\mathcal{F}} t} \left|\psi(t)\right\rangle \tag{5.78}$$

indicated by the subscript I. In the interaction picture, the state $\left|\psi(t)\right\rangle_{\mathrm{I}}$ follows the reduced SEQ

$$i\partial_t \left|\psi(t)\right\rangle_{\mathrm{I}} = V_{\mathrm{I}}(t) \left|\psi(t)\right\rangle_{\mathrm{I}} \tag{5.79}$$

for times $t > 0$ with $V_{\mathrm{I}} := \mathrm{e}^{iH^{\mathcal{F}} t} V(t) \mathrm{e}^{-iH^{\mathcal{F}} t}$. The formal solution is found through an integration from 0 to t as

$$\left|\psi(t)\right\rangle_{\mathrm{I}} = \left|\psi(0)\right\rangle_{\mathrm{I}} + \frac{1}{i} \int_0^t \mathrm{d}t' \, V_{\mathrm{I}}(t') \left|\psi(t')\right\rangle_{\mathrm{I}} \tag{5.80}$$

which is a recursive integral equation. Note, that Eq. (5.80) is an exact solution. Through recursive insertion of the initial state $|\psi(0)\rangle_{\mathrm{I}}$, we find the *Dyson series*

$$\begin{aligned}|\psi(t)\rangle_{\mathrm{I}} = |\psi(0)\rangle_{\mathrm{I}} &+ \frac{1}{i}\int_0^t \mathrm{d}t'\; V_{\mathrm{I}}(t')\,|\psi(0)\rangle_{\mathrm{I}} \\ &+ \frac{1}{(i)^2}\int_0^t \mathrm{d}t' \int_0^t \mathrm{d}t''\; V_{\mathrm{I}}(t')V_{\mathrm{I}}(t'')\,|\psi(0)\rangle_{\mathrm{I}} \\ &+ \dots ,\end{aligned}$$

which is an expansion in terms of orders of the perturbation $V(t)$.

Since we assume the perturbation to be weak, we truncate the Dyson series after the first order of $V(t)$. We assume, that the system is initially in an eigenstate of the Hamiltonian $H^{\mathcal{F}}$ before the perturbation is added. It is time evolved according to

$$|\psi_l^{\mathcal{F}}(t)\rangle = \mathrm{e}^{-iH^{\mathcal{F}}t}\,|\psi_l^{\mathcal{F}}\rangle = \mathrm{e}^{-i\lambda_l t}\,|\psi_l^{\mathcal{F}}\rangle\,. \tag{5.81}$$

With that, we find the transition probability to a different eigenstate $|\psi_k^{\mathcal{F}}(t)\rangle$ of the unperturbed system at time t as

$$\langle\psi_k^{\mathcal{F}}(t)|\psi(t)\rangle = \langle\psi_k^{\mathcal{F}}|\mathrm{e}^{iH^{\mathcal{F}}t}|\psi(t)\rangle = \langle\psi_k^{\mathcal{F}}|\psi(t)\rangle_{\mathrm{I}} \tag{5.82}$$

with the initial state reading $|\psi(0)\rangle_{\mathrm{I}} = |\psi_k^{\updownarrow}\rangle$ in the interaction picture. With the expansion of the perturbed state in terms of the time evolved unperturbed eigenbasis as

$$|\psi(t)\rangle = \sum_k b_k(t)\,\mathrm{e}^{-i\lambda_k t}\,|\psi_k^{\mathcal{F}}\rangle\,, \tag{5.83}$$

we find the coefficient $b_k(t)$ as

$$\begin{aligned}b_k(t) = \langle\psi_k^{\mathcal{F}}(t)|\psi(t)\rangle = \langle\psi_k^{\mathcal{F}}|\psi(t)\rangle_{\mathrm{I}} &= \delta_{k,l} + \frac{1}{i}\int_0^t \mathrm{d}t'\;\langle\psi_k^{\mathcal{F}}|V_{\mathrm{I}}(t)|\psi_l^{\mathcal{F}}\rangle \\ &= \delta_{k,l} + \frac{1}{i}\int_0^t \mathrm{d}t'\;\mathrm{e}^{i(\lambda_k^{\mathcal{F}}-\lambda_l)t}\,\langle\psi_k^{\mathcal{F}}|V(t)|\psi_l^{\mathcal{F}}\rangle\end{aligned} \tag{5.84}$$

in first order of $V(t)$. For that, we plugged in the initial state $|\psi(0)\rangle_{\mathrm{I}} = |\psi_k^{\updownarrow}\rangle$ in the Dyson series. The Delta function vanishes, if we consider transitions between differing initial and final states with $k \neq l$. We choose the perturbation $V(t)$ such that it is possible to separate it into a scalar function $Q(t)$ and a time independent operator $\hat{A}$ which only acts in subsystem $\mathcal{S}$, $V(t) = Q(t)\,\hat{A}\otimes\mathbb{1}_{\mathcal{B}}$. The time dependence in the function is chosen as $Q(t) = \alpha\,\mathrm{e}^{-i\omega t}\Theta(t)$ with a small parameter $\alpha\in\mathbb{R}$ and an incoming electromagnetic wave with frequency ω that models the incoming light onto the quantum system. $\Theta(t)$ ensures, that the perturbation is switched on at time $t = 0$. Then the *transition probability* from the initial state $|\psi_l^{\mathcal{F}}\rangle$ to the final state $|\psi_k^{\mathcal{F}}\rangle$ is given by the squared absolute value of the corresponding coefficient in $|\psi(t)\rangle$,

$$w_{l\to k} = |b_k(t)|^2 = \left|\langle\psi_k^{\mathcal{F}}|A\otimes\mathbb{1}_{\mathcal{B}}|\psi_l^{\mathcal{F}}\rangle\right|^2\cdot\left|\int_0^t \mathrm{d}t'\;\alpha\,\mathrm{e}^{-i\omega t'}\mathrm{e}^{i\omega_{kl}t'}\right|^2 \tag{5.85}$$

with $\omega_{kl} \equiv \lambda_k - \lambda_l$. The matrix element of A as the first term in the result (5.85) allows for scattering between states in subsystem $\mathcal{S}$, while it leaves the bath eigenstates untouched. We can compute the matrix element of the scattering through the decomposition of the full eigenstate $|\psi_l^{\mathcal{F}}\rangle$ in terms of the unperturbed eigenbasis of $\mathcal{S}$ and $\mathcal{B}$, which is detailed in chapter 4. An analytical evaluation of the matrix element is done in Sec. 5.3.2. The time dependent part in Eq. (5.85) evaluates to

$$\left|\int_0^t \mathrm{d}t'\, \alpha\, \mathrm{e}^{-i\omega t'} \mathrm{e}^{i\omega_{kl}t'}\right|^2 = \frac{\alpha^2}{(\omega-\omega_{kl})^2}\left|\mathrm{e}^{-i(\omega-\omega_{kl})t}-1\right|^2 = \frac{4\alpha^2}{(\omega-\omega_{kl})^2}\sin^2\left(\frac{\omega-\omega_{kl}}{2}t\right) = \mathrm{sinc}^2\left(\frac{\omega-\omega_{kl}}{2}t\right)t^2. \tag{5.86}$$

The *transition probability per unit of time* or *transition rate* is given by

$$\Gamma_{l\to k} = \frac{\mathrm{d}}{\mathrm{d}t} w_{l\to k} = |A_{kl}|^2\, 2\alpha^2\, \mathrm{sinc}\left((\omega-\omega_{kl})\, t\right)\cdot t \longrightarrow |A_{kl}|^2\, 2\pi\, \alpha^2 \delta(\omega-\omega_{kl}) \tag{5.87}$$

for $t \to \infty$. This implicitely assumes, that the time of measurement is much larger than the time of transition. We defined the matrix element as $A_{kl} \equiv \langle\psi_k^{\mathcal{F}}|A \otimes \mathbb{1}_{\mathcal{B}}|\psi_l^{\mathcal{F}}\rangle$. The result is obtained by using the fact, that the sinc function with infinitesimal width is a representation of the Dirac delta distribution,

$$\lim_{a\to 0} \frac{\sin\left(\frac{x}{a}\right)}{\pi x} = \delta(x). \tag{5.88}$$

Eq. (5.87) determines the transition rate to a single final state.

In the large system size limit, the energy spacing between neighboring levels becomes very small and we are interested in transition to states of a continuous spectrum. Then, the transition rate to a subset of all total states instead of a single state becomes relevant. For this, we assume that the matrix elements for all those final states in the subset is identical. Since we are considering a small energy window, this is fulfilled, as the scattering element A_{kl} depends on the energy of the initial and final state. With the DOS, we determine the number of states in the energy interval $\mathrm{d}\lambda_k$ to $N_{\mathcal{F}}\rho_{\mathcal{F}}(\lambda_k)\mathrm{d}\lambda_k$. The transition rate is then given by an integral over all possible final states [218]

$$\Gamma_{\mathrm{tot}} = \sum_k \Gamma_{l\to k} = \int \mathrm{d}\lambda_k\, N_{\mathcal{F}}\rho_{\mathcal{F}}(\lambda_k)\, \Gamma_{l\to k} = \int \mathrm{d}\lambda_k\, N_{\mathcal{F}}\rho_{\mathcal{F}}(\lambda_k)\, |A_{kl}|^2\, 2\pi\, \alpha^2 \delta(\omega-\omega_{kl}) \tag{5.89}$$

where the transition rate $\Gamma_{l\to k}$ selects the corresponding final states with the correct energy spacing according to the Delta function $\delta(\omega-\omega_{kl})$. Usually, it is assumed, that the DOS close to the energy λ_k of the final state is approximately constant, as well as the transition rate $\Gamma_{l\to k}$, which depends on the initial and final energies. As we evaluate the transition matrix element A_{kl} in Sec. 5.3.2 analytically, we employ the full form in (5.89) to find the total transition rate. We further specify under which conditions the Delta function approximation in (5.87) is valid. For that, the width of the sinc function in (5.87) can be estimated as the difference between the first zeros left and right of the maximum peak, which gives $\Delta\omega = \frac{2\pi}{t}$. We hence demand two constraints on the spectrum. First, the energy bandwidth in the full energy λ_k must be much greater than the width of the sinc function, $\sigma_{\mathcal{F}} \gg \Delta\omega$. This ensures that with the transition rate $\Gamma_{l\to k}$, we select only a small part of the total spectrum to scatter into and justify its Delta function approximation. Second, for the continuum approximation to be valid, there must be many states that lie inside the energy width prescribed by the width $\Delta\omega$ of the sinc function in $\Gamma_{l\to k}$. This means, that the energy spacing $\delta\lambda$ at λ_k is much smaller than the available width for the scattering, $\delta\lambda \ll \Delta\omega$. Only then the final states can be approximated by their DOS and the scattering is effectively not to a single state at λ_k, but to all states within the energy interval $\Delta\omega$. In total, the two conditions are summarized as [220]

$$\frac{2\pi}{\sigma_{\mathcal{F}}} \ll t \ll \frac{2\pi}{\delta\lambda}. \tag{5.90}$$

In the large system size limit, $d_{\mathcal{F}} \to \infty$, the spectral bandwidth becomes very large $\sigma_{\mathcal{F}} \to \infty$ and the energy spacing approaches zero with $N_{\mathcal{F}}$, $\delta\lambda \to 0$. In this limit, both conditions in (5.90) are fulfilled. The energy uncertainty $\Delta\omega$ is reduced if we consider large times t, which justifies the Delta approximation in (5.87) as long as the number of states in the energy window $\Delta\omega$ is large enough and scales with the total number of states $N_{\mathcal{F}}$.

Note that the chosen time dependent perturbation $V(t) = \alpha\, \mathrm{e}^{-i\omega t}\Theta(t)\,\hat{A} \otimes \mathbb{1}_{\mathcal{B}}$ is not Hermitian as the operator $\hat{A}$ can be non-Hermitian and additionally the exponential function $\mathrm{e}^{-i\omega t}$ is complex valued. To render $V(t)$ Hermitian, we add its conjugate transpose to the total perturbation

$$V(t) = V_1(t) + V_2(t) = \alpha\, \mathrm{e}^{-i\omega t}\Theta(t)\,\hat{A} \otimes \mathbb{1}_{\mathcal{B}} + \alpha\, \mathrm{e}^{i\omega t}\Theta(t)\,\hat{A}^{\dagger} \otimes \mathbb{1}_{\mathcal{B}}, \tag{5.91}$$

which is now Hermitian, $V^{\dagger}(t) = V(t)$ with $V_1(t) = V_2^{\dagger}(t)$. Since the second term contributes as $\delta(\omega + \omega_{kl})$, whereas the first is proportional to $\delta(\omega - \omega_{kl})$, their peak positions differ and we only keep the respective divergent term close to the peak position. This means that the total transition rate is additive in terms of the two individually evaluated terms,

$$\Gamma_{\mathrm{tot}} = \Gamma_{\mathrm{tot}}(V_1) + \Gamma_{\mathrm{tot}}(V_2) \tag{5.92}$$

and they can be treated separately.

5.3.2 Analytical calculation of the transition element

In the following, we calculate the matrix element

$$A_{kl} = \langle \psi_k^{\mathcal{F}} | A \otimes \mathbb{1}_{\mathcal{B}} | \psi_l^{\mathcal{F}} \rangle \tag{5.93}$$

which enters the transition rate in Eq. (5.89). The final objective is to find the transition rate of a scattering, that only acts within the small subsystem $\mathcal{S}$ with a scattering operator A. Without loss of generality, we choose the Hamiltonian in subsystem $\mathcal{S}$, $H^{\mathcal{S}} \propto \sigma_1^z$, such that its eigenstates are given by the spin-up $|{\uparrow}\rangle$ and spin down $|{\downarrow}\rangle$ states on the single site of $\mathcal{S}$. We consider four possibilities for the scattering operator A:

$$A = S_1^+ S_1^- = \begin{pmatrix} 1 & 0 \\ 0 & 0 \end{pmatrix} \tag{5.94}$$

with a scattering $|{\uparrow}\rangle \to |{\uparrow}\rangle$,

$$A = S_1^- = \begin{pmatrix} 0 & 0 \\ 1 & 0 \end{pmatrix} \tag{5.95}$$

with a scattering $|\uparrow\rangle \to |\downarrow\rangle$,

$$A = S_1^+ = \begin{pmatrix} 0 & 1 \\ 0 & 0 \end{pmatrix} \tag{5.96}$$

with a scattering $|\downarrow\rangle \to |\uparrow\rangle$ and

$$A = S_1^- S_1^+ = \begin{pmatrix} 0 & 0 \\ 0 & 1 \end{pmatrix} \tag{5.97}$$

with a scattering $|\downarrow\rangle \to |\downarrow\rangle$. To find the matrix element in (5.93), we represent the full eigenstate in terms of the unperturbed basis,

$$|\psi_l^{\mathcal{F}}\rangle = \sum_{\mu i} c_{\mu i}^{(l)} \, |\psi_\mu^{\mathcal{S}}\rangle \, |\psi_i^{\mathcal{B}}\rangle \tag{5.98}$$

as in Sec. 5.1.1. Then the matrix element of A evaluates to

$$A_{kl} = \langle \psi_\nu^{\mathcal{S}} | A | \psi_\mu^{\mathcal{S}} \rangle \sum_i c_{\nu i}^{(k)*} c_{\mu i}^{(l)}. \tag{5.99}$$

In (5.99), there is only one combination of μ and ν instead of the sum over all possibilities, which would appear according to the representation of the full state in (5.98). This is because we assumed, that A induces only a single scattering between two eigenstates in $\mathcal{S}$, while all other scatterings of eigenstates vanish. Within the setup of $d_{\mathcal{S}} = 1$ and $H^{\mathcal{S}} \propto \sigma_1^z$, this is exemplified by the scattering operators A in (5.94)-(5.97) where only a single entry is nonzero. Depending on the choice of A, the indices μ and ν need to be chosen accordingly such that the matrix element $\langle \psi_\nu^{\mathcal{S}} | A | \psi_\mu^{\mathcal{S}} \rangle$ is nonzero Similar to Sec. 5.1.1, the phases of the coefficients $c_{\mu i}^{(l)}$ are random and average out when we take the expectation value, $\mathbb{E}\left[A_{kl}\right] = 0$. The absolute value however scales inverse to the square root of the Hilbert space dimension, $\mathbb{E}\left[|A_{kl}|\right] \propto N_{\mathcal{F}}^{-\frac{1}{2}}$ as the expected distance in the two-dimensional walk is proportional to $\sqrt{N_{\mathcal{B}}}$ where $N_{\mathcal{B}}$ is the number of elements in the sum. The scaling arises since the coefficients each scale with $N_{\mathcal{F}}^{-\frac{1}{2}}$ due to the normalization of the eigenstate. To find the transition rate, we need to calculate the squared absolute value of (5.99) which is under the expectation value given by

$$\begin{aligned} \mathbb{E}\left[|A_{lk}|^2\right] &= \left|\langle \psi_\nu^{\mathcal{S}} | A | \psi_\mu^{\mathcal{S}} \rangle\right|^2 \mathbb{E}\left[\sum_{i,j} c_{\nu i}^{(k)*} c_{\mu i}^{(l)} c_{\nu j}^{(k)} c_{\mu j}^{(l)*}\right] = \left|\langle \psi_\nu^{\mathcal{S}} | A | \psi_\mu^{\mathcal{S}} \rangle\right|^2 \mathbb{E}\left[\sum_i \left|c_{\nu i}^{(k)}\right|^2 \left|c_{\mu i}^{(l)}\right|^2\right] \\ &= \left|\langle \psi_\nu^{\mathcal{S}} | A | \psi_\mu^{\mathcal{S}} \rangle\right|^2 \sum_i \mathbb{E}\left[\left|c_{\nu i}^{(k)}\right|^2\right] \mathbb{E}\left[\left|c_{\mu i}^{(l)}\right|^2\right] = \left|\langle \psi_\nu^{\mathcal{S}} | A | \psi_\mu^{\mathcal{S}} \rangle\right|^2 \sum_i \mathcal{X}_{\mu i,l} \, \mathcal{X}_{\nu i,k} \\ &= \left|\langle \psi_\nu^{\mathcal{S}} | A | \psi_\mu^{\mathcal{S}} \rangle\right|^2 \int \mathrm{d}E \; (N_{\mathcal{B}} \rho_{\mathcal{B}}(E)) \, \mathcal{X}_\mu^{(l)}\left(E - (\lambda_l - \epsilon_\mu + \eta_\mu^{(l)})\right) \mathcal{X}_\nu^{(k)}\left(E - (\lambda_k - \epsilon_\nu + \eta_\nu^{(k)})\right) \propto \frac{1}{N_{\mathcal{F}}} \end{aligned} \tag{5.100}$$

In the first line, the complex phases of the coefficient are averaged to zero except for the contribution for $i = j$, where the phases cancel out and absolute values arise as a result. As before, we further assume that the coefficients are uncorrelated for $l \neq k$, which is the reason for splitting the expectation value into two contributions in the second line. In the last line, we transfer the sum to the continuum and integrate over the overlap functions with the DOS. As analyzed in chapter 4, the overlap curve $\mathcal{X}_{\mu i,l}$ in terms of the bath energy is peaked at $E_i^{\mathcal{B}} \approx \lambda_l - \epsilon_\mu + \eta_\mu^{(l)}$, where $\eta_\mu^{(l)}$

denotes the shift from the expected position at $t = 0$. Analogous to Sec. 5.1.1, the overlap curves are approximated as a Lorentzian with an area prefactor that takes the normalization into account,

$$\mathcal{X}_\mu^{(l)}(E, \lambda_l) \approx \frac{1}{N_\mathcal{F} \rho_\mathcal{F}(\lambda_l)} \frac{\gamma_\mu^{(l)}}{\pi} \frac{1}{\left(E - (\lambda_l - \epsilon_\mu + \eta_\mu^{(l)})\right)^2 + \left(\gamma_\mu^{(l)}\right)^2}. \tag{5.101}$$

In this approximation, the background Gaussian profile according to the variance model σ_{ij}^2 of the perturbation matrix $\tilde{X}$, c.f. Eq. (4.59) for the single peak model, is omitted. It introduces a natural energy cutoff due to the locality of the perturbation, which is much larger than the width of the Lorentzian and therefore plays a minor role at energies close to the Lorentzian peak. Since the overlaps scale as $\mathcal{X}_\mu^{(l)} \propto \frac{1}{N_\mathcal{F}}$, the squared absolute value of the matrix element of A in (5.100) scales with $\frac{1}{N_\mathcal{F}}$ as well. At first glance, this appears unphysical, as the intensity of the scattering between two eigenstates decreases with system size. To resolve this, we note that the level spacing also decreases with the Hilbert space dimension as $\frac{1}{N_\mathcal{F}}$. In order to select a single final state for the scattering, the energy window of final states to scatter into must also be proportional to $\frac{1}{N_\mathcal{F}}$, which means that it approaches zero as $N_\mathcal{F} \to \infty$. The measurement time to obtain this scattering diverges, $t \to \infty$ with the system size and is therefore not available in experiment. For any constant nonzero energy window to scatter into, the number of states in that window scales proportional to $N_\mathcal{F}$, which cancels the $\frac{1}{N_\mathcal{F}}$ proportionality of the single state-to-state scattering. This is captured in (5.89) by the integral over the DOS. Inserting the shape of the approximate Lorentzian overlap curve in (5.101) into the equation for the square magnitude of the matrix element (5.100), we obtain

$$\begin{aligned}
\mathbb{E}\left[|A_{lk}|^2\right] &= \frac{\left|\langle\psi_\nu^\mathcal{S}|A|\psi_\mu^\mathcal{S}\rangle\right|^2}{N_\mathcal{F}^2 \rho_\mathcal{F}(\lambda_l)\, \rho_\mathcal{F}(\lambda_k)} \frac{\gamma_\mu^{(l)}\, \gamma_\nu^{(k)}}{\pi^2} \int \mathrm{d}E \, \frac{N_\mathcal{B}\rho_\mathcal{B}(E)}{\left(E - (\lambda_l - \epsilon_\mu + \eta_\mu^{(l)})\right)^2 + \left(\gamma_\mu^{(l)}\right)^2} \frac{1}{\left(E - (\lambda_k - \epsilon_\nu + \eta_\nu^{(k)})\right)^2 + \left(\gamma_\nu^{(k)}\right)^2} \\
&\approx \left|\langle\psi_\nu^\mathcal{S}|A|\psi_\mu^\mathcal{S}\rangle\right|^2 \frac{N_\mathcal{B}\rho_\mathcal{B}(E_0)}{N_\mathcal{F}^2 \rho_\mathcal{F}(\lambda_l)\, \rho_\mathcal{F}(\lambda_k)} \frac{\gamma_\mu^{(l)}\, \gamma_\nu^{(k)}}{\pi^2} \int \mathrm{d}E' \, \frac{1}{(E')^2 + \left(\gamma_\mu^{(l)}\right)^2} \frac{1}{(E' - \Delta E)^2 + \left(\gamma_\nu^{(k)}\right)^2},
\end{aligned} \tag{5.102}$$

where we defined

$$\begin{aligned}
E_0 &= \frac{1}{2}\left[(\lambda_l - \epsilon_\mu + \eta_\mu^{(l)}) + (\lambda_k - \epsilon_\nu + \eta_\nu^{(k)})\right], \\
E' &= E - (\lambda_k - \epsilon_\nu + \eta_\nu^{(k)}), \\
\Delta E &= (\lambda_k - \lambda_l) - \left[(\epsilon_\nu - \eta_\nu^{(k)}) - (\epsilon_\mu - \eta_\mu^{(l)})\right].
\end{aligned}$$

The integral in Eq. (5.102) simplifies to a convolution between the two Lorentzians, one from the initial and one from the final state and the scattering matrix element is proportional to their overlap. The resulting integral then depends on the distance between the peaks of the Lorentzians ΔE. To obtain this result, we approximated the DOS of the bath as constant in the energy range where the integral has its main contribution. Since the distance of the Lorentzians ΔE is on the order of the energy difference in subsystem $\mathcal{S}$, it is much smaller than the spectral bandwidth of the DOS of $\mathcal{B}$ and the change of the DOS is negligible for this result. The DOS of $\mathcal{B}$ is evaluated at their mean position E_0, which is the approximate position of the maximum value of the product of the two Lorentzians with comparable widths $\gamma_\mu^{(l)}$ and $\gamma_\nu^{(k)}$. The convolution of two Lorentzians again returns a Lorentzian. This becomes apparent when considering the characteristic function $\varphi_X(t)$ of a normalized Lorentzian $f(x; x_0, \gamma)$ with width γ and center position x_0,

$$\varphi_X(t) = \mathbb{E}\left[\mathrm{e}^{iXt}\right] = \int_{-\infty}^{\infty} \frac{\gamma}{\pi} \frac{1}{(x - x_0)^2 + \gamma^2} \mathrm{e}^{ixt} = \mathrm{e}^{ix_0 t - \gamma|t|}, \tag{5.103}$$

which is the Fourier transform of the Lorentzian. The *convolution theorem* states that the Fourier transform $\mathcal{F}$ of a convolution ($\star$) is equal to the product of the Fourier transforms of the individual functions, $\mathcal{F}\{f \star g\} = k \cdot \mathcal{F}\{f\}\mathcal{F}\{g\}$. k is a normalization factor that depends on the definition of the Fourier transform. The convolution of two Lorentzians $f_1(x; x_1, \gamma_1)$ and $f_2(x; x_2, \gamma_2)$ evaluates to

$$\{f_1(x; x_1, \gamma_1) \star f_2(x; x_2, \gamma_2)\}(x) = \mathcal{F}^{-1}\left\{\mathrm{e}^{ix_1 t - \gamma_1 |t|}\, \mathrm{e}^{ix_2 t - \gamma_2 |t|}\right\} = \frac{\gamma_1 + \gamma_2}{\pi} \frac{1}{(x - (x_1 + x_2))^2 + (\gamma_1 + \gamma_2)^2}, \tag{5.104}$$

where the widths and the shifts of the two Lorentzians add up for the resulting Lorentzian according to the exponential shape of the characteristic functions. Using the result (5.104) to find the result of the Lorentzian overlap in (5.102), we get

$$\mathbb{E}\left[|A_{lk}|^2\right] \approx \left|\langle\psi_\nu^{\mathcal{S}}|A|\psi_\mu^{\mathcal{S}}\rangle\right|^2 \frac{N_{\mathcal{B}}\rho_{\mathcal{B}}(E_0)}{\pi N_{\mathcal{F}}^2 \rho_{\mathcal{F}}(\lambda_l)\rho_{\mathcal{F}}(\lambda_k)} \frac{\gamma_\mu^{(l)} + \gamma_\nu^{(k)}}{(\Delta E)^2 + \left(\gamma_\mu^{(l)} + \gamma_\nu^{(k)}\right)^2} \tag{5.105}$$

for the expectation value of the squared magnitude of the matrix element A_{lk}. We insert this into the final equation for the transition rate (5.89) and obtain

$$\begin{aligned} \Gamma_{\mathrm{tot}} &= \left|\langle\psi_\nu^{\mathcal{S}}|A|\psi_\mu^{\mathcal{S}}\rangle\right|^2 \frac{2\alpha^2}{N_{\mathcal{S}}} \frac{\rho_{\mathcal{B}}(E_0)}{\rho_{\mathcal{F}}(\lambda_l)} \int \mathrm{d}\lambda_k \, \frac{\gamma_\mu^{(l)} + \gamma_\nu^{(k)}}{(\Delta E)^2 + \left(\gamma_\mu^{(l)} + \gamma_\nu^{(k)}\right)^2} \, \delta(\omega - (\lambda_l - \lambda_k)) \\ \Leftrightarrow \Gamma_{\mathrm{tot}}(\omega) &= \left|\langle\psi_\nu^{\mathcal{S}}|A|\psi_\mu^{\mathcal{S}}\rangle\right|^2 \frac{2\alpha^2}{N_{\mathcal{S}}} \frac{\rho_{\mathcal{B}}(E_0)}{\rho_{\mathcal{F}}(\lambda_l)} \frac{\gamma_\mu^{(l)} + \gamma_\nu^{(k)}}{\left[\omega - \left((\epsilon_\nu - \eta_\nu^{(l)}) - (\epsilon_\mu - \eta_\mu^{(k)})\right)\right]^2 + \left[\gamma_\mu^{(l)} + \gamma_\nu^{(k)}\right]^2}. \end{aligned} \tag{5.106}$$

The total transition rate due to a time dependent scattering $V(t)$ which acts in the small subsystem $\mathcal{S}$ is also a Lorentzian in terms of the ingoing frequency ω of the harmonic perturbation. This effect is called *natural broadening*, as it introduces a finite lifetime due to the nonzero width of the Lorentzian. This can be seen by a Fourier transform back to the time domain with (5.103), where the width introduces an exponential decay in time. This width originates from the Lorentzians, which appear in the representation of exact eigenstates of the full quantum system in terms of the unperturbed and uncoupled eigenstates of $\mathcal{S}$ and $\mathcal{B}$. The scattering in $\mathcal{S}$ due to the time dependent perturbation $V(t)$ effectively scatters the Lorentzians in the bath $\mathcal{B}$ belonging to different eigenstates $|\psi_l^{\mathcal{F}}\rangle$ and $|\psi_k^{\mathcal{F}}\rangle$ of the full system. This scattering is proportional to the overlap of the Lorentzians, which is maximal if the difference of full eigenvalues matches the distance of the Lorentzian peaks, $\Delta E = (\lambda_k - \lambda_l) - \left[(\epsilon_\nu - \eta_\nu^{(k)}) - (\epsilon_\mu - \eta_\mu^{(l)})\right] = 0$. The transition rate in (5.106) is then written as a function of ω by matching the energy difference of the states of the full quantum system with the ingoing frequency due to energy conservation. The peak of $\Gamma_{\mathrm{tot}}(\omega)$ is found not at the difference of the bare energy levels in $\mathcal{S}$, but at the difference of the renormalized energy levels $\epsilon_\mu - \eta_\mu^{(l)}$, which are shifted due to the influence of the coupling X between $\mathcal{S}$ and $\mathcal{B}$ proportional to t. The shifted energy levels appear in the Boltzmann factors on the diagonal of the reduced density matrix $\rho^{l,\mathcal{S}}$ in subsystem $\mathcal{S}$ of a single full eigenstate, as discussed in Sec. 5.1.1 with the result for large system sizes in Eq. (5.24). It is therefore possible to measure the shifted energy levels in the small subsystem $\mathcal{S}$ which enter the canonical distribution through a time dependent perturbation that scatters the eigenstates in $\mathcal{S}$ only.

5.3.3 Numerical results

To compare the analytical calculation of the scattering in subsystem $\mathcal{S}$ due to a perturbation $V(t)$ on the full quantum system in Sec. 5.3 and 5.3.2 to the numerical results, we decompose the full eigenstate with an SVD, c.f. Sec. 2.1.4,

$$|\psi_l^{\mathcal{F}}\rangle = \sum_\mu \kappa_\mu^{(l)} |\phi_\mu^{l,\mathcal{S}}\rangle \otimes |\phi_\mu^{l,\mathcal{B}}\rangle = \sum_\mu |\phi_\mu^{l,\mathcal{S}}\rangle \otimes |\tilde{\phi}_\mu^{l,\mathcal{B}}\rangle \,, \tag{5.107}$$

where $|\phi_\mu^{l,\mathcal{S}}\rangle$ and $|\phi_\mu^{l,\mathcal{B}}\rangle$ are the singular vectors in $\mathcal{S}$ and $\mathcal{B}$ respectively. The singular values $\kappa_\mu^{(l)}$ can be absorbed into the singular vectors of the bath, $|\tilde{\phi}_\mu^{l,\mathcal{B}}\rangle \equiv \kappa_\mu^{(l)} \left|\phi_\mu^{l,\mathcal{B}}\right\rangle$. For small perturbations t, the eigenstates in $\mathcal{S}$ are not mixed, since their level spacing is much larger than t. This means, that the singular vectors in $\mathcal{S}$ are almost equal to the eigenstates, $|\phi_\mu^{l,\mathcal{S}}\rangle \approx |\psi_\mu^{\mathcal{S}}\rangle$. Following from that, the singular vectors in $\mathcal{B}$ are approximately given by the overlap coefficients $c_{\mu i}^{(l)}$ in terms of the bath eigenbasis,

$$|\tilde{\phi}_\mu^{l,\mathcal{B}}\rangle \approx \sum_i c_{\mu i}^{(l)} |\psi_i^{\mathcal{B}}\rangle \,. \tag{5.108}$$

In the numerical analysis, we also choose $H^{\mathcal{S}} \propto \sigma^z$. The matrix element of the perturbation operator A can then be represented through

$$A_{kl} = \langle\psi_k^{\mathcal{F}}|A|\psi_l^{\mathcal{F}}\rangle = \langle\psi_\nu^{\mathcal{F}}|A|\psi_\mu^{\mathcal{F}}\rangle \; \langle\tilde{\phi}_\nu^{k,\mathcal{B}}|\tilde{\phi}_\mu^{l,\mathcal{B}}\rangle = \langle\tilde{\phi}_\nu^{k,\mathcal{B}}|\tilde{\phi}_\mu^{l,\mathcal{B}}\rangle \,, \tag{5.109}$$

where one scattering between the two eigenstates in $\mathcal{S}$ is singled out according to the construction of the scattering operator A in (5.94)-(5.97). Consequently, the matrix element $\langle\psi_\nu^{\mathcal{F}}|A|\psi_\mu^{\mathcal{F}}\rangle$ of eigenstates of $\mathcal{S}$ in (5.109) is one for one choice of μ and ν and zero for all other with each A in (5.94)-(5.97). In the numerical analysis, we employ Eq. (5.109) to find the squared magnitude of the matrix element

$$|A_{kl}|^2 = \left|\langle\tilde{\phi}_\nu^{k,\mathcal{B}}|\tilde{\phi}_\mu^{l,\mathcal{B}}\rangle\right|^2 \tag{5.110}$$

and compare it to the analytical result in (5.105). Throughout the whole numerical investigation, the second moment of the bath Hamiltonian is normalized to $\tau\left((H^{\mathcal{B}})^2\right) = 1$.

Fig. 5.10 shows the singular vector overlap (5.110) in a numerical analysis with a total system size of $d_{\mathcal{F}} = 13$ sites, while subsystem $\mathcal{S}$ consists of one site of the full quantum system. The overlap is computed in intervals of width $\Delta\lambda \approx 0.4$ around different investigated points of full energy λ_l. The Hamiltonian $H^{\mathcal{S}}$ is normalized such that its eigenvalues are $\epsilon_1 = -0.1$ and $\epsilon_2 = +0.1$. The result is averaged in terms of bins in the energy difference $\lambda_k - \lambda_l$ of the scattered states, where the number of bins is chosen to be equal to the number of states in the energy window $\Delta\lambda$ to mimic the actual number of data points in the corresponding interval according to the DOS. The squared magnitude of the singular vector overlap is plotted on a logarithmic scale for the four possible scattering combinations of μ and ν individually. For each choice of μ and ν, we notice a main peak close to $\lambda_k - \lambda_l \approx \epsilon_\nu - \epsilon_\mu$, which matches the expected energy difference due to the scattering of different states in $\mathcal{S}$ under the perturbation operator A. The maximum peak position coincides with the distance of the Lorentzians in the eigenbasis of $\mathcal{B}$ from the overlaps $\mathcal{X}_\mu^{(l)}$ and $\mathcal{X}_\nu^{(k)}$. Additionally, there are secondary peaks in Fig. 5.10 which are located at the other energy differences $\epsilon_\nu - \epsilon_\mu$ in subsystem $\mathcal{S}$. Those peaks originate from the fact, that each overlap curve $\mathcal{X}_\mu^{(l)}$ has secondary Lorentzian peaks at the position of the main Lorentzian peaks of the other overlap curves $\mathcal{X}_\nu^{(l)}$ with $\nu \neq \mu$. It is based on the observation

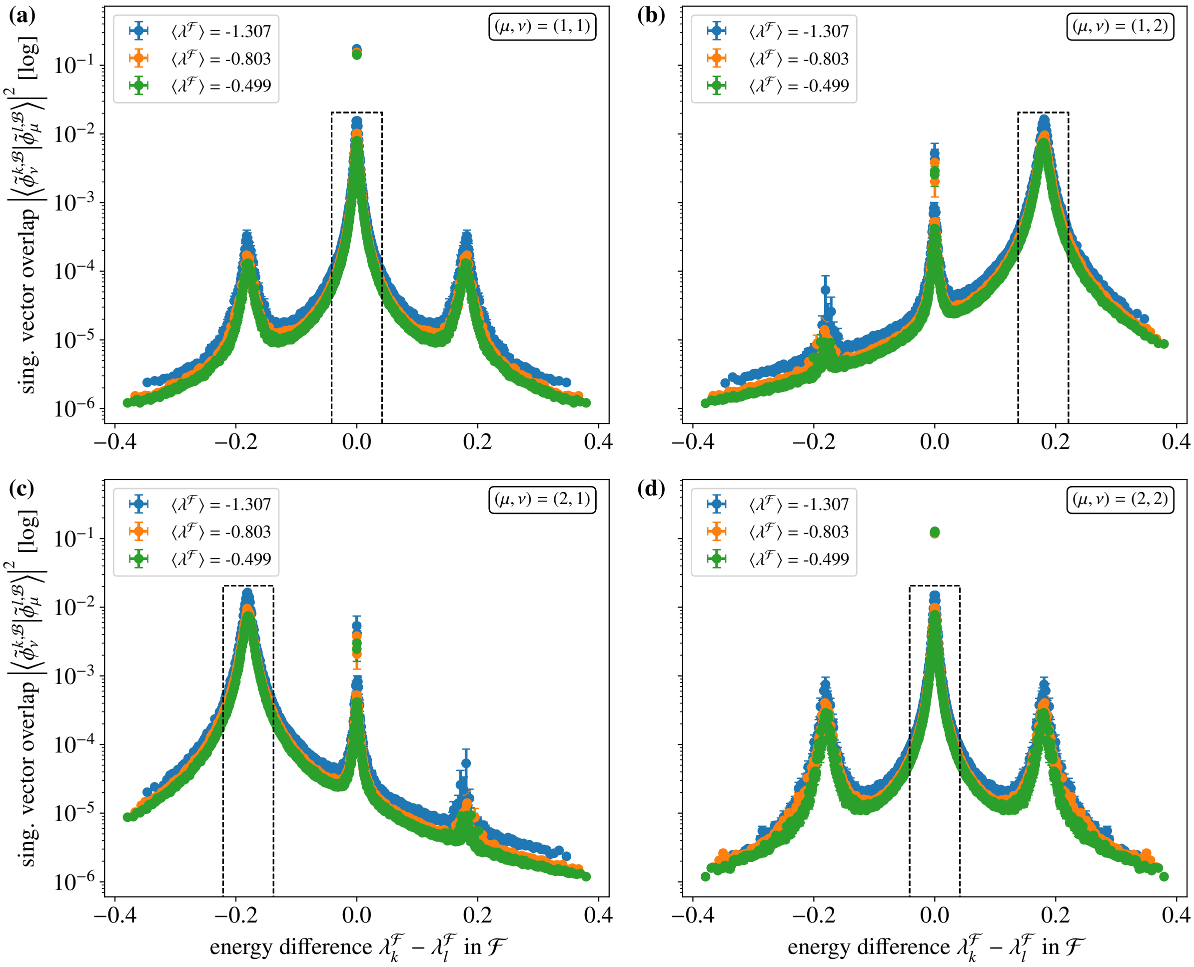

Figure 5.10: Squared absolute value of overlaps of the singular vectors in the bath $\mathcal{B}$ obtained from the SVD of eigenstates of the full quantum system at different eigenvalues λ_l and $\lambda_k^{\mathcal{F}}$. The overlaps are computed in terms of three different intervals of width $\Delta\lambda^{\mathcal{F}} \approx 0.4$ centered around the mean full energy $\langle \lambda^{\mathcal{F}} \rangle$ noted in the legend of the plots. The singular vectors used for the computation of the overlap are rescaled by their corresponding singular values κ_μ, $|\tilde{\phi}_\mu^{\mathcal{B}}\rangle \equiv \kappa_\mu |\phi_\mu^{\mathcal{B}}\rangle$. The result is represented on a logarithmic scale in terms of the energy difference of the full quantum states, $\lambda_l - \lambda_k^{\mathcal{F}}$. To find the overlap curves, we average the results in each energy interval around $\langle \lambda^{\mathcal{F}} \rangle$ in terms of bins, where the number of bins is chosen to match the number of states in the corresponding interval. $\mathcal{S}$ and $\mathcal{B}$ are connected through an interaction matrix X with a variance of $t = 2.44 \times 10^{-3}$. The full quantum system contains $d_{\mathcal{F}} = 13$ sites, of which $\mathcal{S}$ has one site, giving rise to two singular vectors in $\mathcal{S}$ and $\mathcal{B}$ with $\mu, \nu = 1, 2$. Consequently, there are four possible scatterings shown in **(a)** $(\mu, \nu) = (1, 1)$, **(b)** $(\mu, \nu) = (1, 2)$, **(c)** $(\mu, \nu) = (2, 1)$ and **(d)** $(\mu, \nu) = (2, 2)$. Sections of the scattering close to the energy difference $\epsilon_\mu - \epsilon_\nu$ in $\mathcal{S}$ in each plot are marked by dashed black rectangles and shown in Fig. 5.11.

in Fig. 4.7, where we plot the overlap curves on a logarithmic scale and the secondary peaks are observable, which cause the secondary peaks in the scattering of the singular vector overlaps. Those secondary peaks however are at least one order of magnitude smaller than the main peaks and therefore play a minor role, as they originate from a higher order term. We show the main scattering peak of the squared magnitude of the singular vector overlap (5.110) in Fig. 5.11 on a linear scale. The depicted energy range is marked by dashed lines in Fig. 5.10. We fit Lorentzian

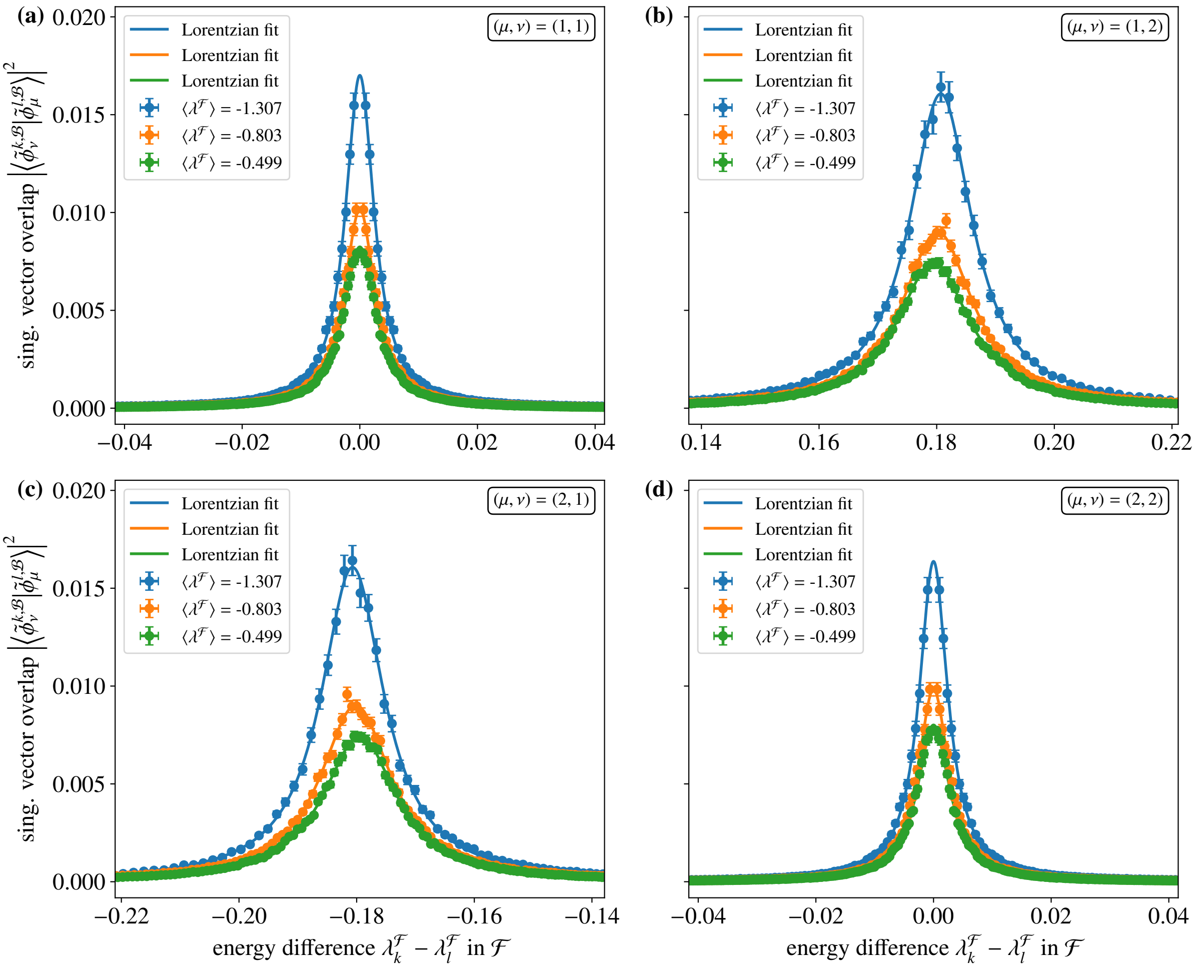

Figure 5.11: Cutouts of Fig. 5.10 marked by dashed rectangles. We show the squared absolute value of overlaps of the singular vectors in the bath $\mathcal{B}$ obtained from the SVD of full eigenstates with eigenvalues $\lambda_l, \lambda_k^{\mathcal{F}}$ at $t = 2.44{\times}10^{-3}$. They are computed in intervals of width $\Delta\lambda^{\mathcal{F}} \approx 0.4$ around the mean $\langle \lambda^{\mathcal{F}} \rangle$ and averaged in bins. With $d_{\mathcal{S}} = 1$, we show all possible scatterings **(a)** $(\mu, \nu) = (1, 1)$, **(b)** $(\mu, \nu) = (1, 2)$, **(c)** $(\mu, \nu) = (2, 1)$ and **(d)** $(\mu, \nu) = (2, 2)$. Additionally, we fit Lorentzians through the data points in each interval and plot the result as joint curves.

curves through the data points for each investigated point of full energy λ_l and each scattering combination of singular states μ and ν individually. The Lorentzians capture the data well and confirm the validity of the fit. This numerical result agrees with the theoretical expectation, that the scattering has the shape of a Lorentzian as obtained from the analytical calculation in (5.105). It once more confirms the approximation of random phases of the overlap coefficient $c_{\mu i}^{(l)} = \langle \psi_\mu^{\mathcal{S}} | \, \langle \psi_i^{\mathcal{B}} | \psi_l^{\mathcal{F}} \rangle$ for different μ, i or l as well as the assumption that the coefficients are uncorrelated, which was employed in the calculation. The Lorentzian in the overlap of the singular vectors of $\mathcal{B}$ in Fig. 5.11 then directly follows from the Lorentzian shape of the overlap curves of the full eigenstates in terms of the unperturbed basis. From the Lorentzian fits in Fig. 5.11 we can read off the fit parameters, which are the scattering height h_s equal to the maximum of the Lorentzian, the scattering center η_s equal to the peak position and the scattering width γ_s equal to the Lorentzian width. This is done for system sizes of $d_{\mathcal{F}} = \{10, 11, 12, 13\}$ sites. The height h_s of the Lorentzian fits is plotted in Fig. 5.12 with respect to the full Hilbert space dimension $N_{\mathcal{F}}$ on a double logarithmic

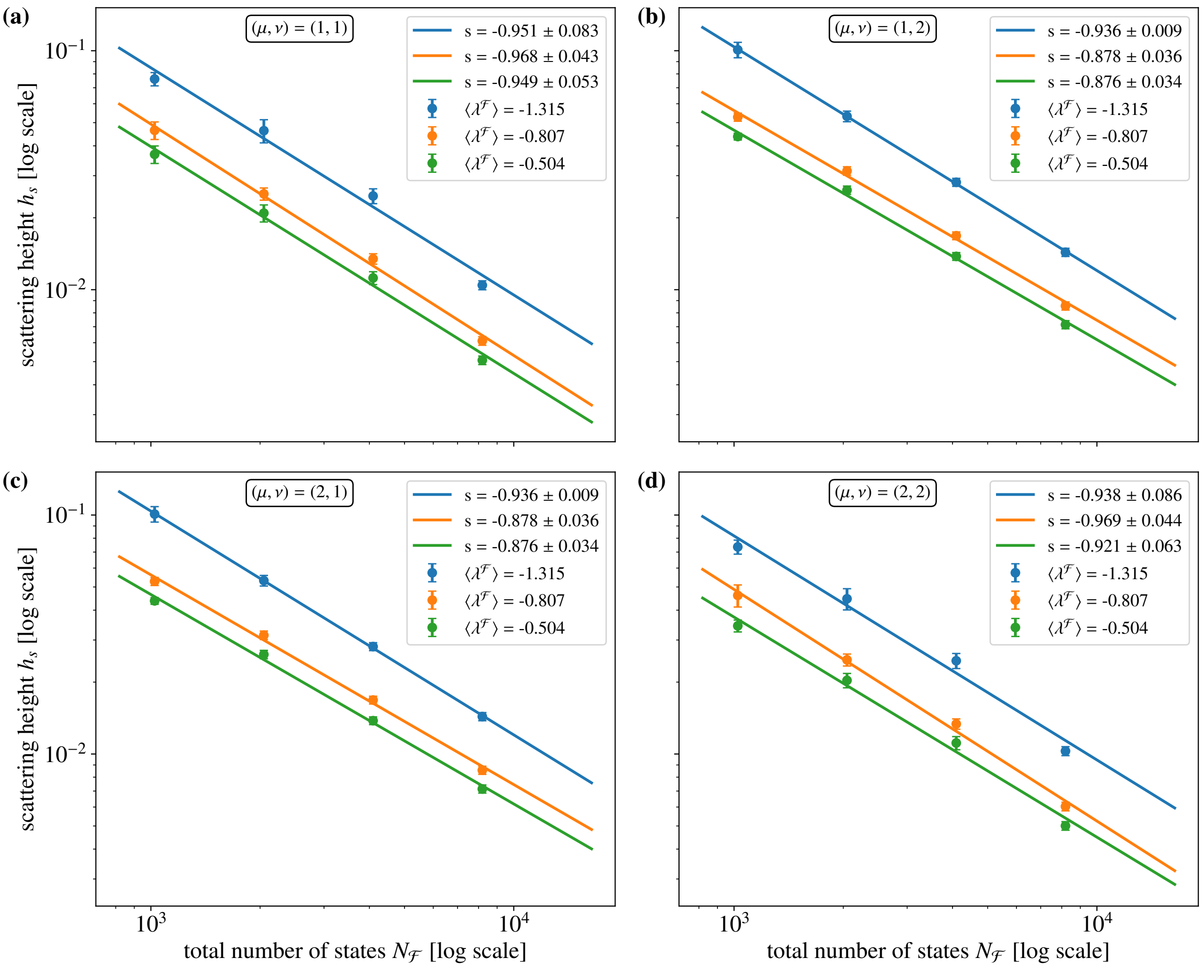

Figure 5.12: Height h_s of the Lorentzian fits for the scattering between singular vectors in the bath $\mathcal{B}$ obtained from the SVD of different full eigenstates. The overlap data is computed in intervals of width $\Delta\lambda^{\mathcal{F}} \approx 0.4$ around the mean $\langle\lambda^{\mathcal{F}}\rangle$ and averaged in bins. The results are additionally averaged over 200 samples of $H^{\mathcal{F}}$. The Lorentzian is fitted close to the expected peak $\lambda_k^{\mathcal{F}} - \lambda_l^{\mathcal{F}} \approx \epsilon_\nu - \epsilon_\mu$ of the singular vector overlaps. The results are obtained for a total system size of $d_{\mathcal{F}} = \{10, 11, 12, 13\}$ sites with $t = \{3.51, 3.02, 2.64, 2.54\} \times 10^{-3}$, while subsystem $\mathcal{S}$ occupies a single site of the full lattice. The data are depicted in terms of the number of total states $N_{\mathcal{F}}$ on a double logarithmic scale. We perform linear fits through the data points, with the slope denoted in the plot legends. We analyze the scatterings **(a)** $(\mu, \nu) = (1, 1)$, **(b)** $(\mu, \nu) = (1, 2)$, **(c)** $(\mu, \nu) = (2, 1)$ and **(d)** $(\mu, \nu) = (2, 2)$.

scale. We add linear fits to the plots, which match the data points well. The linear relation in the double logarithmic plot implies a power law behavior of the scattering height $h_s \propto N_{\mathcal{F}}^s$ with the number of states $N_{\mathcal{F}}$ where s is the slope of the linear fits. Reading off from the legend in Fig. 5.12, we find that the best fit parameters for the slopes are close to $s = -1$, which implies that all data points of the scattering of the singular vectors in $\mathcal{B}$ scale as $\frac{1}{N_{\mathcal{F}}}$. This is expected since the individual Lorentzians scale with $\frac{1}{N_{\mathcal{F}}}$, which implies that their overlap does as well. It agrees with the theoretical scaling in Eq. (5.100). Since we are working in the continuum approximation, the scaling $\frac{1}{N_{\mathcal{F}}}$ is canceled by the number of states in the energy window for the final states, which scales proportional to $N_{\mathcal{F}}$ according to the DOS to combine to a transition rate independent of system size. The scattering center η_s and the scattering width γ_s are plotted in Fig. 5.13 and Fig. 5.14 with respect to a logarithmic scale of the total Hilbert space dimension $N_{\mathcal{F}}$.

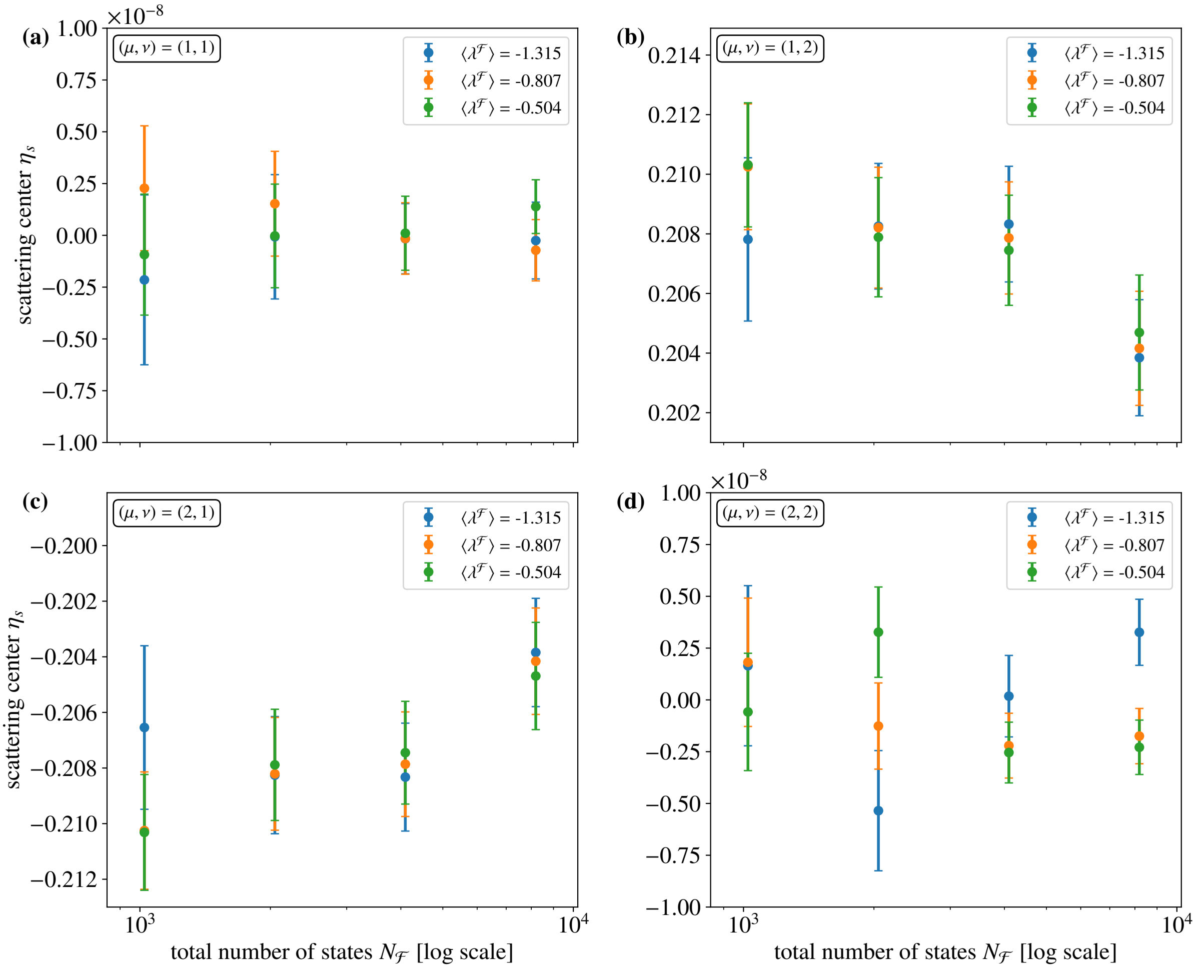

Figure 5.13: Shift η_s of the Lorentzian fits for the scattering between singular vectors in the bath $\mathcal{B}$ obtained from the SVD of different full eigenstates. The overlap data is computed in intervals of width $\Delta\lambda^{\mathcal{F}} \approx 0.4$ around the mean $\langle\lambda^{\mathcal{F}}\rangle$ and averaged in bins. The results are additionally averaged over 200 samples of $H^{\mathcal{F}}$. The Lorentzian is fitted close to the expected peak $\lambda_k^{\mathcal{F}} - \lambda_l^{\mathcal{F}} \approx \epsilon_\nu - \epsilon_\mu$ of the singular vector overlaps. The results are obtained for a total system size of $d_{\mathcal{F}} = \{10, 11, 12, 13\}$ sites with $t = \{3.51, 3.02, 2.64, 2.54\} \times 10^{-3}$, while subsystem $\mathcal{S}$ occupies a single site of the full lattice. The data are depicted in terms of the number of total states $N_{\mathcal{F}}$, which is scaled logarithmically. We analyze the scatterings **(a)** $(\mu, \nu) = (1, 1)$, **(b)** $(\mu, \nu) = (1, 2)$, **(c)** $(\mu, \nu) = (2, 1)$ and **(d)** $(\mu, \nu) = (2, 2)$.

The scattering center η_s of the scattering $\mu = \nu$ in Fig. 5.13**a,d** agrees with zero within the numerical accuracy and is consistent with the fact that we scatter the Lorentzian with itself. In Fig. 5.13**b,c** we expect the scattering center to be located at −0.2 and +0.2 when using the energy difference of the bare levels in subsystem $\mathcal{S}$. The actual data for η_s deviates from those values due to the shifts of the Lorentzian peaks which define the renormalized energy levels $\epsilon_\mu - \eta_\mu^{(l)}$ in $\mathcal{S}$. A comparison to the center position of the Lorentzian peak in the overlaps of the full eigenstate with the unperturbed eigenbasis for $d_{\mathcal{F}} = 13$ sites is done in Fig. 5.15. The scattering widths in Fig. 5.14 decrease slightly with increasing $N_{\mathcal{F}}$. This originates in the decrease of the interaction strength between $\mathcal{S}$ and $\mathcal{B}$ for larger $N_{\mathcal{F}}$ with $t = \{3.51, 3.02, 2.64, 2.54\} \times 10^{-3}$. Since we normalize the second moment of the bath Hamiltonian to $\tau\left((H^{\mathcal{B}})^2\right) = 1$, the local couplings between two spins decrease with system size as the total number of couplings scales with

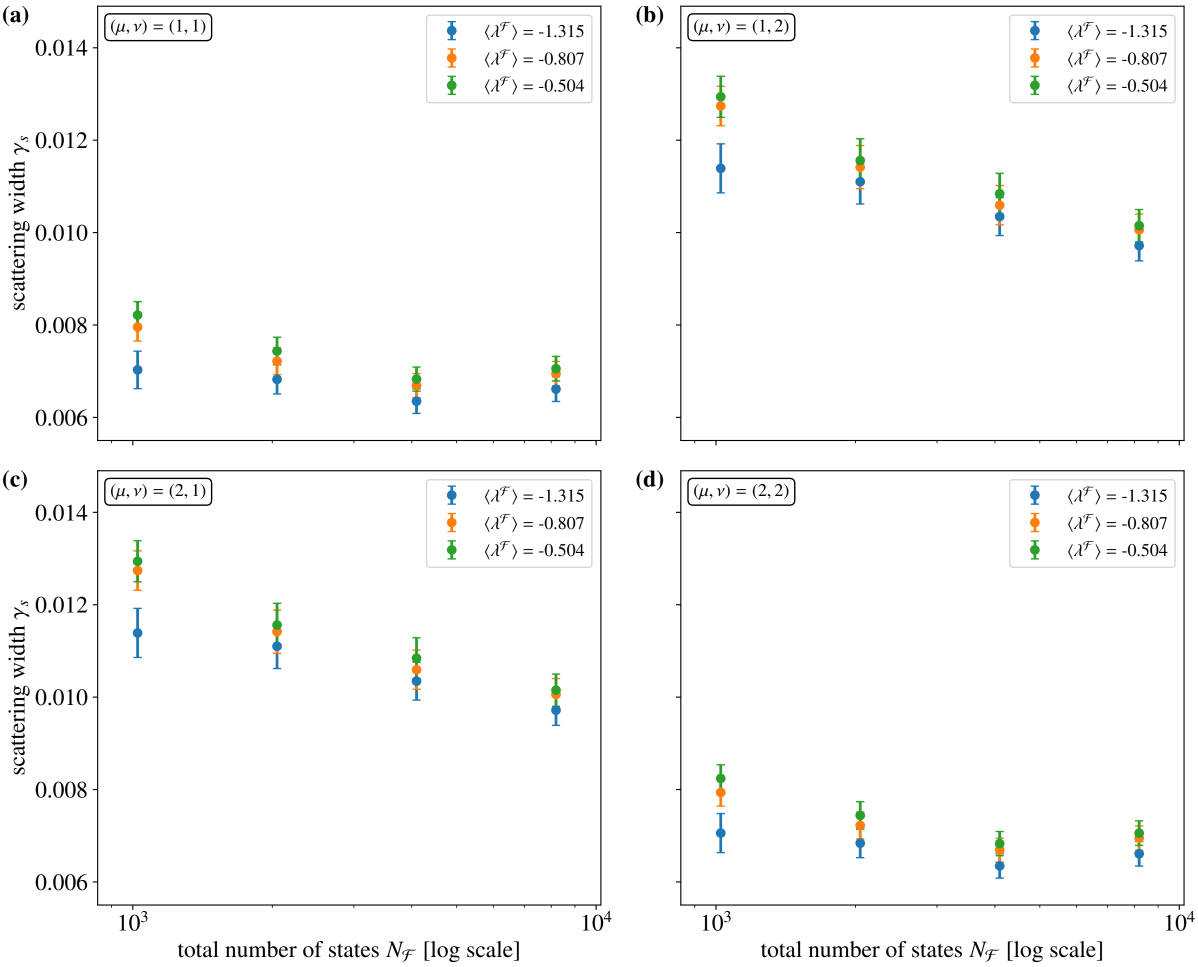

Figure 5.14: Width γ_s of the Lorentzian fits for the scattering between singular vectors in the bath $\mathcal{B}$ obtained from the SVD of different full eigenstates. The overlap data is computed in intervals of width $\Delta\lambda^{\mathcal{F}} \approx 0.4$ around the mean $\langle\lambda^{\mathcal{F}}\rangle$ and averaged in bins. The results are additionally averaged over 200 samples of $H^{\mathcal{F}}$. The Lorentzian is fitted close to the expected peak $\lambda_k^{\mathcal{F}} - \lambda_l^{\mathcal{F}} \approx \epsilon_\nu - \epsilon_\mu$ of the singular vector overlaps. The results are obtained for a total system size of $d_{\mathcal{F}} = \{10, 11, 12, 13\}$ sites with $t = \{3.51, 3.02, 2.64, 2.54\} \times 10^{-3}$, while subsystem $\mathcal{S}$ occupies a single site of the full lattice. The data are depicted in terms of the number of total states $N_{\mathcal{F}}$, which is scaled logarithmically. We analyze the scatterings **(a)** $(\mu,\nu) = (1,1)$, **(b)** $(\mu,\nu) = (1,2)$, **(c)** $(\mu,\nu) = (2,1)$ and **(d)** $(\mu,\nu) = (2,2)$.

the number of sites $d_{\mathcal{F}}$. Therefore, the local couplings in X are reduced by the same factor so that they are always of same magnitude compared to the couplings in $H^{\mathcal{B}}$ and independent of $N_{\mathcal{F}}$, resulting in smaller t for larger $N_{\mathcal{F}}$.

In Fig. 5.15, we compare the scattering center η_s to the position $(\epsilon_\nu - \eta_\nu^{(k)}) - (\epsilon_\nu - \eta_\mu^{(l)})$ expected from the analytical calculation in (5.106). The shifts $\eta_\nu^{(k)}$ are obtained from Lorentzian fits to the overlap curves of full states with the unperturbed eigenbasis of $\mathcal{S}$ and $\mathcal{B}$ as $|\langle\psi_\mu^{\mathcal{S}}|\,\langle\psi_i^{\mathcal{B}}|\psi_l^{\mathcal{F}}\rangle|^2$ and analyzed in detail in chapter 4. Within the scope of the error and the numerical accuracy, the numerically obtained scattering center η_s agrees with the analytical expectation for all investigated values of t. This confirms that the renormalized energy levels in subsystem $\mathcal{S}$ which enter the Boltzmann factors on the diagonal of the reduced density matrix in (5.24) are available through a scattering mediated

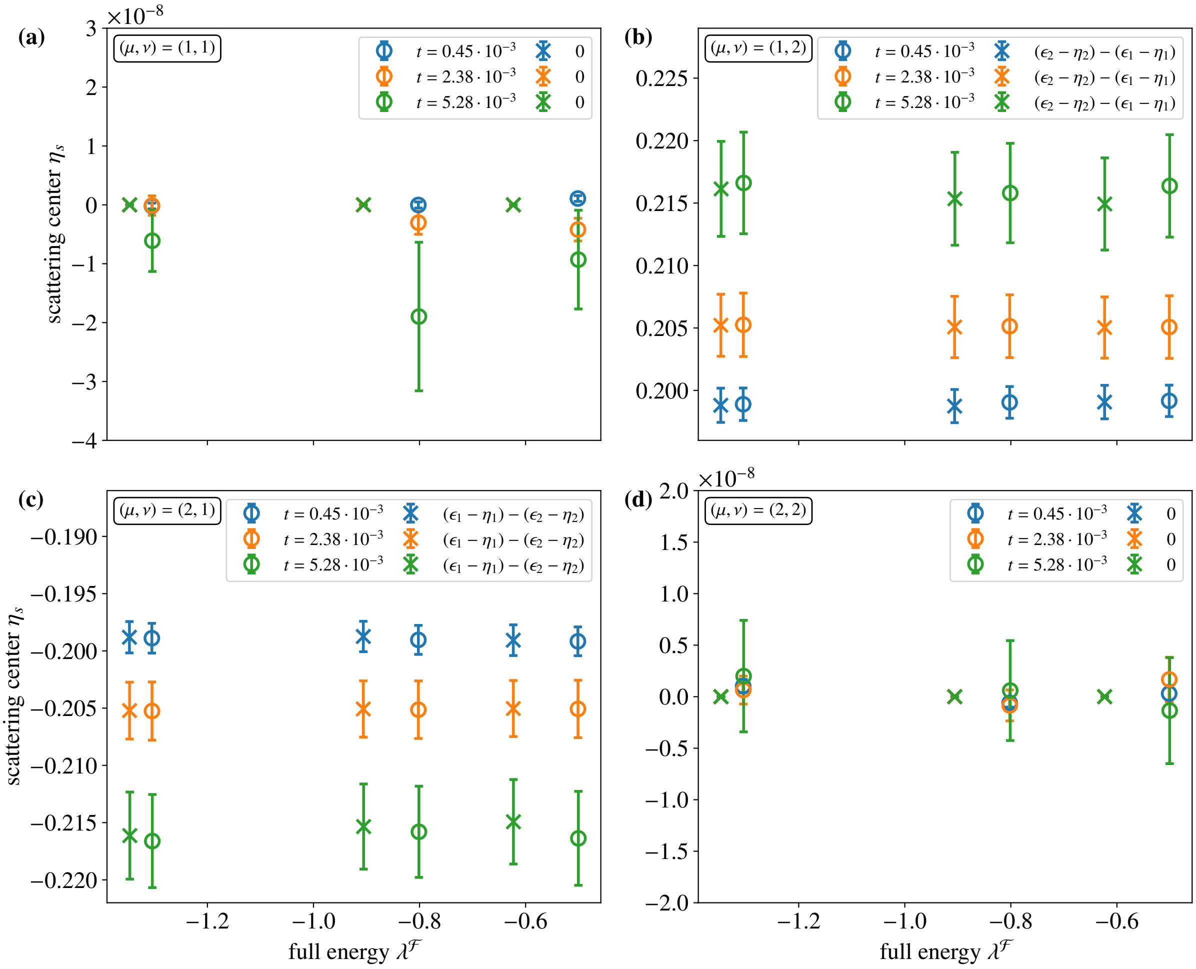

Figure 5.15: Comparison of the scattering center η_s to the center position of the Lorentzian overlaps in the bath for $d_{\mathcal{F}} = 13$ sites and three different values of t. The scattering center is obtained from Lorentzian fits to the squared magnitude of the singular vector overlap in the bath $|\langle\tilde{\phi}_\nu^{k,\mathcal{B}}|\tilde{\phi}_\mu^{l,\mathcal{B}}\rangle|^2$ as in Eq. (5.110). For that, we average the result in intervals of $\Delta\lambda^{\mathcal{F}} \approx 0.4$ around the mean values of $\langle\lambda_l\rangle = \{-1.305, -0.802, -0.501\}$. This is plotted as circles with error bars. The center positions of the overlap curves are obtained from Lorentzian fits to $|\langle\psi_\mu^{\mathcal{S}}|\,\langle\psi_i^{\mathcal{B}}|\psi_l^{\mathcal{F}}\rangle|^2$ using $N_{\text{av}} = 400$ full states around the mean full energies $\lambda_l = \{-1.347, -0.906, -0.623\}$. We then plot the shifted energy levels in $\mathcal{S}$ given by $(\epsilon_\nu - \eta_\nu^{(k)}) - (\epsilon_\nu - \eta_\mu^{(l)})$ as crosses with error bars. All data is additionally averaged over 88 samples of $H^{\mathcal{F}}$. The scatterings are analyzed for **(a)** $(\mu,\nu) = (1,1)$, **(b)** $(\mu,\nu) = (1,2)$, **(c)** $(\mu,\nu) = (2,1)$ and **(d)** $(\mu,\nu) = (2,2)$.

by a time dependent perturbation $V(t)$ which acts only in $\mathcal{S}$. They can hence be measured in an experiment and determine the occupation of the states in the small subsystem $\mathcal{S}$ in terms of a thermal distribution obtained from a single eigenstate of the full quantum system. The scattering width γ_s is compared to the width of the Lorentzian overlap curves in Fig. 5.16. For $\mu \neq \nu$, the expected width of the singular vector overlap is given by $\gamma_1 + \gamma_2$ as shown in Eq. (5.105). This is plotted in Fig. 5.16**b,c** where the analytical prediction agrees with the obtained scattering width γ_s within the scope of their error. For $\mu = \nu$, we find that the scattering width does not agree with $2\gamma_\nu$, but with $\sqrt{2}\gamma_\nu$ as shown in Fig. 5.16**a,d**. This hints at a correlation of the coeffients $c_\mu^{(l)}$ and $c_\mu^{(k)}$ when λ_l is close to λ_k and warrants further investigation that goes beyond the scope of this work.

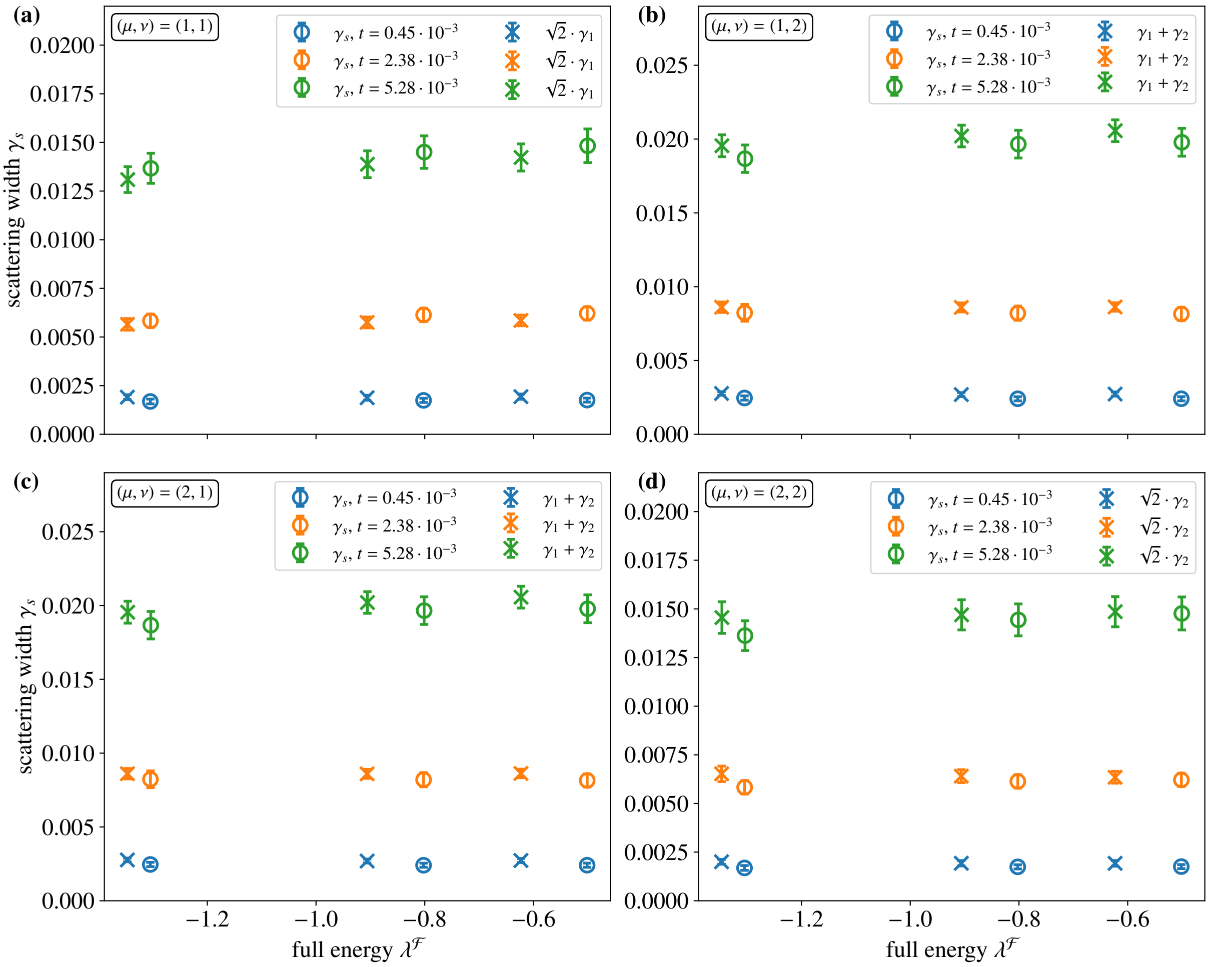

Figure 5.16: Comparison of the scattering width γ_s to the width of the Lorentzian overlap curves in the bath for $d_{\mathcal{F}} = 13$ sites and three different values of t. The scattering width is obtained from Lorentzian fits to the squared magnitude of the singular vector overlap in the bath $|\langle\tilde{\phi}_\nu^{k,\mathcal{B}}|\tilde{\phi}_\mu^{l,\mathcal{B}}\rangle|^2$ as in Eq. (5.110). For that, we average the result in intervals of $\Delta\lambda^{\mathcal{F}} \approx 0.4$ around the mean values of $\langle\lambda_l\rangle = \{-1.305, -0.802, -0.501\}$. This is plotted as circles with error bars. The width of the overlap curves are obtained from Lorentzian fits to $|\langle\psi_\mu^{\mathcal{S}}|\,\langle\psi_i^{\mathcal{B}}|\psi_l^{\mathcal{F}}\rangle|^2$ using $N_{\mathrm{av}} = 400$ full states around the mean full energies $\lambda_l = \{-1.347, -0.906, -0.623\}$. We then plot the width of the overlap peaks with $\sqrt{2}\gamma_\mu$ for $\mu = \nu$ and $\gamma_\mu + \gamma_\nu$ for $\mu \neq \nu$ as crosses with error bars. All data is additionally averaged over 88 samples of $H^{\mathcal{F}}$. The scatterings are analyzed for **(a)** $(\mu, \nu) = (1, 1)$, **(b)** $(\mu, \nu) = (1, 2)$, **(c)** $(\mu, \nu) = (2, 1)$ and **(d)** $(\mu, \nu) = (2, 2)$.

Conclusion

In this thesis, we reported on a joint work with T. Hofmann, R. Thomale and M. Greiter. In our work [3], we investigate the microscopic origin of quantum thermalization. We derive the canonical distribution of statistical mechanics in a subsystem of an isolated quantum system within an exact eigenstate of the full Hamiltonian. Our analysis solely follows from the principles and laws of quantum mechanics and their application to large system with additional constraints of locality and the absence of integrability. This is connected to the ETH [1, 2], which conjectures that a single state of an isolated quantum system exhibits thermal properties at large times when measured in terms of local observables. We hence prove the validity of the ETH in the considered class of local random Hamiltonians without resorting to the concepts of ergodicity or maximal entropy which have to date been employed to obtain the statistical behavior fundamental to the description of statistical mechanics. In contrast to typicality, our approach further does not necessitate any assumptions on the underlying quantum states, which show thermal behavior such as a probability distribution of possible quantum microstates in typicality. With our approach, we investigate the equilibrium phase of quantum thermalization without consideration of equilibration towards the thermal equilibrium.

First, we established the basic concepts of RMT which are needed to perform the analytical calculations within our work. Besides the definition of random variables, Brownian motion, the Stieltjes transform and the resolvent, we derived a stochastic differential equation (SDE) for the Stieltjes and the resolvent given a GUE matrix perturbation of a deterministic matrix by employing Dyson-Brownian motion (DBM). The solutions to the SDEs contain information on the evolution of the eigenvalues and eigenstates of the initial matrix which has been formulated by Allez and Bouchaud [179]. The introduction to RMT is concluded by a description of the equation by Casati and Girko [182], which establishes a recursive equation for the resolvent given a random band matrix perturbation.

We then introduced the quantum system under investigation, which is chosen to be a two-dimensional spin-$1/2$ lattice under open boundary conditions (OBC) described by a random local Hamiltonian that contains random nearest neighbor spin-spin interactions between two sites and random magnetic fields on each individual site. We then briefly outline the DOS that arises in such setups which is described by a Gaussian distribution. The mathematical proof of this statement was first given by Hartmann et al. in [186, 187]. We found an alternative proof which utilizes the moments of the local Hamiltonian [188]. The Gaussian DOS is a crucial ingredient of our approach to quantum thermalization.

The quantum system under investigation is split into a small subsystem $\mathcal{S}$ and a bath $\mathcal{B}$ coupled by a small perturbation X, which contains random local interactions along the boundary of the two subsystems. To determine the properties of a single eigenstate of the full perturbed quantum system, we first examine the structure of the perturbation matrix X. Represented in terms of the unperturbed energy eigenbasis of $\mathcal{S}$ and $\mathcal{B}$ denoted as $\tilde{X}$, it is found to be a random band matrix. We calculate an analytical expression for the element dependent variance of the offdiagonal elements of $\tilde{X}$ depending on the energy of the eigenstates of $\mathcal{S}$ and $\mathcal{B}$. This is labeled as the variance model and is identified to be an appropriately normalized Gaussian distribution in the thermodynamic limit. We further find that the diagonal variance is much larger than the offdiagonal variance with a dominant scaling in the large bath limit. Numerical results obtained by ED confirm the analytical findings. These properties of the perturbation matrix already indicate a thermal behavior as they are equal to the requirements of the ETH when formulated in terms of the matrix elements of local observables.

Going beyond the standard description of the ETH, we insert the variance model into the recursive equation for the resolvent by Casati and Girko. We then extract the overlap between the eigenstates of the full system and the unperturbed product basis of $\mathcal{S}$ and $\mathcal{B}$ from the resolvent analysis. It turns out that the overlap curve in terms of the bath eigenstates close to its peak is described by an appropriately normalized Lorentzian with an additional envelope function originating from the variance structure of the perturbation matrix with an intrinsic energy cutoff arising due to the locality of the perturbation. This is confirmed by an extensive numerical analysis with ED, where we compare the Lorentzian fit parameters to the analytical calculation.

We finish by constructing the reduced density matrix in the small subsystem $\mathcal{S}$ in the energy eigenbasis of $\mathcal{S}$ when starting with the pure density matrix of a single eigenstate of the full Hamiltonian. By a RMT calculation we find that the offdiagonal elements decrease with the dimension of the Hilbert space of the bath while the diagonal entries converge to their thermal value given by the Boltzmann distribution. Both results are confirmed by numerical analysis through a finite size scaling. The Boltzmann distribution on the diagonal is given in terms of shifted energy values in $\mathcal{S}$ where the bare energy eigenvalues are renormalized due to the influence of the perturbation X. The results are reconnected to the ETH in the equilibrium phase where we establish a notion of quantum thermalization based purely on the laws of quantum mechanics. Lastly, we investigate the scattering of the Lorentzians in the bath energies which is triggered by a time dependent scattering that acts only in the subsystem $\mathcal{S}$. A numerical analysis shows that the scattering is sensitive to the renormalized energies in $\mathcal{S}$, which could potentially be probed in an experimental setting such as ultracold atoms.

Outlook

Our analysis of quantum thermalization builds on the application of quantum mechanics to large systems, the random coupling of local degrees of freedom and the absence of integrability. We derive [3] the canonical distribution in a single eigenstate of the isolated quantum system with the eigenstate acting as a thermal bath to its subsystems. This is demonstrated through the reduced density matrix which converges to the canonical density matrix of a thermal equilibrium in the large bath limit. In the calculation we utilize two things. First, we employ the methods of Dyson-Brownian motion applied to random banded matrices. Second, we use that the density of states of a local random Hamiltonian under general circumstances is given by a Gaussian distribution. The analytical findings are confirmed by a numerical study with exact diagonalization. Our approach provides a microscopic derivation of quantum thermalization in the considered class of Hamiltonians without requiring the concepts of maximal entropy or ergodicity, nor requiring any assumption on the quantum states.

Going beyond the generic case, several counterexamples to the ETH have been established. This includes many body localization (MBL) [81–84], a many body extension of Anderson localization featuring localized many body quantum states. The ETH also breaks down for quantum many body scars [54–56], which are typically embedded as single states inside a thermal spectrum. Other examples where the ETH fails are systems with an extensive number of local conserved quantities [112] or finite one-dimensional lattices when approaching an integrable point [41, 43]. With the availability of a microscopic approach to quantum thermalization and the ETH, it may be possible to determine the exact origin of failure of the ETH in those systems which has so far been elusive and primarily explored through numerical analysis. Another direction might be the study of entanglement entropy and how it relates to the present approach, as it did not need to be considered for the derivation in our work. Further research questions arise in relation to the relaxation towards equilibrium, i.e. the mechanism of how initial out-of-equilibrium states converge to the thermal equilibrium. A systematic study of equilibration could address the time scales on which thermalization occurs. Beyond the theory of thermalization, the ETH has been applied to a range of open questions in physics, such as in quantum gravity research. The mechanism of thermalisation explained purely from the laws of quantum mechanics could provide new insights into these topics and generate new ideas where the ETH could be useful for a deeper understanding.

Bibliography

[1] J. M. Deutsch, “*Quantum statistical mechanics in a closed system*”, Physical Review A **43**, 2046 (1991).

[2] M. Srednicki, “*Chaos and quantum thermalization*”, Physical Review E **50**, 888 (1994).

[3] T. Helbig, T. Hofmann, R. Thomale, and M. Greiter, “*Theory of Eigenstate Thermalization*”, to appear (2023).

[4] R. Kubo, *Statistical mechanics: an advanced course with problems and solutions*, (Amsterdam, The Netherlands: Elsevier, 1965).

[5] N. Singh, “*On the foundations of statistical mechanics: a brief review*”, Modern Physics Letters B **27**, 1330003 (2013).

[6] S.-K. Ma, *Statistical Mechanics*, (World Scientific Book, 1985).

[7] R. Feynman, *Statistical Mechanics: A Set Of Lectures*, (Westview Press, 1998).

[8] I. E. Farquhar, “*Ergodic Theory in Statistical Mechanics*”, American Journal of Physics **33**, 973 (1965).

[9] O. Penrose, *Foundations of Statistical Mechanics*, (Pergamon, Oxford, 1970).

[10] E. T. Jaynes, “*Information Theory and Statistical Mechanics*”, Physical Review **106**, 620 (1957).

[11] E. T. Jaynes, “*Information Theory and Statistical Mechanics II*”, Physical Review **108**, 171 (1957).

[12] E. Schrödinger, “*Energieaustausch nach der Wellenmechanik*”, Annalen der Physik **388**, 956 (1927).

[13] E. Schrödinger, *Statistical Thermodynamics, 2nd Edition*, (Cambridge University Press, 1952).

[14] J. v. Neumann, “*Beweis des Ergodensatzes und des H-Theorems in der neuen Mechanik*”, Zeitschrift für Physik **57**, 30 (1929).

[15] M. V. Berry, “*Regular and irregular semiclassical wavefunctions*”, Journal of Physics A: Mathematical and General **10**, 2083 (1977).

[16] M. V. Berry, “*Quantizing a classically ergodic system: Sinai’s billiard and the KKR method*”, Annals of Physics **131**, 163 (1981).

[17] I. Bloch, J. Dalibard, and W. Zwerger, “*Many-body physics with ultracold gases*”, Reviews of Modern Physics **80**, 885 (2008).

[18] T. Langen, R. Geiger, and J. Schmiedmayer, “*Ultracold Atoms Out of Equilibrium*”, Annual Review of Condensed Matter Physics **6**, 201 (2015).

[19] M. A. Cazalilla, R. Citro, T. Giamarchi, E. Orignac, and M. Rigol, “*One dimensional bosons: From condensed matter systems to ultracold gases*”, Reviews of Modern Physics **83**, 1405 (2011).

[20] T. Langen *et al.*, “*Experimental observation of a generalized Gibbs ensemble*”, Science **348**, 207 (2015).

[21] L. D’Alessio, Y. Kafri, A. Polkovnikov, and M. Rigol, “*From quantum chaos and eigenstate thermalization to statistical mechanics and thermodynamics*”, Advances in Physics **65**, 239 (2016).

[22] J. M. Deutsch, “*Eigenstate thermalization hypothesis*”, Reports on Progress in Physics **81**, 082001 (2018).

[23] M. Rigol, V. Dunjko, and M. Olshanii, “*Thermalization and its mechanism for generic isolated quantum systems*”, Nature **452**, 854 (2008).

[24] R. V. Jensen and R. Shankar, “*Statistical Behavior in Deterministic Quantum Systems with Few Degrees of Freedom*”, Physical Review Letters **54**, 1879 (1985).

[25] L. F. Santos and M. Rigol, “*Localization and the effects of symmetries in the thermalization properties of one-dimensional quantum systems*”, Physical Review E **82**, 031130 (2010).

[26] R. Steinigeweg, J. Herbrych, and P. Prelovšek, “*Eigenstate thermalization within isolated spin-chain systems*”, Physical Review E **87**, 012118 (2013).

[27] W. Beugeling, R. Moessner, and M. Haque, “*Finite-size scaling of eigenstate thermalization*”, Physical Review E **89**, 042112 (2014).

[28] R. Mondaini and M. Rigol, “*Eigenstate thermalization in the two-dimensional transverse field Ising model. II. Off-diagonal matrix elements of observables*”, Physical Review E **96**, 012157 (2017).

[29] C. Neuenhahn and F. Marquardt, “*Thermalization of interacting fermions and delocalization in Fock space*”, Physical Review E **85**, 060101 (2012).

[30] H. Kim, T. N. Ikeda, and D. A. Huse, “*Testing whether all eigenstates obey the eigenstate thermalization hypothesis*”, Physical Review E **90**, 052105 (2014).

[31] S. Sorg, L. Vidmar, L. Pollet, and F. Heidrich-Meisner, “*Relaxation and thermalization in the one-dimensional Bose-Hubbard model: A case study for the interaction quantum quench from the atomic limit*”, Physical Review A **90**, 033606 (2014).

[32] R. Steinigeweg, A. Khodja, H. Niemeyer, C. Gogolin, and J. Gemmer, “*Pushing the Limits of the Eigenstate Thermalization Hypothesis towards Mesoscopic Quantum Systems*”, Physical Review Letters **112**, 130403 (2014).

[33] K. R. Fratus and M. Srednicki, “*Eigenstate thermalization in systems with spontaneously broken symmetry*”, Physical Review E **92**, 040103 (2015).

[34] A. Khodja, R. Steinigeweg, and J. Gemmer, “*Relevance of the eigenstate thermalization hypothesis for thermal relaxation*”, Physical Review E **91**, 012120 (2015).

[35] E. J. Torres-Herrera and L. F. Santos, “*Local quenches with global effects in interacting quantum systems*”, Physical Review E **89**, 062110 (2014).

[36] D. J. Luitz and Y. Bar Lev, “*Anomalous Thermalization in Ergodic Systems*”, Physical Review Letters **117**, 170404 (2016).

[37] D. J. Luitz, “*Long tail distributions near the many-body localization transition*”, Physical Review B **93**, 134201 (2016).

[38] T. LeBlond, K. Mallayya, L. Vidmar, and M. Rigol, “*Entanglement and matrix elements of observables in interacting integrable systems*”, Physical Review E **100**, 062134 (2019).

[39] M. Brenes, T. LeBlond, J. Goold, and M. Rigol, "*Eigenstate Thermalization in a Locally Perturbed Integrable System*", Physical Review Letters **125**, 070605 (2020).

[40] J. D. Noh, "*Eigenstate thermalization hypothesis and eigenstate-to-eigenstate fluctuations*", Physical Review E **103**, 012129 (2021).

[41] M. Rigol, "*Breakdown of Thermalization in Finite One-Dimensional Systems*", Physical Review Letters **103**, 100403 (2009).

[42] L. F. Santos and M. Rigol, "*Onset of quantum chaos in one-dimensional bosonic and fermionic systems and its relation to thermalization*", Physical Review E **81**, 036206 (2010).

[43] M. Rigol, "*Quantum quenches and thermalization in one-dimensional fermionic systems*", Physical Review A **80**, 053607 (2009).

[44] A. Polkovnikov, K. Sengupta, A. Silva, and M. Vengalattore, "*Colloquium: Nonequilibrium dynamics of closed interacting quantum systems*", Reviews of Modern Physics **83**, 863 (2011).

[45] J.-H. Jung and J. D. Noh, "*Guide to Exact Diagonalization Study of Quantum Thermalization*", Journal of the Korean Physical Society **76**, 670 (2020).

[46] M. Srednicki and F. Stiernelof, "*Gaussian fluctuations in chaotic eigenstates*", Journal of Physics A: Mathematical and General **29**, 5817 (1996).

[47] M. Srednicki, "*The approach to thermal equilibrium in quantized chaotic systems*", Journal of Physics A: Mathematical and General **32**, 1163 (1999).

[48] J. Richter, J. Gemmer, and R. Steinigeweg, "*Impact of eigenstate thermalization on the route to equilibrium*", Physical Review E **99**, 050104 (2019).

[49] L. P. García-Pintos, N. Linden, A. S. L. Malabarba, A. J. Short, and A. Winter, "*Equilibration Time Scales of Physically Relevant Observables*", Physical Review X **7**, 031027 (2017).

[50] E. Khatami, G. Pupillo, M. Srednicki, and M. Rigol, "*Fluctuation-Dissipation Theorem in an Isolated System of Quantum Dipolar Bosons after a Quench*", Physical Review Letters **111**, 050403 (2013).

[51] S. Pappalardi, L. Foini, and J. Kurchan, "*Quantum bounds and fluctuation-dissipation relations*", SciPost Physics **12**, 130 (2022).

[52] M. Rigol and M. Srednicki, "*Alternatives to Eigenstate Thermalization*", Physical Review Letters **108**, 110601 (2012).

[53] A. Dymarsky, N. Lashkari, and H. Liu, "*Subsystem eigenstate thermalization hypothesis*", Physical Review E **97**, 012140 (2018).

[54] H. Bernien *et al.*, "*Probing many-body dynamics on a 51-atom quantum simulator*", Nature **551**, 579 (2017).

[55] C. J. Turner, A. A. Michailidis, D. A. Abanin, M. Serbyn, and Z. Papić, "*Weak ergodicity breaking from quantum many-body scars*", Nature Physics **14**, 745 (2018).

[56] K. Bull, I. Martin, and Z. Papić, "*Systematic Construction of Scarred Many-Body Dynamics in 1D Lattice Models*", Physical Review Letters **123**, 030601 (2019).

[57] G. Biroli, C. Kollath, and A. M. Läuchli, "*Effect of Rare Fluctuations on the Thermalization of Isolated Quantum Systems*", Physical Review Letters **105**, 250401 (2010).

[58] T. Mori, “*Weak eigenstate thermalization with large deviation bound*”, arXiv preprint arXiv:1609.09776 (2016).

[59] N. Shiraishi and T. Mori, “*Systematic Construction of Counterexamples to the Eigenstate Thermalization Hypothesis*”, Physical Review Letters **119**, 030601 (2017).

[60] D. N. Page, “*Average entropy of a subsystem*”, Physical Review Letters **71**, 1291 (1993).

[61] J. M. Deutsch, “*Thermodynamic entropy of a many-body energy eigenstate*”, New Journal of Physics **12**, 075021 (2010).

[62] J. R. Garrison and T. Grover, “*Does a Single Eigenstate Encode the Full Hamiltonian?*”, Physical Review X **8**, 021026 (2018).

[63] H. Tasaki, “*From Quantum Dynamics to the Canonical Distribution: General Picture and a Rigorous Example*”, Physical Review Letters **80**, 1373 (1998).

[64] J. Gemmer and G. Mahler, “*Distribution of local entropy in the Hilbert space of bi-partite quantum systems: origin of Jaynes’ principle*”, The European Physical Journal B - Condensed Matter and Complex Systems **31**, 249 (2003).

[65] S. Goldstein, J. L. Lebowitz, R. Tumulka, and N. Zanghì, “*Canonical Typicality*”, Physical Review Letters **96**, 050403 (2006).

[66] P. Reimann, “*Canonical thermalization*”, New Journal of Physics **12**, 055027 (2010).

[67] S. Goldstein, “*Typicality and Notions of Probability in Physics*”, *Probability in Physics*, ed. by Y. Ben-Menahem and M. Hemmo, The Frontiers Collection, (Berlin, Heidelberg: Springer, 2012), pp. 59–71.

[68] D. Dürr and W. Struyve, “*Typicality in the Foundations of Statistical Physics and Born’s Rule*”, *Do Wave Functions Jump? : Perspectives of the Work of GianCarlo Ghirardi*, ed. by V. Allori, A. Bassi, D. Dürr, and N. Zanghi, Fundamental Theories of Physics, (Cham: Springer International Publishing, 2021), pp. 35–43.

[69] S. Popescu, A. J. Short, and A. Winter, “*Entanglement and the foundations of statistical mechanics*”, Nature Physics **2**, 754 (2006).

[70] C. Gogolin and J. Eisert, “*Equilibration, thermalisation, and the emergence of statistical mechanics in closed quantum systems*”, Reports on Progress in Physics **79**, 056001 (2016).

[71] N. Linden, S. Popescu, A. J. Short, and A. Winter, “*Quantum mechanical evolution towards thermal equilibrium*”, Physical Review E **79**, 061103 (2009).

[72] S. Goldstein, J. L. Lebowitz, R. Tumulka, and N. Zanghì, “*Long-time behavior of macroscopic quantum systems*”, The European Physical Journal H **35**, 173 (2010).

[73] P. Reimann, “*Typical fast thermalization processes in closed many-body systems*”, Nature Communications **7**, 10821 (2016).

[74] M. Storms and R. R. P. Singh, “*Entanglement in ground and excited states of gapped free-fermion systems and their relationship with Fermi surface and thermodynamic equilibrium properties*”, Physical Review E **89**, 012125 (2014).

[75] L. F. Santos, A. Polkovnikov, and M. Rigol, “*Weak and strong typicality in quantum systems*”, Physical Review E **86**, 010102 (2012).

[76] E. Bianchi and P. Donà, "*Typical entanglement entropy in the presence of a center: Page curve and its variance*", Physical Review D **100**, 105010 (2019).

[77] S. Goldstein, D. A. Huse, J. L. Lebowitz, and R. Tumulka, "*Thermal Equilibrium of a Macroscopic Quantum System in a Pure State*", Physical Review Letters **115**, 100402 (2015).

[78] S. Goldstein, D. A. Huse, J. L. Lebowitz, and R. Tumulka, "*Macroscopic and microscopic thermal equilibrium*", Annalen der Physik **529**, 1600301 (2017).

[79] R. Hamazaki and M. Ueda, "*Atypicality of Most Few-Body Observables*", Physical Review Letters **120**, 080603 (2018).

[80] H. Tasaki, "*Typicality of Thermal Equilibrium and Thermalization in Isolated Macroscopic Quantum Systems*", Journal of Statistical Physics **163**, 937 (2016).

[81] L. Fleishman, D. C. Licciardello, and P. W. Anderson, "*Elementary Excitations in the Fermi Glass*", Physical Review Letters **40**, 1340 (1978).

[82] L. Fleishman and P. W. Anderson, "*Interactions and the Anderson transition*", Physical Review B **21**, 2366 (1980).

[83] B. L. Altshuler, Y. Gefen, A. Kamenev, and L. S. Levitov, "*Quasiparticle Lifetime in a Finite System: A Nonperturbative Approach*", Physical Review Letters **78**, 2803 (1997).

[84] I. V. Gornyi, A. D. Mirlin, and D. G. Polyakov, "*Interacting Electrons in Disordered Wires: Anderson Localization and Low-T Transport*", Physical Review Letters **95**, 206603 (2005).

[85] D. A. Abanin, E. Altman, I. Bloch, and M. Serbyn, "*Colloquium: Many-body localization, thermalization, and entanglement*", Reviews of Modern Physics **91**, 021001 (2019).

[86] P. W. Anderson, "*Absence of Diffusion in Certain Random Lattices*", Physical Review **109**, 1492 (1958).

[87] D. M. Basko, I. L. Aleiner, and B. L. Altshuler, "*Metal–insulator transition in a weakly interacting many-electron system with localized single-particle states*", Annals of Physics **321**, 1126 (2006).

[88] V. Oganesyan and D. A. Huse, "*Localization of interacting fermions at high temperature*", Physical Review B **75**, 155111 (2007).

[89] A. Pal and D. A. Huse, "*Many-body localization phase transition*", Physical Review B **82**, 174411 (2010).

[90] B. Bauer and C. Nayak, "*Area laws in a many-body localized state and its implications for topological order*", Journal of Statistical Mechanics: Theory and Experiment **2013**, P09005 (2013).

[91] R. Mondaini and Z. Cai, "*Many-body self-localization in a translation-invariant Hamiltonian*", Physical Review B **96**, 035153 (2017).

[92] D. A. Huse, R. Nandkishore, and V. Oganesyan, "*Phenomenology of fully many-body-localized systems*", Physical Review B **90**, 174202 (2014).

[93] J. Eisert, M. Cramer, and M. B. Plenio, "*Colloquium: Area laws for the entanglement entropy*", Reviews of Modern Physics **82**, 277 (2010).

[94] D. A. Huse, R. Nandkishore, V. Oganesyan, A. Pal, and S. L. Sondhi, "*Localization-protected quantum order*", Physical Review B **88**, 014206 (2013).

[95] M. Serbyn, Z. Papić, and D. A. Abanin, "*Local Conservation Laws and the Structure of the Many-Body Localized States*", Physical Review Letters **111**, 127201 (2013).

[96] E. Altman and R. Vosk, "*Universal Dynamics and Renormalization in Many-Body-Localized Systems*", Annual Review of Condensed Matter Physics **6**, 383 (2015).

[97] R. Nandkishore and D. A. Huse, "*Many-Body Localization and Thermalization in Quantum Statistical Mechanics*", Annual Review of Condensed Matter Physics **6**, 15 (2015).

[98] F. Alet and N. Laflorencie, "*Many-body localization: An introduction and selected topics*", Comptes Rendus Physique **19**, 498 (2018).

[99] J. Z. Imbrie, "*On Many-Body Localization for Quantum Spin Chains*", Journal of Statistical Physics **163**, 998 (2016).

[100] W. D. Roeck and F. Huveneers, "*Can translation invariant systems exhibit a Many-Body Localized phase?*", arXiv preprint arXiv:1409.8054 (2014).

[101] W. De Roeck and F. Huveneers, "*Scenario for delocalization in translation-invariant systems*", Physical Review B **90**, 165137 (2014).

[102] Z. Papić, "*Weak ergodicity breaking through the lens of quantum entanglement*", arXiv preprint arXiv:2108.03460 [cond-mat] (2021).

[103] S. Moudgalya, B. A. Bernevig, and N. Regnault, "*Quantum many-body scars and Hilbert space fragmentation: a review of exact results*", Reports on Progress in Physics **85**, 086501 (2022).

[104] A. Chandran, T. Iadecola, V. Khemani, and R. Moessner, "*Quantum Many-Body Scars: A Quasiparticle Perspective*", Annual Review of Condensed Matter Physics **14**, 443 (2023).

[105] M. Serbyn, D. A. Abanin, and Z. Papić, "*Quantum many-body scars and weak breaking of ergodicity*", Nature Physics **17**, 675 (2021).

[106] M. C. Gutzwiller, "*Periodic Orbits and Classical Quantization Conditions*", Journal of Mathematical Physics **12**, 343 (1971).

[107] E. J. Heller, "*Bound-State Eigenfunctions of Classically Chaotic Hamiltonian Systems: Scars of Periodic Orbits*", Physical Review Letters **53**, 1515 (1984).

[108] N. Robinson, "*Cold Atoms Bear a Quantum Scar*", Physics **11**, 105 (2018).

[109] C. J. Turner, A. A. Michailidis, D. A. Abanin, M. Serbyn, and Z. Papić, "*Quantum scarred eigenstates in a Rydberg atom chain: Entanglement, breakdown of thermalization, and stability to perturbations*", Physical Review B **98**, 155134 (2018).

[110] J. Keski-Rahkonen, P. J. J. Luukko, S. Åberg, and E. Räsänen, "*Effects of scarring on quantum chaos in disordered quantum wells*", Journal of Physics: Condensed Matter **31**, 105301 (2019).

[111] V. Khemani, C. R. Laumann, and A. Chandran, "*Signatures of integrability in the dynamics of Rydberg-blockaded chains*", Physical Review B **99**, 161101 (2019).

[112] R. Hamazaki, T. N. Ikeda, and M. Ueda, "*Generalized Gibbs ensemble in a nonintegrable system with an extensive number of local symmetries*", Physical Review E **93**, 032116 (2016).

[113] N. J. Hitchin, G. B. Segal, and R. S. Ward, *Integrable Systems: Twistors, Loop Groups, and Riemann Surfaces*, (OUP Oxford, 2013).

[114] E. Kaminishi, T. Mori, T. N. Ikeda, and M. Ueda, "*Entanglement pre-thermalization in a one-dimensional Bose gas*", Nature Physics **11**, 1050 (2015).

[115] T. Langen, R. Geiger, M. Kuhnert, B. Rauer, and J. Schmiedmayer, “*Local emergence of thermal correlations in an isolated quantum many-body system*”, Nature Physics **9**, 640 (2013).

[116] M. Rigol, V. Dunjko, V. Yurovsky, and M. Olshanii, “*Relaxation in a Completely Integrable Many-Body Quantum System: An Ab Initio Study of the Dynamics of the Highly Excited States of 1D Lattice Hard-Core Bosons*”, Physical Review Letters **98**, 050405 (2007).

[117] A. C. Cassidy, C. W. Clark, and M. Rigol, “*Generalized Thermalization in an Integrable Lattice System*”, Physical Review Letters **106**, 140405 (2011).

[118] M. Greiner, O. Mandel, T. W. Hänsch, and I. Bloch, “*Collapse and revival of the matter wave field of a Bose–Einstein condensate*”, Nature **419**, 51 (2002).

[119] K. Winkler *et al.*, “*Repulsively bound atom pairs in an optical lattice*”, Nature **441**, 853 (2006).

[120] S. Will *et al.*, “*Time-resolved observation of coherent multi-body interactions in quantum phase revivals*”, Nature **465**, 197 (2010).

[121] S. Will, T. Best, S. Braun, U. Schneider, and I. Bloch, “*Coherent Interaction of a Single Fermion with a Small Bosonic Field*”, Physical Review Letters **106**, 115305 (2011).

[122] S. Will, D. Iyer, and M. Rigol, “*Observation of coherent quench dynamics in a metallic many-body state of fermionic atoms*”, Nature Communications **6**, 6009 (2015).

[123] M. Gring *et al.*, “*Relaxation and Prethermalization in an Isolated Quantum System*”, Science **337**, 1318 (2012).

[124] A. M. Kaufman *et al.*, “*Quantum thermalization through entanglement in an isolated many-body system*”, Science **353**, 794 (2016).

[125] G. Clos, D. Porras, U. Warring, and T. Schaetz, “*Time-Resolved Observation of Thermalization in an Isolated Quantum System*”, Physical Review Letters **117**, 170401 (2016).

[126] Y. Tang *et al.*, “*Thermalization near Integrability in a Dipolar Quantum Newton’s Cradle*”, Physical Review X **8**, 021030 (2018).

[127] S. Trotzky *et al.*, “*Probing the relaxation towards equilibrium in an isolated strongly correlated one-dimensional Bose gas*”, Nature Physics **8**, 325 (2012).

[128] L. Xia *et al.*, “*Quantum distillation and confinement of vacancies in a doublon sea*”, Nature Physics **11**, 316 (2015).

[129] T. Kinoshita, T. Wenger, and D. S. Weiss, “*A quantum Newton’s cradle*”, Nature **440**, 900 (2006).

[130] J.-y. Choi *et al.*, “*Exploring the many-body localization transition in two dimensions*”, Science **352**, 1547 (2016).

[131] A. J. Daley, H. Pichler, J. Schachenmayer, and P. Zoller, “*Measuring Entanglement Growth in Quench Dynamics of Bosons in an Optical Lattice*”, Physical Review Letters **109**, 020505 (2012).

[132] R. Islam *et al.*, “*Measuring entanglement entropy in a quantum many-body system*”, Nature **528**, 77 (2015).

[133] H. Pichler, G. Zhu, A. Seif, P. Zoller, and M. Hafezi, “*Measurement Protocol for the Entanglement Spectrum of Cold Atoms*”, Physical Review X **6**, 041033 (2016).

[134] L. Childress *et al.*, “*Coherent Dynamics of Coupled Electron and Nuclear Spin Qubits in Diamond*”, Science **314**, 281 (2006).

[135] M. E. Beverland *et al.*, "*Spectrum Estimation of Density Operators with Alkaline-Earth Atoms*", Physical Review Letters **120**, 025301 (2018).

[136] J. Berges, K. Boguslavski, S. Schlichting, and R. Venugopalan, "*Turbulent thermalization process in heavy-ion collisions at ultrarelativistic energies*", Physical Review D **89**, 074011 (2014).

[137] S. Wall *et al.*, "*Quantum interference between charge excitation paths in a solid-state Mott insulator*", Nature Physics **7**, 114 (2011).

[138] D. N. Basov, R. D. Averitt, D. van der Marel, M. Dressel, and K. Haule, "*Electrodynamics of correlated electron materials*", Reviews of Modern Physics **83**, 471 (2011).

[139] S. D. Geraedts, R. Nandkishore, and N. Regnault, "*Many-body localization and thermalization: Insights from the entanglement spectrum*", Physical Review B **93**, 174202 (2016).

[140] L. D'Alessio and A. Polkovnikov, "*Many-body energy localization transition in periodically driven systems*", Annals of Physics **333**, 19 (2013).

[141] A. Lazarides, A. Das, and R. Moessner, "*Equilibrium states of generic quantum systems subject to periodic driving*", Physical Review E **90**, 012110 (2014).

[142] K. Ji and B. V. Fine, "*Nonthermal Statistics in Isolated Quantum Spin Clusters after a Series of Perturbations*", Physical Review Letters **107**, 050401 (2011).

[143] M. Bukov, L. D'Alessio, and A. Polkovnikov, "*Universal high-frequency behavior of periodically driven systems: from dynamical stabilization to Floquet engineering*", Advances in Physics **64**, 139 (2015).

[144] P. Ponte, A. Chandran, Z. Papić, and D. A. Abanin, "*Periodically driven ergodic and many-body localized quantum systems*", Annals of Physics **353**, 196 (2015).

[145] J. Eisert, M. Friesdorf, and C. Gogolin, "*Quantum many-body systems out of equilibrium*", Nature Physics **11**, 124 (2015).

[146] D. Marolf and J. Polchinski, "*Gauge-Gravity Duality and the Black Hole Interior*", Physical Review Letters **111**, 171301 (2013).

[147] J. Maldacena and L. Susskind, "*Cool horizons for entangled black holes*", Fortschritte der Physik **61**, 781 (2013).

[148] J. Maldacena, S. H. Shenker, and D. Stanford, "*A bound on chaos*", Journal of High Energy Physics **2016**, 106 (2016).

[149] S. Khlebnikov and M. Kruczenski, "*Locality, entanglement, and thermalization of isolated quantum systems*", Physical Review E **90**, 050101 (2014).

[150] L. Bombelli, R. K. Koul, J. Lee, and R. D. Sorkin, "*Quantum source of entropy for black holes*", Physical Review D **34**, 373 (1986).

[151] M. Srednicki, "*Entropy and area*", Physical Review Letters **71**, 666 (1993).

[152] S. W. Hawking, "*Gravitational Radiation from Colliding Black Holes*", Physical Review Letters **26**, 1344 (1971).

[153] J. D. Bekenstein, "*Black Holes and Entropy*", Physical Review D **7**, 2333 (1973).

[154] J. Bun, J.-P. Bouchaud, and M. Potters, "*Cleaning large correlation matrices: Tools from Random Matrix Theory*", Physics Reports, Cleaning large correlation matrices: tools from random matrix theory **666**, 1 (2017).

[155] G. Livan, M. Novaes, and P. Vivo, *Introduction to Random Matrices*, vol. 26, SpringerBriefs in Mathematical Physics, (Cham: Springer International Publishing, 2018).

[156] M. Potters and J.-P. Bouchaud, *A First Course in Random Matrix Theory: for Physicists, Engineers and Data Scientists*, (Cambridge: Cambridge University Press, 2020).

[157] E. P. Wigner, "*Characteristic Vectors of Bordered Matrices With Infinite Dimensions*", The Annals of Mathematics **62**, 548 (1955).

[158] H. F. Trotter, "*Eigenvalue distributions of large Hermitian matrices; Wigner's semi-circle law and a theorem of Kac, Murdock, and Szegö*", Advances in Mathematics **54**, 67 (1984).

[159] J. F. Shriner, G. E. Mitchell, and T. von Egidy, "*Fluctuation properties of spacings of low-lying nuclear levels*", Zeitschrift für Physik A Hadrons and Nuclei **338**, 309 (1991).

[160] J.-P. Bouchaud and M. Potters, "*Two short pieces around the Wigner problem*", Journal of Physics A: Mathematical and Theoretical **52**, 024001 (2018).

[161] W. Beugeling, R. Moessner, and M. Haque, "*Off-diagonal matrix elements of local operators in many-body quantum systems*", Physical Review E **91**, 012144 (2015).

[162] J. Wang *et al.*, "*Eigenstate Thermalization Hypothesis and Its Deviations from Random-Matrix Theory beyond the Thermalization Time*", Physical Review Letters **128**, 180601 (2022).

[163] O. Bohigas, M. J. Giannoni, and C. Schmit, "*Spectral properties of the Laplacian and random matrix theories*", Journal de Physique Lettres **45**, 1015 (1984).

[164] P. Bourgade and H.-T. Yau, "*The Eigenvector Moment Flow and Local Quantum Unique Ergodicity*", Communications in Mathematical Physics **350**, 231 (2017).

[165] P. Bourgade, H.-T. Yau, and J. Yin, "*Random band matrices in the delocalized phase, I: Quantum unique ergodicity and universality*", arXiv preprint arXiv:1807.01559 (2018).

[166] G. Cipolloni, L. Erdős, and D. Schröder, "*Eigenstate Thermalization Hypothesis for Wigner Matrices*", Communications in Mathematical Physics **388**, 1005 (2021).

[167] A. Adhikari, S. Dubova, C. Xu, and J. Yin, "*Eigenstate Thermalization Hypothesis for Generalized Wigner Matrices*", arXiv preprint arXiv:2302.00157 (2023).

[168] D. Facoetti, P. Vivo, and G. Biroli, "*From non-ergodic eigenvectors to local resolvent statistics and back: A random matrix perspective*", Europhysics Letters **115**, 47003 (2016).

[169] P. von Soosten and S. Warzel, "*Non-ergodic delocalization in the Rosenzweig–Porter model*", Letters in Mathematical Physics **109**, 905 (2019).

[170] R. Allez and J.-P. Bouchaud, "*Eigenvector dynamics: General theory and some applications*", Physical Review E **86**, 046202 (2012).

[171] R. Allez and A. Guionnet, "*A diffusive matrix model for invariant β-ensembles*", Electronic Journal of Probability **18**, 1 (2013).

[172] R. Allez, J. Bun, and J.-P. Bouchaud, "*The eigenvectors of Gaussian matrices with an external source*", arXiv preprint arXiv:1412.7108 (2015).

[173] L. Benigni, "*Eigenvectors distribution and quantum unique ergodicity for deformed Wigner matrices*", Annales de l'Institut Henri Poincaré, Probabilités et Statistiques **56**, 2822 (2020).

[174] E. Bogomolny and M. Sieber, “*Eigenfunction distribution for the Rosenzweig-Porter model*”, Physical Review E **98**, 032139 (2018).

[175] K. Truong and A. Ossipov, “*Eigenvectors under a generic perturbation: Non-perturbative results from the random matrix approach*”, Europhysics Letters **116**, 37002 (2016).

[176] A. Einstein, “*Über die von der molekularkinetischen Theorie der Wärme geforderte Bewegung von in ruhenden Flüssigkeiten suspendierten Teilchen*”, Annalen der Physik **322**, 549 (1905).

[177] P. Mörters and Y. Peres, *Brownian Motion*, Cambridge Series in Statistical and Probabilistic Mathematics, (Cambridge: Cambridge University Press, 2010).

[178] F. J. Dyson, “*A Brownian-Motion Model for the Eigenvalues of a Random Matrix*”, Journal of Mathematical Physics **3**, 1191 (1962).

[179] R. Allez and J.-P. Bouchaud, “*Eigenvector dynamics under free addition*”, Random Matrices: Theory and Applications **03**, 1450010 (2014).

[180] P. Bourgade, “*Random band matrices*”, arXiv preprint arXiv:1807.03031 (2018).

[181] P. Bourgade, J. Huang, and H.-T. Yau, “*Eigenvector statistics of sparse random matrices*”, Electronic Journal of Probability **22**, 1 (2017).

[182] G. Casati and V. Girko, “*Wigner’s semicircle law for band random matrices*”, De Gruyter Section: Random Operators and Stochastic Equations **1**, 15 (1993).

[183] D. Shlyakhtenko, “*Random Gaussian band matrices and freeness with amalgamation*”, International Mathematics Research Notices **1996**, 1013 (1996).

[184] S. Sugimoto, R. Hamazaki, and M. Ueda, “*Test of the Eigenstate Thermalization Hypothesis Based on Local Random Matrix Theory*”, Physical Review Letters **126**, 120602 (2021).

[185] J. S. Cotler, G. R. Penington, and D. H. Ranard, “*Locality from the Spectrum*”, Communications in Mathematical Physics **368**, 1267 (2019).

[186] M. Hartmann, G. Mahler, and O. Hess, “*Gaussian Quantum Fluctuations in Interacting Many Particle Systems*”, Letters in Mathematical Physics **68**, 103 (2004).

[187] M. Hartmann, G. Mahler, and O. Hess, “*Spectral Densities and Partition Functions of Modular Quantum ystems as Derived from a Central Limit Theorem*”, Journal of Statistical Physics **119**, 1139 (2005).

[188] T. Hofmann, T. Helbig, R. Thomale, and M. Greiter, “*Universal Eigenvalue Distribution for Locally Interacting Quantum Systems*”, to appear (2023).

[189] T. Hofmann, “*Eigenstate thermalization and random matrix theory*”, Dissertation, Julius Maximilians Universität, Würzburg (2023).

[190] I. S. Dhillon and B. N. Parlett, “*Multiple representations to compute orthogonal eigenvectors of symmetric tridiagonal matrices*”, Linear Algebra and its Applications **387**, 1 (2004).

[191] E. Anderson, *LAPACK Users’ Guide*, (Philadelphia, PA: Society for Industrial and Applied Mathematics, 1999).

[192] E. Polizzi, “*Density-matrix-based algorithm for solving eigenvalue problems*”, Physical Review B **79**, 115112 (2009).

[193] P. T. Peter Tang and E. Polizzi, "*FEAST As A Subspace Iteration Eigensolver Accelerated By Approximate Spectral Projection*", SIAM Journal on Matrix Analysis and Applications **35**, 354 (2014).

[194] G. W. Anderson, A. Guionnet, and O. Zeitouni, *An Introduction to Random Matrices*, Cambridge Studies in Advanced Mathematics, (Cambridge: Cambridge University Press, 2009).

[195] Y. W. Sokhotski, "*On definite integrals and functions used in series expansions*", St. Petersburg (1873).

[196] J. Plemelj, *Problems in the sense of Riemann and Klein*, (New York, Interscience Publishers, 1964).

[197] H. A. Kramers, "*La diffusion de la lumière par les atomes*", Atti Cong. Intern. Fisica, (Transactions of Volta Centenary Congress) Como **2**, 545 (1927).

[198] R. d. L. Kronig, "*On the Theory of Dispersion of X-Rays*", JOSA **12**, 547 (1926).

[199] D. Hilbert, *Grundzüge einer allgemeinen Theorie der linearen Integralgleichungen*, (Leipzig, B. G. Teubner, 1912).

[200] R. Durrett, "*Probability: Theory and Examples*", Cambridge series in statistical and probabilistic mathematics (2019).

[201] K. Itô, *Stochastic integral*, (Proceedings of the Imperial Academy 20, Publisher: The Japan Academy, 519, 1944).

[202] K. Itô, *On stochastic differential equations*, (Memoirs of the American Mathematical Society, 1951).

[203] D. W. Stroock and K. Itô, "*Kiyosi Itô: selected papers*", New York: Springer-Verlag (1987).

[204] J. M. Burgers, "*A Mathematical Model Illustrating the Theory of Turbulence*", *Advances in Applied Mechanics*, ed. by R. Von Mises and T. Von Kármán, vol. 1, (Elsevier, 1948), pp. 171–199.

[205] A. Eden, "*On Burgers' original model of turbulence*", Nonlinearity **3**, 557 (1990).

[206] Memoirs Of The American Mathematical Society and No 4, *On Stochastic Differential Equations*, (American Mathematical Society, 1951).

[207] F. John, *Partial differential equations*, (New York : Springer-Verlag, 1982).

[208] E. Schmidt, "*Zur Theorie der linearen und nichtlinearen Integralgleichungen*", Mathematische Annalen **63**, 433 (1907).

[209] A. Ekert and P. L. Knight, "*Entangled quantum systems and the Schmidt decomposition*", American Journal of Physics **63**, 415 (1995).

[210] A. Peres, "*Higher order Schmidt decompositions*", Physics Letters A **202**, 16 (1995).

[211] E. P. Wigner, "*On the statistical distribution of the widths and spacings of nuclear resonance levels*", Mathematical Proceedings of the Cambridge Philosophical Society **47**, 790 (1951).

[212] E. P. Wigner, "*Random Matrices in Physics*", SIAM Review **9**, 1 (1967).

[213] J. W. Lindeberg, "*Eine neue Herleitung des Exponentialgesetzes in der Wahrscheinlichkeitsrechnung*", Mathematische Zeitschrift **15**, 211 (1922).

[214] M. Hartmann, G. Mahler, and O. Hess, "*Existence of Temperature on the Nanoscale*", Physical Review Letters **93**, 080402 (2004).

[215] T. Carleman, "*Sur les fonctions quasi-analytiques*", Comptes rendus du V^{e} Congrès des Mathématiciens Scandinaves, Helsingfors, 181 (1922).

[216] W. Voigt, *Über das Gesetz der Intensitätsverteilung innerhalb der Linien eines Gasspektrums*, (Sitzungsberichte München, 25, 1912).

[217] B. H. Armstrong, "*Spectrum line profiles: The Voigt function*", Journal of Quantitative Spectroscopy and Radiative Transfer **7**, 61 (1967).

[218] E. Fermi, *Nuclear Physics: A Course Given by Enrico Fermi at the University of Chicago*, (University of Chicago Press, 1974).

[219] P. A. M. Dirac, "*The quantum theory of the emission and absorption of radiation*", Proceedings of the Royal Society of London. Series A, Containing Papers of a Mathematical and Physical Character **114**, 243 (1927).

[220] F. Schwabl, *Quantum Mechanics, 4th Edition*, (Springer, 2007).

List of acronyms

The following list is a collection of all acronyms used in this work.

jPDF	Joint Probability Density Function
nDOS	Normalized Density Of States
DBM	Dyson-Brownian Motion
DOF	Degrees Of Freedom
DOS	Density Of States
ED	Exact Diagonalization
ETH	Eigenstate Thermalization Hypothesis
FWHM	Full Width At Half Maximum
GOE	Gaussian Orthogonal Ensemble
GSE	Gaussian Symplectic Ensemble
GUE	Gaussian Unitary Ensemble
HWHM	Half Width At Half Maximum
IID	Independent Identically Distributed
MBL	Many Body Localization
MRRR	Algorithm Of Multiple Relatively Robust Representations
OBC	Open Boundary Conditions
ODE	Ordinary Differential Equation
PDE	Partial Differential Equation
PDF	Probability Density Function
QFT	Quantum Field Theory
RMT	Random Matrix Theory
SDE	Stochastic Differential Equation
SEQ	Schrödinger Equation
SVD	Singular Value Decomposition
TRS	Time Reversal Symmetry

List of publications

1. **Tobias Helbig**, Tobias Hofmann, Ching Hua Lee, Ronny Thomale, Stefan Imhof, Laurens W. Molenkamp, and Tobias Kiessling, *Band structure engineering and reconstruction in electric circuit networks*, Phys. Rev. B **99**, 161114(R) (2019).

2. Tobias Hofmann, **Tobias Helbig**, Ching Hua Lee, Martin Greiter, and Ronny Thomale, *Chiral Voltage Propagation and Calibration in a Topolectrical Chern Circuit*, Phys. Rev. Lett. **122**, 247702 (2019).

3. Raul Stühler, Felix Reis, Tobias Müller, **Tobias Helbig**, Tilman Schwemmer, Ronny Thomale, Jörg Schäfer, and Ralph Claessen, *Tomonaga–Luttinger liquid in the edge channels of a quantum spin Hall insulator*, Nat. Phys. **16**, 47-51 (2020).

4. Ching Hua Lee, Amanda Sutrisno, Tobias Hofmann, **Tobias Helbig**, Yuhan Liu, Yee Sin Ang, Lay Kee Ang, Xiao Zhang, Martin Greiter, and Ronny Thomale, *Imaging nodal knots in momentum space through topolectrical circuits*, Nat. Comm. **11**, 4385 (2020).

5. **Tobias Helbig**, Tobias Hofmann, Stefan Imhof, Mohamed Abdelghany, Tobias Kiessling, Laurens W. Molenkamp, Ching Hua Lee, Alexander Szameit, Martin Greiter, and Ronny Thomale, *Generalized bulk–boundary correspondence in non-Hermitian topolectrical circuits*, Nat. Phys. **16**, 747–750 (2020).

6. Tobias Hofmann, **Tobias Helbig**, Frank Schindler, Nora Salgo, Marta Brzezińska, Martin Greiter, Tobias Kiessling, David Wolf, Achim Vollhardt, Anton Kabaši, Ching Hua Lee, Ante Bilušić, Ronny Thomale, and Titus Neupert, *Reciprocal skin effect and its realization in a topolectrical circuit*, Phys. Rev. Research **2**, 023265 (2020).

7. Sebastian Weidemann, Mark Kremer, **Tobias Helbig**, Tobias Hofmann, Alexander Stegmaier, Martin Greiter, Ronny Thomale, and Alexander Szameit, *Topological funneling of light*, Science **368**, 6488 (2020).

8. Alexander Stegmaier, Stefan Imhof, **Tobias Helbig**, Tobias Hofmann, Ching Hua Lee, Mark Kremer, Alexander Fritzsche, Thorsten Feichtner, Sebastian Klembt, Sven Höfling, Igor Boettcher, Ion Cosma Fulga, Libo Ma, Oliver G. Schmidt, Martin Greiter, Tobias Kiessling, Alexander Szameit, and Ronny Thomale, *Topological Defect Engineering and PT Symmetry in Non-Hermitian Electrical Circuits*, Phys. Rev. Lett. **126**, 215302 (2021).

9. Patrick M. Lenggenhager, Alexander Stegmaier, Lavi K. Upreti, Tobias Hofmann, **Tobias Helbig**, Achim Vollhardt, Martin Greiter, Ching Hua Lee, Stefan Imhof, Hauke Brand, Tobias Kießling, Igor Boettcher, Titus

Neupert, Ronny Thomale, and Tomáš Bzdušek, *Simulating hyperbolic space on a circuit board*, Nat. Comm. **13**, 4373 (2022).

10. Anffany Chen, Hauke Brand, **Tobias Helbig**, Tobias Hofmann, Stefan Imhof, Alexander Fritzsche, Tobias Kießling, Alexander Stegmaier, Lavi K. Upreti, Titus Neupert, Tomáš Bzdušek, Martin Greiter, Ronny Thomale, and Igor Boettcher, *Hyperbolic matter in electrical circuits with tunable complex phases*, Nat. Comm. **14**, 622 (2023)

11. Hendrik Hohmann, Tobias Hofmann, **Tobias Helbig**, Stefan Imhof, Hauke Brand, Lavi K. Upreti, Alexander Stegmaier, Alexander Fritzsche, Tobias Müller, Udo Schwingenschlögl, Ching Hua Lee, Martin Greiter, Laurens W. Molenkamp, Tobias Kießling, and Ronny Thomale, *Observation of cnoidal wave localization in non-linear topolectric circuits*, Phys. Rev. Research **5**, L012041 (2023).

Acknowledgements

This thesis would not have been possible without the constant support, help and encouragement of a lot of people, for which I am immensely grateful.

First and foremost I would like to thank my PhD advisor and mentor Prof. Dr. Martin Greiter for giving me the opportunity to do my PhD with him, for his support and for his patient guidance throughout our research projects. He conceptualized the idea of how to approach the fundamental aspects of quantum thermalization, which is the topic of this thesis and our joint work together with Tobias Hofmann and Prof. Dr. Ronny Thomale. His deep insights and ingenious ideas have kept me excited about physics and his example inspires me to pursue a career in physics. I appreciate that he has always taken the time to engage in numerous discussions with Tobi and me, from which I have learned so much. I am grateful to have the opportunity to work with him and beyond that to call him a friend.

I want to particularly thank my colleague and close friend Tobias Hofmann, with whom I constantly worked since the start of my master thesis. Over the past five years, I have always been able to count on him and talk to him about both professional and personal matters, for which I am forever grateful. We first worked together on topological electric circuits and then in the PhD together joined Martin in the study of the mechanism of quantum thermalization. His insightful thoughts and brilliant ideas as well as his unwavering commitment are a major driving force for the success of our joint projects. I very much enjoy our discussions and always gain a more profound understanding of physics after talking to him. I hope that he will also pursue a career in physics and to have the opportunity to work with him again. I wish him all the best for his future path after the PhD.

I am also very grateful to Prof. Dr. Ronny Thomale for his unwavering support and for giving me the opportunity to work at the TP1 since I started my Bachelor thesis with him. I deeply appreciate his guidance in research and beyond as well as his valuable advice and vast experience, which he is always willing to share with me. Since I met him in the 4th semester, I have enjoyed working with him within the inspiring atmosphere he is creating. More than that, I am very happy to have him as a friend. His unparalleled knowledge of physics and his quick grasp of physical concepts have always impressed me and inspire me on my future path.

Many thanks also go to my friends Wolfgang, Roman, Robin, Philipp and Kerstin, who have accompanied me on my path for many years. Thank you for all your support and for the amazing time we spend together.

I also deeply thank my whole family for their constant support and love with special heartfelt thanks to my brothers Luca and Oskar, my mother Sonja and my step father Dirk, my father Roland and my step mother Beate, and my step

sister Anna. Thank you for your patience, your unwavering support and guidance through the ups and downs of life and for always believing in me.

I further thank my wife Lina so much for her neverending support and unconditional love, which I appreciate every day and for which I am eternally grateful. It is hard to put in words how fortunate I am to have you by my side.

Many thanks also go to

- Tilman Schwemmer, who was my office mate together with Tobi. I really enjoyed the inspiring and motivational atmosphere in our office as well as our physics discussions, with a special thanks to Tilman for enduring the many discussions in the office between Tobi and me.
- Hendrik Hohmann, Janik Potten, Alexander Stegmaier, Alexander Fritzsche, Tom Oeffner and Ludwig Bordfeldt from the TP1 next to Tobias Hofmann and Prof. Dr. Martin Greiter who have taken their time to proof read parts of my thesis.
- Dr. Tobias Müller and Dr. Florian Goth for building and maintaining the IT infrastructure at the TP1. Especially Tobi always had a helping hand and I could turn to him when in need of professional and competent advice in IT questions, software, programming and physics in general.
- everyone contributing to and at the TP1 for providing such a friendly and uplifting atmosphere at the institute. I so much enjoyed our business trips together and the many occasions we shared a cake in the coffee room. Thank you for this very nice time at the institute in Würzburg. Additional to the TP1 members I already mentioned I would like to thank the current and former members Dr. Maciej Bieniek, Armando Consiglio, Matteo Dürrnagel, Lukas Elter, Dr. Mario Fink, Dr. Pratyay Ghosh, Dr. Michael Klett, Dr. David Riegler, Dr. Vera Schnells, Jannis Seufert, Yasin Silyanoglu, Riccardo Sorbello, Nora Taufertshöfer, Dr. Lavi Upreti, Anja Wenger and Dr. Xianxin Wu.
- the secretaries Nina Brust and Madalina Koch for their great help in dealing with the bureaucratic matters during my PhD and my time at the TP1.
- Tobias Hofmann, Alexander Stegmaier, Alexander Fritzsche, Hendrik Hohmann, Dr. Lavi Upreti, Prof. Dr. Martin Greiter and Prof. Dr. Ronny Thomale at the TP1 for our joint work on the theoretical aspects of topological electrical circuits including numerous discussions and efforts to conceptualize novel ideas.
- Prof. Dr. Ching Hua Lee at the National University of Singapore for sharing his deep mathematical insights and impactful ideas within the work on topolectric circuits.
- Stefan Imhof, Hauke Brand, Dr. Tobias Kießling and Prof. Dr. Laurens W. Molenkamp from the EP3 at the University of Würzburg for providing an experimental platform to investigate topological electrical circuits and for the relentless efforts to implement our theoretical ideas experimentally.
- Nora Salgo, Nelson Herbosa Labiano, Michael Denner, Dr. Marta Brzezińska, Patrick Lenggenhager, Prof. Dr. Tomáš Bzdušek, Achim Vollhardt, Dr. Frank Schindler and Prof. Dr. Titus Neupert at the University of Zürich for fruitful discussions surrounding non-Hermitian physics and topolectric circuits as well as for experimentally implementing several theoretical circuit models through the “Elektronikwerkstatt”.

- Mark Kremer, Sebastian Weidemann and Prof. Dr. Alexander Szameit at the University of Rostock for hosting the workshop in Greifswald, for fruitful discussions on non-Hermitian physics and for experimentally implementing the topological light funnel in a photonic mesh lattice with fiber loops.
- Anffany Chen and Prof. Dr. Igor Boettcher at the University of Alberta for insightful discussions on electric circuits and on hyperbolic lattices.
- Iman Ahmadabadi and Prof. Dr. Mohammad Hafezi at the University of Maryland for intriguing discussions on photonics and electric circuits.
- Philipp Grimm, Benedikt Schurr, Thorsten Feichtner and Prof. Dr. Bert Hecht from the EP5 at the University of Würzburg for valuable discussions on plasmonic systems, topology and the experimental implementation of the SSH model in gold nano-optics.
- Raul Stühler, Dr. Felix Reis, Prof. Dr. Jörg Schäfer and Prof. Dr. Ralph Claessen from the EP4 at the University of Würzburg for insightful discussions on the quantum spin Hall effect and for having the opportunity to contribute to a research project on the edge channels of a quantum spin Hall insulator.
- Jonas Erhardt, Alexander Stegmaier, Florian Nöhrig and Janik Schwind for working through many exercise sheets and lab courses with me as well as the time spent together during our studies, with and outside of physics.
- the German Academic Scholarship Foundation (Studienstiftung des deutschen Volkes) for providing the primary funding of my PhD through a PhD scholarship, as well as for intellectual discussions and for having the opportunity to take part in a “Sommerakademie”.
- the Deutsche Forschungsgemeinschaft (DFG, German Research Foundation) for further funding through Project-ID 258499086 - SFB 1170 and through the Würzburg-Dresden Cluster of Excellence on Complexity and Topology in Quantum Matter - ct.qmat Project-ID 390858490 - EXC 2147.